The effects of soil heterogeneity on the performance of horizontal ground loop heat exchangers

by

Richard Blake Simms

A thesis
presented to the University of Waterloo
in fulfillment of the
thesis requirement for the degree of
Master of Applied Science
in
Civil Engineering

Waterloo, Ontario, Canada, 2012

I hereby declare that I am the sole author of this thesis. This is a true copy of the thesis, including any required final revisions, as accepted by my examiners.

I understand that my thesis may be made electronically available to the public.

Abstract

Horizontal ground loop heat exchangers (GLHE) are widely used in many countries around the world as a heat source/sink for building conditioning systems. In Canada, these systems are most common in residential buildings that do not have access to the natural gas grid or in commercial structures where the heating and cooling loads are well balanced. These horizontal systems are often preferred over vertical systems because of the expense of drilling boreholes for the vertical systems. Current practice when sizing GLHEs is to add a considerable margin of safety. A margin of safety is required because of our poor understanding of *in situ* GLHE performance. One aspect of this uncertianty is in how these systems interact with heterogeneous soils. To investigate the impact of soil thermal property heterogeneity on GLHE performance, a specialized finite element model was created. This code avoided some of the common, non-physical assumptions made by many horizontal GLHE models by including a representation of the complete geometry of the soil continuum and pipe network. This model was evaluated against a 400 day observation period at a field site in Elora, Ontario and its estimates were found to be capable of reaching a reasonable agreement with observations. Simulations were performed on various heterogeneous conductivity fields created with GSLIB to evaluate the impact of structural heterogeneity. Through a rigorous set of experiments, heterogeneity was found to have little effect on the overall performance of horizontal ground loops over a wide range of soil types and system configurations. Other variables, such as uncertainty of the mean soil thermal conductivity, were shown to have much more impact on the uncertainty of performance than heterogeneity. The negative impact of heterogeneity was shown to be further minimized by: maintaining a 50 cm spacing between pipes in trenches; favouring multiple trenches over a single, extremely long trench; and/or using trenches greater than 1 m deep to avoid surface effects.

Acknowledgements

In the past two years I have received guidance and aid from many people, without which I would have been lost. I would especially like to thank my partner in crime, Simon Haslam, for his advice, editorial help, and COP curves; David Brodrecht, for his experience and perspective; my supervisor James Craig for his time, wisdom, and understanding; and Jasper Huang, Stephen Constable, Julian Martin, Gurbir Brar, and Evan Campbell for taking the time to edit my thesis.

I must also thank the Ontario Centres of Excellence, the Natural Sciences and Engineering Research council of Canada, and NextEnergy for their financial support.

Dedication

This is to dedicated to my mother, who finished her thesis six months before I finished mine. Love you, Mom!

Contents

List of Tables

List of Figures

List of Symbols

Symbol	Unit	Description
k	W m^{-1} K^{-1}	Thermal conductivity
q	W m^{-2}	Heat flux
c	J kg^{-1} K^{-1}	Specific heat capacity
ρ	kg m^{-3}	Density
ρc	J K^{-1} m^{-3}	Volumetric heat capacity
α	m^2 s^{-1}	Thermal diffusivity
ϕ	(-)	Porosity

Table 1: Variables used, their units and description.

Chapter 1

Introduction

Direct and indirect use of geothermal resources are currently a major source of alternative renewable energy and use has been projected to grow considerably over the next decade (Bertani, 2012; Lund et al., 2011). The largest use of geothermal energy is in the direct conditioning of buildings where ground loops are used as the heat source/sink for heat pump systems. Horizontal Ground Loop Heat Exchangers (GLHEs) are commonly used when geoexchange is implemented for smaller buildings or when there is a large amount of space available. Vertical GLHEs require the drilling of vertical boreholes, which tends to be much more expensive compared to trenching for horizontal GLHEs provided there is enough available land to lay out the system in a horizontal configuration (Florides and Kalogirou, 2007). A horizontal GLHE is typically buried in 1-2 m deep trenches that are dug in parallel. Trenches are typically 1.5 m wide, the width of the excavator bucket used to dig the trench. In these installations 4 pipes usually run parallel in each trench, although there are other configurations such as a looping slinky which are used in practice (Fujii et al., 2012; Florides and Kalogirou, 2007). According to the Canadian

GeoExchange Coalition[1], there are currently over 15,000 of these systems registered as installed for residential buildings in Canada.

GLHEs work in conjunction with heat pumps (Figure 1.1), which transfer heat from cooler areas to warmer areas through the application of mechanical energy, to provide an efficient means of conditioning the air in buildings. A heat pump's efficiency is rated as a Coefficient Of Performance (COP), for every 1 kWh of energy put into a heat pump, it will provide its COP rating in heat energy (e.g. a heat pump with a COP of 4 will produce 4 kWh of heat for every 1 kWh of energy spent running the heat pump). The COP depends upon the temperature of the fluid that the heat pump is using as a source/sink. GLHEs act as a source/sink and are used to improve the temperature of this fluid to increase the COP of the heat pump. Higher geoexchange temperatures will increase the heat pump COP when the heat pump is providing heating and lower geoexchange temperatures will increase the heat pump COP when the heat pump is providing cooling. Other measurements of heat pump efficiency used in the HVAC industry are Seasonal Energy Efficincy Ratio (SEER), Energy Efficency Ratio (EER), and Seasonal Performance Factor (SPF). These measurements are easily convertible to EER (Hendron and Engebrecht, 2010) and then to COP (EER = COP x 3.412).

GLHEs function by circulating a fluid through a network of pipes. The fluid is usually water mixed with an environmentally safe antifreeze solution. Common antifreeze additives include ethanol, methanol, sodium chloride, and propylene/ethylene glycol (Banks, 2009). The fluid temperature will moderate to the surrounding soil temperature as it travels through the pipe. The temperature of the fluid returning from the ground loop is referred to as the Entering Water Temperature (EWT). EWT controls the COP of the heat pump.

[1]CGC Market Transformation Progress Meter: http://www.geo-exchange.ca/en/

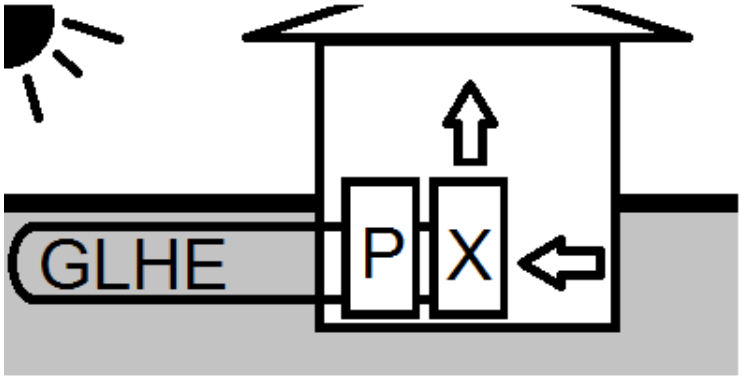

Figure 1.1: Schematic of a GLHE setup: a fluid is circulated in the GLHE where heat transfer occurs between the fluid and surrounding soil. The fluid returns to the heat pump (P). The temperature is then upgraded by the heat pump for using in conditioning the building air, here represented by an air heat exchanger (X).

The pipes are typically made of high-density polyethylene which provides a safe enclosure for the fluid as it travels through the ground loop and heat transfer occurs between the fluid and surrounding soil. The high durability of the plastic allows loop designers to provide warranties of 50 years for their systems (Florides and Kalogirou, 2007). For larger energy requirements (>1 ton heating/cooling), multiple trenches are typically installed. These trenches will be fed by a single manifold using a "reverse return" configuration to balance the fluid flow between trenches by maintaining consistent pipe length between network branches (e.g. Rawlings (1996)) by ensuring constant pressure differential between trenches.

The correct sizing of the GLHE requires an estimate of the building energy load and estimates of the subsurface soil properties. Due to the uncertianty in the estimates of both these parameters, loops are typically oversized. Oversizing is costly in two ways: greater installation expense and increased operational cost. At the time of installation, an oversized GLHE requires extra trenching and extra pipe. An oversized loop also requires greater pump power and/or throughput, which increases the cost of operating the loop.

Improving our understanding of how GLHEs work in the subsurface may provide insights for improving loop performance and design practices. The objective of this thesis is to outline the impact of heterogeneity in soil thermal properties on the performance of horizontal GLHEs. Achieving this objective through field scale experiments would have been costly and difficult to control, so a numerical modelling approach was taken. A numerical model capable of evaluating the impacts of non-homogeneous soil properties must include a representation of those non-homogeneous soil thermal properties in the soil continuum. Two of the key heat transport pathways that should be emphasized for an investigation involving heterogeneity are both heat flux between pipes within a GLHE trench and between trenches, as well as heat flux from the ground surface to the buried GLHE. Year-long simulations of GLHEs using ensembles of realizations of heterogeneous fields must be conducted to determine the statistical distribution of observed performance impacts. A model used for GLHE simulations must be capable of representing a discrete pipe network, heterogeneous thermal fields, dynamic surface boundary conditions, and be computationally efficient so that a statistically significant number of heterogeneous conductivity fields can be evaluated. Existing numerical models were evaluated but all were found lacking in one or more of the requirements therefore a new numerical code was created for this investigation.

The performance of vertical systems and borehole heat exchangers has been well investigated in the literature and there are multiple excellent numerical models and analytical solutions that are available. Despite their prevalence, horizontal systems have received less attention (Spitler, 2005). Piechowski (1999) developed a code for simulating thermal response tests in horizontal GLHEs using the two-dimensional finite difference method. This model performed quite well over short time periods, due to its radial geometry, but would not be appropriate for simulations conducted on the scale of years. More modern numerical

models, such as those done by Fujii et al. (2012) in FEFLOW, use full three-dimensional geometry but sacrifice some of the near pipe accuracy with other assumptions such as the use of a bar heat exchanger to approximate the ground loop sitting in a trench. FEFLOW, and other models like FEFLOW (such as Hydrogeosphere,MODFLOW), take advantage of existing ground water transport codes that already include heat transfer and apply them to geo-exchange systems. Unfortuntately, hydrogeology models lack tool for simulating the pipe network as a discrete model. Analytical solutions, such as the work done by Philippe et al. (2011), provide balance between model performance and accuracy but do so by making many simplifying assumptions. One of the goals of this thesis is to create a new model with different and more physically accurate assumptions than has been attempted in prior works. This model will be capable of representing the physical geometry of a horizontal GLHE pipe network, the physical geometry of the soil surrounding such a GLHE, and the surface boundary conditions that have a major impact on loop performance.

A GLHE installation in Elora, Ontario was used as a field site (Haslam, 2013). Instrumentation was installed to build a real-world data set with which to support model design and facilitate model validation. This data set included inlet and outlet temperatures of the GLHE, HVAC power usage, and temperature time series for a variety of points and cross sections in and around the soil surrounding the buried GLHE (Haslam, 2013). This data set is unique because of the long monitoring period, the high spatial discretization, and the full scale nature of the GLHE. A more complete description of this dataset can be found in Haslam (2013). These data were used in the parametrization, calibration, and testing of the numerical model developed for the heterogeneity investigation.

Chapter 2 details the creation of a new model for horizontal GLHEs. In Chapter 3, the model is used to estimate the parameters of the soil around the GLHE in Elora,

Ontario using over 400 days of temperature observations around the loop. Estimation of this nature is very different than the Thermal Response Tests (TRT) that are typically performed to evaluate soil properties as temperature data outside of the ground loop is available over a long period of time. The investigation of the impact of heterogeneity on GLHE performance is in Chapter 4.

Chapter 2

Numerical model development

2.1 Introduction

For the purpose of investigating the impact of heterogeneous thermal properties on the performance of GLHEs a new numerical code was developed. Existing numerical models tend to focus on vertical simulations ((Al-Khoury et al., 2005; Al-Khoury and Bonnier, 2006; Al-Khoury et al., 2010; Diersch et al., 2011a,b)). More general subsurface process modelling packages such as the comprehensive HydroGeoSphere (Therrien et al., 2005), capable of simulating multiple processes and their interactions, cannot handle the physics involved with fluid flow through continuous pipes within the soil. HydroGeoSphere and FEFLOW are computationally expensive, coupled with other transport phenomena that were superfluous to this study, and use very specialized meshes which need to be carefully adjusted depending upon the layout of the GLHE being simulated. In this study, a model was required which could allow for a conductivity field with a fine enough discretization to accommodate the scale of heterogeneity expected. This required discretization, particularly

in handling important near-pipe effects,would be prohibitive using existing models when performing simulations on a timescale of years.

Existing modelling codes specifically designed for horizontal GLHE simulation tend to use simplified geometry, too simple to include a heterogeneous conductivity field. For example, the general purpose modelling environment TRNSYS (TRNSYS, 2010) includes a GLHE component as part of its included packages. The included GLHE model uses fully explicit time stepping which necessitates the use of time steps on the order of seconds to predict in-pipe fluid temperatures, which would be prohibitive for multi-year simulations. As well, the model uses a radial coordinate system and is limited to representing GLHEs as straight, cylindrical pipes in straight, cylindrical bodies of soil. Correction coefficients can be used to transform the planar surface boundary condition to a radial equivalent but the model is still incapable of including spatially varying thermal properties in soil surrounding the pipe or inter-pipe effects. Esen et al. (2007) developed a numerical explicit finite difference model specific to horizontal GLHEs but this model is of limited utility for this investigation because it assumes homogeneity of soil thermal properties, symmetric heat transfer in the soil, and no pipe-to-pipe thermal interactions. To solve GLHE problems more expediently, analytical and semi-analytical models using mixed coordinate systems and transforms have been developed for horizontal homogeneous systems (Ingersoll and Plass, 1948; Claesson and Dunand, 1983; Philippe et al., 2011). Philippe et al. (2011) provides a useful literature review of horizontal analytical models. These models are extremely fast and accurate but, again, are limited by the assumption of homogeneity. Development of faster and more accurate models for horizontal GLHEs has been highlighted for further research and development (Spitler, 2005).

There have been other models developed that do not have these limitations. A recent

paper on slinky modelling, by Fujii et al. (2012), investigating the performance of horizontal slinky loops used a more complex geometry for the soil continuum where the GLHE trench was simulated as being 2 m below the ground surface in a semi-infinite soil. The drawback of their approach was that the pipe network was approximated as a bar heat exchanger and as such, simulating pipe-to-pipe thermal interactions would not be physically based. The use of triangular elements makes the mapping of heterogeneous fields a challenging problem and the specialized nature of the grid means that the continuum would have to be remeshed when changing pipe configurations. Their approach was limited by the bar heat exchanger assumption employed. By not simulating separate pipes it would be impossible to simulate pipe-to-pipe interactions and a unidirectional flow direction cannot be assumed off-hand for a non-slinky pipe configuration.

To investigate the impact of heterogeneity on GLHE performance, it is desirable to use a model that uses a regular mesh, simplifying the process of generating heterogeneous fields; can respect the geometry of the problem with a full, discrete pipe network buried below the ground surface; is capable of representing the ground surface boundary condition correctly; is capable of simulating, and sensitive to, the arrangements of the pipes in a GLHE trench; and fast enough that it would be tractable to simulate a sufficient number of GLHEs in heterogeneous fields to determine the statistical importance of heterogeneity.

Al-Khoury et al. (2005) observed that the scales involved with modelling vertical geothermal heating systems are extremely disproportionate, where the pipe is hundreds of meters long with a diameter of only a few centimetres. These extreme aspect ratios also appear in horizontal systems. This makes the task of modelling GLHEs challenging as it is difficult to take an off-the-shelf FEM tool and apply it to the problem.

A key component of this thesis was the development of HEN, short for Heat Exchanger

Network, which is an aggregated model which couples a 3D finite element model for solving the heat conduction equation in a soil continuum to a 1D branching pipe heat exchanger network model.

The two models are carefully coupled so as to maximize efficiency. The linear system of equations are solved through the use of the BiCGSTAB algorithm (van der Vorst, 1992) using an iLU preconditioner (Saad, 2000). This approach guarantees convergence and the preconditioner provides constant convergence rates as the sparse matrix grows in size. These numerical solvers function extremely well for the matrix structures which are created by HEN and converge quickly.

The in-pipe network simulation code is unique to this model. Typically, trenches (or wells) are treated as discrete systems where in-pipe flow rates must be continuous. HEN includes the ability to model the header trench and the manifolds, conserving mass and energy at pipe junctions. This allows HEN to simulate realistic, complex GLHE layouts where a manifold has multiple pipe trenches attached to it. To do this the network code allows the branching and merging of pipe sections. This can cause stability problems for a numerical solver, but the properties of the algorithms developed here ensure numerical convergence to a solution.

2.2 Physics of soil heat transfer

The model created to simulate heat flow in and around the GLHE is physically based. Heat transfer is one of the fundamental processes involved with the first law of thermodynamics.

The first law for a closed system,

$$\delta Q - \delta W = dE \tag{2.1}$$

demonstrates the relationship between variation of heat transfer (δQ) [J] into or from the system, work (δW) [J] done by or on the system, and the change internal of energy (dE) [J] of the system. Heat transfer and work are path dependent quantities. The energy conservation is given by:

$$\frac{dE}{dt} = q - w \tag{2.2}$$

where E [J] is the energy in a closed system, q [W] is the net rate of heat transfer to the system, and w [W] is the net rate of work transfer from the closed system. The standard engineering thermodynamics sign convention is used here, where q is positive when heat enters through the system boundaries. Heat transfer can be defined as the energy interaction driven by the temperature difference, the actual mechanism of heat transfer can be conduction, convection, and/or radiation between a system and its environment. As a system is subjected to a moving force field, work is the integral of the force field as the system travels along a path. The rate of work is positive when the system does work on its environment. There are several different types of work: magnetic, electrical, or mechanical.

The second law of thermodynamics states that heat can only flow spontaneously from hot to cold (high temperature to low temperature). An input of energy is needed for heat to be transferred from a cold region to a hot one (e.g. as is done by a refrigerator).

Soil heat transfer concepts are developed in the following sections. First, heat transport mechanics in solids and fluid are discussed. These concepts are then combined in terms

of interconnected particles surrounded by a fluid. These concepts are finally extended to discuss heat transfer in the soils that make up the material around horizontal GLHEs.

2.2.1 Fourier's Law

Thermal conduction occurs when a temperature gradient exists between any two points in a medium. Thermal energy is transferred through the collisions of molecules and the spreading vibration of atoms. The one dimensional expression for the heat flux due to conduction in the x direction (q_x) [W m^{-2}] through an object of cross sectional area A is given by Fourier's law of heat conduction:

$$q_x = -kA\frac{dT}{dx} \tag{2.3}$$

where dT/dx is the temperature slope. This expression also serves as the definition of thermal conductivity, k [W m^{-1} K^{-1}], which is a function of the material and its internal structure. Equation 2.3 is analogous to the Darcy law of fluid flow through a porous medium. In three dimensions, Fourier's Law becomes:

$$q_x = -kA\frac{\partial T}{\partial x},\ q_y = -kA\frac{\partial T}{\partial y},\ q_z = -kA\frac{\partial T}{\partial z} \tag{2.4}$$

using vector notation this can be further generalized to

$$\vec{q} = \mathbf{k}\vec{\nabla}T \tag{2.5}$$

where $\vec{q}$ is the heat flux, $\mathbf{k}$ is the conductivity tensor, and $\vec{\nabla}T$ is the temperature gradient.

2.2.2 Thermal conductivity

Thermal Conductivity of Solids

The thermal conductivity is governed by the elastic moduli of the material in which the heat transfer is occurring. Soils are predominately isotropic even though they are composed of individual grains that are individually anisotropic because the grains are not uniformly oriented within the soil (Penner, 1963). In this study, only isotropic heat conduction will be considered.

Thermal Conductivity of Fluids

In investigation of heat transfer in porous media and soils, it is important to understand the influence of the gas and liquid phases. The presence of a highly conductive pore fluid (e.g. water) will raise the conductivity of the combined material (solid and liquid) substantially. A poorly conducting fluid (e.g. air) will lower it. The magnitude of the conductivity change is dependent upon the porosity of the solid containing the pore fluid. The thermal properties of a soil will be dependent upon the level of saturation of that soil. In a fully saturated soil all the pores will be filled with water; in an unsaturated soil they will all be filled with air. It is important to understand the thermal conductivity of gases and liquids, specifically those that fill the pores of soil surrounding the in-ground heat loop.

Different liquids and gases will have different thermal conductivities, and gases (but not liquids) at high pressures will be more conductive than the same gases at lower pressures. The thermal conductivity of fluids tends to increase with the temperature of the fluid; this rate of increase is much faster in gases than it is in solids or liquids. Water with high salinity will have a higher thermal conductivity than pure water. Seawater has a thermal

conductivity of 0.60 $\frac{\mathrm{W}}{\mathrm{m \cdot K}}$ which is slightly greater than the thermal conductivity of pure water (0.57 $\frac{\mathrm{W}}{\mathrm{m \cdot K}}$) (Sharqawy et al., 2010)).

The impact of groundwater flow is dealt with in §2.2.4.

Thermal Conductivity of Soils

The thermal conductivity of saturated and unsaturated porous materials depends on the composition, geometric micro-structure, and the degree of surface contact between the solids and pore fluids (Kovalenko and Flanders, 1991). Heat transfer in porous media and rock is mainly conductive with radiative and convective heat transfer typically being negligible in comparison (Kovalenko and Flanders, 1991). The components of the soil having thermal properties that are temperature dependent make the aggregated thermal properties of the soil temperature dependent (Sugawara and Yoshizawa, 1961). Typical values for soil thermal properties and soil components are presented in Table 2.1. For a more complete list of properties see Appendix J.

Table 2.1: Value ranges for typical soils and soil constituent materials (for a more complete collection of values refer to Appendix J).

Material	Thermal Conductivity $\frac{\mathrm{W}}{\mathrm{m \cdot K}}$	Heat Capacity $\frac{\mathrm{J}}{\mathrm{m^3 \cdot K}} \times 10^{-6}$	Thermal Diffusivity $\frac{\mathrm{m^2}}{\mathrm{s}} \times 10^{-6}$
Saturated soil[1]	0.50 - 2.20	2.96 - 4.02	0.12 - 0.74
Unsaturated soil [1]	0.06 - 0.30	0.58 - 1.28	0.10 - 0.24
Quartz [2]	8.40	1.92	4.38
Water [2]	0.57	4.18	0.14
Air (still to turbulent) [3]	0.025 - 125	0.0012	20.5 - 10^7

[1](Labs, 1979b)
[2](Farouki, 1986)
[3](Oke, 1987; Farouki, 1986)

2.2.3 Specific heat capacity and thermal diffusivity

The specific heat of a substance is the amount of heat required to raise the temperature of one kilogram of that substance by one degree Kelvin. Specific heat at constant pressure, c_p [J kg^{-1} K^{-1}], and the specific heat at constant volume, c_v [J kg^{-1} K^{-1}], of a pure substance can be different. For an incompressible substance, the specific heat at constant pressure is equal to the specific heat at constant volume and is referred to as simply the specific heat, c ($c_p = c_v = c$). Thermal inertia refers to the amount of energy required for a finite sample to increase in temperature by 1 degree. The thermal inertia per unit of sample volume, or the specific heat capacity of a medium, is represented by ρc where ρ [kg m^{-3}] is density. If the heat transfer to a finite sample is constant, then the temperature will rise faster when the specific heat capacity, ρc, is smaller.

Temperature changes can prompt a phase change, for example heating ice will cause the ice to melt. The energy associated with these changing states is referred to as the specific heat of phase change. There are different specific heats depending upon which phase change is occurring. The melting of ice requires a different quantity of energy than the evaporation of water. These phase changes are reversible and can act as a temperature buffer.

Thermal diffusivity, α [m^2 s^{-1}], is another relevant heat transfer parameter; it is determined by the ratio of thermal conductivity to heat capacity:

$$\alpha = \frac{k}{\rho c} \tag{2.6}$$

Substances with high thermal diffusivity will rapidly equilibrate with their surrounding system. Diffusivity can also be thought of as the speed at which a temperature change at

a boundary will propagate through a medium. See Table 2.1 for example values of heat capacity and thermal diffusivity.

2.2.4 Groundwater flow and convection

Chiasson et al. (2000) demonstrated that high rates of ground water flow can play a significant role in the dissipation of heat around geothermal pipes over long time scales by using AQUA3D to examine the effects of groundwater flow on the performance of GLHEs. The flow of groundwater constantly refreshes the medium adjacent to the pipes; an order of magnitude increase in the rate of groundwater flow will translate to almost an order of magnitude increase in apparent thermal conductivity. In horizontal systems, the impact of a regional flow gradient would likely play a different role, due to the different orientation of the system and the typically smaller water fluxes in the unsaturated zone. Vertical pressure gradients would likely be much more important than horizontal gradients.

While the problem of ground water flow and horizontal GLHEs is an interesting one, it is not the focus of this investigation. A pipe system buried in an environment subject to a regional flow would be more capable at absorbing (or producing) thermal energy than an equivalent system buried in an environment that was not subject to regional flow. Thus, in an investigation of spatial heterogeneity, the assumption that groundwater flow does not play a major role in heat dissipation around a horizontal GLHE is a conservative one.

Fluids have an added mechanism of heat transfer, gravity driven convection. Gravity driven convection is the tendency of hotter fluids to rise and colder fluids to fall causing movement due to density changes of the fluid which is controlled by temperature. A temperature gradient across a fluid will induce a density gradient which induces a current

in the fluid, this current will advect the fluid so that the warmer regions will mix with the colder regions. Density gradients can be caused by other mechanisms such as the addition of ions. Convection is ignored in this thesis as the density gradients would be too small to induce convection through the porous media.

The effect of free heat convection on GLHE performance would be very similar to the effect of groundwater flow and would increase heat transfer away from the pipe.

2.2.5 Phase change

A major source/sink of energy in a GLHE can be the water within the soil matrix changing phase. The latent heat released by freezing is equivalent that needed to heat the same mass of liquid water from 0°C to 80°C, a potentially significant source of energy.

In the soil around a real GLHE, the thermal properties will change with temperature. Generally, as substances warm they become less conductive. The magnitude of this effect is relatively minor ($\sim$1% for the materials and temperatures expected in a GLHE) and neglecting it should have minimal impact. However, the change of thermal properties is quite large when you consider water in liquid form versus its ice form. The ice form of water has four times the thermal conductivity of the liquid form.

The freezing of pore water around a GLHE has a positive effect on loop performance. Latent heat is released which can be recovered by the geoexchange fluid and the cylinder of ice around the piping increases the effective radius of the pipe, further boosting performance. Unfortunately, for this to occur the loop must be operating at a very cold temperature (< 0 °C). At these temperatures, the operation of the loop pump becomes more expensive and there is increased risk of damaging the HVAC equipment.

2.2.6 Geothermal gradient

The model of the soil continuum does not include a geothermal flux on its deepest boundary. As can be seen in Figure 2.1, the heat flow from deep subterranean sources in the area of the field site is well under 40 $\frac{\text{mW}}{\text{m}^2}$. This flux is dwarfed by the total incoming solar radiation of over 1300 $\frac{\text{mW}}{\text{m}^2}$ during a solar minimum (Kopp and Lean, 2011). The heat coming in from the top boundary is greater by a factor of over 10^4. Any influence of the geothermal gradient on the temperature of the soil around the horizontal ground loop should be completely overshadowed by the influence of the surface fluxes.

It can be shown that the effect of the geothermal flux on the bottom boundary of a GLHE is nearly negligible. Examining a hypothetical simple system of an 4 m deep block of soil exposed only to a geothermal flux, it can be shown that the impact of 40 $\frac{\text{mW}}{\text{m}^2}$ is negligible on to a horizontal GLHE. Over the course of 1 year, the energy per square meter is 1.26 MJ which is enough to raise the temperature of a 4 m deep block of soil by ~ 0.25 °C. The effect is minimal enough that it was not considered as a factor in this investigation of soil heterogeneity.

2.3 Continuum model

Creating, parametrizing, and calibrating a model incorporating all soil heat transfer mechanisms is unnecessary for an investigation into the impacts of soil heterogeneity at the scale of a horizontal GLHE. Here, we will consider heat transfer due to conduction in a a heterogeneous soil with isotropic thermal conductivity. The temperature perturbations caused by phase changes will be neglected as will the effects of convection and groundwater flow.

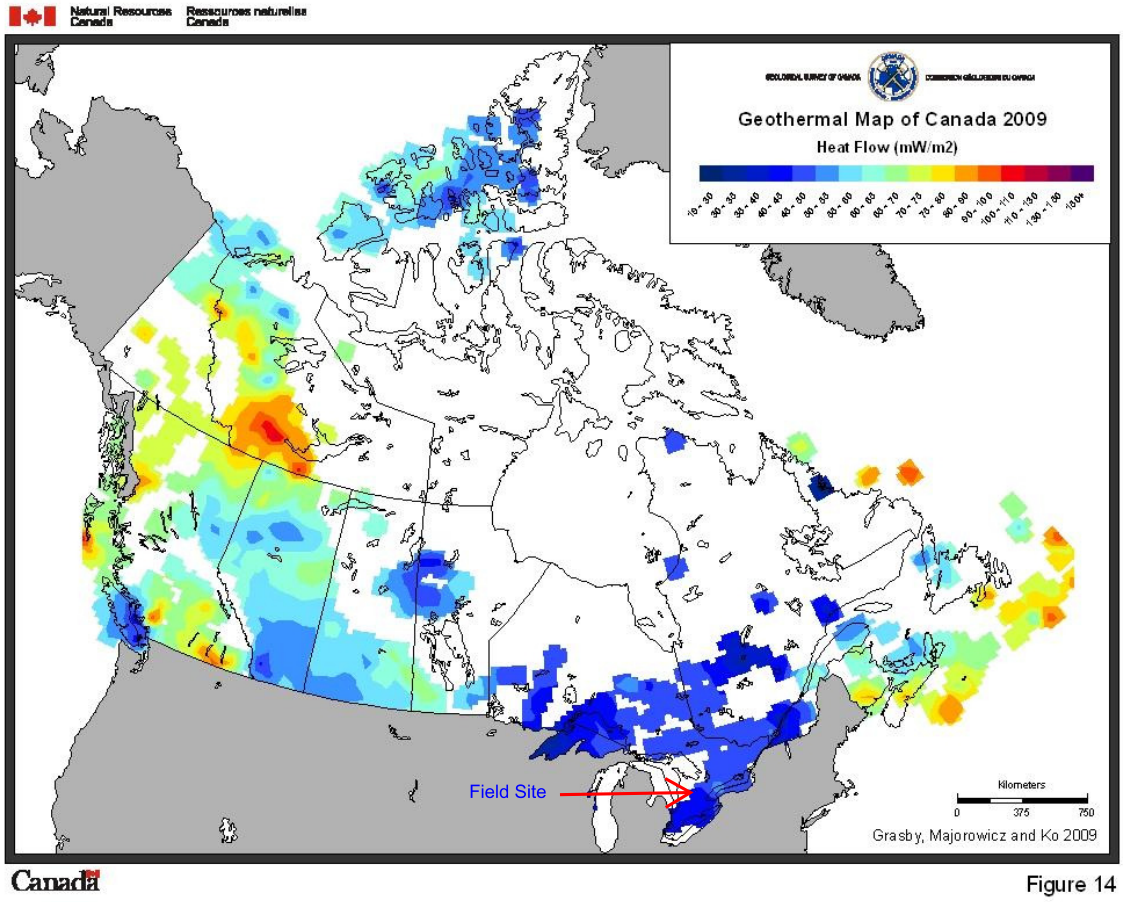

Figure 2.1: Map of geothermal heat flow to surface in Canada (Grasby et al., 2009)

The continuum model in HEN handles the simulation of 3D transient heat transfer in the soil around the GLHE pipes. Heat transfer is driven by temperature gradients, as per Fourier's Law, which can be included in an energy balance leading the following heat equation:

$$\rho c \frac{\partial T}{\partial t} = \vec{\nabla} \cdot (\boldsymbol{k} \cdot \vec{\nabla} T) + \vec{q} \tag{2.7}$$

where $\vec{q}$ [W m^{-3}] is the local volumetric heat flux from the GLHE, $\boldsymbol{k}$ [W m^{-1} K^{-1}] is the thermal conductivity tensor of the media (in this document the tensor $\boldsymbol{k}$ is typically referred to as $k \cdot \boldsymbol{I}$, where $\boldsymbol{I}$ is the unit matrix, corresponding to isotropic conductivity), ρc [J K^{-1} m^{-3}] is the volumetric heat capacity, and ∇T [K m^{-1}] is the temperature gradient.

The derivation of the 3D finite element model follows from Istok's (1989) derivation of a solution for transient saturated groundwater flow (full derivation is provided in Appendix B), which obeys an analogous governing equation. The governing partial differential Equation 2.7 was discretized spatially by the Galerkin finite element method using brick elements with trilinear weighting functions. The conductivity and capacity matrices were created by using Gauss Legendre quadrature on isoparametric elements transformed using the Jacobian. The resulting equation for the residual from each element is

$$\begin{aligned}
R_i^{(e)} &= -\iiint_{V^{(e)}} N_i^{(e)} \left[\frac{\partial}{\partial x}\left(K\frac{\partial \hat{T}^{(e)}}{\partial x}\right) + \frac{\partial}{\partial y}\left(K\frac{\partial \hat{T}^{(e)}}{\partial y}\right) + \frac{\partial}{\partial z}\left(K\frac{\partial \hat{T}^{(e)}}{\partial z}\right) + \vec{q}^{(e)} - \rho c \frac{\partial \hat{T}^{(e)}}{\partial t} \right] dx\, dy\, dz \\
&= -\iiint_{V^{(e)}} N_i^{(e)} \left[\frac{\partial}{\partial x}\left(K\frac{\partial \hat{T}^{(e)}}{\partial x}\right) + \frac{\partial}{\partial y}\left(K\frac{\partial \hat{T}^{(e)}}{\partial y}\right) + \frac{\partial}{\partial z}\left(K\frac{\partial \hat{T}^{(e)}}{\partial z}\right) \right] dx\, dy\, dz \\
&\quad - \iiint_{V^{(e)}} N_i^{(e)} \vec{q}^{(e)} dx\, dy\, dz \\
&\quad + \iiint_{V^{(e)}} N_i^{(e)} \rho c \frac{\partial \hat{T}^{(e)}}{\partial t} dx\, dy\, dz
\end{aligned}$$

which, when the residuals are set to zero, can approximated and written as a simple sparse linear system:

$$0 = \mathbf{K}\vec{T} - \mathbf{C}\frac{\vec{T}}{dt} + \vec{q} \tag{2.8}$$

The time derivative is solved with the Crank-Nicholson (Crank and Nicolson, 1947) method:

$$\mathbf{C}\frac{\vec{T}^{t+1} - \vec{T}^{t}}{\Delta t} = \mathbf{K}\frac{\vec{T}^{t+1}}{2} + \mathbf{K}\frac{\vec{T}^{t}}{2} + \frac{\vec{q}^{t+1}}{2} + \frac{\vec{q}^{t}}{2} \tag{2.9}$$

Note that the flux weighting scheme used in the pipe-to-soil continuum interaction did not use isoparameteric elements so element shapes were limited to rectangular prisms. The temporal term of the equation was approximated through the use of the Crank-Nicholson method; the selection of this semi-implicit method guarantees the numerical stability of the temporal derivative. The lumped element formulation was used for generating the global capacity matrix used for the time stepping. All methods were implemented in C++, based on the original FORTRAN algorithms of Istok (1989).

Boundary conditions applied to the surface of the soil continuum at the time of matrix generation act as a known surface temperature (Figure 2.2). This ensures minimal matrix size, by reducing degrees of freedom; and does so in an efficient manner, by avoiding regeneration of the conductivity matrix. This method of prescribing surface boundary conditions is in contrast to other models such as those which build upon the work of Nam et al. (2008), who presented a surface energy balance formulation which acts as a Neumann flux boundary condition. The surface flux term used in their study was comprised of total solar radiation, downward atmospheric radiation, upward long wave radiation, sensible heat flux, and latent heat flux. To calculate each of these components, atmospheric and surface variables must be taken into account: sky radiation, solar radiation, albedo, water

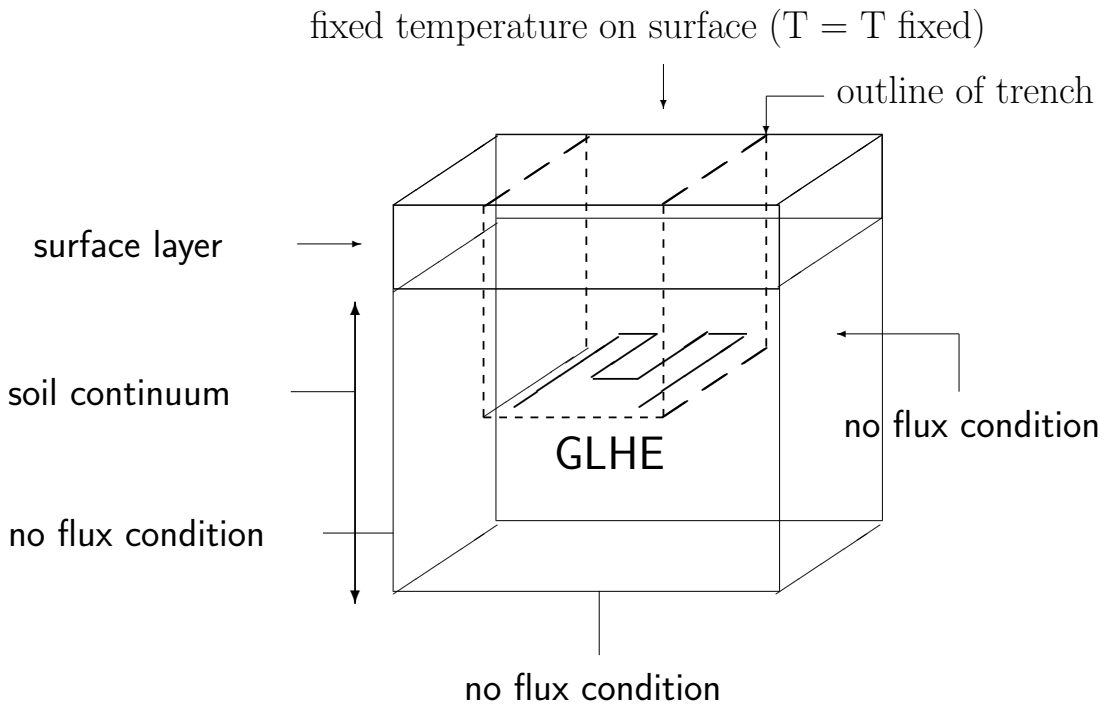

Figure 2.2: Soil continuum domain diagram (not to scale) illustrating boundary conditions on the sides, surface, and bottom. An example trench and rabbit GLHE is included for reference.

vapour pressure,degree of cloudiness, air temperature, ground surface temperature, wind velocity at surface, surface roughness, and ground surface moisture. Unfortunately, at the Elora field site (Haslam, 2013) which this investigation is based around only a small subset of these variables were measured. The near-surface soil temperature sensor was selected as the next best approximation of conditions at the field site. It should also be noted that for the model of Nam et al. (2008) to be applied to the field site it would have to have been modified to account for the effects of snow cover in winter. A covering of snow would change the behaviour of surface energy fluxes (Taniguchi, 1985).

The side and bottom planes of the model domain are parametrized as Neumann zero flux boundaries (Figure 2.2). The assignment of zero flux boundaries to the sides of the

model domain are a reflection of what is expected in typical GLHE installations. Horizontal GLHEs are placed in trenches side by side coming off of a common manifold (e.g. Figures 4.25 and 4.26 showing three trenches coming off a single manifold). Assuming that each trench draws a similar amount of energy from the ground, the flux that crosses the plane dividing each trench from its neighbouring trenches will be zero. When only a single trench is being simulated (e.g. Figures 3.6 and 3.7 of a single rabbit trench), the assignment of zero flux boundary conditions on the sides of the domain parallel to the trench us a conservative assumption because the model will treat those sides as if there is an equivalent trench placed an equivalent distance on the other side of the domain boundary. Depending upon the relative importance or horizontal heat flow this assumption can be relaxed by increasing the domain size on either side of the trench so the edges of the domain are far enough away that the influence of the GLHE is not felt and all heat flow is vertical (like in Figures 4.25 and 4.26).

The assignment of a zero flux boundary to the bottom of the domain has been discussed in §2.2.6.

The resulting model simulates heat transfer in all directions and incorporates the relevant boundary conditions and source terms required to represent a GLHE. Features of the model include the ability to use:

- non-uniform initial temperature distributions;
- prescribed ground surface temperatures (if the temporal density of the surface boundary temperatures does not match the temporal discretization of the model then the temperatures are projected linearly to estimate the boundary values in between time scales);

- non-uniform element sizes; elements are rectangular prisms (a uniform grid can be generated automatically) which allow a straightforward mapping of heterogeneous fields to elements and allow the modeller to use coarse elements in areas where less detail is required to speed up computation;

- element by element soil properties (compatible with GSLIB (Deutsch and Journel, 1992) output and scalable to non-uniform grids through the use of the harmonic mean (Johansen, 1975));

- support for both lumped and consistent formulations of the the FEM method for calculating the capacity matrix, the use of the default lumped method is preferred due to its superior spatial convergence properties;

- three dimensional graphical animations of thermal fields (through the use of the open source Visualization ToolKit (Schroeder et al., 2003)); and

- monitoring temperatures at discrete spatial points over the timeperiod of a model run.

The model includes many advanced features while still maintaining a short run time. However, there are a number of limitations to the code. Specifically: groundwater flow, convection (due to its probably negligible impact on performance and challenges associated with creating a numerical code to handle it), phase change (minor impact when not considering temperatures near 0°C), and the effects of the geothermal gradient have been omitted from the model.

By default, the continuum model does not account for the volume of the continuum that is displaced by the GLHE pipes. In the interest of physical consistency, the user has

the option of integrating out the sub volume that the pipe occupies. A discussion of this problem and the derivation of the solution implemented in the code is in Appendix A. This is required to ensure that model converges with increasing grid resolution. Because of the extreme ratio of the pipe radius relative to the soil continuum dimensions the inclusion/exclusion of this volume has negligible impact on the performance of a typical model run. Removing the volume may, however improve the numerical stability of the model.

The soil continuum model performance was compared to the Theis solution (Theis, 1935) on a simple domain. Agreement between the model and the analytical solution were found to be acceptable (Appendix E).

2.4 Pipe model

The heat flux, $\vec{q}$, to the continuum from the pipe is determined by a 1D FEM pipe model coupled with the continuum system. The pipe model simulates the advection-dispersion of heat in a pipe, also using linear shape functions. The equation governing heat transfer in the system is:

$$\frac{\partial T_p}{\partial t} = -v\frac{\partial T_p}{\partial \overline{x}} + (D_L + \alpha_f)\frac{\partial^2 T_p}{\partial \overline{x}^2} - \frac{K_p}{\rho \cdot c_p \cdot L}(T_p - T) \tag{2.10}$$

where $T_p(\overline{x}, t)$ [K] is the temperature of the fluid in the pipe, $v(t)$ [m s^{-1}] is the velocity of the fluid within the pipe, $D_L(v)$ [m^2 s^{-1}] is the longitudinal dispersivity caused by mechanical mixing in the pipe flow (Sittel et al., 1968), α_f [m^2 s^{-1}] is the thermal diffusivity of the fluid in the pipe (which has a very similar effect to temperatures within the pipe as the mechanical mixing), ρ [kg m^3] and c_p [J kg^{-1} K^{-1}] are the density and specific heat

capacity of the heat exchanger fluid and L [m] is the effective thickness of the pipe wall. The other two parameters, K_p [W m^{-1} K^{-1}] and T [K], describe the interaction of the pipe with the soil continuum; K_p is a representative thermal conductivity of the pipe wall, and $T(\overline{x}, t)$ is the temperature of the soil continuum immediately adjacent to the outside of the pipe wall obtained from the solution of equation 2.7 at distance $\overline{x}$ down the pipe. The combination of the L, K_p, c_p and ρ, terms gives the steady state thermal resistance between the fluid in the pipe and the soil on the outside of the pipe.

The temperatures within the pipe are assumed to be at a pseudo steady state. That is, the temperature profile in the pipe is assumed to reach steady state within each timestep taken by the continuum model, and for every timestep taken by the continuum model the steady state profile in the pipe model will be recalculated. With this assumption, Equation 2.10 becomes:

$$0 = -v\frac{\partial T_p}{\partial \overline{x}} + (D_L + \alpha_f)\frac{\partial^2 T_p}{\partial \overline{x}^2} - \frac{K_p}{\rho \cdot c_p \cdot L}(T_p - T) \tag{2.11}$$

A derivation for the finite element pipe model can be found in Appendix C.

The dominant mechanism for heat transfer along the pipe is advection. High velocity values relative to longitudinal dispersion, i.e. a high Peclet number, make the fully transient numerical problem difficult and unstable without inhibitively small timesteps. This is one of the reasons that a successive steady state approximation is used. In a successive steady state formulation, the steady state in-pipe system is updated every timestep with the new boundary conditions imposed by T, the temperature of the soil continuum adjacent to the pipe. This assumption relies upon the fact that the pipe residence time is on the order of minutes, much less than the timescale of temperature changes within the soil continuum. The impact of this assumption is discussed in Haslam (2013).

The pipe model will output the rate at which energy is being extracted from the ground, the total energy extracted from the ground, and the temperature of the fluid for each time step in the simulation. The pipe model is steady state for each timestep being considered. Because the fluid residence time, t_R, is much shorter than the continuum model timesteps ($t_R = 6$ min in the field, the continuum model timestep is parametrized by the user but is typically around 30 minutes), it is assumed that within each timestep the temperature of the fluid will be equivalent to a steady state. In 1D advective-dispersive systems, without source effects, steady state is reached in less than $2 \times t_R$. Typically the model temporal discretization is coarse enough that multiple circulations of the exchanger fluid occur within each time step of the continuum model. The outlet condition is a passive boundary using a virtual node to specify advection-only out of the domain.

The longitudinal dispersion due to in-pipe mechanical mixing is calculated according to Sittel et al. (1968), this term is then added to the thermal diffusivity of the fluid in the pipe to determine the final, aggregate, parameter $(D_L(v) + \alpha_f)$.

The inlet boundary condition can either be a fixed temperature or defined as a temperature difference between the inlet and outlet temperature (referred to here as the "delta" condition). The second option allows only the energy load to be specified, this option is more consistent with heat pump operation which is tasked with providing a set amount of energy to a HVAC unit. To understand how this is calculated, consider a GLHE that has a flow rate of 0.001 $\frac{\mathrm{m}^3}{\mathrm{s}}$ with a fluid that has a volumetric capacity of 4 $\frac{\mathrm{MJ}}{\mathrm{m}^3\mathrm{K}}$. To extract energy from the ground at the rate of 4 kW of energy from this GLHE then the calculation of the temperature delta across the heat pump is:

$$
\begin{aligned}
\Delta T =& F(\text{energy load}, \text{fluid heat capacity}, \text{flow rate}) \\
=& \frac{\text{energy load}}{\text{flow rate} \times \text{fluid heat capacity}} \\
=& \frac{4 \text{ kW}}{0.001 \frac{\text{m}^3}{\text{s}} \times 4 \frac{\text{MJ}}{\text{m}^3\text{K}}} \\
=& \frac{4 \text{ kW}}{4 \frac{\text{kW}}{\text{K}}} \\
=& 4 \text{ K}
\end{aligned}
$$

or more colloquially, the temperature delta is the temperature that the volume of fluid corresponding to 1 second of flow would change in 1 second when a energy load of the required amount is applied to that volume. If the energy load is specifying that energy must being removed from the soil then the fluid entering the GLHE must necessarily be lower than the fluid returning from the ground loop and vice versa.

The time steps of the boundary condition do not have to match the temporal discretization of the model. Temperatures are projected linearly to estimate the boundary values in between time scales, just as the surface boundaries are.

The coupling of the pipe model with the soil continuum is bidirectional. The soil continuum temperatures are used to determine the temperature adjacent to the pipe, T. The energy fluxes from the pipe, calculated by the pipe model, are used as a distributed source term in the continuum model, $\vec{q}$. The generation of this flux distribution is done on an element by element basis using a path integral of the element interpolation functions. A detailed derivation can be found in Appendix D. The type of coupling implemented in HEN is referred to as iterative coupling and, in the case of HEN, follows the algorithm:

1. Assign initial temperatures to the soil continuum (uniform or non-uniform)
2. Use the soil temperatures surrounding the pipe network to generate the Dirichlet boundary condition for the pipe model
3. Solve the steady state pipe model for the fluid temperatures inside the pipe
4. Calculate the energy fluxes between the pipe and the surrounding soil
5. Map the energy fluxes leaving the pipes to degrees of freedom in the soil continuum, these fluxes act as a source term to the continuum model
6. Advance one timestep in the continuum model, updating the soil temperatures
7. Go to Step 2

2.5 Numerical implementation

The system of equations resulting from the finite element approximation of the continuum equations was solved using the stabilized bicongugate gradient (BiCG-STAB) method with incomplete LU preconditioning (Saad, 2000; van der Vorst, 1992). The Thomas algorithm was used for solving the tridiagonal matrices for the pipe model if the model was for a single pipe system, multi-pipe systems were solved using the same techniques as the continuum solver.

Both the in-pipe and continuum models require the generation and solution of very large matrices. The matrices are sparse, systematically populated, with a banded structure (although they are non-symmetric). The only exception of this is the in-pipe model when the delta boundary condition is used, which causes fill-in in the extreme corners of the matrix. The extremely poor conditioning of this particular matrix requires to use of the BiCG-STAB solver which is capable of converging regardless of condition number.

The matrix storage and generation was handled by code originally produced by Dr. James Craig, modified by the author to be compatible with the dense matrix library Armadillo (Sanderson, 2010). The library, written in C++, uses dynamic compressed row storage and has a matrix-vector multiplication algorithm that is capable of scaling linearly with the number of non-zero elements in a matrix.

To test the convergence properties of HEN, a model of a generic GLHE was created. The model runs were parametrized so that the element width (across the loop) and heights were the same, the element length (in the direction of the loop) was 10 times the size of the element width. The model domain was 5 m wide by 60 m long by 7 m deep (with grid elements 0.1 m wide by 1 m long by 0.1 m deep for the nodal placement test). The surface boundary condition was applied at the thickness of 1 element width, temperatures for the surface condition were taken from the Elora field site (Haslam, 2013). A 30 minute timestep was used to cover a timeperiod of 400 days. The soil thermal conductivity was 2.0 $\frac{\mathrm{W}}{\mathrm{m \cdot K}}$ and the soil heat capacity was 3.328×10^6 $\frac{\mathrm{J}}{\mathrm{m^3 K}}$. Pipe volumes were integrated out of the soil continuum to ensure convergence with decreasing element widths.

The pipe was laid out in a rabbit configuration (Figure 2.3) 1.5 m below ground surface with a trench width of 1.8 m, the total length of pipe was 191.8 m sitting in a 50 m long trench. Load to the pipe model was applied as a temperature delta, supplied again by the Elora field site (Haslam, 2013). Material datasheets provided the thermal conductivity and geometry of the HDPE pipes used at the field site. The flow rate was set at 946 $\frac{\mathrm{cm^3}}{\mathrm{s}}$. The fluid in the pipes was parametrized as a 20% ethanol/80% water solution, the heat capacity of this mixture was calculated to be $3.73 \frac{\mathrm{MJ}}{\mathrm{m^3 K}}$. The mixing ratio (combined thermal diffusivity and mechanical mixing) was 0.167 $\frac{\mathrm{m^2}}{\mathrm{s}}$. Parameter values for the pipe network model were based on the Elora field site (Haslam, 2013).

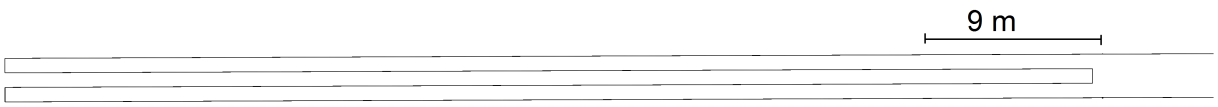

Figure 2.3: Rabbit trench layout

The coupled nature of these models can lead to some nonstandard convergence properties. Pipe outlet temperatures from a convergence test are presented in Figure 2.4 showing the temperature difference as average absolute error and maximum absolute error between a run with a fine discretization compared to a series of runs with coarser discretization. As would be expected, the run with the largest overall temperature difference is the coarsest run which was discretized to 0.6 m in the horizontal and vertical directions. With a monotonically converging model one would expect to see improvement in model performance with an increase in element count. The convergence shown in Figure 2.4 meets the criteria of monotonic convergence. The two lines, max error and average error, were taken as the maximum temperature difference and average temperature difference between the simulated temperatures using the element widths specified and the temperatures from a simulation using 0.05 m element widths. Note that the location of the pipes in these convergence runs was selected so that it always ran through the nodes of the soil continuum elements.

The soil continuum model is sensitive to the relative location of the pipes and the nodes of the finite elements. Figure 2.5 shows the temperature difference between the three off-node placements illustrated in Figure 2.6 compared to an on node placement, all applied to a rabbit trench. Figure 2.7 is provided as a reference to illistrate the relation between relative source location and node placement.

The relative impacts of having the pipe being placed mid element in one of the X or

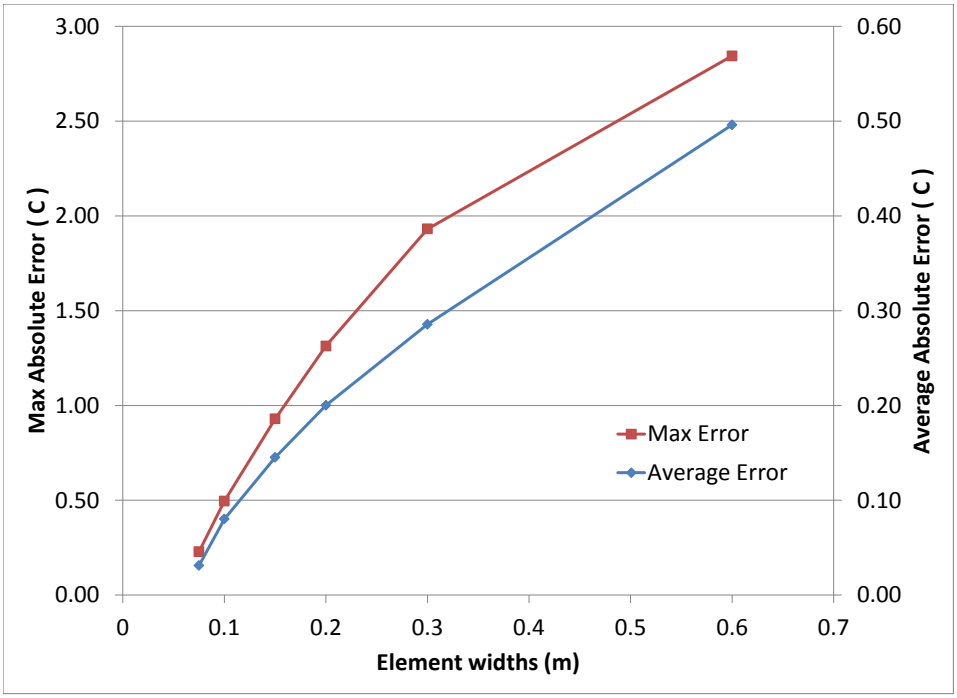

Figure 2.4: Convergence of GLHE outlet temperatures (relative to a 0.05 m discretization). Average absolute error and maximum absolute error are shown.

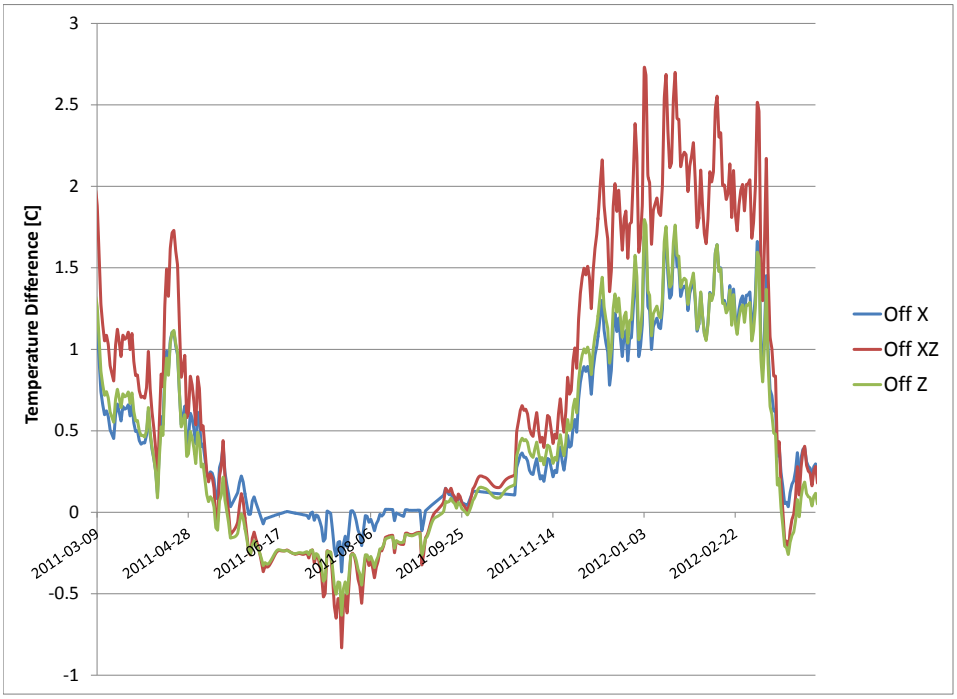

Figure 2.5: The outlet temperature differences between an on-node pipe model placement and three off-node placements of a rabbit loop GLHE in a homogeneous soil

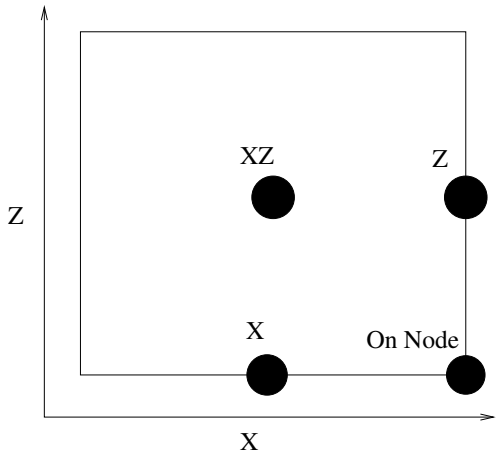

Figure 2.6: The locations of the four pipe locations (circles) relative to the element (square)

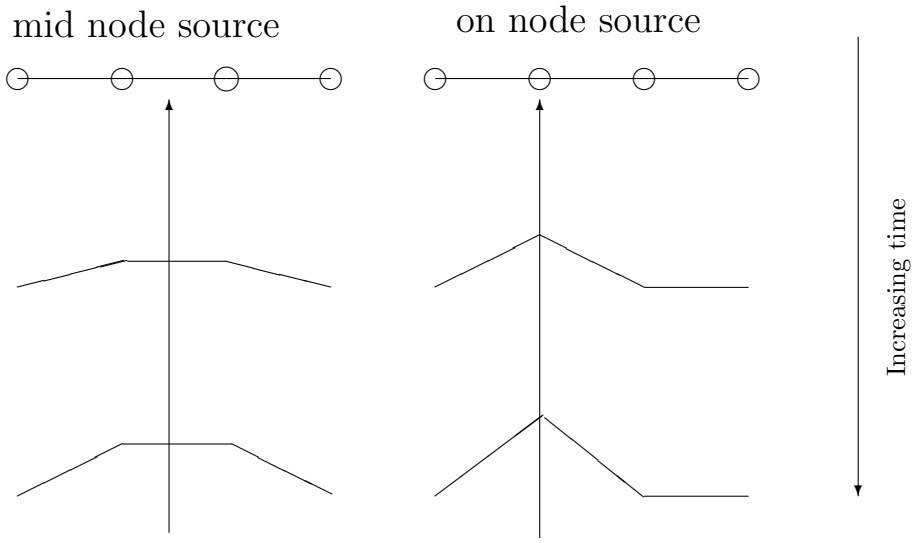

Figure 2.7: Having the source location in the middle of an element (left) causes the temperature field, shown with node locations as circles at the top of the figure, to develop in a more spread out manner relative to a model having a source located on a node (right)

Z axes were very similar. The combined effect of placing the pipe off both the X and Z had a larger deviation than the runs which were only off axis in one direction. If the pipe positioning had not been specified so that it always intersected nodes, Figure 2.4 would not have displayed such consistent convergence properties because of the dependency upon relative pipe-to-element placements.

The performance discrepancies caused by different placements of pipes within the finite element mesh are caused by the interpolation functions not fully resolving the thermal gradients within the element (see Figure 2.7 for a visual reference). Steady state temperature fields around a near point source such as a pipe are best described by a logarithmic function of radial distance with a high gradient near the point source and a rapidly decaying gradient farther away from the source. The linear continuum elements used in HEN can only roughly approximate this radially symmetric logarithmic decay. When a pipe is running through a node then the exponential heat spike is approximated in all directions as a linear peak. When a pipe is running through the center of an element then the flux associated with the pipe must be distributed to all the nodes of that element equally so instead of a peak, a plateau is formed. Heat disperses more quickly from the plateau than the peak and so different outlet temperatures are reported by the model. For a grid with a cross section of 10 cm by 10 cm the difference of outlet temperatures between a pipe network that runs through the centres of the cross sectional area compared to a pipe network that runs through the nodes of the grid will will not exceed 1 °C. This issue should diminish as $\Delta x \to 0$.

2.6 Example investigation

A hypothetical ground loop was created to demonstrate the simulation capabilities of HEN. The modelled GLHE pipe network was designed as a traditional 6 ton system with 6 rabbit loops coming off a simple reverse return manifold. The loop system was buried 1.5 m below ground surface in a heterogeneous soil with mean thermal conductivity of 1.5 $\frac{\mathrm{W}}{\mathrm{m \cdot K}}$. The heat capacity was assigned to be 2495840.25 $\frac{\mathrm{J}}{\mathrm{m^3 K}}$. Input files and instructions are provided in Appendix F.

The surface boundary condition and energy load were assigned according to data collected at the Elora, Ontario field site (Haslam, 2013). A simulation period of 1300 days, about 3.5 years, was used with boundary conditions and GLHE energy loadings created based on an extrapolation of 400 days of available field data from the Elora field site. Figure 2.8 shows the surface boundary condition and energy requirement being used in this example simulation. Note the inverse relationship between the near surface ground temperature and the energy requirement of the GLHE. When the building requires the most amount of heat it corresponds to the minimum near ground surface temperature. Likewise, when the building is rejecting heat to the ground at the highest rate, which occurs in spurts in the summer months, it corresponds to the maximum near ground surface temperatures. In mechanical engineering terms, the heating and cooling energy loads are highly unbalanced. The joules required from the ground over the heating season are greater than the joules rejected to the ground during the cooling season. In the first year of operation, the annual heating and cooling energies required of the GLHE observed at the field site were 48.9 MWh and -1.29 MWh respectively (negative energy load indicates cooling energy), an unbalance of 47.6 MWh. This means that over time, for the performance of the GLHE

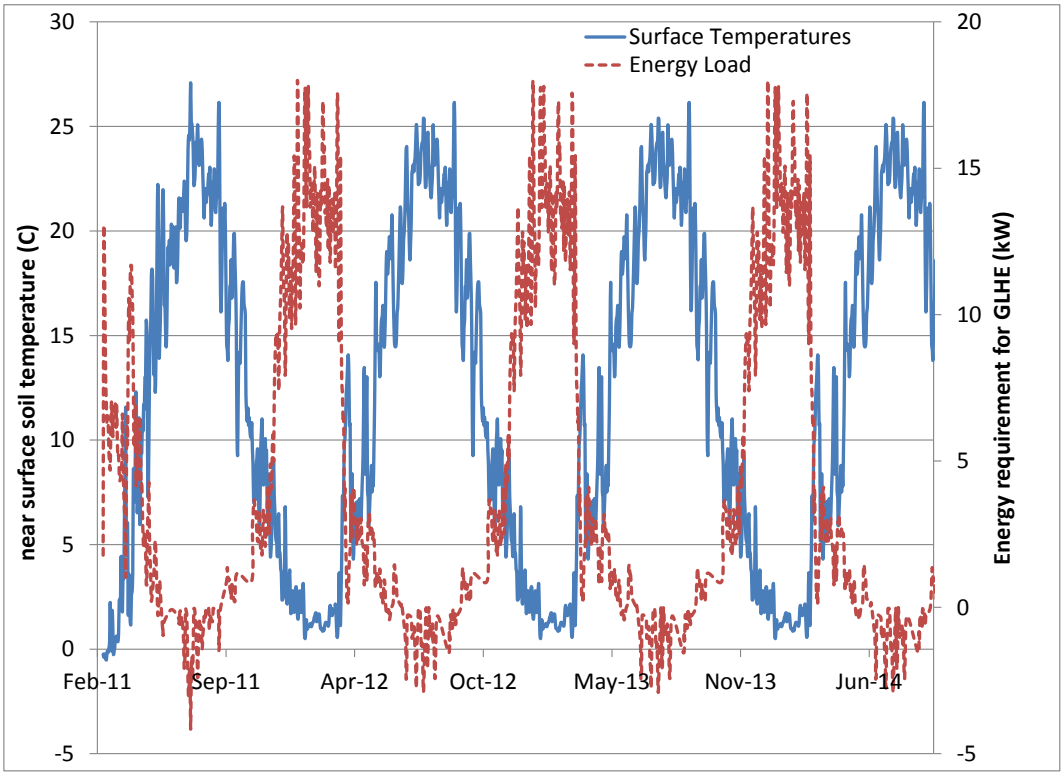

Figure 2.8: Example boundary conditions for the energy requirement of the GLHE and the surface temperature

not to degrade, energy from the ground surface must come down to the level of the loop to recharge it.

The pipe layout in this example represents a 6 ton system, similar to the field site in Elora (Haslam, 2013). Figure 2.9 shows 6 parallel trenches, each of 45 m length, with a rabbit layout present in each trench. Note that the manifold is piped in the standard reverse return header arrangement to ensure even pressure differential within each pipe trench. The dimensions of the domain are reported in Figures 2.9 and 2.10.

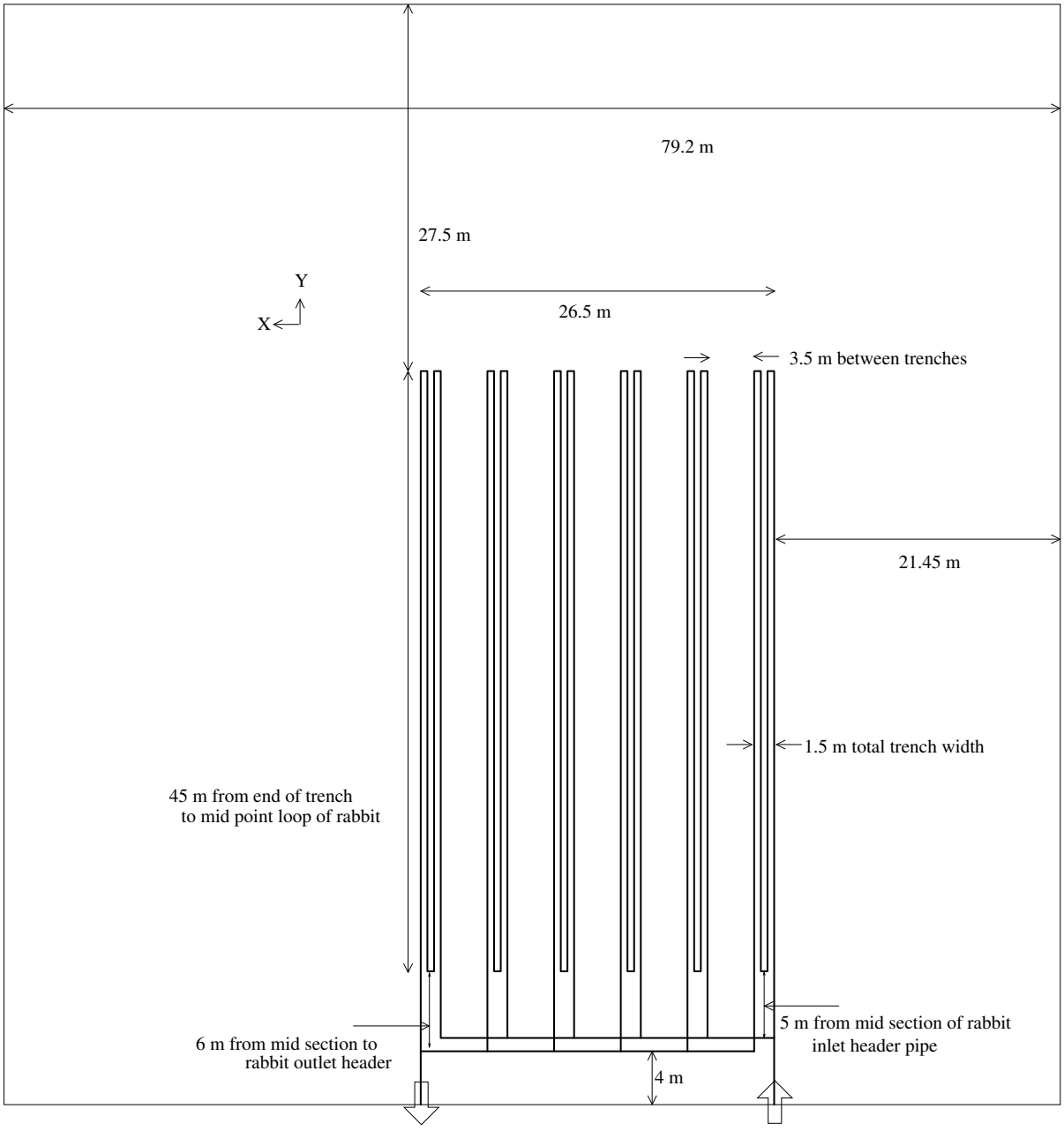

Figure 2.9: Example HEN run diagram in the XY plane.

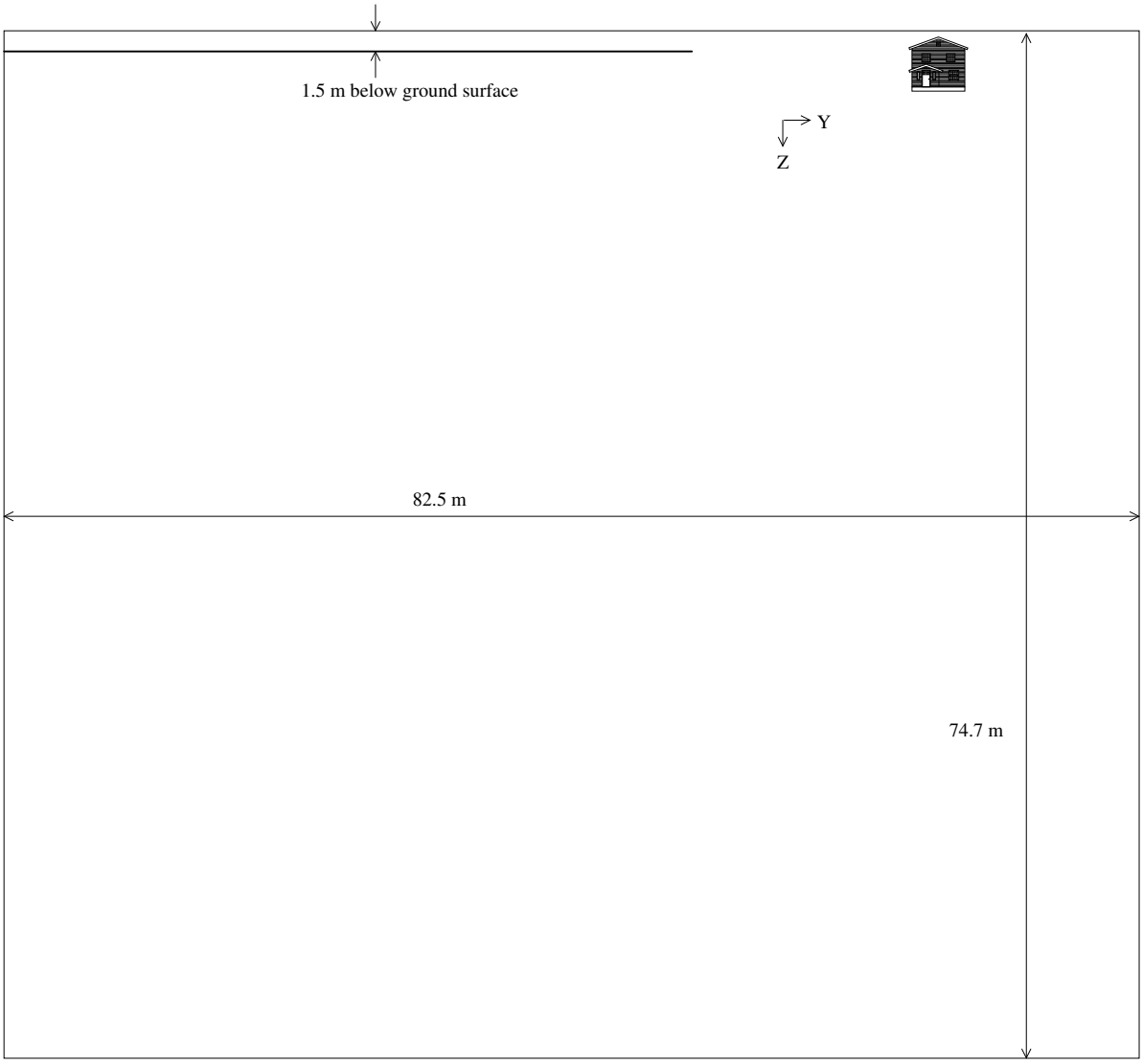

Figure 2.10: Example HEN run schematic diagram in the YZ plane. House illustrates which boundary is the ground surface.

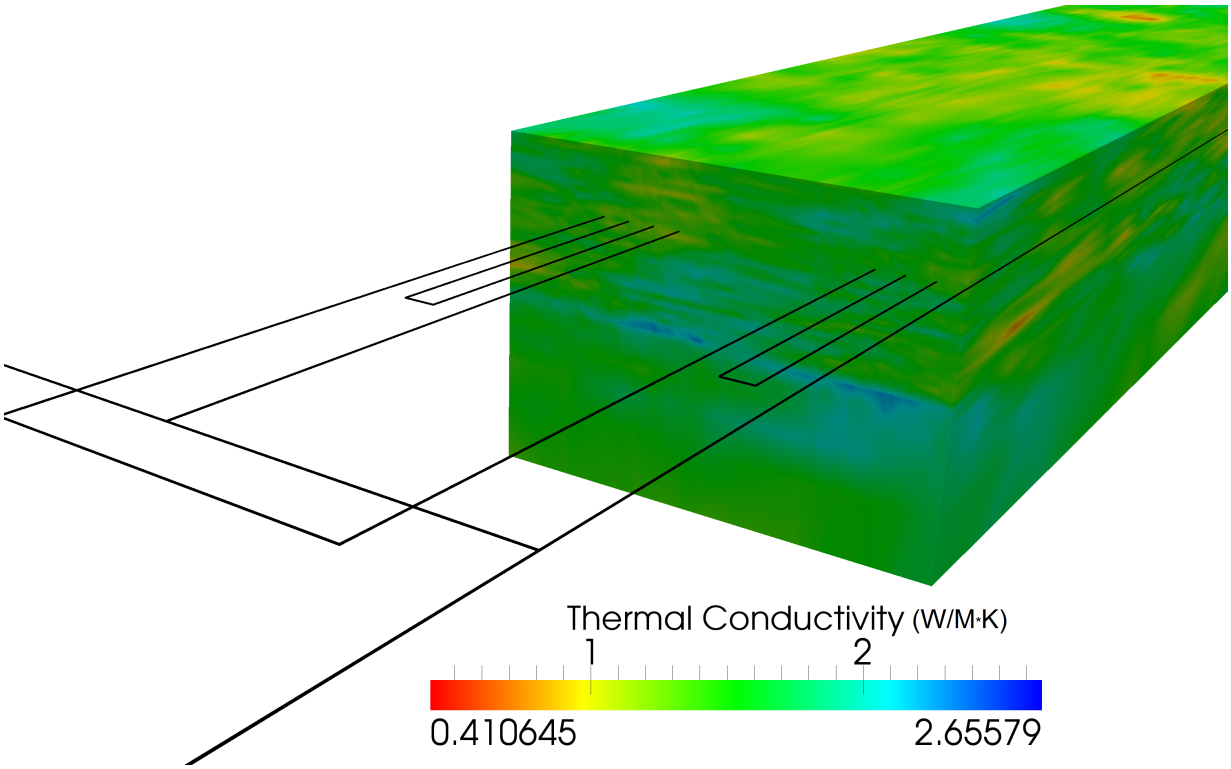

Figure 2.11: Thermal conductivity field applied in the example run

Soil thermal conductivity was parameterized to have a mean value of 1.5 $\frac{\mathrm{W}}{\mathrm{m \cdot K}}$. The property was distributed throughout the soil with this mean and having a standard deviation of 0.225 $\frac{\mathrm{W}}{\mathrm{m \cdot K}}$. A visualization of some of the thermal conductivities is provided in Figure 2.11. Note the vertical anisotropy in the structure of heterogeneity, with much more variation occurring in the vertical direction and much less in the horizontal directions. The extreme high and low values for conductivity fall within the possible range of thermal conductivities that could be expected to be present at the field site but they would never occur in large clumped sections. This lack of clumping of extreme values is largely consistent with the generated heterogeneous field. Figure 2.11 shows a rendering of a portion of the thermal conductivity field. Note that the rendered domain is much smaller than the total model domain, displaying values only immediately adjacent to the pipe network. The displayed

areas of Figures 2.11 and 2.12 are nearly identical with the only difference being the cut out in Figure 2.12.

2.6.1 Output

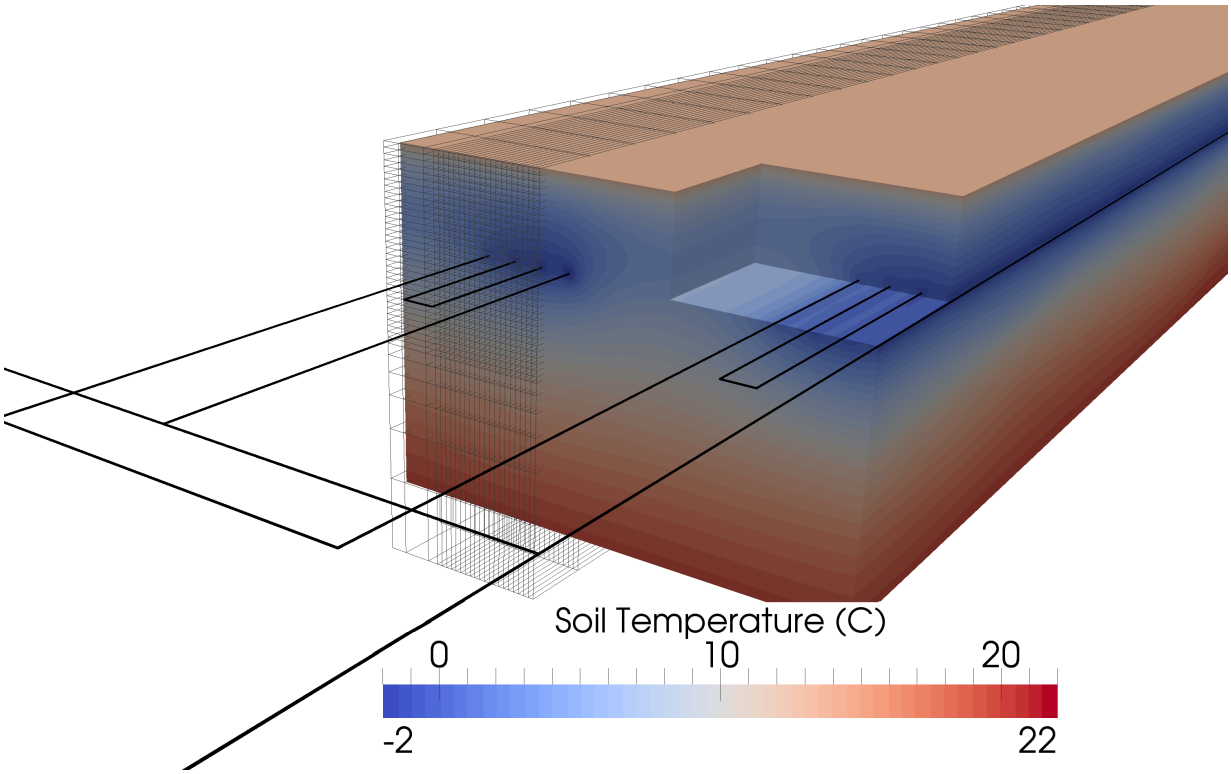

Figure 2.12: Example run thermal field. T = 50 days.

Figure 2.12 shows the thermal field at a mid point in the simulation (T = 50 days). The figure shows the two trenches nearest to the beginning of the GLHE (refer to schematic in Figure 2.9). The grid discretization can be seen on the left of the image; the mesh was highly discretized around the pipe (dx, dy = 10 cm) and coarsened farther away from the pipe. The total number of degrees of freedom was 632,500. This is done to increase both the speed and stability of the model. It is late spring in this image (mid May) and the

ground surface is substantially warmer than the soil around the pipes, over the summer this warming travelled down to the level of the pipes and provided large amounts of energy reserves for the following winters. The inlet pipes are colder than the outlet pipes in each trench section (inlet pipes are to the viewer's right in Figures 2.11 and 2.12). This is because the cold fluid is entering on the right and cools the surrounding soil quicker than the warmer fluid to left, which has warmed after travelling through the trench. Note that despite the presence of heterogeneity in the thermal conductivity of the soil, the temperatures of the system are largely consistent with what would be expected in a homogeneous medium. A full analysis of the temperature field indicates a minimum temperature of -5.3 °C (winter around pipes) and a maximum temperature of 27.0782 °C (summer surface) over the entire 1300 day run period.

From the development of thermal profiles around groups of pipes seen in large scale simulations, there is supporting evidence to conclude that the bar heat exchanger approximation made in investigations such as Fujii et al. (2012) may be appropriate for simulating the development of thermal fields around horizontal GLHEs in homogeneous fields. There has been no work done in this thesis to evaluate what kind of translation would be required to approximate the pipe to a bar for the sake of the pipe model. In the continuum model the replacement of a 4 pipe trench with a single bar as a representative source/sink would do little to change the thermal field development.

Over the 1300 day simulation period of the model run, the EWT did not degrade (Figure 2.13), a phenomena common in vertical loops. The loop field appears to fully reset during the summer months; energy from the surface recharges the ground loop allowing the loop to function despite a 50:1 load imbalance. This was the first academic verification of this phenomena using a correct geometry at the time of the study. Industry practitioners

have long held this as a truth of ground loop designed and it appears to be well founded.

Long period simulations of horizontal systems including correct geometry have not been conducted before. Figure 2.13 shows the EWT of this large scale loop simulation.

2.6.2 Pipe wall conductivity

To demonstrate the use of HEN as an investigative tool, four simulations were conducted to evaluate the impact of pipe wall thermal conductivity on the performance of the GLHE. This is a brief example of the capabilities of HEN, for a more thorough investigation into the impact of pipe wall thermal conductivity see Raymond et al. (2011b) who examine pipe wall variation in the context of steady state and transient heat transfer vertical GLHE. There are multiple options for piping. High density polyethylene (HDPE) pipe is the most common piping for these systems because of its high strength and durability and its compatibility with multiple antifreeze solutions. Thermally enhanced pipes, such as GEOPERFORMX®, have been developed with the premise that by increasing the thermal conductivity of the pipe wall the overall performance of the GLHE will increase. Four pipe conductivities were examined, the parameters are presented in Table 2.2.

Table 2.2: Pipe thermal conductivities investigated

Pipe wall thermal conductivity	Description
0.19 $\frac{\mathrm{W}}{\mathrm{m \cdot K}}$	Unrealistically low conductivity
0.40 $\frac{\mathrm{W}}{\mathrm{m \cdot K}}$	Typical 3608 HPDE pipe used in GLHE
0.60 $\frac{\mathrm{W}}{\mathrm{m \cdot K}}$	Enhanced thermal conductivity
0.80 $\frac{\mathrm{W}}{\mathrm{m \cdot K}}$	Slightly greater than GEOPERFORMX®'s advertised conductivity

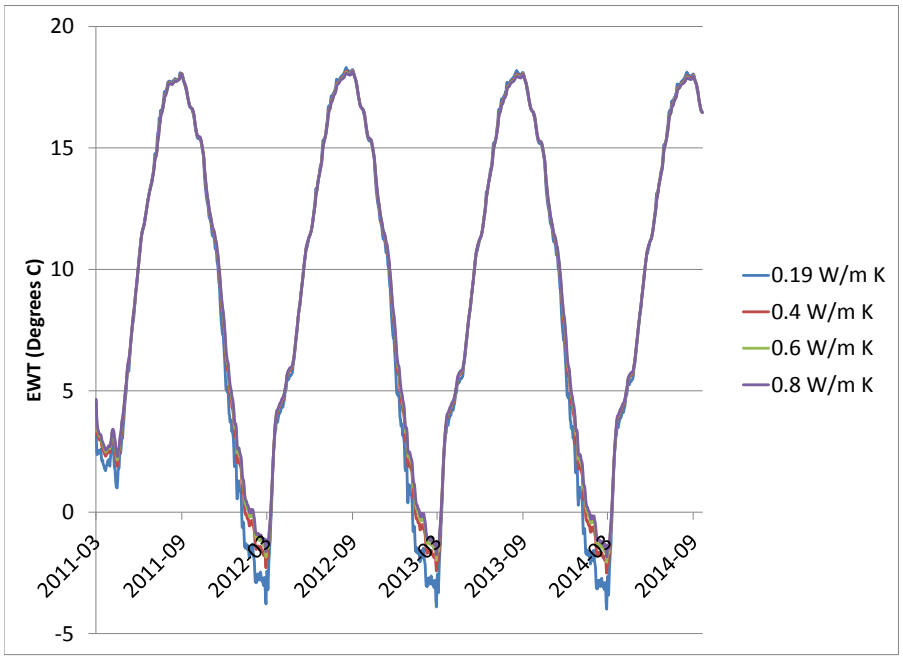

Figure 2.13: Absolute EWT for various pipe wall conductivities

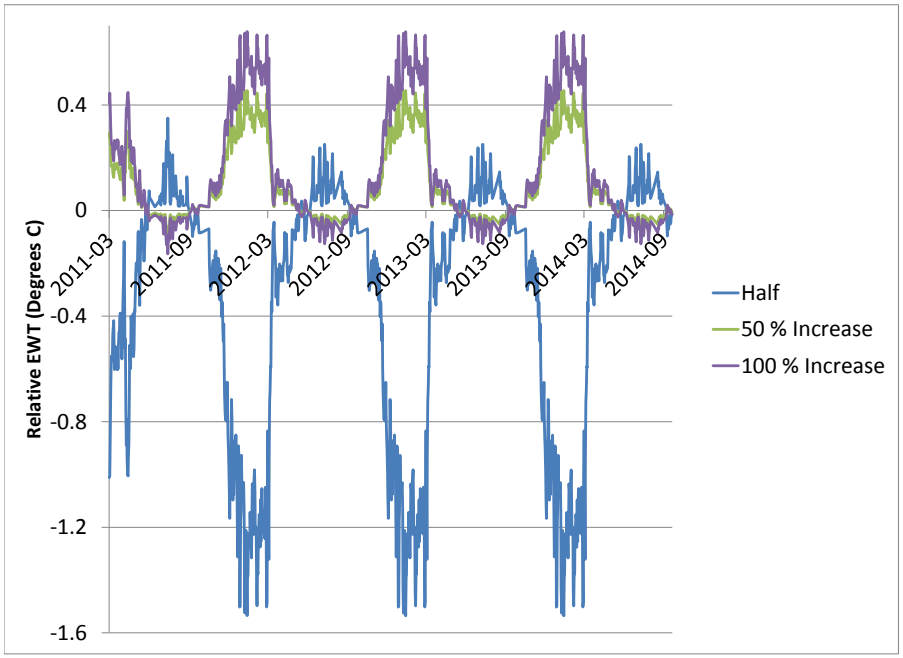

Figure 2.14: EWT difference relative to the 0.4 $\frac{\mathrm{W}}{\mathrm{m \cdot K}}$ pipe wall run

The key variable in GLHE performance is the temperature of the fluid within the GLHE returning to the HVAC system. This is the temperature that controls the coefficient of performance of the heat pump. Figures 2.13 and 2.14 show the absolute outlet temperatures of the GLHE and the outlet temperatures relative standard HDPE pipe, respectively. The overall thermal profiles that the different pipe conductivities produced overlap almost perfectly; differences in temperature are best seen by looking at the relative comparison (Figure 2.14). Two observations are apparent in this figure: increasing the thermal conductivity of the pipe increases the return temperature heating periods and decreases it during cooling periods, and there are diminishing returns to increasing the pipe thermal conductivity. The diminishing returns are particularly noticeable when looking at the run where the pipe thermal conductivity was halved, decreasing outlet temperatures by over 1.5 °C during heating seasons, and comparing to to doubling the pipe thermal conductivity, which only increased outlet temperatures by 0.6 °C during heating seasons. These temperatures would mean the heat pump would run at a lower the COP and the costs associated with running the loop pump would increase. The use of higher conductivity HDPE piping would lead to increased performance but analysing the economic viability of using the more expensive plastics is outside the scope of this these.

An interesting observation in the figures, which has long assumed to be the case by practitioners in the geothermal industry, is that there is no observable performance degradation over time with these horizontal loops. Despite the unbalanced, heating dominated, load, the loop appears to fully recharge every summer. The thermal conductivity of the pipe walls does not affect this behaviour.

Results of this investigation can be related to the study by Raymond et al. (2011b), who were the first to quantify the performance improvement of using thermally enhanced pipes,

and the general conclusions are similar. Both investigations demonstrate that performance can be expected to improve through the use of thermally enhanced piping. The temperature improvements seen by going from pipes with 0.4 $\frac{\mathrm{W}}{\mathrm{m \cdot K}}$ walls to pipes with higher thermal conductivity were modelled to be a decrease of 1 °C in summer months and an increase of 0.6 °C in winter months for vertical boreholes (Raymond et al., 2011b). For the horizontal systems simulated here a decrease of 1 °C in summer months and an increase of 0.6 °C in winter months is modelled (Figure 2.14). A difference in the relative magnitudes is to be expected for a variety of reasons: here horizontal systems are investigated instead of vertical, the loads using in the simulations presented here are taken from field measurements instead of generated by another code, and the pipe layout being simulated may be oversized for the amount of load being applied at the site.

2.6.3 Conclusion

HEN has been demonstrated to be capable of simulating a residential GLHE on a multi-year timescale. A simple investigation into the effects of altering pipe wall conductivities was preformed and the general results appear to correlate well with a previous study (Raymond et al., 2011b). Both studies show increased performance with increasing pipe wall conductivity. In relation to this thesis, HEN has been shown to be capable of simulating field scale GLHE with complex surface temperature timeseries and GLHE loadings in a numerically stable manner within a tractable period of time on a modest computer. The next chapter will discuss the capabilities of HEN in the context of recreating real world datasets.

Chapter 3

Estimation of properties in the field

3.1 Introduction

The thermal conductivity and heat capacity of the soil around a potential GLHE are the most important variables when sizing a geothermal loop. A more conductive environment will increase the effective volume of the soil around each pipe section from which energy may be extracted. This increased effective volume means that GLHE can be sized smaller and still meet the building energy requirements, lowering installation costs. As part of this study, soil properties were estimated using data collected at the Elora field site (Haslam, 2013) and a parameter estimation algorithm. Values estimated here will be used in future sections for evaluating the impact of heterogeneity. The thermal property estimates will also be useful for evaluating assessing whether the GLHE at the site was over- or under-designed.

There are a variety of inverse modelling techniques capable of determining thermal properties from temperature profile timeseries. The approach used in this paper turns the

inverse modelling problem into a problem of optimization, using a simple one dimensional model, similar to the strategy employed by Nicolsky et al. (2007) in their inverse modelling work where soil thermal properties were estimated through the application of a simple forward modelling code and made an optimization problem to fit the model to insitu temperature measurements of a saturated soil. Nicolsky et al. used a comprehensive model which included multiple mechanisms for heat transfer such as phase change and moisture migration. Here, the model used can only represent a limited number of physical phenomena, so this investigation will be less detailed. Other studies using inverse modelling to determine thermal properties of various substances are Jarny et al. (1991), who applied a similar method for investigating inverse heat transfer problems in multidimensional systems, and Cocco Mariani and Coelho (2009) who examined freezing and thawing in foods using inverse models.

Simplified inverse modelling is already a staple of vertical GLHE design. Thermal Response Tests (TRTs) are performed by matching exchange fluid temperatures to those predicted from analytical line-source models. The parameter estimation done here is more complex. The model includes the full geometry of the GLHE and the field data are actual soil temperatures rather than exchange fluid temperatures.

For inverse modelling, two models were created. The first model was of a one-dimensional vertical column of soil with off pipe sensors at the field site, sufficiently far away from the GLHE to avoid interference, at the field site. This model is detailed in §3.3. The second model was designed to simulate the soil temperatures near and around the rabbit trench at the field site. This model is detailed in §3.4.

This chapter details the parameter estimation of thermal conductivities at the field site in Elora, Ontario. First, formulation of the optimization problem and objective function

will be discussed. Second, results of an iterative optimization will be presented. Third, the runs will be examined and the best estimate of thermal diffusivity will be selected. In the final section, an inverse model of the field site's GLHE (Haslam, 2013) will be used to attempt to recreate the temperatures measured at the monitoring cross sections.

3.2 Algorithm design

3.2.1 Objective function

The objective function to be minimized was chosen to be a sum of squared errors between the modelled results and the temperature timeseries measured at the Elora Field Site (Haslam, 2013) in the soil and at the HVAC unit. Using the notation of Nicolsky et al. (2007), the objective function, J, is given by

$$J(\mathcal{C}) \approx \sum_{i}^{NS} w_i \int_{t_s}^{t_e} \left(T_{\text{modelled}}(t, \mathcal{C}) - T_{\text{obs}}(t)\right)^2 dt \tag{3.1}$$

where $\mathcal{C}$ is the vector of parameters controlling the thermal conductivity and initial conditions of the soil profile; T_{obs} is the observed temperature timeseries in the field at location i (from Haslam (2013)); T_{modelled} is the simulated temperature timeseries in the field at location i; NS is the number of field observation locations where valid temperature data was available. The modelled temperature was calculated using HEN, parametrized by $\mathcal{C}$ over the time period $[t_s, t_e]$ that was the time span of the data available at the field site; and w_i was the weight assigned observation location i.

The goal of parameter estimation is to minimize this objective function. The optimal set of parameters, $\mathcal{C}_{opt}$, is the one that minimizes $J(\mathcal{C})$, i.e., T_{modelled} will be highly correlated

to T_{obs}. It is possible that the non-linearities in the problem meant that multiple local minimima existed.

3.2.2 Optimization algorithm

The dynamically dimensioned search algorithm (DDS) (Tolson and Shoemaker, 2007) was used to identify the optimal parameter set. The algorithm, originally designed for parametrizing environmental models, was selected due to its excellent performance at problems involving expensive objective functions. Each of the vertical model evaluations took approximately 20 seconds to compute and each of the full pipe network model evaluations took approximately 1 hour to compute.Therefore, it was important for the algorithm to converge in a limited number of objective function evaluations.

The parameters used in DDS are the defaults recommended by the creators of the algorithm. The maximum number of objective function evaluations was set to 10,000 for the vertical model and 100 for the second model. The DDS neighbourhood size parameter was set to 0.2.

DDS does not employ a gradient based search but it was still possible that the algorithm could have gotten "stuck" in a local minima. In an attempt to avoid this, multiple restarts were used in all optimization runs (reported in each section).

3.2.3 Influencing factors

What can be learned from parameter estimation is limited by the relative complexity of the physics being simulated. The simplicity of the first, vertical profile, model means that there were only two influencing factors: initial conditions and thermal diffusivity, which

could be changed to get the model to more closely match what was being seen in the field. If thermal diffusivity is increased then changes to the surface temperature perturbations will propagate farther, faster, and decay less as they travel down from the surface. A high thermal diffusivity is achieved when thermal conductivity is high and heat capacity is low.

The other influencing factor, initial conditions, play a large role at early time periods in the modelling run. Initial conditions will not matter much if there is a long run up period in the model where soil temperatures will naturally reach realistic values. But if there is no run up period then initial conditions could potentially play a very large role in the model's ability to recreate what is being seen in the field. In all of the models runs using optimal parameter sets presented in this chapter, the system reached dynamic thermal equilibrium in less than 3 days.

The second model, of a full trench GLHE, is affected by more influencing factors. The initial condition and thermal diffusivity are still important but now the roles of the GLHE load and soil thermal conductivity and heat capacity come into play. Having more independent parameters that are important to the development of the thermal fields at the observation points can make the parameter estimation exercise more difficult. In §3.4 parameter values estimated using the vertical model were used to limit the number of parameters being calibrated in the trench model. The recreation of the initial conditions at the time of field data collection was not attempted.

3.3 Vertical profile model

The first parameter estimation exercise was to estimate the soil thermal diffusivity and initial temperature profile using a one-dimensional vertical column model. The total squared

error between the daily averages of the field data and modelled timeseries was used as the objective function (Equation 3.1 with weights from Table 3.3). The field site (Haslam, 2013) has 4 sensors approximately 50 cm apart at this location which were used in the objective function. The vertical grid was finely discretized: 5 cm elements over a 700 cm domain (Figure 3.1). The model was run over a period of 508 days which was the extent of the available field data. Fifteen minute timesteps were used for the forward timestepping. The field data, collected on a five minute interval, was converted to daily averages. This was done to improve the numerical stability of the model by smoothing out the daily surface temperature fluctuations and because the timestep sizes were already longer than the the field data resolution (5 minutes in the field vs. 15 minutes in the model). The use of an average is justifiable as the calibration point closest to the boundary condition is still far enough down that diurnal temperature variations were not observed in the temperature data. The HEN parameter set is presented in Table 3.1.

Table 3.1: Base column model for inverse runs

Parameter	Value
Base dimensions	5 cm by 5 cm
Total depth of domain	7 m
Surface depth for Dirichlet condition	5 cm
Element vertical dimensions are	5 cm
Total time	508 days
Calibration period start time	December 1, 2010
Run up time	0 days
Time step size	15 minutes

Initial conditions were found to have a large effect on the ability of a column model to recreate the thermal profiles observed at the field site. It was found in initial parameter estimation attempts that uniform initial temperature was a poor estimate of actual initial

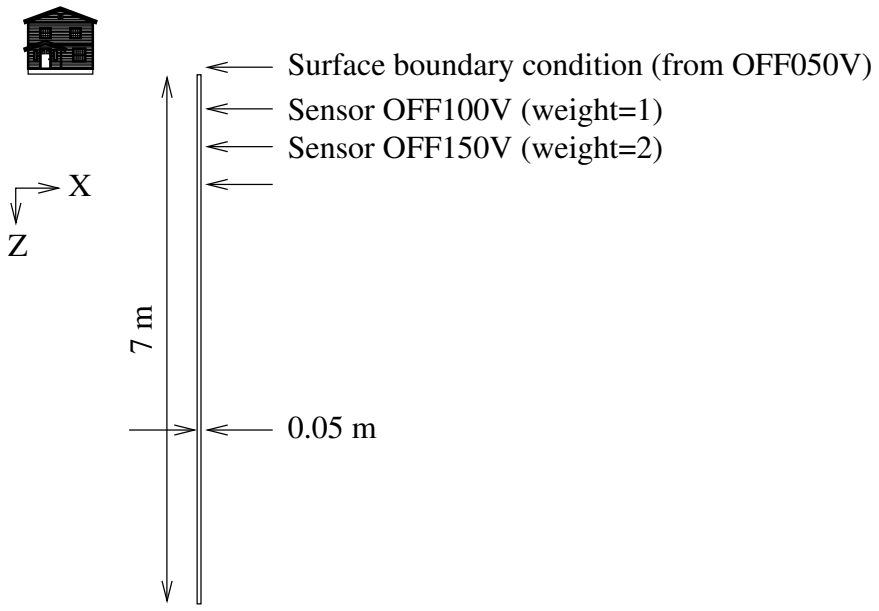

Figure 3.1: Vertical column model domain and sensor locations

conditions in the ground. The model, capable of handling arbitrary initial conditions, was used to investigate an appropriate non-uniform initial condition to include in the model. Initial conditions were generated by an empirically validated mathematical method developed by Labs (1979b) to predict soil temperature as a function of depth and time. The formula is:

$$T_{(x,t)} = T_m - A_s \exp\left(-x\sqrt{\left(\frac{\pi}{365\alpha}\right)}\right) \cos\left[\frac{2\pi}{365}\left(t - t_0 - \frac{x}{2}\sqrt{\left(\frac{365}{\pi\alpha}\right)}\right)\right] \tag{3.2}$$

where $T(x,t)$ is the temperature [°C] of the ground at depth x [m] on day t [d]; t_0 [d] is the phase constant, representing the day of minimum surface temperature; T_m is the mean annual ground temperature [°C]; A_s, the annual temperature amplitude at the surface [°C]; and α is thermal diffusivity in per day units [m^2 d^{-1}]. The equation will satisfy the governing energy Equation 2.7 provided Equation 3.2 is used for the initial temperature

distribution and ground surface boundary condition. Use of this equation can be found in energy simulations of below ground structures such as those of Al-Temeemi and Harris (2004).

The equation produces a sinusoidal temperature curve that decays exponentially with depth (see e.g. Figure 3.2 which shows a single temperature profile beside the annual range of vertical temperature profiles). At the depths considered here, the sinusoidal part of the curve can be difficult to pick out. The amplitude, A_s, controls the magnitude of the waves, T_m controls the value of infinitely deep temperature, and t_0 controls the phase angle of the curve.

The only variable assigned without estimation was t_0. The start of the model run period was December 1st, the 335th day of the year. Other variables (T_m, A_s, t_0) were estimated by DDS. To ensure there was no interplay between the thermal diffusivity being used in the model run and the one used to calculate the initial condition, another variable, $\alpha_{initial}$, was used. This was done because the soil diffusivity present in the field site after the installation of the GLHE may have been different than the thermal diffusivity present before excavation, which would have been the diffusivity that had the greatest impact on the development of the initial temperatures.

The complete parameter set being investigated is presented in Table 3.2. Note that heat capacity is a fixed parameter. Heat capacity was selected to be fixed because the nature of a 1D column model with a single forcing function of a time-varying Dirichlet boundary condition meant that only the aggregate parameter of thermal diffusivity could be estimated. Thermal diffusivity was estimated by fixing heat capacity as a set value and estimating thermal conductivity. Estimates for thermal conductivity here are completely dependent upon the assumed heat capacity and should not be considered representative of

Table 3.2: Parameters and their bounds

Parameter	Minimum	Maximum
Thermal conductivity	0.01 $\frac{W}{m \cdot K}$	3.50 $\frac{W}{m \cdot K}$
Physical analogue: thermal conductivity	less than peat soil	greater than solid rock
Heat capacity	2,900,000 $\frac{J}{m^3 K}$	2,900,000 $\frac{J}{m^3 K}$
Physical analogue: heat capacity	Saturated sandy soil, 40% pore volume	
Mean annual temperature	2 °C	20 °C
From:	Hart and Couvillion (1986)	
Annual surface temperature variation	25 °C	35 °C
From:	Reasonable range of surface temperatures[1]	
Coldest day of the year (Julian days)	15	46
From:	Between January and February[2]	
Thermal diffusivity for initial condition	0.00864 $\frac{m^2}{day}$	0.1296 $\frac{m^2}{day}$
From:	Oke (1987)	

Table 3.3: Locations of monitoring points

Reference Sensor	Weight	Distance from surface (specified by OFF050V)
OFF100V	1	45 cm
OFF150V	2	95 cm
OFF200V	4	145 cm

conditions at the field site.

The calibration process was set up so, that for every objective function evaluation, an initial thermal profile for the model domain would be generated through the use of Equation 3.2. HEN would then be run for the timeperiod specified, recording temperature timeseries at the depths of the three field sensors as per Table 3.3 and Figure 3.1. The sum of the squared errors between the modelled time series and the observed timeseries

[1] http://climate.weatheroffice.gc.ca/climate_normals/results_e.html?stnID=5051& lang=e& dCode=1& StationName=TORONTO & SearchType=Contains& province=ALL& provBut=& month1=0& month2=12

[2] (http://www.weather.com/weather/wxclimatology/monthly/graph/CAXX1415?from=month_bottomnav_undeclared)

was then calculated and weighted (according to Table 3.3). The combined sum of squared errors was then returned as the value of the objective function. In this manner the initial conditions and thermal diffusivity were both estimated.

To test for any impacts on model performance due to the disparity between the initial conditions generated using Equation 3.2 and the governing equation (Equation 2.7), a non-physical initial condition was created. This initial condition had a 3 °C spike placed at an arbitrary location, chosen here to be 1.35 m below the surface. HEN was then run using this initial condition set and the resulting temperature timeseries at the shock location was compared to an equivalent, unshocked system. The two models converged quickly, at $time_{model}$=1 day the two time series were equal to 3 significant figures. At $time_{model}$=2 days there were 4 signifigant figures and after $time_{model}$=6 days the two timeseries were equal to 5 signifigant figures. On a 400 day simulation, the attenuation rates of these shocks were rapid enough that they considered negligible in this investigation.

Results

Results from the parameter estimation are presented in Table 3.4. Note that the thermal diffusivity was determined very consistently between restarts, indicating that there is likely a single optimal diffusivity for the domain. Figure 3.2 shows the initial temperature profile as determined by DDS. It can be seen that in the first 2 m of soil the equation is almost linear, and the a larger section of the curve must be examined to see its true shape. Since the deepest sensor is less than 2 m below the surface, the initial temperature profile is being estimated without the benefit of field data to evaluate the estimation. The profile generated from the analytical model is assumed to be correct.

Figure 3.3 shows the final comparison of modelled temperature and measured at the

Table 3.4: Estimate parameters after 14 restarts

Parameter	Mean	Range
Thermal conductivity	1.74 $\frac{\mathrm{W}}{\mathrm{m \cdot K}}$	1.73705 - 1.74295 $\frac{\mathrm{W}}{\mathrm{m \cdot K}}$
Heat capacity	2,900,000 $\frac{\mathrm{J}}{\mathrm{m^3 K}}$	fixed
Thermal diffusivity	6.01 $\times 10^{-7} \frac{\mathrm{m^2}}{\mathrm{s}}$	6.00-6.02 $\times 10^{-7} \frac{\mathrm{m^2}}{\mathrm{s}}$
Initial Conditions:		
Mean annual temperature	11.1 °C	10.262-11.948 °C
Annual surface temperature range	28.0 °C	25.71-30.29 °C
Coldest day of the year	36.9 Julian days	33.89-40.0 Julian days
Thermal diffusivity of initial condition	15.0 $\times 10^{-7} \frac{\mathrm{m^2}}{\mathrm{s}}$	14.733-15.277 $\times 10^{-9} \frac{\mathrm{m^2}}{\mathrm{s}}$

2 m location. The model overestimates the temperature by about 1 °C in the summer of 2011 and underestimates the temperature in the spring of 2012. This is potentially due to a large temperature spike in March which would have melted snow at the surface and sent warm ground water percolating down through the soil. Heat transfer due to ground water advection was not included in the simulation.

Other parameter estimation attempts

A variety of parameter sets and model configurations were attempted before converging on the final parameter set presented in this section. Model attempts using a uniform initial condition did a poor job of recreating the observed temperature timeseries, even when run up periods were used. The use of a model run up changed the estimated thermal diffusivity, indicating the sensitivity of the parameter estimation process to early timeperiods in the field and modelled data. When a run up period was used for the parameter set presented in this section the thermal diffusivity was estimated to be lower. This may also suggest soil thermal diffusivity at the field site varied over the data collection period.

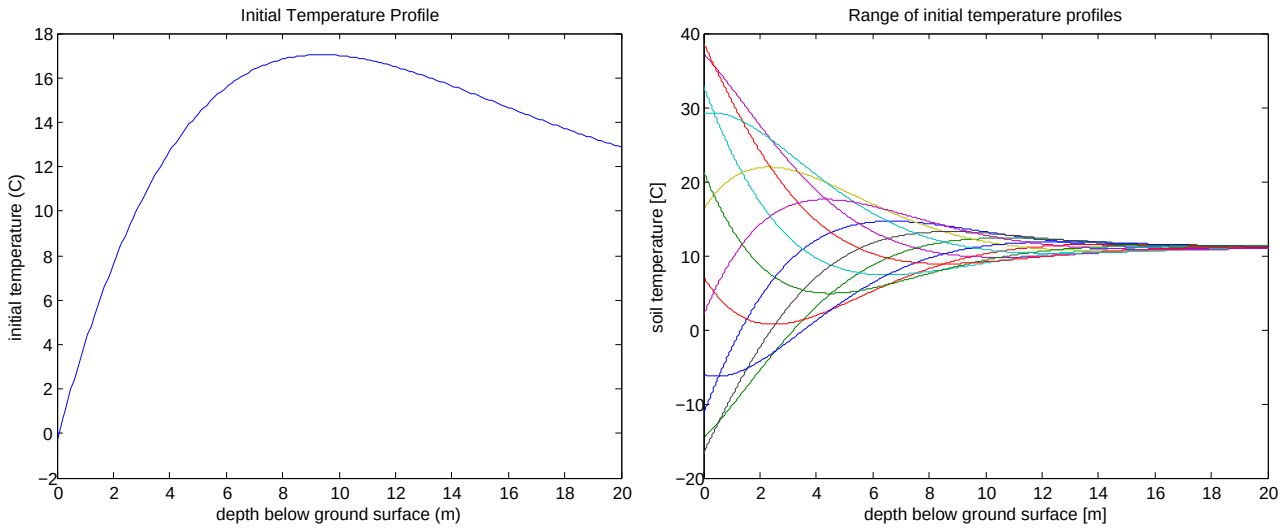

Figure 3.2: Initial vertical temperature profile (left). An annual range of vertical profiles (right) generated with Equation 3.2 is provided for context.

The locations of the observation sensors, as parametrized in the model, were modified from what was measured in the field (Haslam, 2013) to find what is presented in Table 3.3 through a manual calibration process to improve the fit between the vertical column model and the field data. It is possible that the distances between the sensors, measured just before the off trench monitoring site was backfilled, changed during the backfilling process. The weights were also tweaked to determine sensitivities to the weighting scheme. Weighting appears to only slightly affect the estimated parameters and the differences between the optimal modelled timeseries were not visibly changed. The weighting scheme selected for the final parameter estimation, presented here, was the one that emphasized the lower sensors over the higher sensors without discarding information.

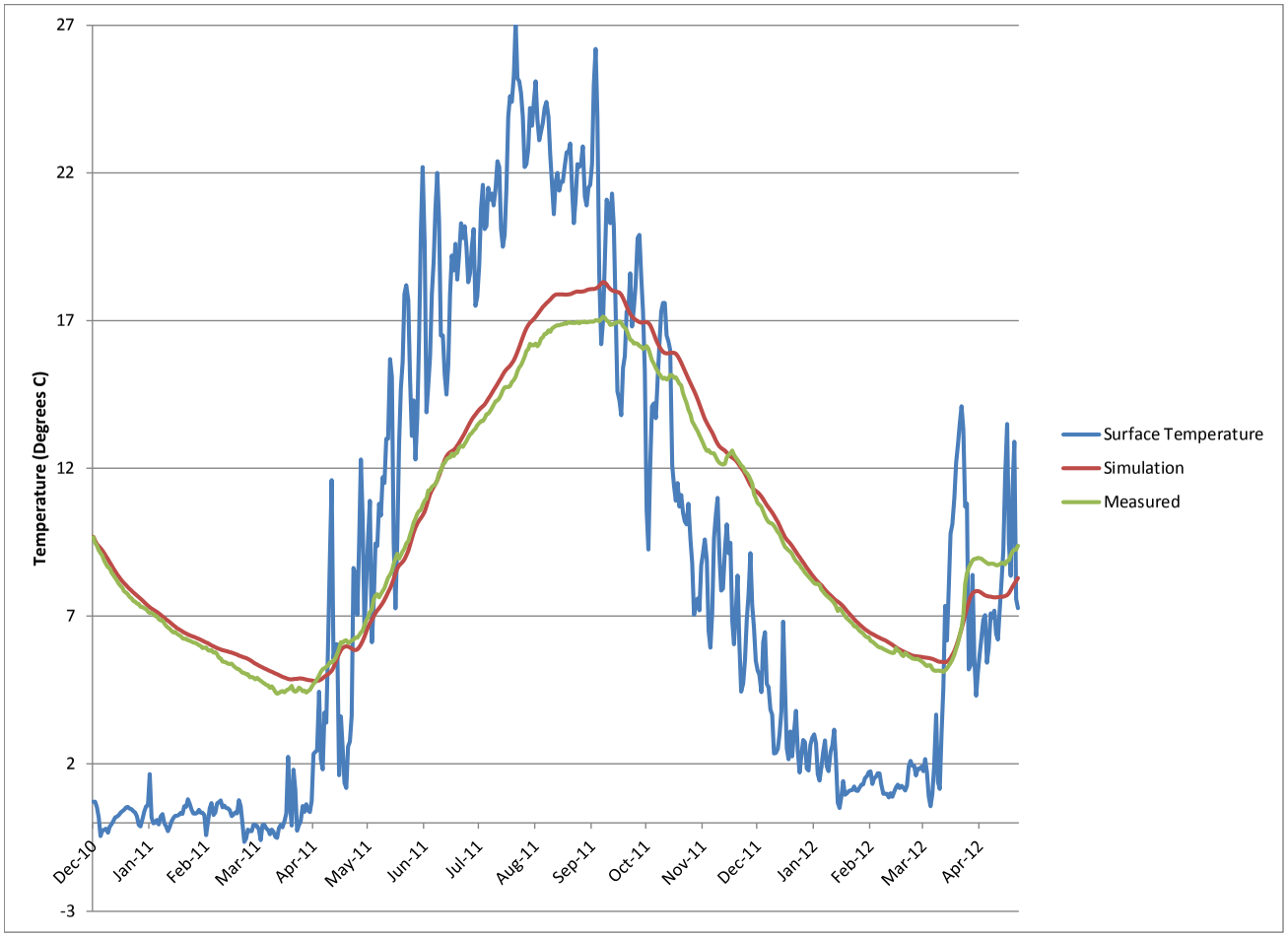

Figure 3.3: Comparison of model using estimated values to field results, 200 cm deep location. The comparisons for the other sensors are presented in Figure 3.4.

3.3.1 Discussion

The mean effective thermal diffusivity of the soil continuum at the field site and the initial vertical temperature profile were estimated in this section. The diffusivity was well within what could be expected based on the literature similar soils whose compositions are predominantly sandy clay (Table 3.2). Estimated initial conditions were slightly more suspect.

The assumption of uniform initial temperatures was found to be much worse than a non-linear initial condition based on a decaying sinusoid for the purposes of recreating the temperature time series recorded at the field site. Because the formula of Labs (1979a) uses empirical numbers based on seasonality at the location of the field site to estimate temperature at depth, reasonableness of these parameters in the initial condition can be evaluated. From Table 3.4: the mean annual temperature is 11 °C, a fair assumption based on background groundwater temperatures in the region (Hart and Couvillion, 1986); the annual surface temperature range is 28 °C, which is a little low for southern Ontario but if the snow blanket effect is considered it becomes less unreasonable; the coldest day of the year is in early February. The estimated thermal diffusivity of the initial condition is the only value does not appear to fit in well with literature values. A thermal diffusivity of 15.0 $\times 10^{-7} \frac{\mathrm{m}^2}{\mathrm{s}}$ for the analytical is more than double the estimated thermal diffusivity from the continuum model. From Appendix J, the diffusivity is outside the diffusivity of the high-end of aquifers: Materials that could have this magnitude of diffusivity are rock, ice, or other components with low heat capacity and high thermal conductivity. This suggests that the installation process of the sensors, where an excavator dug up and subsequently buried a 2 m deep soil column, disturbed the background temperature. This disturbance likely changed the initial temperatures in the area of the sensors. The formula

used was intended for natural systems subject to varying surface temperature and some of its parameters may have been bastardized to fit a perturbed soil.

A secondary objective of this parameter estimation exercise was to compare the thermal properties estimated to be in the field to the thermal properties assumed by the loop designer of the GLHE at the field site. In this case the designer was using the commercial software GLD2012, which contains soil thermal properties for a variety of soils the majority of which are sourced from Farouki (1982). The designer selected a damp silt/clay as the soil type which GLD lists as having a thermal diffusivity of 6.45×10^{-7} $\frac{\mathrm{m}^2}{\mathrm{s}}$. This compares quite favourably to the estimated value of 6.01 $\times 10^{-7}$ $\frac{\mathrm{m}^2}{\mathrm{s}}$ from Table 3.4. This lends evidence to support the methods used in this parameter estimation and suggests that the ground loop designer had a good grasp for the thermal diffusivity of the field site.

The model was capable of approximating what was happening at the field site away from the loop. This suggests that the heat transfer at the Elora field site is conduction dominated. Discrepancies appeared from a probable melting event in the spring of 2012 but this appears to a one time occurrence and is not part of the day-to-day behaviour of the column. Values estimated with the vertical model were used as a starting point in the following sections where heat flow in the subsurface around a GLHE was simulated to estimate soil thermal conductivity and heat capacity.

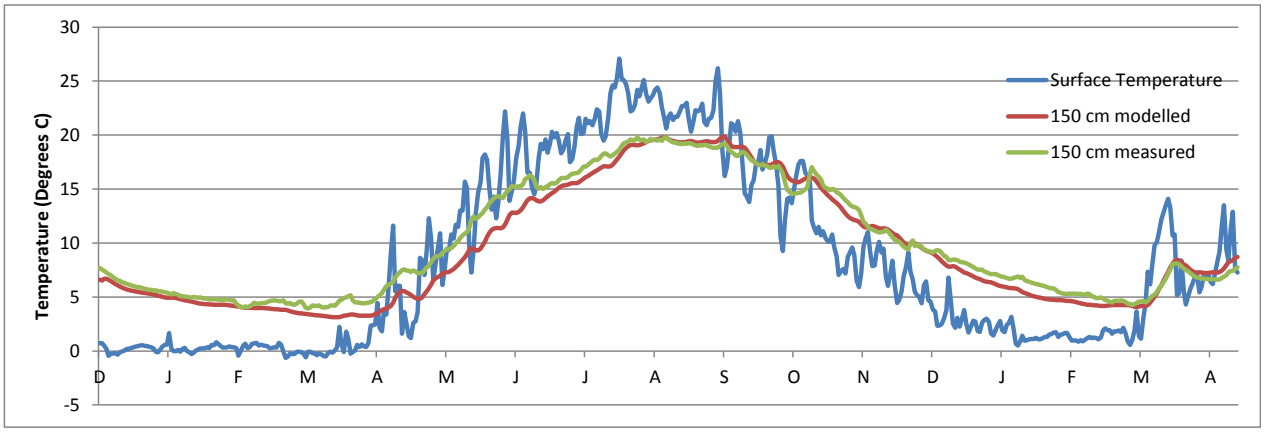

(a) 150 cm deep

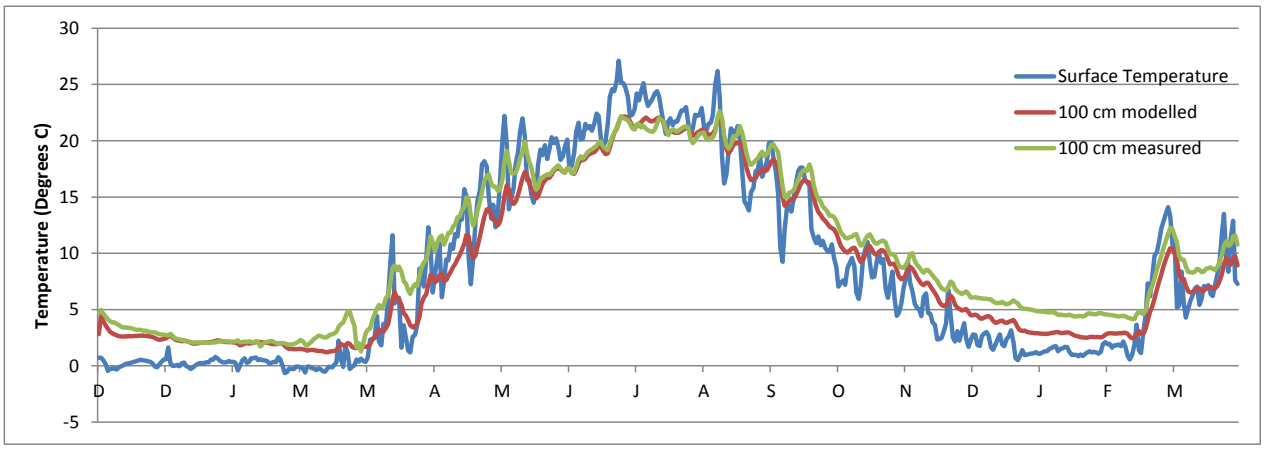

(b) 100 cm deep

Figure 3.4: The shallower calibration points

3.4 Trench inverse modelling

3.4.1 Single trench system

The thermal diffusivity is the ratio of thermal conductivity to heat capacity and can be thought of as the thermal inertia of a substance. A soil with low thermal inertia will quickly respond to fluctuations in surface temperature whereas a soil with a higher thermal inertia will be slower to equilibrate. In a modelled system where there are only fixed temperature boundary conditions, thermal conductivity and volumetric heat capacity cannot be determined uniquely through calibration, but when source and sink terms are introduced this changes and unique determination becomes possible. To accomplish this, a parameter estimation experiment was conducted investigating an active GLHE.

At the Elora field site (Haslam, 2013), the soil temperature around the GLHE was monitored with particularly dense instrumentation on the the rabbit loop trench. A cross-section of this trench was monitored with 32 thermocouples monitoring temperatures between the pipes in the trench, temperatures, extending beside the trench, and the temperature above and below the trench. For the parameter estimation, 16 of these sensors were selected (Figure 3.5). Sensors were chosen based on the quality of recorded temperatures in the first 400 days of monitoring. None of the sensors attached to the ground loop pipe were used; sensors directly adjacent to the pipe are more sensitive to errors made in estimating their location. The parameter estimation objective was to minimize the sum of squared errors between the time series recorded in the field and the temperature time series generated by the model. Equal weighting of observations was applied. It was not possible to determine if one sensor was more accurate than another (and therefore deserving of a higher weight), only whether or not a sensor was functioning.

An initial model of the rabbit loop GLHE in this trench was developed using parameters estimated from the previous section. The time period being investigated is different than in the previous section: data on the on energy load placed on the GLHE by the HVAC unit was not collected until March 7, 2011, so this was used as the start date. Initial temperatures around the GLHE were generated using the column model from the previous section, this time assuming that temperature only varied with depth. This assumption would cause the model to overestimate the temperature immediately adjacent to the GLHE because it neglects the energy removed by the GLHE from November to March. This overestimation should not play a large role in the parameter estimation due to the relatively long timeperiod of 400 days being investigated which should decrease the sensitivity of the estimation to initial conditions. One of the benefits of using initial conditions generated using the column model was that all shocks due to the initial conditions had already been attenuated.

The modelled rabbit trench was 45 m long and had a 5 m lead from the manifold (which placed it outside of the modelling domain, see Figure 2.3). The geometry of the layout did not exactly reflect the geometry of the field site. In the field site, 10 m from the end of the rabbit loop the trench makes a 90 degree turn. It has been assumed that, given the elongated nature of the trench, such a turn will not affect loop performance in a meaningful way and that the trench can be approximated by a model that has a loop without a turn. The model domain was 5 m across the trench, 72.5 m in the direction of the trench, and 74.7 m deep (Figures 3.6 and 3.7). A wider domain was also used (see Chapter 4 and Figures 4.3 and 4.4). The wider domain had dimensions 54.2 m across the trench, 72.5 m in the direction of the trench, and 74.7 m deep.

Energy use loadings to the ground loop were taken from data collected at the HVAC

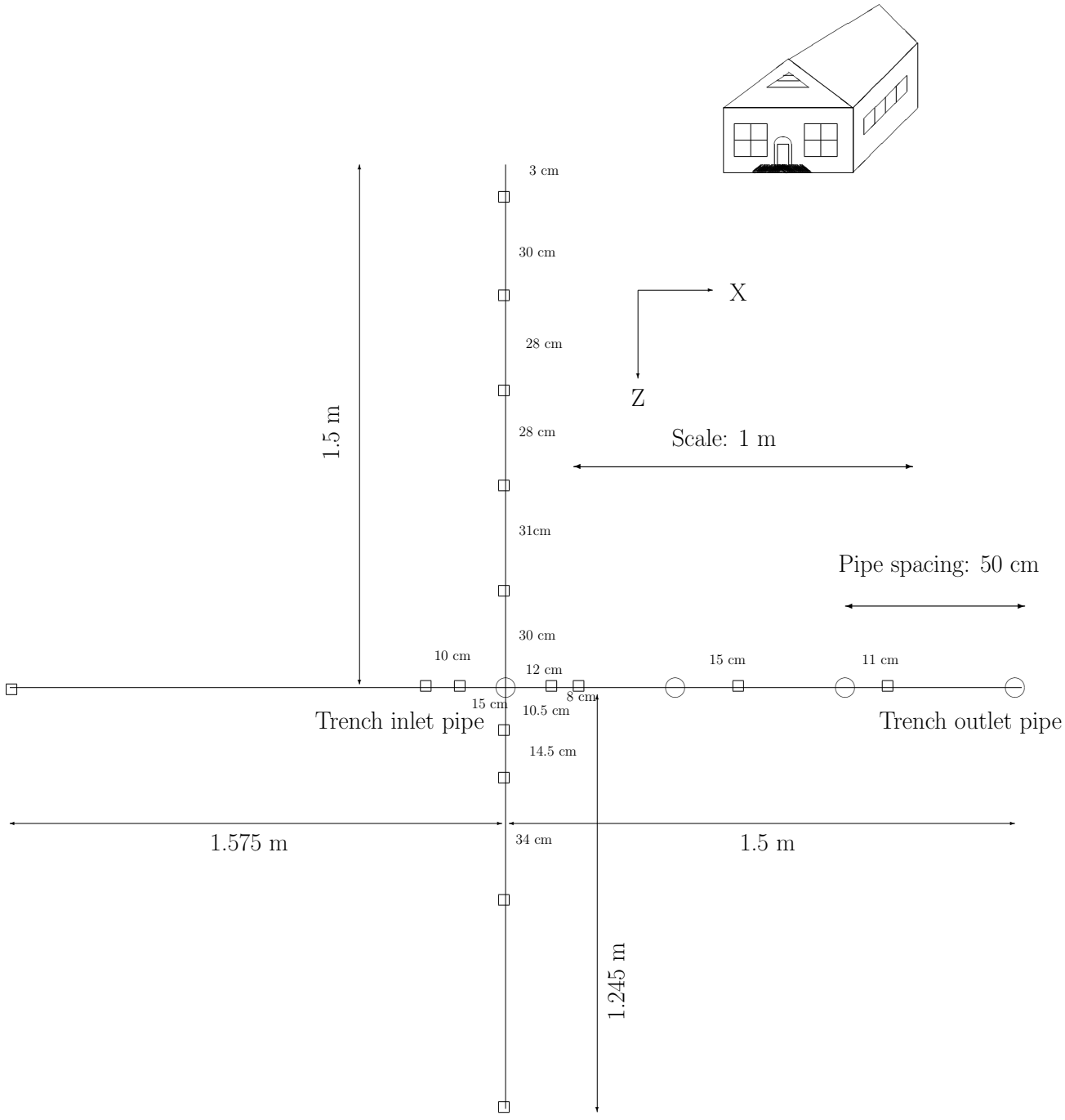

Figure 3.5: Location of field site thermistors in the rabbit loop cross section. The locations of the sensors are indicated by squares, the locations of the pipes by circles. Fluid coming from the manifold enters on the pipe in the left side of the trench on this diagram and exits through the rightmost trench. See Appendix G for a more detailed description.

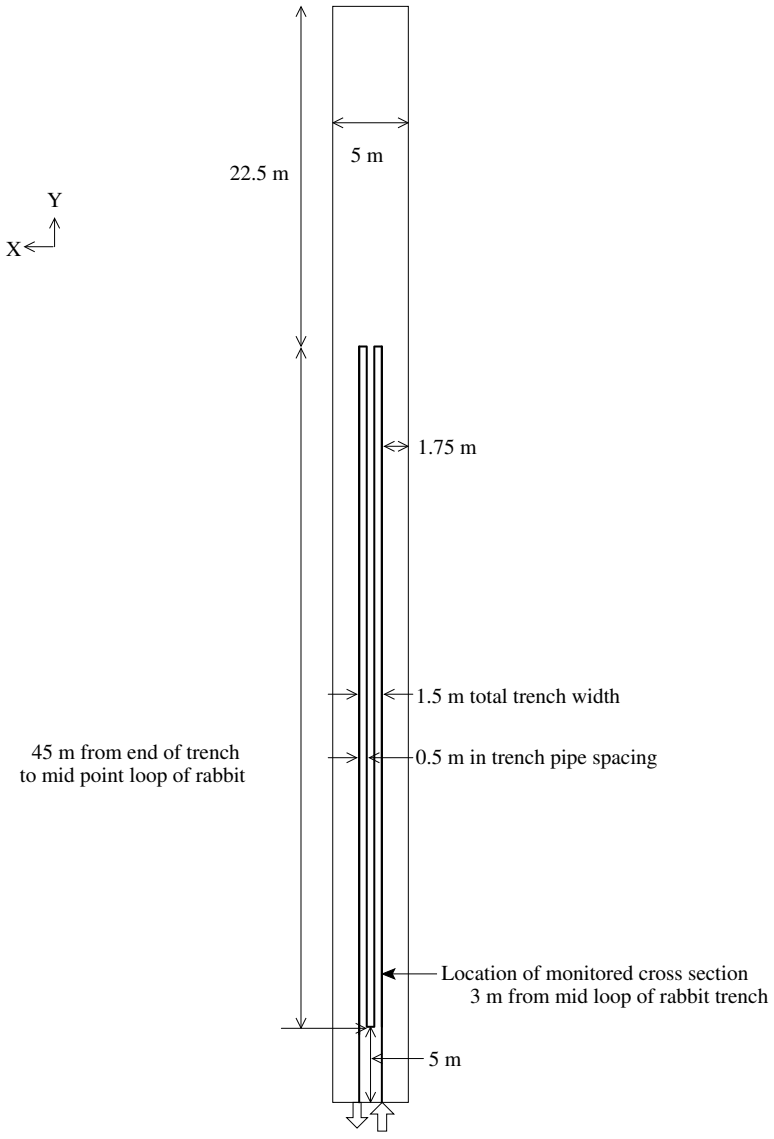

Figure 3.6: Narrow trench schematic diagram in the XY plane.

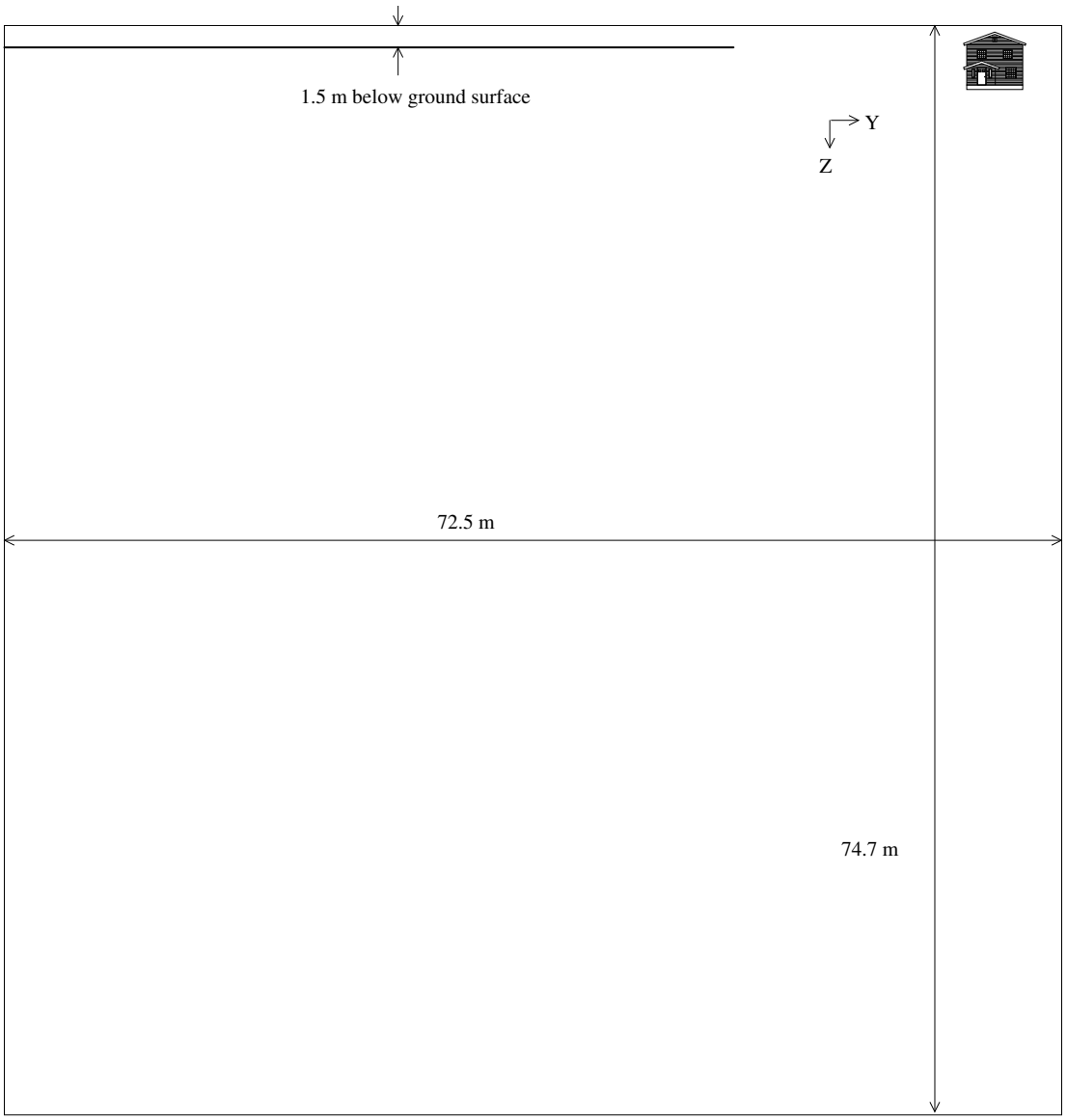

Figure 3.7: Narrow trench schematic diagram in the YZ plane. House illustrates which boundary is the ground surface.

unit inside the house (Haslam, 2013). The rabbit trench is one of six pipe sections coming off the manifold so the energy draw was assumed to be a percentage of the total energy drawn by the HVAC system. The assumed load was 14% of the total load. One sixth ($\sim$17%) of the total load was not assumed because it is plausible that some of the energy from the GLHE is being gained in the manifold and header trench components. The ground surface boundary condition was again assigned as a specified temperature based on measurements of the off pipe temperature sensor closest to the ground surface. This top sensor may not be a good indicator of actual surface temperatures above the rabbit trench because horizontal variations in temperature are likely when an area the size of the rabbit trench is considered. Unfortunately, there was no better source of surface temperature information (see §4.5 for a discussion of the ground surface boundary condition).

Due to the large areal extent of the rabbit loop, the computational cost of the model was quite high. The model included over 60,000 elements for the soil continuum and another 3000 elements for the pipe network. Non-uniform element sizes were used to reduce the number of elements away from the ground loop. As compared to the the run time of model of the first inverse model, the time to evaluate each objective function was very high. A different approach to optimization was required. Instead of the 10,000 runs used previously the maximum number of objective function evaluations was cut to 100. Two optimization problems were solved: one where only thermal conductivity was being estimated, with heat capacity being calculated from the thermal diffusivity determined above; and another with both thermal conductivity and the percentage of the total building energy load handled by this trench. The percentage load was assigned to be 14% of the total load. The two optimization scenarios were created because the thermal conductivity and heat capacity, with the ratio between them fixed by thermal diffusivity, are likely to be highly correlated

with the percentage load parameter. DDS runs were created for each of the conductivity only and conductivity and load runs. Another algorithm, *fmincon* (part of the MATLAB optimization toolkit), was evaluated for use as an optimization algorithm but was not used because it was found to have difficulty determining a gradient with the inverse trench objective function.

The thermal conductivity was assumed to be between 0.25 $\frac{\mathrm{W}}{\mathrm{m \cdot K}}$ and 3.00 $\frac{\mathrm{W}}{\mathrm{m \cdot K}}$ and the percentage load was assumed to be between 8% and 30% of the total (Haslam, 2013).

The intention was that, with the presence of a source term, it would be possible to estimate the magnitude of the soil thermal conductivity and heat capacity given that the diffusivity had already been estimated from the vertical profile model.

Results

The best objective function values and the associated estimated parameters are presented in Table 3.5. The size of the objective function indicates the magnitude of the deviation of the model from the field data (using sum of squared error). Two soil continuum domains were considered: narrow and wide (Figure 3.8). The narrow domain contains the trench and simulates soil temperatures 1.75 m to either side of the trench (Figure 3.6). Because of the narrowness of the domain and the boundary conditions for the subsurface, the model will behave as if there are two equivalent trenches on either side of the modelled trench.

In the wider domain, the model provided a slightly better fit to the field data with the objective functions being consistently lower by around 5×10^3 (Table 3.5). The better objective function translated to a 0.03 °C improvement to the average absolute error between the modelled temperatures and the observed field temperatures. This suggests that the

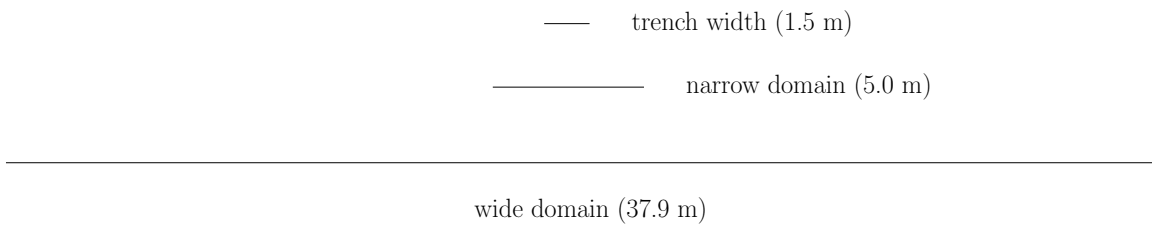

Figure 3.8: Narrow and wide inverse soil continuum domains relative sizes. The trench width is included for scale.

near-infinite domain (Figure 4.3) used in this run was a more accurate approximation of reality than the limited domain used in the narrow runs. However, the parameters estimated in narrow domain were very close to the parameter sets estimated using the wide domain. This closeness in parameter sets supports that there was minimal horizontal energy flux at 5 m away from a GLHE trench that has been operated for 400 days. See Figure 3.11 for an example timeseries comparison between the modelled data and the observed field data. Full results are presented in Appendix G.

The DDS - Conductivity run (wide) estimated a conductivity of 1.20 $\frac{\mathrm{W}}{\mathrm{m \cdot K}}$, which would suggest a saturated clay-like soil. The DDS - Both run (wide) estimated a conductivity of 2.86 $\frac{\mathrm{W}}{\mathrm{m \cdot K}}$, which would suggest a saturated sandy soil. When compared to substances and aquifers presented in Appendix J the first value is well within expected values whereas the later value is outside of the literature soil values.

For the conductivity only runs, the estimated thermal conductivities were in the the middle of the range of expected conductivities. For the runs where both conductivity and percentage load were being estimated, the values of thermal conductivity and percentage load were in the high end of their parameter ranges. This was likely due to the lack of independence between the parameters. If the estimated thermal conductivity is corrected by the factor that the percentage load is different from the fixed percentage load, more

Table 3.5: Parameter estimations runs based on the trench model

Run Name	Best Obj. Function $\times 10^5$	Avg. Abs. Error °C	Objective Function Count restarts x count	Thermal Conductivity $\frac{W}{m \cdot K}$	Percentage Load %
narrow domain, 400 day optimization					
DDS - Both	2.002	1.207	2x100	2.99	29.4
DDS - Cond.	2.064	1.233	2x100	1.29	14.0
wide domain, 400 day optimization					
DDS - Both	1.957	1.176	2x100	2.86	29.9
DDS - Cond.	2.019	1.205	2x100	1.20	14.0

reasonable thermal conductivities values appear. The following example calculation is using values from the wide domain DDS - Both estimation:

$$\text{adjusted conductivity} = (\text{est. conductivity}) \times (\text{fixed \% load}) \div (\text{est. \% load}) \tag{3.3}$$

$$1.34 \frac{W}{m \cdot K} = 2.86 \frac{W}{m \cdot K} \times 14\% \div 29.9\% \tag{3.4}$$

which much more closely matches the estimated 1.20 $\frac{W}{m \cdot K}$ estimated in the wide domain DDS - Conductivity only run.

The outputs of both models were examined using the optimal parameter sets estimated by DDS. Observations at some calibration locations matched the optimally parameterized model more closely than others. Generally, the closer a location was to the GLHE or the ground surface, the model did a better job of recreating the temperatures observed at those locations. The model had particular difficulty with the temperatures below the ground loop, with the model systematically simulating soil temperatures 5 °C colder than observed in the field. Full results and further discussion of these runs are presented in Appendix G.

It was a possibility that there were differences between the surface conditions and/or the ground structure of the rabbit loop cross section and the off-loop vertical profile. If vertical profiles had been available at multiple locations around the field site it may have been possible to estimate the variation that could be expected by having a vertical profile at a different location.

The effect of uncertainty in the location of the field sensors was not examined. Locations of the probes were carefully surveyed when they were installed and positions were known to within an inch (Haslam, 2013). However, the processes of backfilling the trenches could have moved the sensors beyond this range.

It is difficult to explain the estimation of 29.9% load found in the DDS - Both run. This load was approximately was the load the loop was expected to carry (there are six 1-ton loops in the GLHE network at the field site, so $\sim$16% was expected) and was very close to the upper bound of 30% placed on the optimization algorithm. The rabbit loop may be taking more than a sixth of the load at the site but it is unlikely that it would be taking this much more than that. The more likely explanation is that the there is a direct correlation between the pipe load and the thermal conductivity of the surrounding soil. Since the thermal diffusivity was fixed, the only parameter being optimized around the pipe was amount of energy required to affect a temperature change in the adjacent soil. A higher heat capacity would have had an equivalent effect as a decreased pipe load (see calculation in Equation 3.4).

3.4.2 Four trench system

An inverse model was created that included four trenches with geometry similar to that of the trenches in the field site. The size of the modelled domain was increased to nearly double that of the wide domain, used for the single trench, to accommodate all four trenches. The trench with the observation points around it was still placed within a highly discretized part of the mesh, however, the three other trenches were in a coarser part of the mesh. It was hoped that the presence of the other loops, adjacent to the highly monitored rabbit trench, would have made it possible for HEN to more accurately match the temperature timeseries observed in the field. The model domain and pipe network are presented in Figure 3.9 and 3.10.

The pipe network for this four-trench model includes a full manifold with a reverse-return header. The pipe sections in the non-observation trench that run perpendicular to the direction of the trench were removed to limit oscillations that can arise from the presence of elbows in the network. The pipe model automatically balances the loads between the trenches so that if one trench is generating a larger temperature differential than its neighbours it will be supporting more of the network's total load.

Two parameter estimations were performed with parameters similar to the previous section. The first was with thermal conductivity and percentage of total field load as targets. The second had thermal conductivity only as the target parameter. The range of thermal conductivity considered remained the same as the single trench system, from 0.5 $\frac{\mathrm{W}}{\mathrm{m \cdot K}}$ to 3.0 $\frac{\mathrm{W}}{\mathrm{m \cdot K}}$. Percentage loads were increased to 56% of total system load for the fixed load case, four times that of the single trench load; the range of loads considered when the load was set to variable was from 20% to 66%.

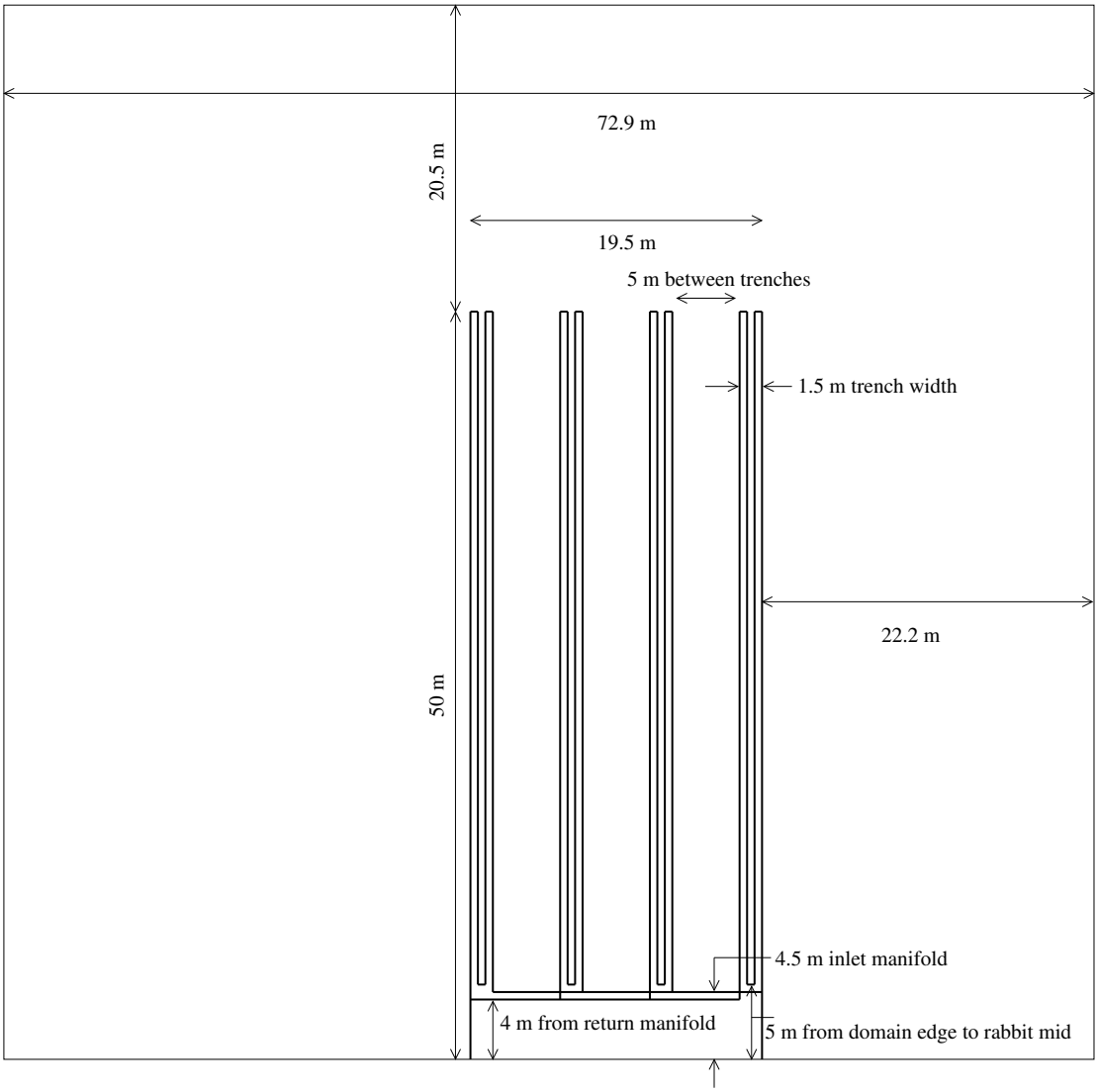

Figure 3.9: Four trench inverse model diagram in the XY plane.

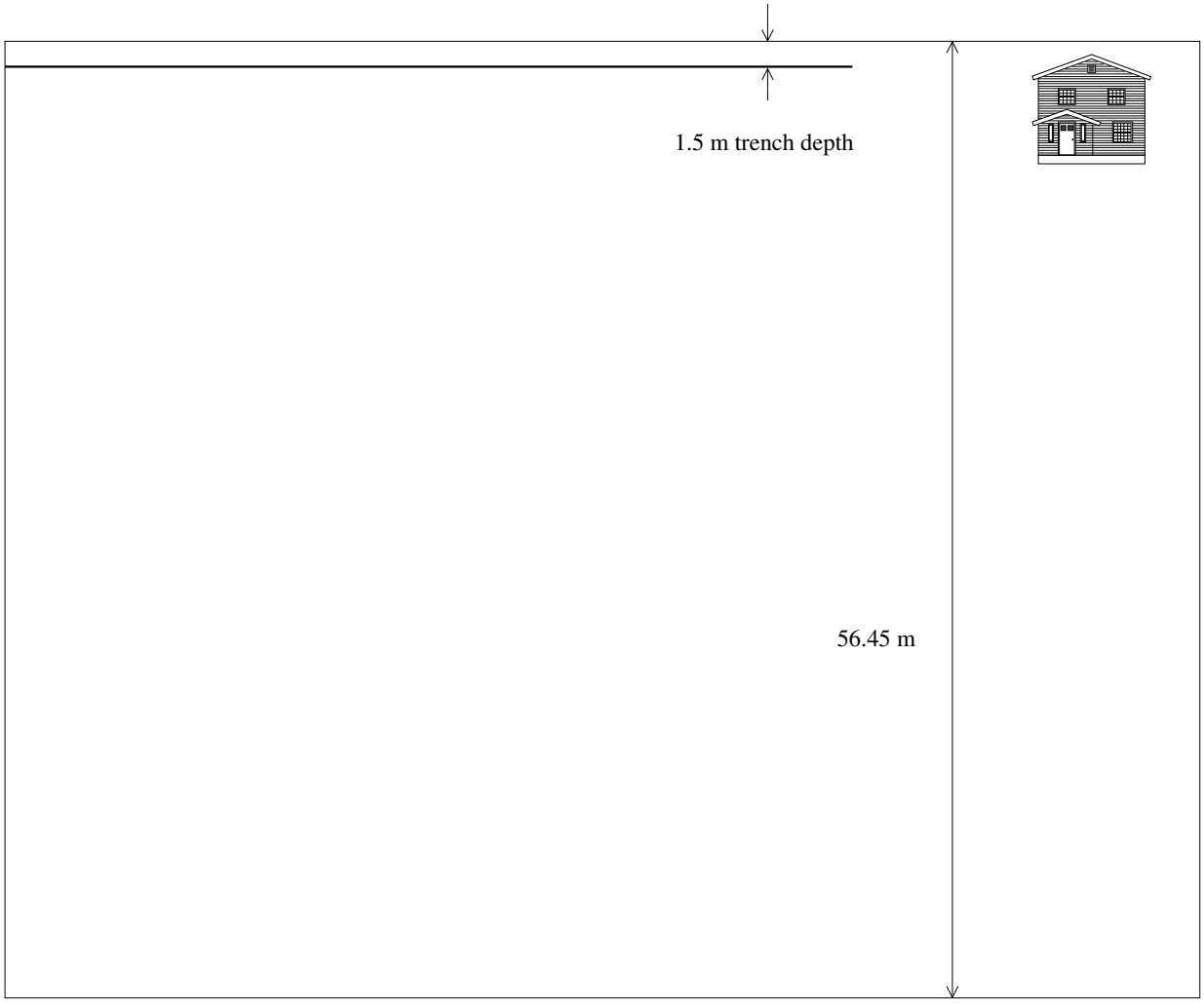

Figure 3.10: Four trench inverse model schematic diagram in the YZ plane. House illustrates which boundary is the ground surface.

Table 3.6: Parameter estimations runs based on the four trench model

Run Name	Best Obj. Function $\times 10^5$	Avg. Abs. Error °C	Objective Function Count restarts x count	Thermal Conductivity $\frac{W}{m \cdot K}$	Percentage Load %
DDS - Both	2.125	1.256	2x100	1.1338	65.3
DDS - Cond.	2.157	1.261	2x100	0.9497	56.0

Results of the four-trench parameter estimation are presented in Table 3.6. When it came to recreating the field observations, these models appear to perform worse than single, narrow trench inverse models but better than the single, wide domain trenches (Table 3.6). The visual difference between the four trench simulated timeseries and the single trench simulated timeseries was minimal (Figure 3.11) manifesting as a slight increase in yearly temperature varitation when going from the single trench to the four trench. This left the best method for comparison as the value of the optimal objective function. None of the structural problems seen in the previous runs appear to be alleviated by the inclusion of the three trenches beside the monitored trench. As with the single trench estimations, the load and conductivity runs produced slightly tighter fits than their conductivity only equivalents.

A simple model such as the single trench model will not always outperform a complex model such as the four trench model (Hill, 2006). When a more complicated model under performs a less complicated model it suggests that the conceptual model of the system used in the complex model is somehow flawed, and the addition of more complex processes hinders the ability of the complex model to approximate reality.

In conjunction with the previous inverse trench results, the four trench run seems to suggest that there are noticeable effects from having a pseudo-infinite domain or otherwise the narrow domain trench would be the best fit. The wide trench domain had the best fit,

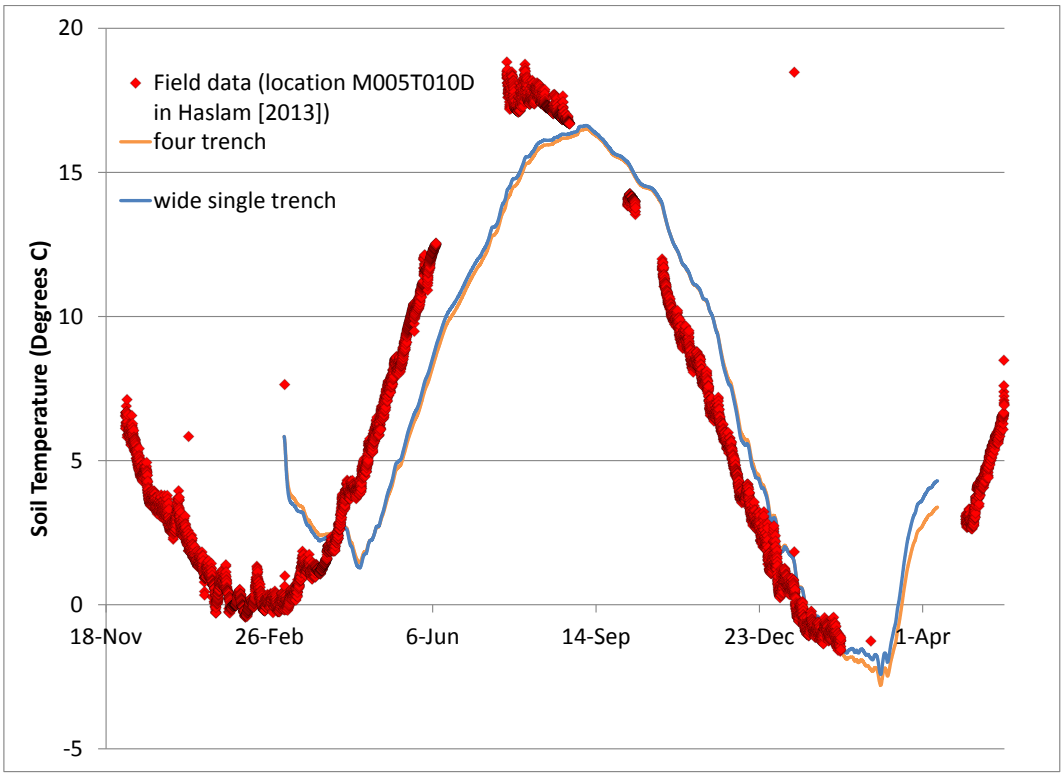

Figure 3.11: Temperature timeseries for field location approximately 10 cm beneath the inlet pipe (Haslam, 2013). The four trench results were taken from the four trench DDS - Both run; single trench results from the single wide trench DDS - Both run. Both modelled timeseries were created using their respective estimated optimal parameter sets.

implying that trench to trench interactions were less important than the inclusion of far field areas.

The pipe-to-pipe interactions may not be quite physically correct in the four trench simulation. The simulated temperature-time profiles of the sensors that are towards a slinky trench (Haslam, 2013), away from the monitored rabbit loop, appear to more closely match the observed timeseries as the model runs using the narrow domain. The four trench simulation appears to perform well initially but the simulated timeseries diverges over time.

The coarseness of the mesh around the outer trenches may have enhanced the effect that the adjacent trenches had on the monitored trench. This could cause the temperature of the simulated temperature field that lies between the trenches to be too low, making the four trench model fit poorly.

The only certain observation that can be taken away from this calibration exercise is that adjacent trenches, even if they are spaced 4.5 m apart as they are in the field site, can interact in a level that is at least measurable through modelling and parameter estimation.

3.4.3 Fit to pipe temperatures

While the fit to the field temperatures appear to be amicable, HEN had difficulty recreating the thermal profiles of the geoexchange fluid. Parameters estimated by DDS runs minimizing the difference between the simulated GLHE outlet temperature and temperatures observed at the Elora field site came up with field conductivities that were much higher than realistic soils ($> 3.5\ \frac{\mathrm{W}}{\mathrm{m \cdot K}}$) and percentage loads which were too low to be reasonable (<10% per loop on a 6 loop system, implying the manifold and header trench are responsible for 40% of the total energy). Even with these unrealistic parameters the fit

to the field data was poor. An alternative approach was taken. The field sensors were assumed to be affected by the temperature inside the house, and that this effect could be accounted for with a simple correction scheme, allowing for a tighter fit between the modelled and observed data. Two correction approaches were investigated. The first was a temperature bump, which took the modelled GLHE temperatures and shifted them all up or down based on a single factor. The second was a linear temperature scale that had the original temperature bump with an added linear scaling factor applied to the temperature. Other parameters for this run, the thermal conductivity and percentage load, were taken from the best wide trench run which was found to be the best fit to the soil temperature sensors.

The objective functions were similar to the original objective function of Equation 3.1 with the addition of new terms and the reduction to a single timeseries comparison. For the temperature bump runs the objective function becomes:

$$J(bump) = \int_{t_s}^{t_e} \left((T_{\text{modelled}}(t, \mathcal{C}) + bump) - T_{\text{field}}(t) \right)^2 dt \tag{3.5}$$

and for the temperature scale runs,

$$J(bump, scale) = \int_{t_s}^{t_e} \left((scale \times T_{\text{modelled}}(t, \mathcal{C}) + bump) - T_{\text{field}}(t) \right)^2 dt \tag{3.6}$$

where the parameters *bump* and *scale* are two new parameters in the optimization algorithm. Note that a positive *bump* means that the temperature simulated by HEN was lower than the observed field temperatures. It was difficult to put constraints on these optimization parameters as they did not have physical analogues. The *scale* was expected to be around 1 and the bump was expected to be close to 0 °C. The temperature *bump* was

constrained to fall within -5 °C and 10 °C. Temperature *scale* was constrained to be within 0.1 (one tenth of the temperature range) and 2 (double the temperature range). These two new objective functions had the benefit of only requiring a single HEN evaluation from which all the outlet temperatures could be scaled, therefore the number of objective function evaluations was increased to 10,000 from the previous 100.

Note that the T_{field} considered in both objective functions was the temperatures seen by the heat pump when the GLHE was active. Field data was also available for when the GLHE was inactive but the inclusion of inactive periods would be less correct than excluding them because of the way HEN simulates the GLHE as always being in the active state.

Results

The original modelled timeseries, created from the optimal estimated parameters found in the wide domain DDS - Both run, for the EWT was generally too cold (Figure 3.12). Temperatures in the modelled timeseries only matched the observed field EWT for a brief period at the start of the cooling season in late October and early November. The application of an optimal temperature bump significantly improved the fit, and the application of a linear scale to the modelled EWT improved it further (Table 3.7). Despite the improvement of fit gained by scaling the EWT timeseries, neither scaling technique fully captures the pattern of the field data (Figure 3.12). The use of the temperature bump overestimated the EWT in the field from August through November and underestimated it in the heating season of January and February. The linear scaling underestimated the EWT during the recovery period through June, July, and August, then overestimated it at the start of the cooling season. Both of the scaling techniques were likely negatively affected

by the presence of outliers in the field data; field data outliers that were warmer than the equilibrated loop temperatures would have skewed both scaling runs upward making the fit between the non-outlying field data and the scaled EWT timeseries poorer.

Table 3.7: Scaling factors optimization results

Run Name	Best Objective Function $\times 10^4$	Avg. Abs. Error °C	Objective Function Count restarts x count	*scale* (−)	*bump* °C
DDS - Bump	1.4527	1.325	2x10,000	1.00	2.87
DDS - Scale	0.6910	0.909	2x10,000	0.76	4.18

Should the original EWT timeseries have been close to an optimal match of the field data the temperature bump would have been estimated to be approximately zero and the temperature scaling factor would have been estimated to be approximately one. From Table 3.12: the optimal temperature bump was found to be 2.87 °C and the optimal temperature scale was 0.76 (with an associated bump of 4.18 °C). These parameters show that HEN was likely underestimating the absolute EWT and overestimating the range in which it oscillates every year. Some of this difference may have been due to the difference in the way that HEN measured EWT and how EWT was measured in the field. EWT in HEN was measured as the temperature of the fluid inside the GLHE as it enters the building and the loop pump was simulated as always being on. EWT in the field was measured as the temperature of the outside of the pipe entering the HVAC unit and the loop pump ran intermittently as required (Haslam, 2013). Insulation was placed around the field sensor in an attempt to isolate the sensor from the indoor temperatures and the field data was parsed so that only temperature measurements taken while the loop pump was running were used. Even with these two precautions taken, the observed field data showed outliers skewed in the direction of the indoor temperature ($\sim$ 21 °C). It is possible

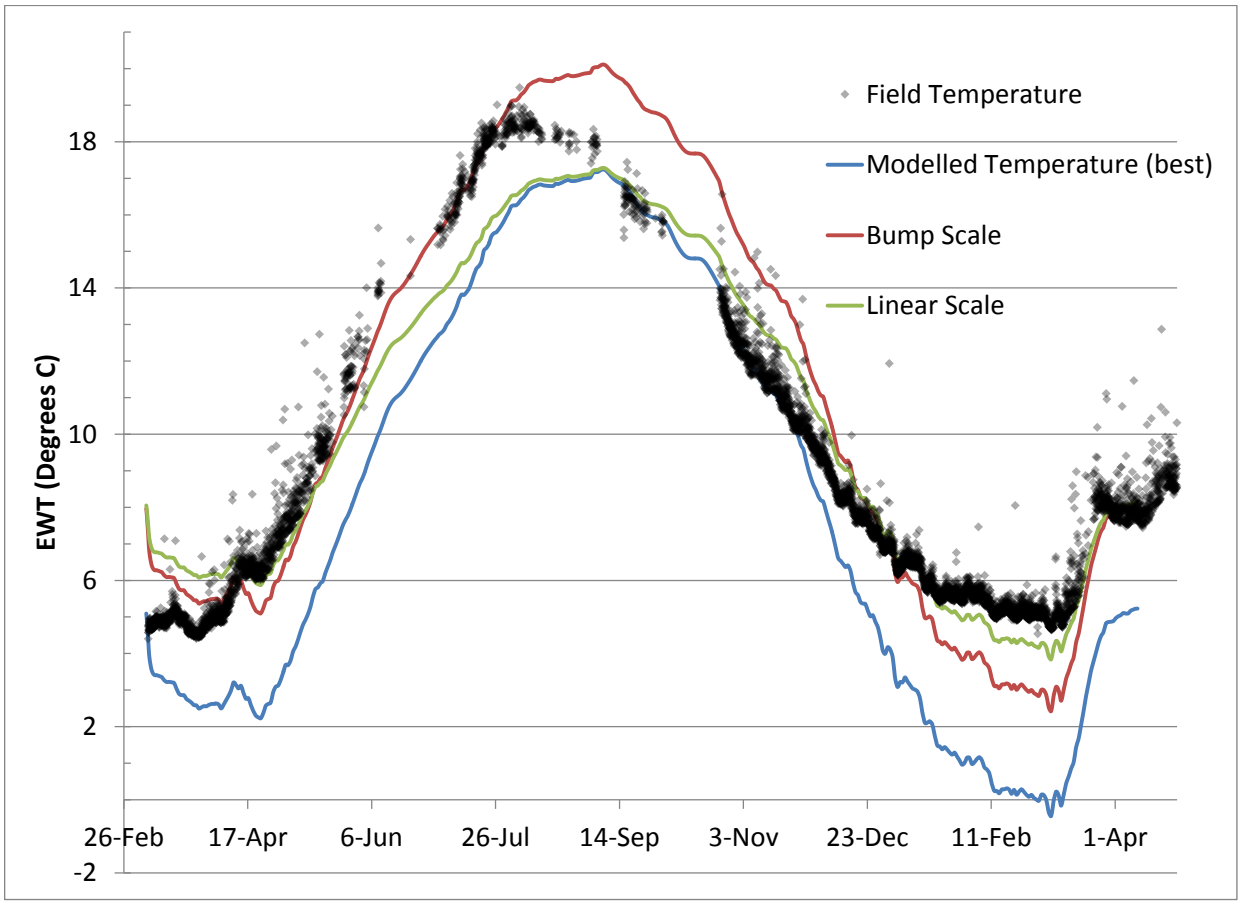

Figure 3.12: Temperatures for the best single trench run compared against observed temperatures in the field. The two scaled temperatures match the field data much more closely. Note the outliers in the field data are likely taken before the temperature at the sensors has equilibrated with the temperature of the loop.

that the indoor temperature and the loop pump cycling make a direct comparison between the loop temperatures measured in the field and those simulated by HEN an inappropriate basis for an objective function.

The parameters collected in this scaling estimation should not be used to scale the temperatures in HEN. They have been used here as a means of investigating where HEN may be lacking in its ability to simulate a real-world EWT timeseries. Importantly, the general trends of the EWT timeseries created by HEN appear to do a reasonable job of recreating an observed timeseries. Only a simple scaling is required to make the modelled data closely match the observed field data, suggesting that HEN is capturing much of the physical processes of horizontal GLHE operation.

3.5 Conclusion

Thermal models of the subsurface around the Elora field site (Haslam, 2013) are capable of reasonably approximating the temperatures seen in the field site. This suggests the the physics included in HEN are representative enough to simulate thermal profiles around GLHEs. The problem of recreating observed soil temperatures with a numerical model is a difficult one. A perfect match would require a model simulate many complex physical processes and be perfectly parametrized. Given the somewhat inconsistent and error-prone field data (Haslam, 2013), this may be an impossibility. HEN still performed well, suggesting that conductive heat flow was the dominant form of energy movement in the shallow subsurface and around GLHE at the Elora field site.

The effective homogeneous parameter values of the soil at the field site were more difficult to ascertain. The optimal parameters estimated in this section were close to the

conductivity and heat capacity values being used by GLHE designers, suggesting accuracy in the parameter estimation experiment and that local GLHE experts have a good grasp of soil conditions.The complexity of the problem and the inter-related variables make getting precise and accurate estimates of heat capacity and thermal conductivity difficult without a controlled thermal response test.

The model matched some of the observed temperatures well and others poorly. There are physical mechanisms that, although secondary to the main physical mechanism of conduction, were likely coming into play in a way that makes them difficult to ignore when considering year-long timescales. The simplification of the surface boundary as a fixed temperature boundary, the lack of phase change (the model tended to get overly cold in winter, likely because latent heat of phase change was not included as an energy source), and water flow within the subsurface limit the ability of the model to match the observations.

Some options in this parameter estimation investigation were not exercised due to computational constraints. The trench depths could have been a target variable. Sensor location uncertainty could have been taken into account. Thermal diffusivity could have been estimated using the sensors around the trench as well as the off loop sensors. It was not clear that any one of these items would have significantly improved the model fit but a future, more in-depth analysis should take into account these variables.

This procedure of inverse modelling is similar to TRTs done by geoexchange installers. As discussed in Raymond et al. (2011a), a pump and heat source are attached to a GLHE to circulate heated fluid through the loop. Temperatures of inlet and outlet fluids are monitored. These temperatures can then be analysed and fit to analytical solutions such as the various line-source models. Through this type of test, the installer can often determine

the effective thermal conductivity and heat capacity of the subsurface. These tests can be highly accurate with thermal conductivity being estimated to within 7% of its actual value (Raymond et al., 2011a). The parameter estimation discussed in this chapter gives parameters that produce a much poorer fit to observed data when compared to TRTs. TRTs have the benefit of having a known heat flow rate which is either constant or highly controlled. This contrasts with conditions at the Elora field site (Haslam, 2013) where loads vary at the whim of the homeowner. TRTs are also conducted over a limited time period, which means that the assumptions which go into a line-source model are rarely violated. Again, this contrasts with the 400 day timeperiod considered in this investigation where it is not appropriate to neglect inter-pipe and surface effects..

A secondary objective of this parameter estimation was to evaluate the capability of HEN to simulate temperatures in the soil around a GLHE. While it appeared to be missing some physical mechanisms of heat transfer and storage, the model performed well in general, matching basic trends in the observed data set. The final test of HEN was to see if this ability to simulate the soil temperature field meant that the model could also accurately simulate the temperature of the geoexchange fluid where it was found that scaling factors were required.

Figure 3.12 shows geoexchange temperatures simulated in the optimized single trench system plotted against the hourly average of the temperatures seen coming into the HVAC system. The modelled temperatures clearly start cold, the load from the HVAC system is ramped up over the first day, and continue to get colder throughout the simulation. It may be that the physical mechanisms discussed as being missing play a crucial role in recharging the temperature immediately adjacent the pipe and the model diverges from reality because of this omission.

The exact matching of the simulated and observed temperatures was not expected. The field observations are hourly averages of a system that was turning on and off over potentially much shorter intervals. These rapid on/off switches were not simulated by HEN, which was supplied with the daily heat load of the building. The pump in HEN was treated as always being on and the temperatures of the GLHE fluid were always in equilibrium with the soil, whether there was heat required by the HVAC system or not. With the field monitoring equipment, most of these rapid on/off events were captured (Haslam, 2013). When the system was on it was extracting an instantaneous load that would have been higher than the load simulated in HEN, which meant that the temperatures in the field data should have been more extreme than the simulated temperatures. Figure 3.12 shows that the measured heat pump inlet temperatures oscillated over a relatively thick band, whereas the simulated temperatures did not oscillate over short timeperiods. These extremes were mitigated by the averaging of the field data into 1 hour chunks, but the band over which the field data oscillated should have, in theory, been wide enough that the simulated data would fall within it. Referring to Figure 3.12 this is clearly not the case. In early time the model was systematically too cold, which could be acceptable as model parametrization could be adjusted to compensate for systematic differences, but then the modelled EWT timeseries falls within in the band of field data around September of the first year of operation before falling well below the band as heating season began in late November. During the late spring and early fall months the GLHE spent a large portion of its time off because no heating was required (Haslam, 2013). The more important timeperiods were the winter months where the full capacity of the GLHE was required. The temperature timeseries produced by an optimized HEN model for the second winter of operation was clearly too cold.

The temperature of the ground loop appeared to get progressively cooler (Figure 3.12). This observation of the simulated temperature results may be due to the extremely imbalanced nature of the load on the GLHE. Assuming no energy recharge through the top boundary, a quick back-of-the-envelope calculation shows that if the ground loop is run at the loads measured at the field site for a period of 400 days then the temperature of a 7 m X 4 m X 50 m volume will have to drop by 6 °C to generate the required energy. This is close to the temperature drop seen in Figure 3.12 but is an unfair explanation because HEN includes temperature recharge through the ground surface boundary condition. This quick calculation assumes that the block of soil would have its temperature lowered uniformly, which is not physically correct because the temperature should have to drop by a greater amount immediately adjacent to the pipe relative the temperature drop farther away from the pipe.

To summarize, HEN was deemed capable of simulating vertical and horizontal heat transfer in the soil continuum around the GLHE at the Elora field site (Haslam, 2013). With these capabilities, HEN is a useful tool for evaluating loop interference and design. Where the model fell short was in recreating heat pump inlet temperatures seen by the HVAC system. Further study would be required to determine if this misrepresentation of the GLHE temperatures is something that was systemic of the way HEN was designed or if it was because the GLHE temperature were not one of the optimization targets of the original parameter estimations and soil temperature was insufficiently correlated to in-pipe temperature.

Chapter 4

Performance of horizontal GLHEs in heterogeneous soils

4.1 Introduction

Soil thermal conductivity and heat capacity are typically assumed to be completely homogeneous when modelling GLHEs (e.g. Esen et al. (2007); Eskilson (1987); Giardina (1995); Ingersoll and Plass (1948); Mei (1986)). The use of uniform thermal properties throughout the model domain makes the problem of modelling geothermal systems much more tractable by reducing the parameterization required for a model run and improving the mathematical properties of the underlying system of equations. Analytical models of heterogeneous systems are rare and, when they do exist, are for limited specialized applications.

Measurements of field properties, when available, are averaged using an appropriate technique to get a representative property value for the entire system. Bundschuh and

Arriaga (2010) list 8 different methods for averaging geological parameters in heterogeneous environments; selection of a good averaging technique requires knowledge of the orientation of the heterogeneities. In soil, thermal properties are traditionally averaged through the use of the harmonic mean (Johansen, 1975).

The use of the homogeneity assumption has been justified in the past by a cursory examination of a sufficiently large block of soil placed between two constant temperatures acting as a thermal resistor. The thermal resistance of characteristics of the soil block can be shown to be equivalent to that of a homogeneous medium with a certain thermal conductivity, despite the heterogeneity of its internal structure. However, this assumption is only valid for systems where the sources and sinks are separated from one another on a scale that is much greater than the scale of heterogeneity.

The impact of heterogeneous subsurface thermal properties on horizontal ground loop performance has not been examined in detail before. Vertical heterogeneities have been shown to impact thermal fluxes in the subsurface (Shen et al., 1995). Signorelli et al. (2007) examined the influence of vertical heterogeneities on results of a vertical borehole thermal response test (TRT) using a line source model. They found the inhomogeneous case would return a higher or lower effective thermal conductivity depending upon whether the TRT was performed using heat injection or heat extraction, and that the ordering of the heterogeneities affected the TRT. The investigation was limited to two layers, vertically stratified. Signorelli et al. (2007) estimated that the heterogeneous test cases showed the resulting conductivity from a homogeneous case was generally within 10% of an equivalent heterogeneous case that had two layers: the first of conductivity 2 $\frac{\mathrm{W}}{\mathrm{m \cdot K}}$ and the second of conductivity 4 $\frac{\mathrm{W}}{\mathrm{m \cdot K}}$. Fujii et al. (2009) developed field techniques capable of evaluating these heterogeneities in vertical boreholes. Ferguson (2007) conducted a study of the impact of

heterogeneous hydraulic conductivities on the performance of open loop systems. In his study, Ferguson assigned soil thermal conductivities as a random, normally distributed, variable with no spatial correlation. He found that heterogeneity increased the effective thermal diffusivity of the subsurface. None of these studies dealt with horizontal loops. No prior investigations on the impacts of heterogeneity on the performance of horizontal GLHEs were found by the author.

To understand the relative importance of the impact of heterogeneity, its impact should be compared to other causes of performance uncertainty. In a review of TRTs using concepts from the field of hydrogeology (Raymond et al., 2011a), the typical uncertainty associated with the measurement of soil thermal conductivity was estimated to be $\pm 7\%$ on a measurement of 2.5 $\frac{\mathrm{W}}{\mathrm{m \cdot K}}$. Since TRTs are rarely applied to horizontal systems, this level of uncertainty associated with the measured thermal conductivity can be thought of as a minimum level of uncertainty that must be shown to exist to be able to conclude that structural heterogeneity of soil thermal properties is impactful on the overall performance of a horizontal GLHE.

When a GLHE designer plans a loop installation, the soil thermal properties of interest are heat capacity and conductivity. In this work conductivity can be thought of as "an effective thermal conductivity" after Farouki (1986) which represents heat transfer capability via conduction but implicitly includes some effects of convection and radiation. To simplify the investigation, heat capacity was assigned as a uniform property and conductivity was represented using spatially correlated fields. Holding heat capacity constant while varying thermal conductivity effectively varied the thermal diffusivity of the medium.

Table 4.1: Geostatistical terms and symbols.

Term	Symbol	Description
lag	h	Distance from the reference point, typically the horizontal axis of the variogram chart.
correlation length	a	Lag at which the semivariance achieves a plateau. This parameter is sometimes referred to as the integral scale.
sill	c	Semivariance value of the plateau.
nugget	n	Semivariance at zero distance due to subscale variability.

4.2 Geostatistical terminology

It was assumed that the properties of the subsurface may be represented as a spatially correlated random variable. Statistical tools may then be used to create 3D fields of soil thermal properties in the area around the GLHE.

Variograms are functions that provide an expression for the spatial dependence of a spatial random field (Kitanidis, 1997) expressed as a monotonically increasing semivariance as a function of distance between sampling points. A list of the relevant geostatistical terms is provided in Table 4.1.

Multiple variograms models exist and each represents the spatial correlations in a slightly different manner. The most often encountered are spherical, exponential, Gaussian, and power. In this study, exponential was the selected to be the base variogram model (See §4.3 for discussion). Spherical and Gaussian variograms were also investigated.

These have the forms (Deutsch and Journel, 1992):

$$\text{Exponential: } \gamma(h) = c\left(1 - \exp\left(-\frac{h}{a}\right)\right) \tag{4.1}$$

$$\text{Spherical: } \gamma(h) \begin{cases} = c\left(1.5\frac{h}{a} - 0.5\left(\frac{h}{a}\right)^3\right), & \text{if } h \leq a \\ = c & \text{if } h > a \end{cases} \tag{4.2}$$

$$\text{Gaussian: } \gamma(h) = c \cdot \left(1 - \exp\left(-\frac{h^2}{a^2}\right)\right) \tag{4.3}$$

Variograms have directionality. For a full, three dimensional representation of variability three orthogonal variograms are required. In the study of soil, the two variograms that describe the horizontal plane were assumed to be equivalent, the vertical variance can be very different from horizontal variance so this direction often has its own variograms. The resulting field had spatial variations in all directions and was vertically anisotropic with respect to correlation length.

4.3 Geostatistical description of thermal conductivity

In order to assess the impacts of heterogeneity on GLHE performance the heterogeneity of the soil in which the system is installed must first be characterized. The thermal properties of soil vary in space and time. There are more porous and less porous areas; areas dominated by soil organics versus areas dominated by in-organics. In time, the moisture content can fluctuate considerably and changing temperature will cause changes in thermal properties. Most noticeable is the change in thermal properties as the pore water freezes. For the purpose of this investigation, temporal changes in thermal properties were ignored.

One of the challenges with assessing the impact of heterogeneity on horizontal GLHEs was that there have not been any studies looking at the spatial distribution of thermal properties of the subsurface in which a horizontal GLHE would typically be installed. In the past, the lack of information on spatial correlation has meant that authors have either assumed homogeneous conditions (e.g. Fujii et al. (2009)) or non-spatially correlated randomness (e.g. Ferguson (2007)). The only study investigating soil thermal property distributions found by the author was one performed by Usowicz et al. (1996). The study examined 220 measurements of topsoil properties in an agricultural field and analysed them using both classical and geo- statistics. Unfortunately the measurements were only made in two dimensions, without any vertical profiling, and the variograms they collected would not be sufficient for an investigation at the depth of a horizontal GLHE.

A 3D semivariogram description of a property requires the variogram form, correlation length (both vertical and horizontal), nugget effect, sill value, mean, and anisotropy ratio be known. Since the literature was lacking in the information required for this investigation, reasonable assumptions were made. To check the impact of these assumptions, multiple values of all semivariogram parameters, except nugget effect and anisotropy ratio of the correlation length, were considered.

The nugget effect was assumed to be zero. Because the model used for this study only accepts discrete thermal property values for block elements this assumption was effectively superficial. Adjacent element blocks were far enough apart (5 cm) that near field correlations (or lack of correlation) could not be observed.

The thermal conductivity of the soil around a GLHE can be expected to be within the range of 0.25 - 2.20 $\frac{\mathrm{W}}{\mathrm{m \cdot K}}$ (see Appendix J). Mean conductivities ranging between 0.5 - 1.5 $\frac{\mathrm{W}}{\mathrm{m \cdot K}}$ were considered here as the thermal conductivity in shallow horizontal systems is

generally expected to be lower than the thermal conductivity around deep vertical systems. Deeper systems are typically fully saturated and drilled into consolidated material whereas shallow systems are above the water table and place in unconsolidated sediment. Due to the lack of prior investigations, putting a boundaries on what the sill values could be was more challenging. Sill values considered were 0, 0.1, 0.2, 0.4, and 0.6 $\frac{\mathrm{W}}{\mathrm{m \cdot K}}$. The sill value 0.2 $\frac{\mathrm{W}}{\mathrm{m \cdot K}}$ was taken from the topsoil study by Usowicz et al. (1996) by squaring the standard deviation that they found. The thermal diffusivity, and from it the calculated heat capacity, were taken from parameters estimated in the inverse modelling chapter (Chapter 3).

The field of hydrogeology has long considered spatial heterogeneity of subsurface properties to play an important role in groundwater transport phenomena (Sudicky, 1986; LeBlanc et al., 1991; Dagan, 1994). This importance has led to multiple studies detailing comprehensive statistical models of hydraulic conductivity and permeability (Rehfeldt et al., 1992; Woodbury and Sudicky, 1991; Mohanty et al., 1991). Empirical relationships using parameters such as grain size, porosity, and grain orientation can provide good approximations of hydraulic parameters (Schwartz and Zhang, 2002). These variables are very similar to the variables that are used in empirical equations for thermal conductivity and heat capacity in the de Vries (1963) model. It was assumed here that spatial distributions of soil components that cause spatial variations in hydraulic conductivity would cause variations in thermal conductivity at a similar spatial scale.

The variogram form found in the studies considered was an exponential type. Limitations in the software being used to generate the fields in this study prevented the author from evaluating alternative variogram models. The vertical and horizontal correlation lengths of Rehfeldt et al. (1992) were selected as the most appropriate: 1.6 m in the vertical axis and 12.8 m in the horizontal axes. A non-spatially correlated field was considered.

This field had correlation lengths of 0 m for both the vertical and horizontal. Other correlation lengths such as the 5.1 m horizontal and 0.64 m vertical from the study of Woodbury and Sudicky (1991) were not used because of the highly homogeneous nature of the Borden sand being investigated.

All statistical distributions were considered to be normal Gaussian. Usowicz et al. (1996) found that, with a sample size of 220 measurements, there was a skew of 0.274 and a kurtosis of 1.929 for thermal conductivity. The skew is small enough that it was neglected in this study. The kurtosis value indicates that the distribution of values is more clustered around the mean than a true Gaussian distribution.

4.4 Synthetic model of soil thermal conductivity heterogeneity

Working with the theoretical ranges of thermal conductivity and the variance structure from hydrological properties, a synthetic statistical model of thermal conductivity was created (Table 4.2) which was used as a basis for the generation of ensembles of heterogeneous thermal conductivity fields.

Table 4.2: Synthetic model

Parameter	Value
Model Type	Exponential
Sill	0.2
Nugget	0.0
Correlation length (horizontal)	12.8 m
Correlation length (vertical)	1.6 m

Conductivity fields were realized in three dimensions. The grid was oblong, 10 cm

across by 125 cm long by 10 cm deep. The longest axis was in the same direction that the pipes were laid out in the field. This was done to limit the number of elements for the numerical modelling of the soil and to improve the resolution of the model radially around the pipe. These elements covered a volume that was 54.4 m across by 72.5 m long by 74.7 m deep (see Figures 4.3 and 4.4 for a schematic diagram of the model domain). For reference, the amount of soil that would normally be excavated to install a 600 foot GLHE pipe in a rabbit orientation would be 1.5 m across by 45 m long by 1.5 m deep. The realized fields were made up of over 20 million elements.

The software GSLIB (Deutsch and Journel, 1992) was used to create the spatially correlated fields. To ensure that a thermal conductivity field that respected the correlation lengths listed in Table 4.2 could be simulated with the spatial bounds of a typical GLHE a test case was created. The sill value was normalized to 1. GSLIB reproduced the theoretical variograms well when considering smaller domains. Figure 4.1 shows the modelled field compared against theoretical variograms and the match was quite good. Unforunately, when the full scale field was simulated the modelled field variograms did a poor job of recreating their theoretical counterparts (Figure 4.2). The blue and black lines, which are nearly co-incident, on this figure are two separate realizations of the same field using different seeds which were supposed to conform to the theoretical variogram represented by the red lines.

GSLIB appeared to have difficulty reproducing the theoretical variograms when larger fields were considered. Part of the difference may have been attributable to the tools used to analyse the generated fields provided by GSLIB, but after a quick check of the overall standard deviation it became clear that the problem was in the field itself. The standard deviation for the runs in Figure 4.2 are 0.879 and 0.866 for the blue and black

lines, respectively. The square of those standard deviations nicely matches the sill value of the chart. The means of the resulting fields were both within 0.004 from the targeted mean.

The field generated by GSLIB clearly does not match the theoretical variograms that was parameterized to produce. All correlation lengths and standard deviations given in this chapter should be taken as parameters to GSLIB rather than actual theoretical variogram parameters. No attempt was made to correct the fields to fit the variogram. A naive approach of scaling the field to increase the sill value would mean that the variograms would not match at the small distances. As such, no scaling or other correction techniques were applied to the generated fields.

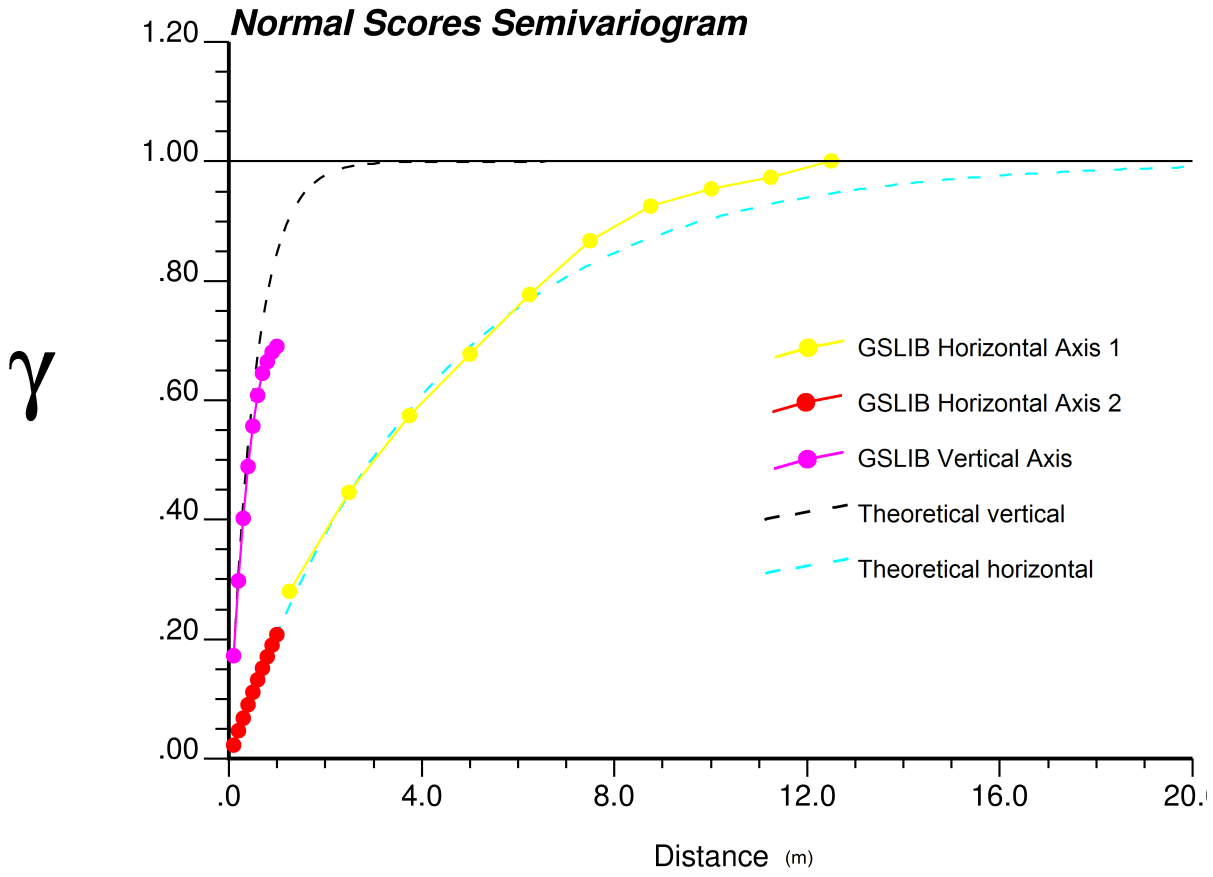

Figure 4.1: Theoretical variograms compared with variograms calculated for a field with a coarse discretization at small scale.

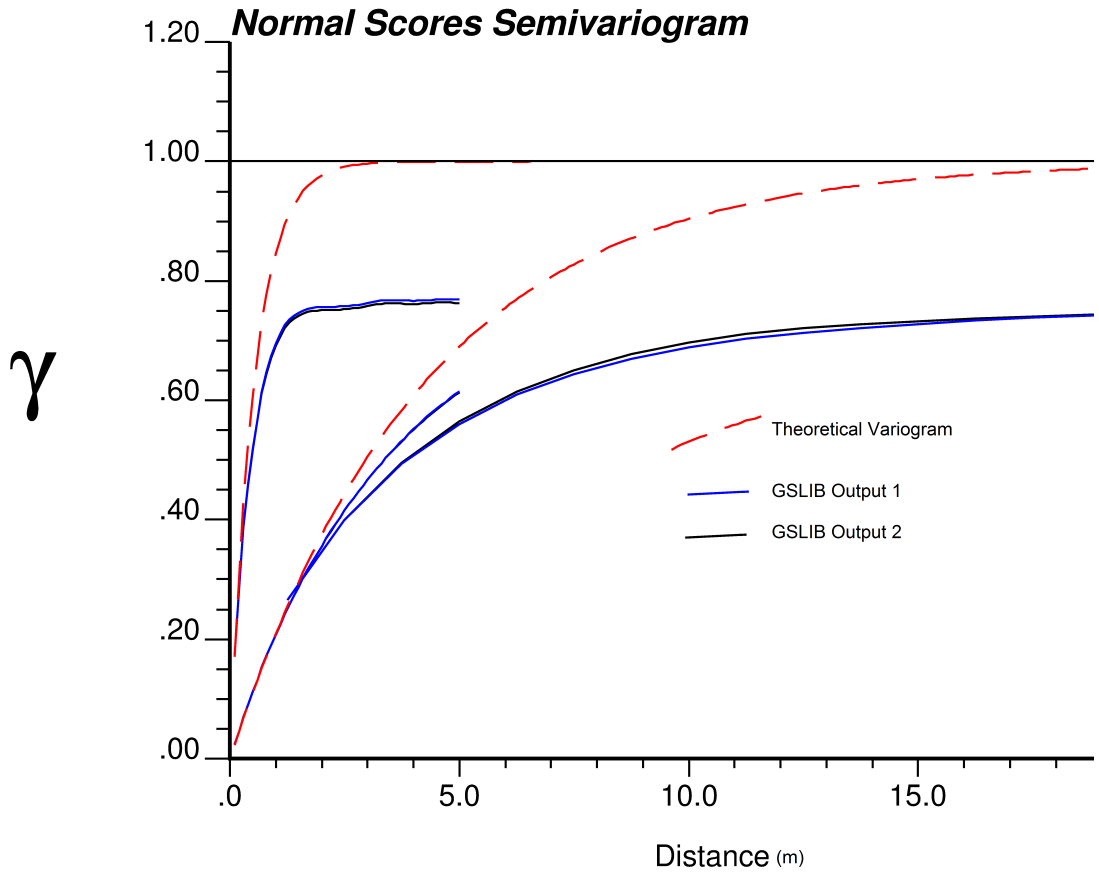

Figure 4.2: Theoretical variograms compared with variograms calculated for a large field at full scale.

4.5 Computational model of the GLHE

The hypothetical GLHE being simulated using the HEN model was a single rabbit loop in a 45 m long trench with a 5 m lead from the edge of the model domain (see schematic diagram of the model domain in Figures 4.3 and 4.4). This configuration was loosely modelled after that of the Elora field site (Haslam, 2013). Recall that HEN was created with the purpose of being used for heterogeneity investigations using full pipe geometry (see Chapter 2). The trench was 1.5 m wide and buried to a depth of 1.5 m. Pipe thermal properties were taken to be those of high density polyethylene pipe. A 80% water/20% ethanol mixture was used as the heat exchange fluid. Loads to the pipe were prescribed as being one seventh (14%) of the total loads seen at the Elora Field Site (there are 6 loops coming off a single manifold with a long header trench), loads typical of a retrofitted brick farmhouse in southern Ontario (§2.6) (Haslam, 2013).

The surface boundary was a Dirichlet condition, prescribed by the temperature time series collected by the shallowest sensor at the Elora Field Site (Haslam, 2013). All other boundary conditions were no flux (Neumann) conditions. The domain was made large enough that, over the time periods simulated, the field around the GLHE would behave as if there was an infinite horizontal domain. The geothermal flux coming up from the earth is small enough that it can be ignored for horizontal installations (see §2.2.6). The initial temperature of the soil was determined by running the model, without the pipe, for three months with only the forcing function of the surface temperature. The resulting thermal field used as the initial condition had vertically varying temperatures.

The physical dimensions of the simulated domain match the domain being generated in GSLIB. The 23 million individual elements of the conductivity file would be overwhelming

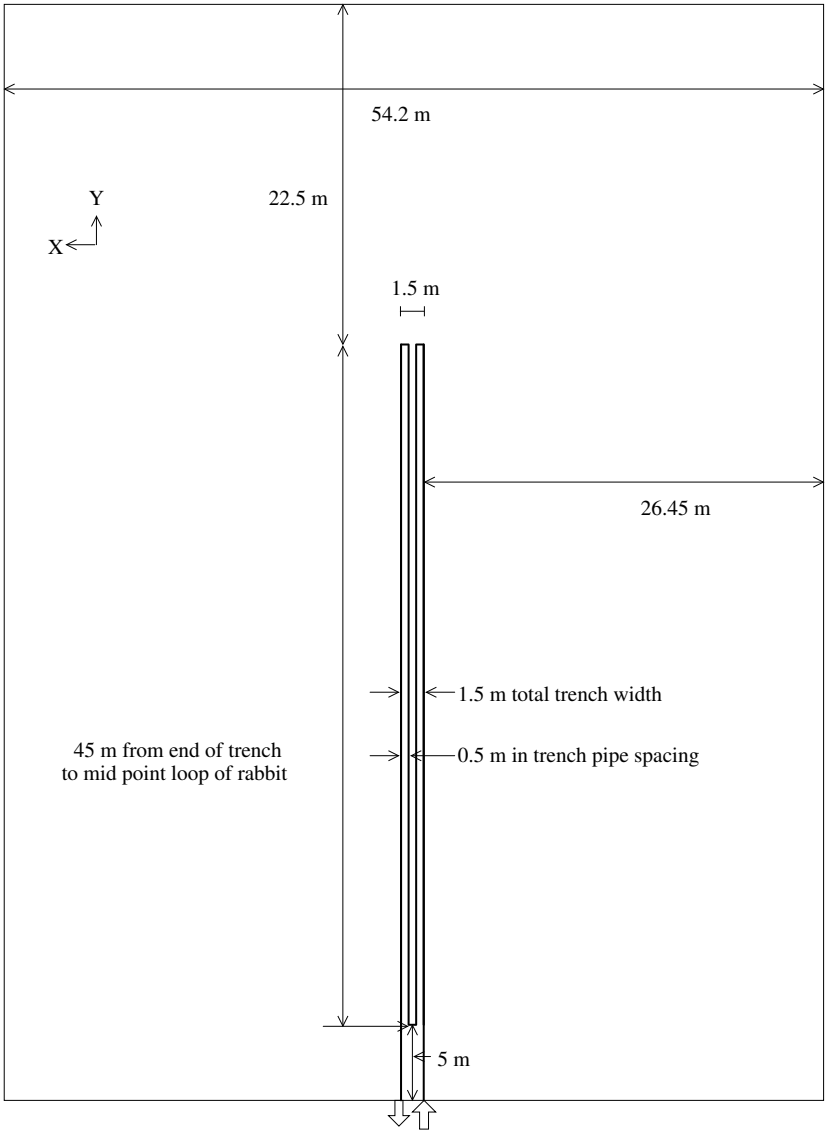

Figure 4.3: Single trench schematic diagram in the XY plane.

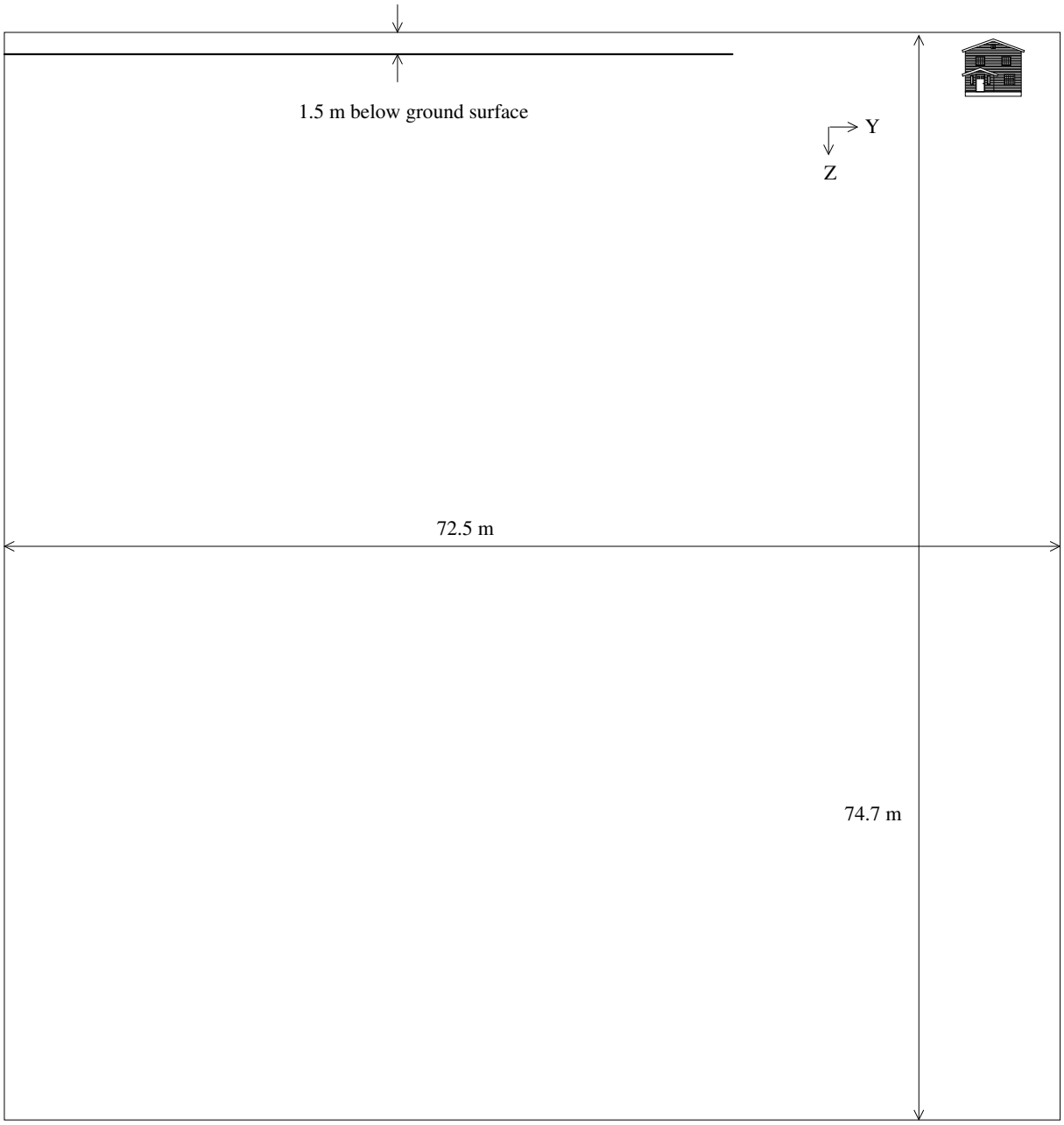

Figure 4.4: Single trench schematic diagram in the YZ plane. House illustrates which boundary is the ground surface.

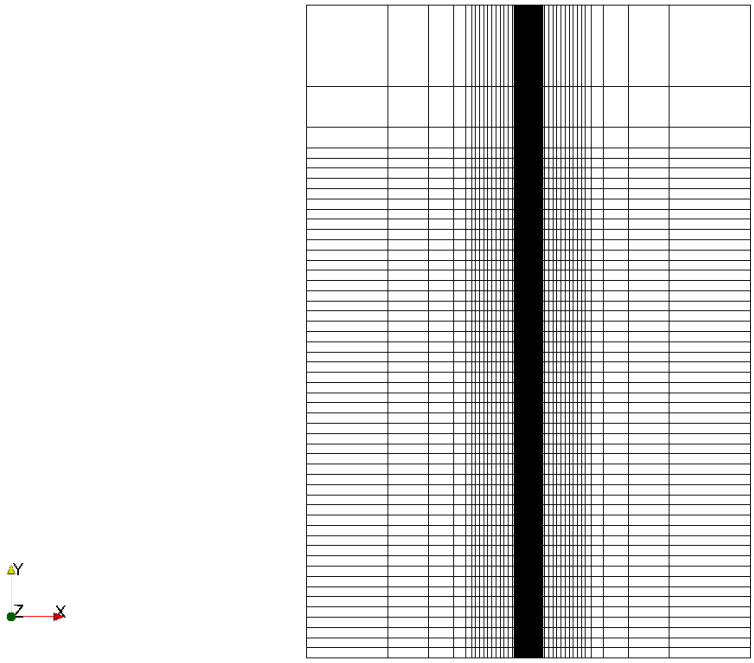

Figure 4.5: Element grid in the X-Y plane in which the ground loop is buried

for a transient computational model and as such the generated conductivities were upscaled to fit a non-uniform grid (Figure 4.5), which was coarse near the edges of the domain and match the discretization of the conductivity values in the immediate area around the pipe. For the grid cells which were large enough to contain multiple GSLIB elements the harmonic mean of the thermal conductivities was assigned. The non-uniform grid contained 115,056 degrees of freedom.

The time period being simulated was 365 days beginning the 7^{th} of March, 2011, using a timestep of 30 minutes. Entering water temperatures (EWT) to the heat pump were output hourly and were used as a basis for comparison between conductivity field realizations.

The temperature profiles away from the pipe in the X and Z directions were also

recorded. For each heterogeneity realization, two HEN runs were performed: one with the pipe present and one without the pipe. The differences in the temperature fields caused by the presence of the ground loop was then examined to determine the specific influence of the GLHE.

The systematic generation of conductivity fields with GSLIB and running of models was facilitated through the use batch scripts and the model execution framework OSTRICH(Matott, 2010). OSTRICH, originally designed for running optimization algorithms on models, was used for its scalability and flexible configuration.

One of the concerns in assessing the impact of heterogeneity was whether the scale of heterogeneity investigated could be properly resolved by the model. A grid convergence test was conducted to determine an appropriate element size to investigate the heterogeneity fields. The outputs of models using element faces from 60 cm by 60 cm through 5 cm by 5 cm were examined and it was determined that outputs converge to a sufficient level when the element faces were 10 cm by 10 cm.

A series of runs were constructed to find an appropriate element size to investigate the fields. The element size was refined downward from 60 cm by 60 cm faces to 5 cm by 5 cm faces with convergence being found suitable at 10 cm by 10 cm faces. The 10 cm by 10 cm model faces were used in this study.

Shocks from the initial soil temperature profile in the soil continuum model, resulting from the inclusion of heterogeneity, were found to dissipate to a level where they had no discernible impact on EWT within 1 day of simulation time. On a 365 day simulation, the initial condition would have a negligible effect on GLHE performance analysis.

4.6 Analysis techniques

4.6.1 Cost analysis

Two metrics were used for comparing relative performance of GLHEs over the year. The first was the average COP value, and the second was the annual expense of running the GLHE. Due to the nature of heat pump performance curves, a direct comparison of entering water temperature between various heterogeneity realizations was not considered the most appropriate method of comparison. Instead, the EWTs calculated by the model were processed to determine the corresponding effective heat pump COP (see the heating and cooling COP curves in Figures 4.6a and 4.6b). The wattage requirement of the HVAC system was then divided by the COP and aggregated to determine the total energy required to extract/inject thermal energy. This can be written as:

$$\sum_{time} \frac{\text{Wattage Requirement}}{\text{COP from Curve}(EWT)} = \text{Aggregate Wattage Used} \tag{4.4}$$

Note that this method of comparison was not strictly correct. Because of the quasi-steady state approximation, the model could only report the average EWT. However, a more appropriate EWT for determining the COP of the heat pump is only the EWT when the heat pump is running. These running temperatures would have been more extreme than an average temperature that includes the off time between pump cycles. These extreme temperatures were not simulated in the model. If they were, this would lead to lower modelled COPs. However, the method of comparison is still useful because a change in the average temperature indicates there are changes in temperature extremes.

The curve used to determine COP from entry water temperature was taken from a Cli-

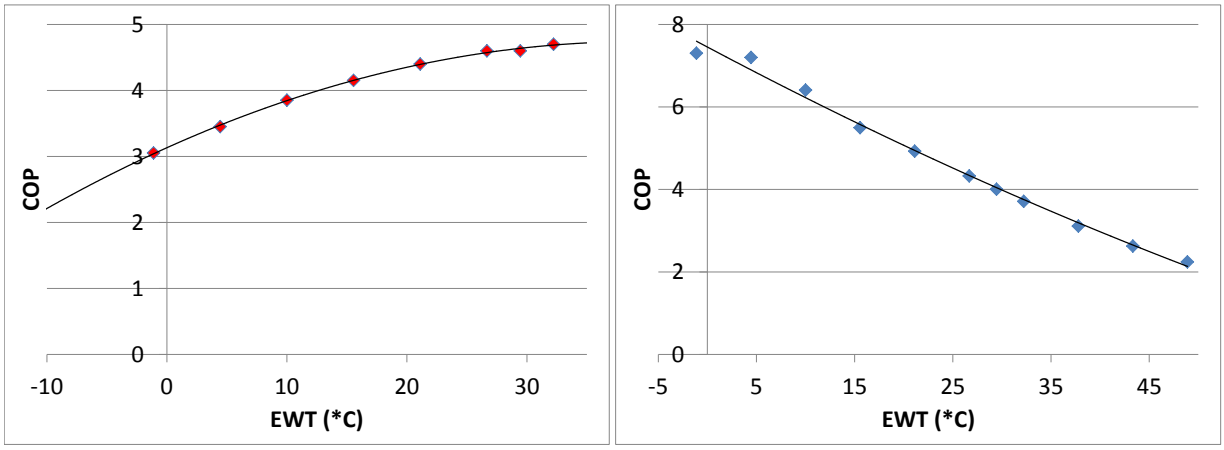

(a) Heating mode (b) Cooling mode

Figure 4.6: COP curves for a ClimateMaster Tranquillity 27® TTV072 Closed Loop Water-to-Air geothermal heat pump heat pump as a function of EWT.

mateMaster Tranquillity 27® TTV072 Closed Loop Water-to-Air geothermal heat pump (ClimateMaster, 2010) (the same heat pump used at the Elora field site (Haslam, 2013)). The flow rate used to select the COP curves was based on the Elora site flow rate (Haslam, 2013). The curve used for when the system was in heating mode followed:

$$\text{COP} = -0.001038 \times EWT^2 + 0.081732 \times EWT + 3.132452 \quad \text{(Figure 4.6a)} \tag{4.5}$$

For cooling mode a reversing valve is used and the heat pump curve changes, following the equation:

$$\text{COP} = -0.000346 \times EWT^2 + 0.104857 \times EWT + 7.383829 \quad \text{(Figure 4.6b)} \tag{4.6}$$

The pertinent curve was selected based on the sign of the wattage load at each time step.

The wattage was also converted to a dollar value by taking a fixed electricity price of \$0.08 per kWh. This conversion puts the loop performance into context. This dollar

amount does not take into account the expenses involved with pumping fluid through the loop or any other load that was not the heat pump. These extra costs are omitted because they may also be temperature sensitive (e.g., the loop pump could be expected to draw more power when the temperature of the geoexchange fluid drops because of the increase in viscosity of the liquid) and by not considering them the investigation could be simplified. Note that the dollar amount only reflects the costs of running one ton of a six ton system. The energy that was modelled to have been consumed by the heat pump was also reported.

4.6.2 Statistical analysis

One of the focus questions of this study was to show the extent to which heterogeneity impacts the performance of the GLHE. A Monte Carlo approach was used to determine statistical significance using formulas detailed in Morgan and Henrion (1992):

$$m = p(1-p)\left(\frac{c}{\Delta p}\right)^2 \tag{4.7}$$

where m is sample size, in this case the number of heterogeneity realizations; p is the percentile being estimated; c is the confidence level, units are in standard deviations from normal; and Δp is the number of percentiles to either side of p that we are trying to be confident the percentile is between. So to be 95% certain ($c = 2$) that the actual 90th percentile is between the estimates of the 85th and 95th percentile ($\Delta p = 0.05$) it can be calculated that the number of model evaluations required are:

$$m = 0.10(1-0.10)\left(\frac{2}{0.05}\right)^2 = 144 \tag{4.8}$$

To determine if heterogeneity tends to increase or decrease the performance of a GLHE, it must be shown that the mean of the performance of the heterogeneous runs was different that the performance of a homogeneous run. To accomplish this, refer to the formula from Morgan and Henrion (1992):

$$m > \left(\frac{2cs}{w}\right)^2 \tag{4.9}$$

where w is the width of the range over which we are confident the mean is in and s is the standard deviation of the sample population.

These calculations were performed for every ensemble of heterogeneity experiments to verify that the heterogeneous cases were statistically distinguishable from the equivalent homogeneous case.

Charts of the empirical cumulative distribution functions were created for a variety of GLHE performance diagnostics for the various ensembles being examined. On these charts the means of the heterogeneous runs and their homogeneous equivalents could easily be compared. These charts were used as the standard comparison procedure for all investigations detailed in this chapter.

4.7 Results and discussions

4.7.1 Base case

A base run was created as detailed in §4.4 and §4.5. This base run respected the parameters of a typical ground loop and the soil thermal property fields were parametrized to represent a good approximation for the level of heterogeneity present in the thermal properties of the soil around this typical ground loop.

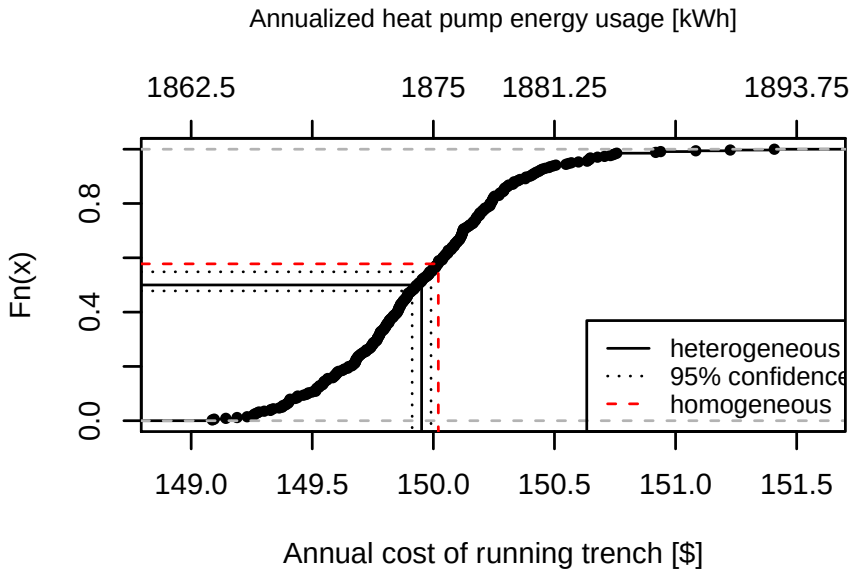

Figure 4.7: Performance data representing the approximate costs of running the base case loop for a period of 365 days

Figure 4.7 shows the ECDF of the performance metric created for this base case. Over the 365 day period being simulated, the expected costs of running the ground loop fall within a $2.50 range about a mean of $149.95. This represents a relatively uncertainty associated with the cost and performance of the GLHE; less than 2% of the total cost of running the loop. The distribution was skewed towards higher costs; there was a long tail above the 95th percentile. The lower 95% confidence interval, which has been selected as its corresponding value on the ECDF line, was slightly closer to the 50% ECDF value than the upper 95% confidence interval. This type of skew appeared in most of the heterogeneous fields examined in this study.

As can be seen in Figure 4.7, the performance statistic for the homogeneous run falls outside of the 95% confidence interval of the mean of the heterogeneous runs indicating that the presence of heterogeneity in soil thermal properties, on average, slightly improved

the performance of a GLHE relative to a GLHE buried in an equivalent homogeneous medium.

The electricity costs of running the GLHE/HVAC system at the Elora field site were $1,444 for the first year of measured operation (Haslam, 2013). Of that, $1,087 went to the electrical costs of running the heat pump. The approximate yearly cost of ∼$900, estimated by multiplying the expected costs from Figure 4.7 by 6 (the number of ground loops present at the field site), was within %20 of the value determined by Haslam (2013). Note that the value from Haslam (2013) was based on field measurements rather than simulated temperatures and COP conversions. The field analysis included time-of-use energy rates and has a much finer temporal resolution.

Appendix I.4 contains full charts of the various performance statistics collected for the base case.

4.7.2 Days of exceedence

When the fluid in a ground loop drops below a certain temperature the loop the loop must be turned off. This is done because it is no longer economical to run the loop at such a low temperature or, more importantly, it can be done to avoid damaging HVAC equipment connected to the loop. Under these conditions, a backup source of heat must be used because the GLHE is unavailable. The use of such backup energy sources is much more costly than using the ground loop and, if no backup is present, then there will be no temperature conditioning available for the attached building. Under less strenuous conditions, it can still be useful to know when the temperature of the fluid returning from the GLHE has dropped below a certain point in order to perform a cost-benefit analysis

of using the loop.

To illustrate the impact of heterogeneity on the temperature of the geoexchange fluid "days of exceedence" charts were created (for an example see Figure 4.8). These charts plot the number of days that the temperature of the GLHE falls below a specific value over the period of one year. The days of exceedence is determined by counting the number of simulated temperatures that are below a given temperature. A log axis is used for the number of days so the lines of the charts are truncated as it is not possible to represent zero days of exceedence. Error bars on this chart represent the bounds that 95% of all runs fell within.

The loads being applied in this investigation were heating dominate in accordance to the Elora field site (Haslam, 2013). For a cooling dominated load, it would be more informative to plot the number of days that the GLHE temperature is a above a certain value.

Days of exceedence is a useful metric even when the ground loop is operating well within its normal temperature range. Comparatively short timeperiods of cold loop temperatures can make a difference between a successful loop design and one that fails when it is needed most.

Figure 4.8 shows the days of exceedence for the base case along with the range in the expected amount of time at each EWT (the range was selected as the 95th percentile of EWTs of the heterogeneous ensemble). The large error bars on the lowest EWT are because many of the runs did not drop to -1 °C at any point, but there was a run that spent an aggregate of 5 days at or below that temperature. The variances in the amount of time spent at each temperature were not strongly correlated to EWT.

The days of exceedence charts shown in following sections, comparing multiple ensem-

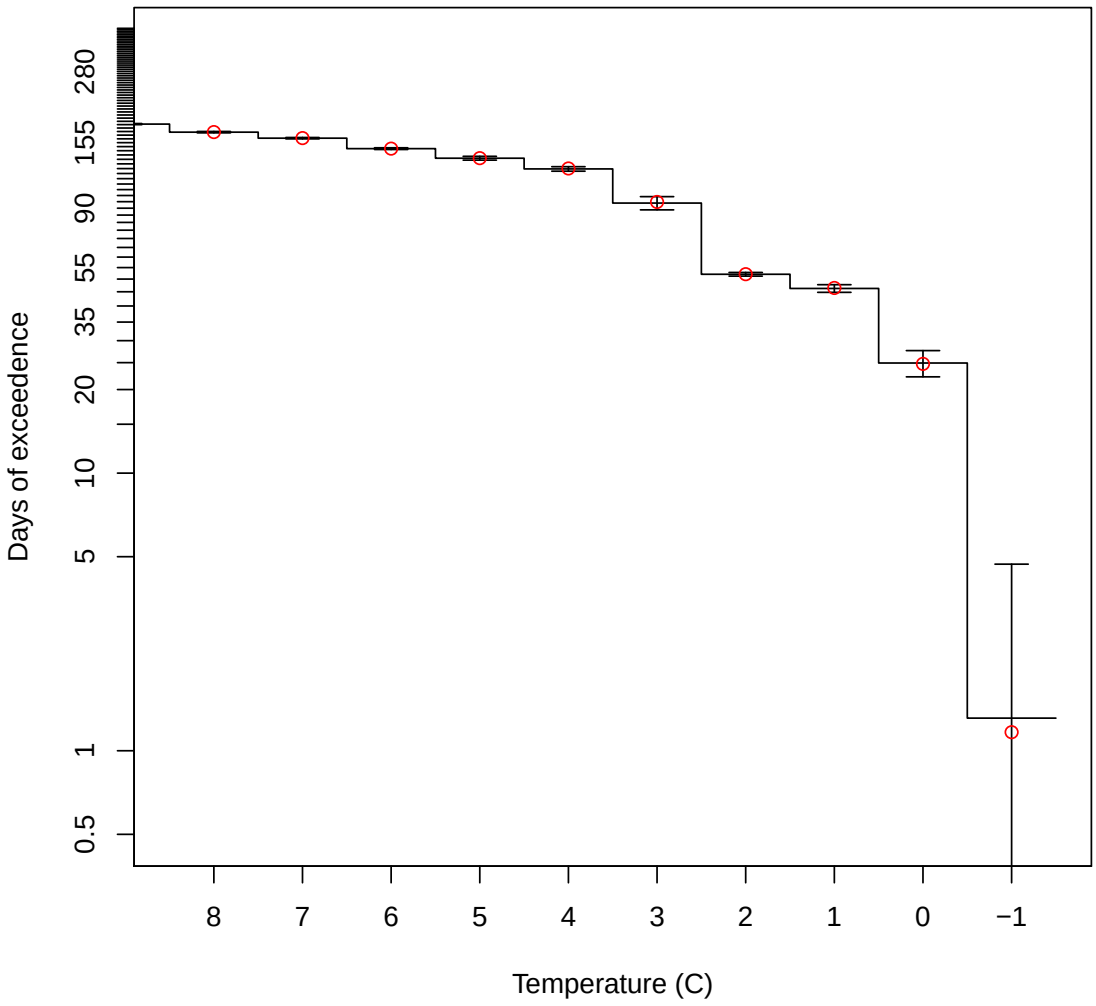

Figure 4.8: Base case: days of exceedence. The bars on the values indicate the 95% confidence interval. The circles are the days of exceedence of the homogeneous run.

bles, are useful for comparing the amount of time during which the GLHE is producing low entering water temperatures. If the relative importance that the GLHE designer places on temperature extremes (freezing) is much higher than general efficiency then overall system then the days of exceedence analysis may be the most important form of analysis. Design decisions that have an effect on the lowest temperatures in the loop may be the most important decisions when systems are not being deliberately over-designed.

4.7.3 Impacts of heterogeneity structure

The soil thermal conductivity distributions for the highest and lowest performing thermal conductivity fields were analysed. The goal was to identify structural properties that made these fields perform better or worse than their equivalent homogeneous field. Figures 4.9, 4.10, 4.11, and 4.12 all show the distribution of thermal conductivity values in various cross sections. The figures were taken from two realizations of the conductivity field, the one that performed best according to the performance metric and the one that performed the worst according to the performance metric. The colour coding indicates how many standard deviations from the mean the thermal conductivity of an element was. A cell coloured deep red was 4 standard deviations higher than the mean, a cell coloured deep blue was 4 standard deviations lower than the mean. The figures in the X-Y plane, 4.9 and 4.10, are in the same plane that the GLHE was situated in. The figures in the X-Z plane, 4.11 and 4.12, are at Y = 18 m which is labelled in the X-Y cross sections as a black line. Relative to the GLHE, the cross sections are just 13 m passed the loop back point on the manifold end of the rabbit loop. The pipe is 1.5 m from the surface in these cross sections.

The worst performing heterogeneity realizations tended to have a high thermal conductivity region approximately at the midpoint of the length of the trench. In Figure 4.10 this

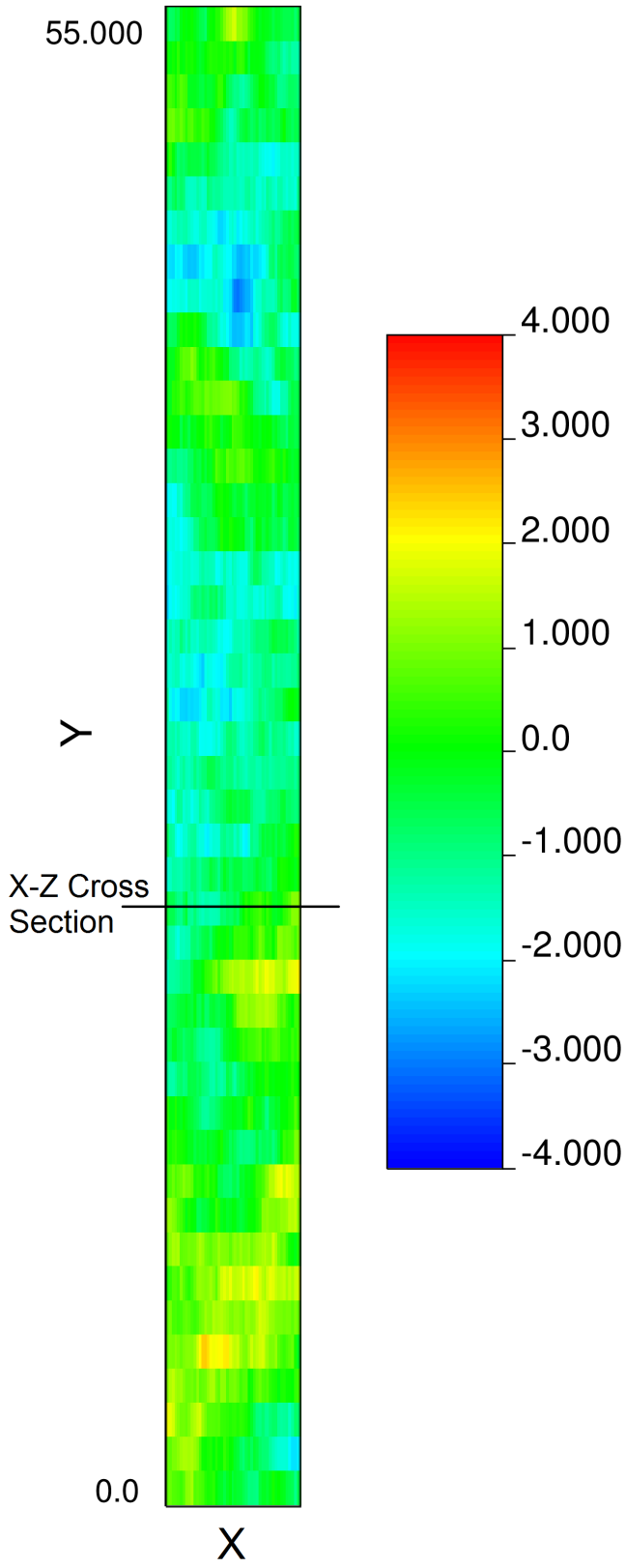

Figure 4.9: XY Cross section of the trench elements at the level of the GLHE (1.5 m) for a high performing run.

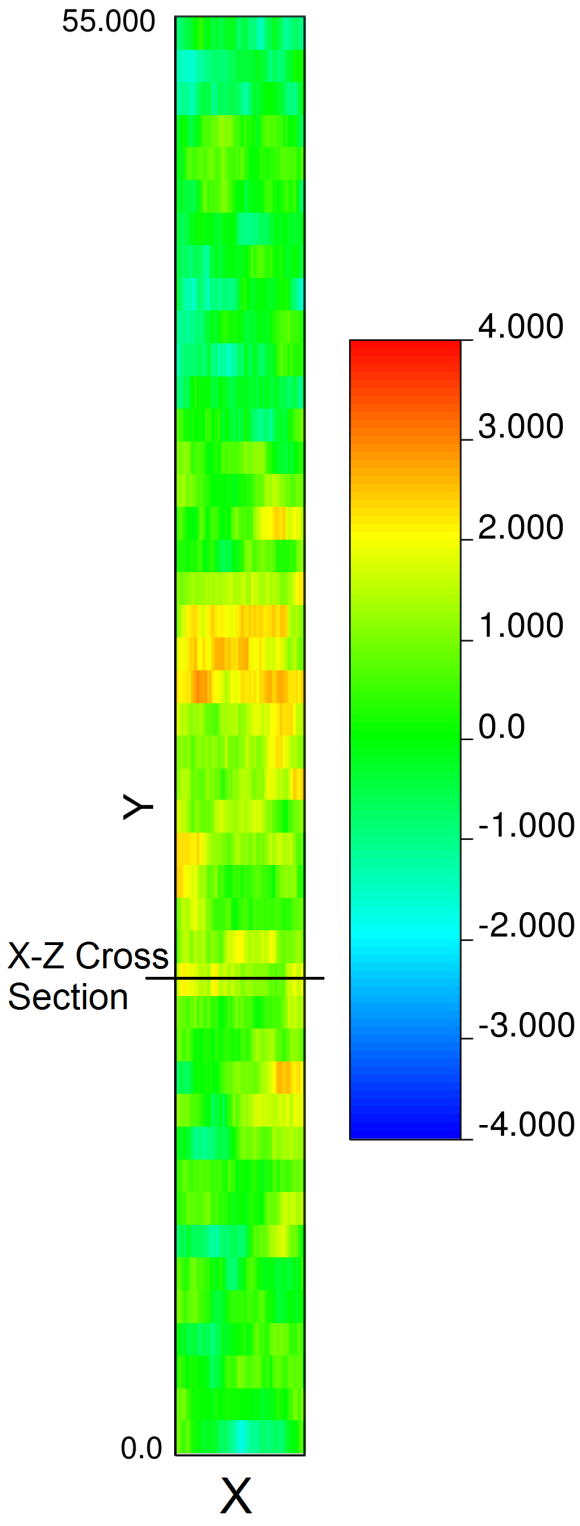

Figure 4.10: XY Cross section of the trench elements at the level of the GLHE (1.5 m) for a low performing run.

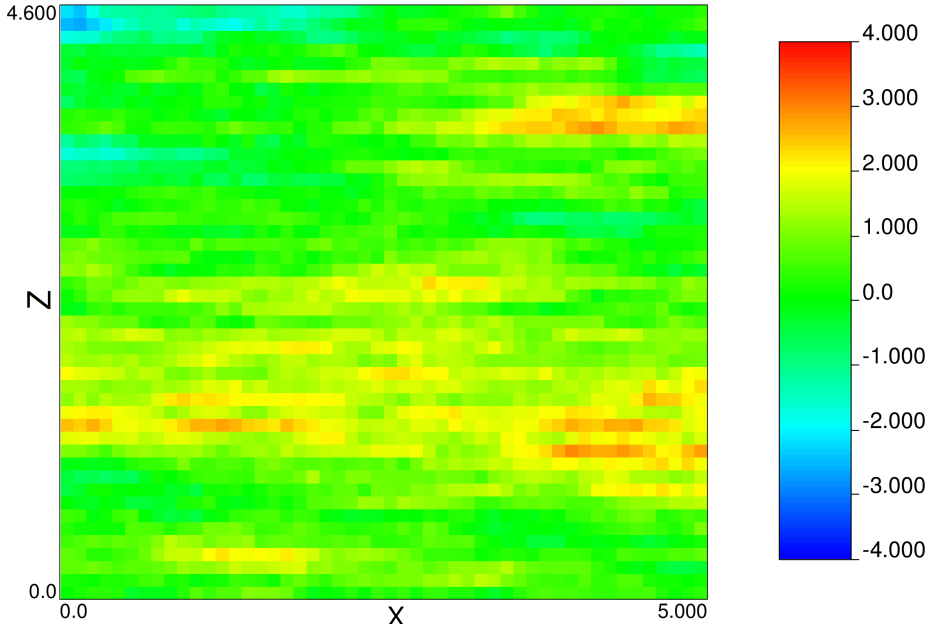

Figure 4.11: XZ Cross section of the trench elements at the level of the GLHE for a high performing run. The cross section is 13 m from the loopback point in the rabbit trench.

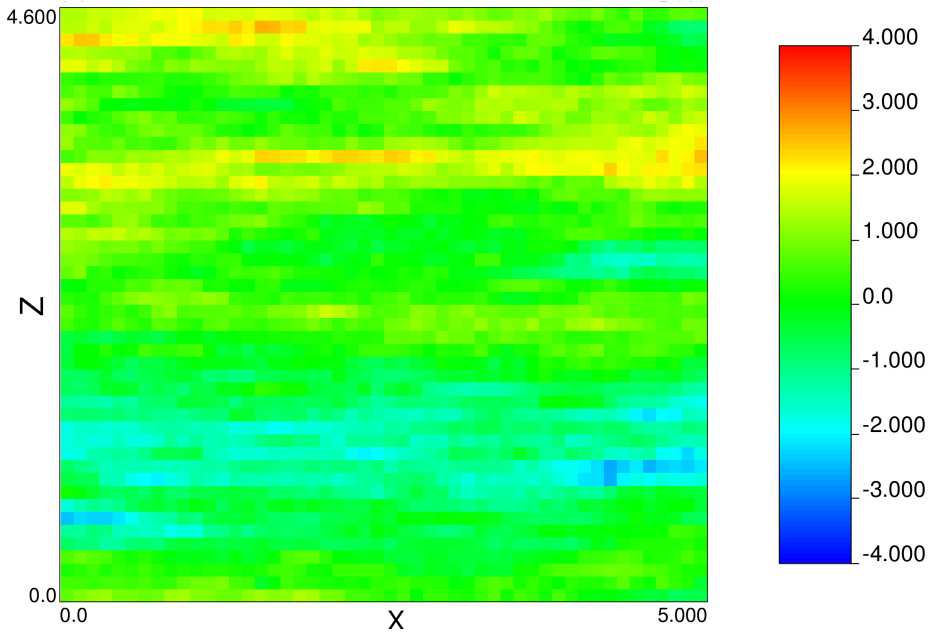

Figure 4.12: XZ Cross section of the trench elements at the level of the GLHE for a low performing run. The cross section is 13 m from the loopback point in the rabbit trench.

region was very pronounced. On average, poor performing realizations also had relatively high thermal conductivity between the surface and the ground loop. This would increase the thermal diffusivity, lowering the thermal resistance between the surface and the ground loop. The increased thermal diffusivity would mean that in the winter, when the surface is coldest, the cold from the surface would be quickly transmitted down to the level of the ground loop. This surface connectivity appeared to play a larger role than short circuiting.

The highest performing realizations did not have obvious zones of high thermal conductivity around the GLHE. There were sections of high thermal conductivity and sections of low thermal conductivity but no one trend dominates the field in the area of the GLHE. Figure 4.11 shows what appears to be a commonality between high performing runs, this realization had a low thermal conductivity layer at the surface boundary and a higher thermal conductivity beneath the GLHE. These combined factors, insulation from the surface and well distributed thermal conductivity around the loop, are supposed to be the cause of the observed high performance. Similar empirical observations have been made by contractors working in the field. In some places where the depth of the underlying bedrock is shallow enough, the pipes are laid on the bedrock and excellent performance is seen because the overburden acts as an insulator and isolates the high thermal conductivity rock, linking the GLHE to deeper reservoirs.

Insulation of the ground surface to the GLHE clearly plays an important role in enhancing the performance. When the top boundary has high thermal resistivity and the bottom boundary has low thermal resistivity there is a larger effective volume to pull energy from. With this larger volume comes increased performance. There may be problems long term with this set up because of the minimal surface interactions preventing summer recharge of the thermal energy in the soil, but it seems unlikely as the surface boundary still appears

to be well connected with the rest of the system.

The worst performers tended to have high conductivity around around the pipes. This may seem counter intuitive as it could be expected that having a higher conductivity immediately around the pipes would improve performance. However, a high conductivity region immediately around the piping system allows thermal short-circuiting to occur. Heat transfer takes place between the pipes, reducing the effective length of the trench as there is a smaller thermal gradient in the far reaches of the trench with which to draw energy from the surrounding soil.

Heat transfer pathways appeared to be the most important factor when considering a GLHE in a heterogeneous medium. Heat transfer pathways from surface to the loop were observed to be damaging to loop performance. Heat transfer pathways between pipes were observed to be damaging to the efficiency of the systems. High conductivities connecting soil beneath and to the sides of the GLHE were observed increasing the effective volume of the trench and improved loop performance.

The actual temperature differences seen in the return temperature of the GLHE between runs in the ensemble were small. These results were similar to those found by Ferguson (2007) who examined heterogeneity in the context of open loop systems. Ferguson noted that, while the temperature deviations were small, the total amount of energy was sensitive to heterogeneous structures. Energy recovery was not measured in the investigation detailed in this thesis because of the way the pipe boundary conditions were applied, which ensured that the total energy recovered did not vary between realizations.

According to the results presented here, heterogeneity does more to improve performance than it does to hurt it. Refer to Appendix I.2 for further examples of high and low performing structures.

4.7.4 Temperature profile in heterogeneous systems

The presence of heterogeneity appeared to have little impact on the development of the fluctuating thermal profile around a GLHE. A temperature profile was taken at the level of the buried pipe, with the profile being taken in the direction away from the coldest pipe (this cross section was centred about the inlet pipe, 8.5 m from the edge of the domain (Figure 4.3)). The temperature perturbation was calculated by taking the difference in thermal profiles of the heterogeneous field with a GLHE present and the same heterogeneous field without a GLHE. Figure 4.13 displays the temperature deviation from the undisturbed temperature profile caused by the having a GLHE installed in a soil and run for 365 days. Note that the thermal profile for the homogeneous equivalent, in red, almost completely overlaps the mean profile of the heterogeneous runs, in black. The impact of surface effects on the profile are controlled for and the only differences are caused by the GLHE. The uncertainty induced by heterogeneity is almost unnoticeable relative to the magnitude of thermal draw-down in the vicinity of the GLHE. Of all temperatures in the ensemble, 95% were less than 0.5 °C from the homogeneous case, demonstrating just how minor an effect heterogeneity had on thermal profile development.

Temperature profiles for other runs were generated (Appendix I.1); the profiles were largely unremarkable. Little changed relative to the base case presented in this section. Doubling the standard deviation of the heterogeneous field had only a small effect on the horizontal thermal structure. The exception was the zero correlation length ensemble, which produced a thermal field around the GLHE with almost zero variance at all distances.

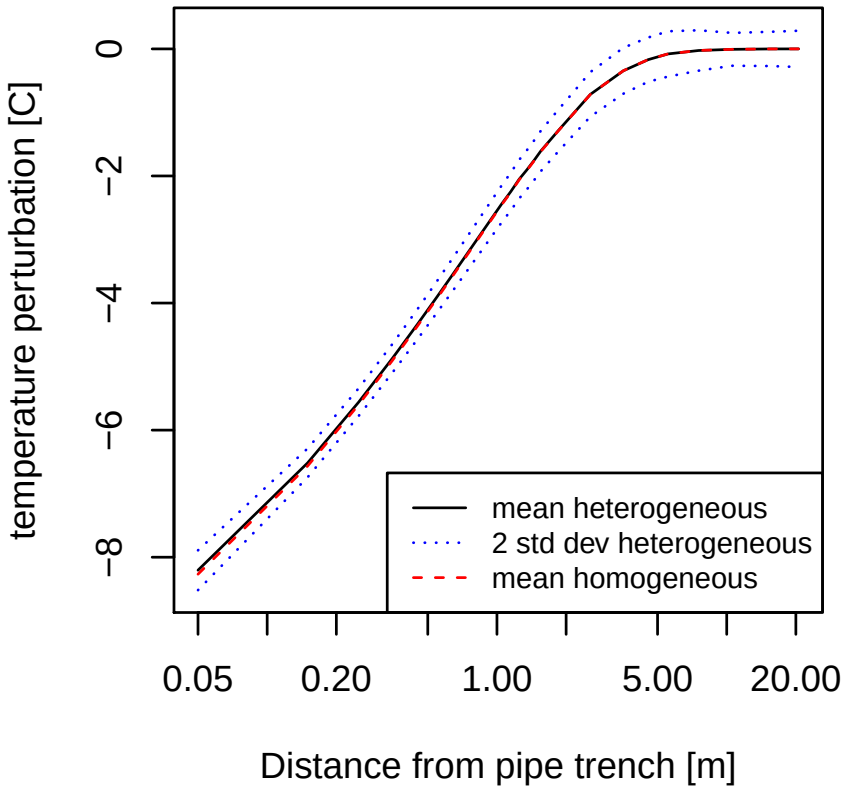

Figure 4.13: Temperature profile away from the pipe nearest the inlet of the GLHE

4.7.5 Thermal conductivity mean and variance

The mean and standard deviation of the thermal conductivity fields used in the base case were taken from specific case studies. To further generalize the impacts of heterogeneity on performance, conductivity fields were generated with a range of means and standard deviations.

Ensembles were made for soils with mean conductivities of 1.5 $\frac{\mathrm{W}}{\mathrm{m \cdot K}}$, 1.25 $\frac{\mathrm{W}}{\mathrm{m \cdot K}}$, 1.0 $\frac{\mathrm{W}}{\mathrm{m \cdot K}}$, 0.75 $\frac{\mathrm{W}}{\mathrm{m \cdot K}}$, and 0.5 $\frac{\mathrm{W}}{\mathrm{m \cdot K}}$. As would be expected, the performance of the GLHE decreased with decreasing thermal conductivity (Figure 4.14) due to the colder temperatures of the heat exchanger fluid in the lower conductivity fields (Figure 4.15). Note that the thermal diffusivity was not corrected for the different thermal conductivities. That is, the ensemble using 0.75 $\frac{\mathrm{W}}{\mathrm{m \cdot K}}$ would have had half the thermal diffusivity of the 1.5 $\frac{\mathrm{W}}{\mathrm{m \cdot K}}$ ensemble. This would have affected the propagation and attenuation of thermal pulses from the surface.

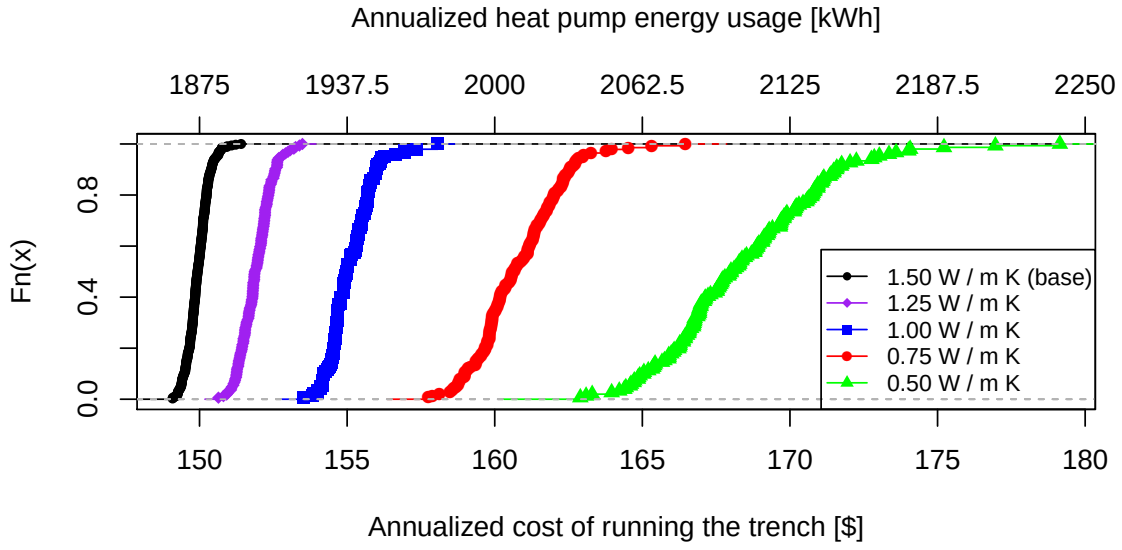

Figure 4.14: ECDF of heterogeneous realizations with a variety of mean conductivities.

The standard deviation for all the mean conductivity runs was set to 0.2 $\frac{\mathrm{W}}{\mathrm{m \cdot K}}$, so the

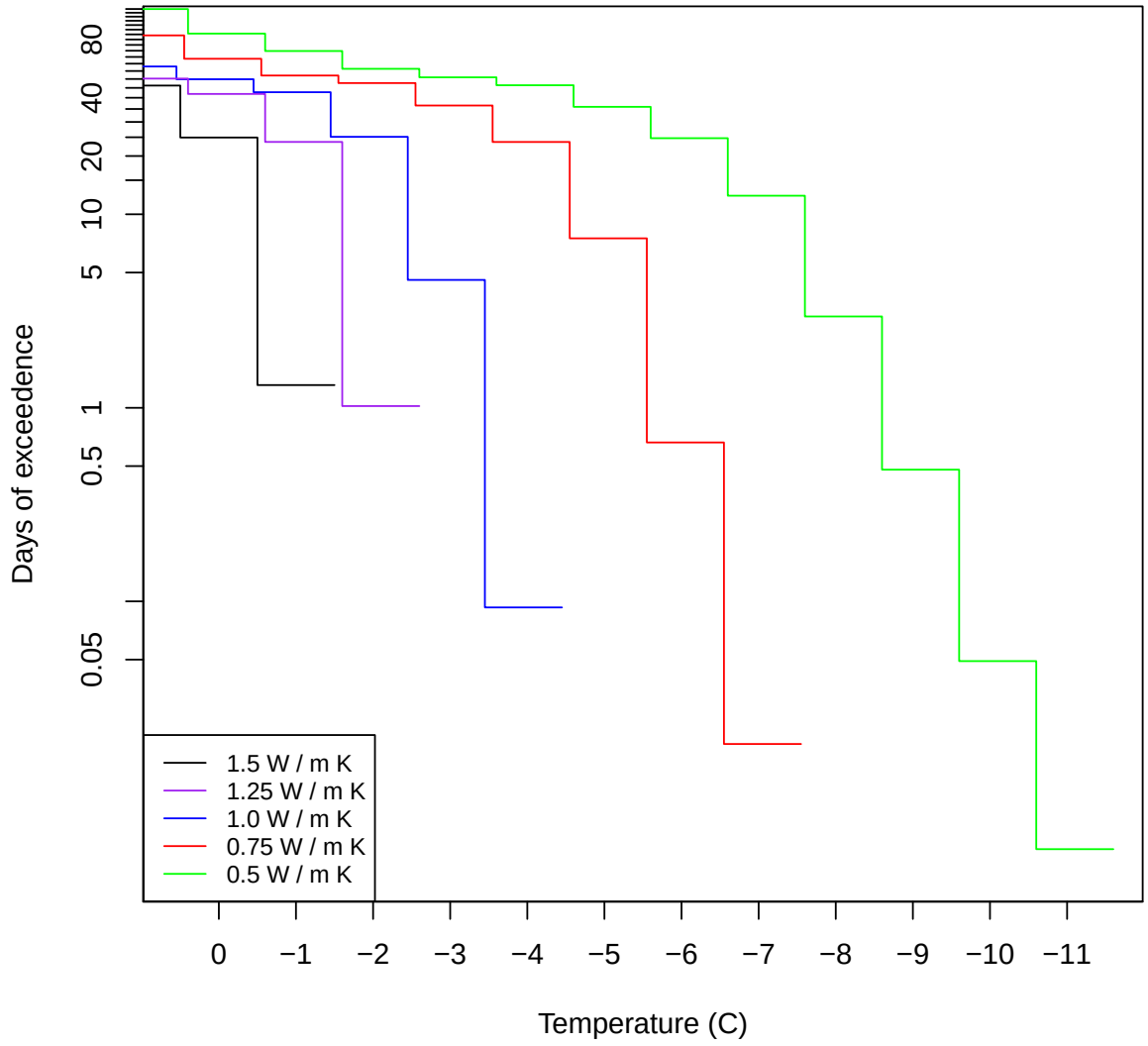

Figure 4.15: Days of exceedence for the various thermal conductivities. Decreasing thermal conductivity of the soil continuum lowers the expected return temperature of the geoexchange fluid. The lines are offset slightly in the temperature axis to improve the readability of the chart.

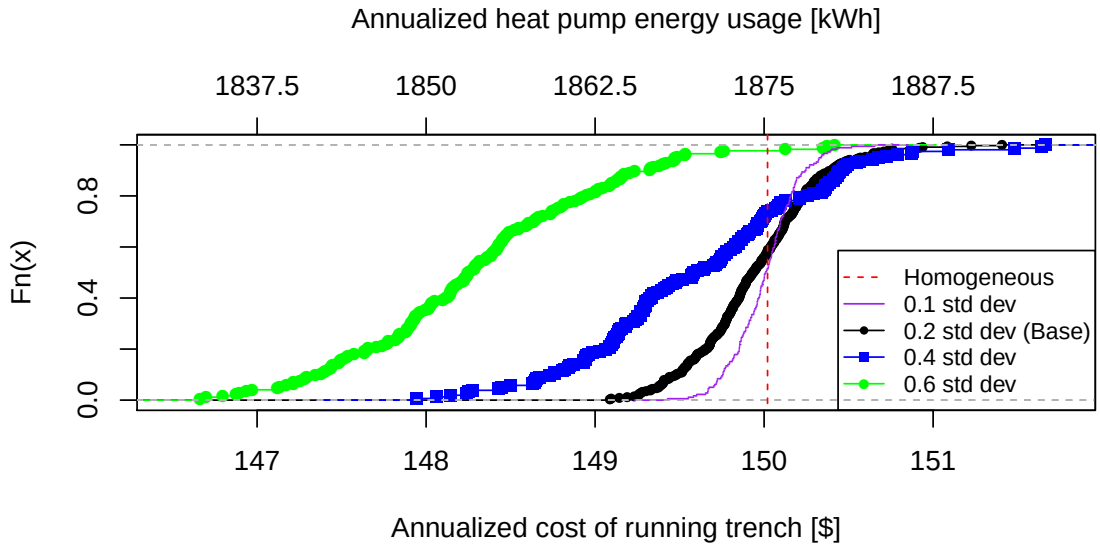

Figure 4.16: ECDF of heterogeneous realizations with same mean but variable standard deviations for the thermal conductivity field.

increase in the range of performance values for lower mean thermal conductivities seen in Figure 4.14 could be explained by the relative increase in the size of the standard deviation compared to the magnitude of the mean. This explanation plays well with the results of the standard deviation analysis presented in Figure 4.16 where when the standard deviation was increased there was a corresponding increase in the range of performance values.

To investigate the impact of standard deviation, the mean conductivity was held constant at 1.5 $\frac{\mathrm{W}}{\mathrm{m{\cdot}K}}$ and standard deviation was varied from 0.1 $\frac{\mathrm{W}}{\mathrm{m{\cdot}K}}$ to 0.6 $\frac{\mathrm{W}}{\mathrm{m{\cdot}K}}$. GLHE performance tended to increase with increasing variations in the thermal conductivity (Figure 4.16). The ECDFs still overlap, even for the 0.6 $\frac{\mathrm{W}}{\mathrm{m{\cdot}K}}$ standard deviation run, but the median values showed a strong trend of decreasing with increasing standard deviation. The EWT corresponded well with this observation. Figure 4.17 shows the days of exceedence plots for the standard deviations. The time spent at the colder temperatures decreased with increasing standard deviation of the thermal conductivity field.

While the results of mean conductivity investigation were largely expected, the results from the standard deviation runs were not. Relative to the base case it was seen that the

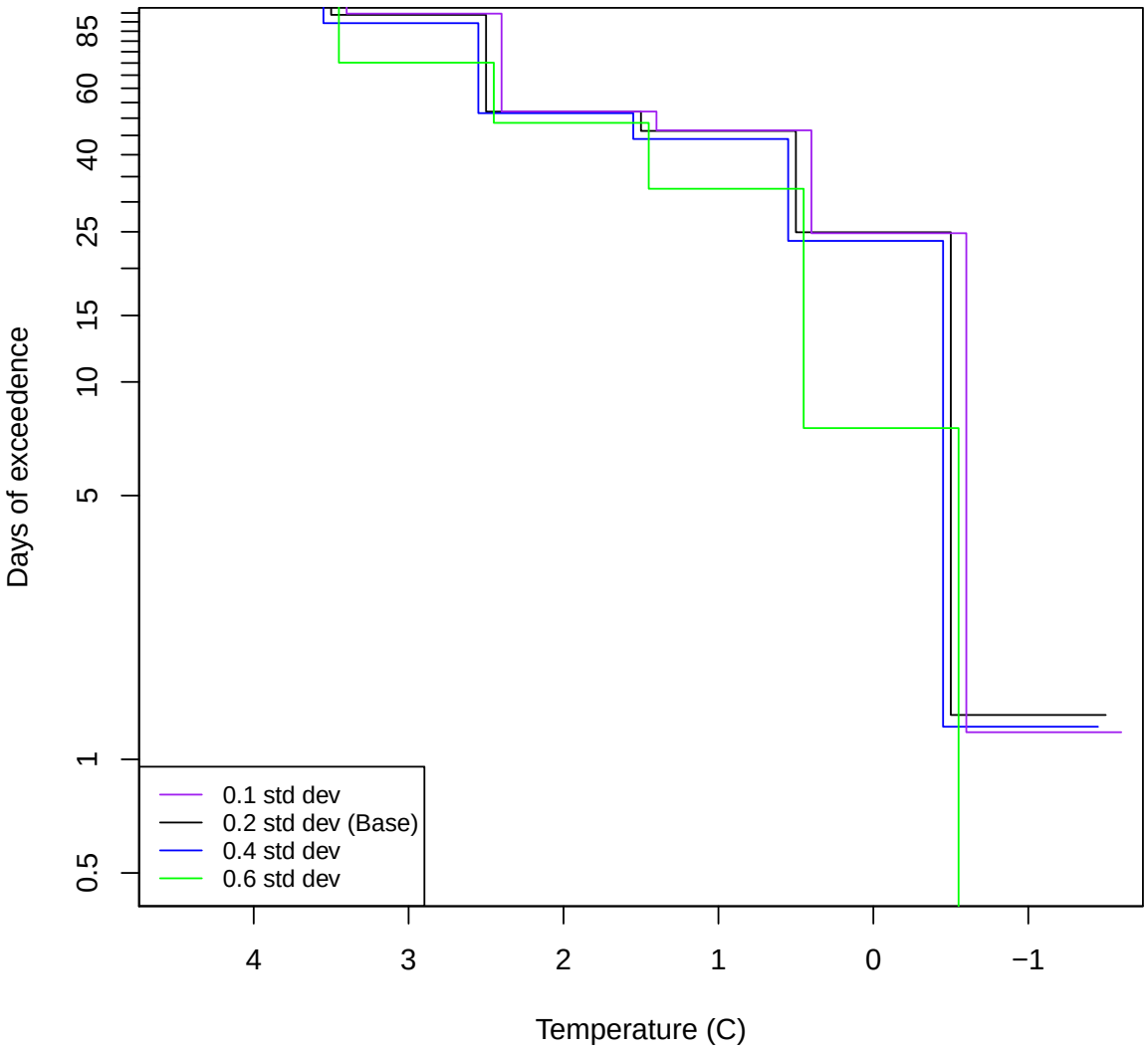

Figure 4.17: Days of exceedence for the various standard deviations. Increasing the standard deviation increases the outlet temperature. The lines are offset slightly in the temperature axis to improve the readability of the chart.

presence of heterogeneity was capable of increasing and decreasing the performance of a GLHE but, on average, the performance would increase with increasing heterogeneity. The standard deviation ECDFs show that, with high variances, heterogeneity had a predominantly positive impact on the loop performance. Impacts of structural factors must have shifted so that negative impacts due to short circuiting became minor relative to the general increase in thermal diffusivity caused by high levels of heterogeneity. This observation correlates well with the results of the zero correlation lengths field in the following section (§4.7.6). Full results for the various means and thermal conductivities are presented in Appendix I.6.

4.7.6 Correlation lengths

The correlation lengths of the thermal conductivity fields were taken from studies on spatial variations of hydraulic conductivity under the assumption that both properties would vary on a similar scale. To assess the impact of this assumption, an additional test was performed to evaluate the impact that correlation length of heterogeneous fields has on the performance of GLHEs (Figure 4.18).

The base correlation lengths (L) were used as a reference point; fields with higher ($2L$) correlation lengths and fields with lower ($L/2$) correlation lengths were examined. These ratios were applied to the vertical and horizontal correlation lengths to preserve the anisotropy in the heterogeneity structures (see §4.4 for ratio and explanation). A field with a correlation length of zero (no spatial correlation) was also examined. Results from these runs are presented in Appendix I.4. Only the zero correlation length field consistently outperformed the homogeneous field. All other correlation lengths produced fields that could over- or under-perform the homogeneous case. In the context of correlation lengths,

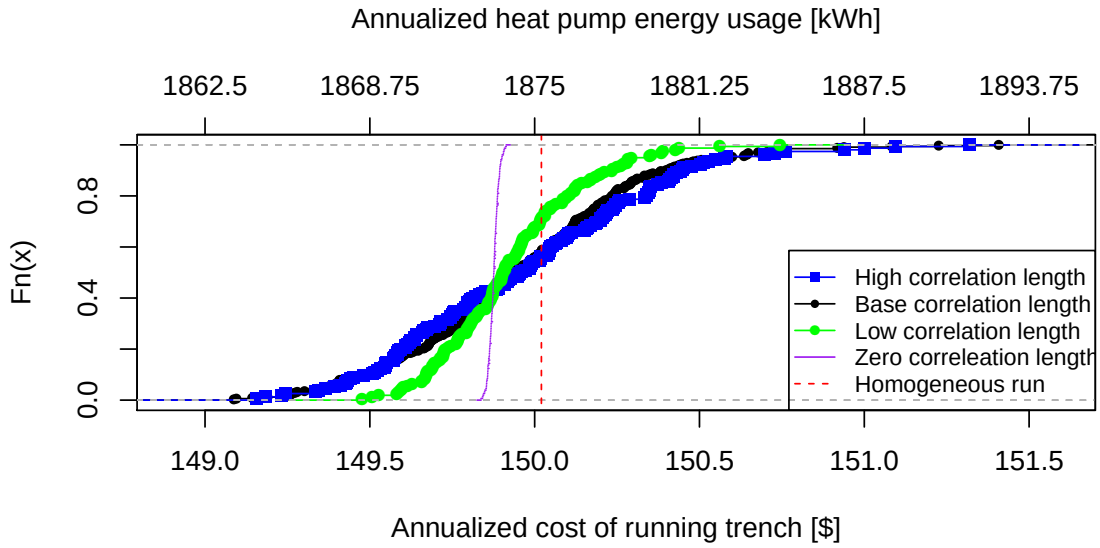

Figure 4.18: Comparison of ECDFs the performance of a rabbit GLHE in fields of varying correlation length

the homogeneous run should be considered the infinite correlation length case.

The base correlation length had performance values ranging over approximately $2.50. Doubling the correlation length appears to narrow the performance range with the range dropping to $2.00, although this could be attributed to fewer runs being evaluated. Halving the correlation length also appears to decrease the range of expected values with the modelling ECDF having a range of $1.50. The zero correlation length runs had the smallest range with all performance metrics falling within a $0.10 range.

The zero and high correlation length thermal conductivity fields appeared to have a predictable impact on the performance of a rabbit GLHE trench. It is possible that, with more runs to provide a more highly resolved ECDF, the high correlation length run would have had a similar ECDF to the base correlation length ECDF. With the data collected in this study, it is difficult to conclude that the longer correlation length would show a larger range of values. The long correlation length could be expected to behave in a manner similar to an equivalent homogeneous field. The doubling of the correlation length presented here means that when there are high conductivity sections between pipes, which

would cause short circuiting, they are also connected to large far-field reservoirs. The two effects may act to counteract one another, limiting the range of expected performance of a GLHE in the field.

For a Gaussian random field with zero correlation lengths, the heterogeneous field had a very small range of performance values. Multiple realizations behaved effectively has a homogeneous medium with slightly higher thermal conductivity. The performance of the GLHE in a homogeneous field with the same mean was worse than the heterogeneous case with over 95% confidence. The probable mechanism was the increased thermal diffusion from point sources that can occur in heterogeneous fields. The mechanism had a small impact on the overall performance: the difference between the mean of the heterogeneous runs and the homogeneous run is just over $0.15, but the impact was present.

The performances of GLHEs in low correlation length fields had a slightly higher mean performance than the base correlation length fields. The skew of the distribution decreased, similar to the decreased skew of the zero correlation length field, and the mean of the performances were statistically different than the homogeneous run. The mean of the half correlation length was lower, meaning better loop performance, than the mean of the zero correlation length field. It would appear that the small, but still present, correlation lengths provided enhanced heat dissipation away from the GLHE without degrading performance as significantly.

A days of exceedence analysis of the correlation lengths further illustrated the similarity of the different fields. Figure 4.19 shows the four correlation lengths examined. The amount of time that the returning temperature was below -1 °C increased with increasing correlation length, but the increase was very small. Difference between the days of exceedence values for the correlation lengths at higher temperatures are indistinguishable on

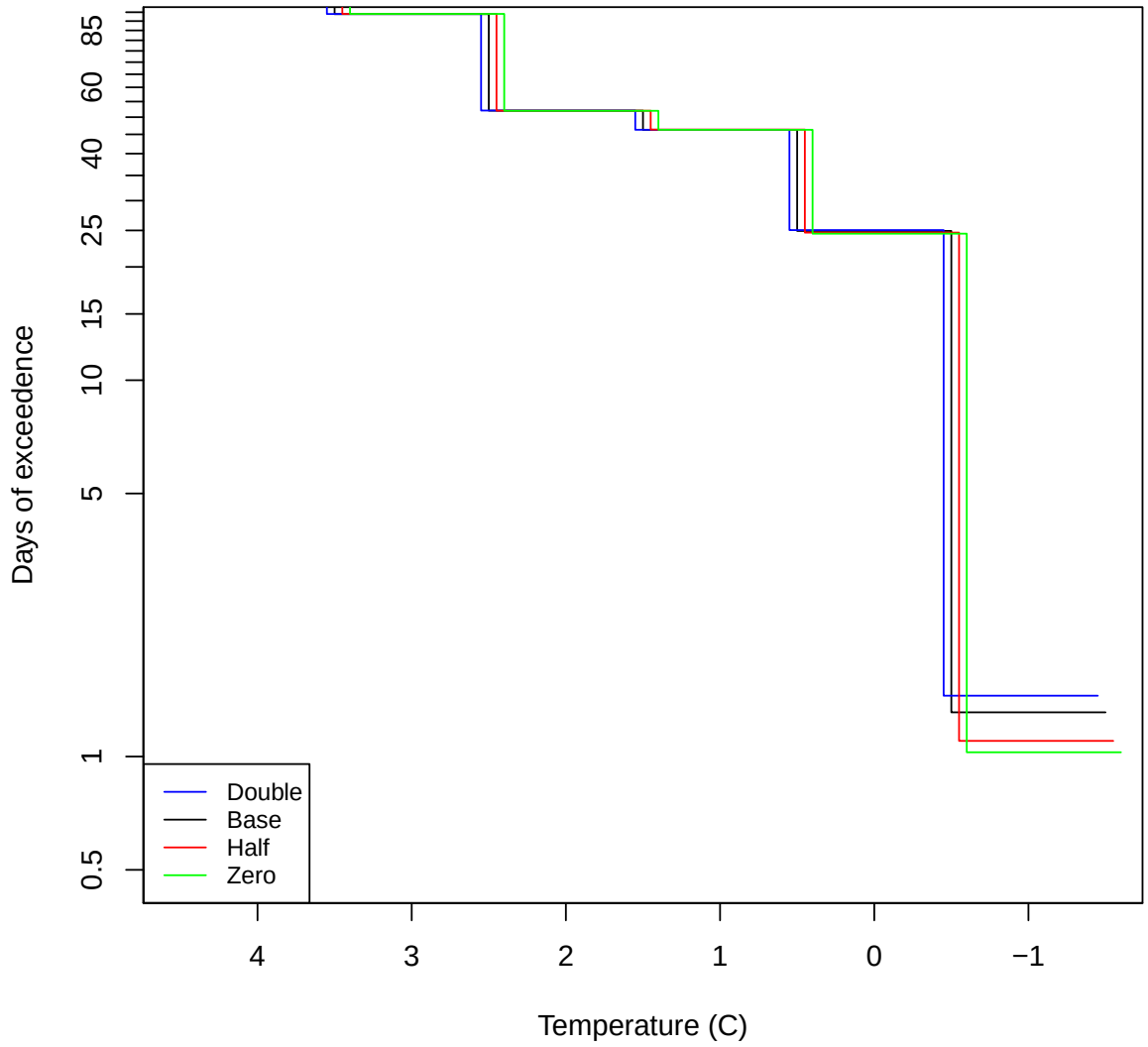

Figure 4.19: Mean days of exceedence for the various correlation lengths. The lines are offset slightly in the temperature axis to improve the readability of the chart.

the log-scale plot. Despite the overlapping performance ECDFs, the base and double correlation length ensembles have different days of exceedence values on the low temperature end.

The impact of correlation length was shown to be very minor in relation to the overall performance of the GLHE. The effect of correlation length appeared to change with scale. A finer grained approach with more model runs would be allow the building of an empirical relationship. Based on the results collected from the correlation length runs, it appears that performance uncertianty will increase with increasing correlation length (to a point) and that very low correlation lengths for thermal conductivity will actually improve GLHE performance.

4.7.7 Trench widths

The widths of the trenches used in GLHE installations are often dependent upon the equipment that the contractor has available to them; trench width plays an important role in loop performance. To examine of the impacts of changing the trench widths of the GLHE, the effective spacing between the pipes were systematically changed. The width of the overall domain remained unaltered while the width of the trench inside that domain was changed. To avoid errors due to inconsistencies in the discretization, there were only three trench widths examined. 0.9 m, 1.2 m, and 1.5 m (base case). This was done to ensure that the placement of the pipes relative to the soil elements was consistent between runs.

The performances of the difference pipe runs are displayed in Figure 4.20. The widest pipe spacing clearly outperformed the narrower trenches. This was expected because of

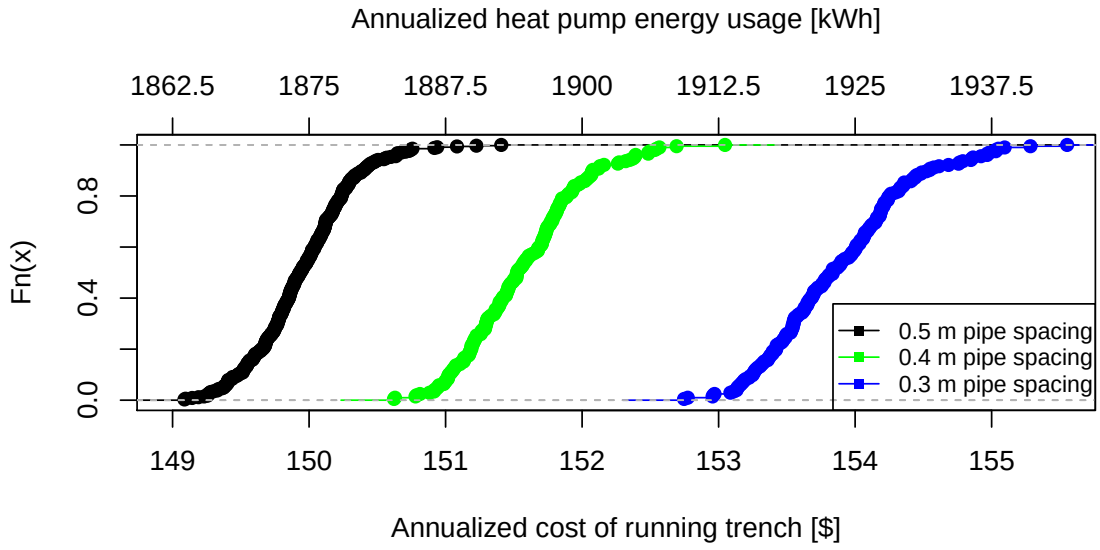

Figure 4.20: Comparison of ECDFs showing the performance of a rabbit GLHE in trenches of varying widths

the larger effective volume that the larger pipe spacing gave the trench. Narrow trenches showed a slightly higher sensitivity to heterogeneity. The band of probable costs for a 0.5 m pipe spacing cover ∼$2.50 compared to the narrow trench with a costs of running the trench ranging from $152.80 to $155.90. The discrepancy was likely due to a more pronounced short circuiting effect made possible by the smaller distances between pipes. The reduced footprint may make the smaller trench more sensitive to thermal insulation or connectivity with the surface. Since the performance of an equivalent homogeneous field falls very close to the same value in each experimental cumulative distribution function (ECDF) the likely explanation would be that both effects are more pronounced and scale with changes in trench width.

The days of exceedence chart (Figure 4.21) clearly shows the impact that decreasing the trench spacing had on the return temperature of the GLHE. The narrower trenches produce colder temperatures for longer periods of time compared the wide trench.

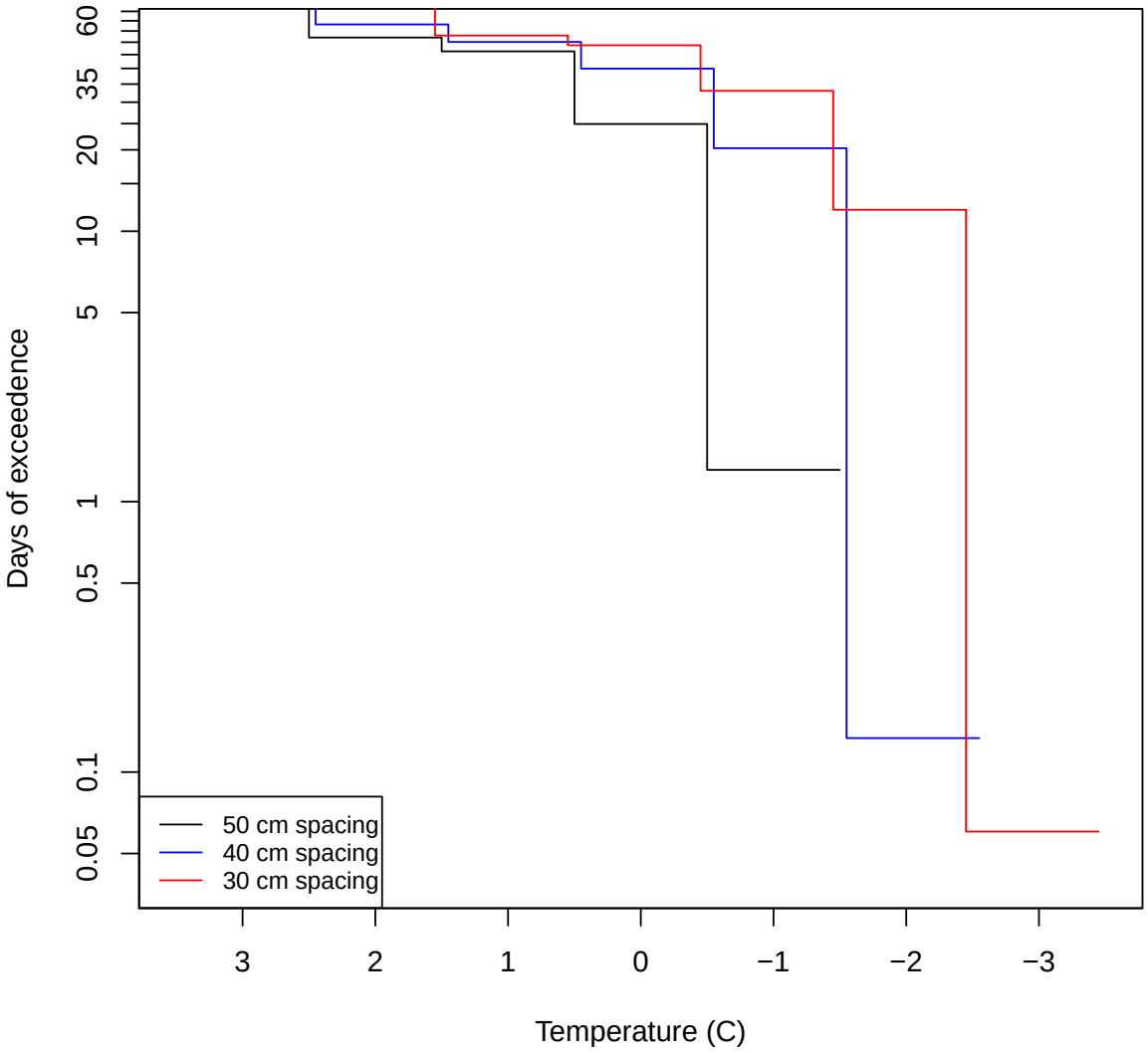

Figure 4.21: Mean days of exceedence for GLHEs of varying trench widths. The 50 cm spacing is the base case. The lines are offset slightly in the temperature axis to improve the readability of the chart.

These results have implications on the design of horizontal GLHE trenches. The current best practice of targeting 50 cm pipe spacing should be continued. Narrowing the pipe spacing clearly makes the GLHE slightly more sensitive to heterogeneity. The level of uncertainty brought on by heterogeneity was enough that a loop with a 0.4 m spacing placed in a well structured soil was capable of matching the performance of a loop with 0.5 m pipe spacing, if that loop was placed in a poorly structured soil.

4.7.8 Trench depth

Changing the depth of the trench dug to install a GLHE should change how that GLHE performs. With greater depth, influences from the surface should decrease because of the larger effective resistance between GLHE and the ground surface. Figure 4.22 shows a comparison between three different GLHE depths in ensembles of heterogeneous conductivity realizations.

The shallow loop performed measurably worse than all the other loops, with a performance metric similar to the trench with a 0.4 m pipe spacing of the previous section (Figures 4.20 and 4.22). The deeper loops, at 2.0 m and 3.0 m below ground surface, performs slightly better when considering the mean of the distributions. The greater depth appears to decrease the variability associated with heterogeneity marginally. These results are contextualized by the days of exceedence chart (Figure 4.23) showing a systematic increase in temperature with depth of burial.

Figure 4.22 was not intuitively interpretable. Theoretically, the greater depth should reduce the short term variability induced by ground surface conditions and reduce the magnitude of temperature peaks seen in winter (cold) and summer (hot). The more moderate

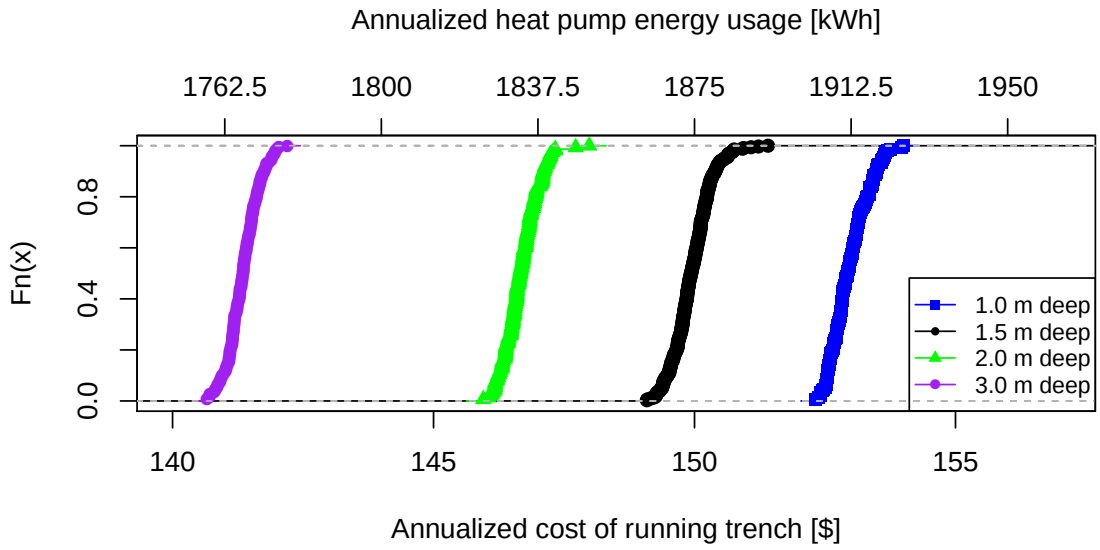

Figure 4.22: ECDFs of performances for GLHEs buried at varying depths

temperatures should generally be good for the performance of a GLHE. A complication arises when the loads on the GLHE are, as they are in the these modelling runs, unbalanced. The shallow GLHE "resets" to the surface temperature much easier than a deeper GLHE. The deeper GLHE has the potential to, over time, develop a thermal field in the soil that does not reach natural background temperatures every summer. Because of this phenomena, the loop's performance will slowly degrade until a new steady state is reached. Due to the relatively short simulation period being used, this phenomena likely had no effect on the presented performance measurements.

The reduced temperature variation induced by surface conditions manifested as a slight decrease in performance variability. At the greater depths most of the performance variation was likely due to the non-surface structural effects, discussed in §4.7.3, such as short circuiting and access to large reservoirs. These lateral structural effects would be expected to come through as being of greater relative influence on performance variability.

These distributions may illustrate limitations of the model's ability to simulate the

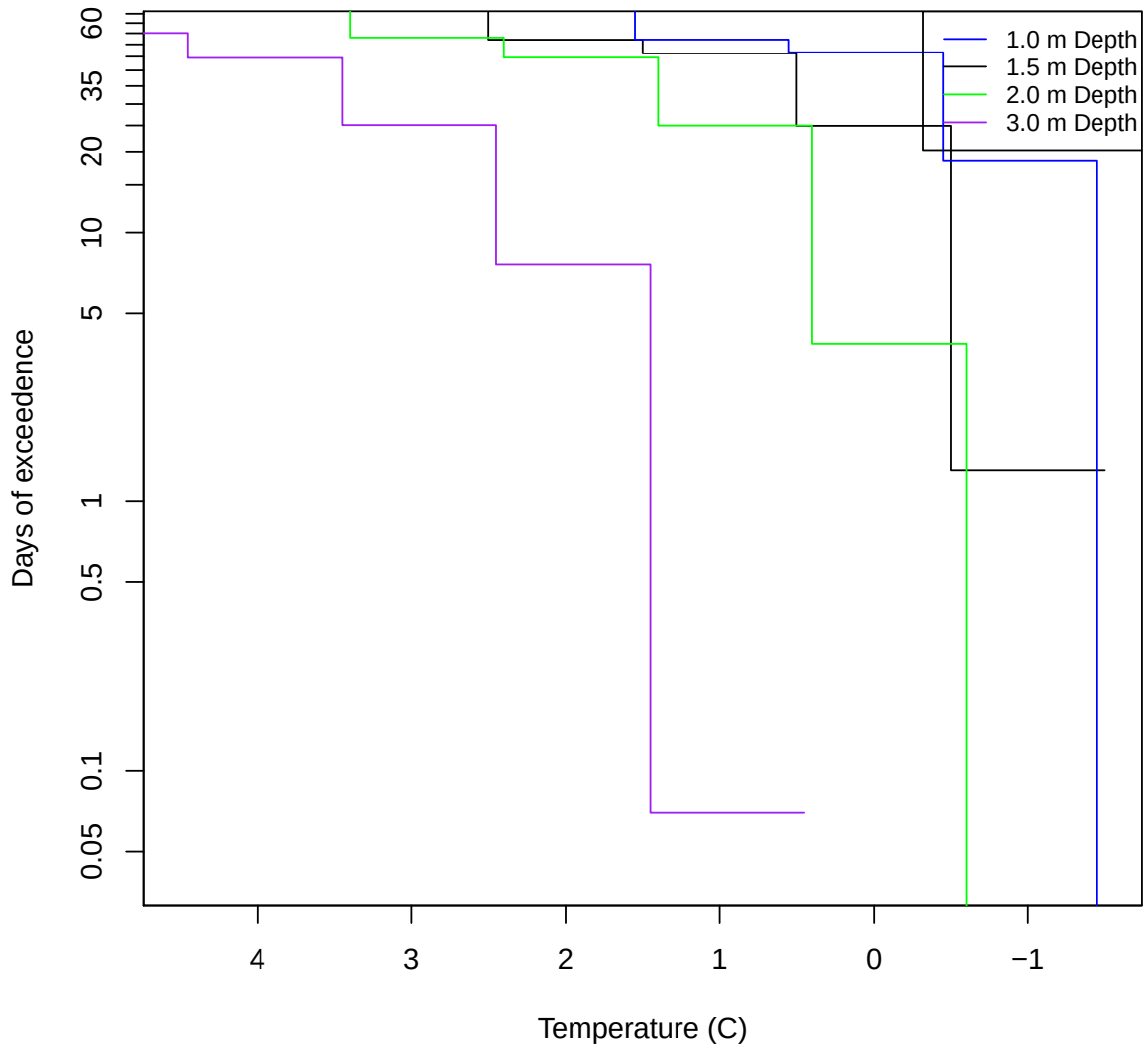

Figure 4.23: Days of exceedence for the various trench depths. As the GLHE is buried deeper in the ground the minimum temperature increases. The lines are offset slightly in the temperature axis to improve the readability of the chart.

physics of the shallow surface. The lack of ground water infiltration in the model may mean the simulation is omitted the most significant form of reset mechanism. This can be seen in some of the inverse modelling results where early spring melts were missed in the simulation (see Chapter 3). The absence of this could mean that the effect of depth was poorly shown by these models. Depending on the depth of the water table this could have a huge effect, if one depth is in the vadose zone and the other is beneath the water table, or a tiny effect, if both depths are in the vadose zone/below the groundwater table.

Full results for the 3.0 m, 2.0 m, and 1.0 m deep runs are presented in Appendix I.3. The 1.5 m deep run is the base case which is presented throughout the heterogeneity appendix.

4.7.9 Triple trench system

Typical GLHE installations involve multiple adjacent trenches connected to a manifold. To assess whether the relation between performance and heterogeneity changed when more than one loop was present in the system an series of model runs was done using three trenches instead of one.

The ensemble for the triple trench system was performed using the same statistical parameters of the base case. Two trenches were added to the system, one each on either side of the trench used in the base case (Figure 4.24). The three trenches were all rabbit loops fed by a common reverse return manifold. The finite element mesh used in the base case was also used for the triple trench system. This meant that the outer loops were situated in more poorly discretized areas of the mesh. The coarser discretization translated to lower fidelity in the thermal field for the outer loops. In spite of the coarser

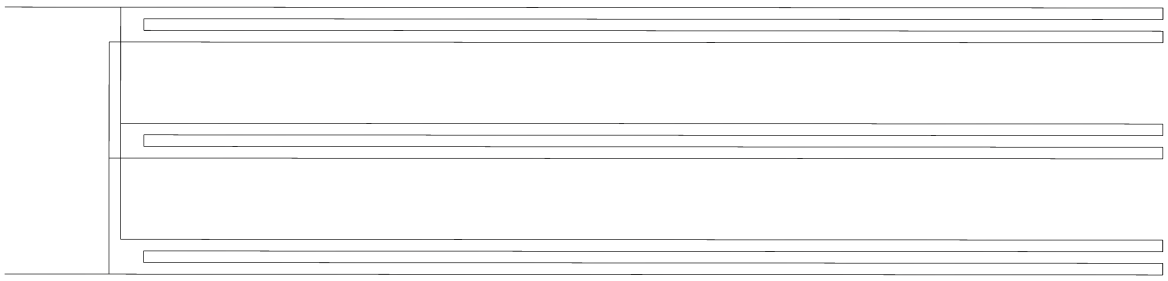

Figure 4.24: Triple trench layout

discretization for the outer loop, the model remained stable. Schematic diagrams of the model domain are provided in Figures 4.25 and 4.26.

Loads were taken to be 3 times that of the base case. This was justifiable because there was now three trenches instead of one. The effect on performance of the added lengths and changing geometry of the manifold were considered negligible.

The ECDF presented in Figure 4.27 shows the distribution of costs for running all three trenches combined. The extremely low discretization around the outer loops should act to increase thermal dispersion away from the ground loop, increasing loop performance. This loss of resolution due to the grid selection may be partially responsible for the relatively good performance seen by the outer trenches.

The relative variability of the performance of a triple trench system was expected to be lower than that of a single trench system. The larger footprint covered a spatial extent that should have been sufficient to average out many of the macro effects of heterogeneity seen in a single trench. Figure 4.27 shows that the range of performance numbers falls within a $5.50 window for the entire 3 trench system, just over double the variation seen in the base case.

The load of a triple trench system has a more complex structure than that of a single

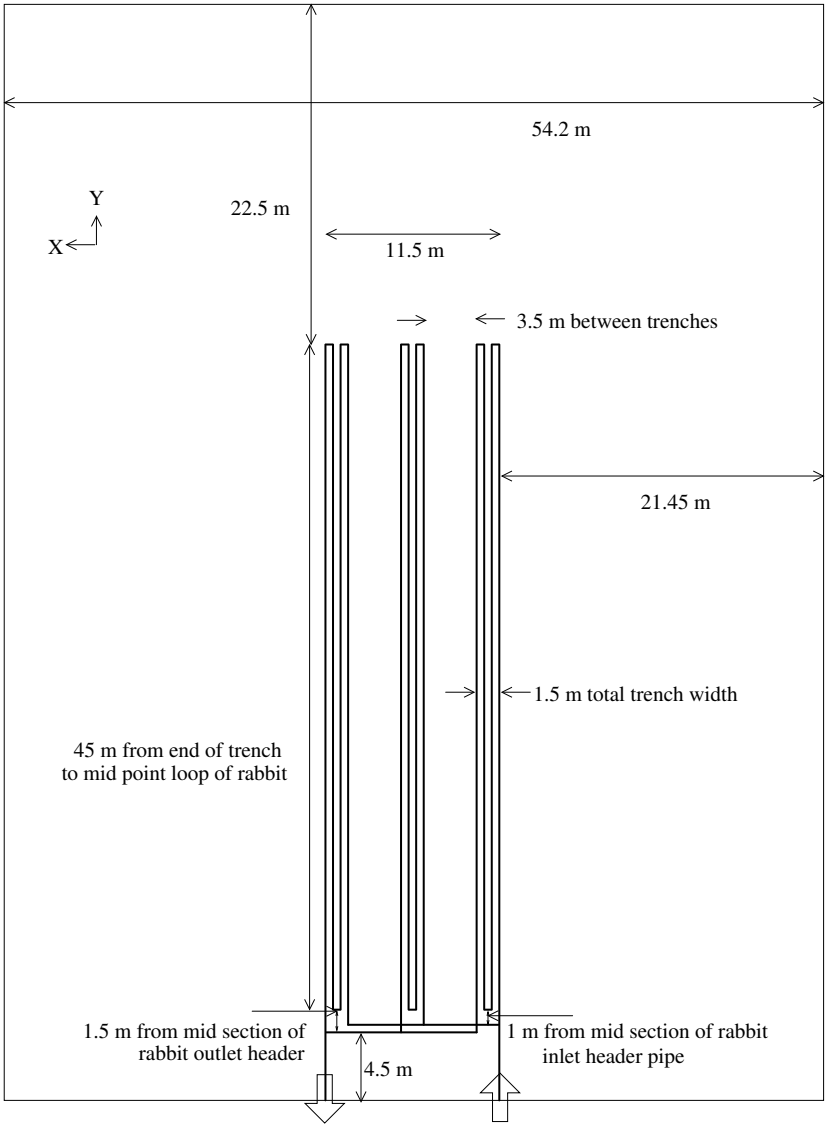

Figure 4.25: Triple trench schematic diagram in the XY plane.

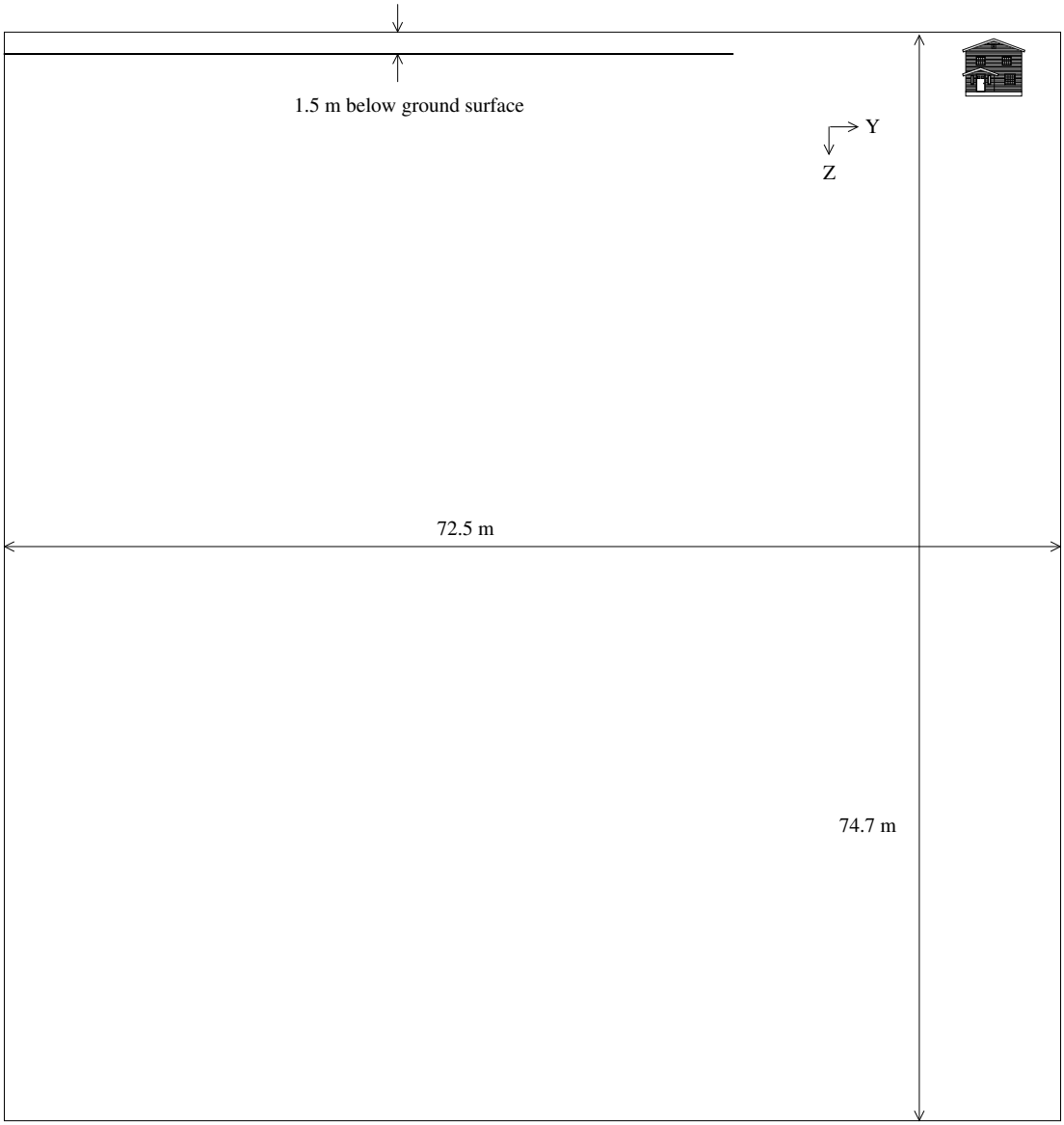

Figure 4.26: Triple trench schematic diagram in the YZ plane. House illustrates which boundary is the ground surface.

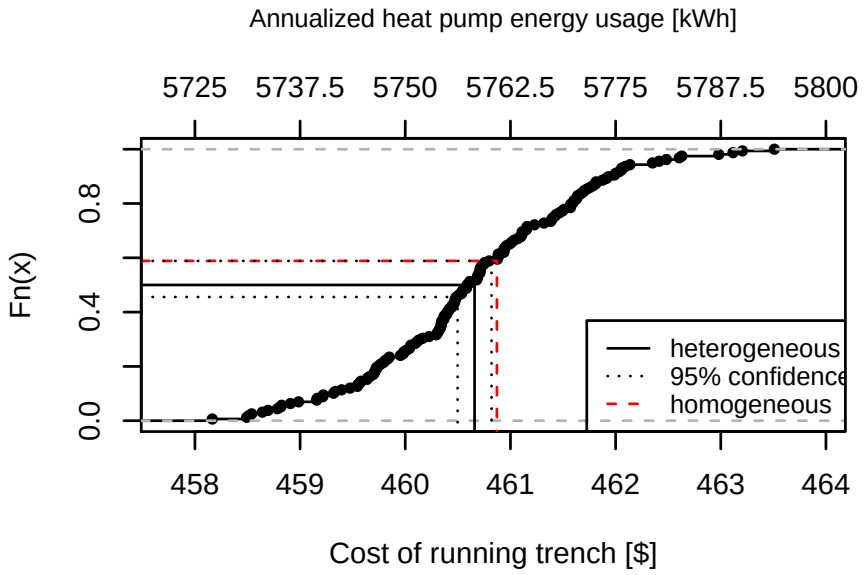

Figure 4.27: ECDF of a three trench system cost in a heterogeneous fields

trench. Temperatures are relatively even when they go into each of the three loops but when they return the temperature of the fluids can vary substantially depending on the thermal field developing around each trench. It would be expected that the outer loops, all else being equal, would carry more of the system load than the inner loop. This kind of load balancing happens intrinsicly in the model just as it would in the real world. Because of the lower load on the middle loop there could be less variation in that loop's performance. But, since the load on the center trench is now itself a variable, there was also the possibility that there would be more variability in its performance. Regardless of the kind of effects that the inner loop sees, the analysis of the performance data was more difficult than any single trench system.

Figure 4.28 shows the ECDF for the performance of the middle pipe. Note that, since the load structure is dynamic, this trench was not necessarily carrying a third of the loop load. The average cost from Figure 4.28 was slightly less than a third of the mean costs of

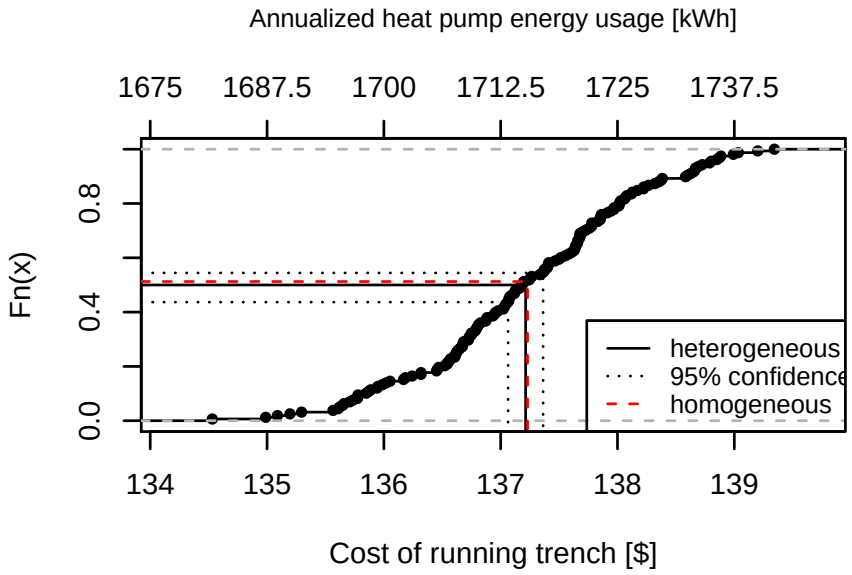

Figure 4.28: ECDF for the middle trench of the three trench system

running all three trenches, potentially due to a smaller load being placed on the middle loop. With lower wattage requirements the expense of extracting that wattage amount decreases. The performance of the homogeneous run was found to be not significantly different than the mean of the heterogeneous runs for the middle loop. For the overall system there was a significant difference between heterogeneous and homogeneous conductivity fields.

The temperature profile with distance has a different structure due to the extra trenches. Figure 4.29 shows how temperatures change away from the center loop. The outer loop is poorly visualized in this plots due to the coarse sampling structure used. Evidence of the smearing effect near loop was apparent when examining the horizontal thermal profile. The smearing was found to act to regulate temperatures near each loop, but farther out the different thermal conductivities came through to produce a more varied thermal profile.

The presence of multiple trenches in a single GLHE has additive performance uncertainty associated with heterogeneity. Systems designed to support 2 or more tons of

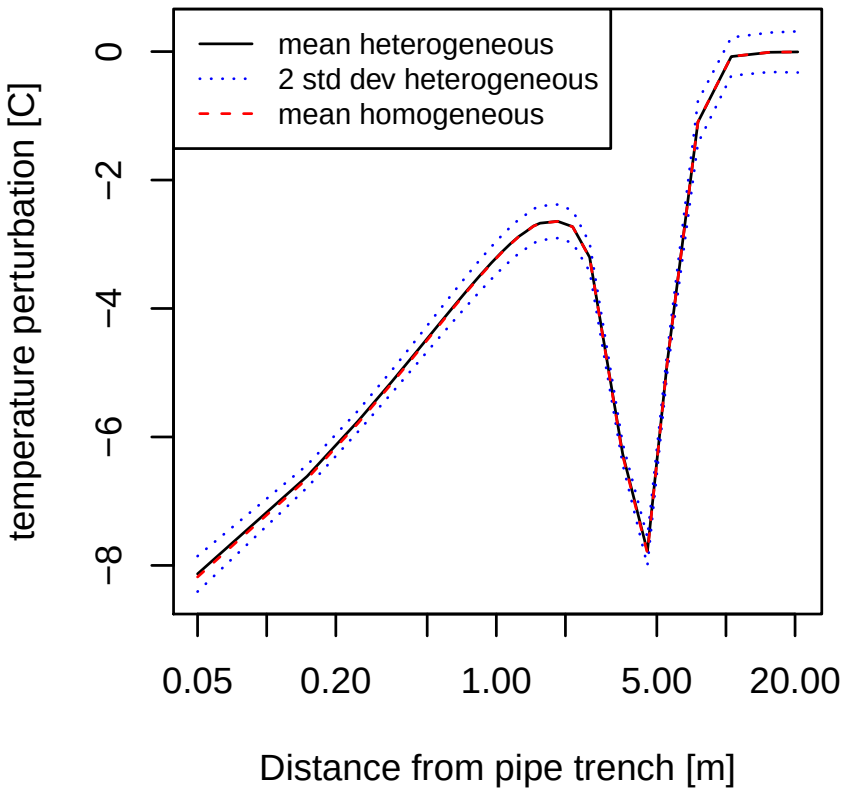

Figure 4.29: Temperature profile away from the pipe.

heating/cooling, enough for a very small townhouse in southern Ontario, are piped as multiple trenches coming off a manifold. The use of multiple trenches appeared to decrease the performance uncertainty relative to a single trench GLHE.

Full results for the triple trench system presented in Appendix I.9.

4.8 Conclusion

Heterogeneity was shown to be a relatively minor source of uncertainty to the expected performance of GLHEs (on the order of 2% of the heat pump expense for running the trench). Presence of heterogeneity in the subsurface has been shown to have a positive (although small) effect, on average, on GLHE performance. Positive and negative structural elements were identified that affect this performance. Specifically, short circuiting between pipes within a trench have a negative impact on performance and bridges to high conductivity reservoirs have a positive impact on performance. In general, the presence of heterogeneity increases the rate of thermal dispersion away from the GLHE.

The profile of the thermal field around a GLHE in a heterogeneous environment was shown to be equivalent to a GLHE in a homogeneous field, with equal probability of a the thermal field being warmer or colder for a given cross section. A smearing effect was identified near to the GLHE pipes which limited the uncertainty in this thermal profile. The smearing acts to control the temperatures near to pipe by acting as a thermal bridge along the trench.

Uncertainty in the mean conductivity was shown to dominate uncertainty of the structure when it comes to performance. Logically, increasing the variance of the thermal conductivity field increased the variance in yearly costs of running the trench, although

less intuitively it also correlated with a statically significant decrease of those costs. This further reinforced the conclusion that heterogeneity is a net positive for GLHE performance.

Correlation lengths of the thermal conductivity fields affected the range of expected performances. For the physically realistic lengths investigated, decreasing the correlation length decreased the range for the expected costs. Increasing the correlation length had little effect on the shape of the ECDF compared to the base case. The mean days of exceedence for all correlation lengths investigated were nearly identical.

Pipe spacing within trenches was shown to have a large effect on the performance of GLHEs. The greater the spacing between pipes the better the performance. Increasing the pipe spacing was shown to slightly decrease the uncertainty associated with heterogeneity. A similar story can be told about trench depths, with GLHE performance increasing with increasing depth of burial. These conclusions come with the caveat that the modelling investigation was performed for the time period of one year and the increasing depth of burial may change the loops ability to reset in summer. The uncertainty from heterogeneous structures did not appear to diminish with depth.

The use of multiple horizontal trenches was shown to decrease the uncertainty associated with heterogeneity. A three trench GLHE in a heterogeneous field was shown to have approximately twice the uncertainty of a single trench system.

The most important results of this investigation may be in the introduction of the days of exceedence charts for design analysis. If design failure can be shown to occur at a specific temperature than the measures taken to limit the amount of time that the GLHE is operating below a certain temperature could be very useful for informing loop design.

This investigation was limited in a number of ways. The GLHE performance ECDFs were generated based on the costs of running the heat pumps according to their COP curves and did not account for other costs (a third of all HVAC costs at the field site were not heat pump related). For example, the expense of running the loop pump would likely increase with a decrease in the viscosity of the exchange fluid. A single heat pump curve was used which corresponded to the heat pump present at the Elora field site (Haslam, 2013), other heat pumps may be more or less sensitive to the temperature of the exchange fluid and that sensitivity will likely vary with temperature. Also, the steady state pipe model used here would not reflect the intermittent nature of a true GLHE. Exchange fluid temperature and pumping expenses would fluctuate rapidly within a pumping cycle, this study only attempted to recreate expenses and temperatures on the timescale of one year.

The load applied to the GLHE in this study may have been too low bring the effects of heterogeneity out. The loop field at the Elora site was known to be over-designed at the time of installation. The parameter estimation exercise of the previous chapter showed that the parameters used for the base case were reasonably close to what could be expected to exist at the field site but this does not account for an over-design of the overall system. If the loads were too low relative to current design guidelines for GLHE then the effects of heterogeneity shown in this study may be lower than what kinds of effects could be expected from a typical GLHE. A series of ensembles were made investigating the impact of increasing the load on the GLHE (results presented in Appendix I.8). A near linear scaling of cost was found with load, e.g. a doubling of the load doubled the cost of running the GLHE and doubled the range of the performance metric.

Despite its limitations, HEN appeared to function as a reliable modelling tool for the problems studied here, where the aim was to recreate thermal fields and to compare soil

thermal conductivity structures. The effects of heterogeneity were shown to be minor in all cases, an observation which supports continued use of the homogeneity assumption commonly made in GLHE models.

Further modelling studies could be made to attempt to account for the limitations highlighted here. A more sophisticated pipe model would be particularly useful but may not be feasible due to the numerical difficulties of modelling an intermittent advection dominated system. Field work would provide the ultimate form of hypothesis testing but the creation of controlled, field scale heterogeneous soils around even a scaled down GLHE may prove effectively impossible.

Chapter 5

Conclusions

The impact of structural heterogeneity of soil thermal properties on the performance of GLHEs has been investigated. The potential influence of such heterogeneity on performance has been shown to be less than 2% of the cost of running a GLHE in a typical heterogeneous environment. Performance uncertainty associated with heterogeneity was shown to be less than uncertainty related to estimated mean conductivity values of a TRT. Considering that ground loop designers do not typically perform even simple TRTs for horizontal loops systems, the results generated as part of this thesis show that heterogeneity is a less important design factor than the effective mean thermal properties. This supports the common assumption that the subsurface soil properties can be treated as homogeneous for the purposes of evaluating loop layouts and energy loadings of horizontal GLHEs. Obtaining accurate mean effective soil thermal properties remains the most important design constraint.

The impact of heterogeneity on the performance of GLHEs, though small, was shown to be non-zero. According to the results collected in preparation of this thesis, a ground

loop designer should consider the following if they wish to limit design safety factors and improve performance for their loops:

- Using pipe spacing of 50 cm minimizes the effects of short-circuiting due to high conductivity zones between pipes, although in this study the limited runs of the 40 cm pipe spacing seems to suggest that it should not be a critical implementation error if some of the pipes are closer; much closer 40 cm will most certainly increase the chance of failure;
- Favouring shorter trenches and the use multiple trenches may further mitigate the effect of heterogeneity; and
- Burying the pipe at least 1.5 m below the surface minimizes surface effects; this has less to do with heterogeneity and more to do with the performance increases seen with greater burial depths.

These three design aspects are within the control of the loop designer and were demonstrated to have an impact on the performance uncertainty of GLHEs.

The uncertainty of performance calculations relied on the calculation of COP using a specific heat pump curve. The performance values reported here are specific to a single heat pump and may not be reproducible using other heat pumps, although general trends are likely to be similar across all heat pumps. Costs other than that of running the heat pump were not considered. The energy requirement for running the loop pumps would likely change with temperature. The magnitude of this change should be smaller than the magnitude of performance change due to temperature changes at the heat pump. Should it become important, the GLHE is likely already in a fault mode (loop temperatures too high

or too low to run economically). The exclusion of loop pump costs makes the performance impacts of heterogeneity estimated in this study conservative because of these fault modes.

An investigation specifically examining fault modes of GLHE would be a valuable target for future work. If the days of exceedence charts were compared to loop outlet temperatures at a field site and an acceptable level of accuracy was possible, GLHE designers would be able to quickly evaluate design decisions and model whether or not those designs are sufficient for the loop load being applied.

This study used physical models that were limited in two ways. Firstly, the processes represented in HEN made a number of assumptions that made the simulations faster and more stable at the expense of physical accuracy. Should more processes and parameters be included in the model, the simulated performance and heterogeneity relationship may change. For example: the addition of phase change which would be expected to decrease the impact of heterogeneity by decreasing the importance of thermal conductivity on loop performance; or the addition of groundwater advection, which would be expected to increase the impact of heterogeneity on loop performance by adding spatially varying convection driven flows. Neither of these examples of omitted processes should be expected to have a significant impact on the performance of horizontal GLHEs, but may be important for vertical systems. Secondly, the heterogeneous thermal conductivity fields generated with GSLIB were made based on variograms that were created by taking literature values from hydro-geology (for spatial relationships) and soil science disciplines (for sill values). An investigation of actual heterogeneity of soil thermal properties in 3D has never been conducted. However, according to modelling results from this study, such an investigation would not be particularly valuable for advancing horizontal GLHE design. Even when very high levels of heterogeneity were assumed, the performance variations never exceeded

5% of the total energy costs.

Ancillary observations made during a trial investigation supported the validity of the commonly used bar heat exchanger approximation (Fujii et al., 2012) and the full reset of horizontal ground loops. The full reset assumption is the commonly used rule-of-thumb that horizontal ground loops do not degrade under unbalanced annual loads unlike vertical loops. The bar heat exchanger assumption simplifies analytical and numerical models by treating the ground loop as a continuous bar instead of discrete trenches. Thermal fields around GLHEs simulated in this study mimicked the shape of a bar, supporting the general validity of this assumption.

Other investigations performed include evaluating the impact of loop pipe thermal conductivity, which was shown to have moderate effect of performance, and estimating the effective homogeneous soil thermal properties at the Elora field site. The parameter estimation demonstrated that conductive heat transfer was the dominant mechanism for energy transfer around a GLHE. There is the potential for further information to be gleaned from the data collected at the field site, but this avenue of investigation was not taken in this thesis. Importantly, parameter estimation using the Elora field data showed that the assumption of conduction only heat transfer and the steady state approximation for the loop flow were both reasonable.

HEN performed as required, facilitating the comparison of heterogeneous thermal conductivity fields with a sufficient degree of speed and precision. To further improve upon the numerical code the use of customized shape functions should be considered. Specialized techniques, such as the enriched finite element method (Belytschko et al., 2009), placed in the soil continuum around the pipe network would ensure that the temperatures in the soil continuum adjacent to the pipe are accurately represented in the numerical approximation.

This is very important because the temperatures adjacent to the pipes are the ones which actually control the effectiveness of the heat exchanger. In the pipe network model, an upwinding method applied to the FEM approximation would improve the numerical stability of the model considerably when a non-branching pipe is being simulated. The application of an upwinding method would not significantly alter the poor numerical characteristics of a branching and merging pipe network but for single trench systems the convergence of the steady state pipe model would be expected to improve significantly.

Recomendations for future parameter estimations challenging to make due to the uniqueness of the field data set (Haslam, 2013) being used. The parameter estimation detailed in this thesis was conducted over a time period which was far longer than other studies in the literature and temperature timeseries were available for the soil around the GLHE whereas most datasets would only record the temperature of the geoexchange fluid as it enters and exits the ground loop. Theoretically, the use of a gradient -based search should be more efficient than a stochastically heuristic search (DDS in this case) for finding the optimal parameter set. The application of an algorithm such as PEST (Doherty, 1994) may provide a more optimal balance between avoiding local minima and an efficient, gradient-based search. Also, the use of the sum of squared errors as the objective function should be investigated. Other error weightings such as sum of absolute error should be considered as it may allow the parameter estimation algorithm to avoid placing too much importance on erroneous field data measurements.

APPENDICES

Appendix A

Derivation and explanation for the removal of the pipe volume from the continuum equations

Accounting for the volume the GLHE piping occupies in the soil continuum is essential to ensure convergence of the overall system as the element discretization is refined. The impact of not removing this volume can be conceptualized when examining the heat capacity of the soil continuum. The energy fluxes from the pipe are assigned to each node in an element occupied by a pipe. The temperature change induced by the flux is based on the heat capacity of the soil in that element. A 30% increase in the volume of the soil in an element will translate directly to an equal decrease in temperature change due to the pipe flux. Depending upon whether the energy load is in cooling or heating, this could cause the model to over- or underestimate the performance of the GLHE.

The effect of the volume of soil displaced by the pipe increases as the ratio between the

displaced volume and the volume of a continuum element increases. For example, a pipe with an outer radius of 3 cm going through a 10 cm x 10 cm x 10 cm element parallel to one of the axes will occupy 28.3% of the volume of that element:

$$\text{Percentage Displaced} = 28.3\% = 100\% \times \frac{\pi 3^2 \times 10}{10 \times 10 \times 10} \tag{A.1}$$

Contrast this to when the same pipe goes through a 20 cm x 20 cm x 20 cm element. The percentage of occupied volume has decreased to 7.07%:

$$\text{Percentage Displaced} = 7.07\% = 100\% \times \frac{\pi 3^2 \times 20}{20 \times 20 \times 20} \tag{A.2}$$

With these coarse elements, the displacement effect is so minimal that error from other areas of the model should overshadow error caused by not accounting for the volume correctly. However, a 30% error in volume of an element could have large impacts on the local conductivity and capacity matrices of that element. This would decrease the accuracy of the model for elements intersecting with the pipe network, a loose of accuracy where accuracy is most needed.

Accounting for this volume is difficult because of the cylindrical volume of the pipe which does not match the coordinate system of the rectangular prism volume of the continuum element. Because of this geometrical complication, simplifying assumptions are made. Only pipes oriented parallel to an axis are considered, this simplifies the modification of the interpolation functions as only a change of variable is required. The pipe is treated as a long, narrow rectangular prism instead of a cylinder. The square cross section distributes the volume in a way that does not strictly conform to the geometry of the original system being modelled. The volume is underestimated in directions of the

major axes perpendicular to the orientation of the pipe and overestimated in directions 90 degrees from the other major axes directions.

The equivalent area of a square cross section can be determined from the pipe radius:

$$\pi(\text{Pipe Radius})^2 = (\text{Square Side Length})^2 \tag{A.3}$$

$$(\text{Square Side Length}) = (\text{Pipe Radius}) \times \sqrt{\pi} \tag{A.4}$$

The derivation follows Istok (1989). The interpolation function of a cubic element is modified with a change of variable so that it respects the boundaries of the new pipe volume. This interpolation function is then integrated using Gauss-Legendre quadrature to perform the numerical integration over the reduced domain. The thermal conductivity and heat capacity of the element are assigned to the subvolume of the pipe rectangular prism. These sub-local element conductivity and capacity matrices are then subtracted from the global matrices to effectively remove their volumes from the continuum.

Let us start by looking at the interpolation functions of a unitless 2 x 2 x 2 cubic element. Each node, i, has interpolation function:

$$N_i = \frac{1}{8}(1 + \varepsilon_i\varepsilon)(1 + \eta_i\eta)(1 + \zeta_i\zeta) \tag{A.5}$$

Where each of the eight nodes has coordinates corresponding to:

i	1	2	3	4	5	6	7	8
ε_i	-1	1	1	-1	-1	1	1	-1
η_i	-1	-1	1	1	-1	-1	1	1
ζ_i	-1	-1	-1	-1	1	1	1	1

(A.6)

Each interpolation function has a partial derivative with respect to each of its variables for use in calculating the local conductivity matrix:

$$\frac{\partial N_i}{\partial \varepsilon} = \frac{\varepsilon_i}{8}(1+\eta_i\eta)(1+\zeta_i\zeta) \tag{A.7}$$

$$\frac{\partial N_i}{\partial \eta} = \frac{\eta_i}{8}(1+\varepsilon_i\varepsilon)(1+\zeta_i\zeta) \tag{A.8}$$

$$\frac{\partial N_i}{\partial \zeta} = \frac{\zeta_i}{8}(1+\varepsilon_i\varepsilon)(1+\eta_i\eta) \tag{A.9}$$

Istok uses these interpolation functions on a unit cube as a basis from which any rectangular prism can be interpolated through the use of a Jacobian to transform the coordinate system. We will still be taking advantage of this transformation technique, but we are only interested in part of this cube, not the entire thing.

Suppose that in the ε direction the pipe has dimensions and locations such that it is bounded by ε_a and ε_b. We would like to transform this variable so that at when ε_t = -1, $\varepsilon = \varepsilon_a$ and when $\varepsilon_t = 1$, $\varepsilon = \varepsilon_b$. This can be accomplished through a linear transform so that $\varepsilon_t = m\varepsilon + b$.

$$\left(\begin{array}{cc|c} -1 & 1 & m \\ 1 & 1 & b \end{array}\right) = \begin{pmatrix} \varepsilon_a \\ \varepsilon_b \end{pmatrix} \tag{A.10}$$

In this manner we derive new variables: ε_t, η_t, and ζ_t. These variables are then substituted into Equation A.7 to create a new equation:

$$N_i = \frac{1}{8}(1 + \varepsilon_i\varepsilon_t)(1 + \eta_i\eta_t)(1 + \zeta_i\zeta_t) \tag{A.11}$$

This new equation contains a reduced interpolation function of the original domain. It is the original interpolation function over the pipe volume being removed transformed to fit in a domain from (-1,-1,-1) to (1,1,1). Using this interpolation function we can perform Gauss Legendre numerical integration using Istok's standard techniques.

Now that we have the correct sub interpolation function for our element we can look at applying them to generate the sub-local conductivity and capacity matrices. The generation of the sub-capacity matrix follows directly from Istok. The conductivity matrix is complicated because of the derivatives of the interpolation functions involved in the FEM derivation. The chain rule must be applied when changing variables.

Each interpolation function has a partial derivative with respect to each of its variables for use in calculating the local conductivity matrix:

$$\frac{\partial N_i}{\partial \varepsilon} = \frac{\partial \varepsilon_t}{\partial \varepsilon}\frac{\varepsilon_i}{8}(1 + \eta_i\eta_t)(1 + \zeta_i\zeta_t) \tag{A.12}$$

$$\frac{\partial N_i}{\partial \eta} = \frac{\partial \eta_t}{\partial \eta}\frac{\eta_i}{8}(1 + \varepsilon_i\varepsilon_t)(1 + \zeta_i\zeta_t) \tag{A.13}$$

$$\frac{\partial N_i}{\partial \zeta} = \frac{\partial \zeta_t}{\partial \zeta}\frac{\zeta_i}{8}(1 + \varepsilon_i\varepsilon_t)(1 + \eta_i\eta_t) \tag{A.14}$$

Where the partial derivative of the replacement variable with respect to the original variable is the m value found calculated using Equation A.10.

With the application of a Jacobian transform and Guass-Legendre quadrature the pipe volume integrals can be performed. The local element conductivity matrices generated through these techniques can be directly subtracted from the global conductivity matrix at the same degrees of freedom of the original soil continuum element. After this final step, the volume taken up by the pipe in a soil element has been accounted for and removed and the model will converge properly with h refinement.

Since this technique can only handle straight sections of pipe, corners must be handled differently. When a pipe takes a corner it is already considered in two sections, the section going into the bend and the section coming out of the bend. Because the method for removing pipes from the continuum as discussed in this section only considered pipes parallel to a major axis, corners are limited to 90° turns. To handle a 90° corner the first pipe section is extended by half of the modified radius calculated in A.4 in the direction of the corner. The section after the corner is then shortened by the same length on the end coming out of the corner. This process is illustrated in Figure A.1.

The sub element conductivity matrices have been checked against an alternative technique. The Gauss Legendre interpolation points in (-1,-1,-1) to (1,1,1) can be translated into the reduced coordinate space using Equation A.10. These translated points are then fed into the element conductivity matrix generator used for generating the full element local conductivity matrix. The resulting matrix needs to be factored by the ratio of the volume of pipe in the element to the volume of the total element. The resulting sub local conductivity matrices calculated using both methods are exactly equal.

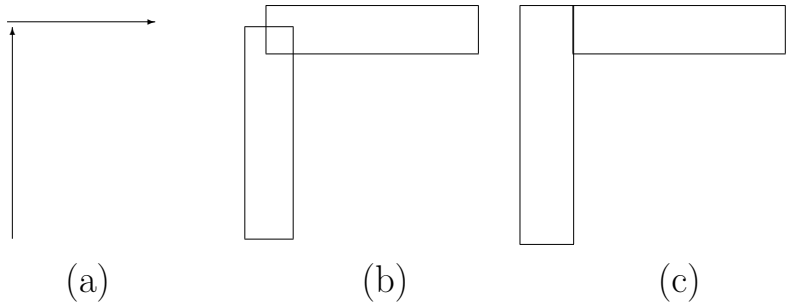

Figure A.1: Pipe volume integral schematic. The vectorized pipe layout (a) would have overlap if the pipes were expanded without modification (b). To correct for this, the first pipe is extended by its radius and the second pipe is shortened by its radius. The resulting pipes do not overlap and full continuity is preserved on corners (c).

Appendix B

Derivation of a finite element solution for heat transport in the soil continuum

Heat transport in the soil continuum is governed by Fourier's Law. In HEN, the three dimensional, transient, with sources/sinks and storage is represented by the governing equation

$$\rho c \frac{\partial T}{\partial t} = \vec{\nabla} \cdot (\boldsymbol{K} \cdot \vec{\nabla} T) + \vec{q} \tag{B.1}$$

where $\vec{q}$ [W m^{-3}] is the local volumetric heat flux from the GLHE, $\boldsymbol{K}$ [W m^{-1} K^{-1}] is the thermal conductivity tensor of the media (in this document the tensor $\boldsymbol{K}$ is typically referred to as $K \cdot \boldsymbol{I}$, where $\boldsymbol{I}$ is the unit matrix, corresponding to isotropic conductivity), ρc [J K^{-1} m^{-3}] is the volumetric heat capacity, and ∇T [K m^{-1}] is the temperature gradient.

HEN solves the equation using Cartesian coordinates and an isotropic conductivity

tensor ($K_x = K_y = K_z$), where Equation B.1 takes the form:

$$\rho c \frac{\partial T}{\partial t} = \frac{\partial}{\partial x}\left(K\frac{\partial T}{\partial x}\right) + \frac{\partial}{\partial y}\left(K\frac{\partial T}{\partial y}\right) + \frac{\partial}{\partial z}\left(K\frac{\partial T}{\partial z}\right) + \vec{q} \tag{B.2}$$

The finite element method will be used to solve this equation numerically. Trilinear shape functions will be used and Galerkin's method will be applied following the solutions detailed Istok (1989).

An approximate solution, $\hat{T}$, which is substituted into equation B.2, the equation is no longer satisfied exactly and becomes:

$$R(x) = \frac{\partial}{\partial x}\left(K\frac{\partial \hat{T}}{\partial x}\right) + \frac{\partial}{\partial y}\left(K\frac{\partial \hat{T}}{\partial y}\right) + \frac{\partial}{\partial z}\left(K\frac{\partial \hat{T}}{\partial z}\right) + \vec{q} - \rho c \frac{\partial \hat{T}}{\partial t} \neq 0 \tag{B.3}$$

where $R(x)$, the residual vector, is defined to be the value of the residual at each node in the finite element mesh. The contributions to the residual vector are defined element-by-element as

$$\begin{aligned}
R_i^{(e)} &= -\iiint_{V^{(e)}} N_i^{(e)} \left[\frac{\partial}{\partial x}\left(K\frac{\partial \hat{T}^{(e)}}{\partial x}\right) + \frac{\partial}{\partial y}\left(K\frac{\partial \hat{T}^{(e)}}{\partial y}\right) + \frac{\partial}{\partial z}\left(K\frac{\partial \hat{T}^{(e)}}{\partial z}\right) + \vec{q}^{(e)} - \rho c \frac{\partial \hat{T}^{(e)}}{\partial t}\right] dx\, dy\, dz \\
&= -\iiint_{V^{(e)}} N_i^{(e)} \left[\frac{\partial}{\partial x}\left(K\frac{\partial \hat{T}^{(e)}}{\partial x}\right) + \frac{\partial}{\partial y}\left(K\frac{\partial \hat{T}^{(e)}}{\partial y}\right) + \frac{\partial}{\partial z}\left(K\frac{\partial \hat{T}^{(e)}}{\partial z}\right)\right] dx\, dy\, dz \\
&\quad - \iiint_{V^{(e)}} N_i^{(e)} \vec{q}^{(e)} dx\, dy\, dz \\
&\quad + \iiint_{V^{(e)}} N_i^{(e)} \rho c \frac{\partial \hat{T}^{(e)}}{\partial t} dx\, dy\, dz
\end{aligned}$$

where $N_i^{(e)}$ (see Equation D.1) is the nodal interpolation function for node i in element e,

$V^{(e)}$ is the volume of element e, R_i^e is the contribution, and

$$\hat{T}^{(e)} = \sum_{i=1}^{n} N_i^{(e)} T_i \tag{B.4}$$

where T_i is the unknown temperature at node i.

The elemental flux derivation is detailed in Appendix D and is only shown here as $\vec{q}^{(e)}$ to show how the elemental flux fits into the derivation of the governing equation. It will be omitted going forward.

Moving forward, the residuals of the approximating governing equation can be further simplified by knowing that the nodal interpolation functions all have an undefined second derivative (see Equation A.7 for the first derivatives of the nodal interpolation functions) and integration by parts to get

$$\begin{aligned} R_i^{(e)} = &- \iiint_{V^{(e)}} K\, N_i^{(e)} \left[\frac{\partial N_i^{(e)}}{\partial x} \frac{\partial \hat{T}^{(e)}}{\partial x} + \frac{\partial N_i^{(e)}}{\partial y} \frac{\partial \hat{T}^{(e)}}{\partial y} + \frac{\partial N_i^{(e)}}{\partial z} \frac{\partial \hat{T}^{(e)}}{\partial z} \right] dx\, dy\, dz \\ &+ \iiint_{V^{(e)}} N_i^{(e)} \rho c \frac{\partial \hat{T}^{(e)}}{\partial t} dx\, dy\, dz \end{aligned} \tag{B.5}$$

The above equation is then expanded to create the combined system of equations for the element e ($\mathbf{K}$ and $\mathbf{C}$ to be defined from the above later)

$$\vec{R}^{(e)} = \mathbf{K}^{(e)} \vec{T}^{(e)} - \mathbf{C}^{(e)} \frac{\vec{T}}{dt} \tag{B.6}$$

which can then be further expanded to the global expanded system

$$\vec{R} = \mathbf{K}\vec{T} - \mathbf{C}\frac{\vec{T}}{dt} \tag{B.7}$$

The capacity matrix, $\mathbf{C}$, is an 8x8 matrix in the brick node formulation used in HEN. It is derived by expanding the heat capacity portion of Equation B.5 to get

$$\mathbf{C}^{(e)} = \iiint_{V^{(e)}} \begin{bmatrix} N_1^{(e)} \\ \vdots \\ N_8^{(e)} \end{bmatrix} [\rho c] \begin{bmatrix} N_1^{(e)} & \cdots & N_8^{(e)} \end{bmatrix} dx\, dy\, dz \tag{B.8}$$

this is referred to as the consistent formulation of the capacity matrix. HEN also implements the lumped formulation where capacity is assigned equally to equally to all nodes in an element. This method of generating the capacity matrix is limited to symmetric elements, which is what HEN uses. The lumped formulation is as follows:

$$\mathbf{C}^{(e)} = \rho c \frac{V^{(e)}}{8} \begin{bmatrix} 1 & & 0 \\ & \ddots & \\ 0 & & 1 \end{bmatrix} \tag{B.9}$$

In HEN, $\mathbf{K}^{(e)}$ is an 8x8 matrix because of the 8 nodes in each brick element. It is derived by expanding the conductivity/double derivative portion Equation B.5 to get

$$\mathbf{K}^{(e)} = \iiint_{V^{(e)}} \begin{bmatrix} \frac{\partial N_1^{(e)}}{\partial x} & \frac{\partial N_1^{(e)}}{\partial y} & \frac{\partial N_1^{(e)}}{\partial z} \\ \vdots & \vdots & \vdots \\ \frac{\partial N_8^{(e)}}{\partial x} & \frac{\partial N_8^{(e)}}{\partial y} & \frac{\partial N_8^{(e)}}{\partial z} \end{bmatrix} \begin{bmatrix} K & 0 & 0 \\ 0 & K & 0 \\ 0 & 0 & K \end{bmatrix} \begin{bmatrix} \frac{\partial N_1^{(e)}}{\partial x} & \cdots & \frac{\partial N_8^{(e)}}{\partial x} \\ \frac{\partial N_1^{(e)}}{\partial y} & \cdots & \frac{\partial N_8^{(e)}}{\partial y} \\ \frac{\partial N_1^{(e)}}{\partial z} & \cdots & \frac{\partial N_8^{(e)}}{\partial z} \end{bmatrix} dx\, dy\, dz \tag{B.10}$$

To solve the conductivity matrix and the consistent formulation of the capacity matrix isoparametric elements were used with a Jacobian matrix to generalize the coordinate system and the integrals were calculated numerically with Gauss Legendre quadrature. The isoparametric nodal interpolation functions from Equations D.1 and node values in Equation A.6 were used to create a Jacobian matrix in a generalized coordinate system $(\varepsilon, \eta, \zeta)$.

$$\mathbf{J}^{(e)} = \begin{bmatrix} \frac{\partial N_1}{\partial \varepsilon} & \cdots & \frac{\partial N_8}{\partial \varepsilon} \\ \frac{\partial N_1}{\partial \eta} & \cdots & \frac{\partial N_8}{\partial \eta} \\ \frac{\partial N_1}{\partial \zeta} & \cdots & \frac{\partial N_8}{\partial \zeta} \end{bmatrix} \begin{bmatrix} x_1 & y_1 & z_1 \\ \vdots & \vdots & \vdots \\ x_8 & y_8 & z_8 \end{bmatrix} \tag{B.11}$$

using the Jacobian the equations for the conductivity matrix and the consistent formulation of the capacity matrix can be rewritten to

$$\mathbf{K}^{(e)} = \int_{-1}^{1}\int_{-1}^{1}\int_{-1}^{1} \begin{bmatrix} \frac{\partial N_1^{(e)}}{\partial \varepsilon} & \frac{\partial N_1^{(e)}}{\partial \eta} & \frac{\partial N_1^{(e)}}{\partial \zeta} \\ \vdots & \vdots & \vdots \\ \frac{\partial N_8^{(e)}}{\partial \varepsilon} & \frac{\partial N_8^{(e)}}{\partial \eta} & \frac{\partial N_8^{(e)}}{\partial \zeta} \end{bmatrix} [\mathbf{J}^{-1}]^T \begin{bmatrix} K & 0 & 0 \\ 0 & K & 0 \\ 0 & 0 & K \end{bmatrix}$$
$$[\mathbf{J}^{-1}] \begin{bmatrix} \frac{\partial N_1^{(e)}}{\partial \varepsilon} & \cdots & \frac{\partial N_8^{(e)}}{\partial \varepsilon} \\ \frac{\partial N_1^{(e)}}{\partial \eta} & \cdots & \frac{\partial N_8^{(e)}}{\partial \eta} \\ \frac{\partial N_1^{(e)}}{\partial \zeta} & \cdots & \frac{\partial N_8^{(e)}}{\partial \zeta} \end{bmatrix} |\mathbf{J}|\, d\varepsilon\, d\eta\, d\zeta \tag{B.12}$$

and

$$\mathbf{C}^{(e)} = \int_{-1}^{1}\int_{-1}^{1}\int_{-1}^{1} \begin{bmatrix} N_1^{(e)} \\ \vdots \\ N_8^{(e)} \end{bmatrix} [\rho c] \begin{bmatrix} N_1^{(e)} & \cdots & N_8^{(e)} \end{bmatrix} |\mathbf{J}| d\varepsilon\, d\eta\, d\zeta \tag{B.13}$$

respectively. Equations B.12 and B.13 were then solved using Guass Legendre quadrature. The general form of this quadrature:

$$\int_{-1}^{1}\int_{-1}^{1}\int_{-1}^{1} f(\varepsilon,\eta,\zeta) d\varepsilon\, d\eta\, d\zeta = \sum_{i=1}^{G_{points}} W_i f(\varepsilon_i,\eta_i,\zeta_i) \tag{B.14}$$

where G_{points} is the number of quadrature points used to evaluate the integral, W_i is the weighting of quadrature point i and $f(\varepsilon_i,\eta_i,\zeta_i)$ is the evaluation of f at quadrature point i. In HEN 8 quadrature points are used: $1/\sqrt{3}$ and $-1/\sqrt{3}$ in each direction of ε, η, and ζ. Each point has a weight of 1.

With this application we have solved for the matrices $\mathrm{K}^{(e)}$ and $\mathrm{C}^{(e)}$ which can be subbed into their global equivalents and we can return to our global equation

$$\vec{R} = \mathbf{K}\vec{T} - \mathbf{C}\frac{\vec{T}}{dt} \tag{B.15}$$

set the residuals to zero and solve

$$\vec{R} = 0 = \mathbf{K}\vec{T} - \mathbf{C}\frac{\vec{T}}{dt} \tag{B.16}$$

The implementation of the timestepping algorithm is dealt with in Chapter 2.

Appendix C

Derivation of a finite element solution for the pipe network model

The notation used in the derivations presented in this appendix deviate from the notations used in the rest of the document. The in-pipe temperatures, T_p elsewhere, are represented by T here to improve the readability of the subscripts in the finite element method. The temperatures of the soil continuum, T elsewhere, are represented by T_{soil}.

Steady state flow in a pipe with advection, dispersion, and convective cooling is described by the following governing equation:

$$0 = -v\frac{\partial T}{\partial x} + (D_L + \alpha_f)\frac{\partial^2 T}{\partial x^2} - \frac{K_p}{\rho \cdot c_p \cdot L}(T - T_{\text{soil}}) \tag{C.1}$$

where $T(x,t)$ is the temperature of the fluid in the pipe as a function of distance in the pipe and time, v $[\frac{\text{m}}{\text{s}}]$ is the velocity of the fluid within the pipe, $D_L(v)$ $[\frac{\text{m}^2}{\text{s}}]$ is the longitudinal dispersivity caused by mechanical mixing in the pipe flow, α_f $[\frac{\text{m}^2}{\text{s}}]$ is the thermal diffusivity

of the fluid in the pipe (a second order effect, along with mechanical mixing), and ρ $[\frac{\text{kg}}{\text{m}^3}]$ and c_p $[\frac{\text{J}}{\text{kg}\cdot\text{K}}]$ are the density and specific heat capacity of the heat exchanger fluid. The other two parameters, K_p $[\frac{\text{W}}{\text{m}\cdot\text{K}}]$ and T_{soil} [K], are used to describe the interaction of the pipe with the soil continuum. K_p is a representative thermal conductivity of the pipe wall and T_{soil} is the temperature of the soil continuum immediately adjacent to the outside of the pipe wall. L is the effective thickness of the pipe wall. The combination of the L, K_p, c_p and ρ, terms gives the steady state thermal resistance between the fluid in the pipe and the soil on the outside of the pipe.

In this appendix, a numerical solution to this partial differential equation at steady state ($\frac{\partial T}{\partial t} = 0$) is developed using the finite element method.

The governing equation can be represented in the simplified form:

$$0 = -A\frac{\partial^2 T}{\partial x^2} + B\frac{\partial T}{\partial x} + C(x)T + D(x) \tag{C.2}$$

The finite element method will be used to solve this equation numerically. Linear shape functions will be used and Galerkin's method will be applied.

An approximate solution, $\hat{T}$, which is substituted into equation C.2, the equation is no longer satisfied exactly:

$$-A\frac{\partial^2 \hat{T}}{\partial x^2} + B\frac{\partial \hat{T}}{\partial x} + C(x)\hat{T} + D(x) = R(x) \neq 0 \tag{C.3}$$

Define the vector R to be the value of the residual at each node in the finite element mesh. The residual at any node i, R_i, represents the error between the true value of temperature and the approximate solution $\hat{T}$ at that node. The residual at each node is a

contribution from each element connected to that node. In general we can write:

$$R_i = \sum_{e=1}^{p} R_i^{(e)} \tag{C.4}$$

where p is the number of elements that are joined to node i.

The contribution of element e to the residual at node i can be obtained from the integral formulation for that node:

$$R_i^{(e)} = \int_{x_i^{(e)}}^{x_j^{(e)}} N_i^{(e)} \left[-A\frac{\partial^2 \hat{T}^{(e)}}{\partial x^2} + B\frac{\partial \hat{T}^{(e)}}{\partial x} + C(x)\hat{T}^{(e)} + D(x) \right] dx \tag{C.5}$$

where $x_i^{(e)}$ and $x_j^{(e)}$ are the coordinates at either end of the element, $N_i^{(e)}$ is the weighting function for node i in element e (as required by Galerkin's method). $C(x)$ and $D(x)$ will be assumed to be constant within each element.

$\hat{T}$ is defined as:

$$\begin{aligned} \hat{T}^{(e)} &= N_i^{(e)} T_i + N_j^{(e)} T_j \\ &= \frac{x_j^{(e)} - x}{L^{(e)}} T_i + \frac{x - x_i^{(e)}}{L^{(e)}} T_j \end{aligned} \tag{C.6}$$

where $L^{(e)}$ is the length of element e.

The terms in equation C.2 were combined to form a system of linear equations:

$$\mathbf{R} = [\mathbf{A} + \mathbf{B} + \mathbf{C}]\vec{T} + \mathbf{D} \tag{C.7}$$

Each of the global matrices will be created by solving local matrices. The creation of each of these local matrices is given in the following pages.

A integral

The integral

$$\int_{x_i^{(e)}}^{x_j^{(e)}} N_i^{(e)} \left[-A \frac{\partial^2 \hat{T}^{(e)}}{\partial x^2} \right] N_i^{(e)\intercal} \, dx \tag{C.8}$$

Can be solved as in Istok (1989) using integration by parts to get a matrix

$$[A^{(e)}] = \frac{A}{L^{(e)}} \begin{bmatrix} 1 & -1 \\ -1 & 1 \end{bmatrix} \tag{C.9}$$

B integral

Next we will determine the contribution to the residual at i from the B term. The integral

$$\int_{x_i^{(e)}}^{x_j^{(e)}} N_i^{(e)} \left[B \frac{\partial \hat{T}^{(e)}}{\partial x} \right] dx \tag{C.10}$$

From the definition of $\hat{T}^{(e)}$ in equation C.6 we can write:

$$\begin{aligned} \frac{\partial \hat{T}^{(e)}}{\partial x} &= \frac{\partial}{\partial x} \left(\frac{x_j^{(e)} - x}{L^{(e)}} T_i + \frac{x - x_i^{(e)}}{L^{(e)}} T_j \right) \\ &= -\frac{1}{L^{(e)}} T_i + \frac{1}{L^{(e)}} T_j \\ &= \frac{1}{L^{(e)}} (-T_i + T_j) \end{aligned} \tag{C.11}$$

To improve readability, the substitutions $x_i^{(e)} = 0$ and $x_j^{(e)} = L^{(e)}$ were made. Substitute

equation C.11 into equation C.10 to get:

$$\int_{x_i^{(e)}}^{x_j^{(e)}} N_i^{(e)} \left[B \frac{\partial \hat{T}^{(e)}}{\partial x} \right] dx \tag{C.12}$$

$$= \int_{x_i^{(e)}}^{x_j^{(e)}} \frac{x_j^{(e)} - x}{L^{(e)}} \left[B \frac{1}{L^{(e)}} (-T_i + T_j) \right] dx \tag{C.13}$$

$$= \frac{x_j^{(e)} x - \frac{x^2}{2}}{L^{(e)}} \Big|_0^L \left[B \frac{1}{L^{(e)}} (-T_i + T_j) \right] \tag{C.14}$$

$$= \frac{\frac{L^{(e)}}{2}}{L^{(e)}} \left[B \frac{1}{L^{(e)}} (-T_i + T_j) \right] \tag{C.15}$$

$$= \frac{1}{2} \left[B \frac{1}{L^{(e)}} (-T_i + T_j) \right] \tag{C.16}$$

$$= \frac{B}{2L^{(e)}} (-T_i + T_j) \tag{C.17}$$

Examining the same integral at node j we have:

$$\int_{x_i^{(e)}}^{x_j^{(e)}} N_j^{(e)} \left[B \frac{\partial \hat{T}^{(e)}}{\partial x} \right] dx \tag{C.18}$$

$$= \int_{x_i^{(e)}}^{x_j^{(e)}} \frac{x - x_i^{(e)}}{L^{(e)}} \left[B \frac{1}{L^{(e)}} (-T_i + T_j) \right] dx \tag{C.19}$$

$$= \frac{\frac{x^2}{2} - x_i^{(e)} x}{L^{(e)}} \Big|_0^L \left[B \frac{1}{L^{(e)}} (-T_i + T_j) \right] \tag{C.20}$$

$$= \frac{\frac{L^{(e)}}{2}}{L^{(e)}} \left[B \frac{1}{L^{(e)}} (-T_i + T_j) \right] \tag{C.21}$$

$$= \frac{1}{2} \left[B \frac{1}{L^{(e)}} (-T_i + T_j) \right] \tag{C.22}$$

$$= \frac{B}{2L^{(e)}} (-T_i + T_j) \tag{C.23}$$

The contributions to the residuals can be written as:

$$[B^{(e)}] = \frac{B}{2L^{(e)}} \begin{bmatrix} -1 & 1 \\ -1 & 1 \end{bmatrix} \tag{C.24}$$

As a sanity check, the units can be examined. Where: L = length, T = time, K = temperature:

$$\frac{B}{2L^{(e)}} \begin{bmatrix} -1 & 1 \\ -1 & 1 \end{bmatrix} = \frac{\frac{L}{T}}{L} K = \frac{K}{T} \tag{C.25}$$

The units work out as expected.

C integral

Now we will examine the contribution from the C term. Here, C is assumed to be constant within each element:

$$\int_{x_i^{(e)}}^{x_j^{(e)}} N_i^{(e)} \left[C\hat{T}^{(e)}\right] dx \tag{C.26}$$

$$= \int_{x_i^{(e)}}^{x_j^{(e)}} \frac{x_j^{(e)} - x}{L^{(e)}} \left[C\left(\frac{x_j^{(e)} - x}{L^{(e)}} T_i + \frac{x - x_i^{(e)}}{L^{(e)}} T_j\right)\right] dx \tag{C.27}$$

$$= \frac{C}{L^{2(e)}} \int_{x_i^{(e)}}^{x_j^{(e)}} (x_j^{(e)} - x)\left((x_j^{(e)} - x)T_i + (x - x_i^{(e)})T_j\right) dx \tag{C.28}$$

$$= \frac{C}{L^{2(e)}} \int_{x_i^{(e)}}^{x_j^{(e)}} \left((x_j^{(e)} - x)^2 T_i + (x - x_i^{(e)})(x_j^{(e)} - x)T_j\right) dx \tag{C.29}$$

$$= \frac{C}{L^{2(e)}} \int_{x_i^{(e)}}^{x_j^{(e)}} \left((x_j^{2(e)} - 2x \cdot x_j^{(e)} + x^2)T_i + ((-1)x^2 + x \cdot x_i^{(e)} + x \cdot x_j^{(e)} - x_i^{(e)} x_j^{(e)})T_j\right) dx \tag{C.30}$$

$$= \frac{C}{L^{2(e)}} \int_{x_i^{(e)}}^{x_j^{(e)}} \left((L^{2(e)} - 2x \cdot L^{(e)} + x^2)T_i + ((-1)x^2 + x \cdot L^{(e)})T_j\right) dx \tag{C.31}$$

$$= \frac{C}{L^{2(e)}} \left((L^{2(e)} \cdot L^{(e)} - L^{2(e)} \cdot L^{(e)} + \frac{1}{3}L^{3(e)})T_i + (\frac{-1}{3}L^{3(e)} + \frac{1}{2}L^{2(e)} \cdot L^{(e)})T_j\right) \tag{C.32}$$

$$= CL^{(e)} \left(\frac{1}{3}T_i + \frac{1}{6}T_j\right) \tag{C.33}$$

This can easily be evaluated for numerical values. The residual at j follows similarly:

$$\int_{x_i^{(e)}}^{x_j^{(e)}} N_j^{(e)} \left[C\hat{T}^{(e)}\right] dx \tag{C.34}$$

$$= \int_{x_i^{(e)}}^{x_j^{(e)}} \frac{x}{L^{(e)}} \left[C\left(\frac{L^{(e)}-x}{L^{(e)}}T_i + \frac{x}{L^{(e)}}T_j\right)\right] dx \tag{C.35}$$

$$= \frac{C}{L^{2(e)}} \int_{x_i^{(e)}}^{x_j^{(e)}} x\left[\left((L^{(e)}-x)T_i + (x)T_j\right)\right] dx \tag{C.36}$$

$$= \frac{C}{L^{2(e)}} \int_{x_i^{(e)}}^{x_j^{(e)}} \left[\left((L^{(e)}x - x^2)T_i + (x^2)T_j\right)\right] dx \tag{C.37}$$

$$= \frac{C}{L^{2(e)}} \left[\left(\left(\frac{L^{3(e)}}{2} - \frac{L^{3(e)}}{3}\right)T_i + \left(\frac{L^{3(e)}}{3}\right)T_j\right)\right] \tag{C.38}$$

$$= CL^{(e)} \left[\left(\left(\frac{1}{2} - \frac{1}{3}\right)T_i + \left(\frac{1}{3}\right)T_j\right)\right] \tag{C.39}$$

$$= CL^{(e)} \left[\left(\left(\frac{1}{6}\right)T_i + \left(\frac{1}{3}\right)T_j\right)\right] \tag{C.40}$$

The contributions to the residuals can be written as:

$$[C^{(e)}] = \frac{CL^{(e)}}{2} \begin{bmatrix} \frac{2}{3} & \frac{1}{3} \\ \frac{1}{3} & \frac{2}{3} \end{bmatrix} \tag{C.41}$$

D integral

D is not a function of T and so can be represented as a vector multiplied by the identity matrix. For node i:

$$\int_{x_i^{(e)}}^{x_j^{(e)}} N_i^{(e)} [D] \, dx \tag{C.42}$$

$$= D \int_{x_i^{(e)}}^{x_j^{(e)}} \frac{x_j^{(e)} - x}{L^{(e)}} dx \tag{C.43}$$

$$= \frac{D}{L^{(e)}} \left(\int_{x_i^{(e)}}^{x_j^{(e)}} x_j^{(e)} \, dx - \int_{x_i^{(e)}}^{x_j^{(e)}} x \, dx \right) \tag{C.44}$$

$$= \frac{D}{L^{(e)}} \left(L^{2(e)} - \frac{L^{2(e)}}{2} \right) \tag{C.45}$$

$$= \frac{DL^{(e)}}{2} \tag{C.46}$$

For node j:

$$\int_{x_i^{(e)}}^{x_j^{(e)}} N_j^{(e)} [D] \, dx \tag{C.47}$$

$$= D \int_{x_i^{(e)}}^{x_j^{(e)}} \frac{x - \cancelto{0}{x_i^{(e)}}}{L^{(e)}} dx \tag{C.48}$$

$$= \frac{D}{L^{(e)}} \left(\int_{x_i^{(e)}}^{x_j^{(e)}} x \, dx \right) \tag{C.49}$$

$$= \frac{D}{L^{(e)}} \left(\frac{L^{2(e)}}{2} \right) \tag{C.50}$$

$$= \frac{DL^{(e)}}{2} \tag{C.51}$$

The resulting element vector is:

$$[D^{(e)}] = \frac{DL^{(e)}}{2} \begin{bmatrix} 1 \\ \\ 1 \end{bmatrix} \tag{C.52}$$

Summary

When each of the submatrices and vectors are assembled together in a global system we have a model for advection-diffusion of temperature in a flowing fluid. The matrix **A** provides the diffusion of the temperature forward and backward in the pipe, matrix **B** translates temperatures forward in the pipe, and matrix **C** handles the energy coming from outside of the pipe.

The resulting system of equations could be modified to be non-steady state by the inclusion of a capacity matrix.

Appendix D

Derivation of the flux weighting scheme used in Standard FEM

The weighting of fluxes from a pipe passing through a cubic element is derived. The approach presented uses a parametrized line integrated from beginning to end. The relative weight of each node inside of the desired element is found, these relative weights then need to be summed to assign the fraction of the pipe flux each node receives.

Definitions:

- Interpolation function (cubic):

$$N_{(i,j,k)}(x,y,z) = \frac{1}{8}(1+ix)(1+jy)(1+kz) \tag{D.1}$$

  Where (i,j,k) are the isoparameteric coordinates of a specific node within the matrix. The function is dependent upon the spatial variables (x,y,z). See Table A.6 for values of (i,j,k) for each node of the rectangular prism.

- Pipe: The pipe is defined as starting at ENTER(a,b,c) and finishing at EXIT(A,B,C).

- Parametrized curve:

  Define a linear curve, $f(t)$, using a system of equations parametrized to t. This line goes through ENTER and EXIT such that $f(0) =$ ENTER and $f(1) =$ EXIT.

$$
\begin{aligned}
f: \; x &= a + t(A - a) = a + t\Delta X \\
y &= b + t(B - b) = b + t\Delta Y \\
z &= c + t(C - c) = c + t\Delta Z
\end{aligned}
$$

  Where $\Delta X = (A - a)$, $\Delta Y = (B - b)$, and $\Delta Z = (C - c)$.

Begin with the field equation of the interpolation function (Equation D.1) and substi-

tute the parametrized curve:

$$N(x,y,z) = \frac{1}{8}(1+ix)(1+jy)(1+kz)$$

$$N(t) = \frac{1}{8}(1+ia+it\Delta X)(1+jb+jt\Delta Y)(1+kc+kt\Delta Z)$$

expanding the first brackets:

$$N(t) = \frac{1}{8}[(1+jb+jt\Delta Y)(1+kc+kt\Delta Z)+ia(1+jb+jt\Delta Y)(1+kc+kt\Delta Z)$$
$$+it\Delta X(1+jb+jt\Delta Y)(1+kc+kt\Delta Z)]$$

then perform a full expansion of the first of the three terms:

$$N(t) = \frac{1}{8}[$$
$$1$$
$$+jb+kc$$
$$+jt\Delta Y+kt\Delta Z$$
$$+jbkc$$
$$+jbkt\Delta Z+kcjt\Delta Y$$
$$+jkt^2\Delta Y\Delta Z$$
$$+ia(1+jb+jt\Delta Y)(1+kc+kt\Delta Z)$$
$$+it\Delta X(1+jb+jt\Delta Y)(1+kc+kt\Delta Z)]$$

expand of the second set of terms:

$$
\begin{aligned}
N(t) = & \frac{1}{8}[\\
& 1 \\
& + ia + jb + kc \\
& + jt\Delta Y + kt\Delta Z \\
& + jbkc + iajb + iakc \\
& + iajbkc \\
& + jbkt\Delta Z + kcjt\Delta Y + iajt\Delta Y + iakt\Delta Z \\
& + iajbkt\Delta Z + iakcjt\Delta Y \\
& + jkt^2\Delta Y\Delta Z + iajkt^2\Delta Y\Delta Z \\
& + it\Delta X(1 + jb + jt\Delta Y)(1 + kc + kt\Delta Z)]
\end{aligned}
$$

expand of the last set of terms:

$$
\begin{aligned}
N(t) = & \frac{1}{8}\big[\\
& 1 \\
& + ia + jb + kc \\
& + it\Delta X + jt\Delta Y + kt\Delta Z \\
& + jkbc + ijab + ikac \\
& + iajbkc \\
& + jkbt\Delta Z + jkct\Delta Y + ijat\Delta Y + ikat\Delta Z + ijbt\Delta X + ikct\Delta X \\
& + ijkbct\Delta X + ijkabt\Delta Z + ijkact\Delta Y \\
& + ijkat^2\Delta Y\Delta Z + ijkbt^2\Delta X\Delta Z + ijkct^2\Delta X\Delta Y \\
& + jkt^2\Delta Y\Delta Z + ijt^2\Delta X\Delta Y + ikt^2\Delta X\Delta Z \\
& + ijkt^3\Delta X\Delta Y\Delta Z\big]
\end{aligned}
$$

We must now integrate with respect to t from START to END, or from $t = 0$ to $t = 1$:

$$\begin{aligned}
\int_0^1 N(t) = \Big[\frac{1}{8} \big[& \\
& + t + iat + jbt + kct \\
& + \frac{1}{2} it^2 \Delta X + \frac{1}{2} jt^2 \Delta Y + \frac{1}{2} kt^2 \Delta Z \\
& + jkbct + ijabt + ikact \\
& + iajbkct \\
& + \frac{1}{2} jkbt^2 \Delta Z + \frac{1}{2} jkct^2 \Delta Y + \frac{1}{2} ijat^2 \Delta Y + \frac{1}{2} ikat^2 \Delta Z + \frac{1}{2} ijbt^2 \Delta X + \frac{1}{2} ikct^2 \Delta X \\
& + \frac{1}{2} ijkbct^2 \Delta X + \frac{1}{2} ijkabt^2 \Delta Z + \frac{1}{2} ijkact^2 \Delta Y \\
& + \frac{1}{3} ijkat^3 \Delta Y \Delta Z + \frac{1}{3} ijkbt^3 \Delta X \Delta Z + \frac{1}{3} ijkct^3 \Delta X \Delta Y \\
& + \frac{1}{3} jkt^3 \Delta Y \Delta Z + \frac{1}{3} ijt^3 \Delta X \Delta Y + \frac{1}{3} ikt^3 \Delta X \Delta Z \\
& + \frac{1}{4} ijkt^4 \Delta X \Delta Y \Delta Z \big] \Big]_0^1
\end{aligned}$$

since all terms when $t = 0$ are zero, evaluate:

$$
\begin{aligned}
\int_0^1 N(t) = & \frac{1}{8}\big[\\
& + 1 + ia + jb + kc \\
& + \frac{1}{2}i\Delta X + \frac{1}{2}j\Delta Y + \frac{1}{2}k\Delta Z \\
& + jkbc + ijab + ikac \\
& + iajbkc \\
& + \frac{1}{2}jkb\Delta Z + \frac{1}{2}jkc\Delta Y + \frac{1}{2}ija\Delta Y + \frac{1}{2}ika\Delta Z + \frac{1}{2}ijb\Delta X + \frac{1}{2}ikc\Delta X \\
& + \frac{1}{2}ijkbc\Delta X + \frac{1}{2}ijkab\Delta Z + \frac{1}{2}ijkac\Delta Y \\
& + \frac{1}{3}ijka\Delta Y\Delta Z + \frac{1}{3}ijkb\Delta X\Delta Z + \frac{1}{3}ijkc\Delta X\Delta Y \\
& + \frac{1}{3}jk\Delta Y\Delta Z + \frac{1}{3}ij\Delta X\Delta Y + \frac{1}{3}ik\Delta X\Delta Z \\
& + \frac{1}{4}ijk\Delta X\Delta Y\Delta Z\big]
\end{aligned}
$$

This integral is for one node, the sum of the integrals must also be calculated to determine the full flux vector. Once the full flux vector is calculated it must be normalized before it can be used as a flux weighting scheme. Normalization ensures energy conservation between the pipe model and soil model.

Appendix E

HEN Benchmark

The Theis solution (Theis, 1935) for transient flow in a fully penetrating confined aquifer was used to benchmark the performance of HEN. Unit transformations converting aquifer properties to thermal properties allowed the solution to be compared to HEN. The formulation of the Theis solution uses some assumptions which are slightly incompatible with HEN:

The pumping well is fully penetrating with infinitesimal diameter HEN treats pipes has having a finite diameter (e.g. a 3/4" pipe) and is a full three dimensional simulation. To limit the impact of having a third dimension the domain was limited to a single element in the Y axis.

The aquifer is confined and infinite in extent There is no mechanic in HEN to simulate a confined system. To approximate the confined nature of the Theis solution the benchmark domain is 300 m from the surface and the surface layer was parameterized to have 10 orders of magnitude lower thermal conductivity. Low pumping

rates, a large domain, and short pumping times were used to approximate an aquifer of infinite extent.

The solution requires a number of other assumptions as well but none of them have major conflicts with the modelling structure HEN uses. In order to satisfy the horizontal flow assumption of the Theis solution, an artificial source term was used instead of a miniature pipe network. This source term was placed 300 m below the ground surface in the corner of the modelling domain. This was done to take advantage of the spatial symmetry of the Theis solution.

The Theis equation (Theis, 1935) is expressed as

$$h_0 - h = s = \frac{Q}{4\pi T} W(u) \tag{E.1}$$

where Q is the pumping rate and T is the transmissivity of the aquifer. The well function $W(u)$ is a function which evaluates an infinite series (not discussed here) and the dimensionless variable u is given by

$$u = \frac{r^2 S}{4Tt} \tag{E.2}$$

where S is the storativity of the aquifer, r is the specific radius of influence to measure the drawdown at, and t is the pumping time.

The calculation of storativity takes special consideration. Thermal storage is a combination of the heat capacity and the thickness of the confined unit. In this case the thickness

	Thermal equivalent	Unit	Value	Details
r	-	m	25,50,75	the distance from the center of the pipe/well to measure drawdown at
S	heat capacity	J m^{-2} K^{-1}	60	energy released per head change per unit surface area
T	thermal conductivity	W K^{-1}	1.24	energy flux over the width of the domain per unit temperature change
t	-	s	-	the time drawdown is measured at
Q	energy load	W	32	the rate of energy extraction or injection

is 1 m, with a unit area of 1 m^2 the storativity is

$$S = \frac{\text{Energy released}}{(\text{unit area}) \times (\text{unit head change})} \tag{E.3}$$

$$= \frac{\text{Energy released}}{(1\text{m}^2) \times (1\text{K})} \tag{E.4}$$

$$= \frac{60 \frac{\text{J}}{\text{m}^3 \cdot \text{K}} \times 1\text{m} \times 1\text{m}^2 \times 1\text{K}}{1\text{m}^2 \cdot \text{K}} \tag{E.5}$$

$$= 60 \frac{\text{J}}{\text{m}^2 \cdot \text{K}} \tag{E.6}$$

These units are slightly different than those specified by Theis ($\frac{\text{m}^3}{\text{m}^3}$) but will cancel out well with the modified transmissivity units.

Transmissivity is defined as conductivity times aquifer thickness. In thermal transport terms it is slightly altered:

$$T = Kb \tag{E.7}$$

$$= 1.24 \frac{\mathrm{W}}{\mathrm{m} \cdot \mathrm{K}} \times 1\mathrm{m} \tag{E.8}$$

$$= 1.24 \frac{\mathrm{J}}{\mathrm{s} \cdot \mathrm{K}} \tag{E.9}$$

All the variables were set up in a C++ program for generating multiple timeseries of the drawdown at different radii using a formulation of the Theis solution by Dr. James Craig. These drawdowns were then compared to an equivalent study performed in HEN. The agreement was found to be acceptable for the timeperiods considered (presented in Figures E.1 and E.2).

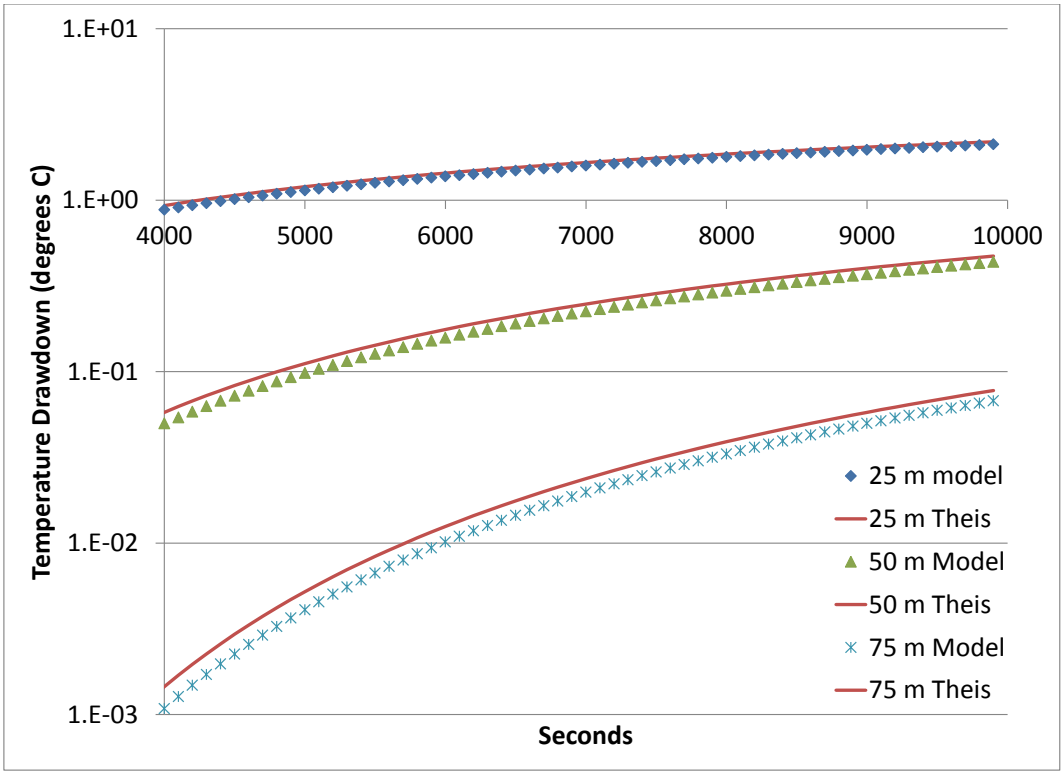

Figure E.1: HEN drawdown plotted against Theis drawdown at different radii from the source location. The temperature axis is in log scale.

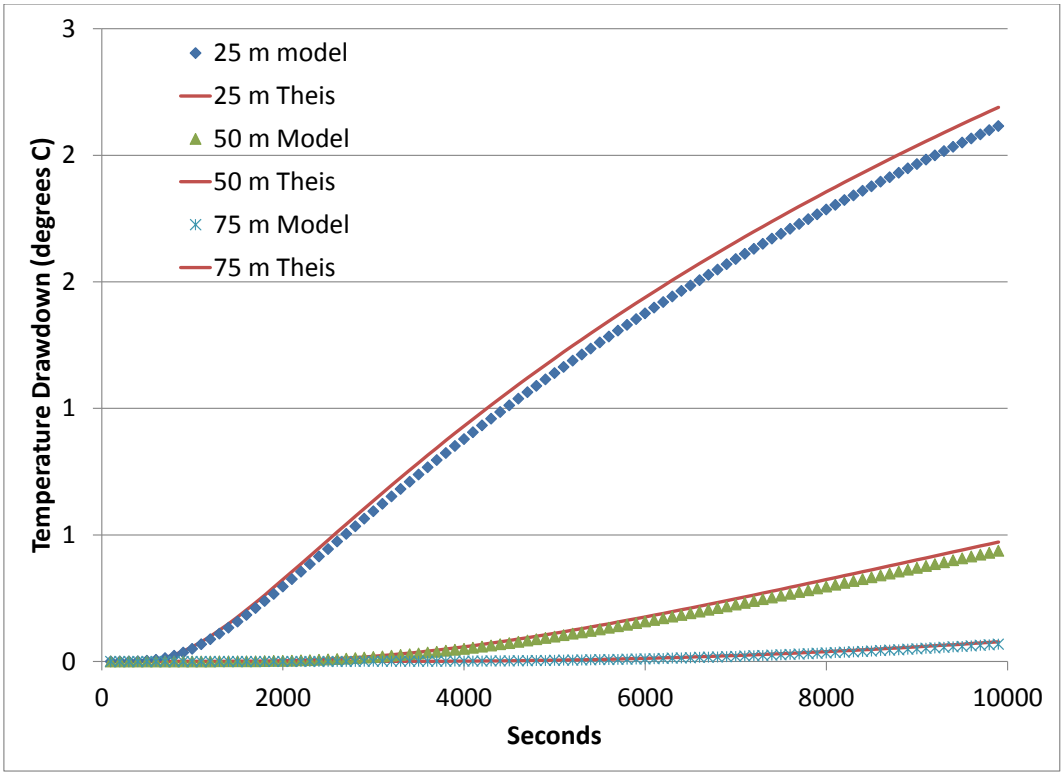

Figure E.2: HEN drawdown plotted against Theis drawdown at different radii from the source location. The temperature axis is in linear scale.

Appendix F

HEN tutorial example

To run the HEN tutorial place all files in a common folder. To perform a heterogeneous run, first run *sgsim.exe* to generate *conductivityVariance.csv* then run *Hen.exe*. HEN needs *input.txt* to be present in the run folder, all other files are referenced by *input.txt* and can be labelled as the user pleases. A list of all relevant input files follows, they have been pared down to a 10 day run from the 1300 day run shown in the tutorial section:

Input files

Hen.exe: The main executable. Looks for *input.txt* in the directory in which it is called.

sgsim.exe: The sequential Gaussian simulation library from GSLIB. Defaults to looking for *sgsim.par* as its input file. Generates a heterogeneous field which can be read directly by HEN.

sgsim.par: The input file for *sgsim.exe*. See Deutsch and Journel (1992) for the user

manual and algorithm description.

conductivityVariance.csv: The output file of *sgsim*. This file can be used by specifying it in *input.txt*. Values in this file represent the number of standard deviations that the thermal conductivity at a specific element is above (positive) or below (negative) the mean. See Appendix H for an example input file. The output line needs to be changed to "conductivityVariance.csv" for the purposes of this tutorial. The dimensions of this file must meet or exceed the dimensions of the specified grid and the discretization must be the same size or finer than the smallest discretization of the soil continuum. For example, if the smallest element in *gridDeclaration.txt* is 0.10 m x 2 m x 0.5 cm then the entire field must have that discretization in *sgsim*.

input.txt: The main HEN input file. Lists all files, controls output, controls timestepping, controls surface boundary, and has a testing option. If desired, a uniform autogenerated grid can be specified in this file. This file uses a strict structure, there are no comment lines. Each comma separated value must be on each line and in the correct format.

gridDeclaration.txt: If specified in *input.txt*, this file provides a custom grid spacing for the soil continuum.

initTemp.txt: If specified in *input.txt*, this file provides an initial temperature of the vertical profile of the soil continuum. If the file is not specified the initial temperature of the entire continuum is set to the first temperature in $OFF050.csv$.

OFF050.csv: This file must be specified in *input.txt*. This file provides a time series of temperatures representing the temperature at the surface of the soil continuum. If the user would like to simulate a no flux boundary then the surface soil parameters

can be tweaked to near infinite resistance in *input.txt*. This will effectively shut down the Dirichlet condition and turn it into a zero flux Neumann condition.

monitoredLocations.txt: If specified in *input.txt* (note: not used in the provided example *input.txt*), this file contains a list of x,y,z locations and files names. When a model run reaches completion, files will be created for each of the locations listed contain the temperature timeseries for that location.

PipeNetwork.txt: If specified in *input.txt*, this file details the GLHE pipe and contains all the relevant model parameters. In this file the user can specify the number of pipe elements to use, whether the pipe volumes should be integrated out of the soil continuum or not, and exchange fluid properties. If the file is not specified with the keyword "nopipe" then a simulation is done of the soil continuum with no GLHE system installed. This can be useful for doing vertical temperature profile simulations.

PipeLoads.csv: This file must be specified in *PipeNetwork.txt*. This file contains the boundary conditions of the pipe model. The boundary conditions are a time series of values which can either be fixed inlet temperature, specified by the "temperature" keyword, or a wattage requirement, specified by starting the second column with the string "watt". The first time in this file must match the first time in the $OFF050.csv$ file specifying the soil boundary condition. The files do not have to have the same time discretization, just the same starting point. For example, the user could use a daily average temperature for the soil boundary and a monthly average inlet temperature for the pipe boundary as long as both timeseries started at the same time.

File listing:

input.txt

```
0.1,1.25,0.1,5,55,4.6,1.5,2495840.25,0.3
discretization, total size, conductivity, capacity, STD DEV
OFF050V.csv,PipeNetwork.txt,condVariance.csv,gridDeclaration.txt,initTemp.txt
Surface temperatures,pipe layout,conductivity variance,gridspacing,initial cond
900,10,96
Timestep size, number of outputs, number of timesteps between each output
true
Save the animations to file, true or false (creates an animations folder)
0.05,1.5,2495840.25
Surface boundary conditions: depth,conductivity,capacity
none
Load monitored locations in this run (called monitoredLocations.txt in tutorial)
lumped
"consistent" or "lumped" FEM for the heat capacity matrices (defaults to lumped)
none
To run a test case include the keyword "test" on the line above. This gives
the user a chance to debug all input files before the continuum matrices
are generated.
```

gridDeclaration.txt

```
# This is a very large grid,
```

```
#
#element counts in each direction x,y,z
250,55,46
# x direction     from 0 to 290 m, one entry per element
14.8,5.6,2.2,1.4,0.8,0.4,0.2,0.1,0.1,0.1,0.1,0.1,0.1,0.1,....
# y direction     from 0 to 82.5 m, one entry per element
1.25,1.25,1.25,1.25,1.25,1.25,1.25,1.25,1.25,1.25,1.25,1.25....
# z direction     from 0 to 74.7 m, one entry per element
0.1,0.1,0.1,0.1,0.1,0.1,0.1,0.1,0.1,0.1,0.1,0.1,0.1,0.1,....
```

OFF050.csv

```
Time, Temperature
2011-03-07 00:00:00,-0.240489694865687
2011-03-08 00:00:00,-0.388135484415784
2011-03-09 00:00:00,-0.230552080692405
2011-03-10 00:00:00,-0.305361601180493
2011-03-11 00:00:00,-0.476600891573355
2011-03-12 00:00:00,-0.514431236455152
2011-03-13 00:00:00,-0.185681221411244
2011-03-14 00:00:00,-0.0668754901129773
2011-03-15 00:00:00,-0.157186420781102
2011-03-16 00:00:00,0.0582694336375198
2011-03-17 00:00:00,0.317797488829456
2011-03-18 00:00:00,2.2348986621235
```

```
2011-03-19 00:00:00,0.612526673717127
2011-03-20 00:00:00,-0.0897722529328462
2011-03-21 00:00:00,1.80414777242845
2011-03-22 00:00:00,1.13058410543761
2011-03-23 00:00:00,-0.265466891081928
2011-03-24 00:00:00,-0.0882702745788606
```

monitoredLocations.txt

```
#FORMAT: x,y,z, name of output file
#for a trench that starts 1.75 m from the x side on the hot loop
#
# Not used in the tutorial example
#
#horizontal entries
0.2250,8.5,1.5,L005T150NModelled.csv
1.5000,8.5,1.5,L005T025NModelled.csv
1.6000,8.5,1.5,L005T010NModelled.csv
1.8770,8.5,1.5,K005T020SModelled.csv
1.9532,8.5,1.5,K005T040SModelled.csv
2.4358,8.5,1.5,J005T110SModelled.csv
2.8930,8.5,1.5,J005T170SModelled.csv
#
#
#vertical entries
```

```
1.75,8.5,2.745,M005T150DModelled.csv
1.75,8.5,2.110,M005T060DModelled.csv
1.75,8.5,1.750,M005T025DModelled.csv
1.75,8.5,1.605,M005T010DModelled.csv
#
1.75,8.5,1.200,N005T030UModelled.csv
1.75,8.5,0.890,N005T060UModelled.csv
1.75,8.5,0.610,Z005T090UModelled.csv
1.75,8.5,0.330,Z005T120UModelled.csv
1.75,8.5,0.030,Z005T150UModelled.csv
```

initTemp.txt

```
# There must be one entry per vertical node, that's one entry per element
# plus one extra
-0.0281282
0.0542769
0.49927
0.926392
1.33993
1.74325
2.13878
2.52814
2.91234
3.29191
```

```
3.66705
4.03777
4.40394
4.76532
5.12167
5.47271
5.81818
6.15785
6.49153
6.81905
7.14027
# rest of file not included in this example.
```

PipeNetwork.txt

```
# Pipe section file
#
# ONLY PART OF THIS FILE IS SHOWN HERE, IT INCLUDES ALL KEY FEATURES
#
# Pipe names start with "P", all the coordinates of the sections follow as
# triplets of numbers separated by commas of the form (x,y,z). Remember to keep
# the pipe network within the confines of the overall grid network. Remember
# that z is the distance below surface (and should therefore be positive).
#
# Loading of the GLHE is specified in a separate file
```

```
LoadingFile PipeLoads.csv
#
# Remove the pipe volumes from the continuum through FEM integration
RemovePipes false
#
#
# The pipes should be numbered starting with zero, incrementing upwards,
# the pipes upstream of a given pipe are specified by numbers after the
# pipe number, e.g. Pipe 2 0 1 indicates pipe 2 has pipes 0 and 1 feeding
# into it
Pipe 0
#
#divide the element into this many finite elements
NumberOfElements 100
#
# Number of sample points around the pipe for grabbing temperatures
SamplingPoints 10
#
# Monitor what's going on in this pipe and output it whenever a normal output
# would be made
Monitored true
#
#
#Flowrate in m^3 / sec
```

```
FlowRate 0.000946254
#
# diameters in m
InternalDiameter 0.0209296
ExternalDiameter 0.02667
#
# mixing ratio is the longitudinal dispersion, units m^2/sec, this is also
# combined with thermal diffusivity
MixingRatio 0.16716216
#
# Heat capacity of the fluid is in Joules per m cubed
VolumetricHeatCapacityOfTheFluid 3728680.00
#
# Conductivity of the pipe wall is in Watts per Meter per Kelvin
ConductivityOfPipeWall 0.19
# First entry section
26.45,0,1.45
26.45,5,1.45

Pipe 1,0
#  the above pipe is labelled pipe 1 and is fed by pipe 0
#divide the element into this many finite elements
NumberOfElements 100
#
```

```
# Number of sample points around the pipe for grabbing temperatures
SamplingPoints 10
#
#Flowrate in m^3 / sec
FlowRate 0.000788545
#
# diameters in m
InternalDiameter 0.0209296
ExternalDiameter 0.02667
#
# mixing ratio is the longitudinal dispersion, units m^2/sec, this is also
# combined with thermal diffusivity
MixingRatio 0.16716216
#
# Heat capacity of the fluid is in Joules per m cubed
VolumetricHeatCapacityOfTheFluid 3728680.00
#
# Conductivity of the pipe wall is in Watts per Meter per Kelvin
ConductivityOfPipeWall 0.19
# second manifold section
26.45,5,1.45
31.45,5,1.45
```

PipeLoads.csv

```
# replace wattageLoad with temperature for fixed temperature boundary condition
# wattageLoad is positive when heat is being extracted from the ground and
# negative when it's being injected into the ground
Date,wattageLoad
2011-03-07 00:00:00,1782.10011637435
2011-03-08 00:00:00,13061.4662675895
2011-03-09 00:00:00,12052.6716215264
2011-03-10 00:00:00,9923.39349816334
2011-03-11 00:00:00,7798.0014120667
2011-03-12 00:00:00,6942.62654031047
2011-03-13 00:00:00,6257.14359095742
2011-03-14 00:00:00,6541.19444536745
2011-03-15 00:00:00,6149.80897737917
2011-03-16 00:00:00,5273.40515209101
2011-03-17 00:00:00,4976.04635364944
2011-03-18 00:00:00,4687.07439360978
2011-03-19 00:00:00,6292.10940903287
2011-03-20 00:00:00,7015.83357239696
2011-03-21 00:00:00,6443.0779062372
2011-03-22 00:00:00,5831.76833539076
2011-03-23 00:00:00,6830.55015153853
2011-03-24 00:00:00,6636.14195784052
2011-03-25 00:00:00,6695.30035013455
```

```
2011-03-26 00:00:00,6932.14331316611
2011-03-27 00:00:00,6146.58029058557
```

Output files

The monitoredLocation outputs are largely self explanatory. Each location specified will have its own output file containing a time series of the temperatures at that location.

The graphical output is a little more interesting. If animations is set to "true" then there will several VTK files created which can be visualized using a program such as ParaView. The folder "animations" will be created and a VTK file will be created for each output step. These VTK files represent the temperature field as it evolves in the model. Other files are pipeLayout.vtk, elementGrid.vtk, and elementConductivityGrid.vtk for visualizing the pipe system, element discretization and grid, and the thermal conductivity distribution in the soil continuum respectively.

EfficiencyOverTime.csv is the most important file, containing the performance analysis of the GLHE and how it evolves with time. It is generated if there is a GLHE present in the model (i.e. the "nopipe" keyword is not specified in *input.txt*).

EfficiencyOverTime.csv

```
Date, EWT, Joules gained in timestep, Watts of in timestep, Delta Temp.
2011-03-08 00:00:00,3.23118,1.17024e+007 ,13002.7, 3.68529,
2011-03-09 00:00:00,2.50514,1.08521e+007 ,12057.9, 3.41751,
2011-03-10 00:00:00,2.37139,8.94104e+006 ,9934.48, 2.81567,
```

...

...

The first column is the timestamp of each output time. This is the corresponding timestamp of the equivalent animation and monitored locations output. The format is the standard ISO date format up to seconds. The second column represents the exchange fluid entering the heat pump after it has been circulated through the GLHE. The unit is degrees Celsius. The third column contains the energy removed from the soil continuum on that timestep in joules. This measurement can be look odd when the model is asked to perform multiple timesteps between outputs, this is not a running count of energy of all timesteps between outputs it is only the energy removed of the timestep of the specified time. The fourth column gives the temperature delta required by the pipe loads if a wattage load is specified, or the generated temperature delta if a fixed inlet temperature is specified.

Further columns will appear in this file if there are pipes with the "Monitored true" line in the pipe network file. These columns will give the exit temperature, joules gained in the previous timestep, and temperature delta of each pipe with this keyword present.

Appendix G

Inverse Trench Model Results

Field thermistor measurements were used as a target for model calibration. Two calibration runs are presented, one that was calibrated to conductivity only (with diffusivity held constant by varying heat capacity), and another calibrated to both thermal conductivity and the percentage load that the rabbit trench would see of the total load. This appendix contains plots of the field data time series against the modelled timeseries.

It will be beneficial to have some understanding of where each of the calibration locations are.

In total 16 thermistor locations were used. All thermistors on the J and K lines were the ones outside of the trench, perpendicular to the orientation of the trench but at the same depth. The suffix "S" denotes this direction. In increasing distance from the trench they are: K00T020S, K00T040S, J005T110S, and J005T170S. Thermistors on the L line are the thermistors placed between the pipes in the rabbit trench. L005T010N and L005T025N are between the pipe coming off the header and the first loop back. L005T150N is between the pipe returning to the header and the second last pipe.

The M line has four thermistors at increasing depth below the pipe coming off the header. M005T010D is the shallowest, just below the pipe; and M005T150D is the deepest. There are five thermistors above the pipe on the N and Z lines. In increasing distance from the pipe these are: N005T030U, N005T060U, Z005T090U, Z005T120U, and Z005T150U. The last is nearly at the ground surface.

G.1 Single trench inverse modelling

The four inverse modelling attempts all produced very similar results. Differences in the domain sizes and optimization variables appeared to have little difference on the final optimized objective function value.

G.1.1 Both Conductivity and Load Estimated: Wide DDS

The model did a very good job recreating the temperatures observed on the L line, whose sensors are located inbetween the rabbit loop pipes.

For sensors farther away at this depth the model did progressively worse with increased distance from the ground loop. There appeared to be a slight time and magnitude shift that is very apparent for sensor J005T170S. At this depth the data seems to suggest that the ground conditions of the rabbit loop and off trench monitoring location are different. The discrepancy could be explained by an increased mean temperature of the ground around the rabbit loop and a slightly higher thermal diffusivity. Note that neither of these parameters were being tweaked during these calibration runs.

Immediately below the pipe M005T010D was closely matched by the model, but lower

down none of the sensors were well replicated by the model. The deepest sensor in particular appears to be consistently 5 K colder than what the model suggests it should be, with a time shift similar to what was seen in the other off pipe sensors.

Above the pipe there was little field data available due to difficulties with the datalogger. What little data was available appears to be recreatable by the model. The sensor closest to the surface, Z005T150U, had so much fluctuation that it would be unlikely that tweaking continuum parameters would improve the model fit. This location would be extremely sensitive to the surface boundary condition and relatively insensitive to everything else.

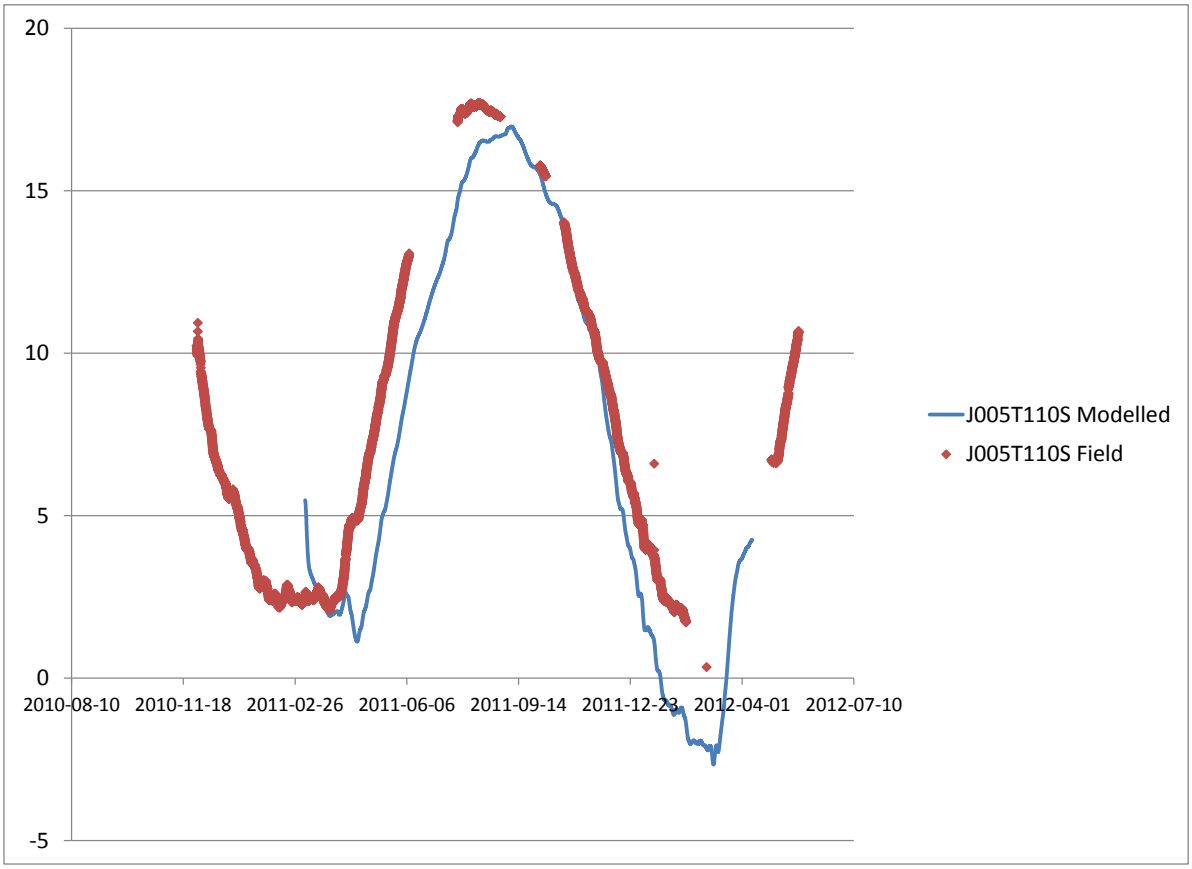
20
15
10
5
0
-5
2010-08-10
2010-11-18
2011-02-26
2011-06-06
2011-09-14
2011-12-23
2012-04-01
2012-07-10
J005T110S Modelled
J005T110S Field

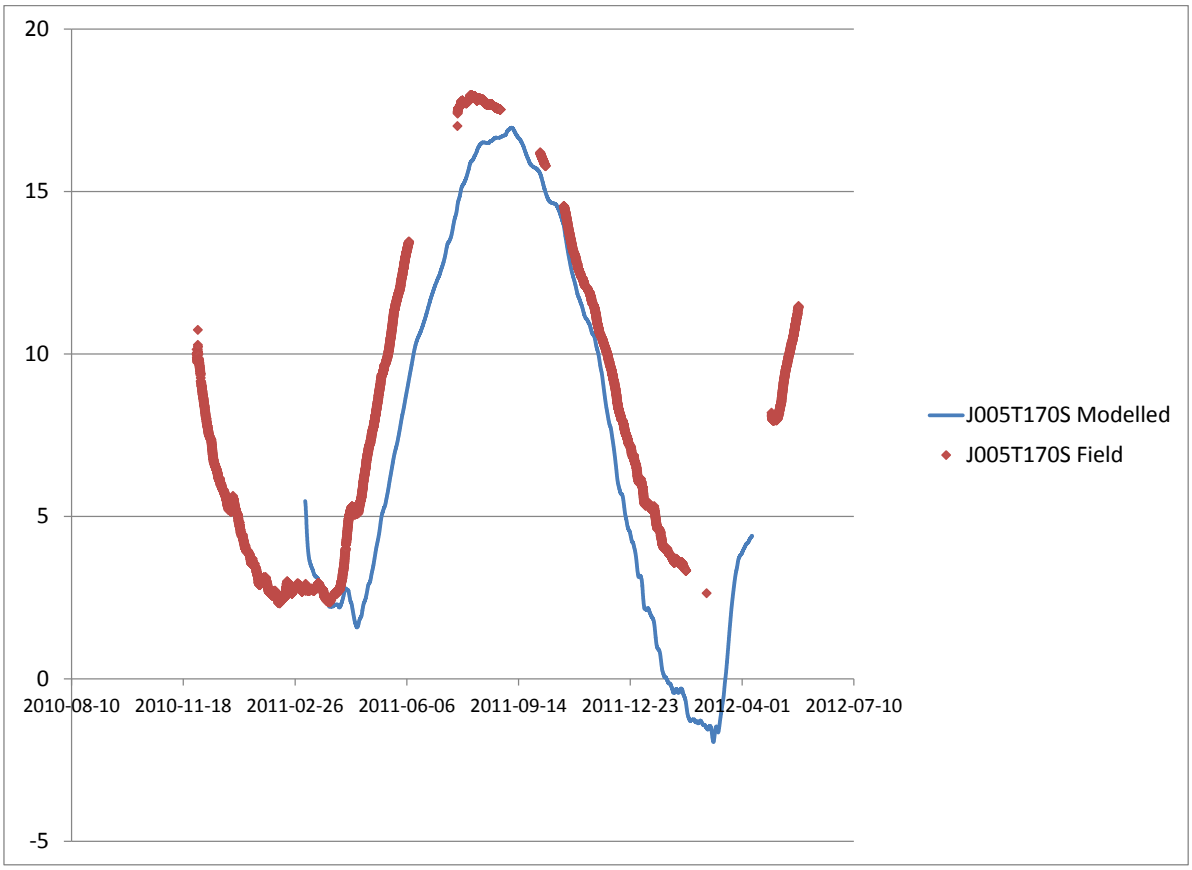
20
15
10
5
0
-5
2010-08-10
2010-11-18
2011-02-26
2011-06-06
2011-09-14
2011-12-23
2012-04-01
2012-07-10
J005T170S Modelled
J005T170S Field

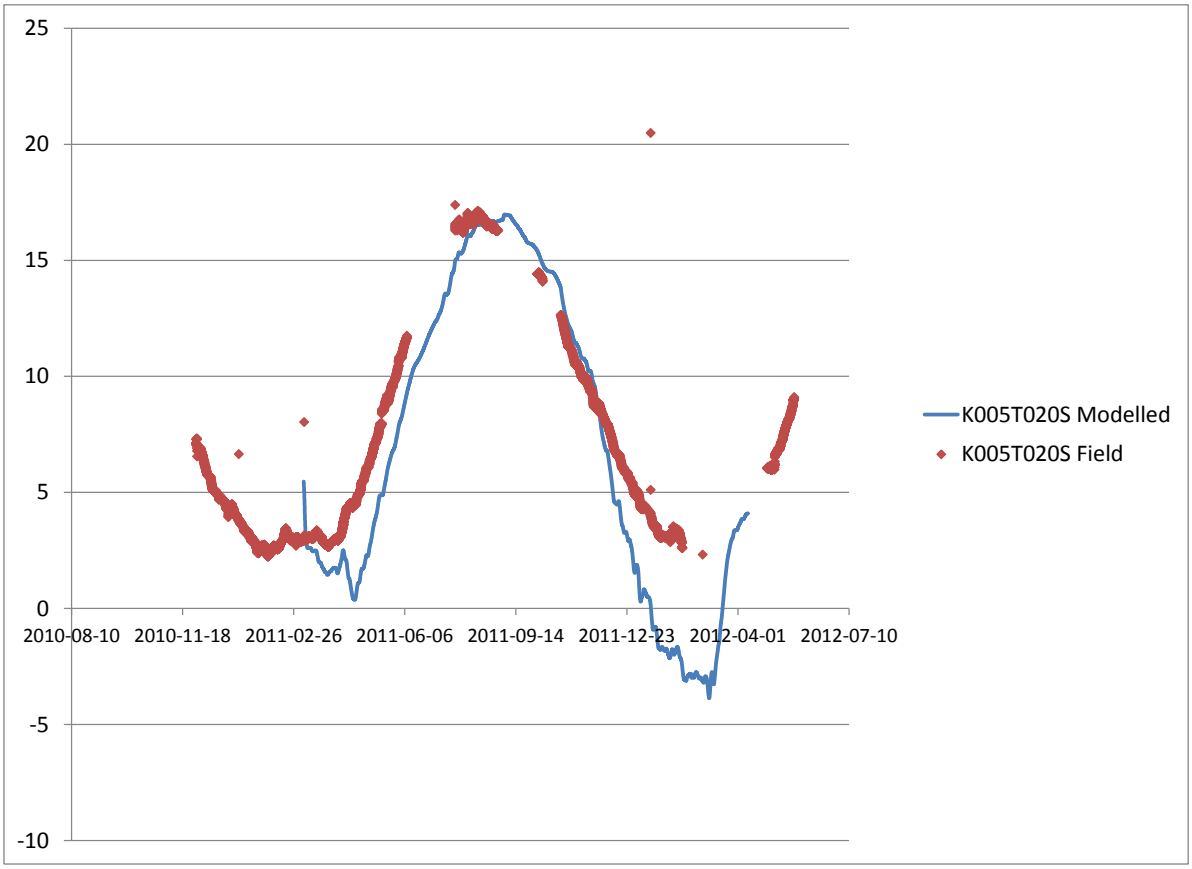
25
20
15
10
5
0
-5
-10
2010-08-10
2010-11-18
2011-02-26
2011-06-06
2011-09-14
2011-12-23
2012-04-01
2012-07-10
K005T020S Modelled
K005T020S Field

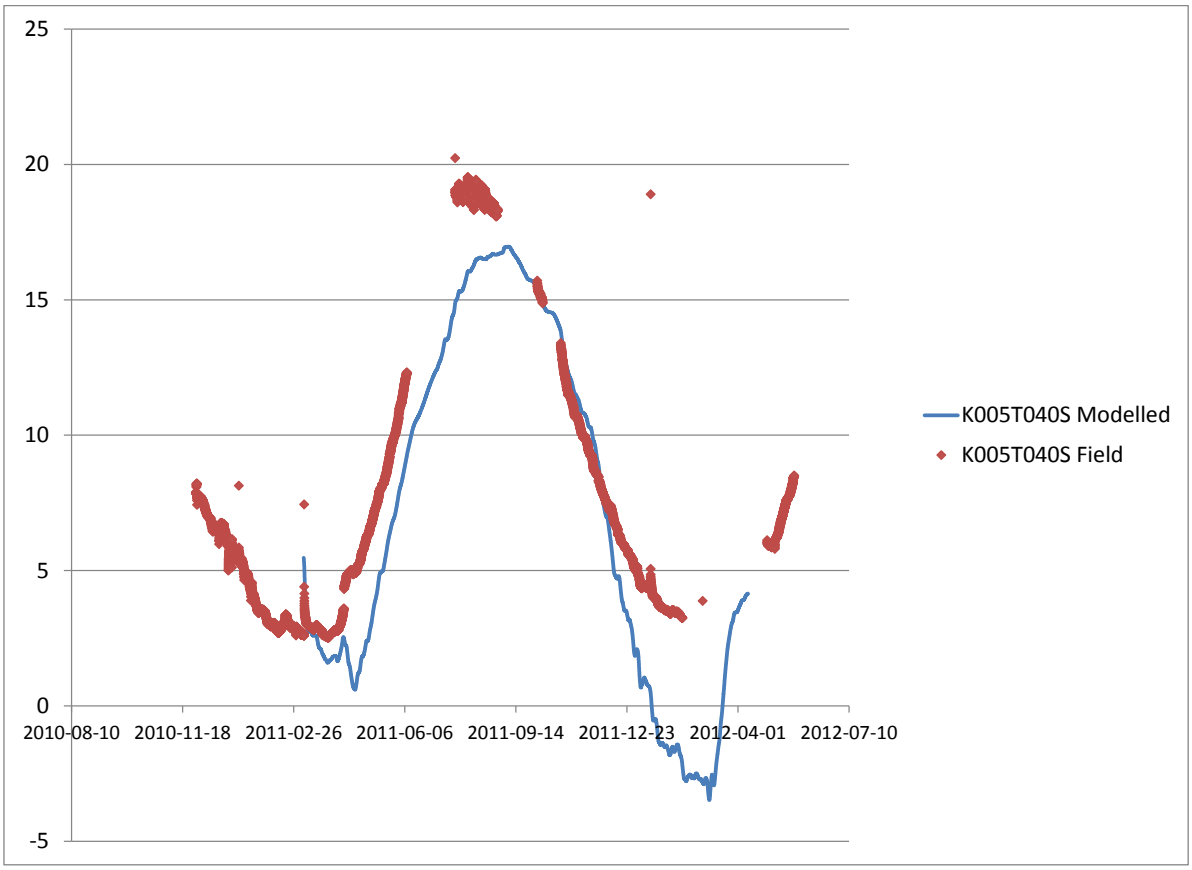
25
20
15
10
5
0
-5
2010-08-10
2010-11-18
2011-02-26
2011-06-06
2011-09-14
2011-12-23
2012-04-01
2012-07-10
K005T040S Modelled
K005T040S Field

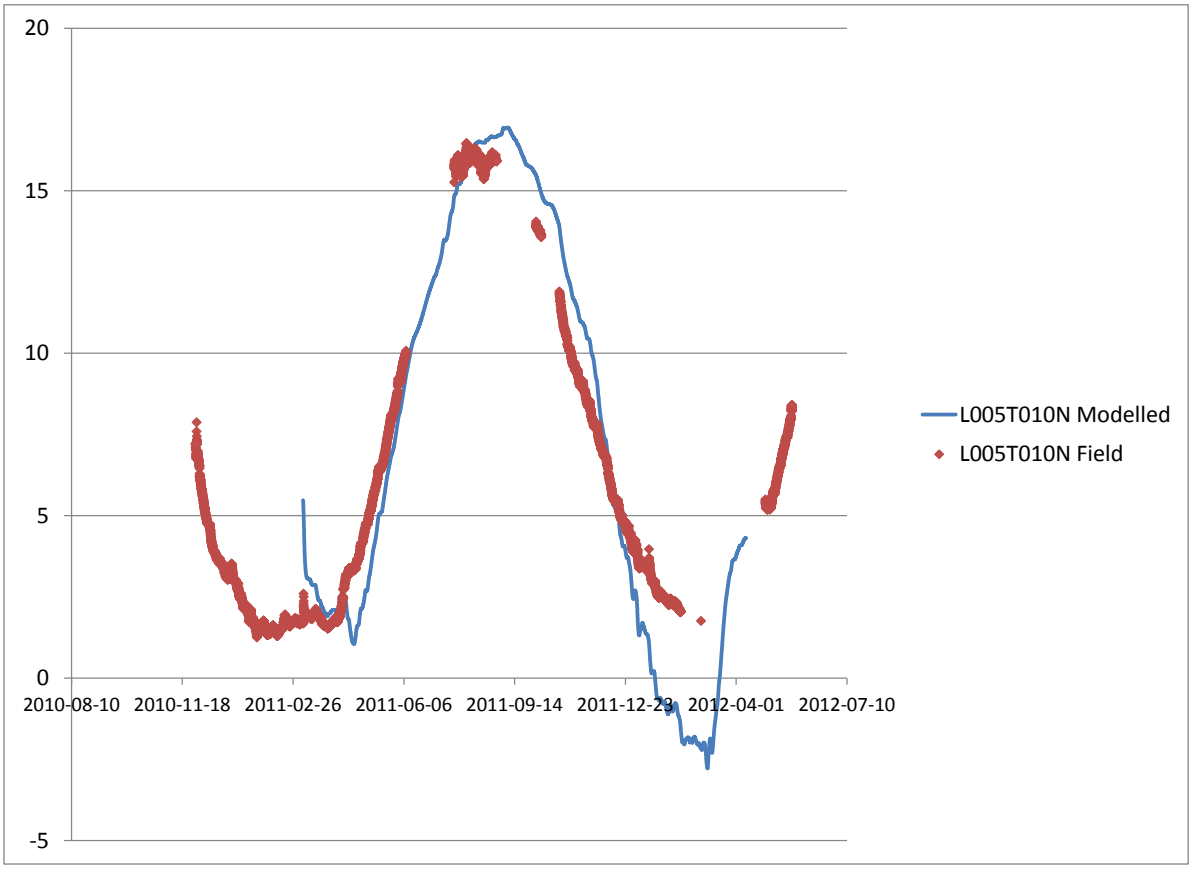
20
15
10
5
0
-5
2010-08-10
2010-11-18
2011-02-26
2011-06-06
2011-09-14
2011-12-23
2012-04-01
2012-07-10
L005T010N Modelled
L005T010N Field

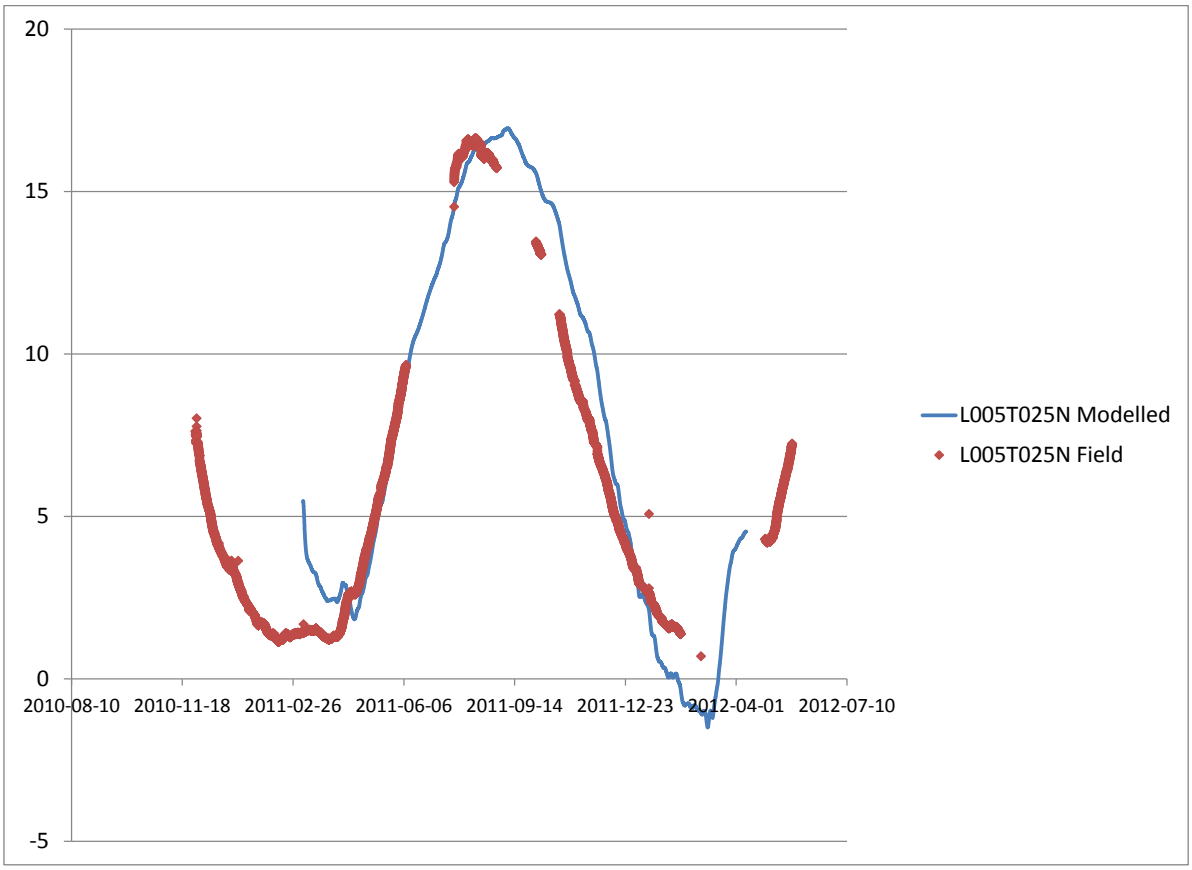
20
15
10
5
0
-5
2010-08-10
2010-11-18
2011-02-26
2011-06-06
2011-09-14
2011-12-23
2012-04-01
2012-07-10
L005T025N Modelled
L005T025N Field

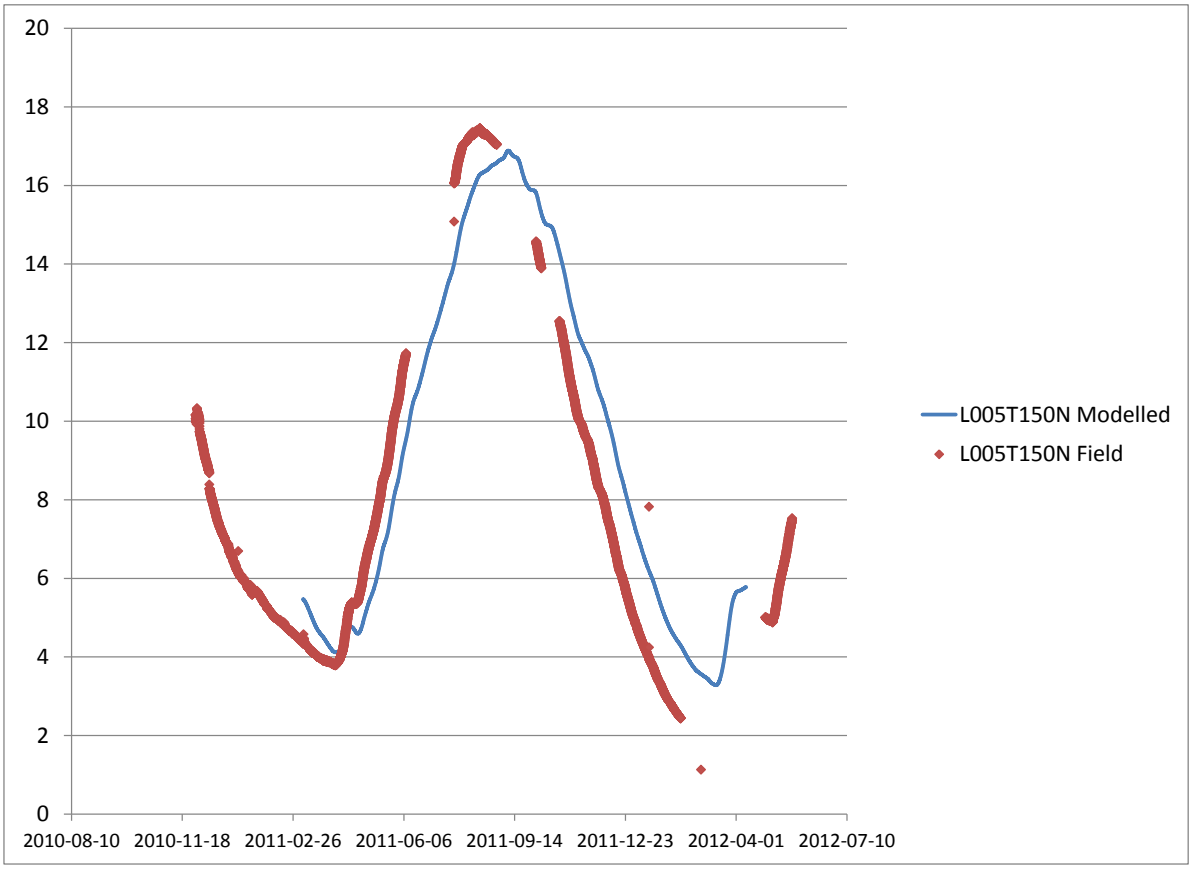
20
18
16
14
12
10
8
6
4
2
0
2010-08-10
2010-11-18
2011-02-26
2011-06-06
2011-09-14
2011-12-23
2012-04-01
2012-07-10
L005T150N Modelled
L005T150N Field

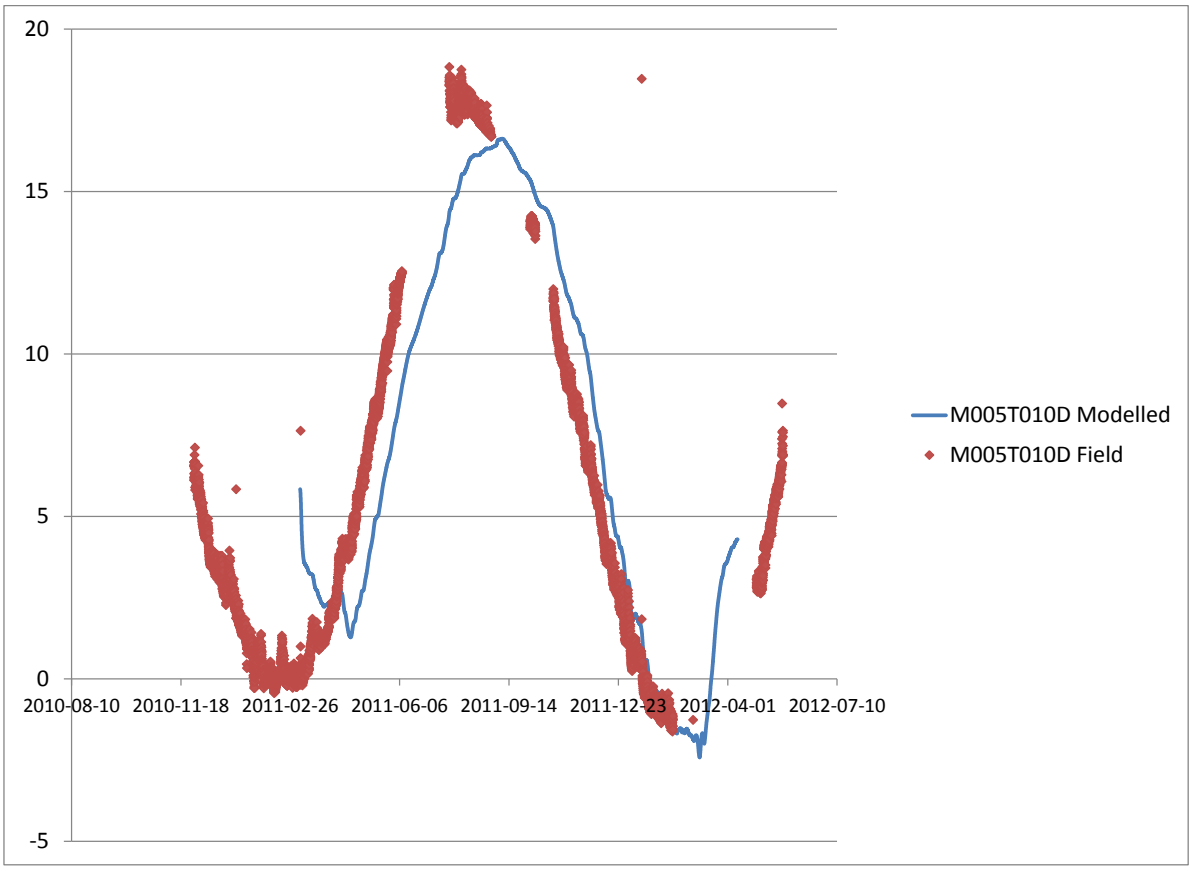
20
15
10
5
0
-5
2010-08-10
2010-11-18
2011-02-26
2011-06-06
2011-09-14
2011-12-23
2012-04-01
2012-07-10
M005T010D Modelled
M005T010D Field

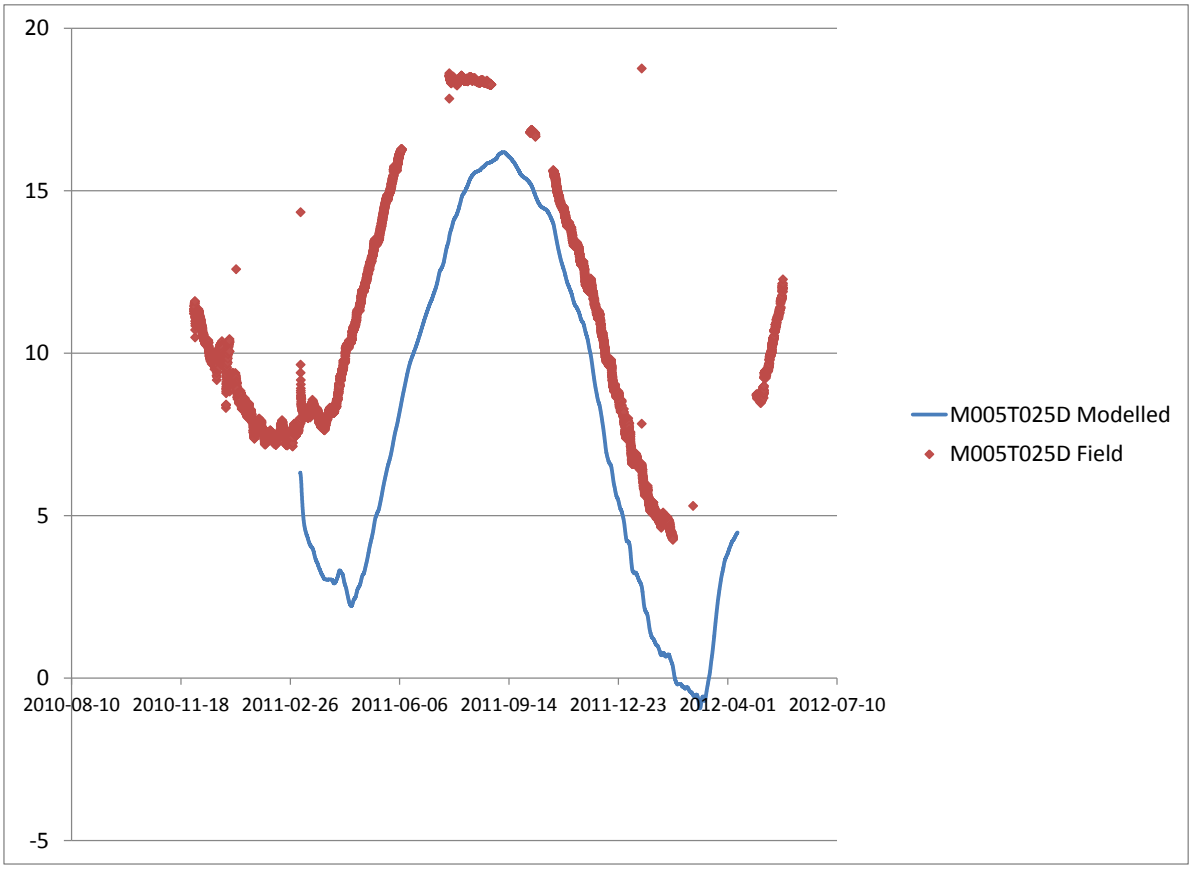
20
15
10
5
0
-5
2010-08-10
2010-11-18
2011-02-26
2011-06-06
2011-09-14
2011-12-23
2012-04-01
2012-07-10
M005T025D Modelled
M005T025D Field

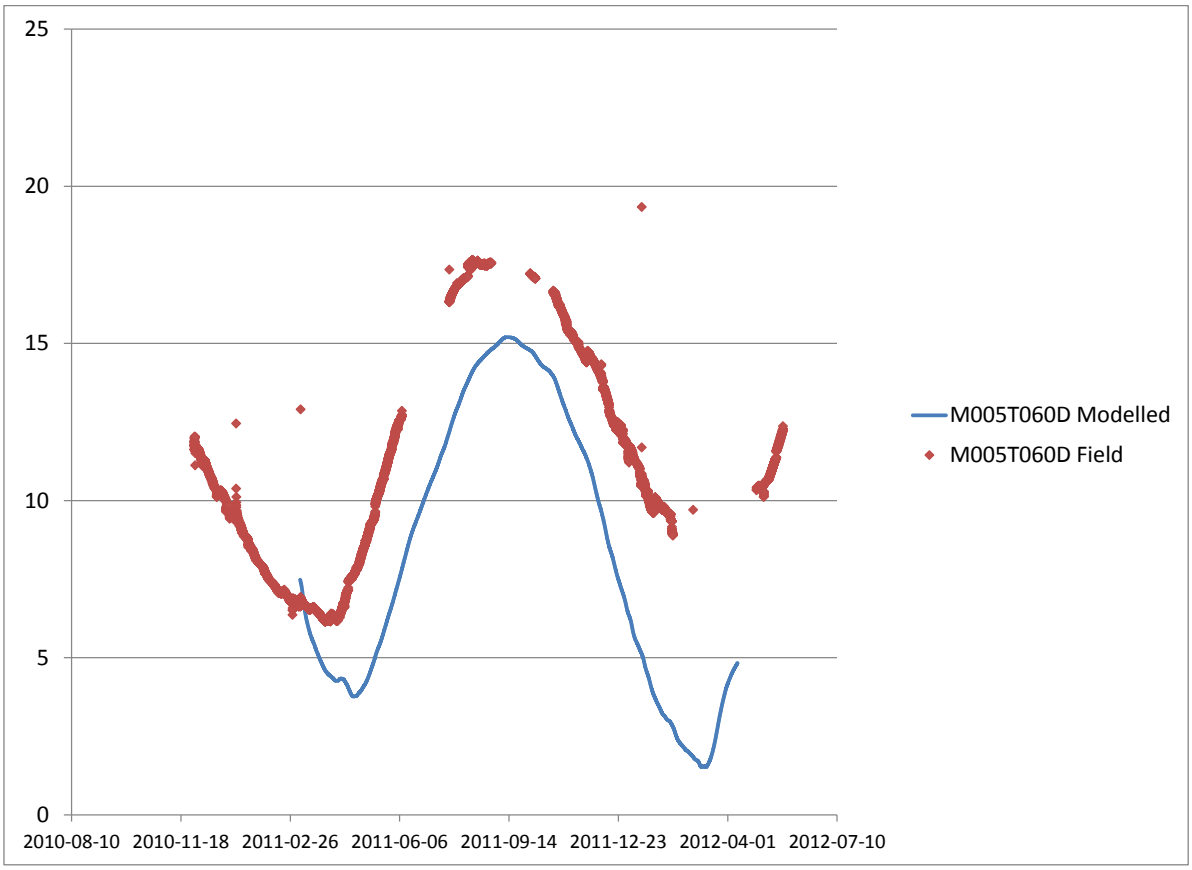
25
20
15
10
5
0
2010-08-10
2010-11-18
2011-02-26
2011-06-06
2011-09-14
2011-12-23
2012-04-01
2012-07-10
M005T060D Modelled
M005T060D Field

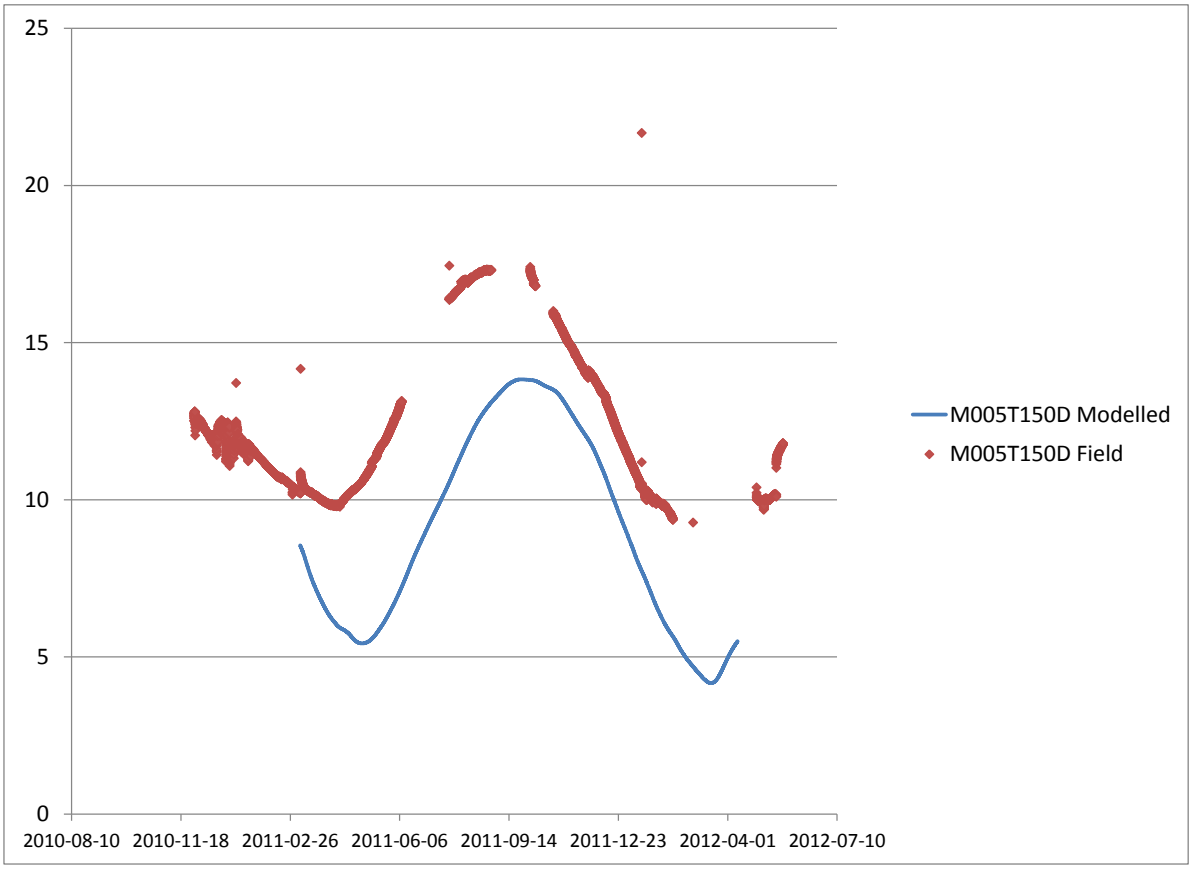
25
20
15
10
5
0
2010-08-10
2010-11-18
2011-02-26
2011-06-06
2011-09-14
2011-12-23
2012-04-01
2012-07-10
M005T150D Modelled
M005T150D Field

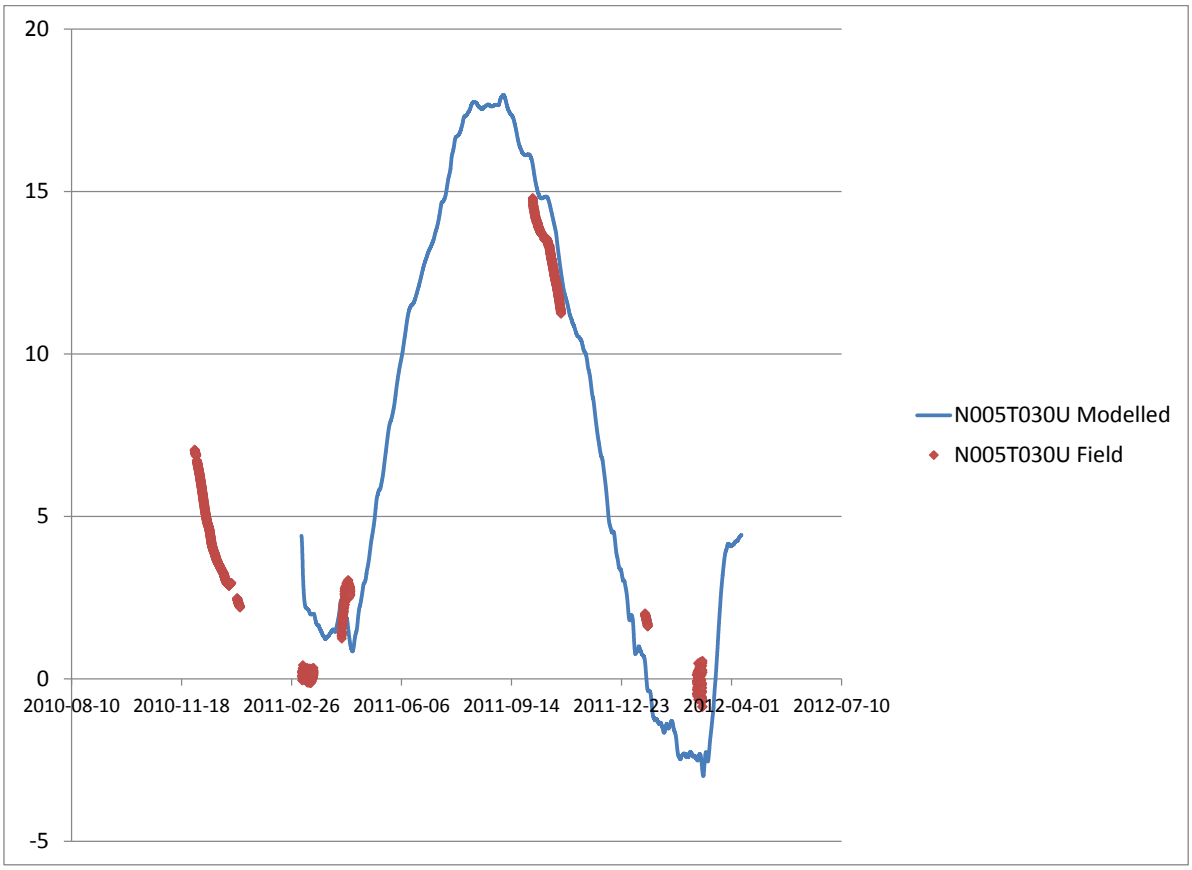
20
15
10
5
0
-5
2010-08-10
2010-11-18
2011-02-26
2011-06-06
2011-09-14
2011-12-23
2012-04-01
2012-07-10
N005T030U Modelled
N005T030U Field

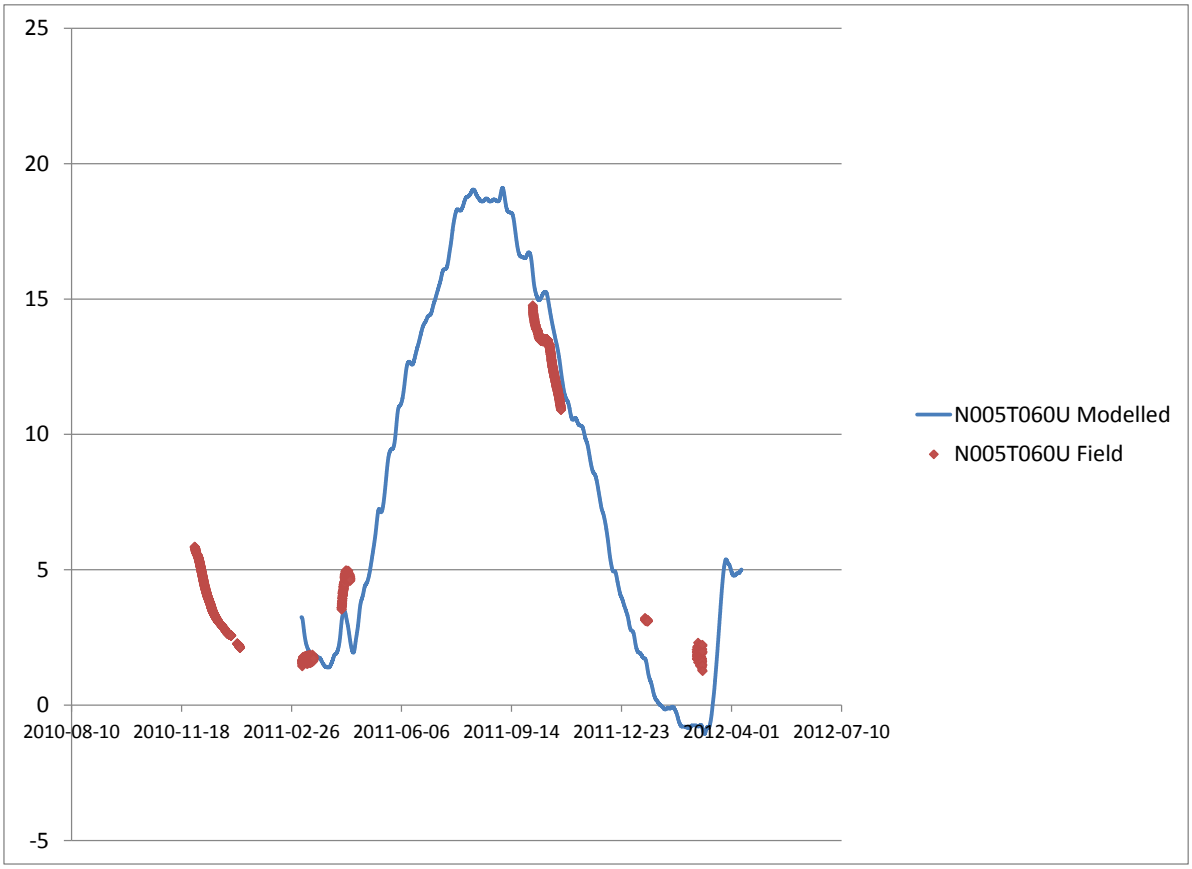
25
20
15
10
5
0
-5
2010-08-10
2010-11-18
2011-02-26
2011-06-06
2011-09-14
2011-12-23
2012-04-01
2012-07-10
N005T060U Modelled
N005T060U Field

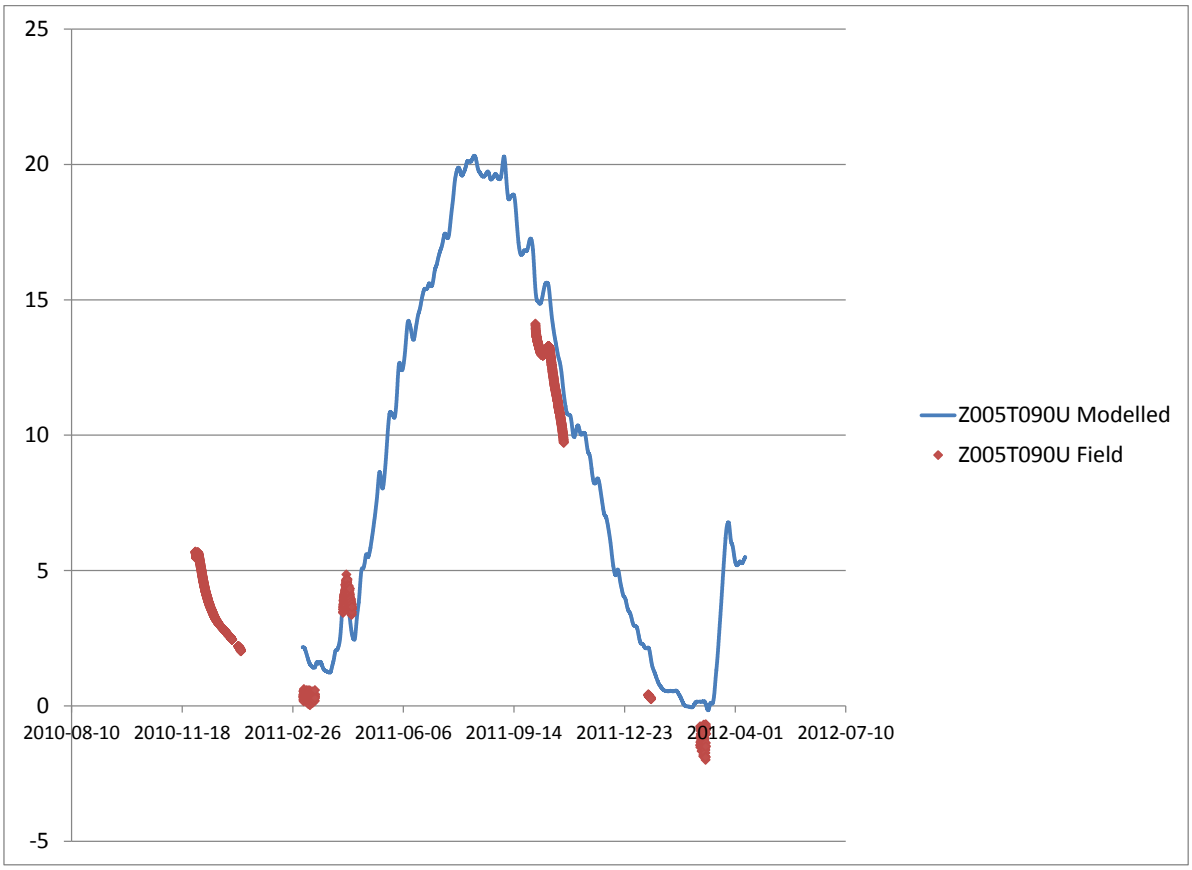
25
20
15
10
5
0
-5
2010-08-10
2010-11-18
2011-02-26
2011-06-06
2011-09-14
2011-12-23
2012-04-01
2012-07-10
Z005T090U Modelled
Z005T090U Field

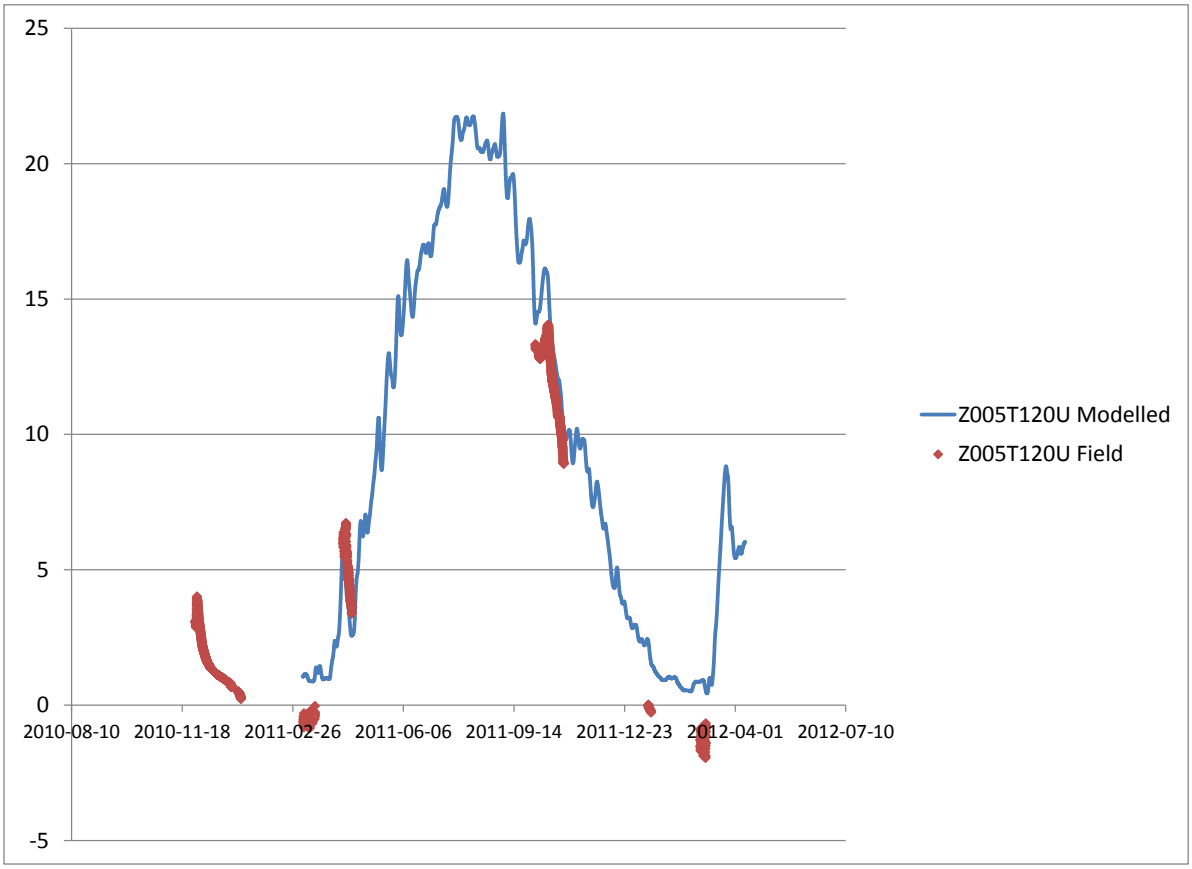
25
20
15
10
5
0
-5
2010-08-10
2010-11-18
2011-02-26
2011-06-06
2011-09-14
2011-12-23
2012-04-01
2012-07-10
Z005T120U Modelled
Z005T120U Field

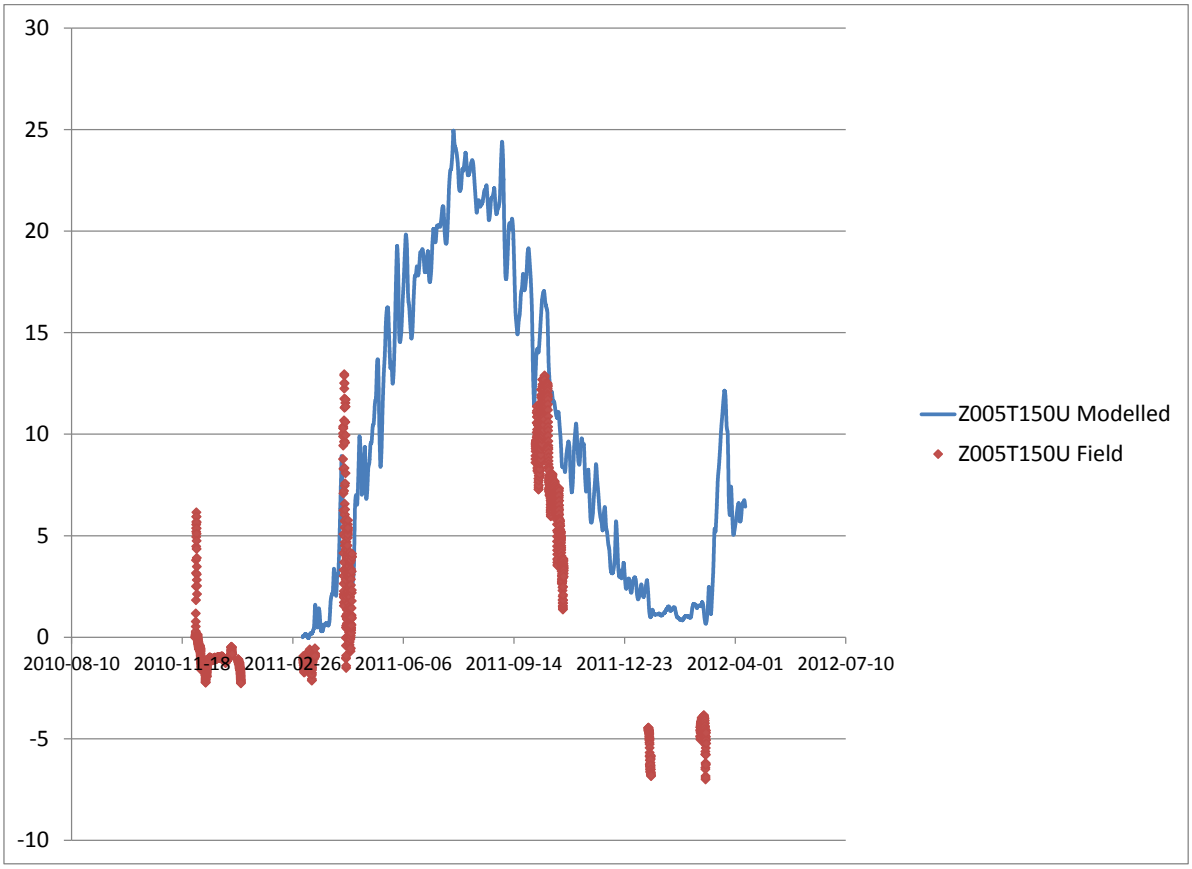
30
25
20
15
10
5
0
-5
-10
2010-08-10
2010-11-18
2011-02-26
2011-06-06
2011-09-14
2011-12-23
2012-04-01
2012-07-10
Z005T150U Modelled
Z005T150U Field

G.1.2 Only Conductivity Estimated: Wide DDS

To the naked eye the model run calibrated to conductivity only produced results identical to the model run calibrated to both thermal conductivity and percentage pipe load. This model calibration run did perform better than the previously detailed run but the differences between to two are impossible to see without calculating the squared errors between the model runs and the field data.

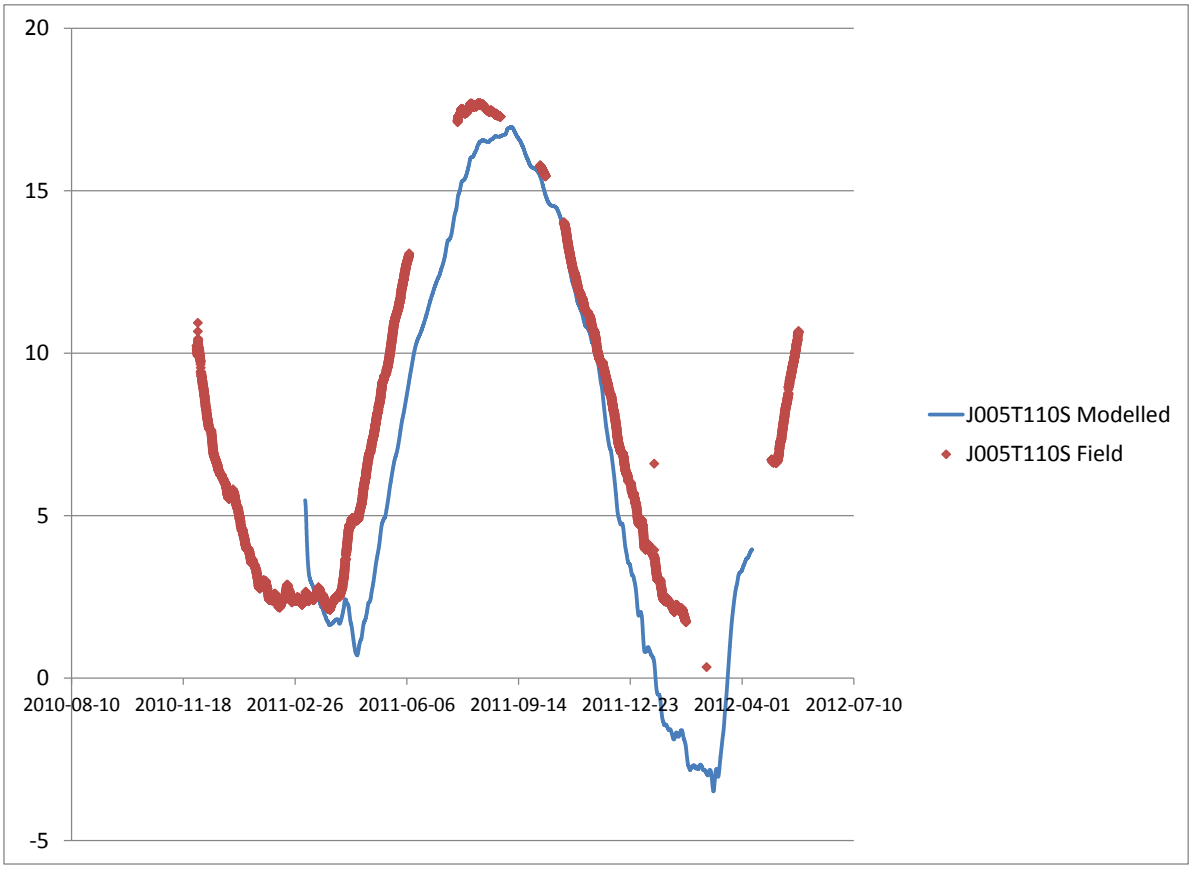
20
15
10
5
0
-5
2010-08-10
2010-11-18
2011-02-26
2011-06-06
2011-09-14
2011-12-23
2012-04-01
2012-07-10
J005T110S Modelled
J005T110S Field

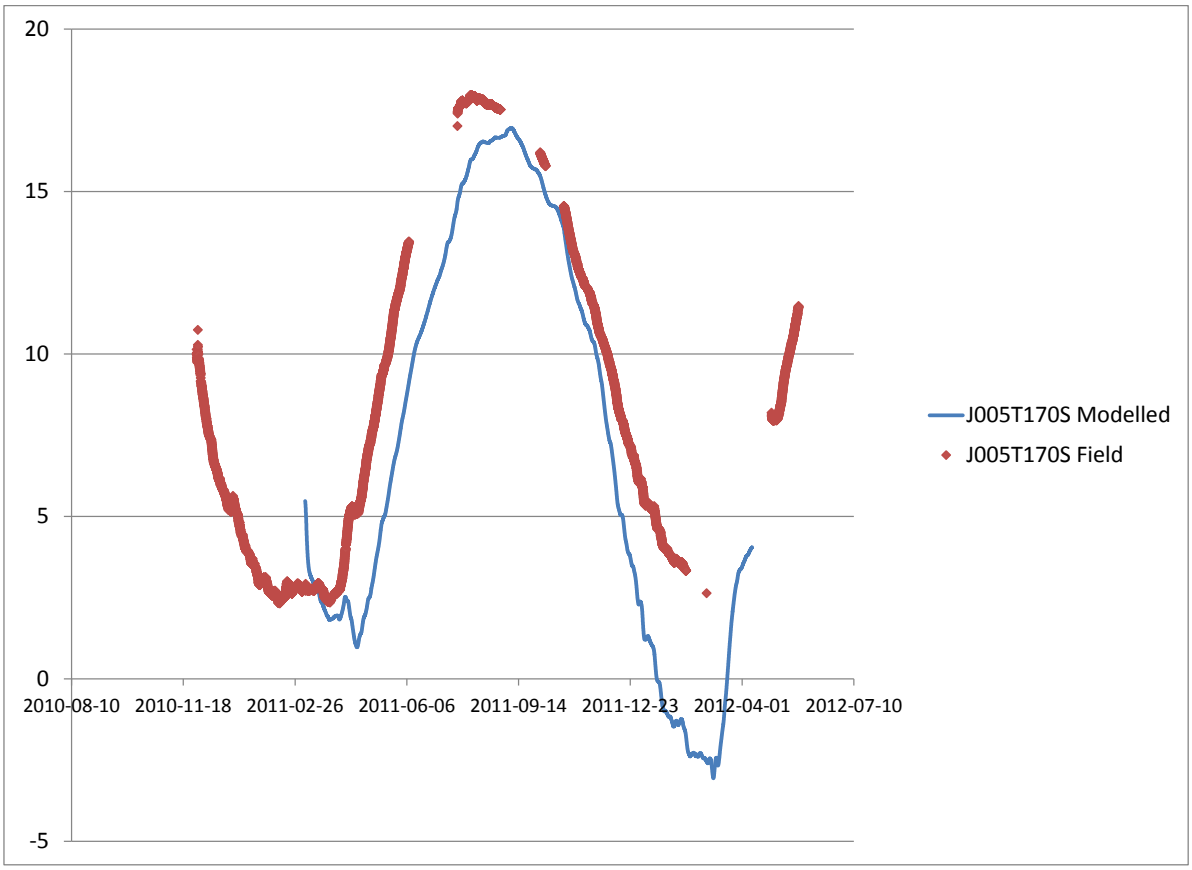
20
15
10
5
0
-5
2010-08-10
2010-11-18
2011-02-26
2011-06-06
2011-09-14
2011-12-23
2012-04-01
2012-07-10
J005T170S Modelled
J005T170S Field

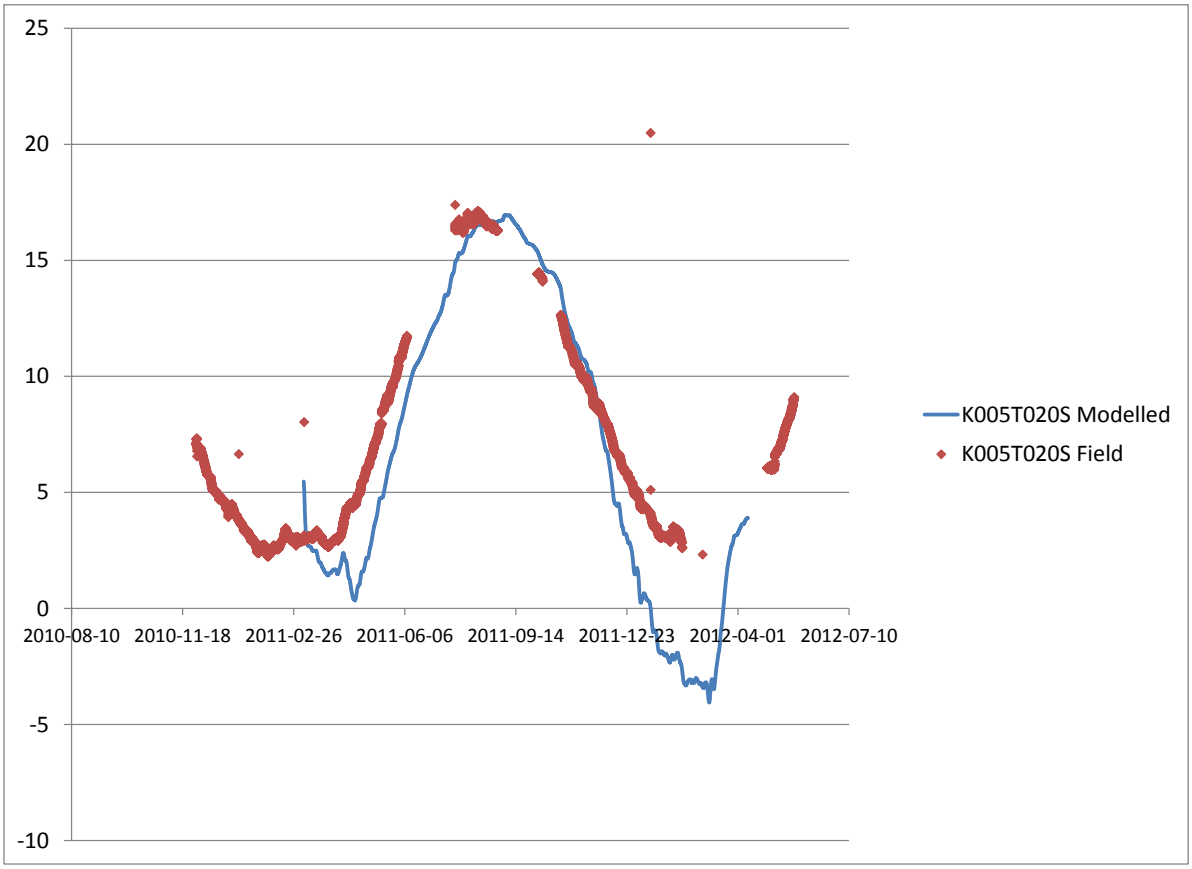
25
20
15
10
5
0
-5
-10
2010-08-10
2010-11-18
2011-02-26
2011-06-06
2011-09-14
2011-12-23
2012-04-01
2012-07-10
K005T020S Modelled
K005T020S Field

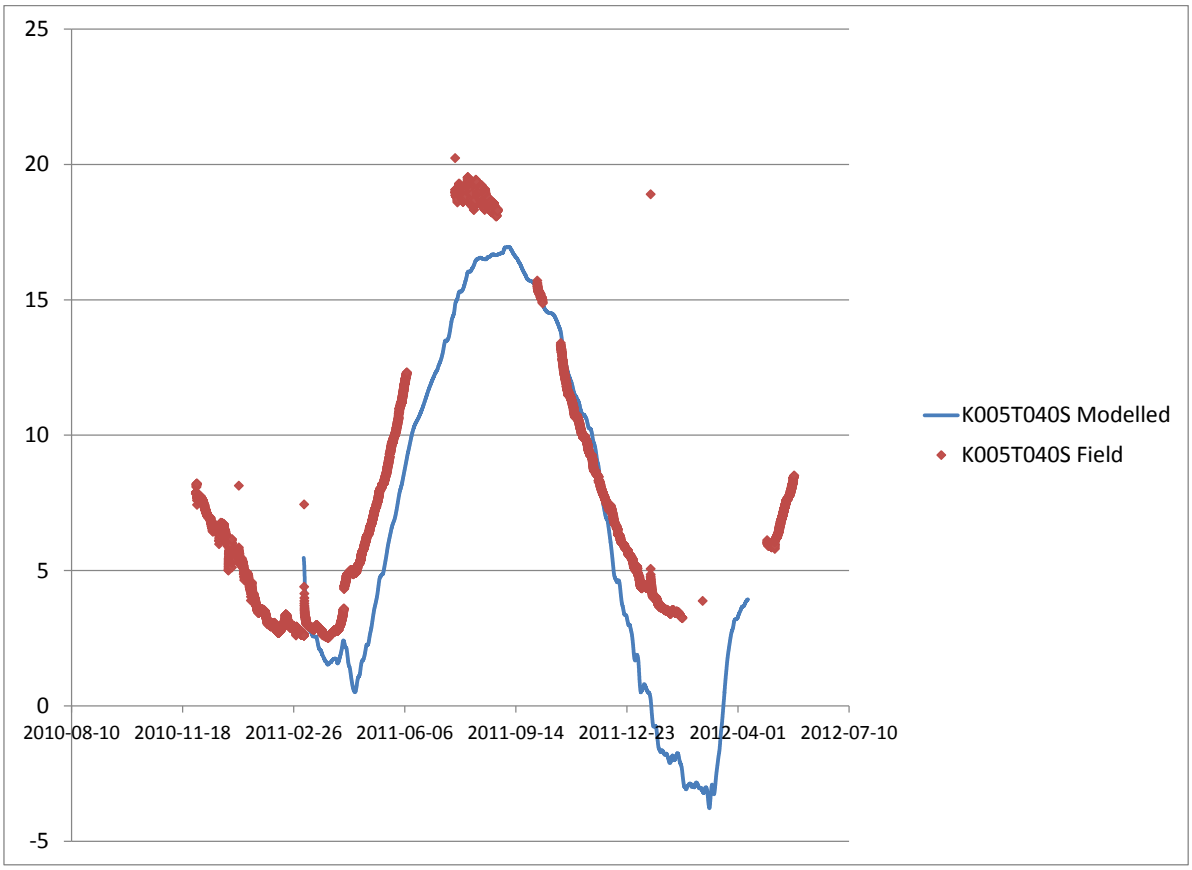
25
20
15
10
5
0
-5
2010-08-10
2010-11-18
2011-02-26
2011-06-06
2011-09-14
2011-12-23
2012-04-01
2012-07-10
K005T040S Modelled
K005T040S Field

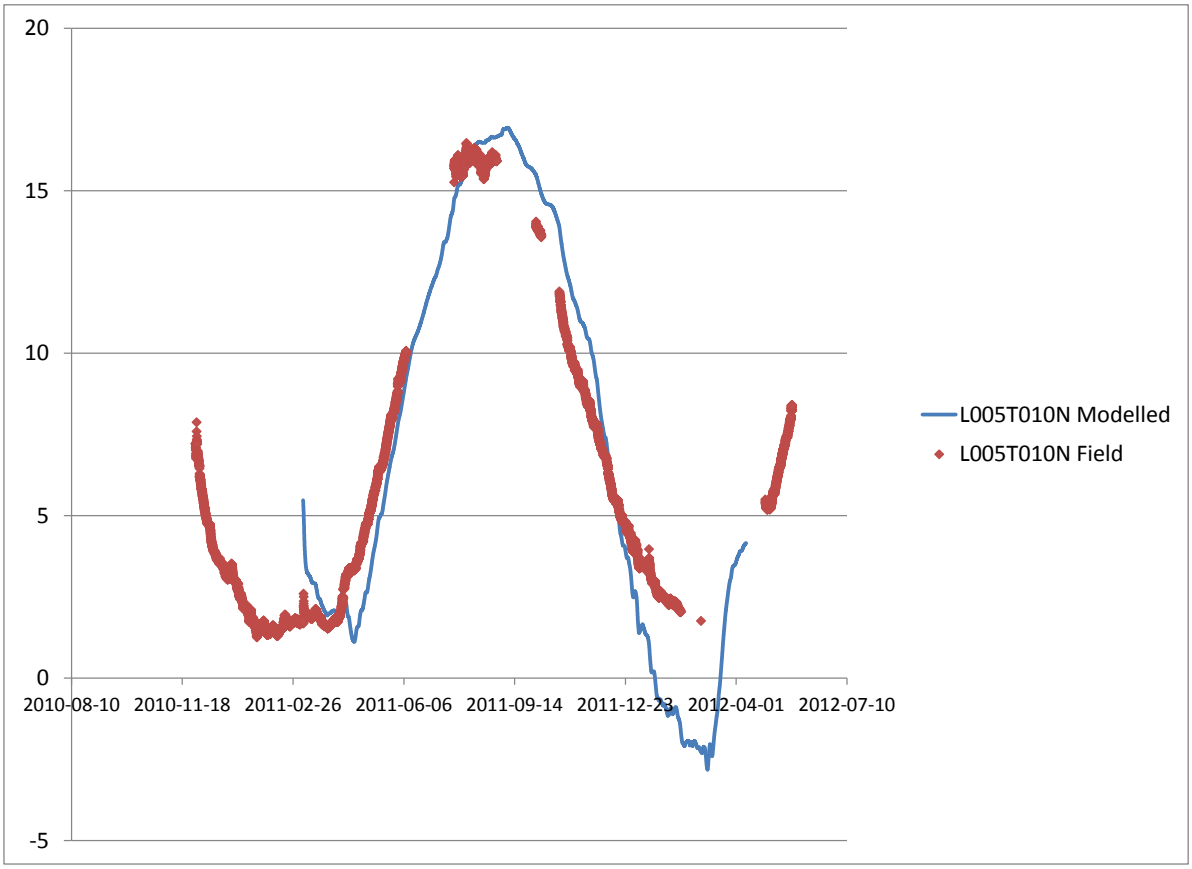
20
15
10
5
0
-5
2010-08-10
2010-11-18
2011-02-26
2011-06-06
2011-09-14
2011-12-23
2012-04-01
2012-07-10
L005T010N Modelled
L005T010N Field

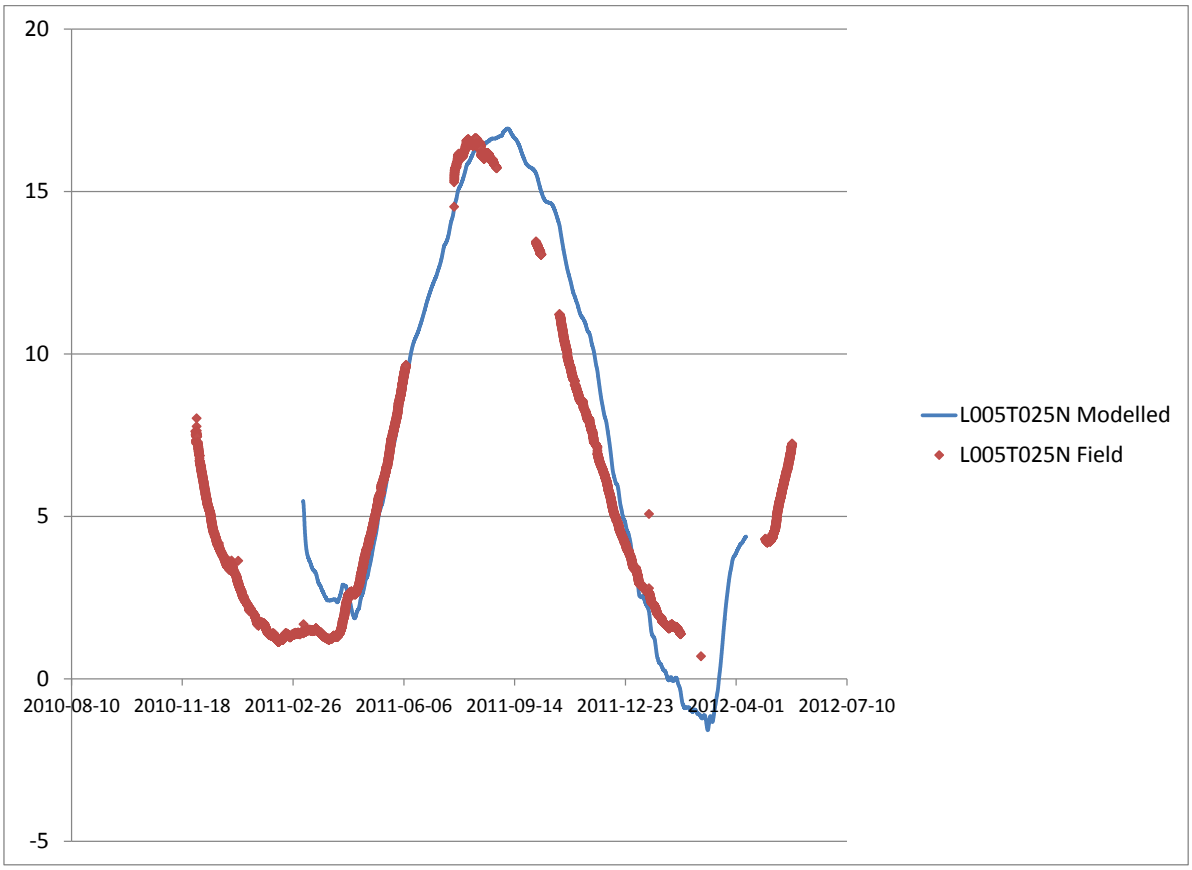
20
15
10
5
0
-5
2010-08-10
2010-11-18
2011-02-26
2011-06-06
2011-09-14
2011-12-23
2012-04-01
2012-07-10
L005T025N Modelled
L005T025N Field

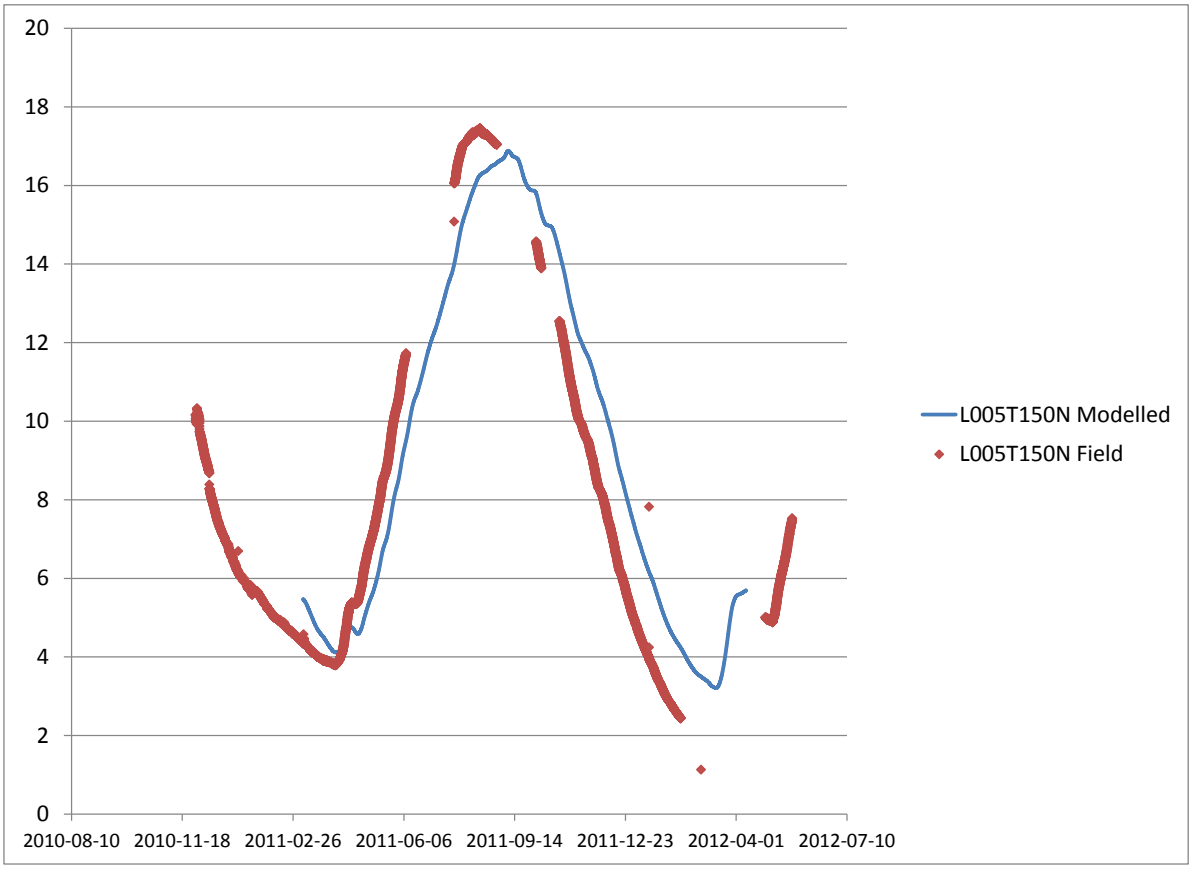
20
18
16
14
12
10
8
6
4
2
0
2010-08-10
2010-11-18
2011-02-26
2011-06-06
2011-09-14
2011-12-23
2012-04-01
2012-07-10
L005T150N Modelled
L005T150N Field

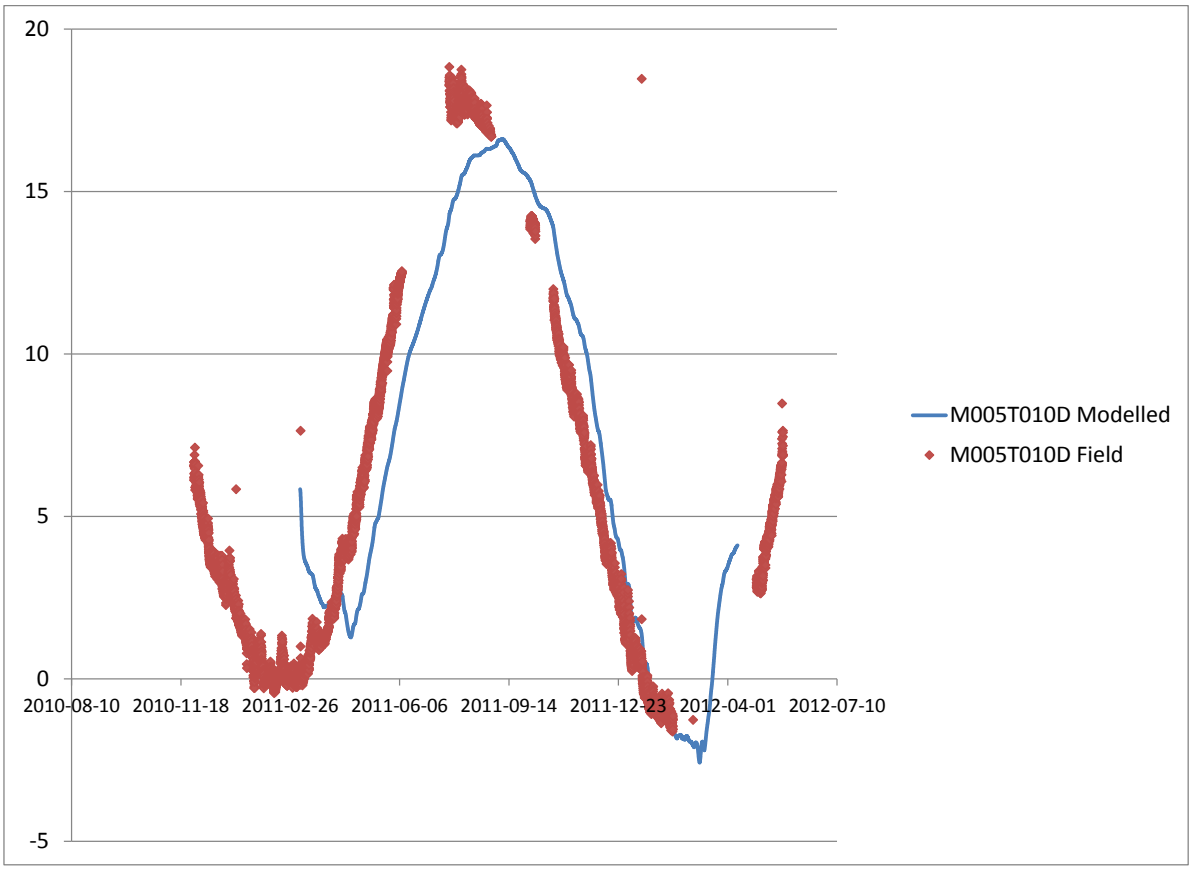
20
15
10
5
0
-5
2010-08-10
2010-11-18
2011-02-26
2011-06-06
2011-09-14
2011-12-23
2012-04-01
2012-07-10
M005T010D Modelled
M005T010D Field

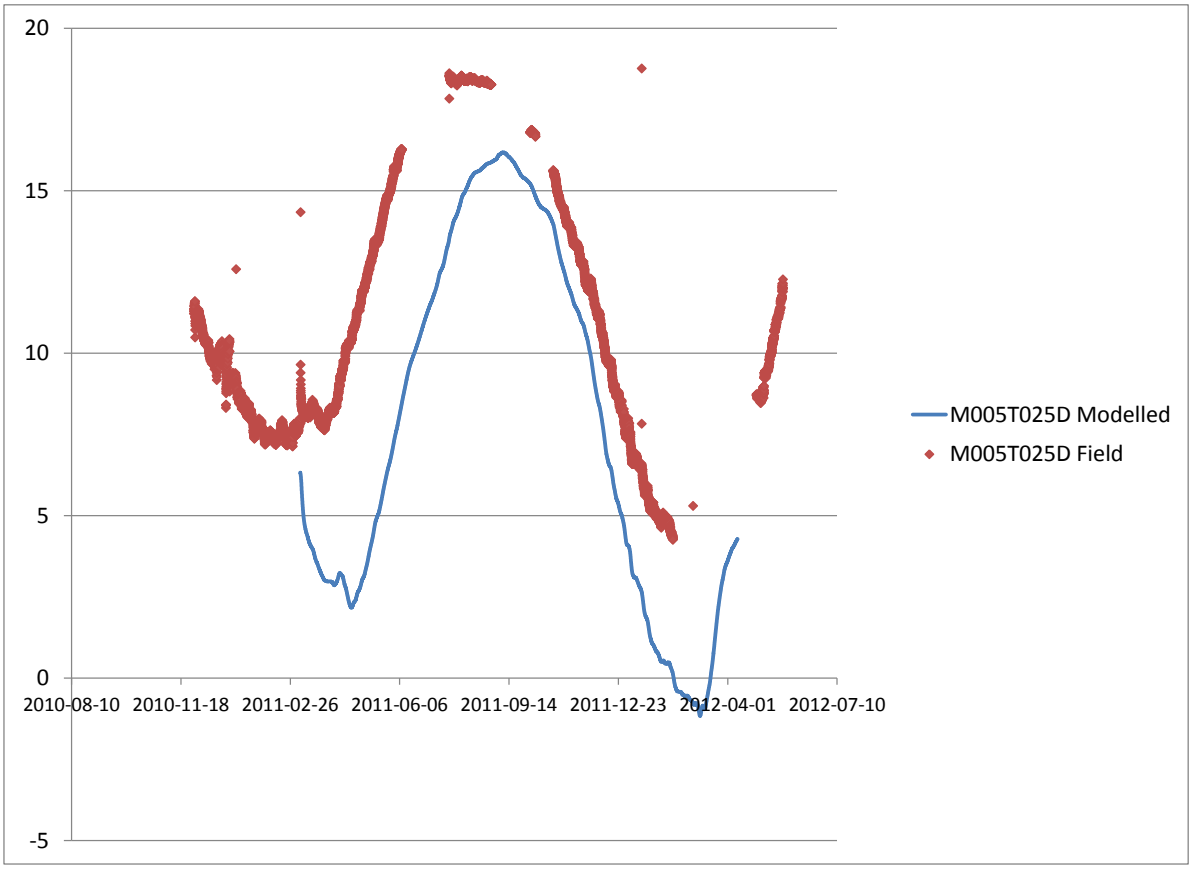
20
15
10
5
0
-5
2010-08-10
2010-11-18
2011-02-26
2011-06-06
2011-09-14
2011-12-23
2012-04-01
2012-07-10
M005T025D Modelled
M005T025D Field

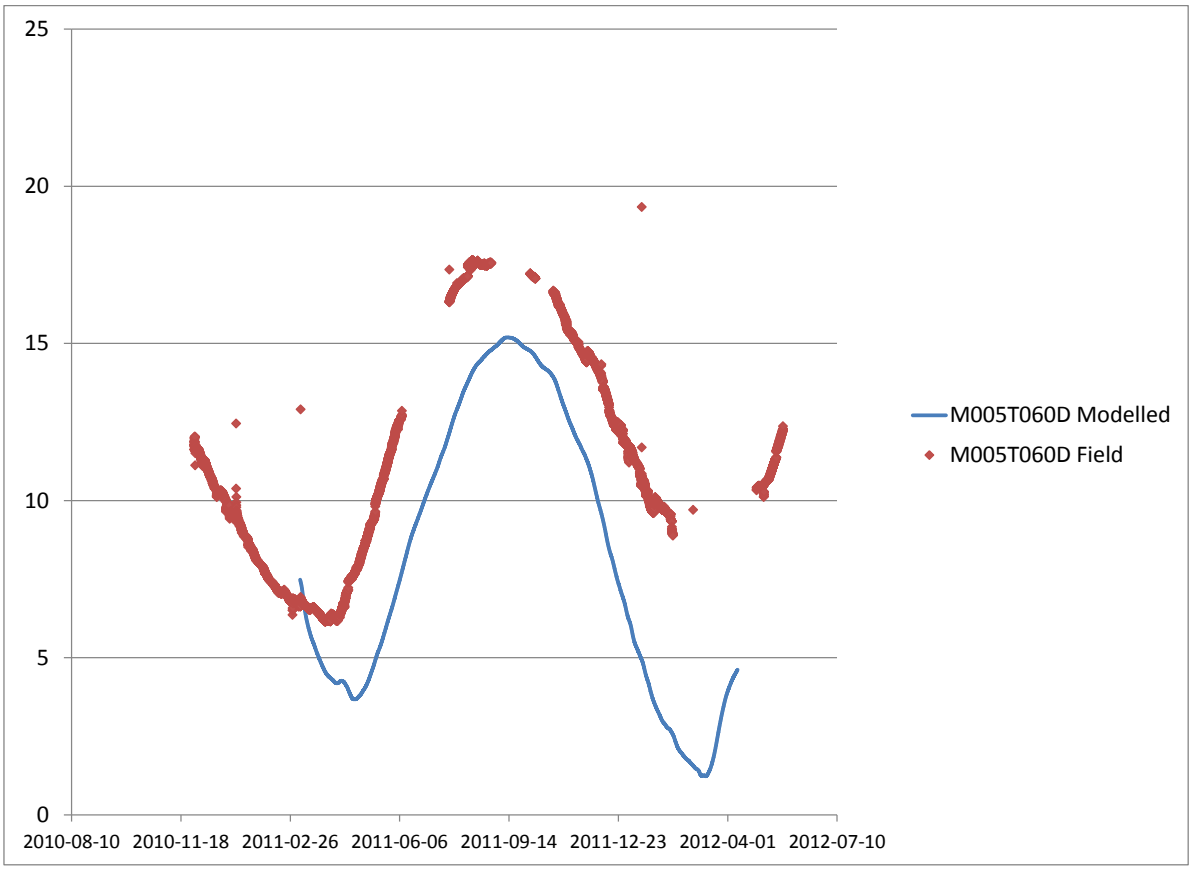
25
20
15
10
5
0
2010-08-10
2010-11-18
2011-02-26
2011-06-06
2011-09-14
2011-12-23
2012-04-01
2012-07-10
M005T060D Modelled
M005T060D Field

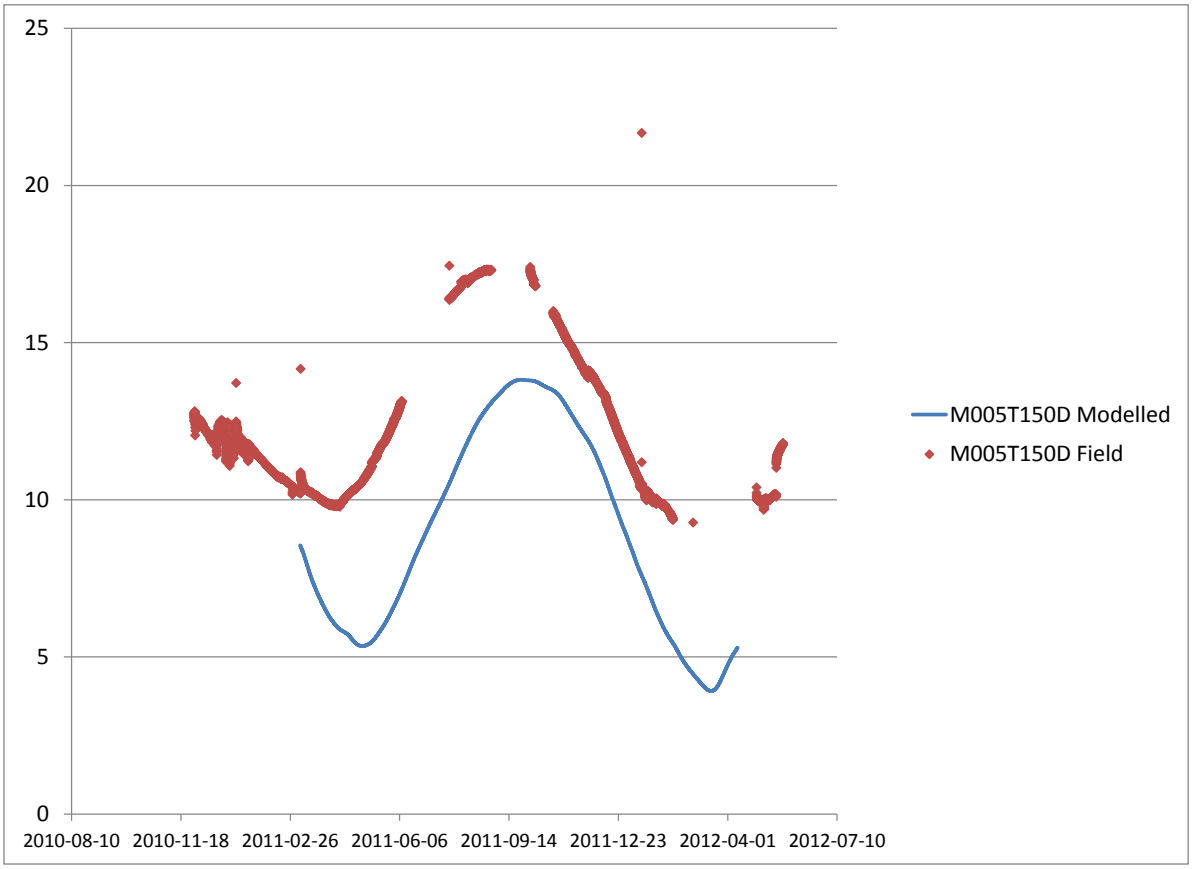
25
20
15
10
5
0
2010-08-10
2010-11-18
2011-02-26
2011-06-06
2011-09-14
2011-12-23
2012-04-01
2012-07-10
M005T150D Modelled
M005T150D Field

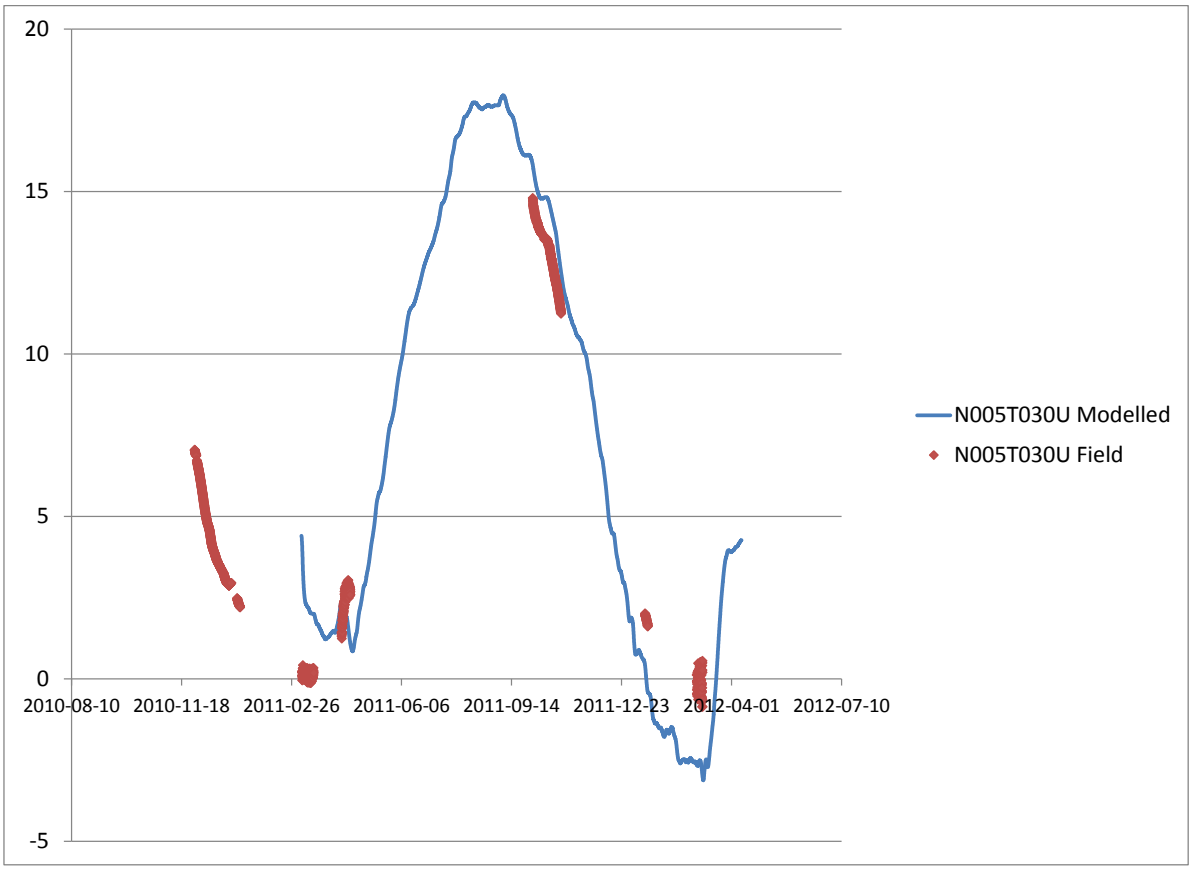
20
15
10
5
0
-5
2010-08-10
2010-11-18
2011-02-26
2011-06-06
2011-09-14
2011-12-23
2012-04-01
2012-07-10
N005T030U Modelled
N005T030U Field

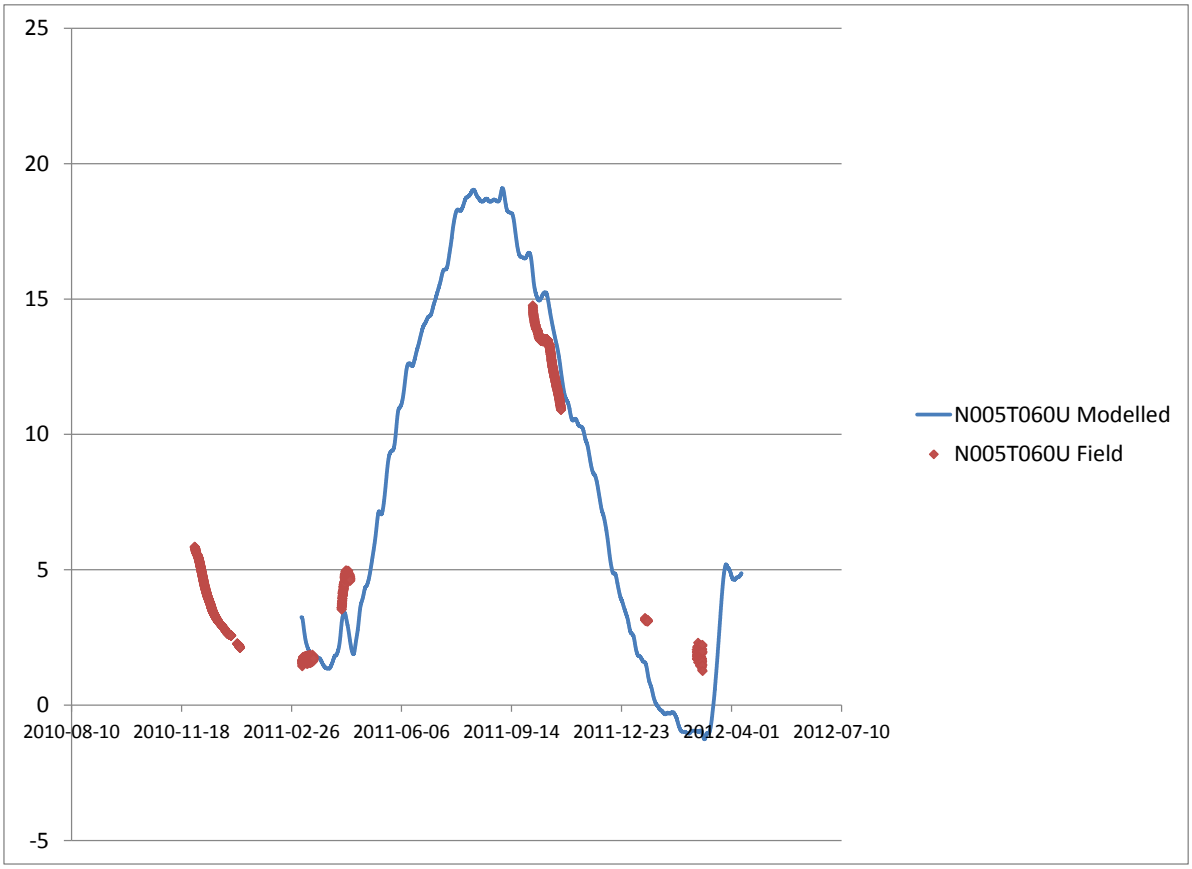
25
20
15
10
5
0
-5
2010-08-10
2010-11-18
2011-02-26
2011-06-06
2011-09-14
2011-12-23
2012-04-01
2012-07-10
N005T060U Modelled
N005T060U Field

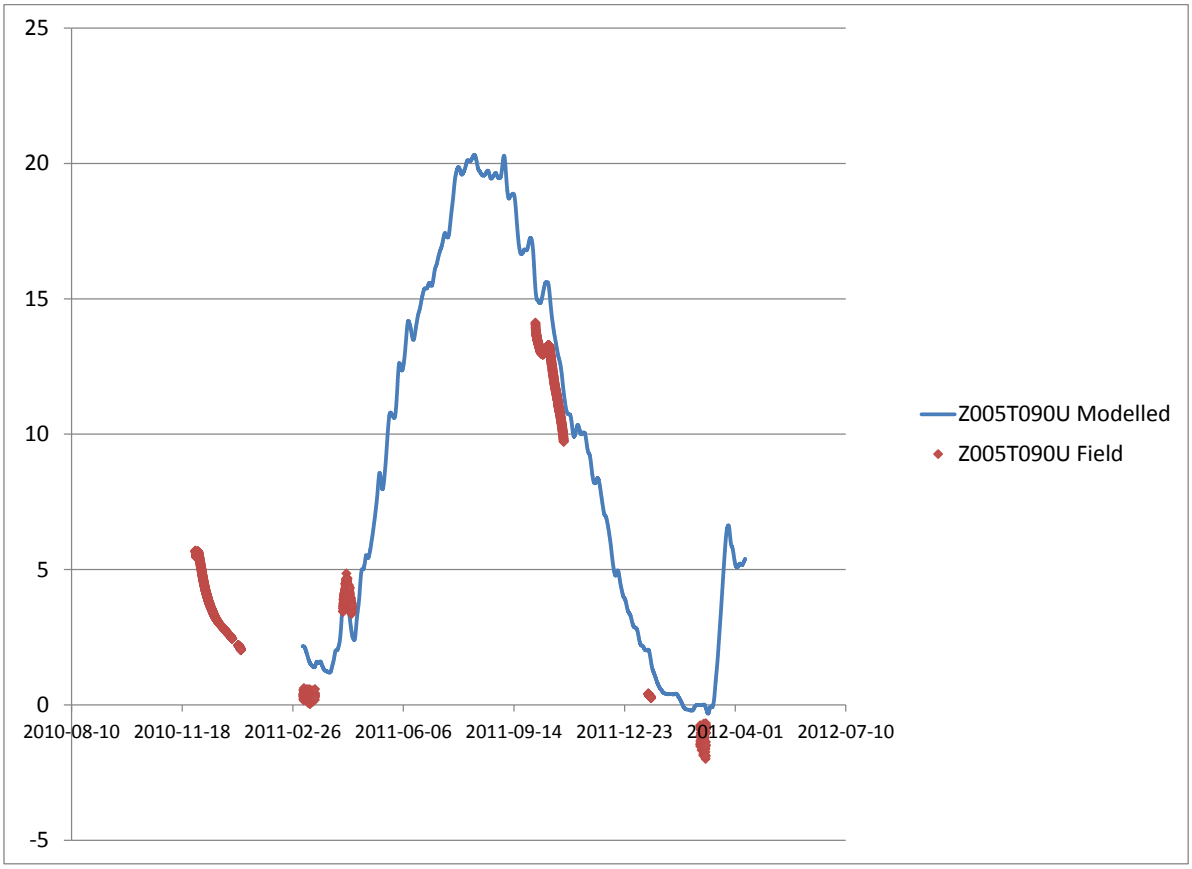
25
20
15
10
5
0
-5
2010-08-10
2010-11-18
2011-02-26
2011-06-06
2011-09-14
2011-12-23
2012-04-01
2012-07-10
Z005T090U Modelled
Z005T090U Field

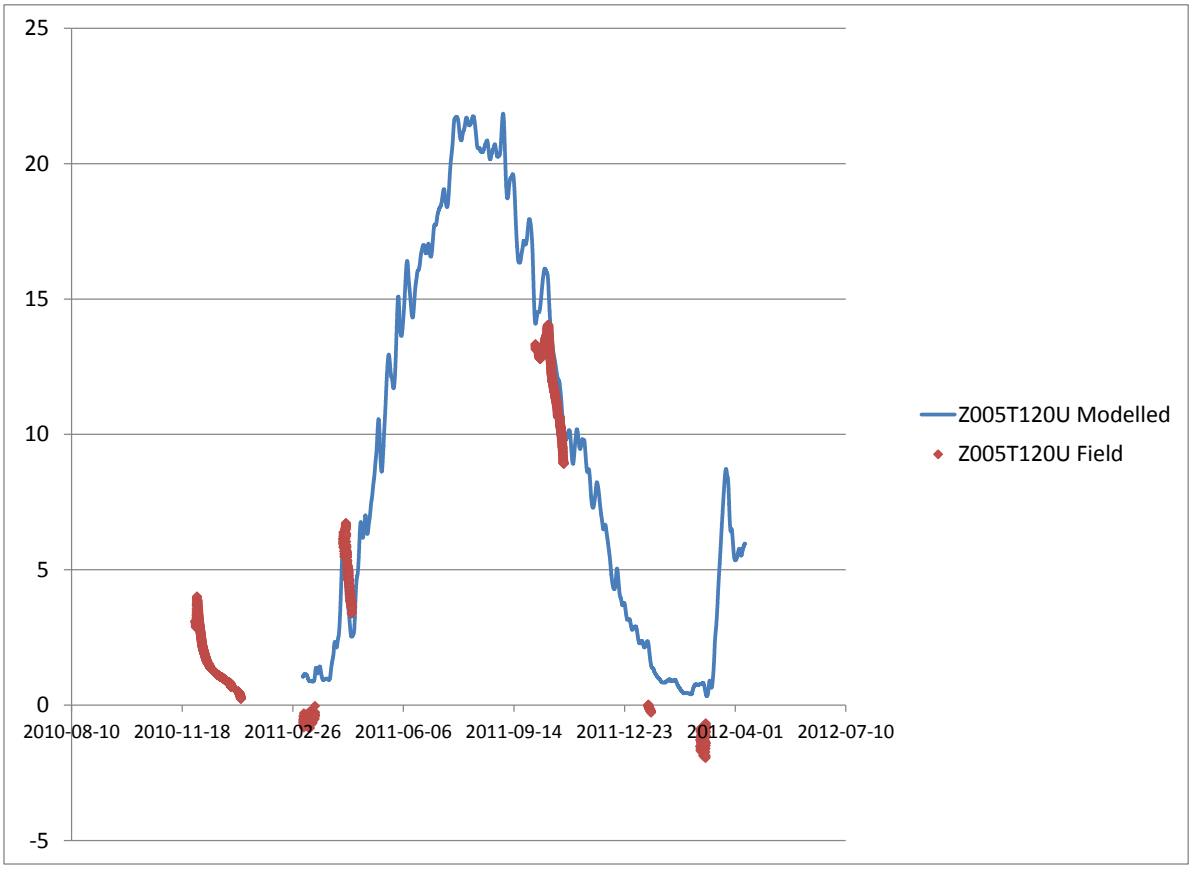
25
20
15
10
5
0
-5
2010-08-10
2010-11-18
2011-02-26
2011-06-06
2011-09-14
2011-12-23
2012-04-01
2012-07-10
Z005T120U Modelled
Z005T120U Field

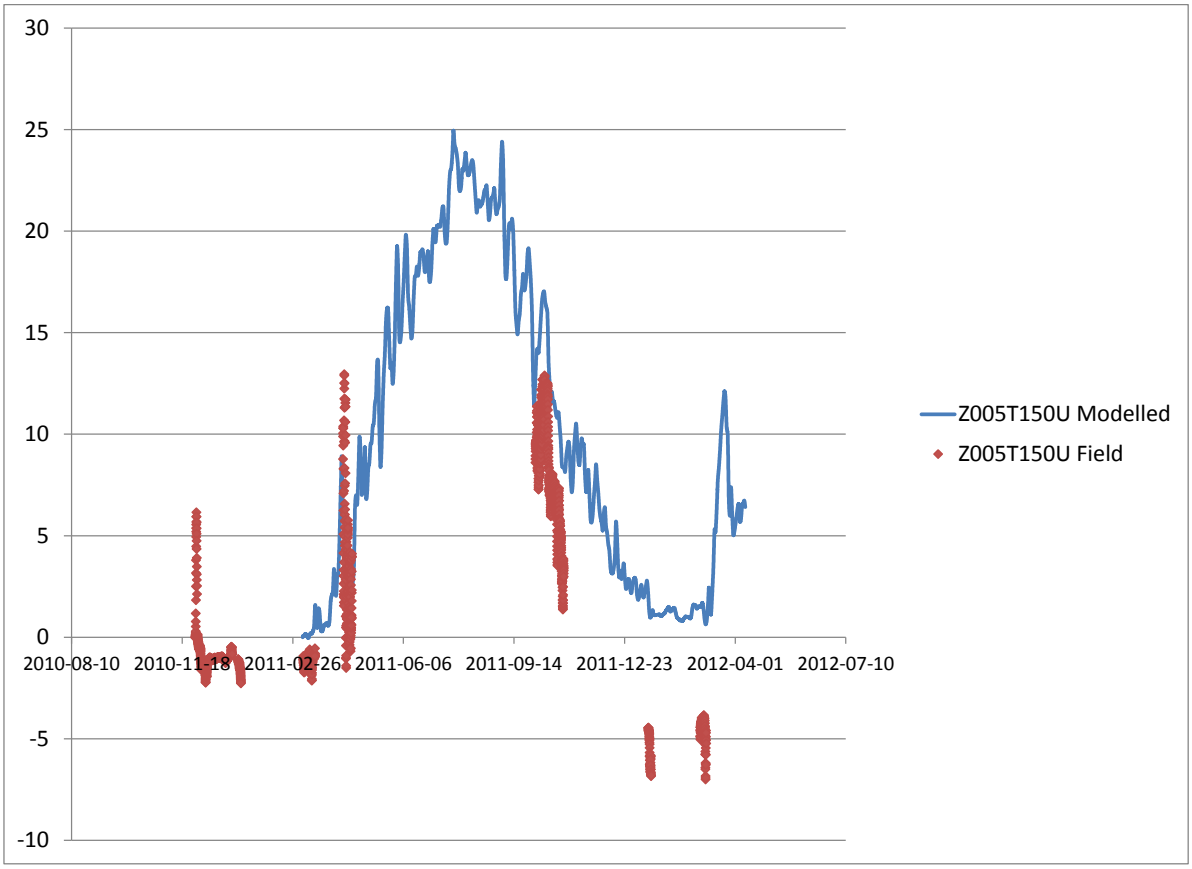
30
25
20
15
10
5
0
-5
-10
2010-08-10
2010-11-18
2011-02-26
2011-06-06
2011-09-14
2011-12-23
2012-04-01
2012-07-10
Z005T150U Modelled
Z005T150U Field

G.1.3 Both Conductivity and Load Estimated: Narrow DDS

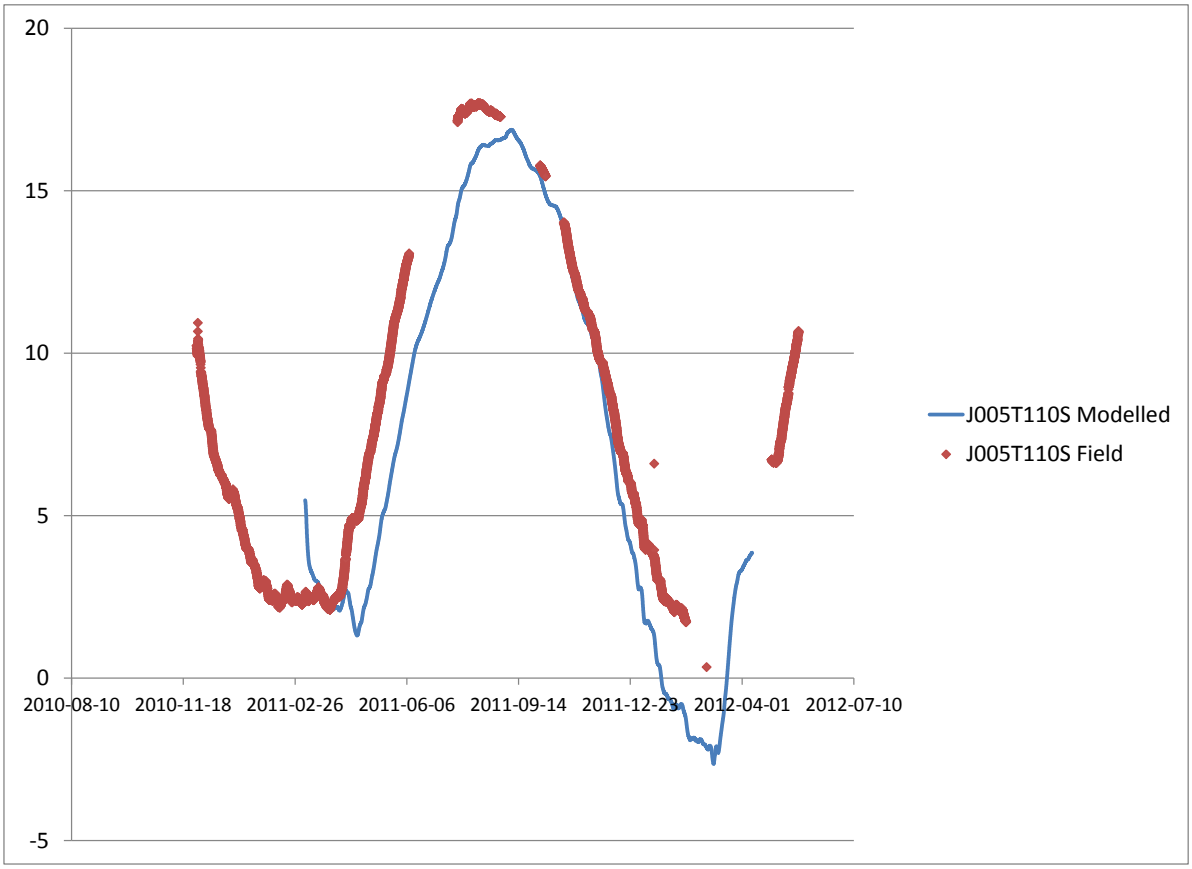
20
15
10
5
0
-5
2010-08-10
2010-11-18
2011-02-26
2011-06-06
2011-09-14
2011-12-23
2012-04-01
2012-07-10
J005T110S Modelled
J005T110S Field

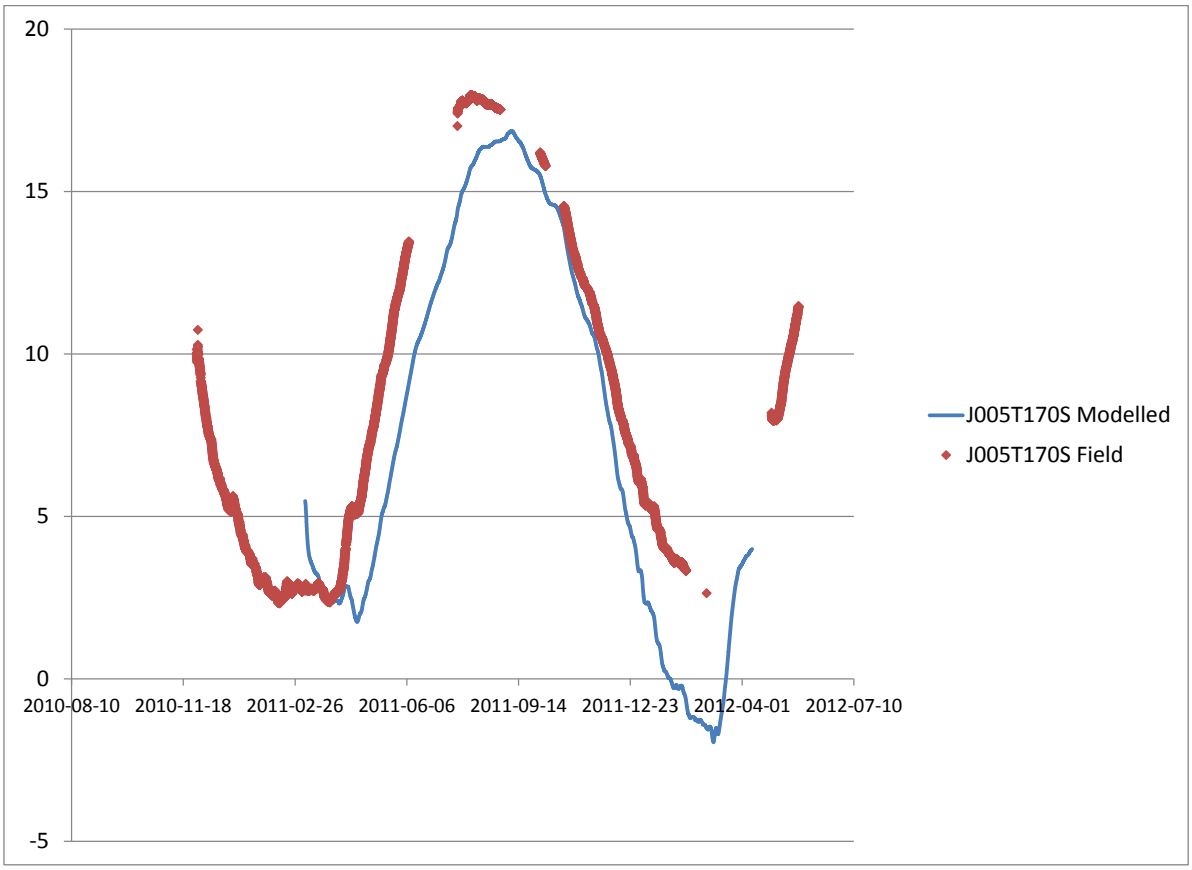
20
15
10
5
0
-5
2010-08-10
2010-11-18
2011-02-26
2011-06-06
2011-09-14
2011-12-23
2012-04-01
2012-07-10
J005T170S Modelled
J005T170S Field

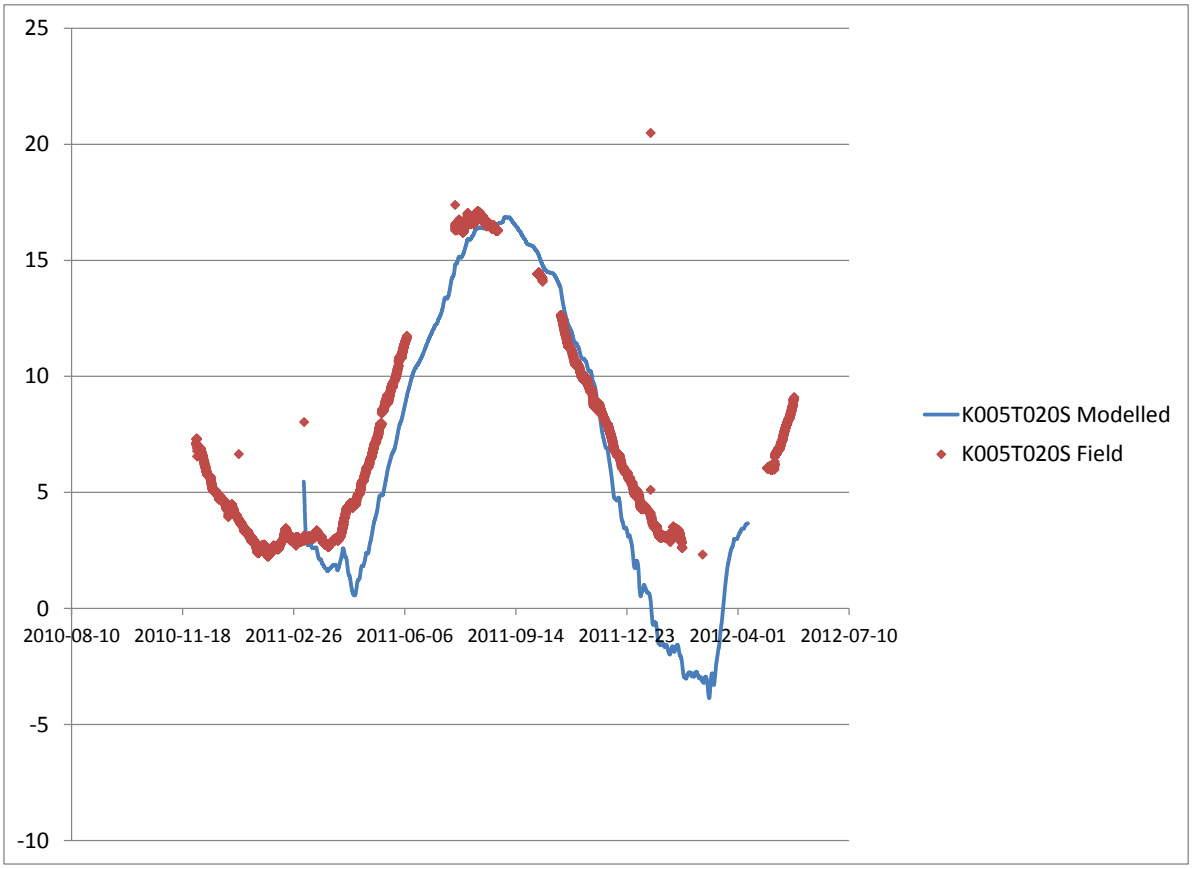
25
20
15
10
5
0
-5
-10
2010-08-10
2010-11-18
2011-02-26
2011-06-06
2011-09-14
2011-12-23
2012-04-01
2012-07-10
K005T020S Modelled
K005T020S Field

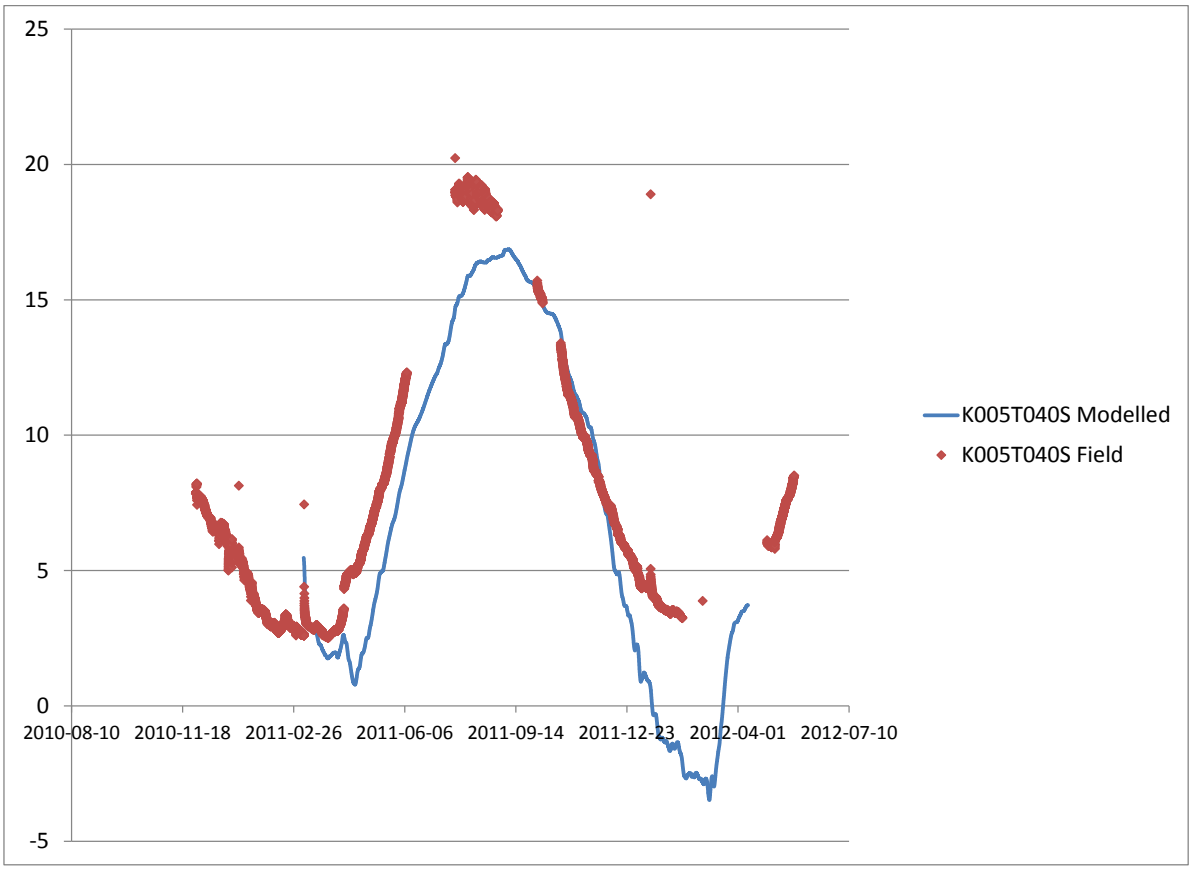
25
20
15
10
5
0
-5
2010-08-10
2010-11-18
2011-02-26
2011-06-06
2011-09-14
2011-12-23
2012-04-01
2012-07-10
K005T040S Modelled
K005T040S Field

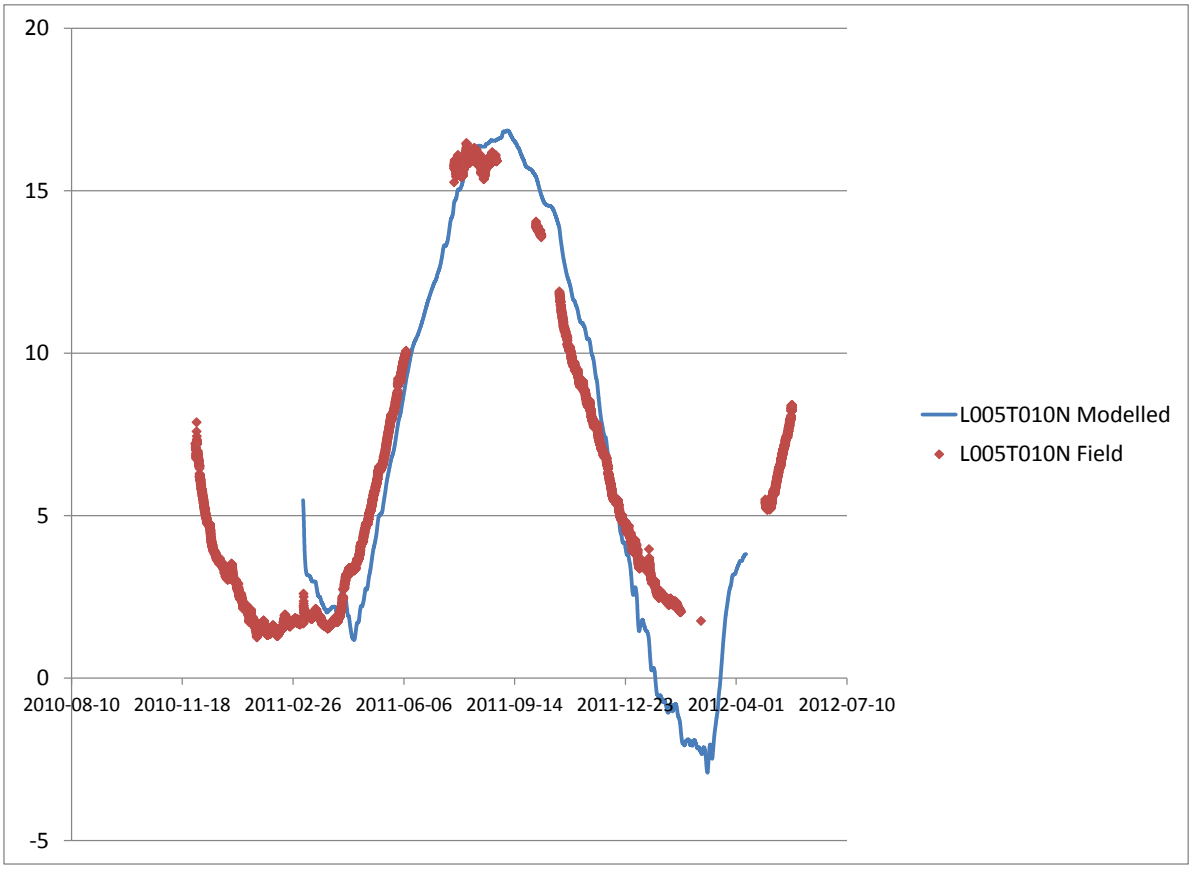
20
15
10
5
0
-5
2010-08-10
2010-11-18
2011-02-26
2011-06-06
2011-09-14
2011-12-23
2012-04-01
2012-07-10
L005T010N Modelled
L005T010N Field

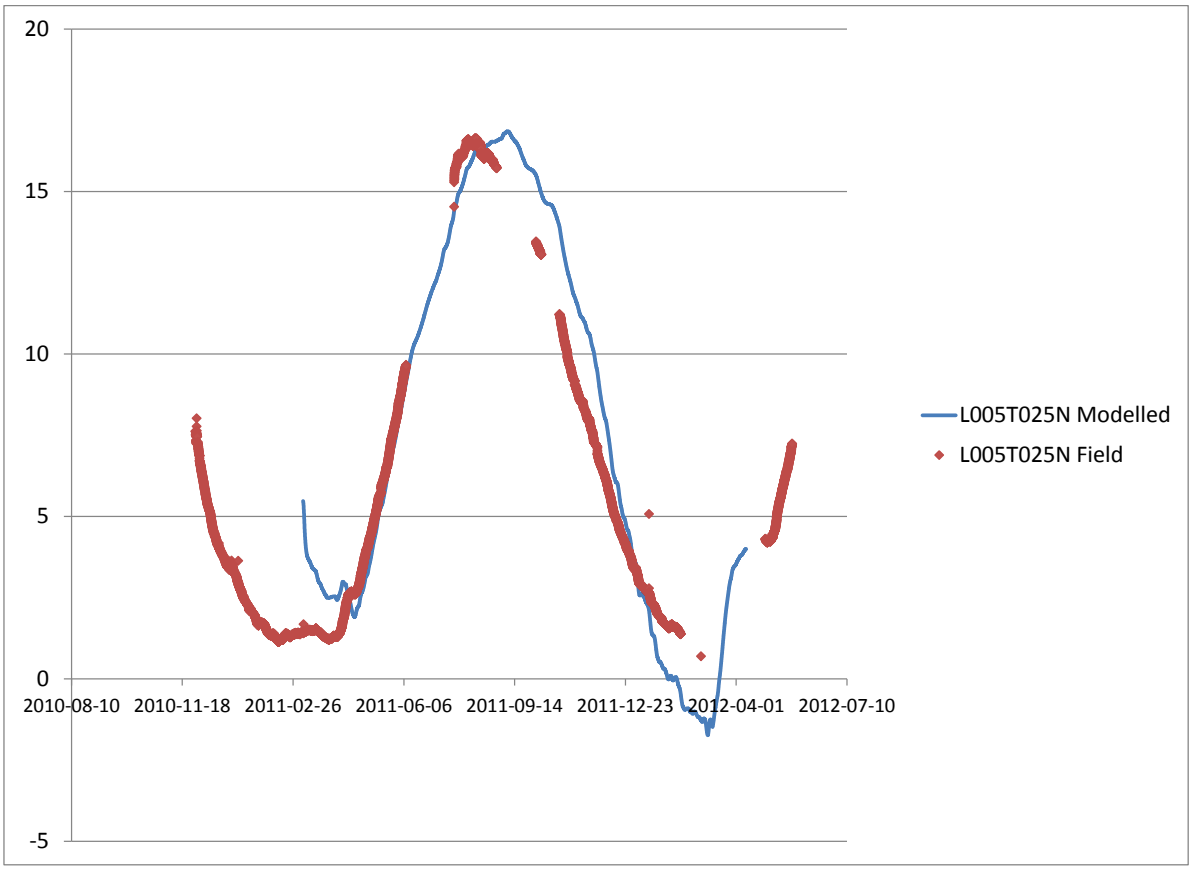
20
15
10
5
0
-5
2010-08-10
2010-11-18
2011-02-26
2011-06-06
2011-09-14
2011-12-23
2012-04-01
2012-07-10
L005T025N Modelled
L005T025N Field

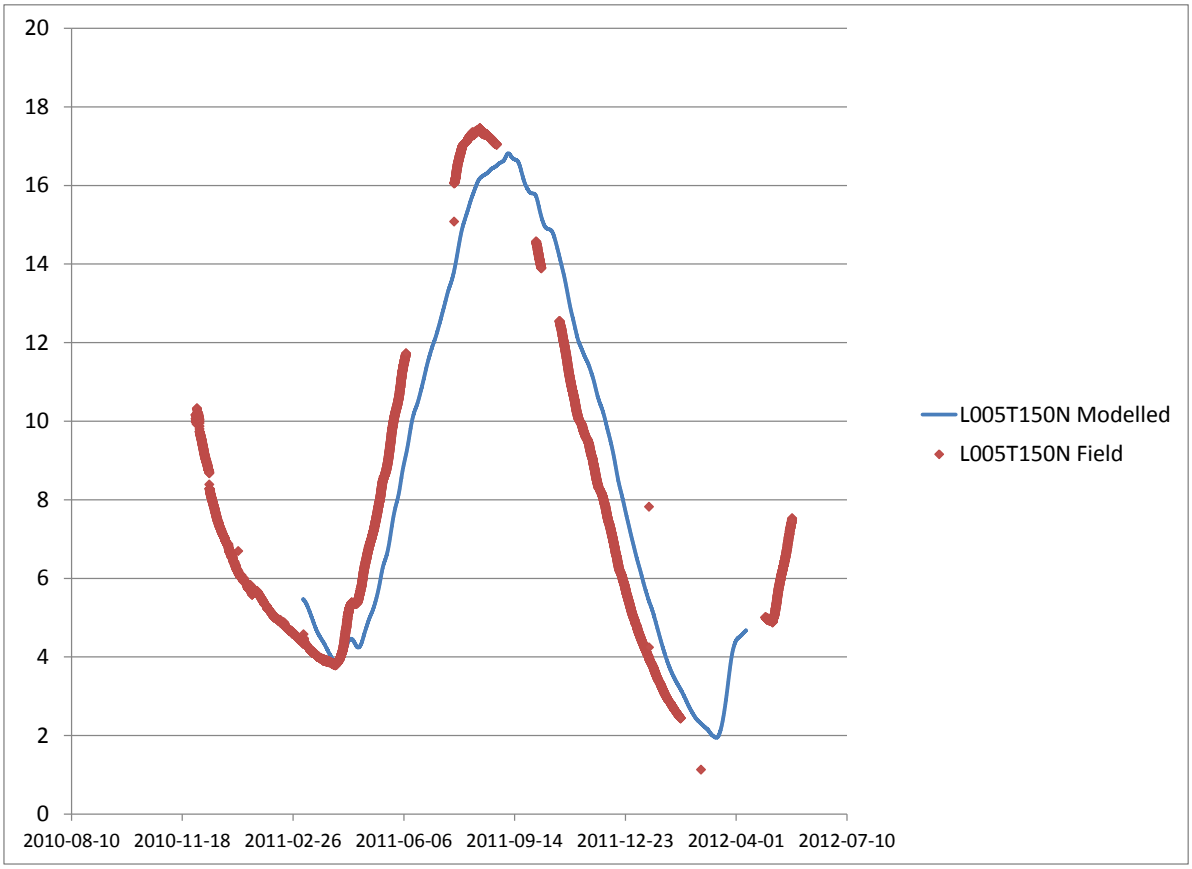
20
18
16
14
12
10
8
6
4
2
0
2010-08-10
2010-11-18
2011-02-26
2011-06-06
2011-09-14
2011-12-23
2012-04-01
2012-07-10
L005T150N Modelled
L005T150N Field

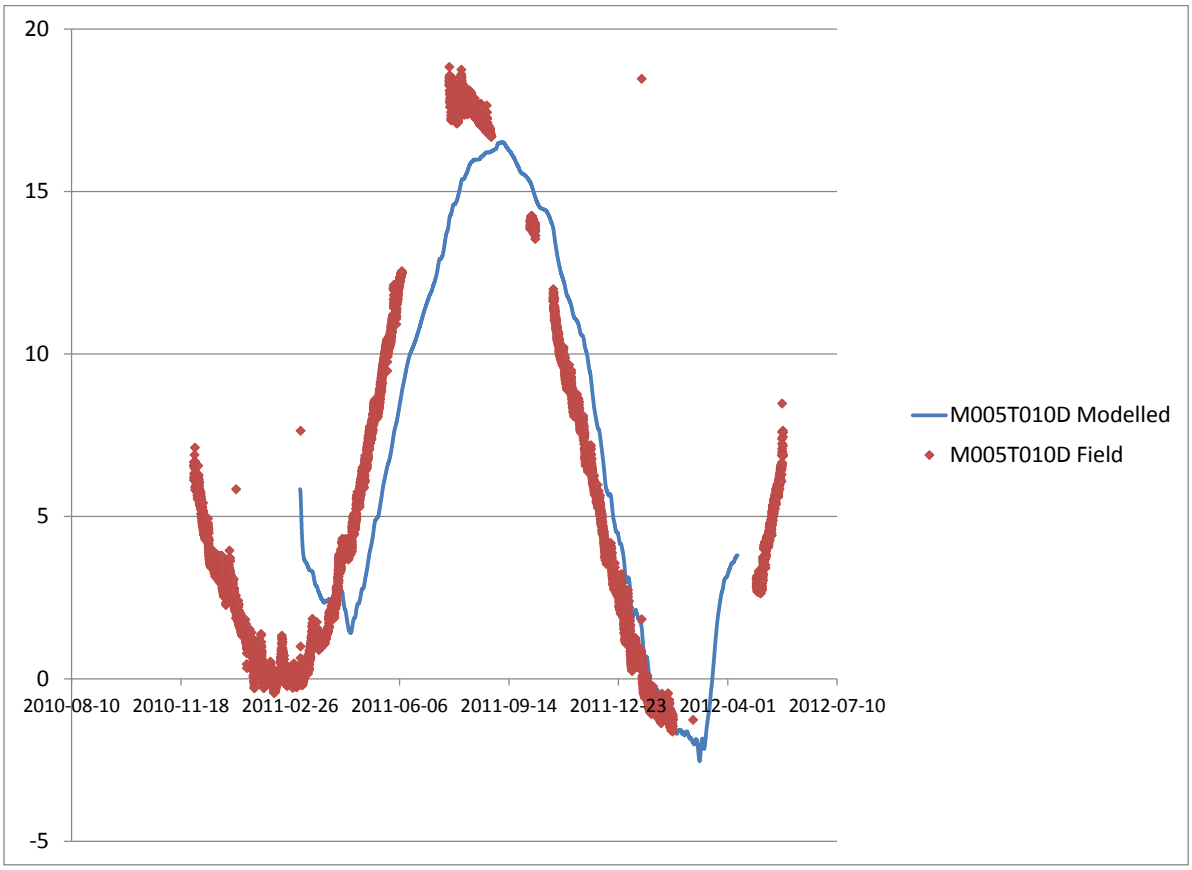
20
15
10
5
0
-5
2010-08-10
2010-11-18
2011-02-26
2011-06-06
2011-09-14
2011-12-23
2012-04-01
2012-07-10
M005T010D Modelled
M005T010D Field

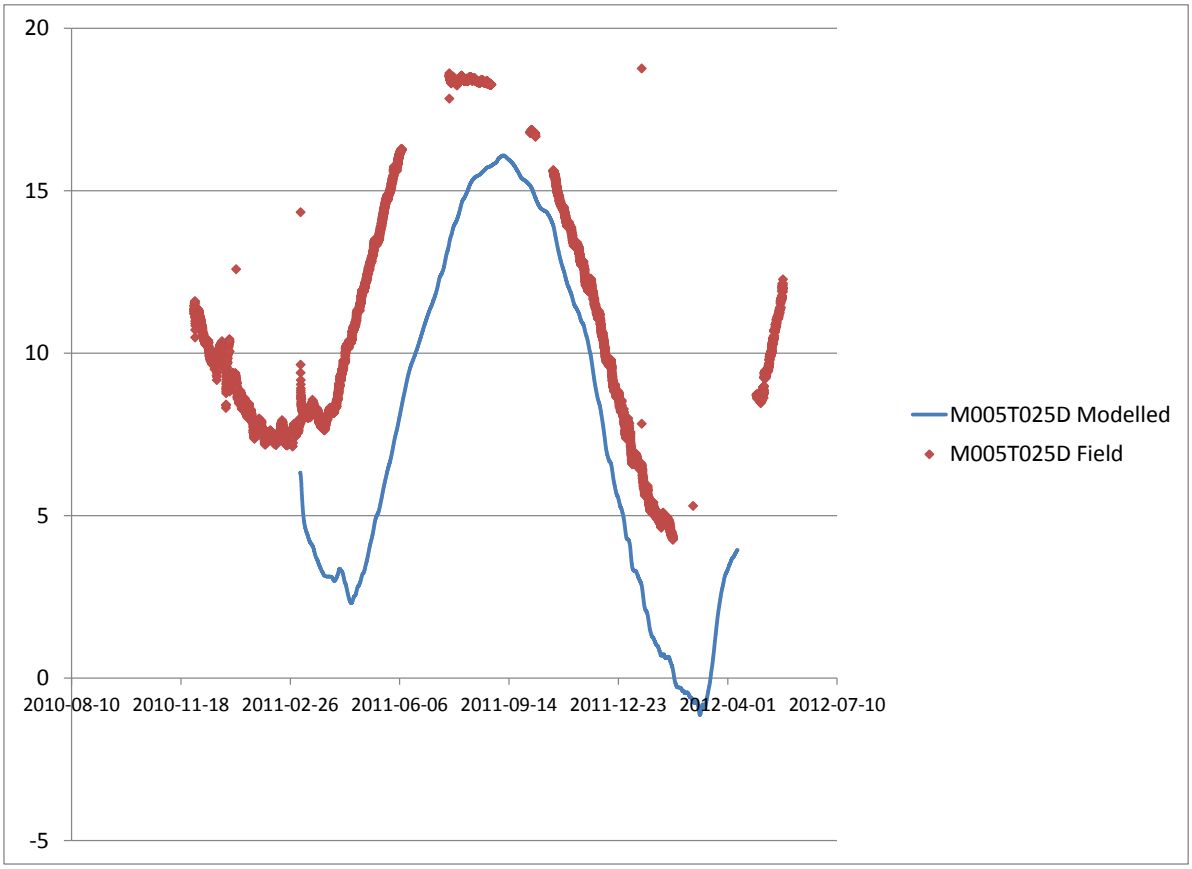
20
15
10
5
0
-5
2010-08-10
2010-11-18
2011-02-26
2011-06-06
2011-09-14
2011-12-23
2012-04-01
2012-07-10
M005T025D Modelled
M005T025D Field

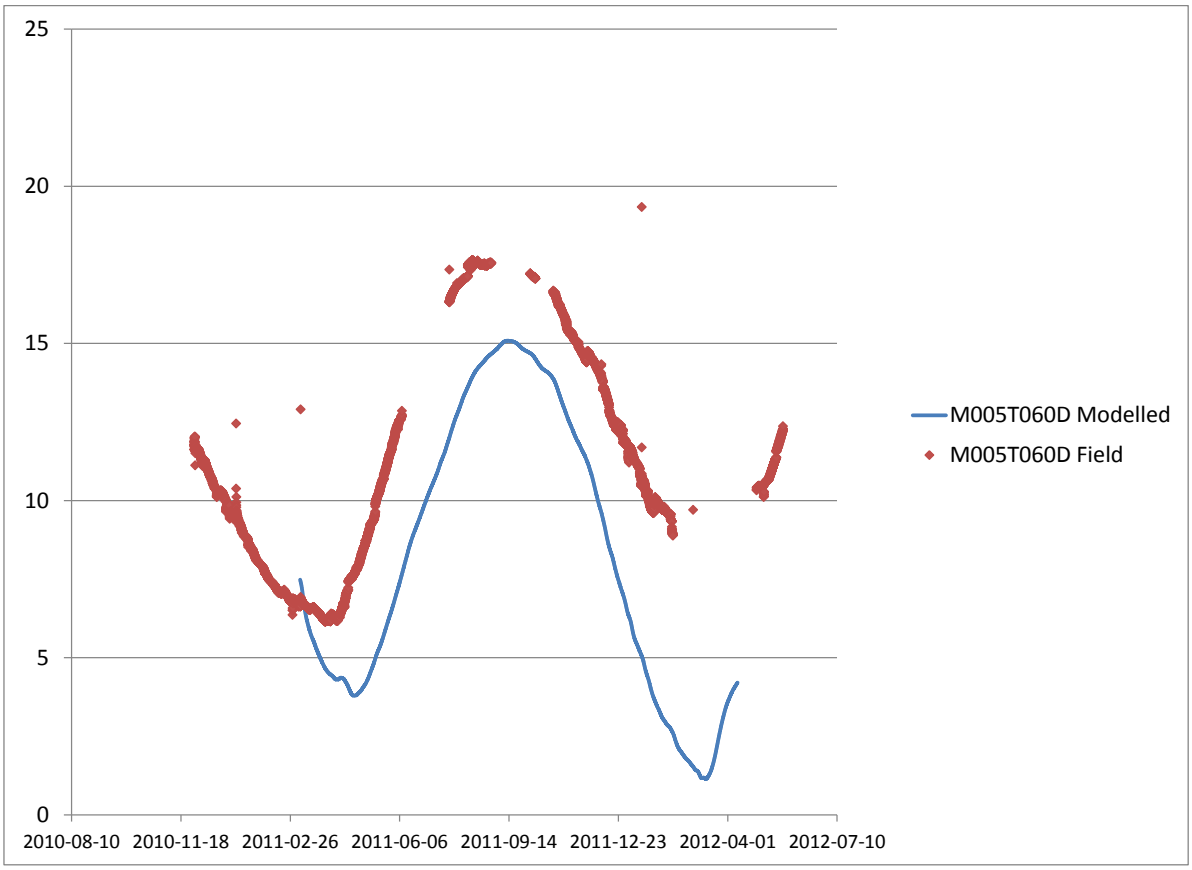
25
20
15
10
5
0
2010-08-10
2010-11-18
2011-02-26
2011-06-06
2011-09-14
2011-12-23
2012-04-01
2012-07-10
M005T060D Modelled
M005T060D Field

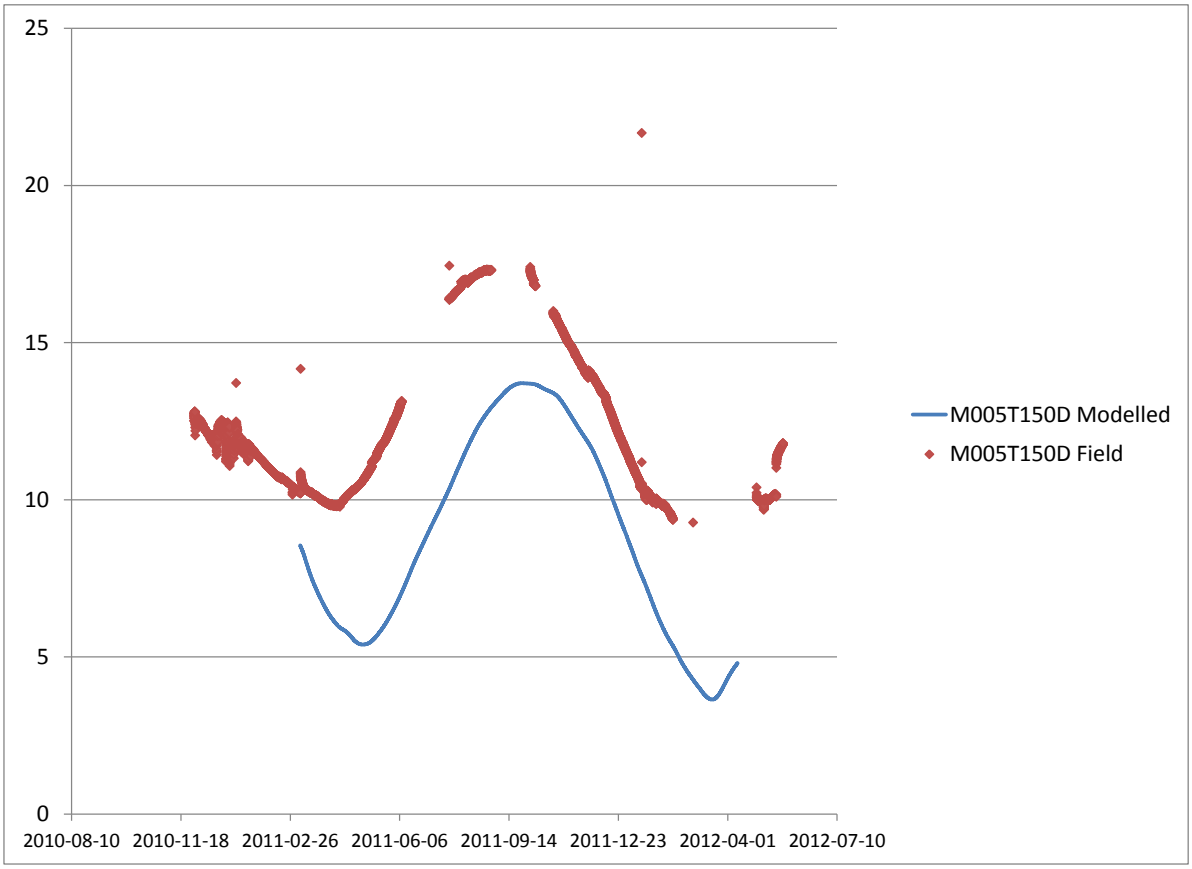
25
20
15
10
5
0
2010-08-10
2010-11-18
2011-02-26
2011-06-06
2011-09-14
2011-12-23
2012-04-01
2012-07-10
M005T150D Modelled
M005T150D Field

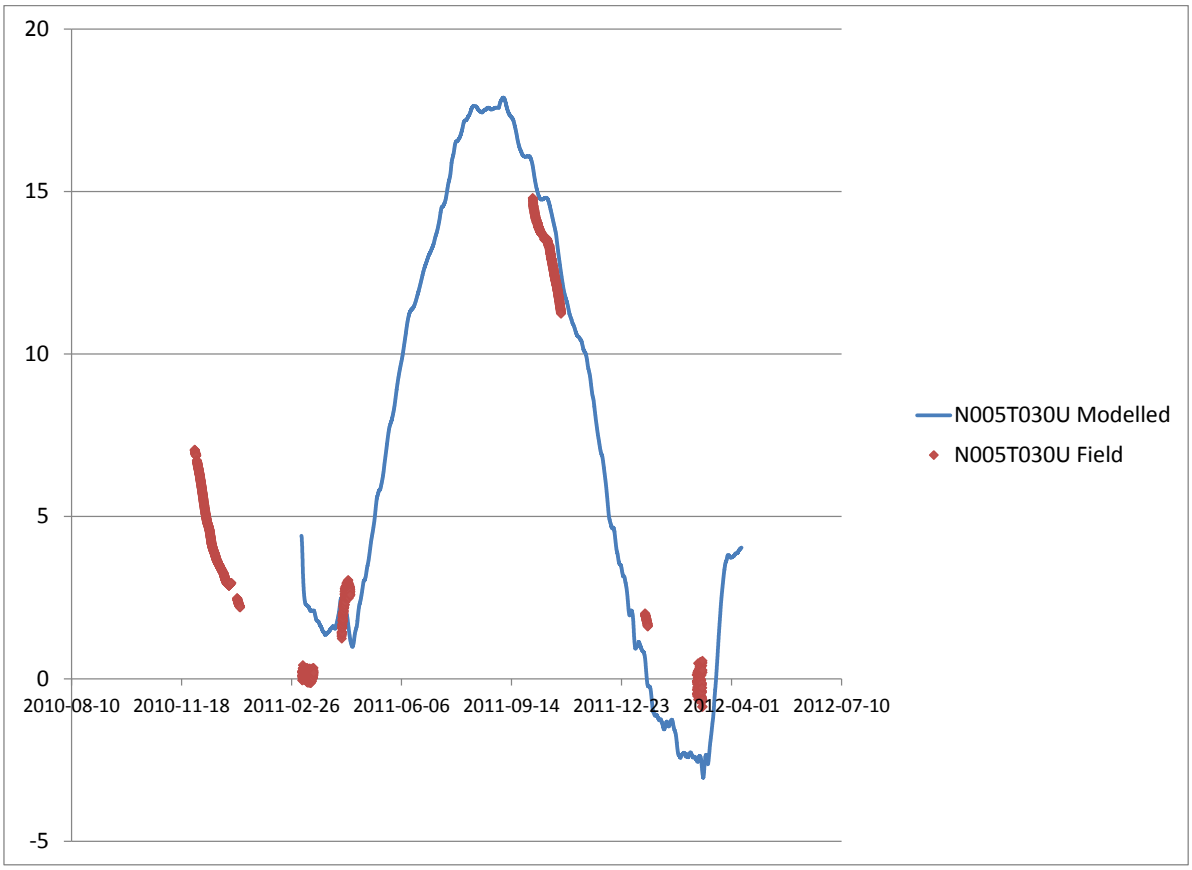
20
15
10
5
0
-5
2010-08-10
2010-11-18
2011-02-26
2011-06-06
2011-09-14
2011-12-23
2012-04-01
2012-07-10
N005T030U Modelled
N005T030U Field

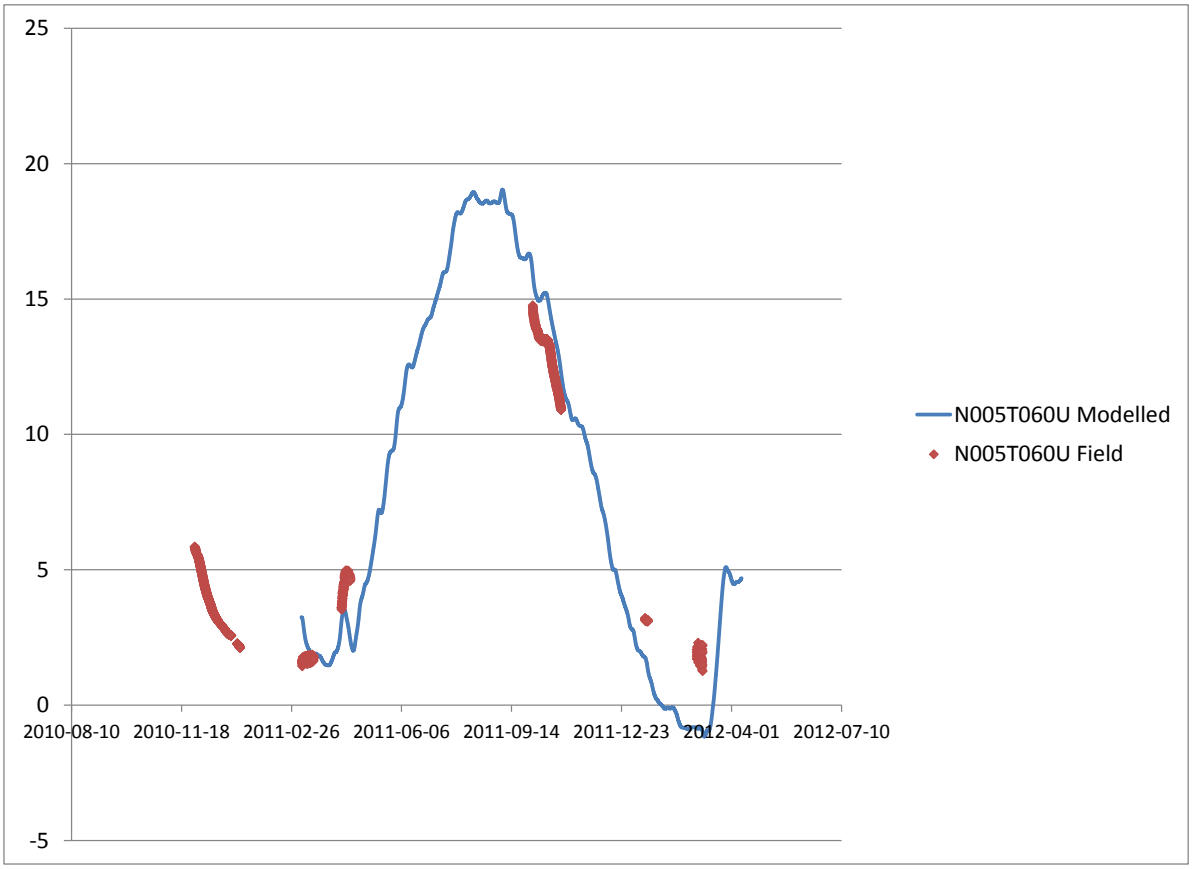
25
20
15
10
5
0
-5
2010-08-10
2010-11-18
2011-02-26
2011-06-06
2011-09-14
2011-12-23
2012-04-01
2012-07-10
N005T060U Modelled
N005T060U Field

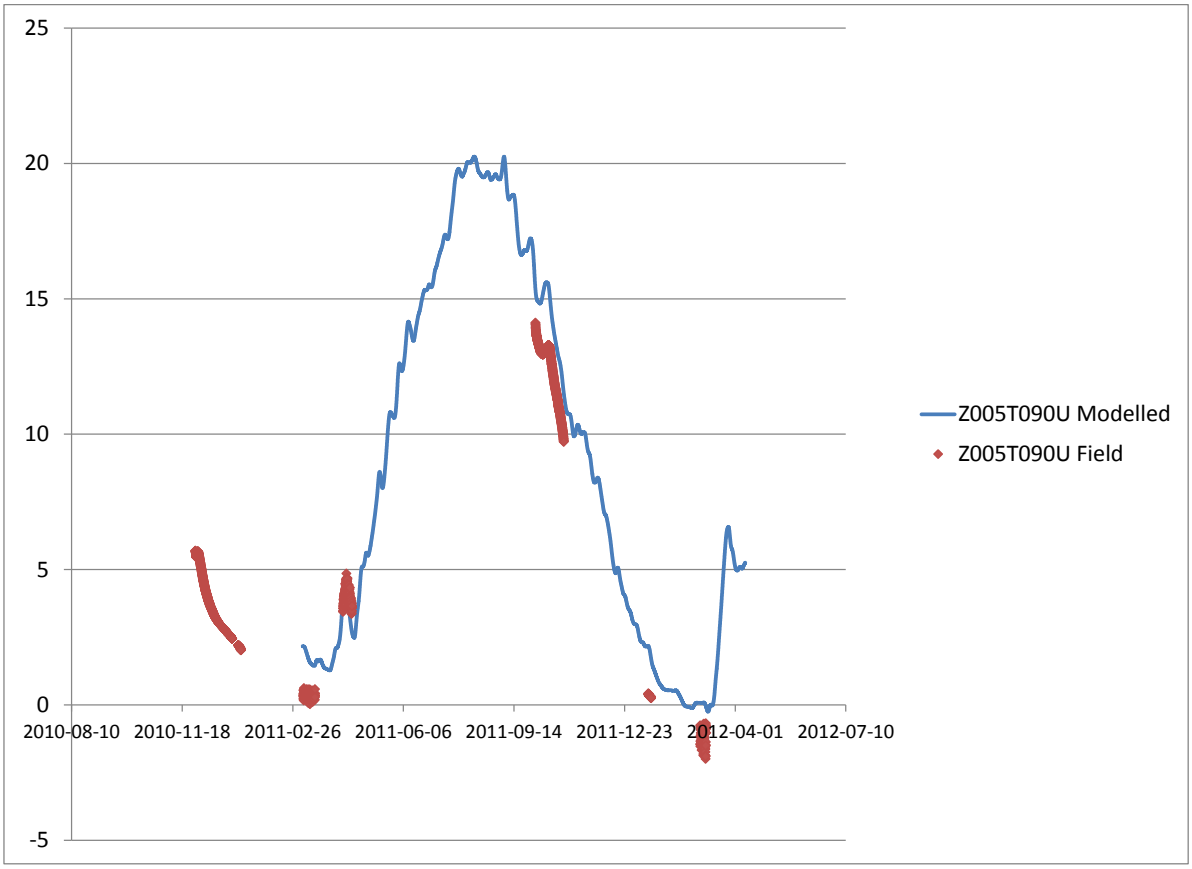
25
20
15
10
5
0
-5
2010-08-10
2010-11-18
2011-02-26
2011-06-06
2011-09-14
2011-12-23
2012-04-01
2012-07-10
Z005T090U Modelled
Z005T090U Field

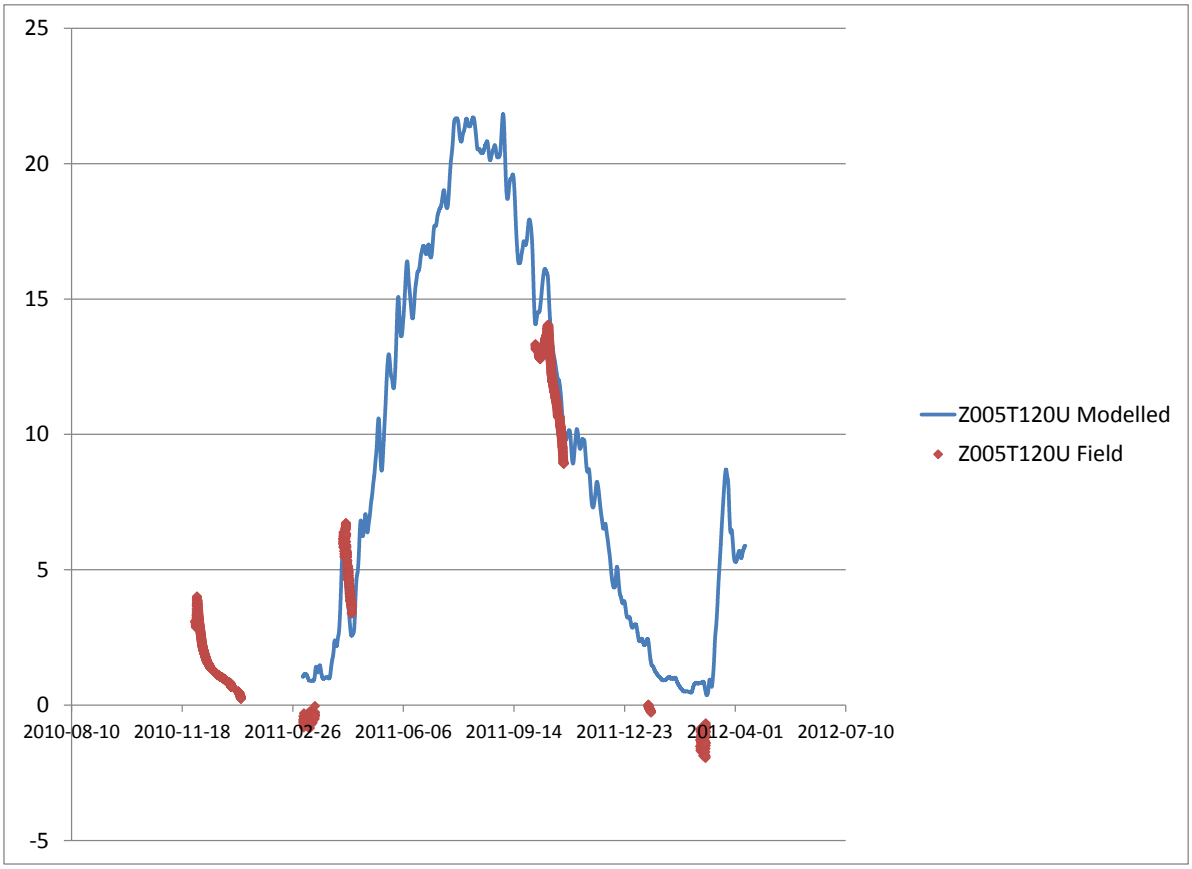
25
20
15
10
5
0
-5
2010-08-10
2010-11-18
2011-02-26
2011-06-06
2011-09-14
2011-12-23
2012-04-01
2012-07-10
Z005T120U Modelled
Z005T120U Field

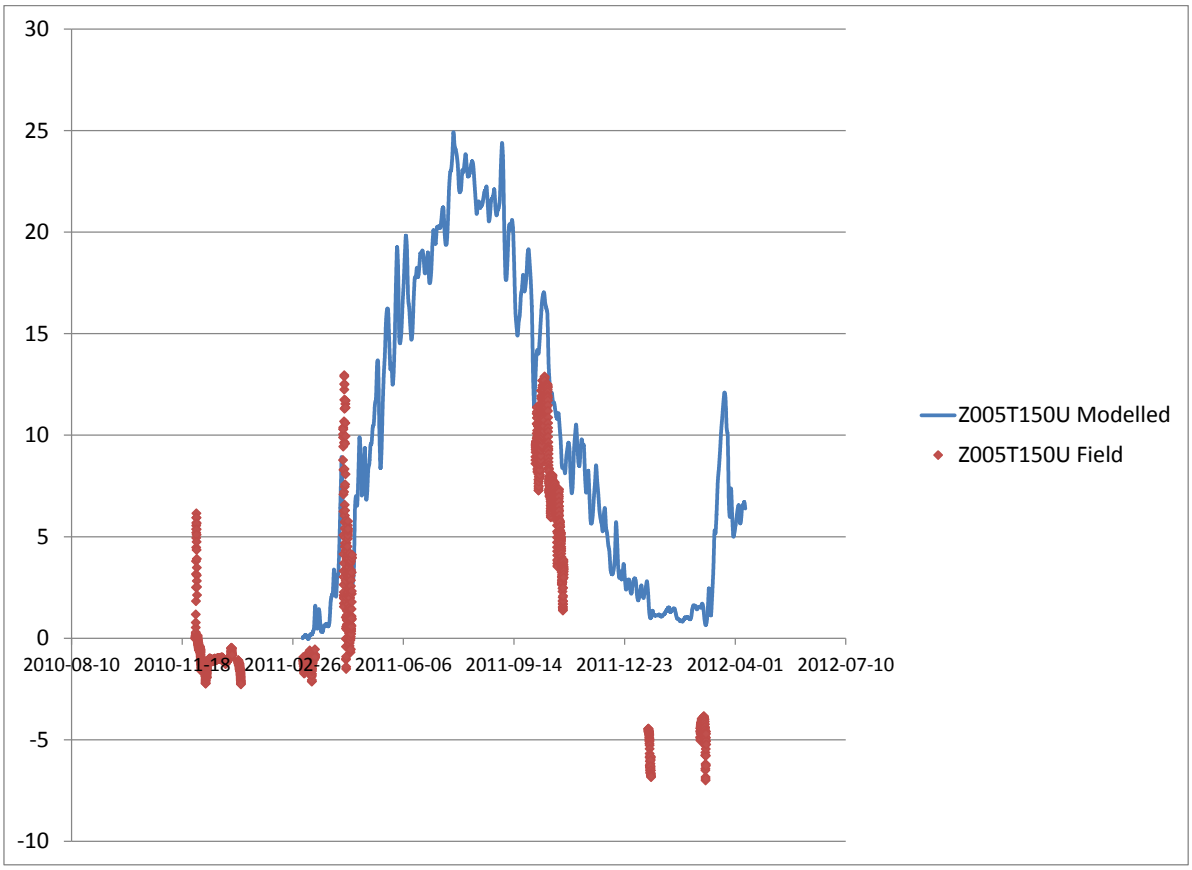
30
25
20
15
10
5
0
-5
-10
2010-08-10
2010-11-18
2011-02-26
2011-06-06
2011-09-14
2011-12-23
2012-04-01
2012-07-10
Z005T150U Modelled
Z005T150U Field

G.1.4 Only Conductivity Estimated: Narrow DDS

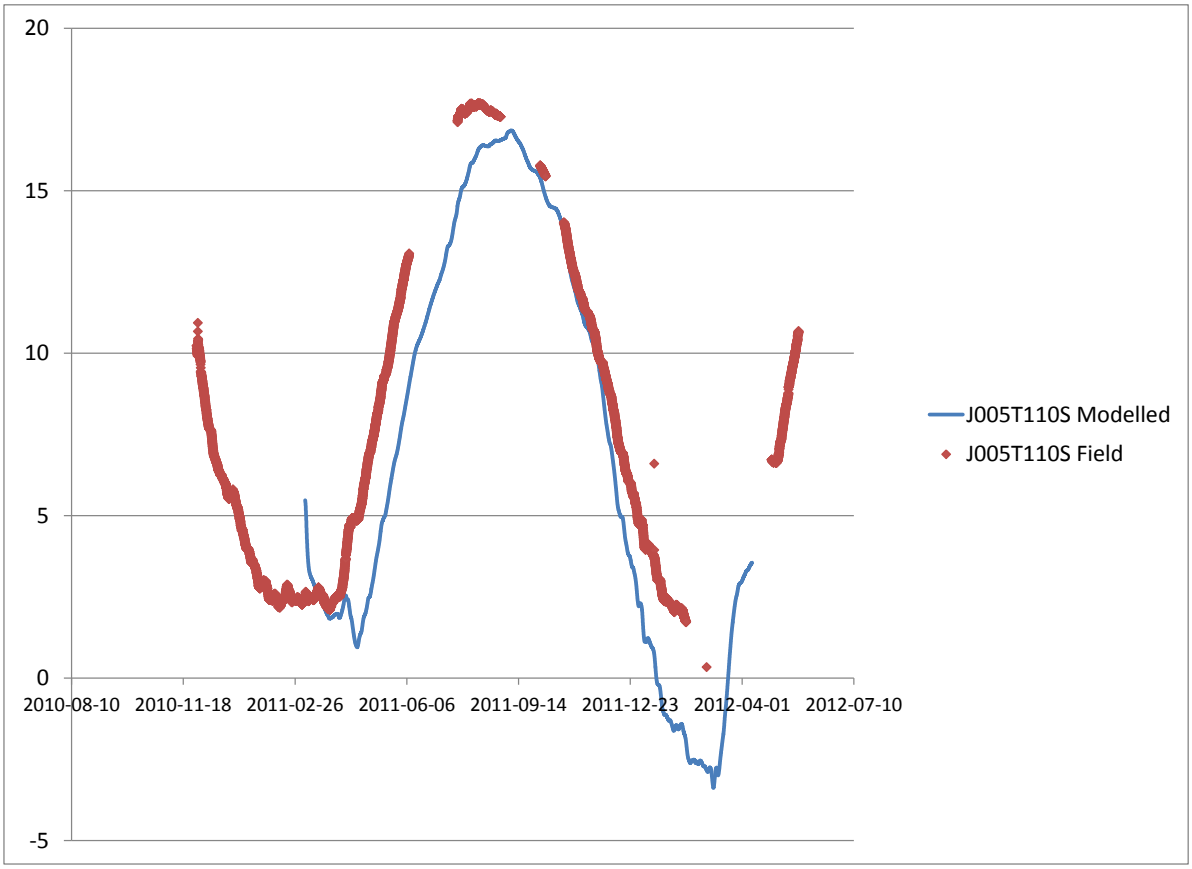
20
15
10
5
0
-5
2010-08-10
2010-11-18
2011-02-26
2011-06-06
2011-09-14
2011-12-23
2012-04-01
2012-07-10
J005T110S Modelled
J005T110S Field

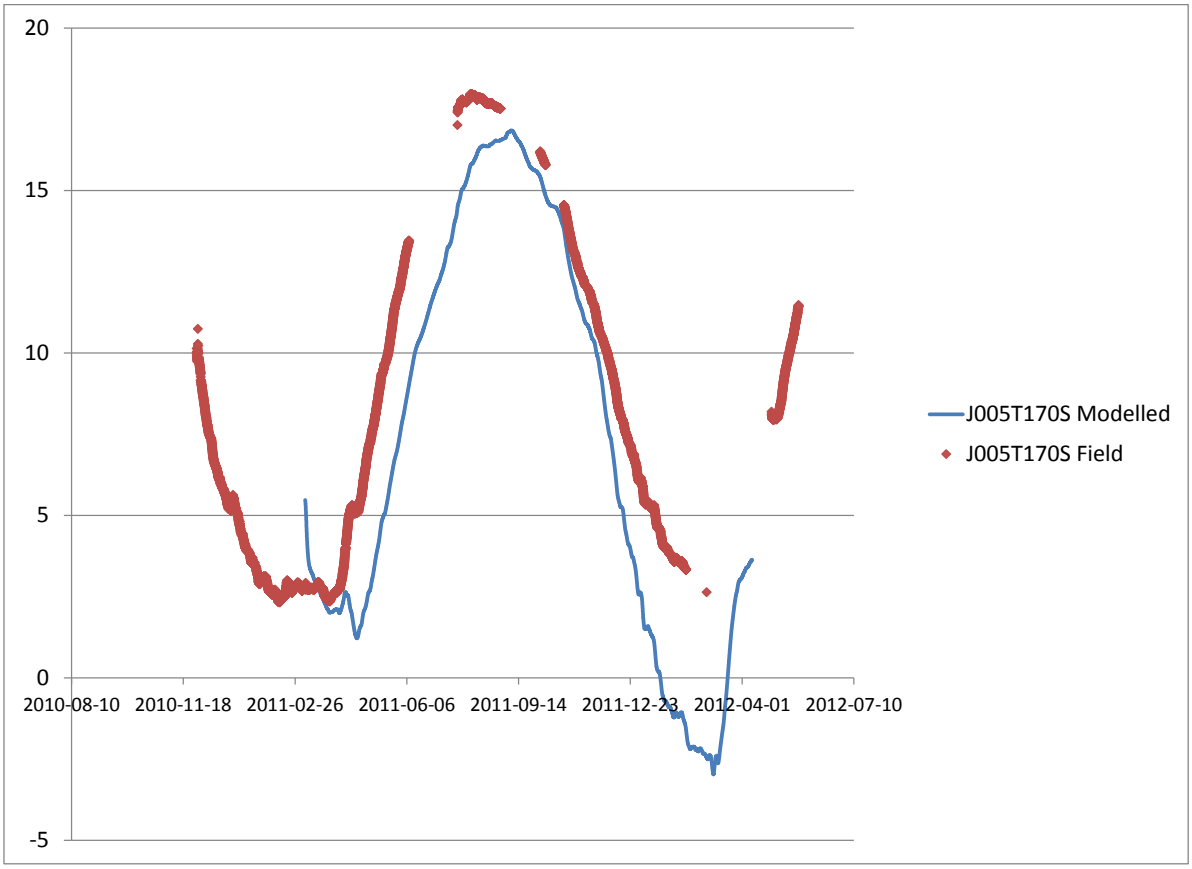
20
15
10
5
0
-5
2010-08-10
2010-11-18
2011-02-26
2011-06-06
2011-09-14
2011-12-23
2012-04-01
2012-07-10
J005T170S Modelled
J005T170S Field

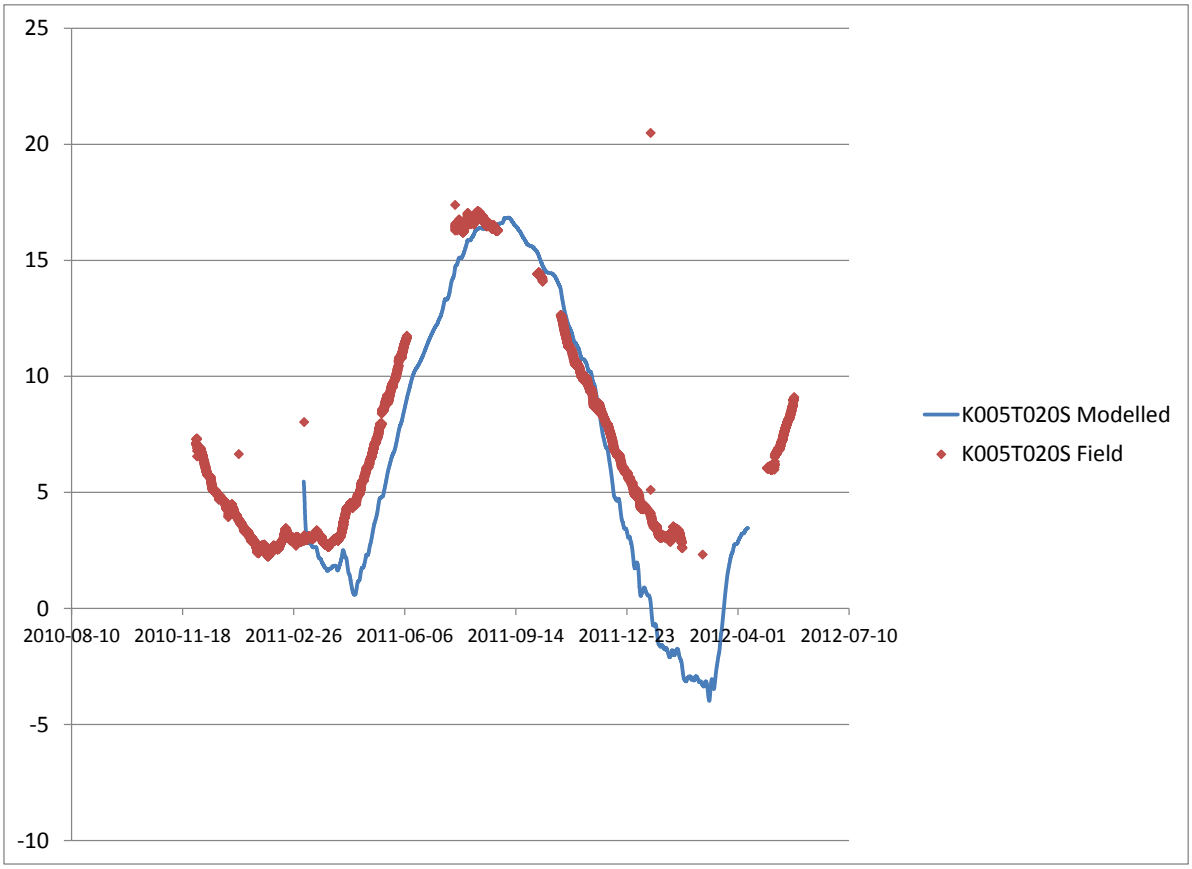
25
20
15
10
5
0
-5
-10
2010-08-10
2010-11-18
2011-02-26
2011-06-06
2011-09-14
2011-12-23
2012-04-01
2012-07-10
K005T020S Modelled
K005T020S Field

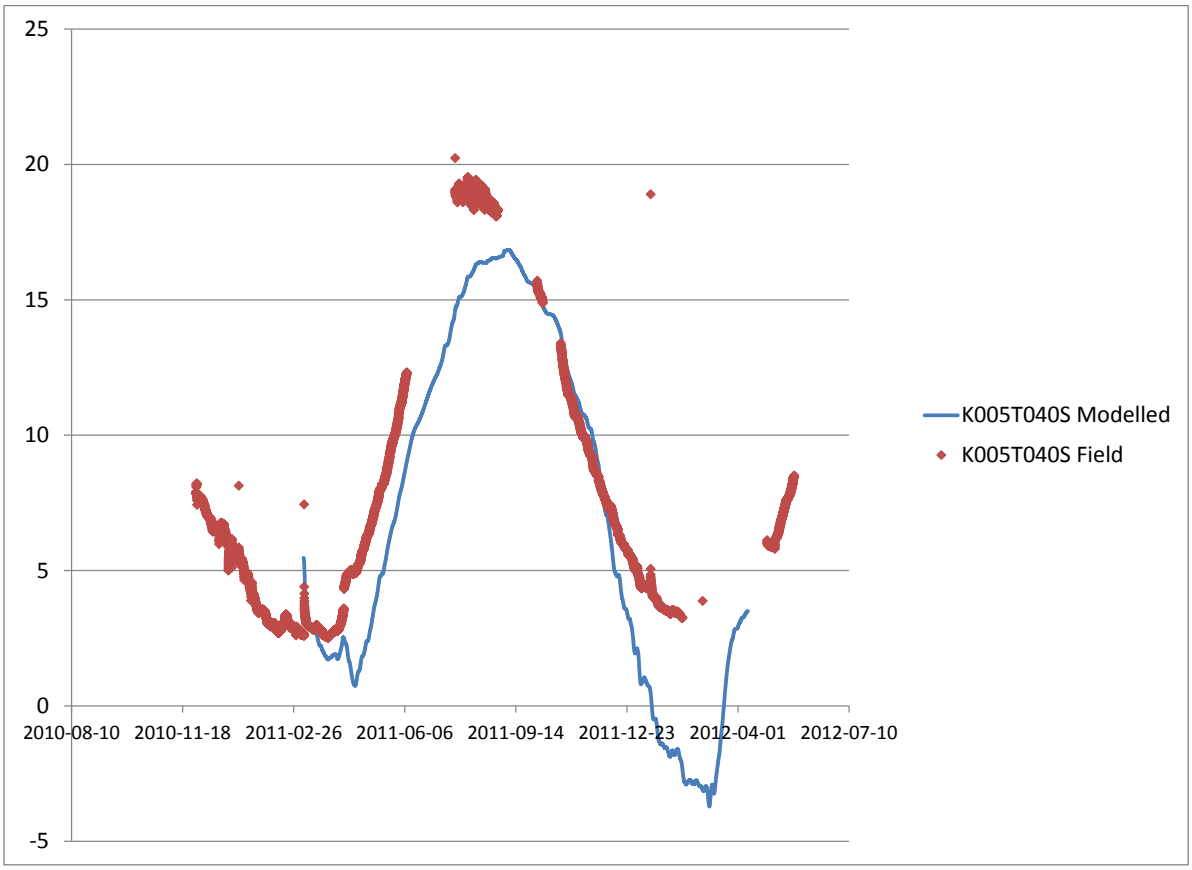
25
20
15
10
5
0
-5
2010-08-10
2010-11-18
2011-02-26
2011-06-06
2011-09-14
2011-12-23
2012-04-01
2012-07-10
K005T040S Modelled
K005T040S Field

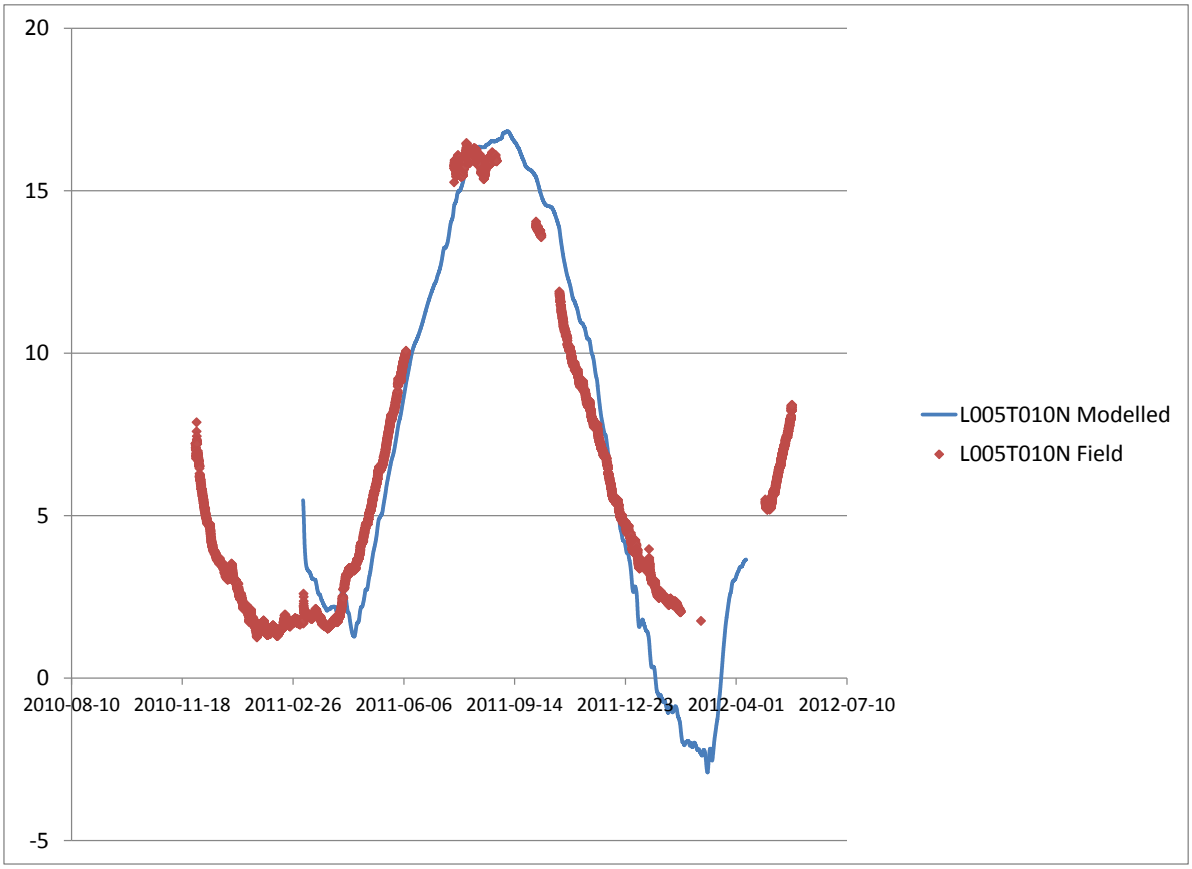
20
15
10
5
0
-5
2010-08-10
2010-11-18
2011-02-26
2011-06-06
2011-09-14
2011-12-23
2012-04-01
2012-07-10
L005T010N Modelled
L005T010N Field

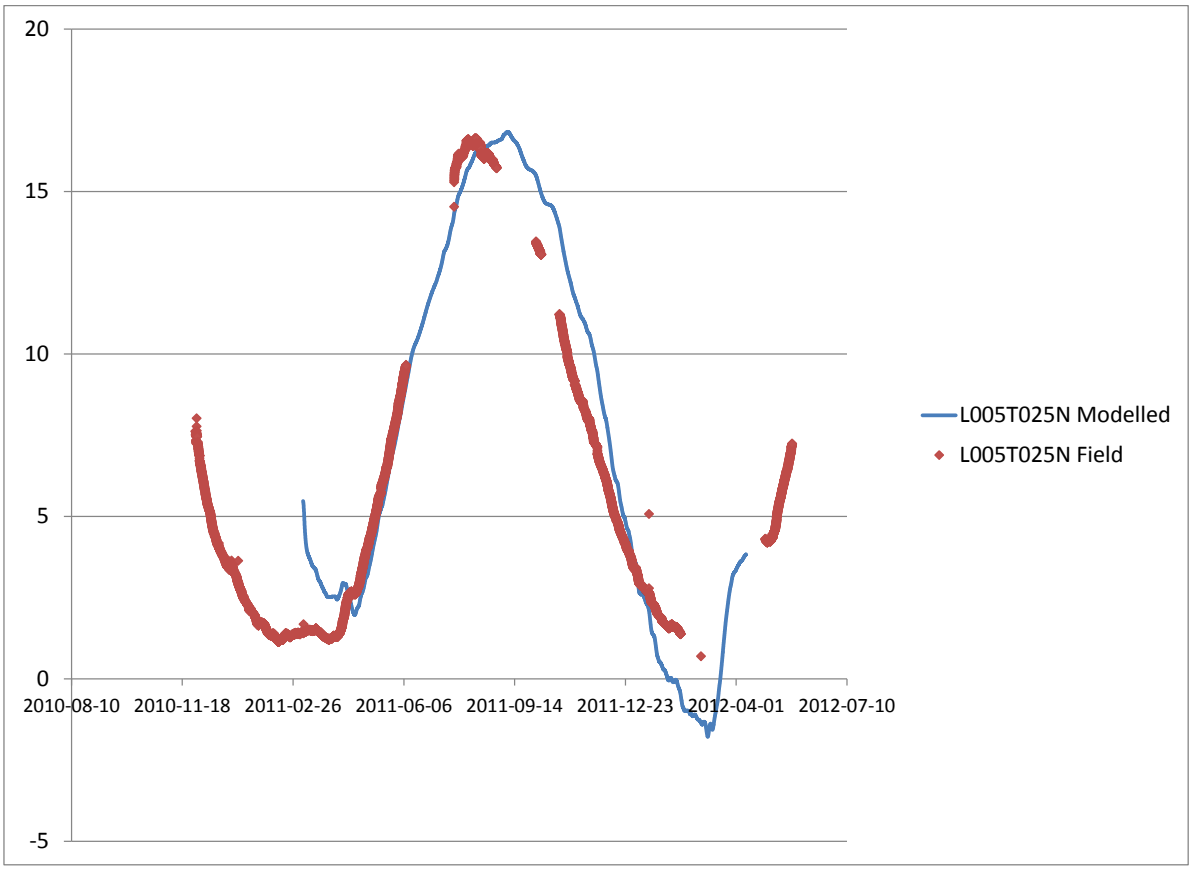
20
15
10
5
0
-5
2010-08-10
2010-11-18
2011-02-26
2011-06-06
2011-09-14
2011-12-23
2012-04-01
2012-07-10
L005T025N Modelled
L005T025N Field

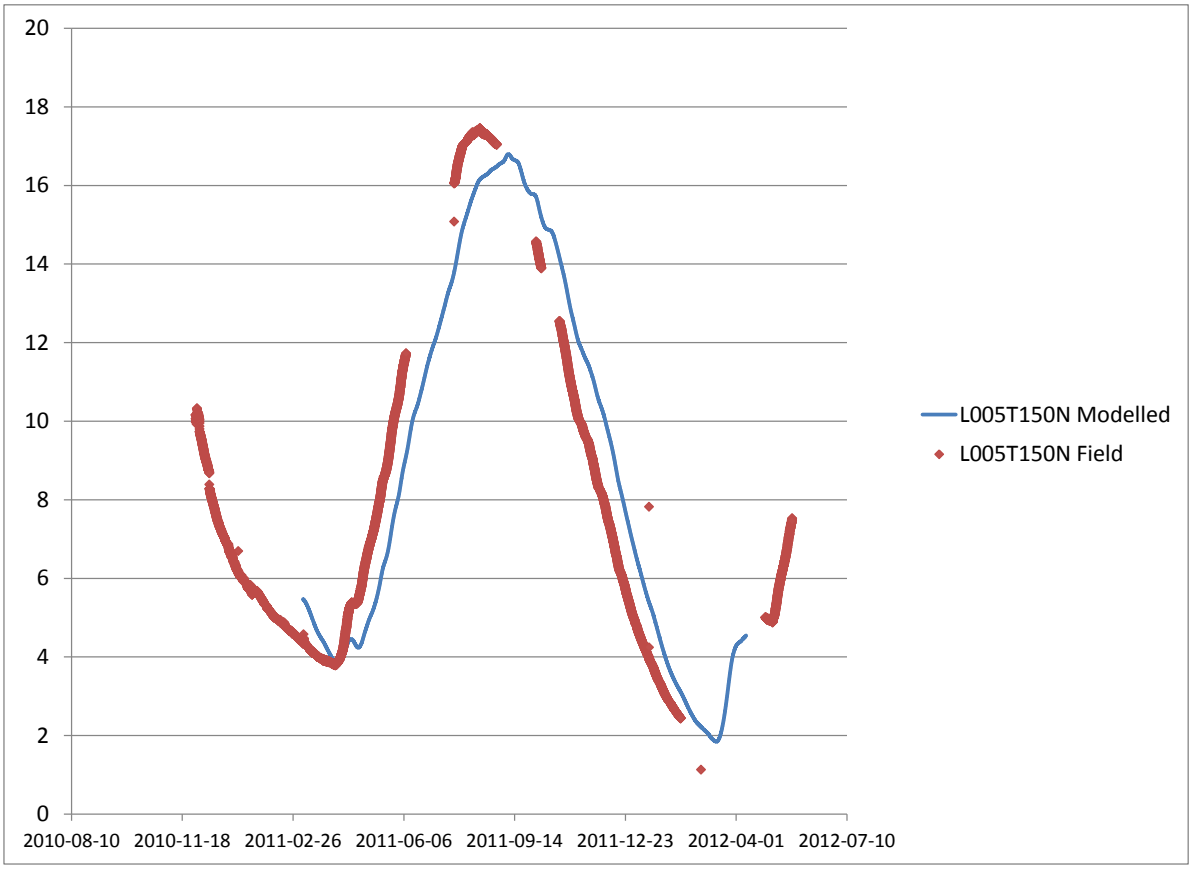
20
18
16
14
12
10
8
6
4
2
0
2010-08-10
2010-11-18
2011-02-26
2011-06-06
2011-09-14
2011-12-23
2012-04-01
2012-07-10
L005T150N Modelled
L005T150N Field

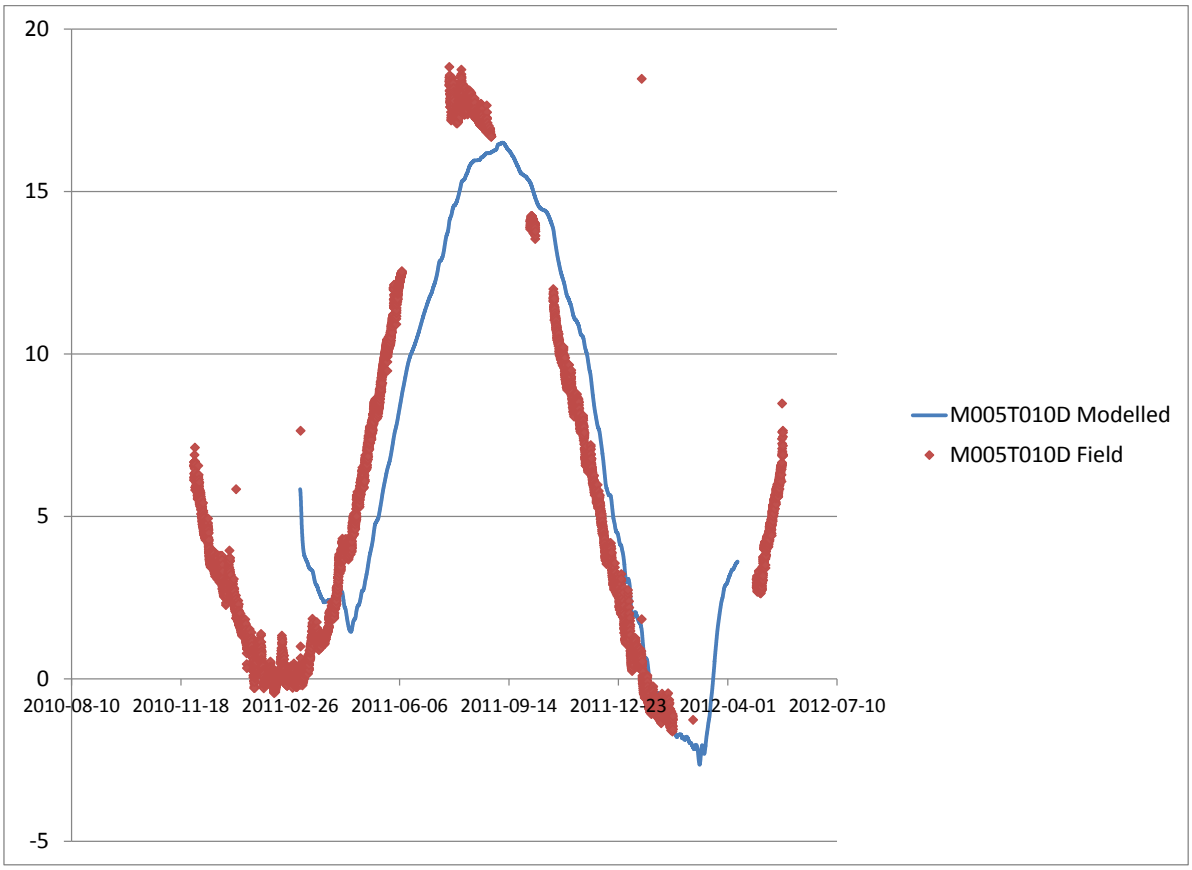
20
15
10
5
0
-5
2010-08-10
2010-11-18
2011-02-26
2011-06-06
2011-09-14
2011-12-23
2012-04-01
2012-07-10
M005T010D Modelled
M005T010D Field

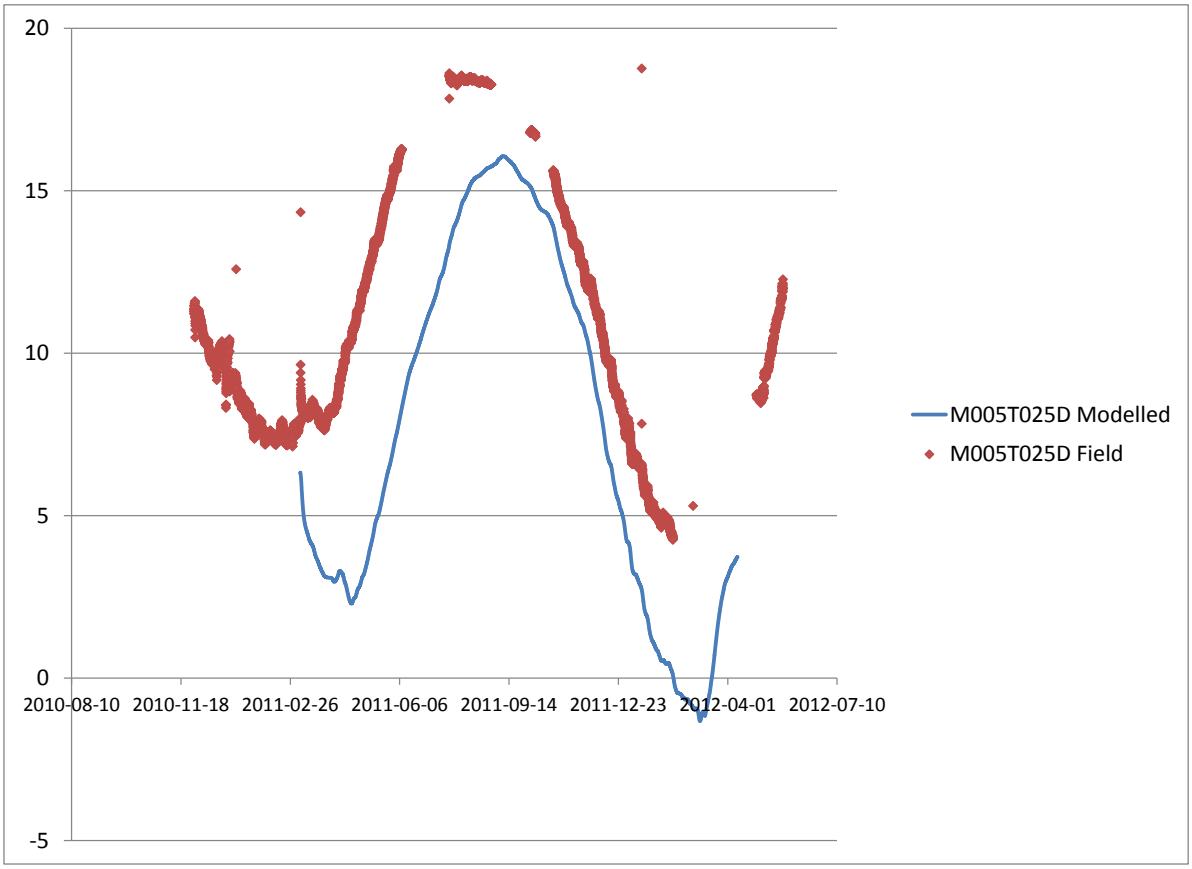
20
15
10
5
0
-5
2010-08-10
2010-11-18
2011-02-26
2011-06-06
2011-09-14
2011-12-23
2012-04-01
2012-07-10
M005T025D Modelled
M005T025D Field

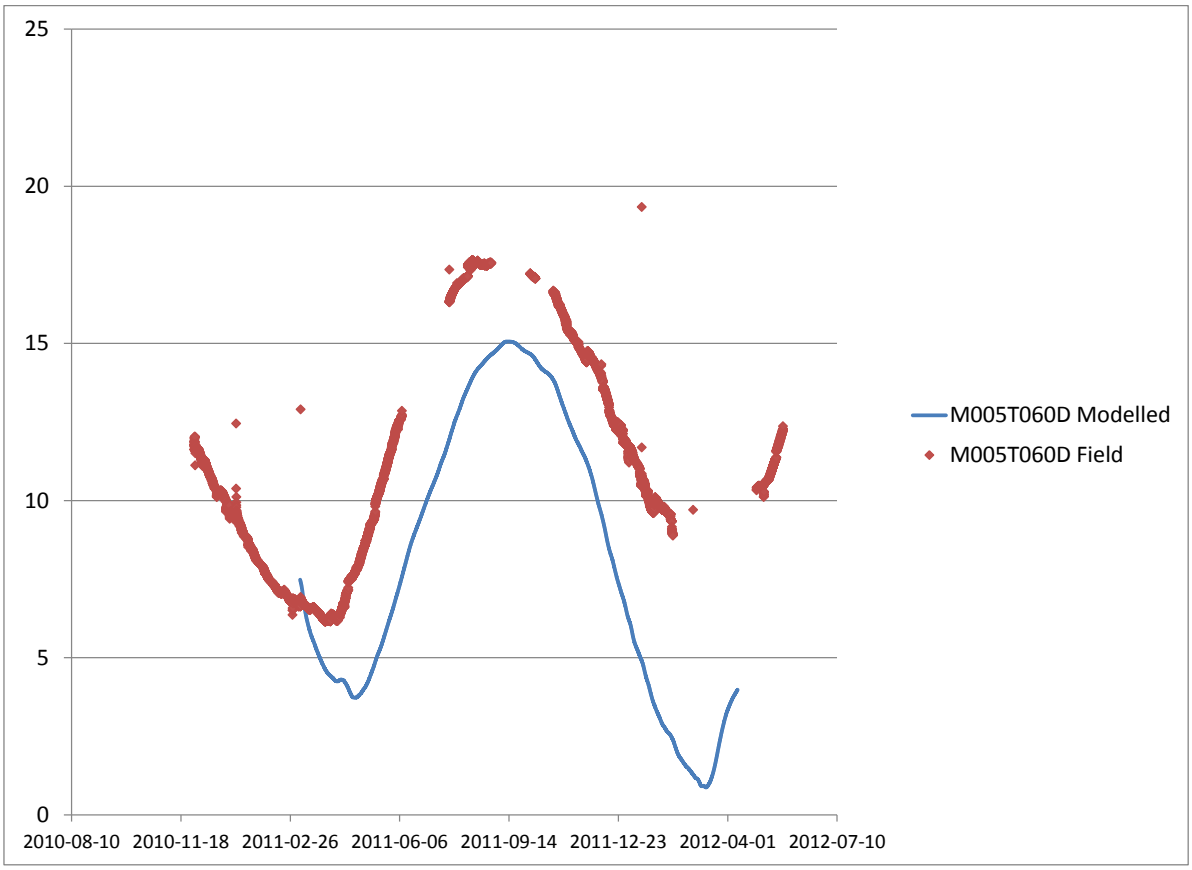
25
20
15
10
5
0
2010-08-10
2010-11-18
2011-02-26
2011-06-06
2011-09-14
2011-12-23
2012-04-01
2012-07-10
M005T060D Modelled
M005T060D Field

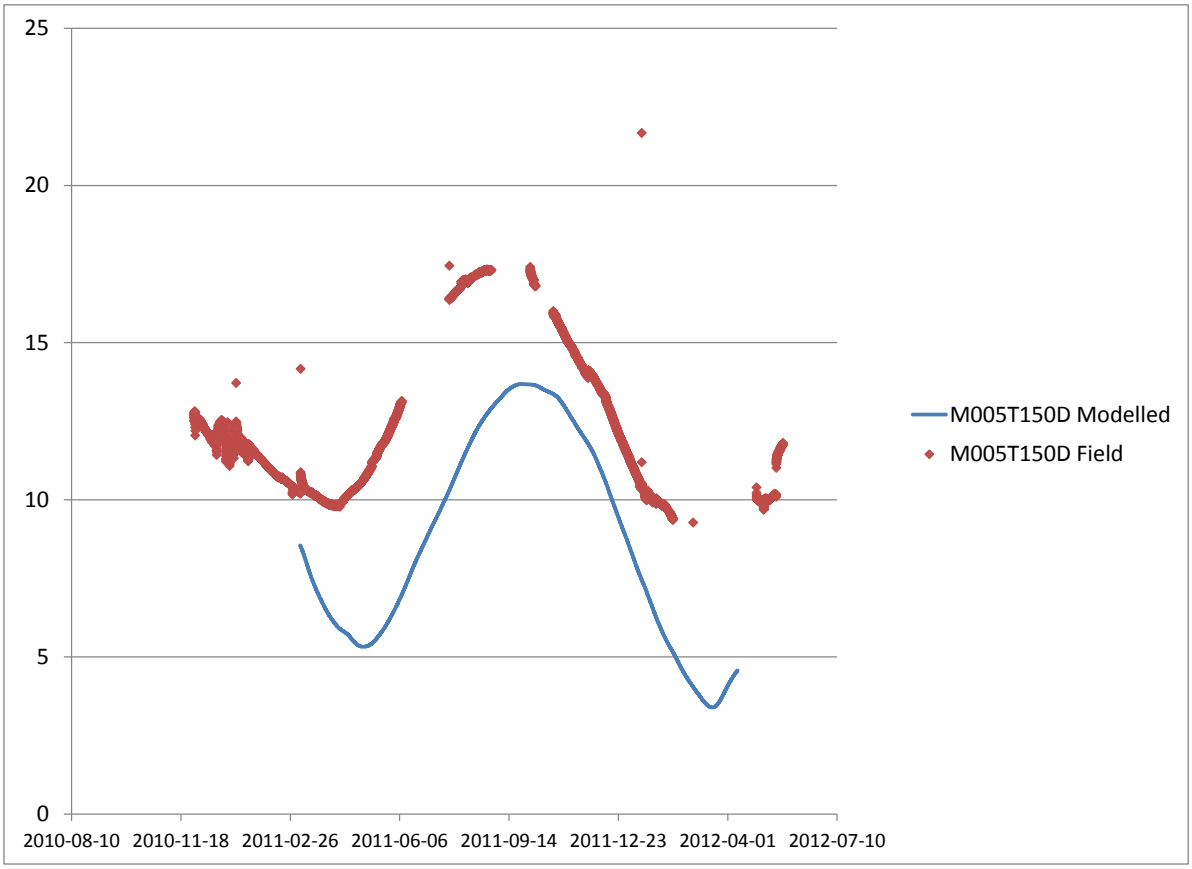
25
20
15
10
5
0
2010-08-10
2010-11-18
2011-02-26
2011-06-06
2011-09-14
2011-12-23
2012-04-01
2012-07-10
M005T150D Modelled
M005T150D Field

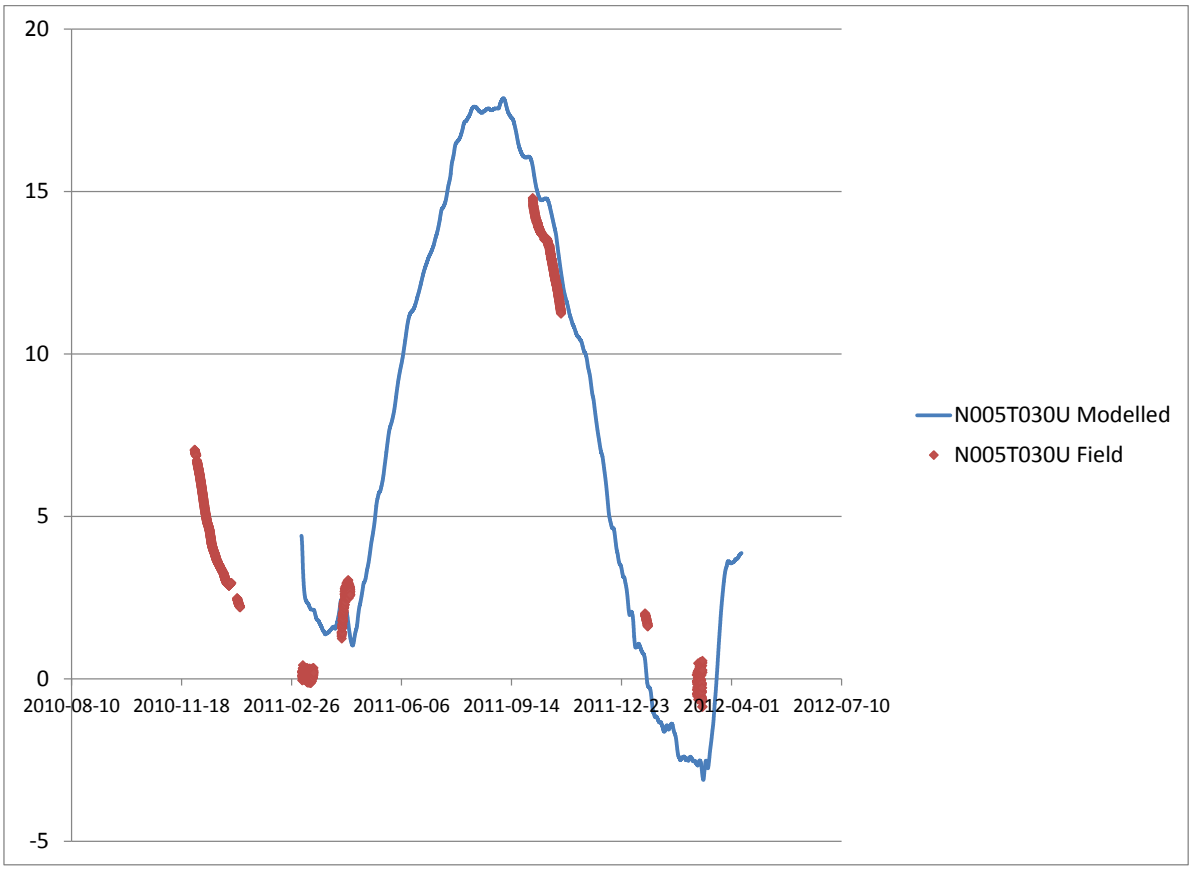
20
15
10
5
0
-5
2010-08-10
2010-11-18
2011-02-26
2011-06-06
2011-09-14
2011-12-23
2012-04-01
2012-07-10
N005T030U Modelled
N005T030U Field

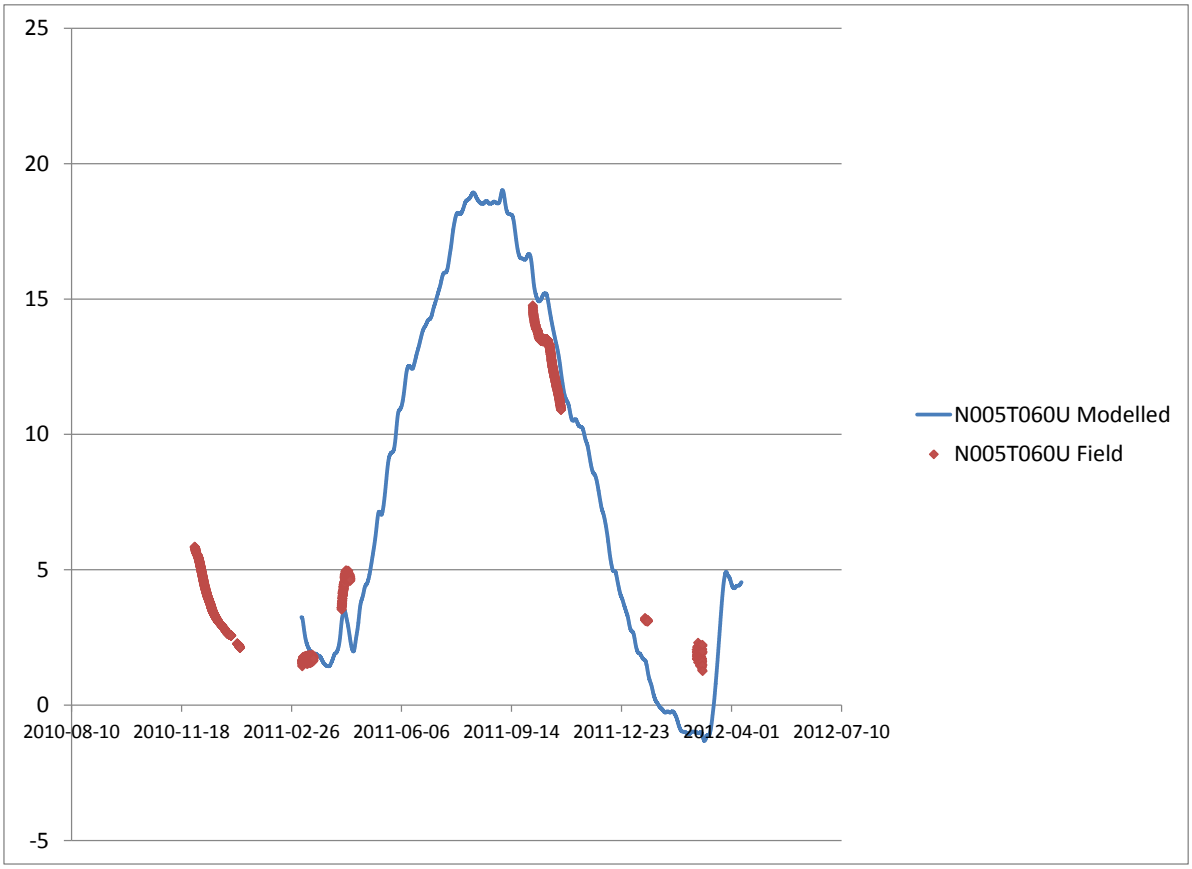
25
20
15
10
5
0
-5
2010-08-10
2010-11-18
2011-02-26
2011-06-06
2011-09-14
2011-12-23
2012-04-01
2012-07-10
N005T060U Modelled
N005T060U Field

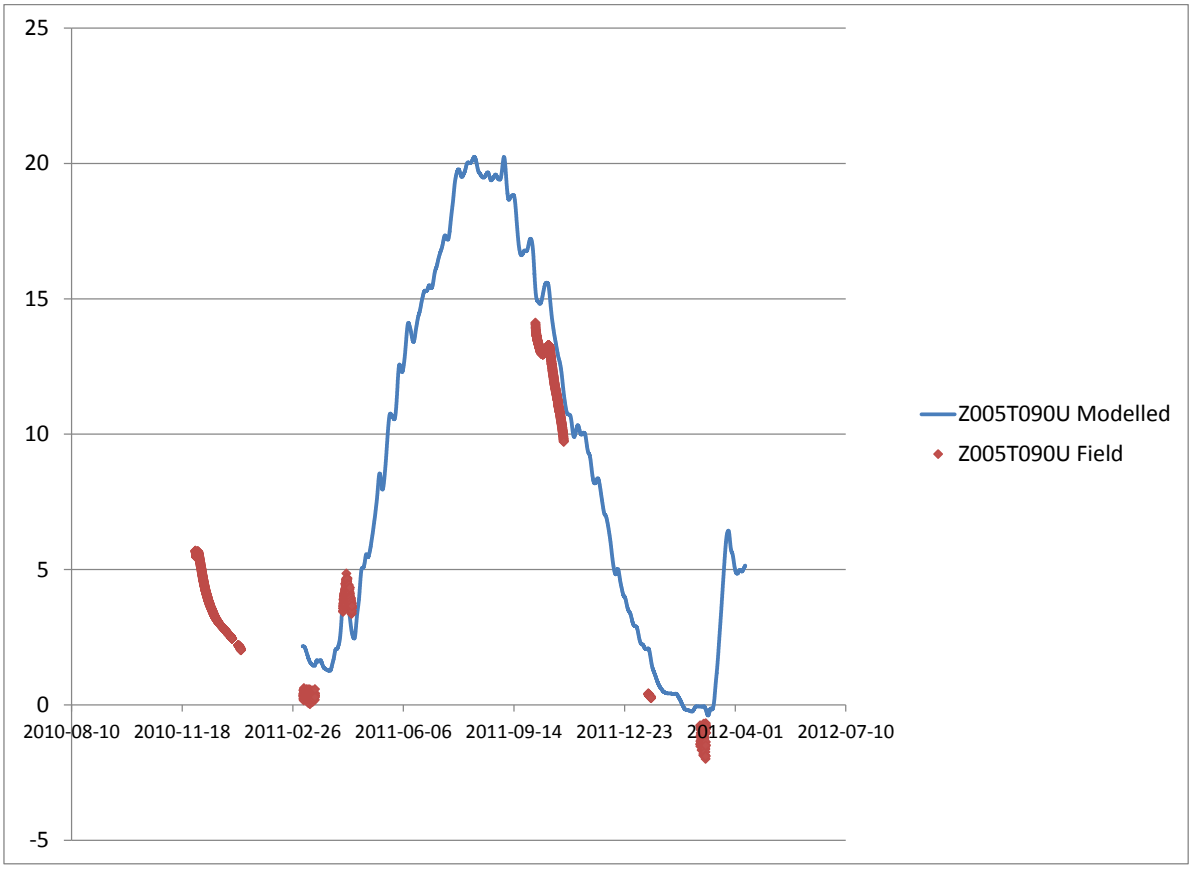
25
20
15
10
5
0
-5
2010-08-10
2010-11-18
2011-02-26
2011-06-06
2011-09-14
2011-12-23
2012-04-01
2012-07-10
Z005T090U Modelled
Z005T090U Field

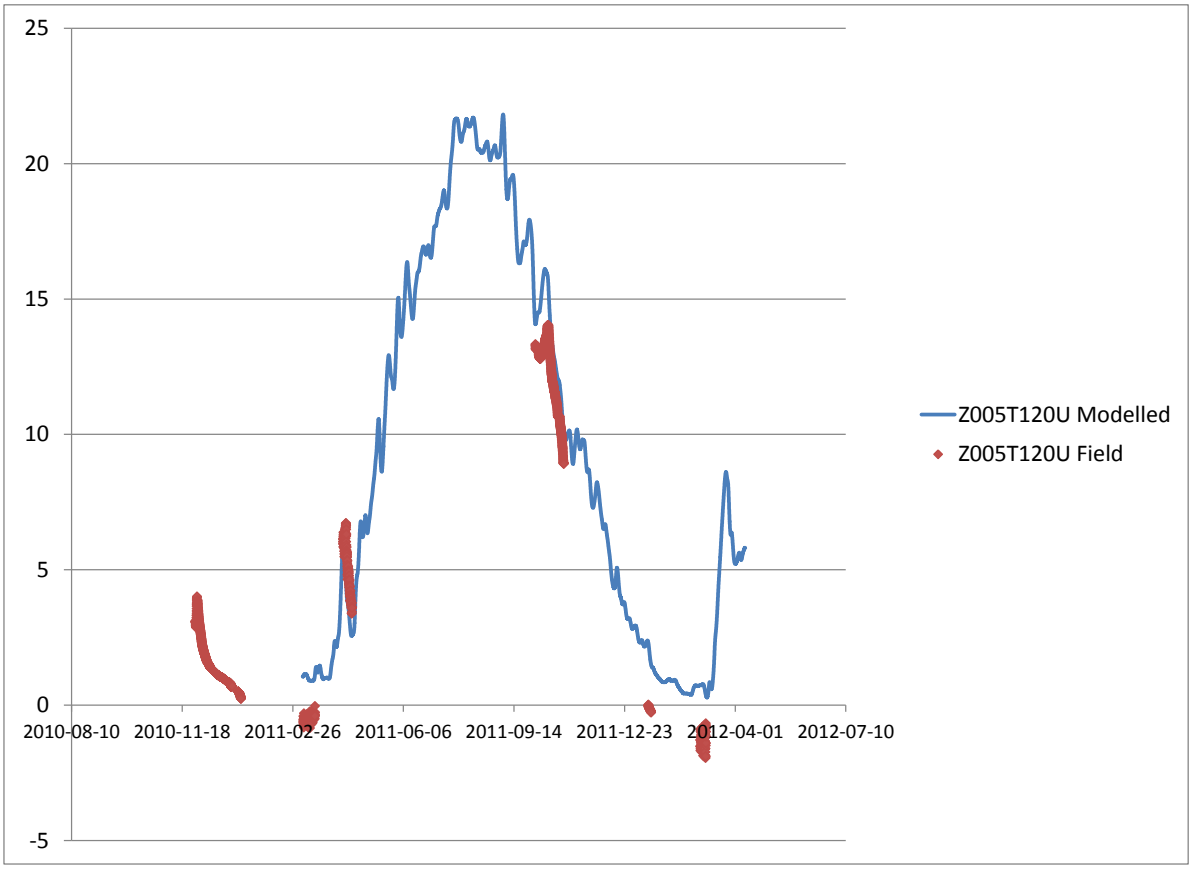
25
20
15
10
5
0
-5
2010-08-10
2010-11-18
2011-02-26
2011-06-06
2011-09-14
2011-12-23
2012-04-01
2012-07-10
Z005T120U Modelled
Z005T120U Field

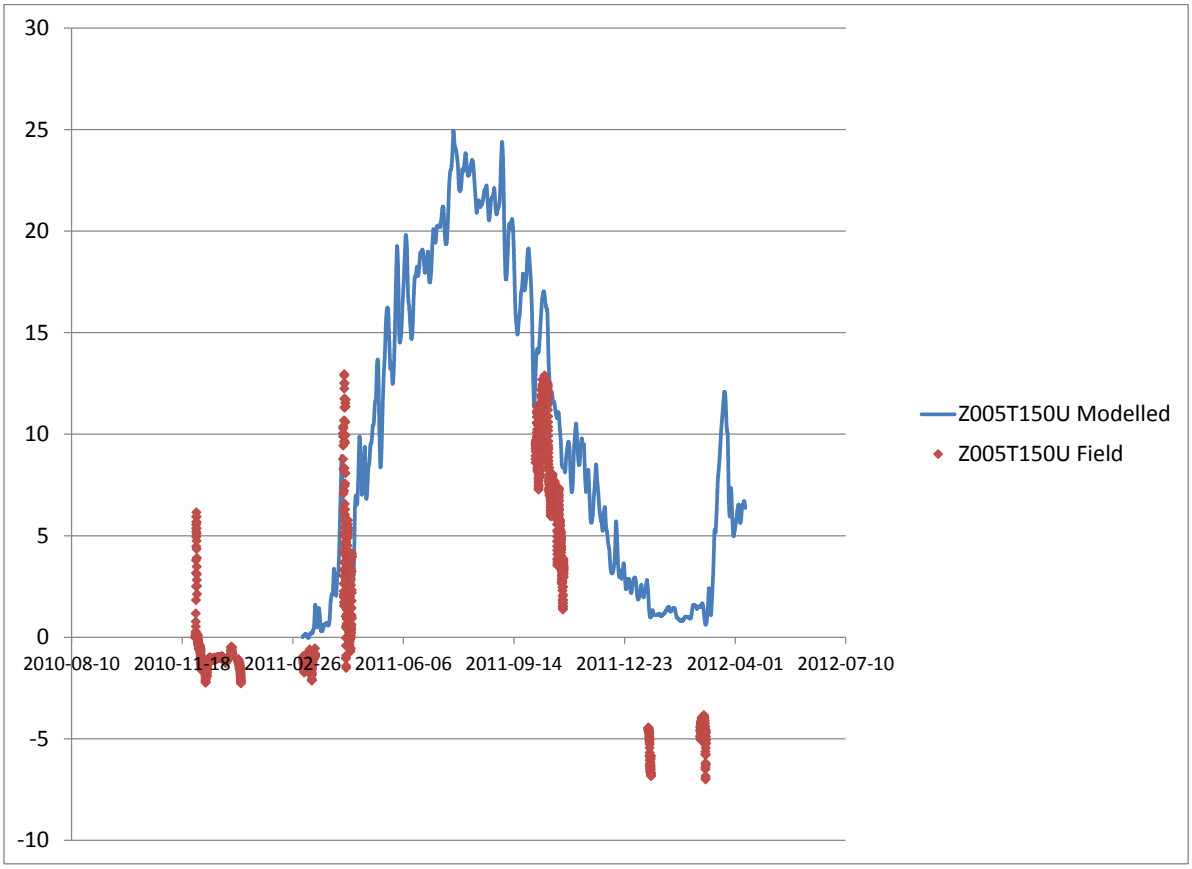
30
25
20
15
10
5
0
-5
-10
2010-08-10
2010-11-18
2011-02-26
2011-06-06
2011-09-14
2011-12-23
2012-04-01
2012-07-10
Z005T150U Modelled
Z005T150U Field

G.2 Four trench inverse modelling

G.2.1 Both - Four trench system

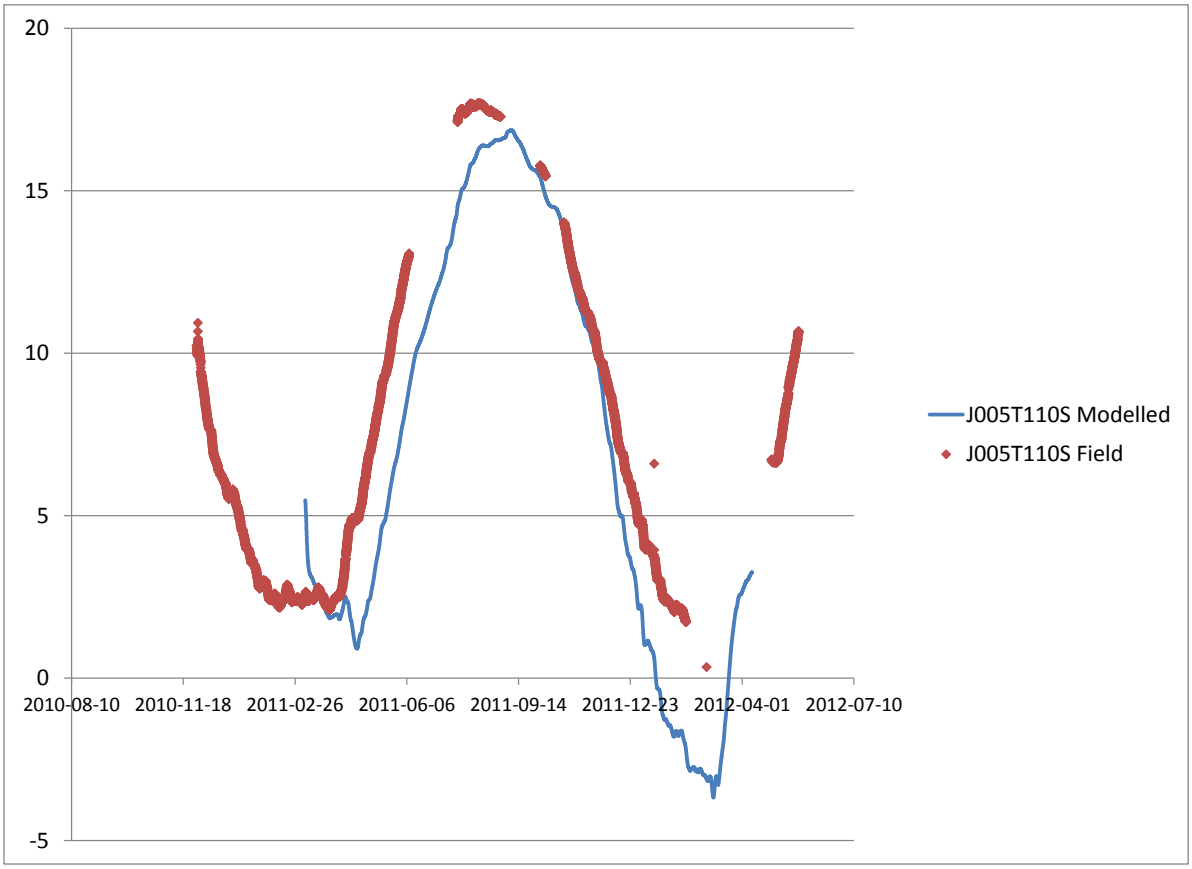
20
15
10
5
0
-5
2010-08-10
2010-11-18
2011-02-26
2011-06-06
2011-09-14
2011-12-23
2012-04-01
2012-07-10
J005T110S Modelled
J005T110S Field

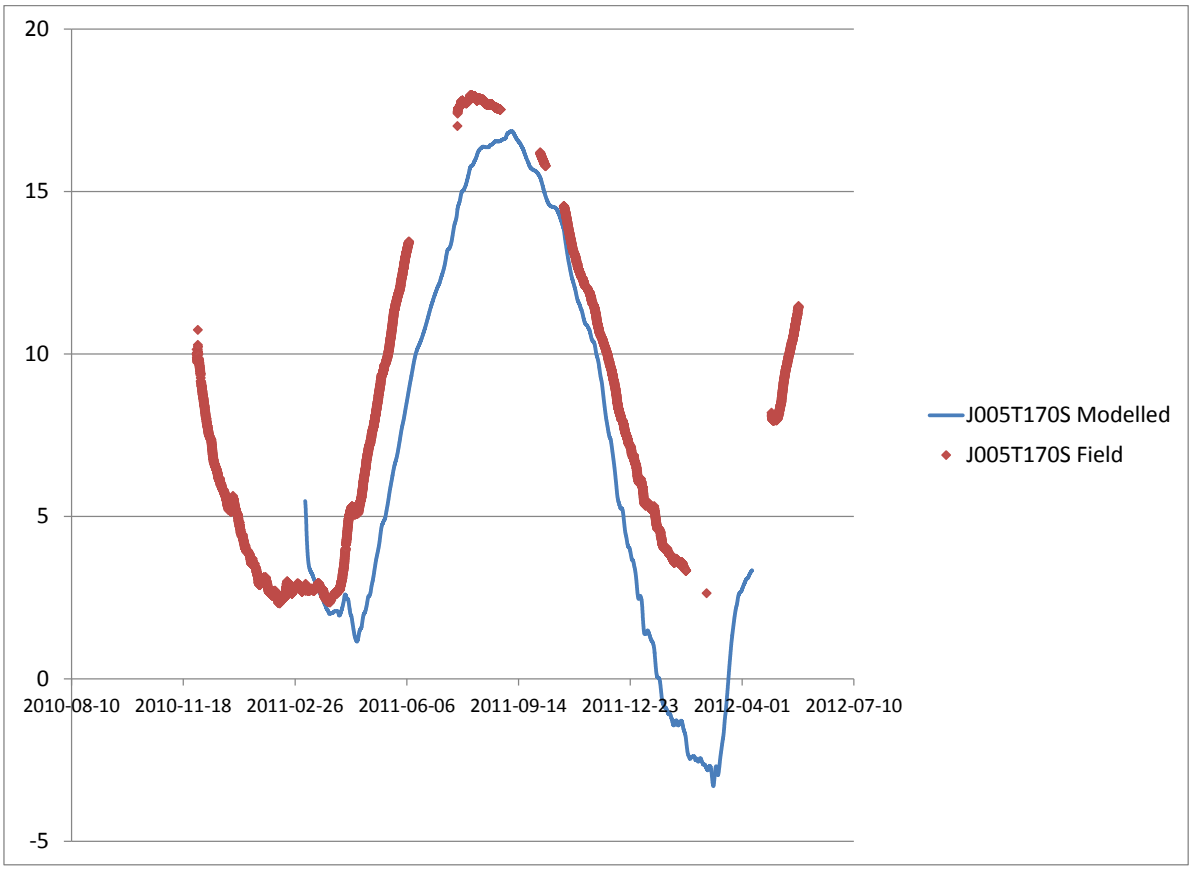
20
15
10
5
0
-5
2010-08-10
2010-11-18
2011-02-26
2011-06-06
2011-09-14
2011-12-23
2012-04-01
2012-07-10
J005T170S Modelled
J005T170S Field

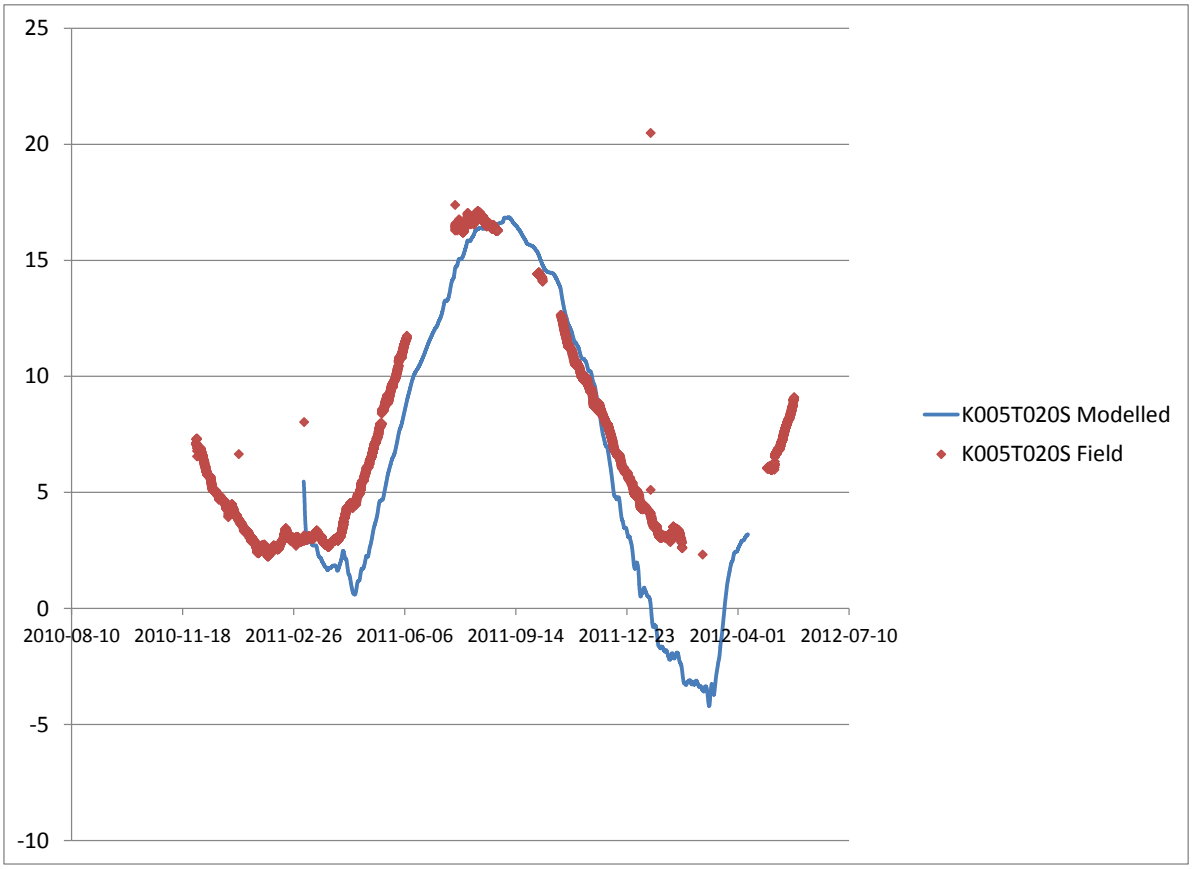
25
20
15
10
5
0
-5
-10
2010-08-10
2010-11-18
2011-02-26
2011-06-06
2011-09-14
2011-12-23
2012-04-01
2012-07-10
K005T020S Modelled
K005T020S Field

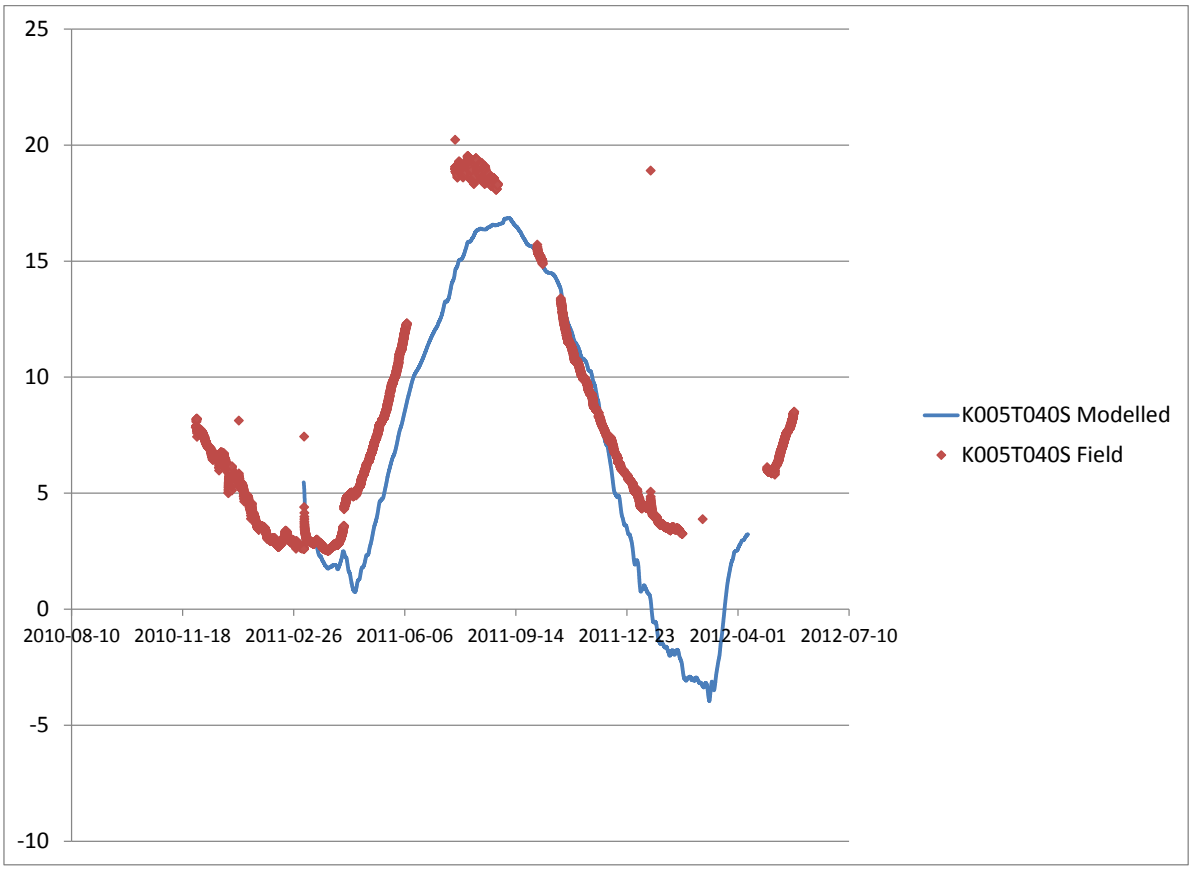
25
20
15
10
5
0
-5
-10
2010-08-10
2010-11-18
2011-02-26
2011-06-06
2011-09-14
2011-12-23
2012-04-01
2012-07-10
K005T040S Modelled
K005T040S Field

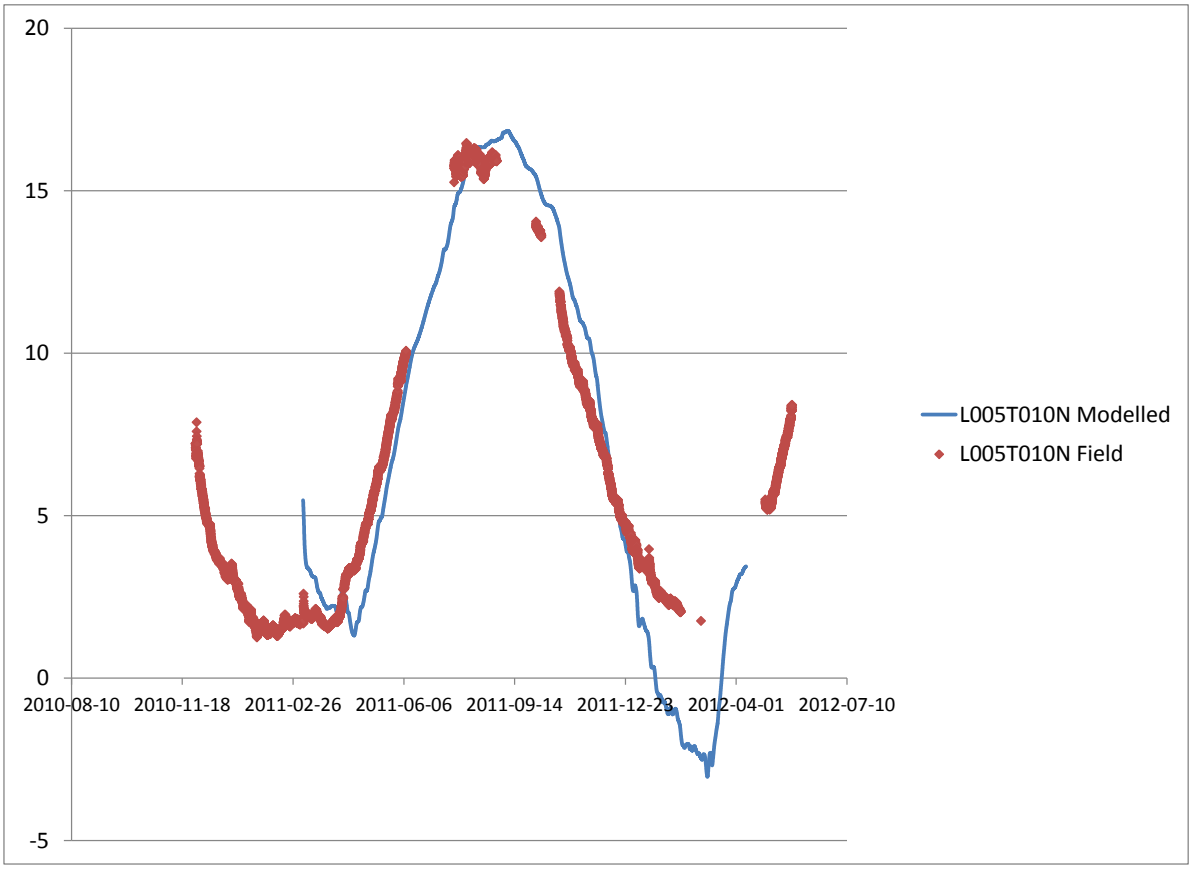
20
15
10
5
0
-5
2010-08-10
2010-11-18
2011-02-26
2011-06-06
2011-09-14
2011-12-23
2012-04-01
2012-07-10
L005T010N Modelled
L005T010N Field

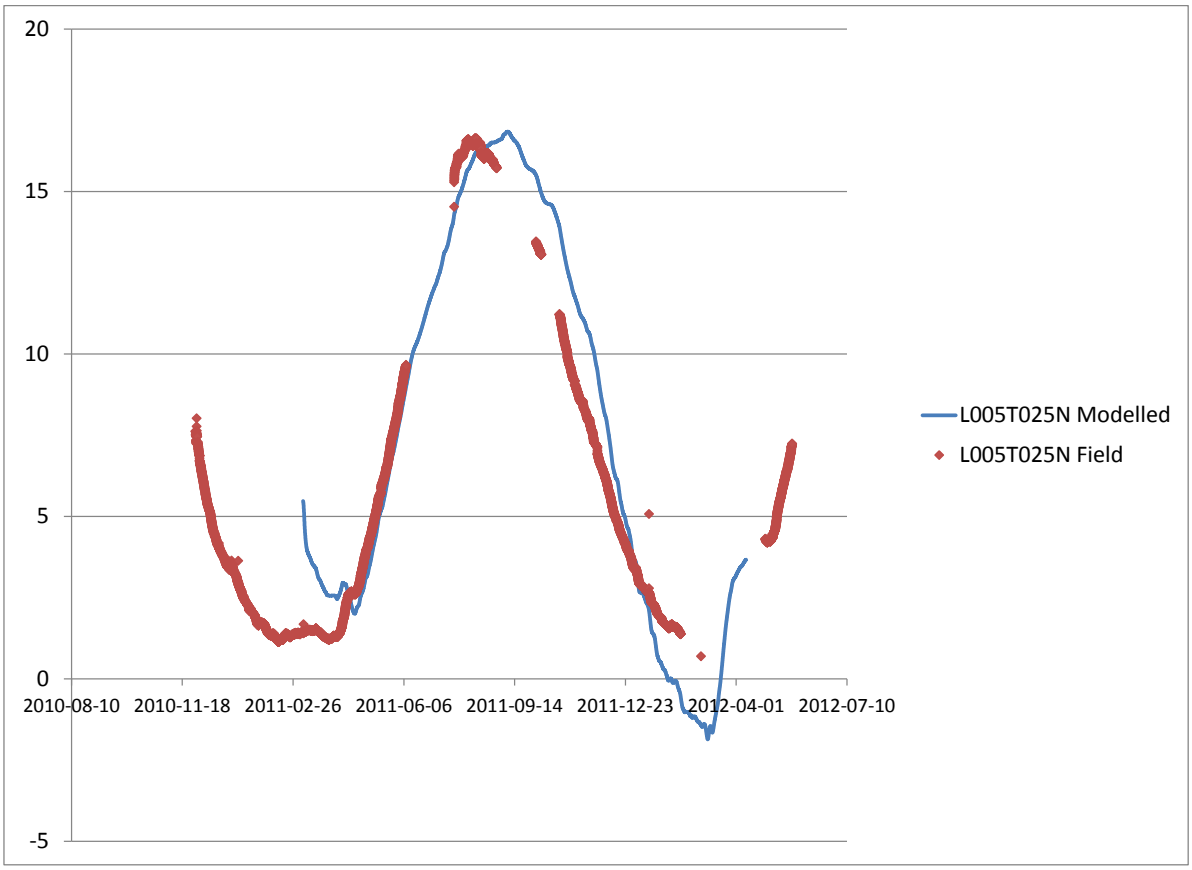
20
15
10
5
0
-5
2010-08-10
2010-11-18
2011-02-26
2011-06-06
2011-09-14
2011-12-23
2012-04-01
2012-07-10
L005T025N Modelled
L005T025N Field

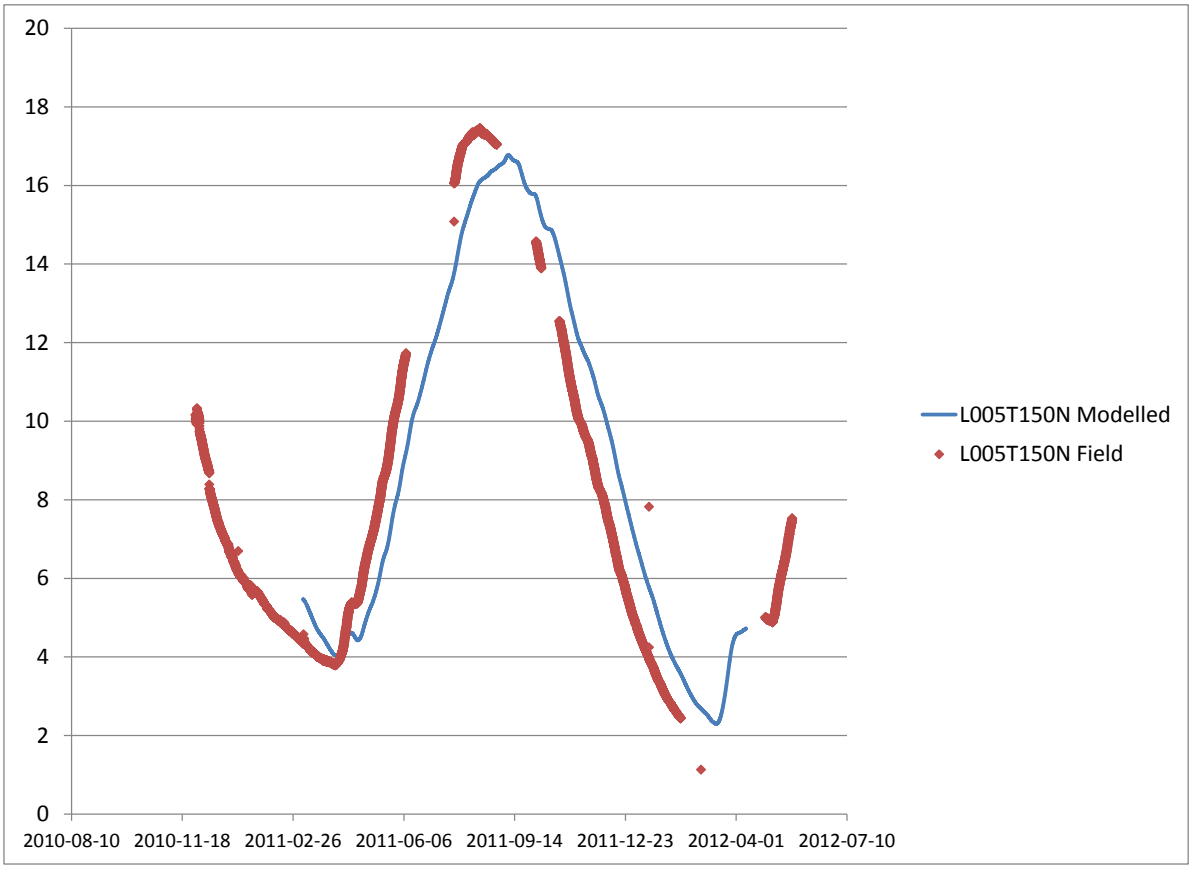
20
18
16
14
12
10
8
6
4
2
0
2010-08-10
2010-11-18
2011-02-26
2011-06-06
2011-09-14
2011-12-23
2012-04-01
2012-07-10
L005T150N Modelled
L005T150N Field

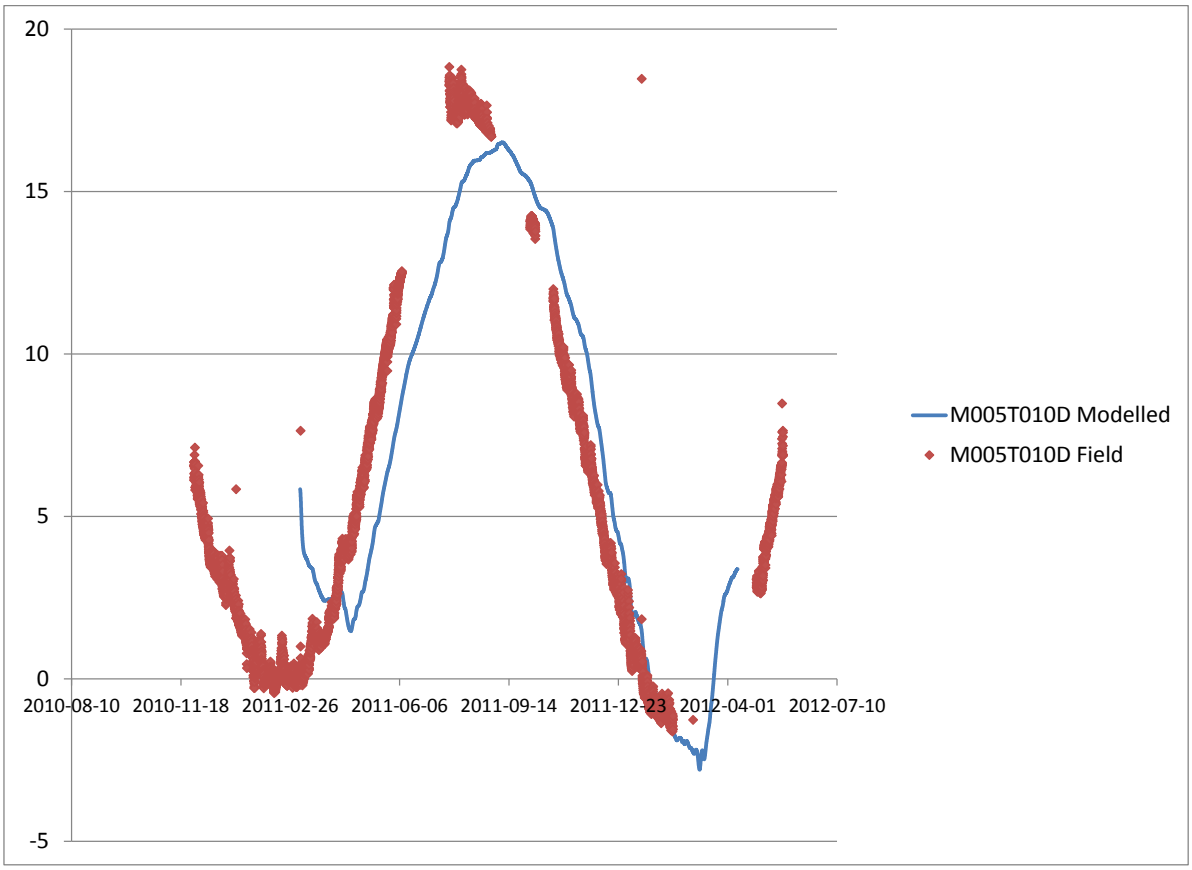
20
15
10
5
0
-5
2010-08-10
2010-11-18
2011-02-26
2011-06-06
2011-09-14
2011-12-23
2012-04-01
2012-07-10
M005T010D Modelled
M005T010D Field

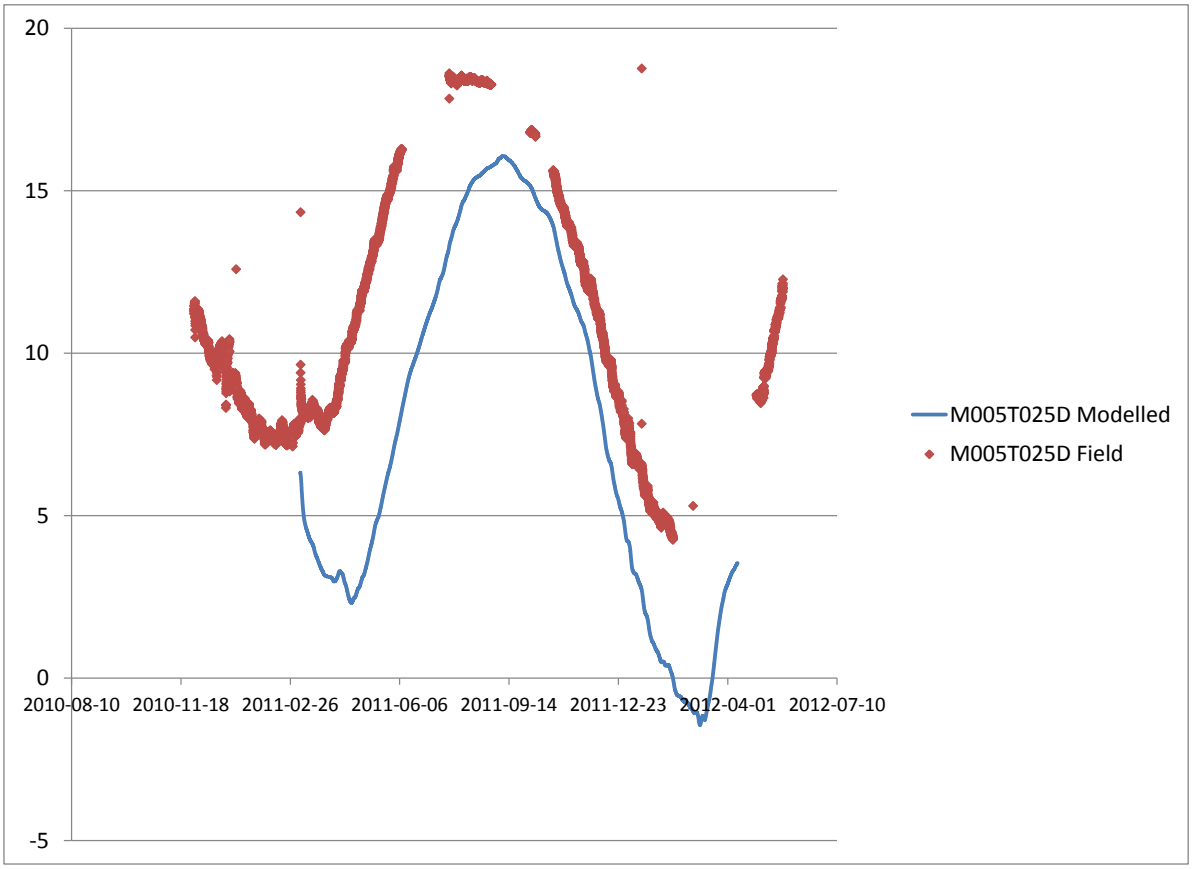
20
15
10
5
0
-5
2010-08-10
2010-11-18
2011-02-26
2011-06-06
2011-09-14
2011-12-23
2012-04-01
2012-07-10
M005T025D Modelled
M005T025D Field

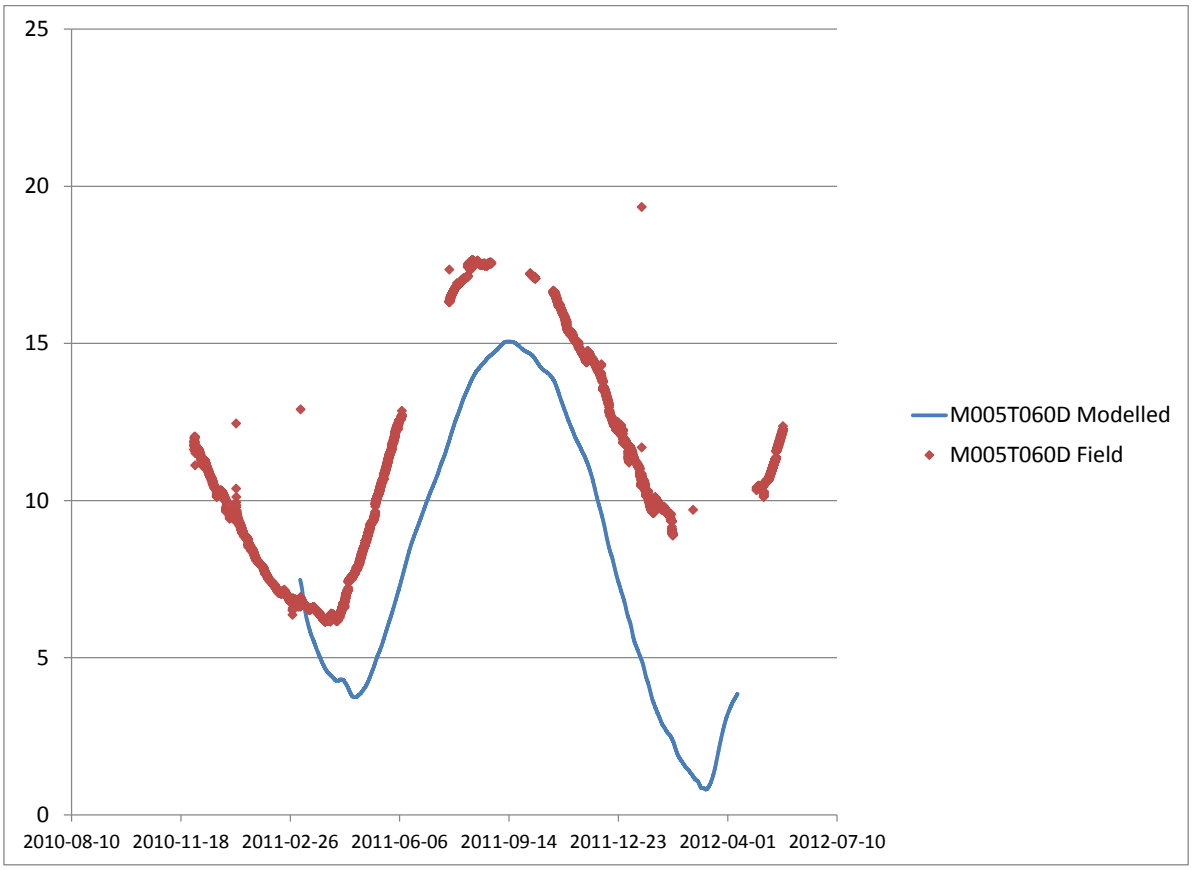
25
20
15
10
5
0
2010-08-10
2010-11-18
2011-02-26
2011-06-06
2011-09-14
2011-12-23
2012-04-01
2012-07-10
M005T060D Modelled
M005T060D Field

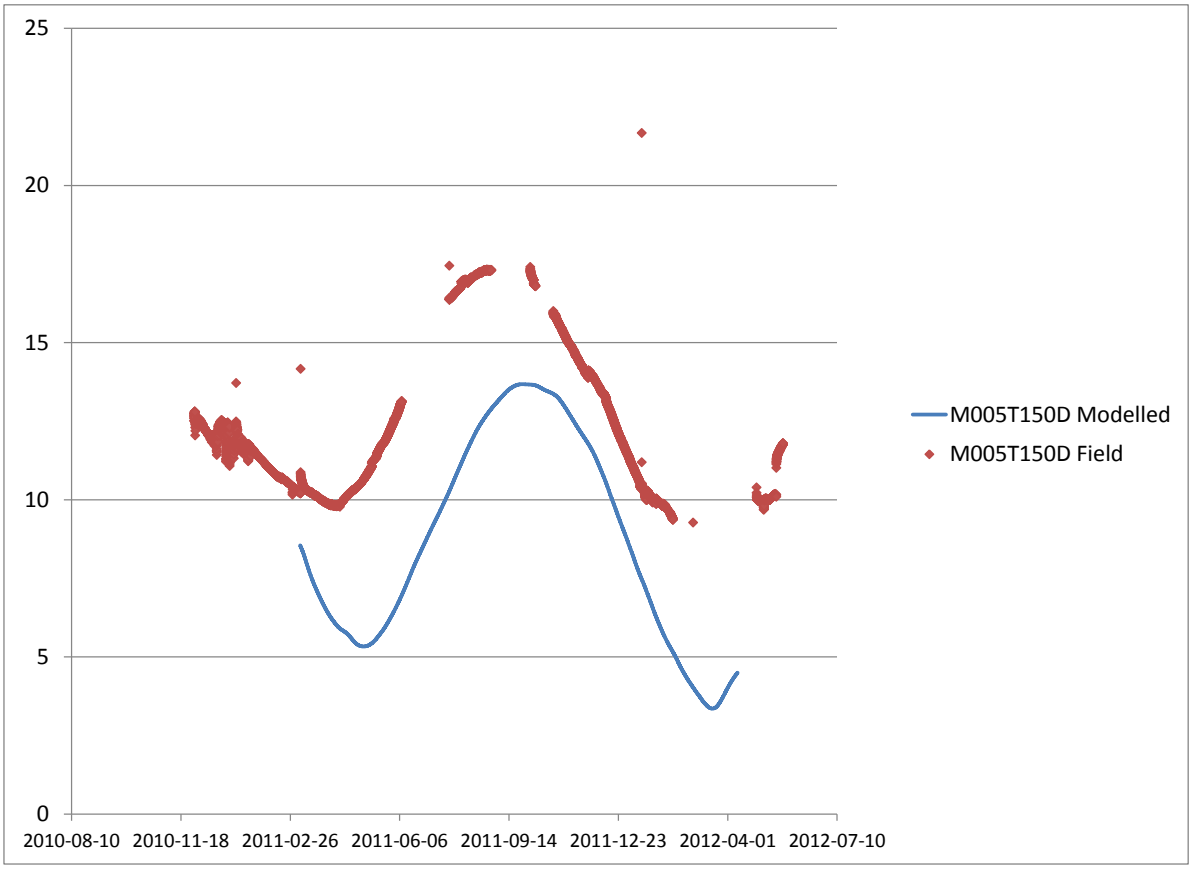
25
20
15
10
5
0
2010-08-10
2010-11-18
2011-02-26
2011-06-06
2011-09-14
2011-12-23
2012-04-01
2012-07-10
M005T150D Modelled
M005T150D Field

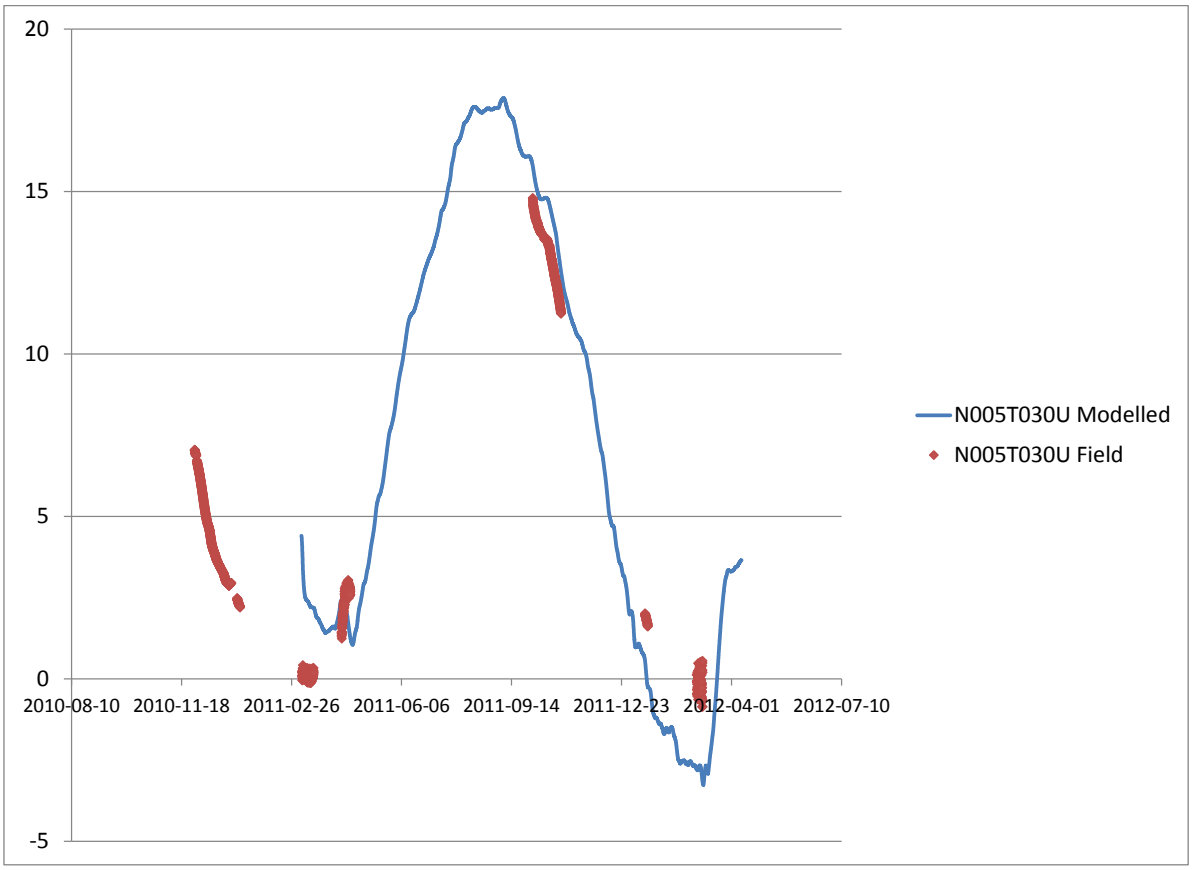
20
15
10
5
0
-5
2010-08-10
2010-11-18
2011-02-26
2011-06-06
2011-09-14
2011-12-23
2012-04-01
2012-07-10
N005T030U Modelled
N005T030U Field

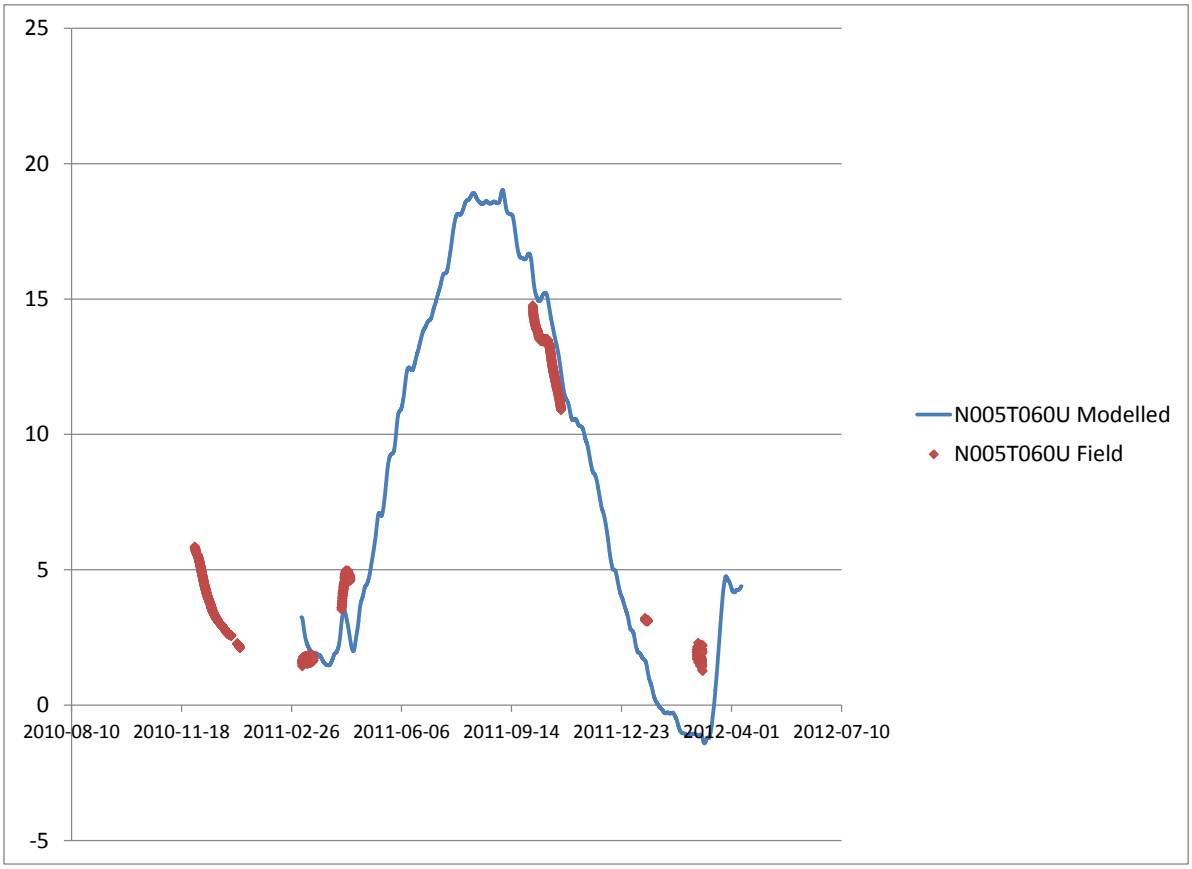
25
20
15
10
5
0
-5
2010-08-10
2010-11-18
2011-02-26
2011-06-06
2011-09-14
2011-12-23
2012-04-01
2012-07-10
N005T060U Modelled
N005T060U Field

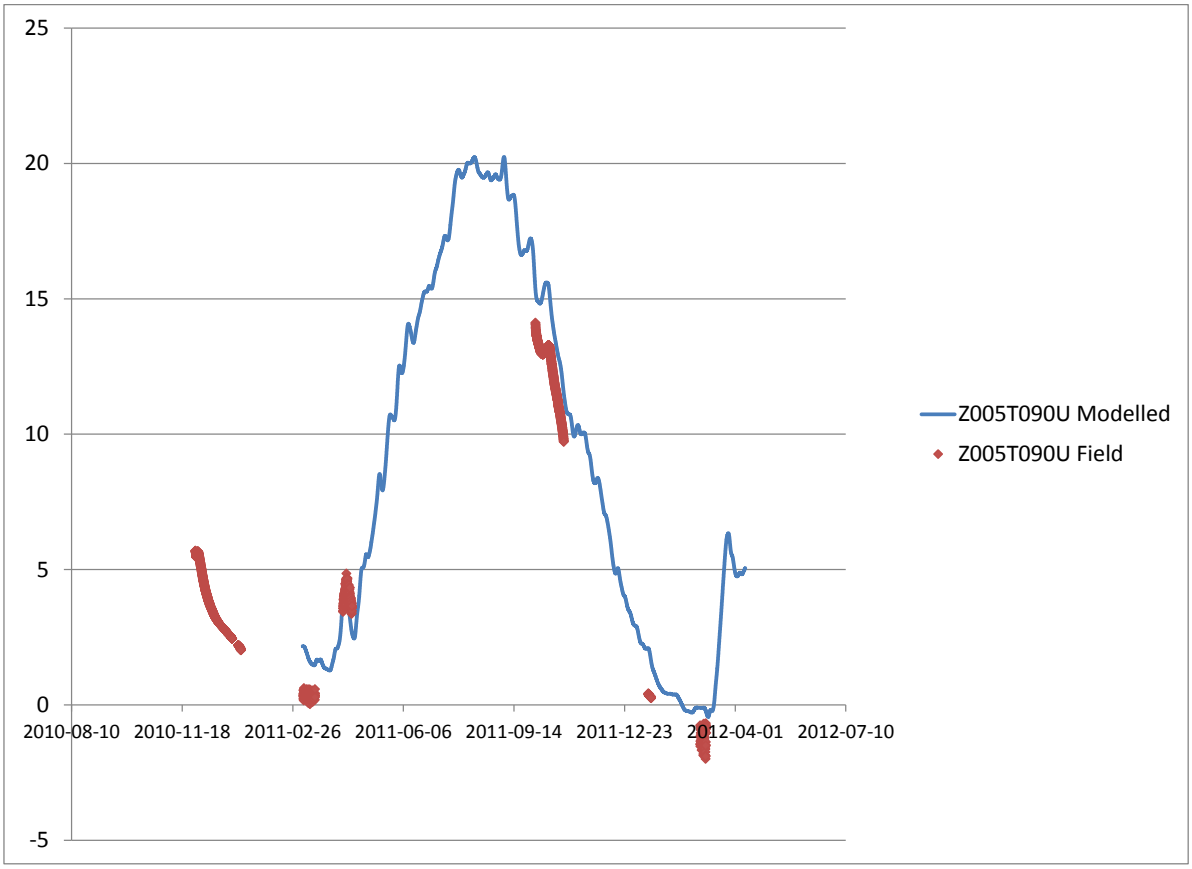
25
20
15
10
5
0
-5
2010-08-10
2010-11-18
2011-02-26
2011-06-06
2011-09-14
2011-12-23
2012-04-01
2012-07-10
Z005T090U Modelled
Z005T090U Field

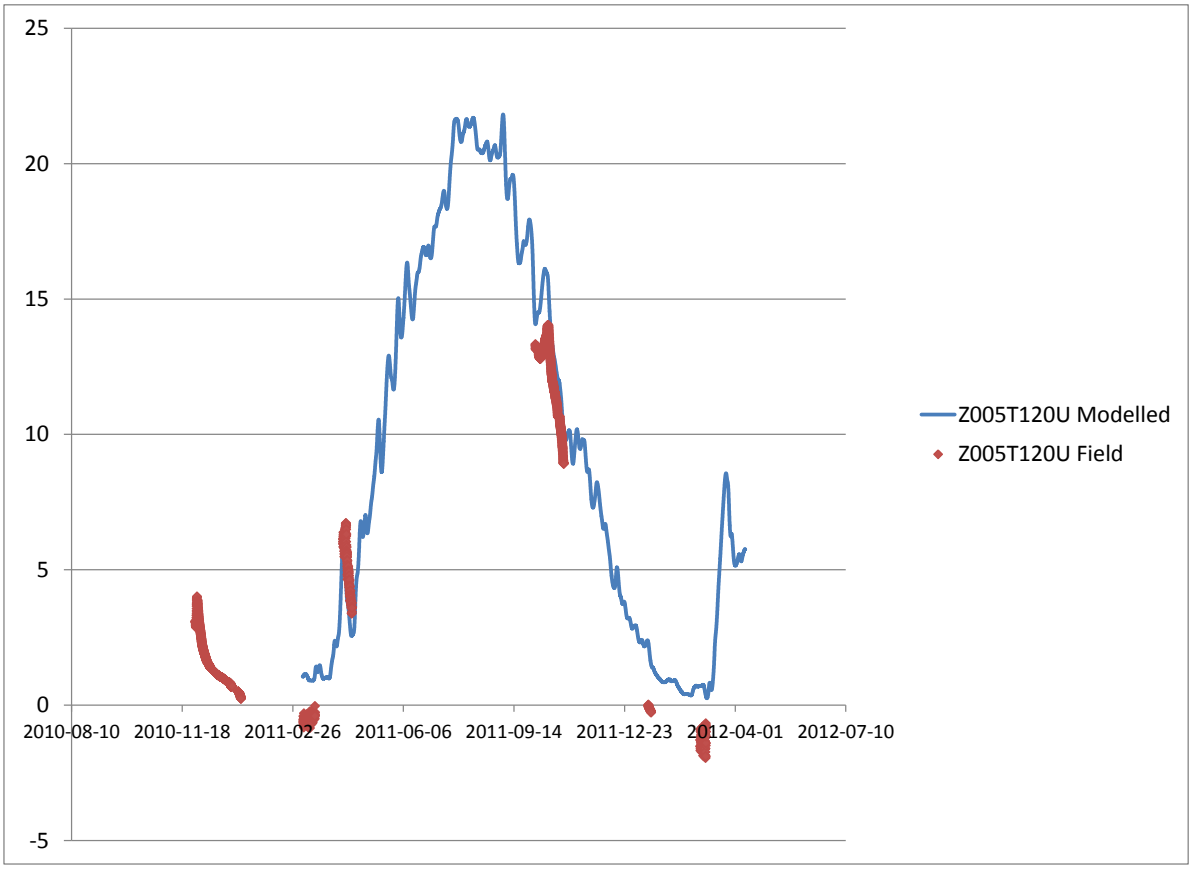
25
20
15
10
5
0
-5
2010-08-10
2010-11-18
2011-02-26
2011-06-06
2011-09-14
2011-12-23
2012-04-01
2012-07-10
Z005T120U Modelled
Z005T120U Field

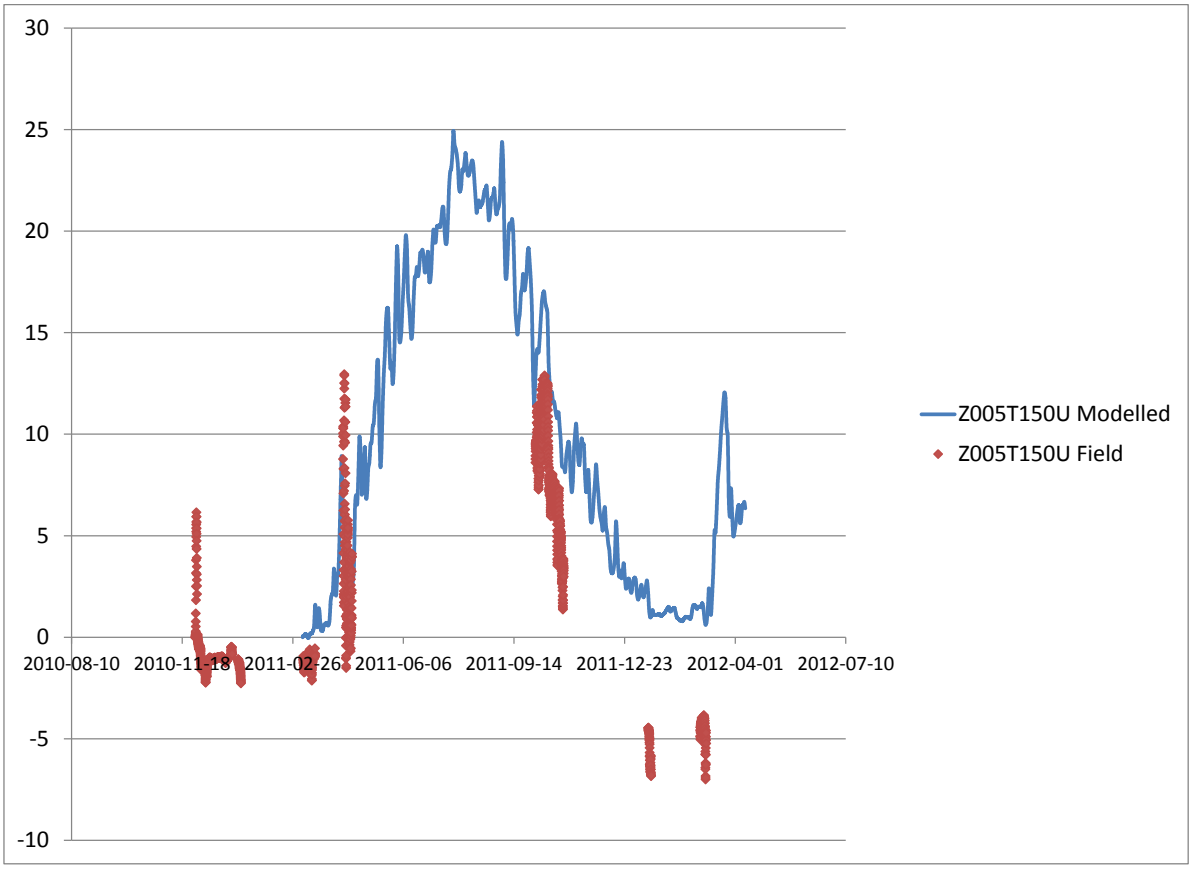
30
25
20
15
10
5
0
-5
-10
2010-08-10
2010-11-18
2011-02-26
2011-06-06
2011-09-14
2011-12-23
2012-04-01
2012-07-10
Z005T150U Modelled
Z005T150U Field

G.2.2 Conductivity only - Four trench system

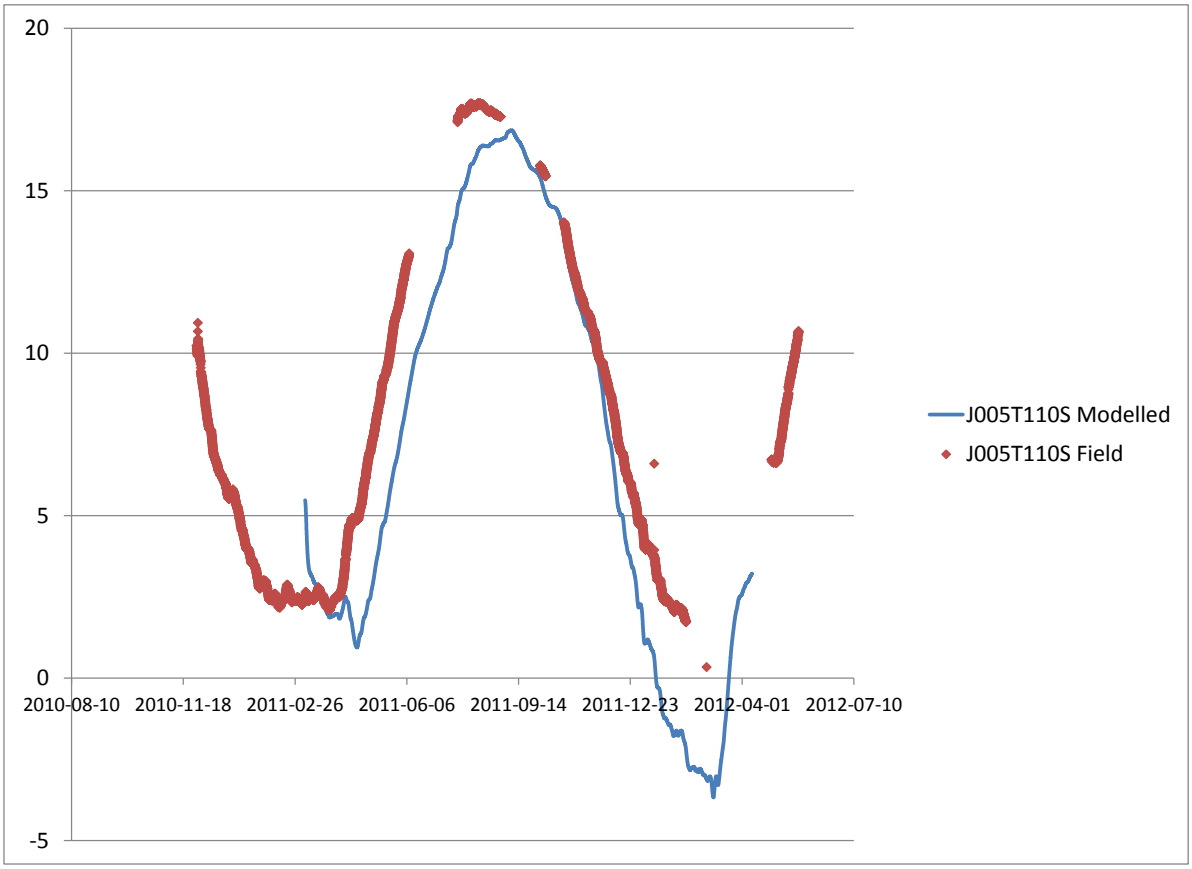
20
15
10
5
0
-5
2010-08-10
2010-11-18
2011-02-26
2011-06-06
2011-09-14
2011-12-23
2012-04-01
2012-07-10
J005T110S Modelled
J005T110S Field

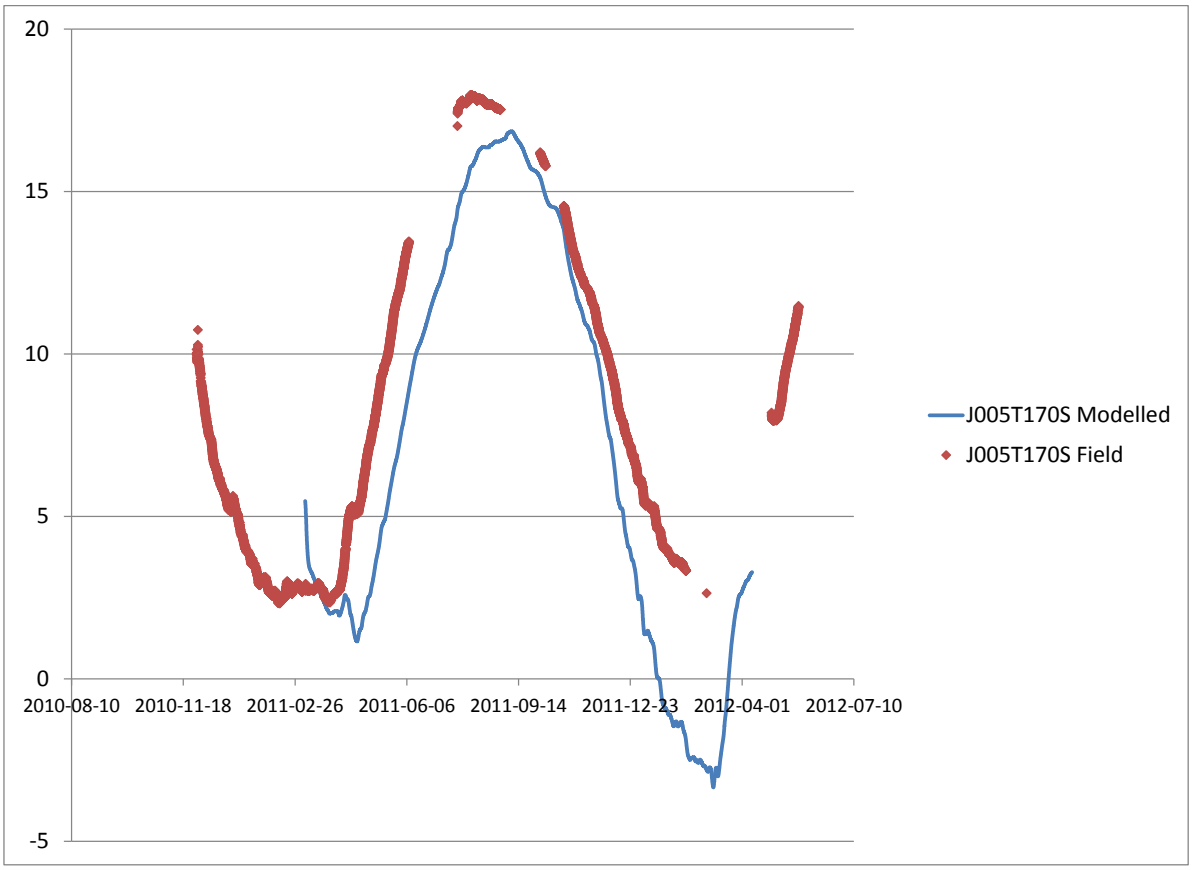
20
15
10
5
0
-5
2010-08-10
2010-11-18
2011-02-26
2011-06-06
2011-09-14
2011-12-23
2012-04-01
2012-07-10
J005T170S Modelled
J005T170S Field

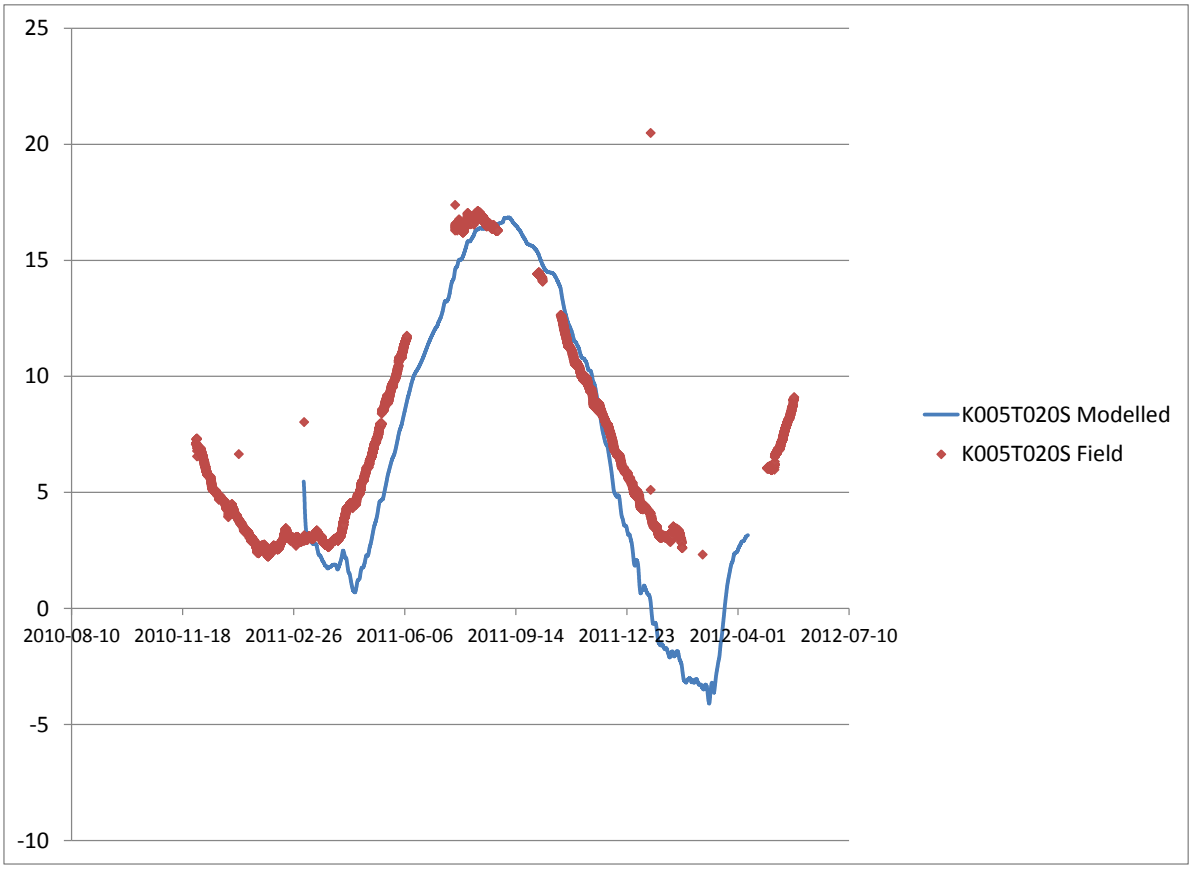
25
20
15
10
5
0
-5
-10
2010-08-10
2010-11-18
2011-02-26
2011-06-06
2011-09-14
2011-12-23
2012-04-01
2012-07-10
K005T020S Modelled
K005T020S Field

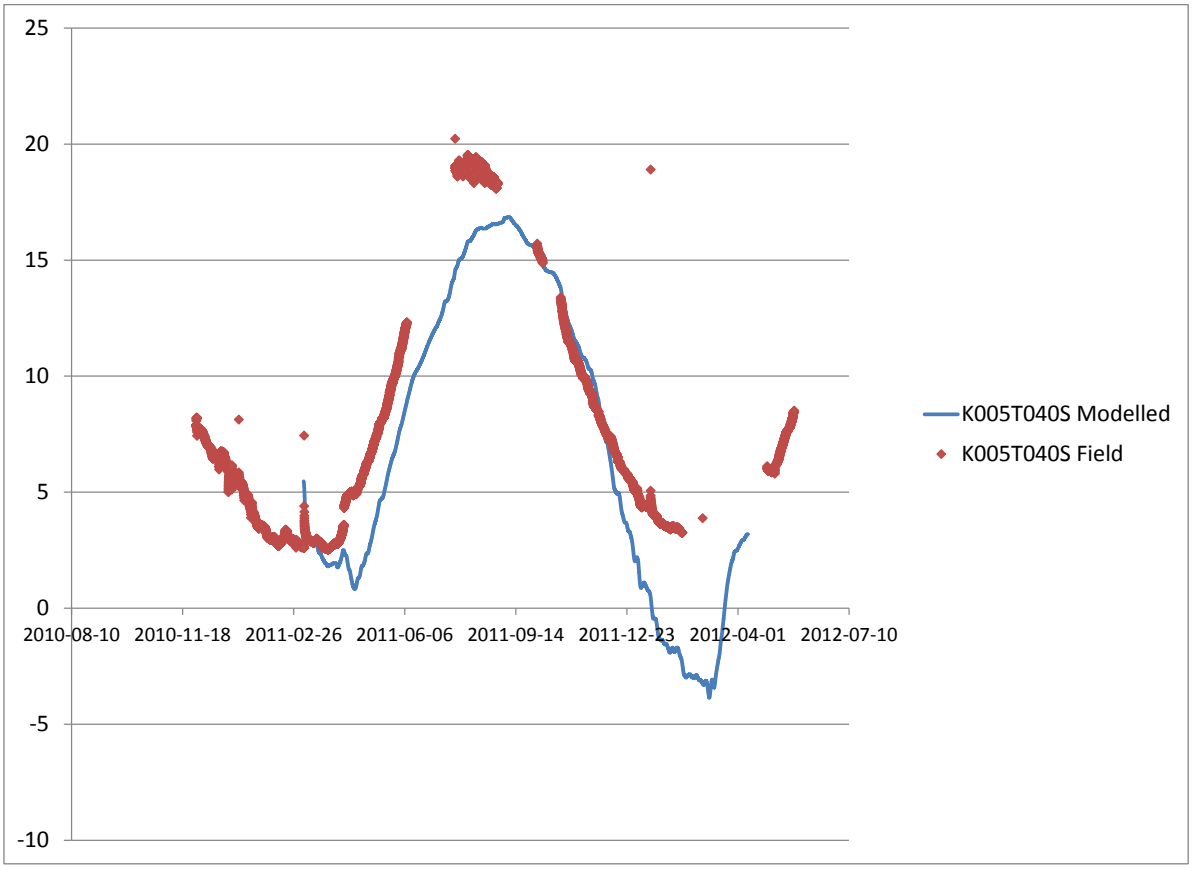
25
20
15
10
5
0
-5
-10
2010-08-10
2010-11-18
2011-02-26
2011-06-06
2011-09-14
2011-12-23
2012-04-01
2012-07-10
K005T040S Modelled
K005T040S Field

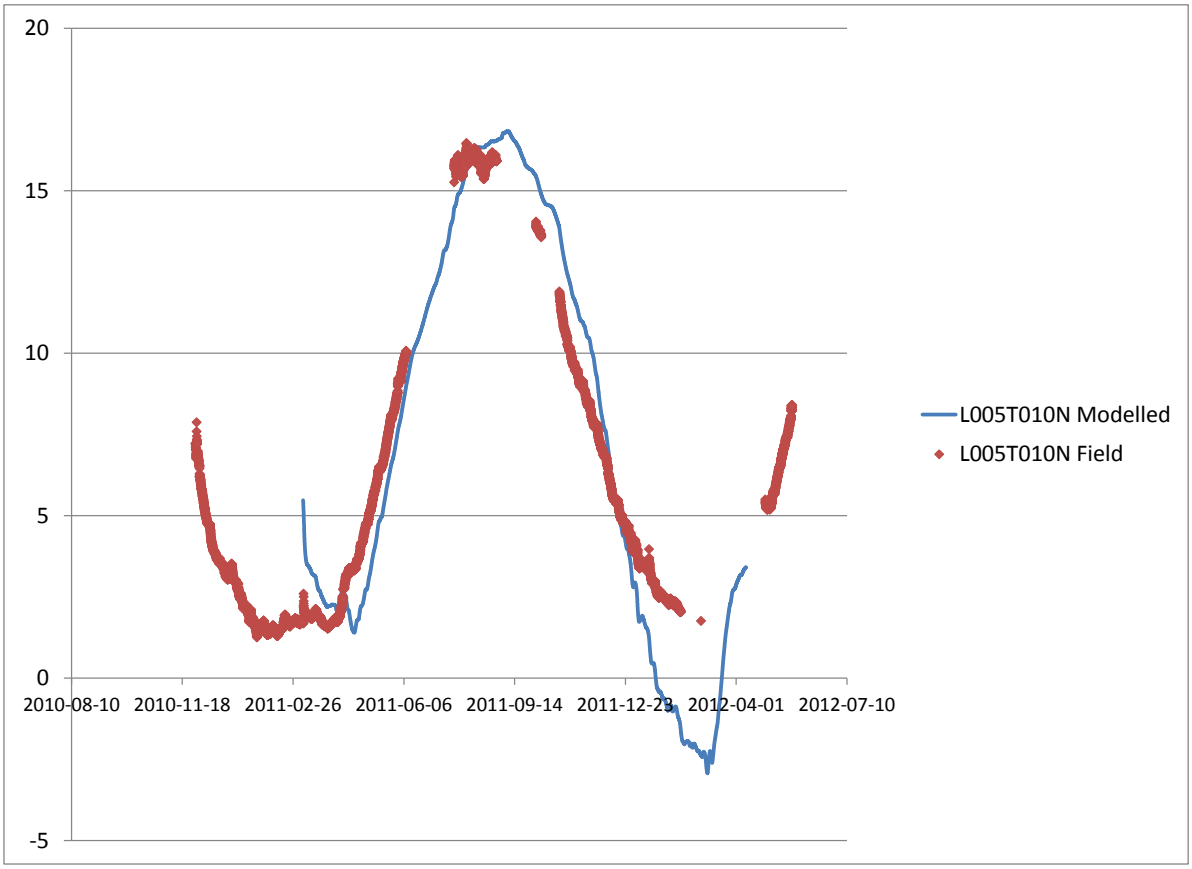
20
15
10
5
0
-5
2010-08-10
2010-11-18
2011-02-26
2011-06-06
2011-09-14
2011-12-23
2012-04-01
2012-07-10
L005T010N Modelled
L005T010N Field

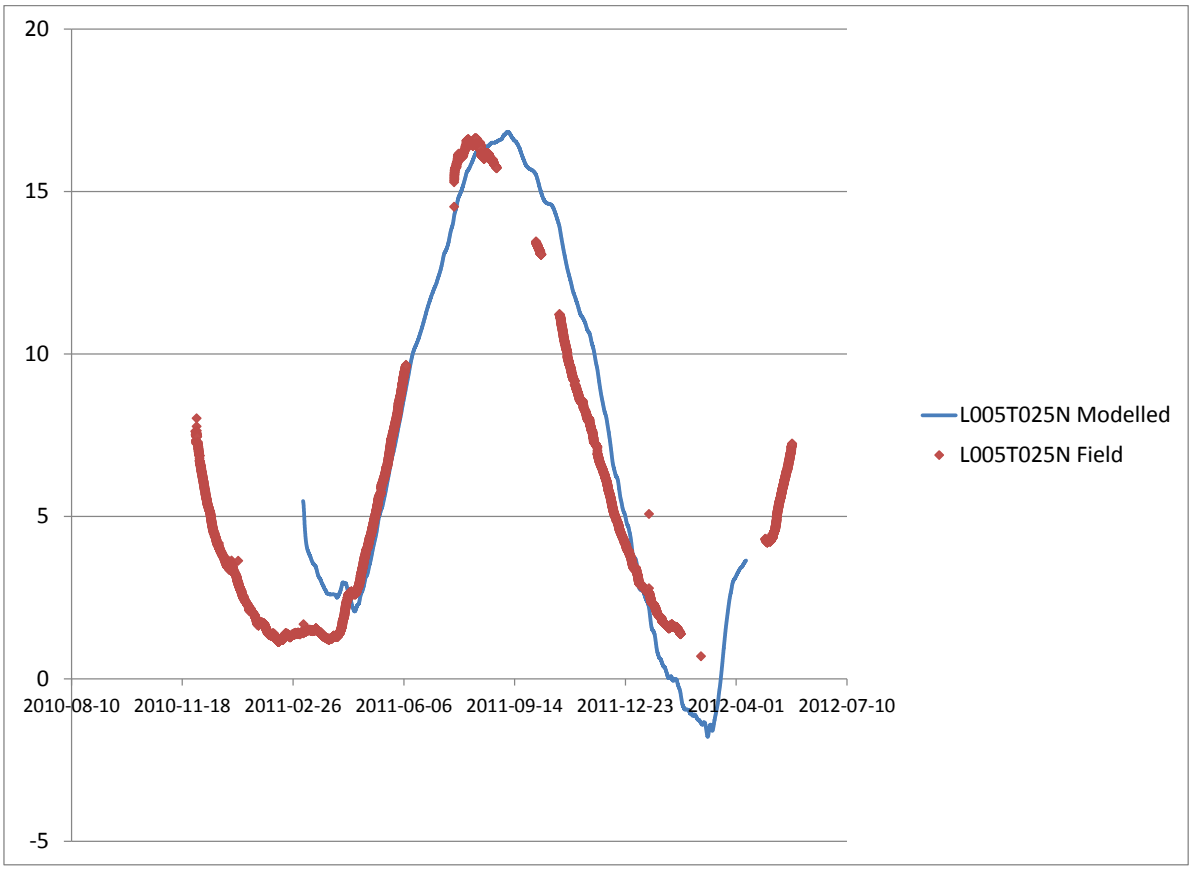
20
15
10
5
0
-5
2010-08-10
2010-11-18
2011-02-26
2011-06-06
2011-09-14
2011-12-23
2012-04-01
2012-07-10
L005T025N Modelled
L005T025N Field

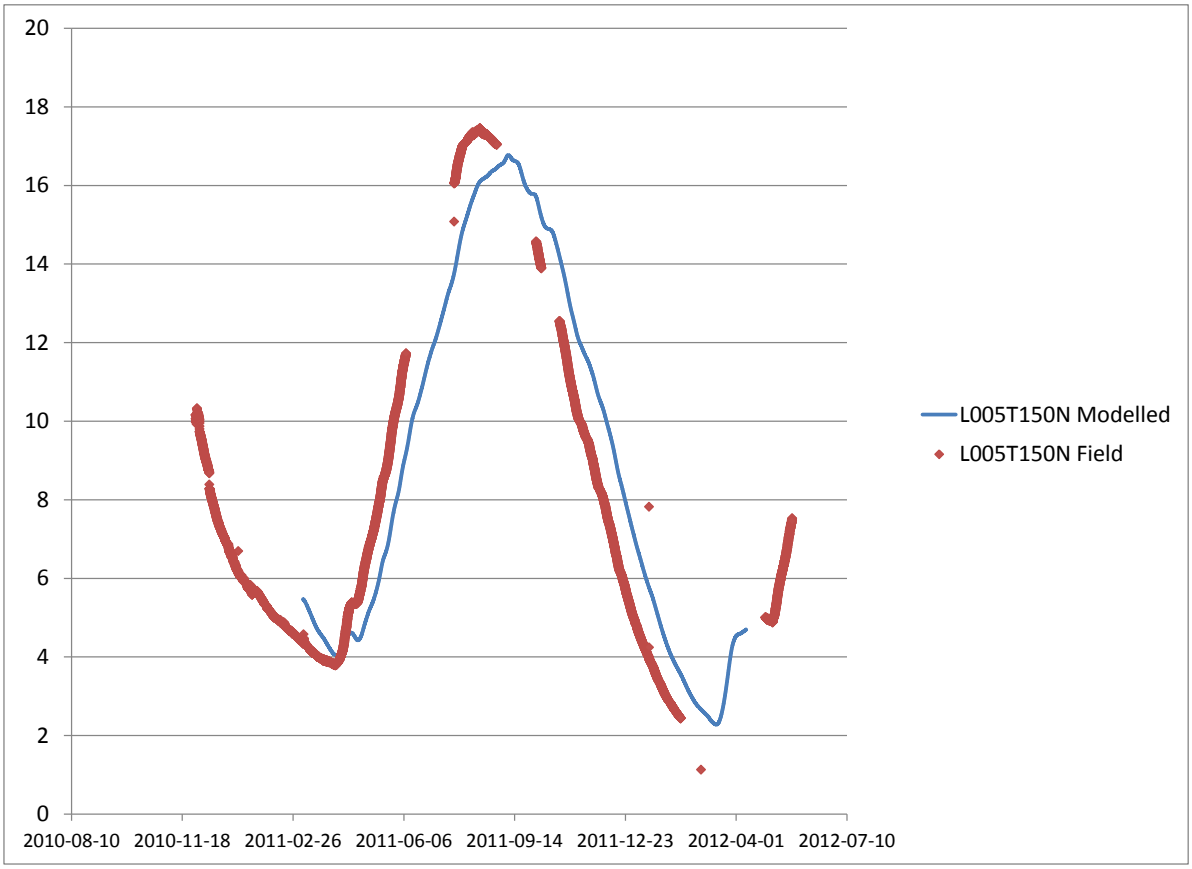
20
18
16
14
12
10
8
6
4
2
0
2010-08-10
2010-11-18
2011-02-26
2011-06-06
2011-09-14
2011-12-23
2012-04-01
2012-07-10
L005T150N Modelled
L005T150N Field

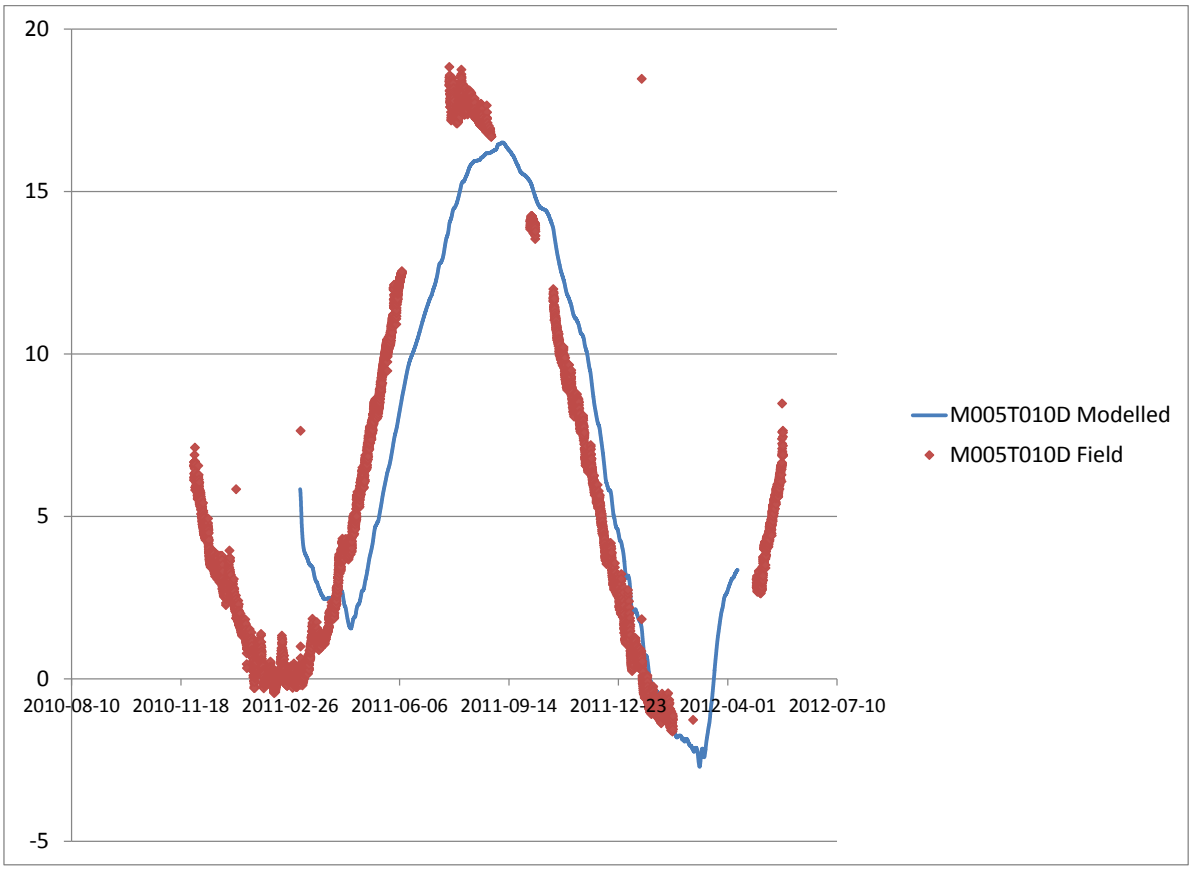
20
15
10
5
0
-5
2010-08-10
2010-11-18
2011-02-26
2011-06-06
2011-09-14
2011-12-23
2012-04-01
2012-07-10
M005T010D Modelled
M005T010D Field

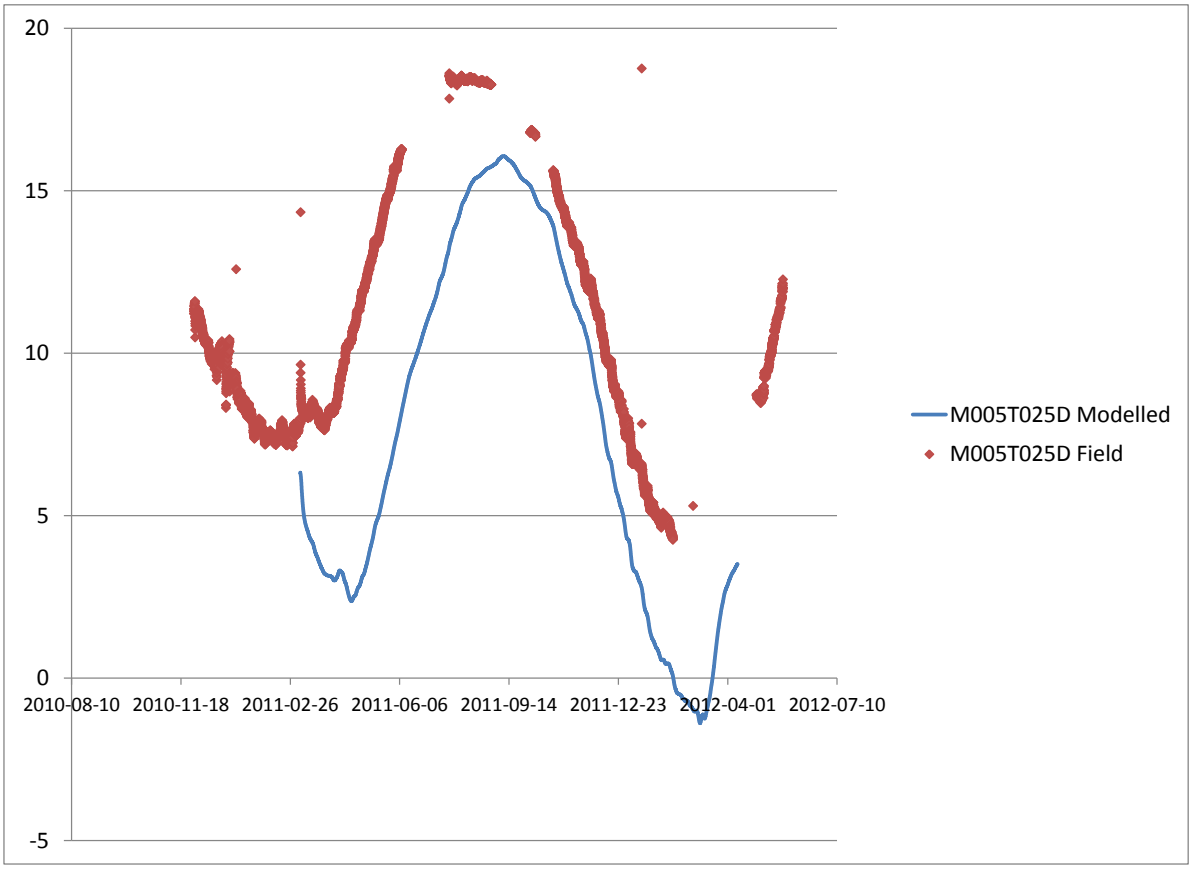
20
15
10
5
0
-5
2010-08-10
2010-11-18
2011-02-26
2011-06-06
2011-09-14
2011-12-23
2012-04-01
2012-07-10
M005T025D Modelled
M005T025D Field

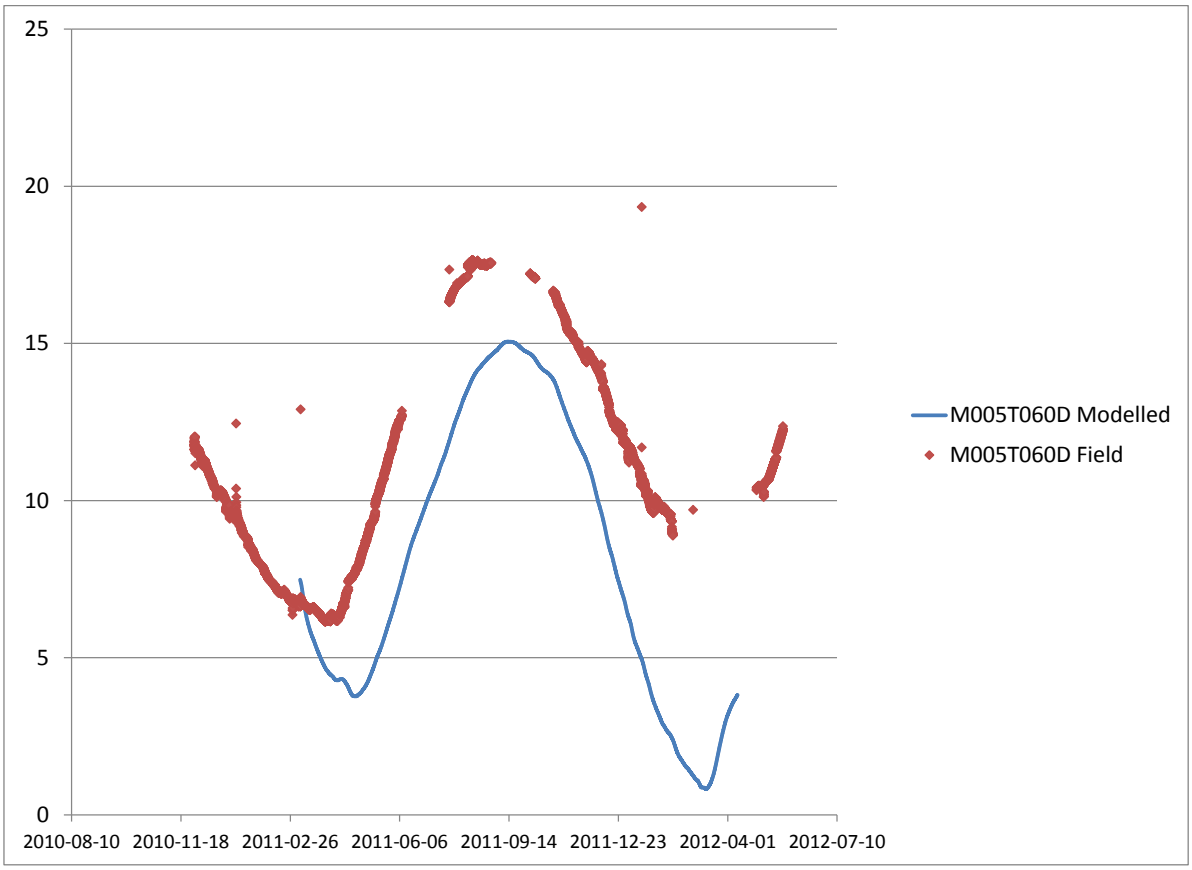
25
20
15
10
5
0
2010-08-10
2010-11-18
2011-02-26
2011-06-06
2011-09-14
2011-12-23
2012-04-01
2012-07-10
M005T060D Modelled
M005T060D Field

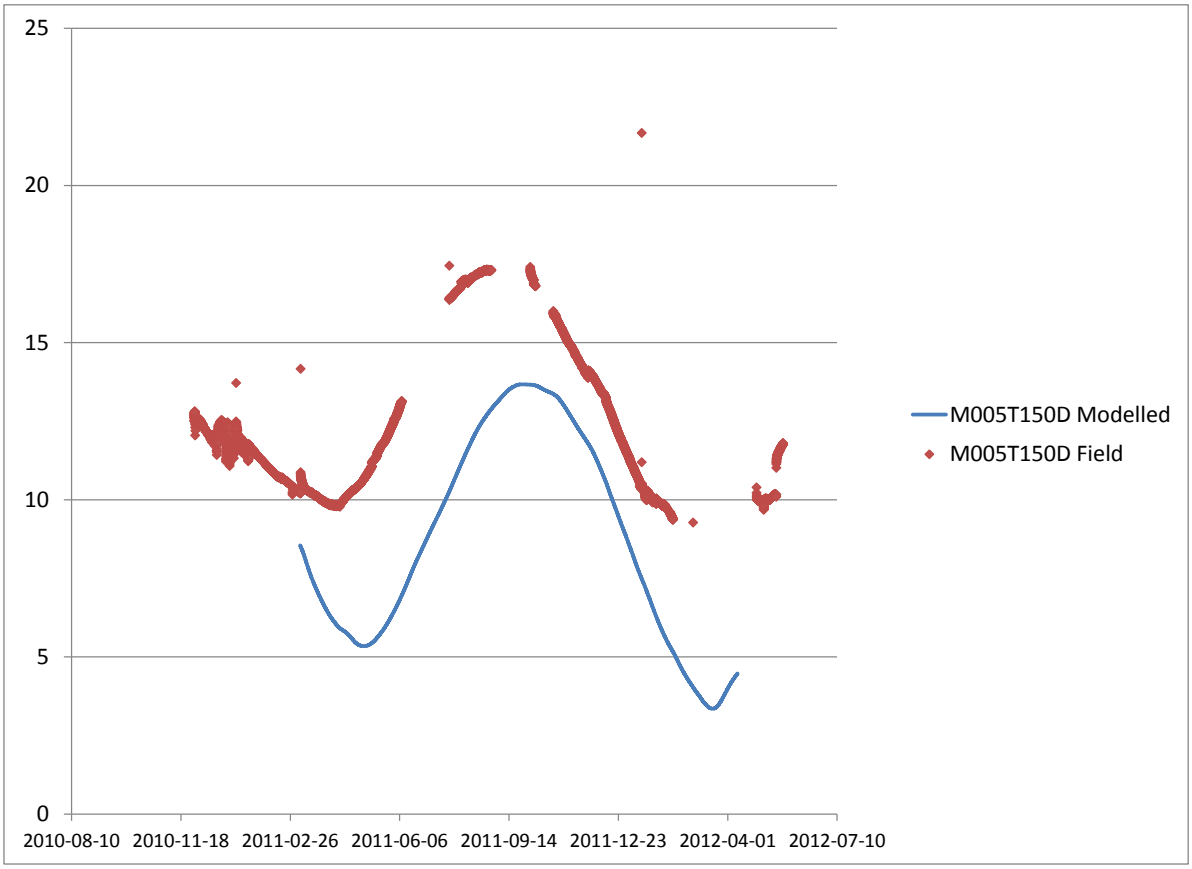
25
20
15
10
5
0
2010-08-10
2010-11-18
2011-02-26
2011-06-06
2011-09-14
2011-12-23
2012-04-01
2012-07-10
M005T150D Modelled
M005T150D Field

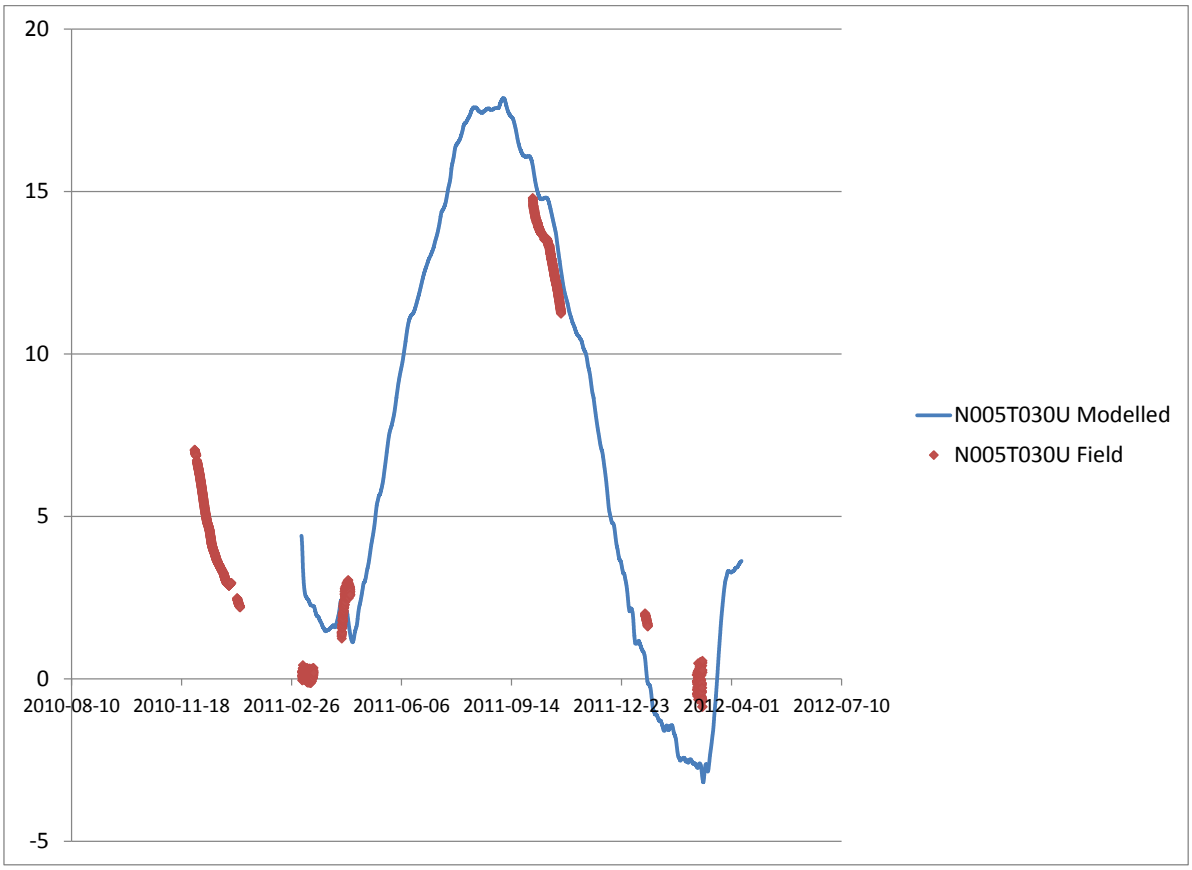
20
15
10
5
0
-5
2010-08-10
2010-11-18
2011-02-26
2011-06-06
2011-09-14
2011-12-23
2012-04-01
2012-07-10
N005T030U Modelled
N005T030U Field

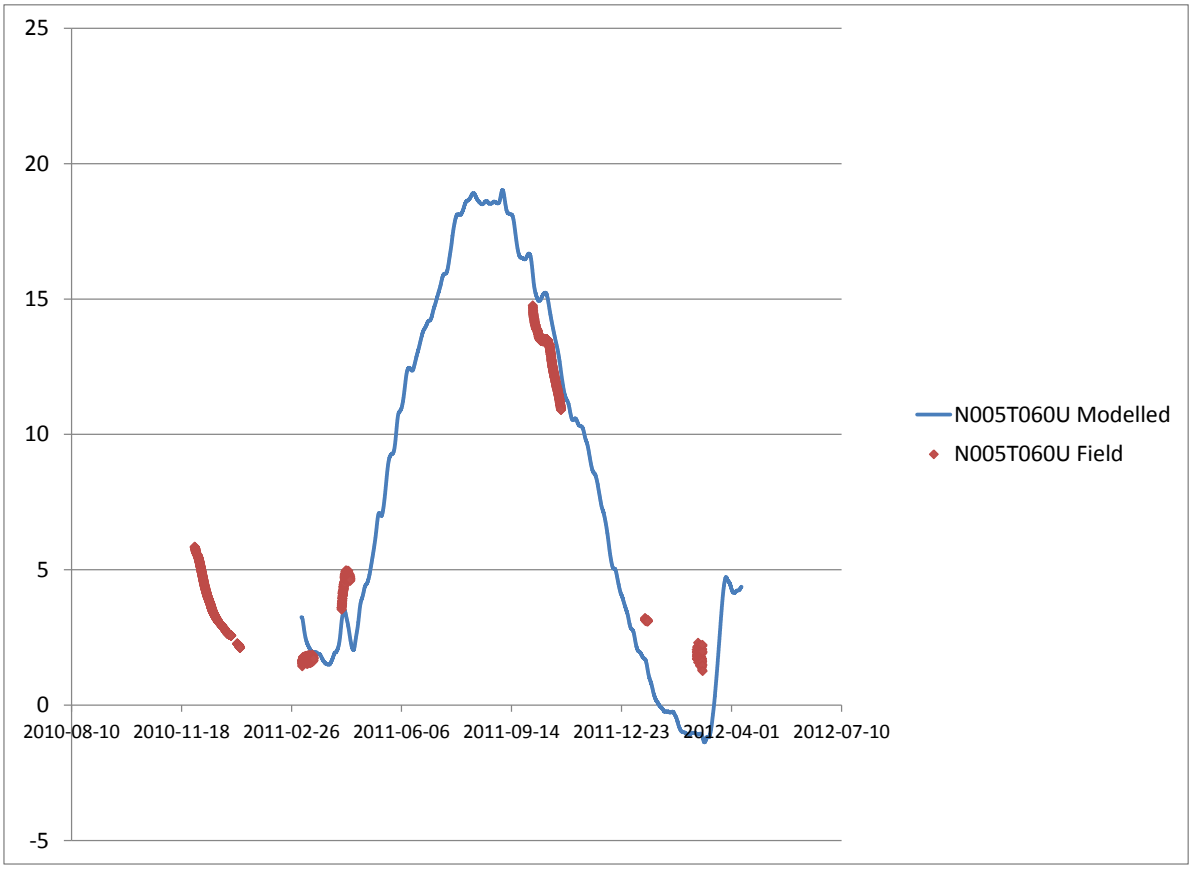
25
20
15
10
5
0
-5
2010-08-10
2010-11-18
2011-02-26
2011-06-06
2011-09-14
2011-12-23
2012-04-01
2012-07-10
N005T060U Modelled
N005T060U Field

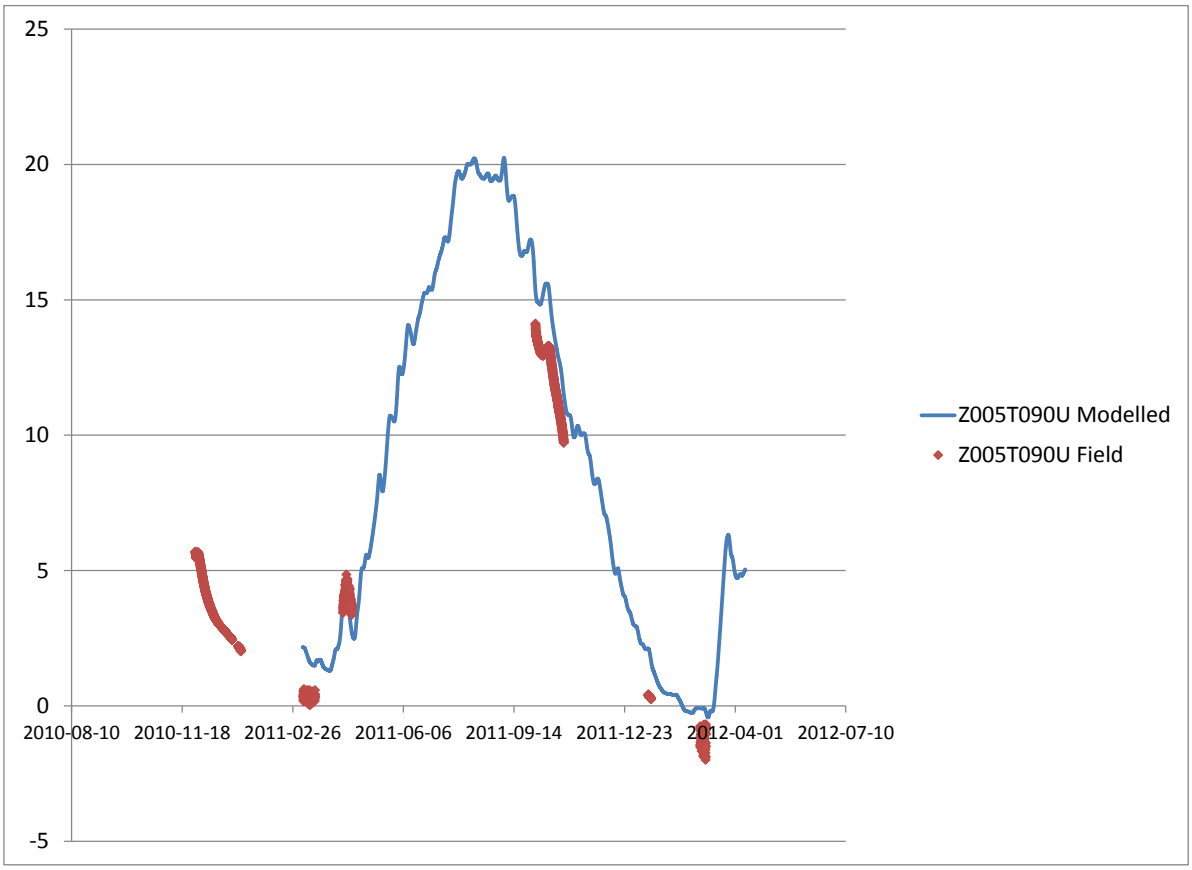
25
20
15
10
5
0
-5
2010-08-10
2010-11-18
2011-02-26
2011-06-06
2011-09-14
2011-12-23
2012-04-01
2012-07-10
Z005T090U Modelled
Z005T090U Field

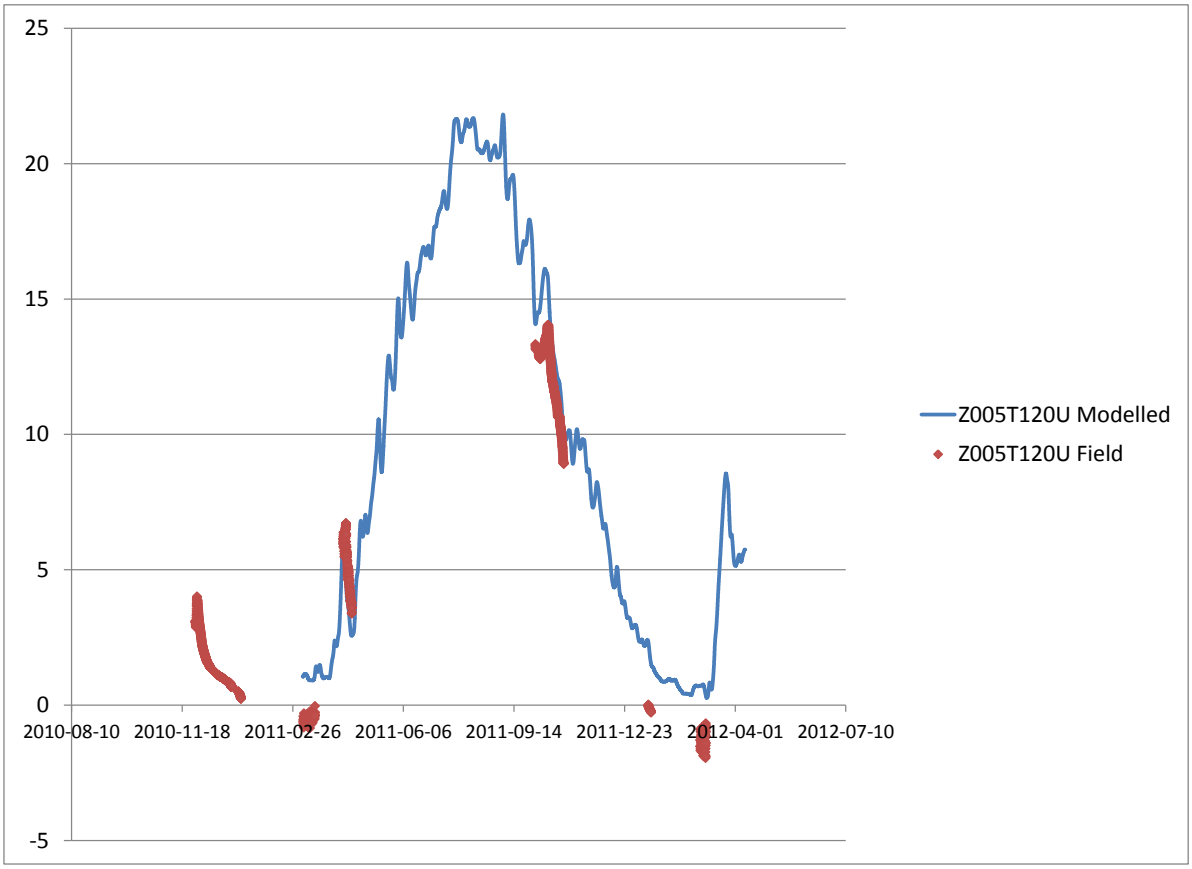
25
20
15
10
5
0
-5
2010-08-10
2010-11-18
2011-02-26
2011-06-06
2011-09-14
2011-12-23
2012-04-01
2012-07-10
Z005T120U Modelled
Z005T120U Field

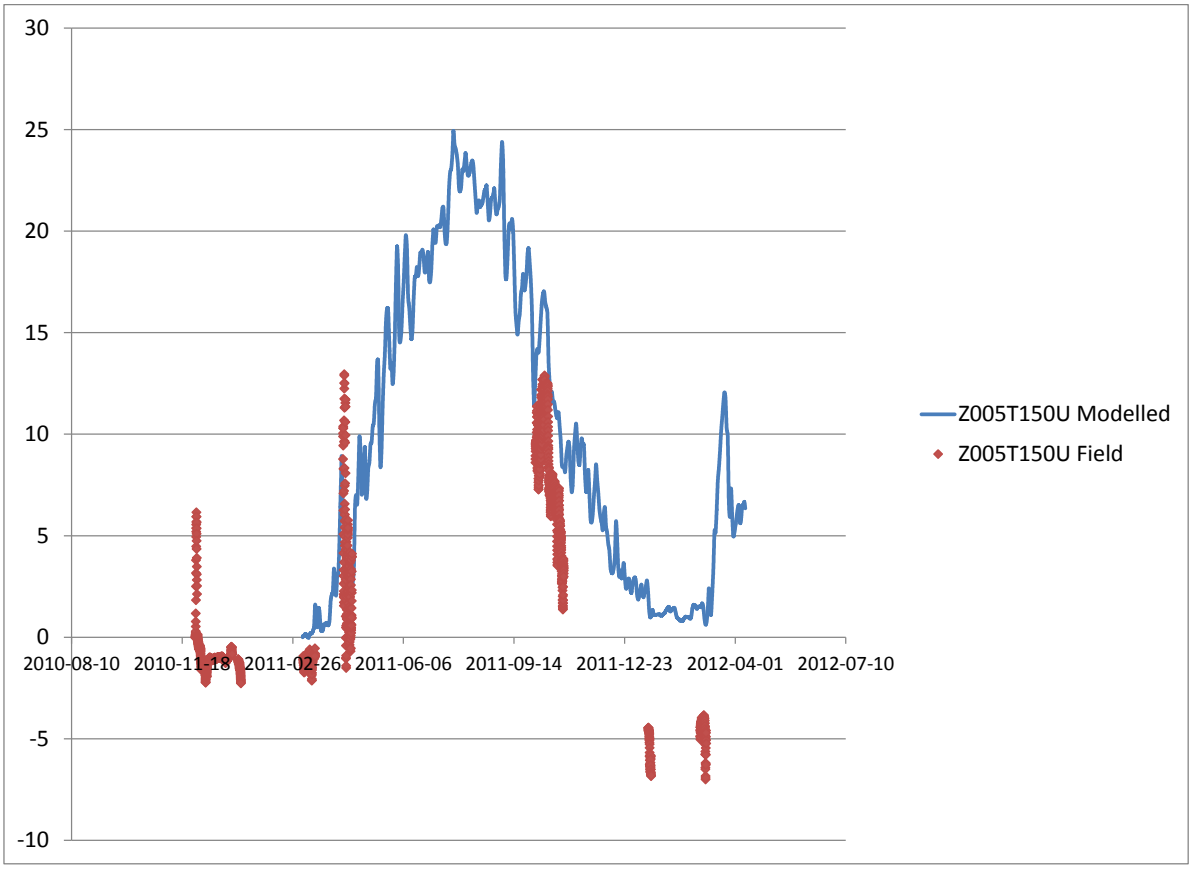
30
25
20
15
10
5
0
-5
-10
2010-08-10
2010-11-18
2011-02-26
2011-06-06
2011-09-14
2011-12-23
2012-04-01
2012-07-10
Z005T150U Modelled
Z005T150U Field

G.3 Pipe temperature

For these inverse model runs the optimization target was to minimize the difference between the modelled inlet temperatures going into the heat pump and the temperature sensor at that location.

G.3.1 DDS Both 550 days

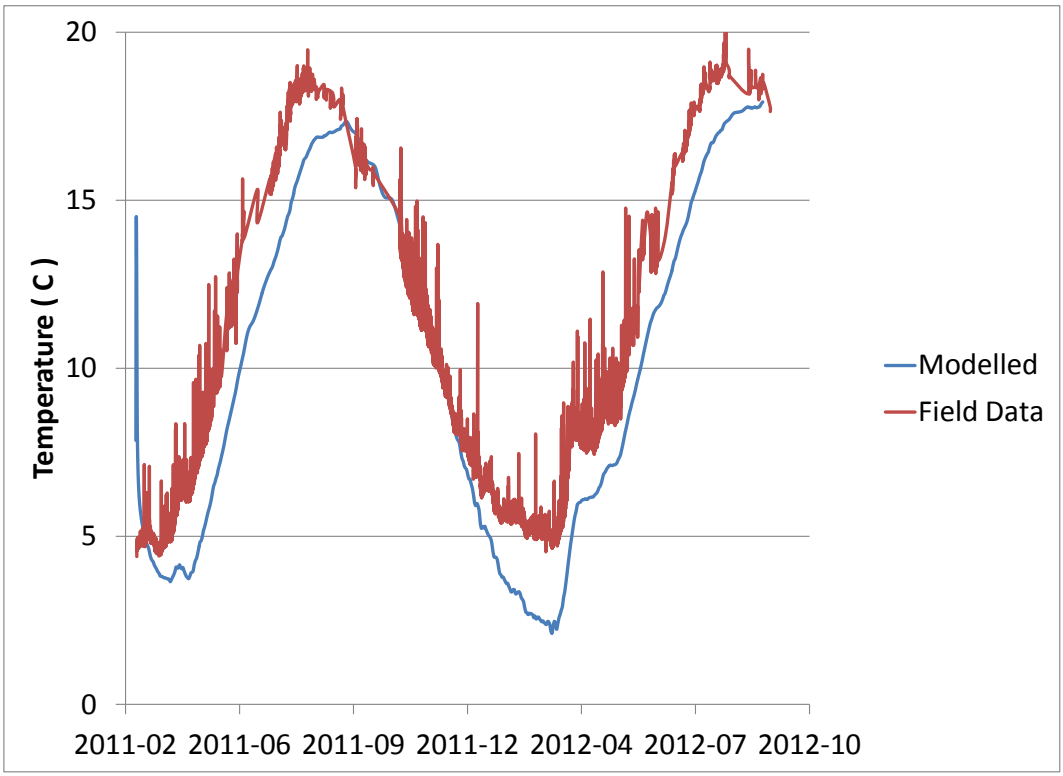

Appendix H

Heterogeneity generation using GSLIB

GSLIB (Deutsch and Journel, 1992) is a collection of opensource geostatistical software libraries. The list of packages and their version numbers presented in Table H.1.

sgsim uses sequential Gaussian simulations to generate spatial correlated random fields. *gam* was used to generate variograms based on these simulated fields. *vmodel* was used to create theoretical variograms of the spatially corellated random space functions which

Table H.1: Version numbers of the components from GSLIB90 which were used in this project

Program	Version Number
sgsim	3.001
gam	2.905
vmodel	2.905
vargplt	2.906
pixelplt	2.905

could then be compared against the spatial distributions of the generated random fields. Results from *vmodel* and *gam* were plotted with *vargplt* for direct comparison of the variograms.

pixelplt was used for visualizing the random fields.

For this project all random fields are normalized so that they have a mean of 0 and a sill variance of 1. From this the numerical model will apply a mean and standard deviation, using the spatial distribution generated by GSLIB. Any conductivities or heat capacities that would be negative due to the applied variance are corrected upwards to 0.

Example parameter files used in this project follow:

1. sgim parameter file
2. gam parameter file
3. vmodel parameter file
4. vargplt parameter file
5. pixelplt parameter file

sgim parameter file

```
                          Parameters for SGSIM
                *********************

START OF PARAMETERS:
nodata                          -file with data
1  2  0  3  5  0                -  columns for X,Y,Z,vr,wt,sec.var.
-1.0e21       1.0e21              -  trimming limits
0                               -transform the data (0=no, 1=yes)
sgsim.trn                       -  file for output trans table
0                               -  consider ref. dist (0=no, 1=yes)
histsmth.out                    -  file with ref. dist distribution
1  2                            -  columns for vr and wt
0.0    15.0                     -  zmin,zmax(tail extrapolation)
1       0.0                     -  lower tail option, parameter
1      15.0                     -  upper tail option, parameter
0                               -debugging level: 0,1,2,3
sgsim.dbg                       -file for debugging output
conductivityVariance.csv        -file for simulation output
1                               -number of realizations to generate
50      0.05    0.1                -grid definition: nx,xmn,xsiz
40      0.625    1.25                -                 ny,ymn,ysiz
46      0.05    0.1                 -                nz,zmn,zsiz
69069                           -random number seed
0     8                         -min and max original data for sim
12                              -number of simulated nodes to use
1                               -assign data to nodes (0=no, 1=yes)
1     3                         -multiple grid search (0=no, 1=yes),num
0                               -maximum data per octant (0=not used)
10.0  10.0  10.0                -maximum search radii (hmax,hmin,vert)
 0.0   0.0   0.0                -angles for search ellipsoid
51    51    11                  -size of covariance lookup table
0     0.60   1.0                -ktype: 0=SK,1=OK,2=LVM,3=EXDR,4=COLC
nodata                          -  file with LVM, EXDR, or COLC variable
4                               -  column for secondary variable
1    0.0                           -   nst, nugget effect
2    1.0  0.0   0.0   0.0          -   it,cc,ang1,ang2,ang3
        12.8  12.8  1.6            -   a_hmax, a_hmin, a_vert
```

gam parameter file

```
                  Parameters for GAM
                  ******************

START OF PARAMETERS:
sgsim.out      -file with data
1   1                -   number of variables, column numbers
-1.0e21     1.0e21    -   trimming limits
gam.out               -file for variogram output
1                     -grid or realization number
50      0.05    0.1              -grid definition: nx,xmn,xsiz
40      0.625    1.25              -                 ny,ymn,ysiz
46      0.05    0.1               -                nz,zmn,zsiz
3  10                 -number of directions, number of lags
 1  0  0              -ixd(1),iyd(1),izd(1)
 0  1  0              -ixd(2),iyd(2),izd(2)
 0  0  1              -ixd(3),iyd(3),izd(3)
0                     -standardize sill? (0=no, 1=yes)
1                     -number of variograms
1   1   1             -tail variable, head variable, variogram type


type 1 = traditional semivariogram
     2 = traditional cross semivariogram
     3 = covariance
     4 = correlogram
     5 = general relative semivariogram
     6 = pairwise relative semivariogram
     7 = semivariogram of logarithms
     8 = semimadogram
     9 = indicator semivariogram - continuous
     10= indicator semivariogram - categorical
```

vmodel parameter file

```
                 Parameters for VMODEL
                 *********************

START OF PARAMETERS:
vmodel.var                    -file for variogram output
3   100                        -number of directions and lags
 0.0   0.0    1             -azm, dip, lag distance
90.0   0.0    1             -azm, dip, lag distance
0.0   90.0    1             -azm, dip, lag distance
1    0.0                         -   nst, nugget effect
2    1.0  0.0   0.0   0.0        -   it,cc,ang1,ang2,ang3
         12.8  12.8  1.6         -   a_hmax, a_hmin, a_vert
```

vargplt parameter file

```
                  Parameters for VARGPLT
                  **********************

START OF PARAMETERS:
vargplt.ps                      -file for PostScript output
6                               -number of variograms to plot
0.0   20.0                      -distance  limits (from data if max<min)
0.0    1.0                      -variogram limits (from data if max<min)
1      1.0                      -plot sill (0=no,1=yes), sill value)
Normal Scores Semivariogram     -Title for variogram
vmodel.var                      -2 file with variogram data
1    2   1   1   10             -  variogram #, dash #, pts?, line?, color
vmodel.var                      -2 file with variogram data
2    2   0   1   6             -  variogram #, dash #, pts?, line?, color
vmodel.var                      -2 file with variogram data
3    2   0   1   5             -  variogram #, dash #, pts?, line?, color
gam.out                        -2 file with variogram data
1    0   0   1   1               -  variogram #, dash #, pts?, line?, color
gam.out                         -2 file with variogram data
2    0   0   1   2               -  variogram #, dash #, pts?, line?, color
gam.out                         -2 file with variogram data
3    0   0   1   11              -  variogram #, dash #, pts?, line?, color

Color Codes for Variogram Lines/Points:
      1=red, 2=orange, 3=yellow, 4=light green, 5=green, 6=light blue,
      7=dark blue, 8=violet, 9=white, 10=black, 11=purple, 12=brown,
      13=pink, 14=intermediate green, 15=gray
```

pixelplt parameter file

```
                  Parameters for PIXELPLT
                  ***********************

START OF PARAMETERS:
gsim.out                          -file with gridded data
1                                 -  column number for variable
-1.0e21  1.0e21                    -  data trimming limits
pixelplt.ps                       -file with PostScript output
1                                 -realization number
50      0.05    0.1                -grid definition: nx,xmn,xsiz
40      0.625    1.25                -                 ny,ymn,ysiz
46      0.05    0.1                 -                nz,zmn,zsiz
2                                 -slice orientation: 1=XY, 2=XZ, 3=YZ
1                                 -slice number
2-D Reference Data                -Title
X                                -X label
Z                                -Y label
0                                   -0=arithmetic, 1=log scaling
1                                   -0=gray scale, 1=color scale
0                                   -0=continuous, 1=categorical
-4.0  4.0  1                     -continuous:  min, max, increm.
4                                   -categorical: number of categories
1     3    Code_One                 -category(), code(), name()
2     1    Code_Two
3     6    Code_Three
4    10    Code_Four


Color Codes for Categorical Variable Plotting:
      1=red, 2=orange, 3=yellow, 4=light green, 5=green, 6=light blue,
      7=dark blue, 8=violet, 9=white, 10=black, 11=purple, 12=brown,
      13=pink, 14=intermediate green, 15=gray
```

Appendix I

Heterogeneity Results

I.1 Heterogeneity Temperature Profiles

The following figures show the near negligible effect that different heterogeneity structures have on the development of the thermal profile around the GLHE.

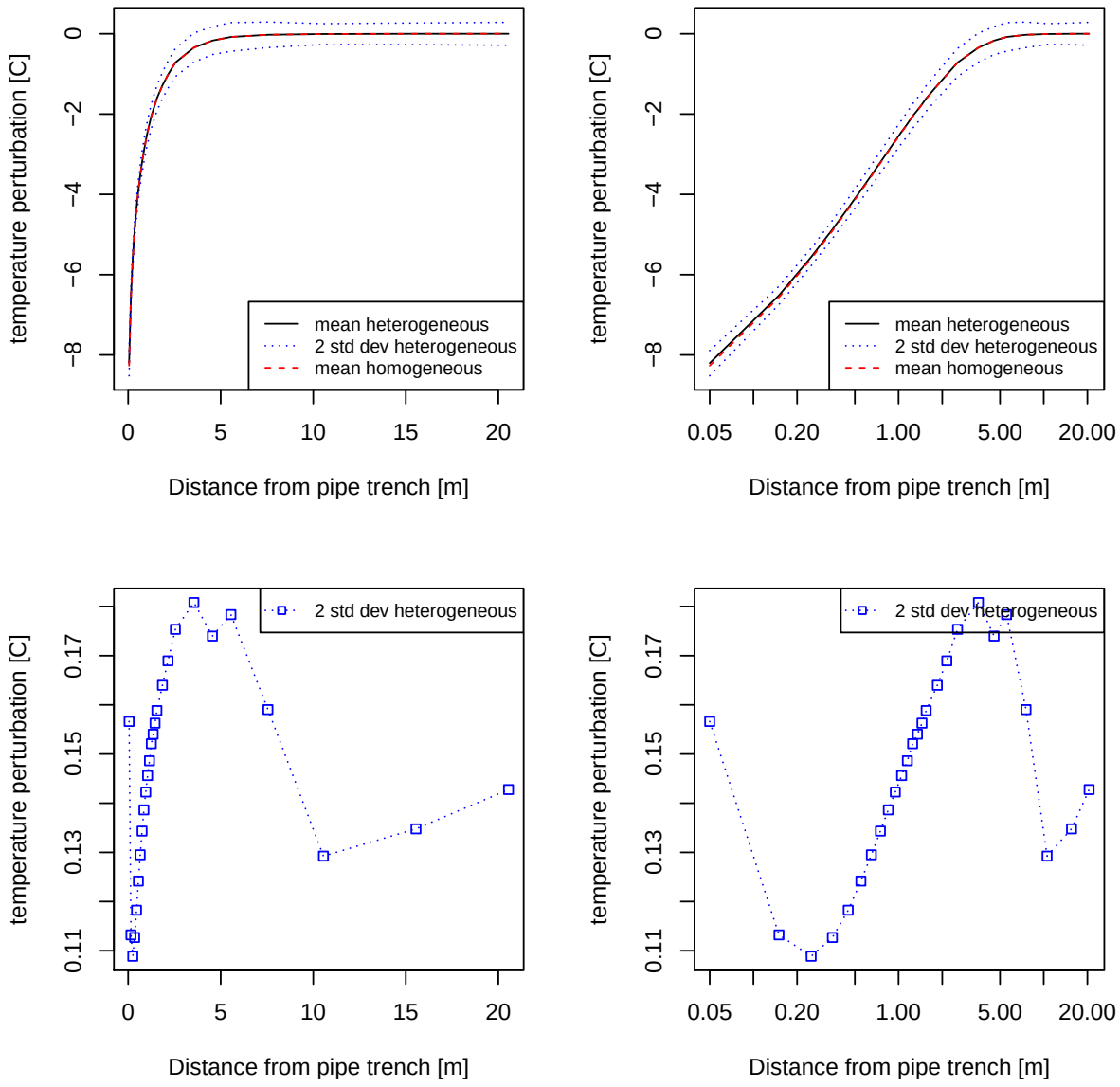

(a) Base case profile

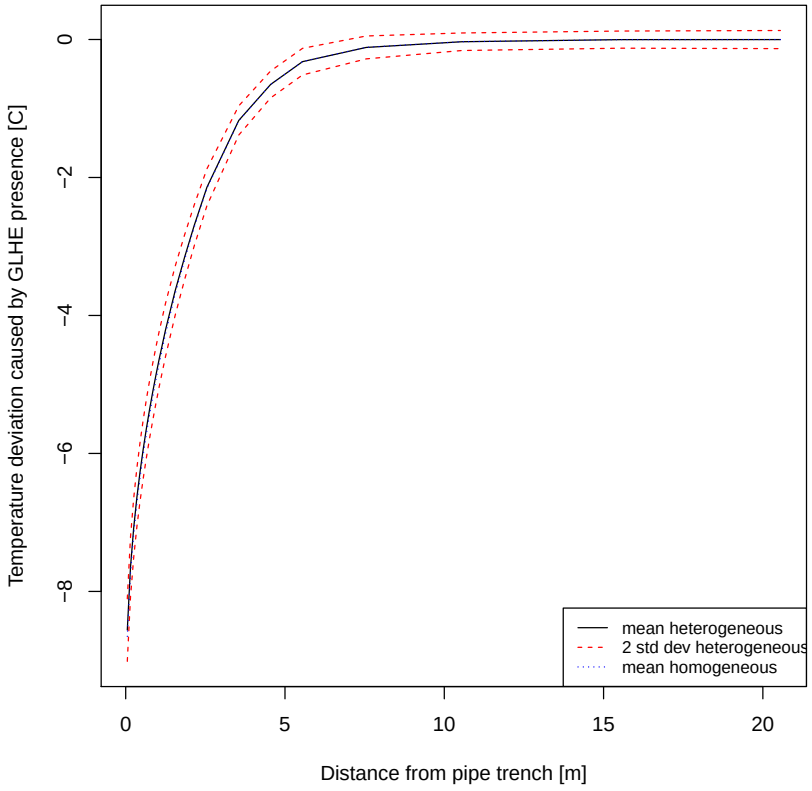

(b) Double the correlation length

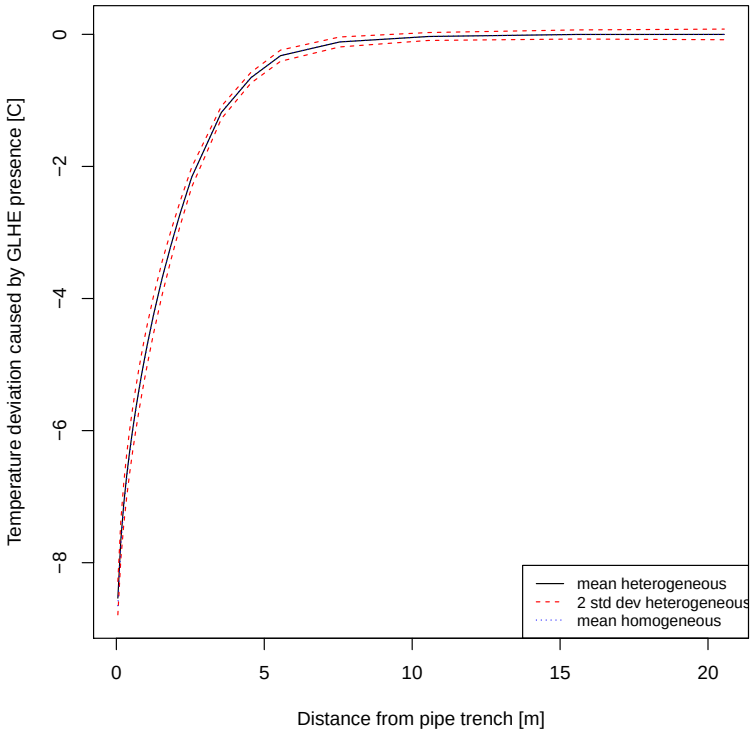

(c) Half the correlation length

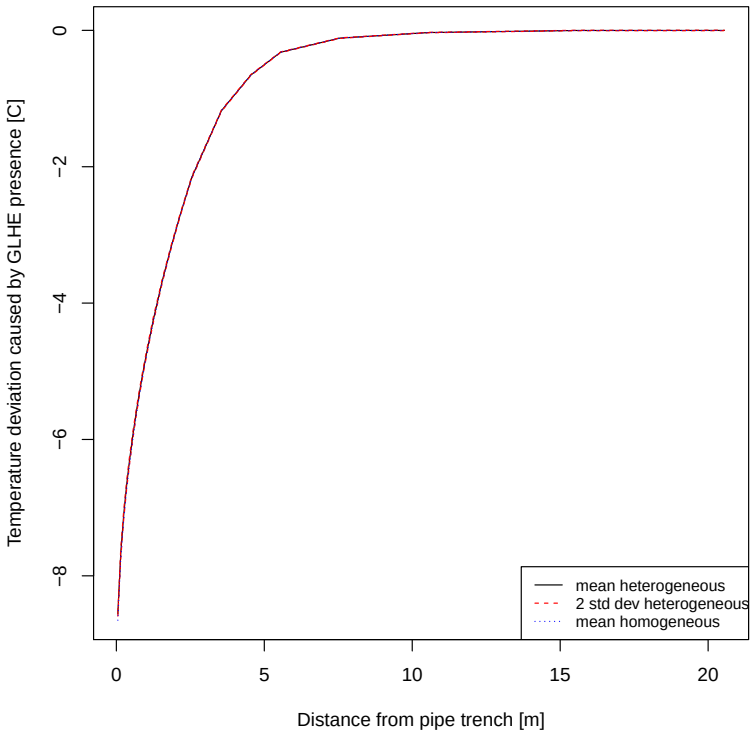

(d) Zero correlation length, or true random

I.2 Heterogeneity Structures

I.2.1 Legend

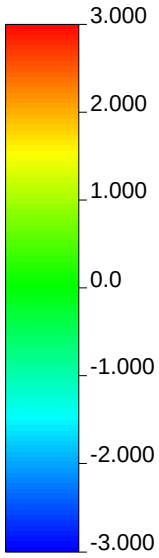

Figure I.1: Legend for the heterogeneity structures. The scale is standard deviations from the mean. Deviations beyond 3 are coloured red and blue for above and below the mean respectively.

What follows are the structures of the top and bottom four runs of the base case

I.2.2 XY cross sections

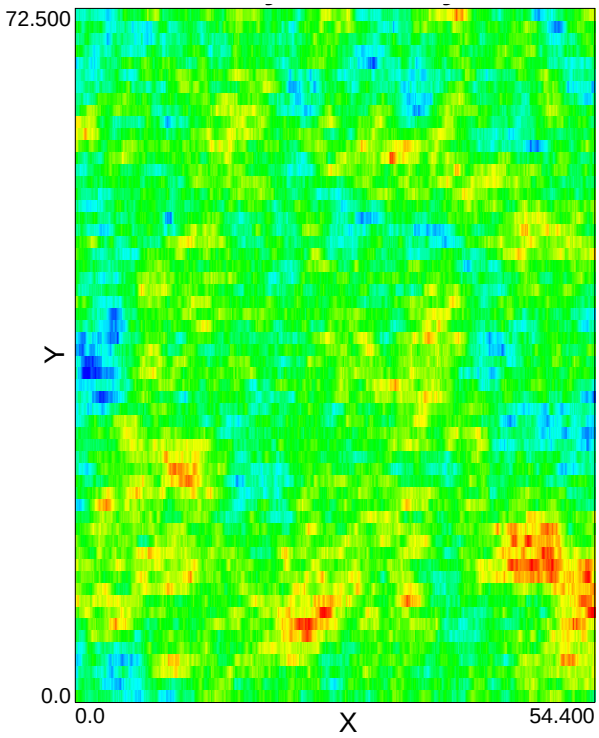

(a) Best

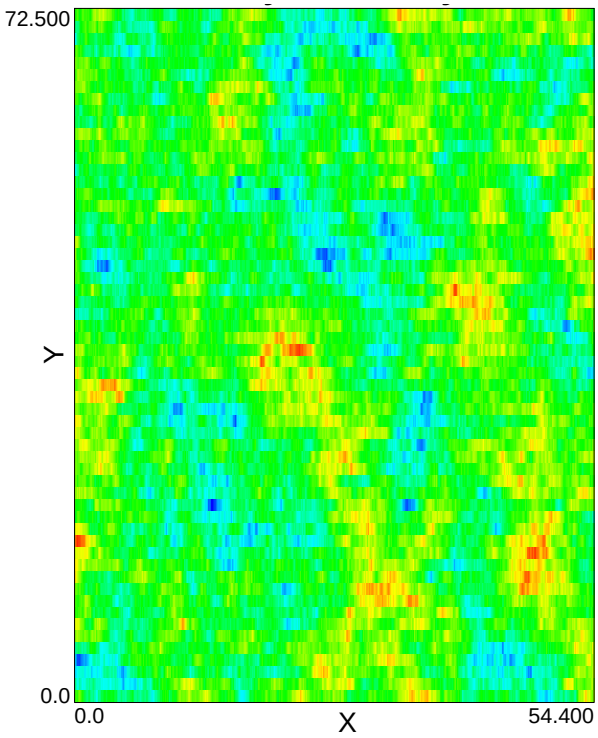

(b) Second best

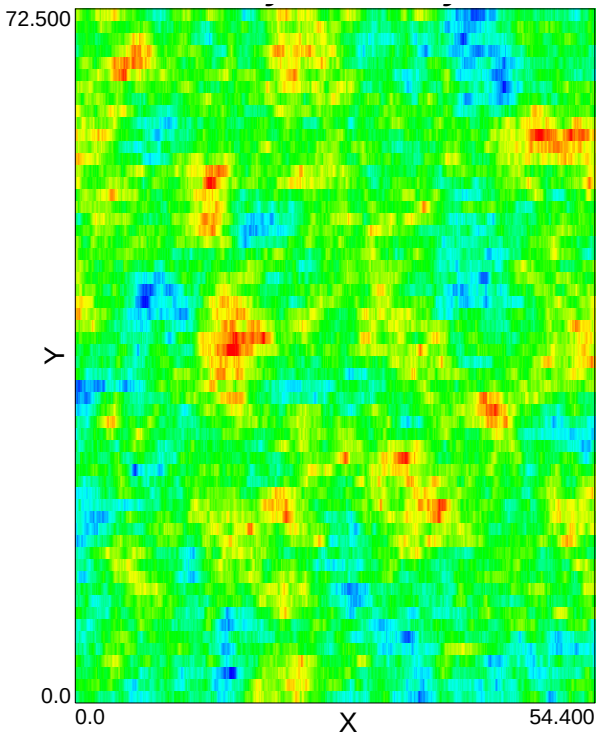

(c) Third best

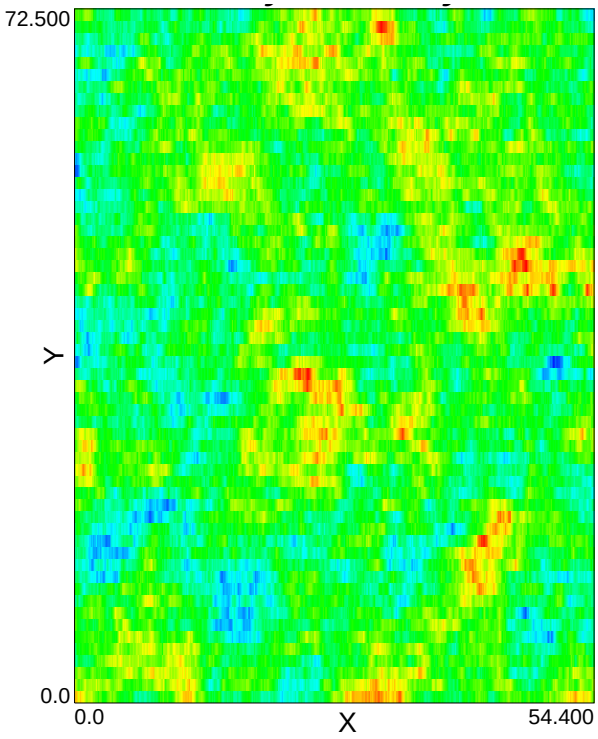

(d) Fourth best

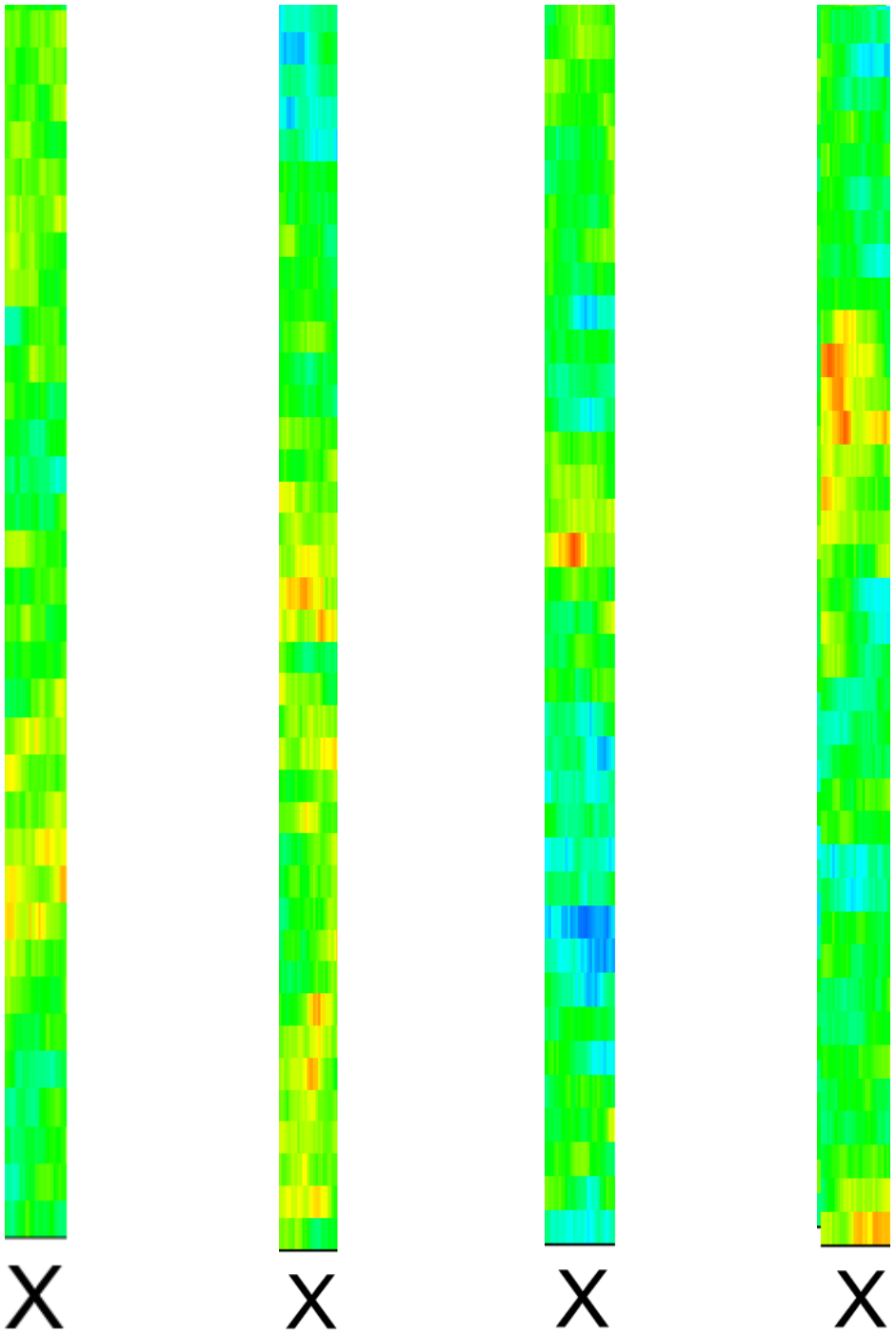

(e) Best (f) Second best (g) Third best (h) Fourth best

Figure I.2: Enlarged XY cross sections over the area in which the GLHE is situated

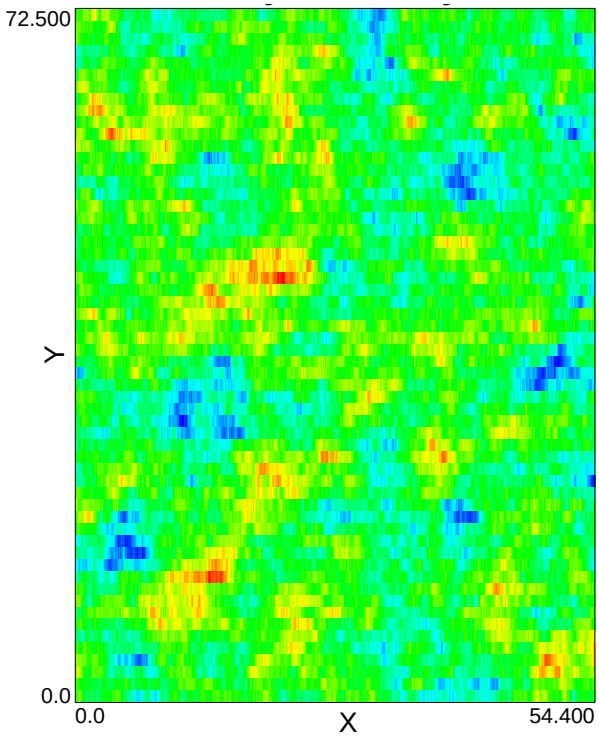

(a) Worst

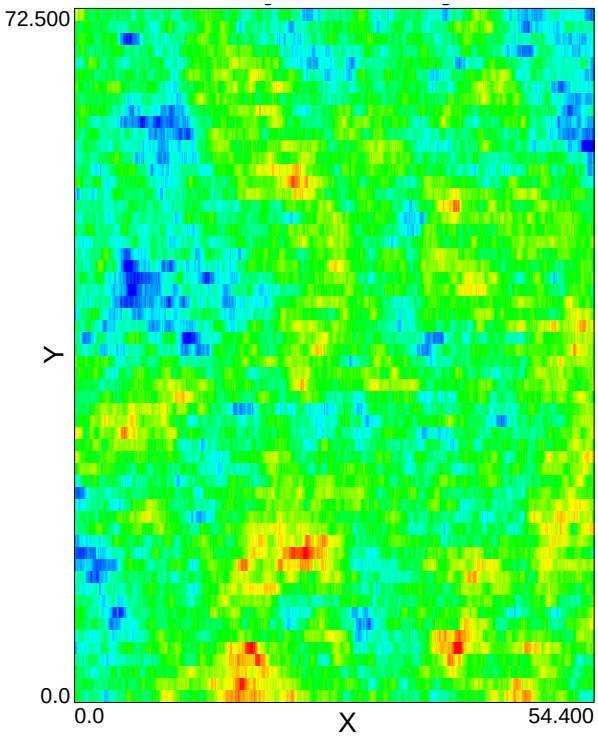

(b) Second worst

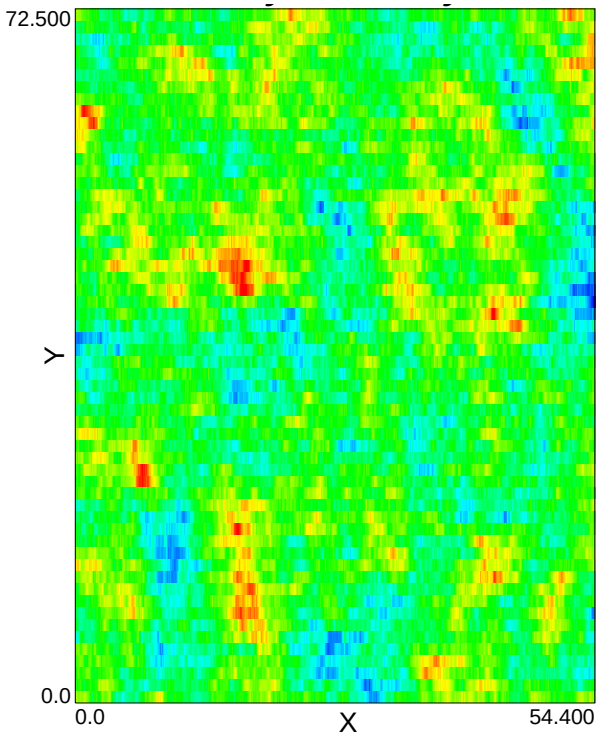

(c) Third worst

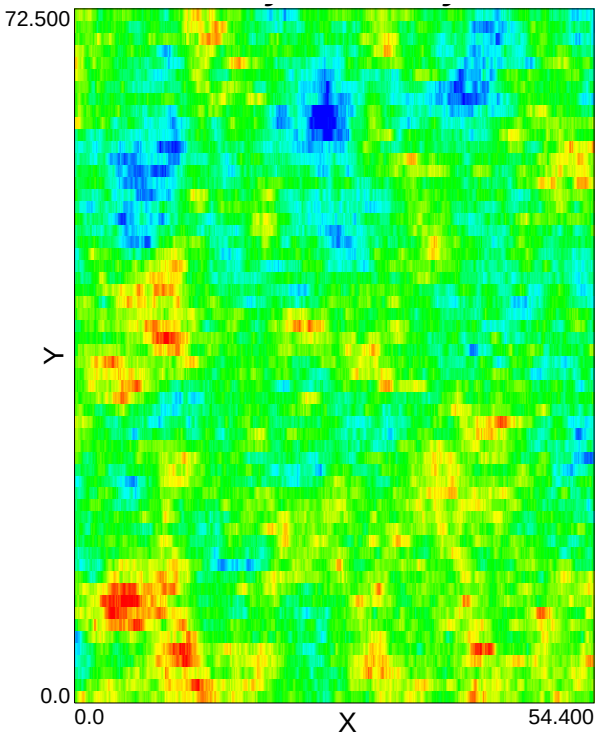

(d) Fourth worst

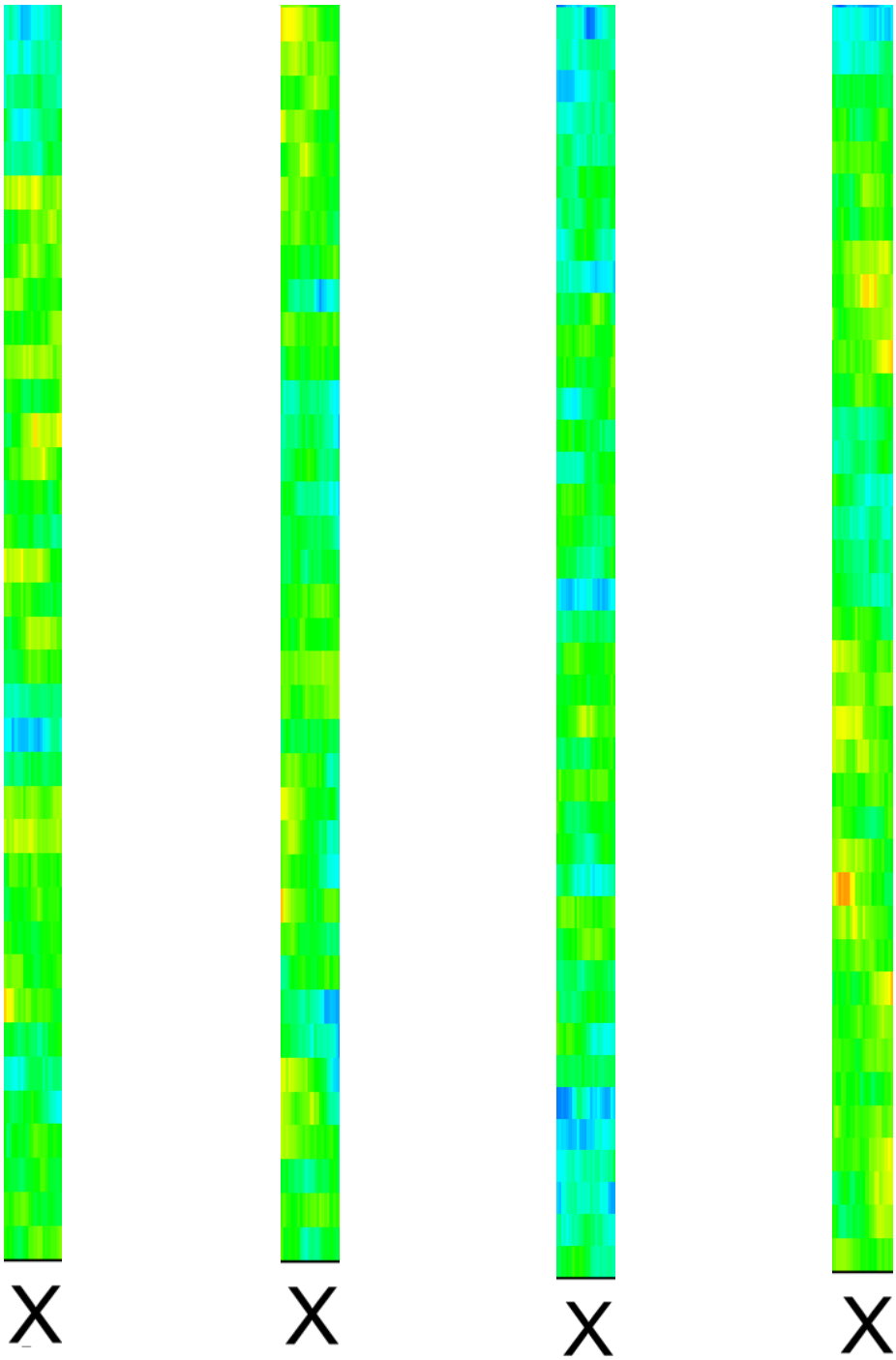

(e) Worst (f) Second worst (g) Third worst (h) Fourth worst

Figure I.3: Enlarged XY cross sections over the area in which the GLHE is situated

I.2.3 XZ cross sections

The XZ cross sections were taken 25 m in from the side of the domain, or 20 m in from the rabbit loop back.

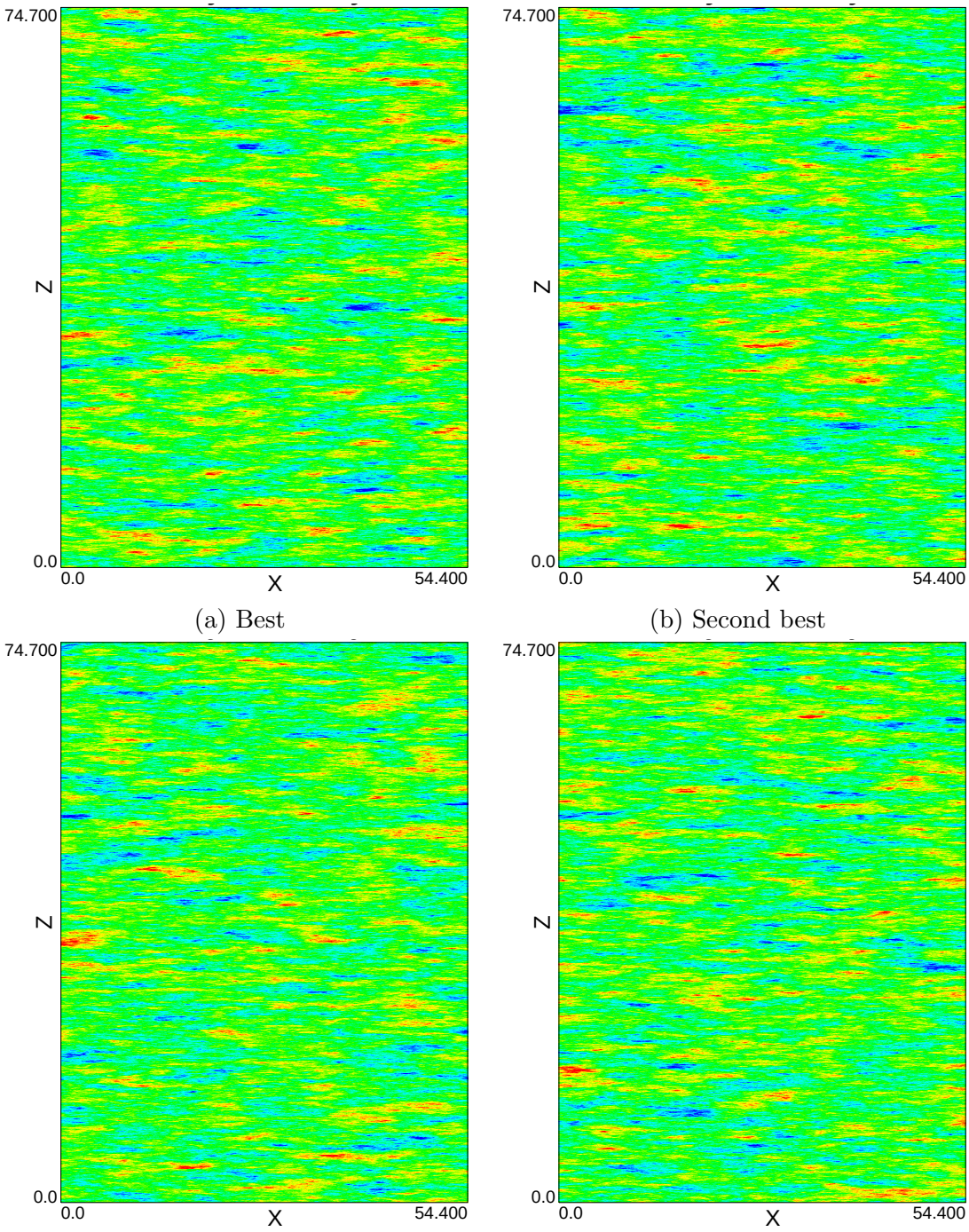

(a) Best

(b) Second best

(c) Third best

(d) Fourth best

Figure I.4

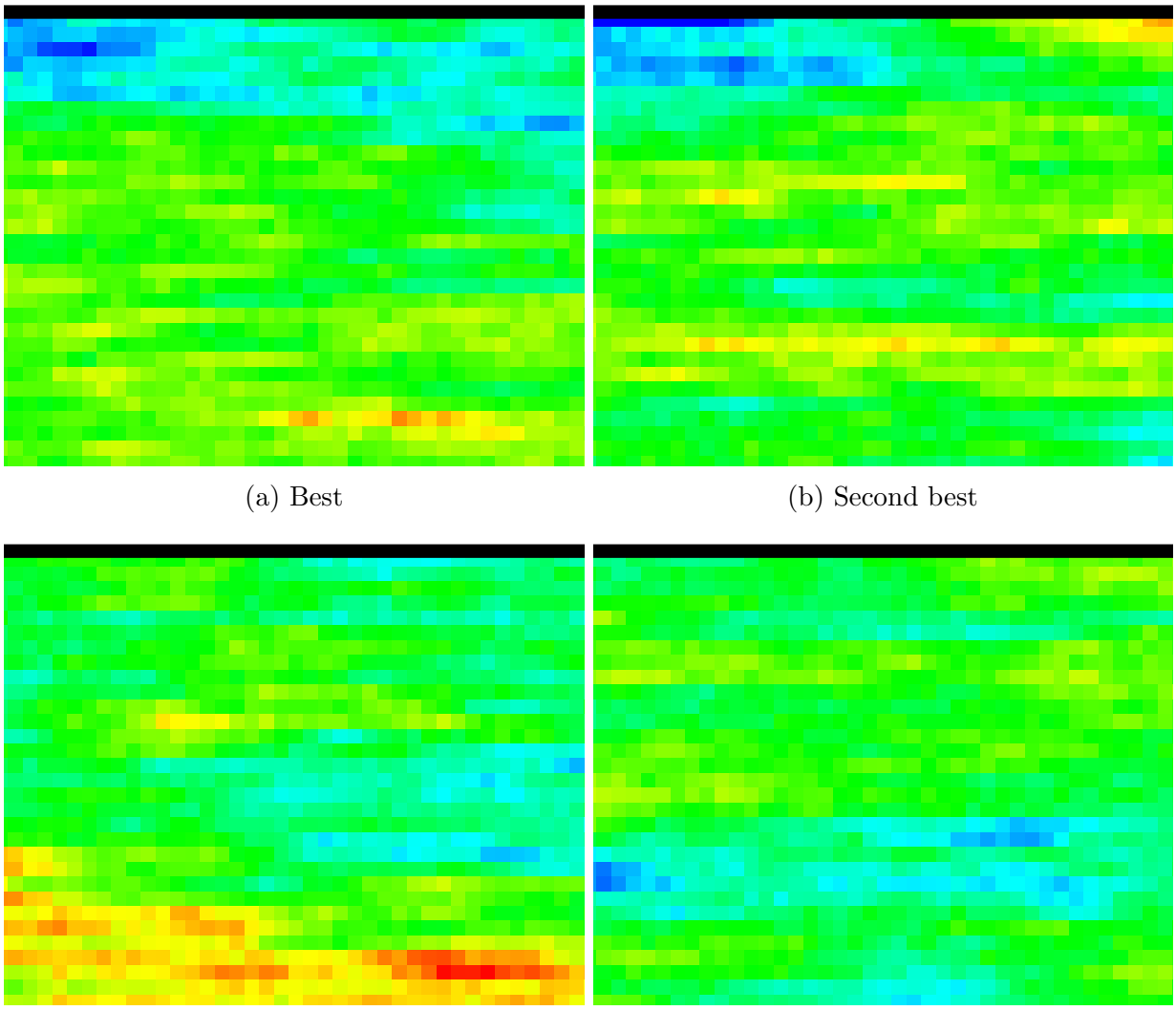

(a) Best

(b) Second best

(c) Third best

(d) Fourth best

Figure I.5

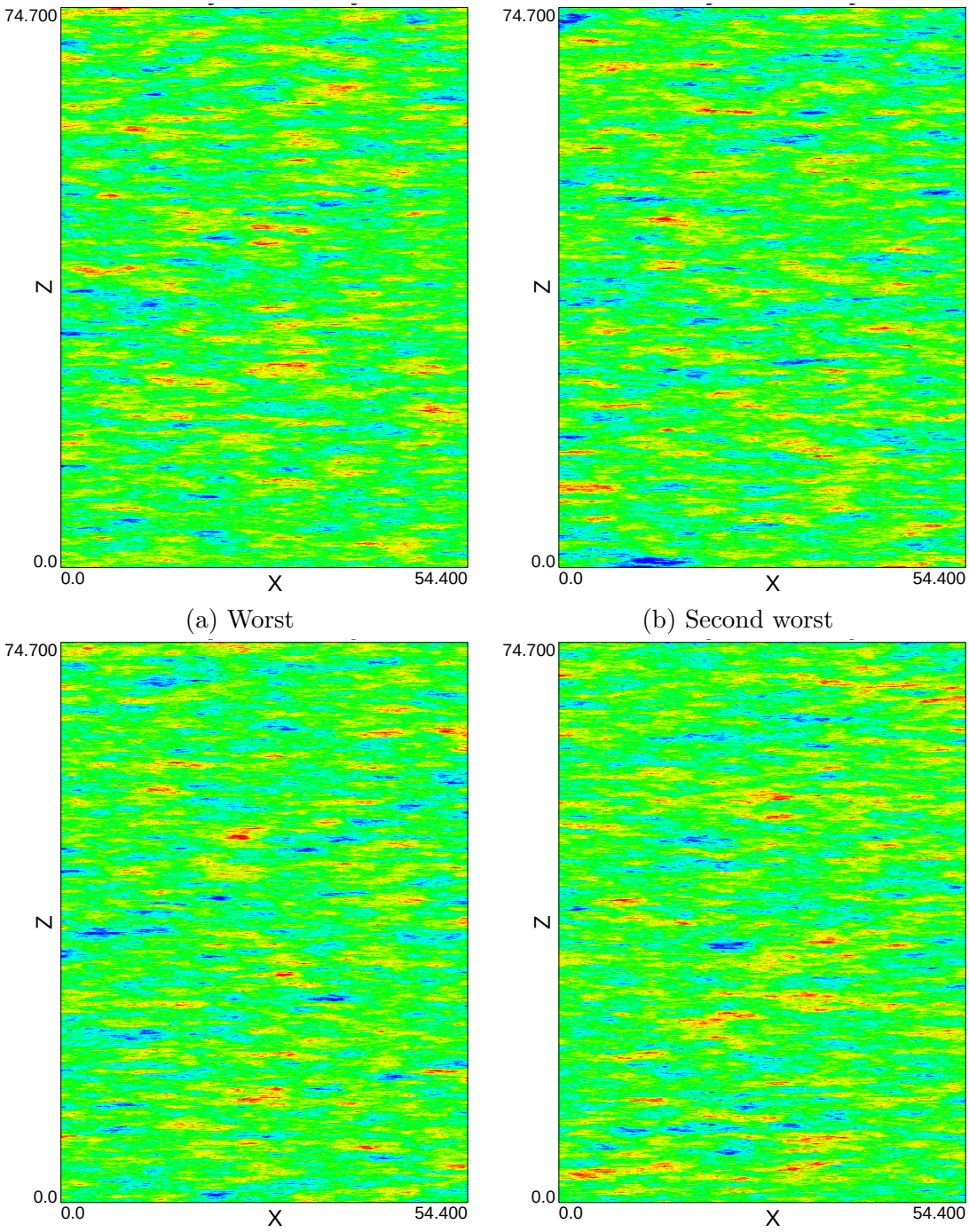

(a) Worst

(b) Second worst

(c) Third worst

(d) Fourth worst

Figure I.6

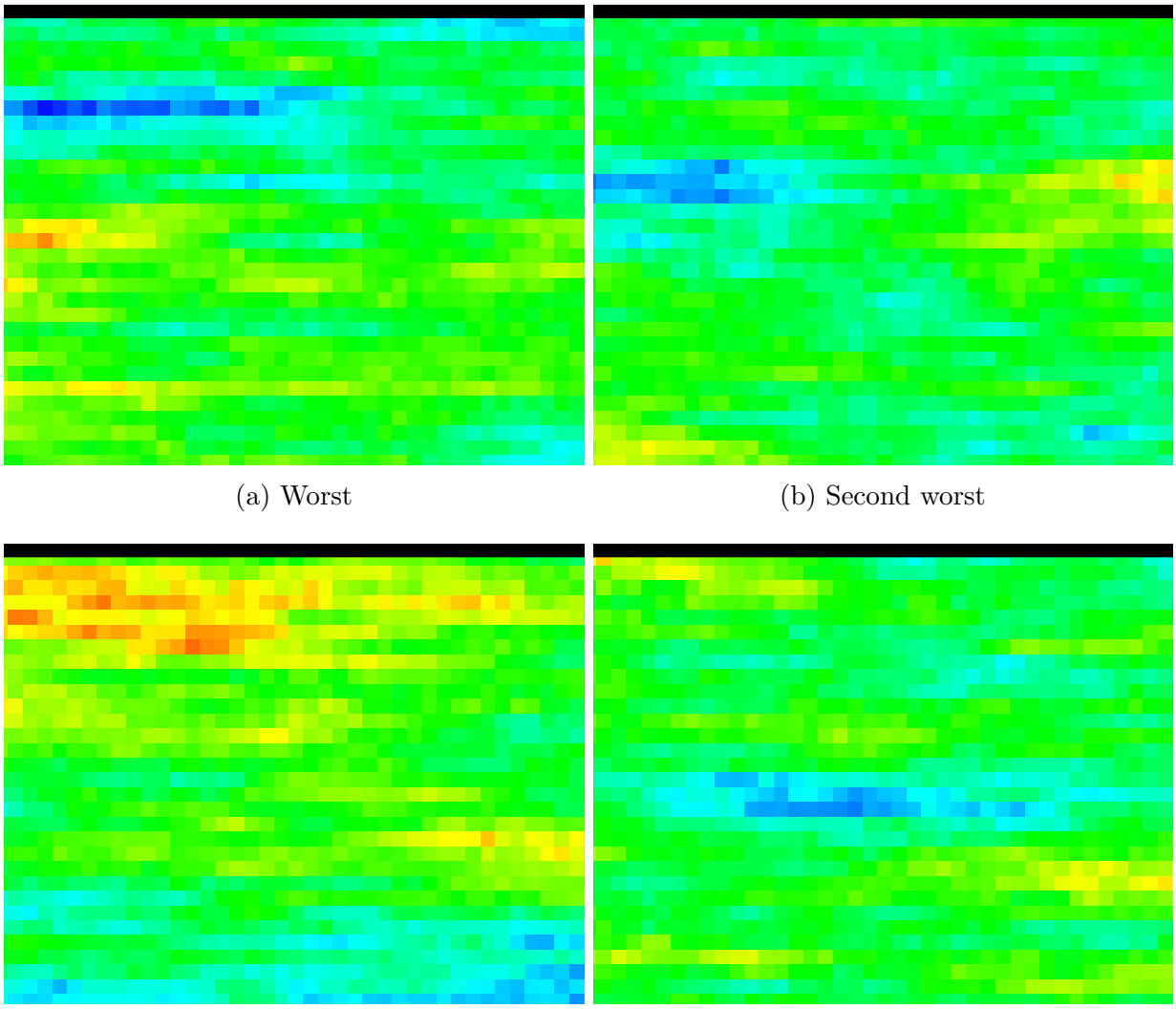

(a) Worst

(b) Second worst

(c) Third worst

(d) Fourth worst

Figure I.7: Enlarged XZ cross sections. The GLHE is situated in approximately the center of these cross sections vertically horizontally. The width of the GLHE is approximately half the width of each figure.

I.3 Heterogeneity Depth Analysis

I.3.1 3.0 m below ground surface

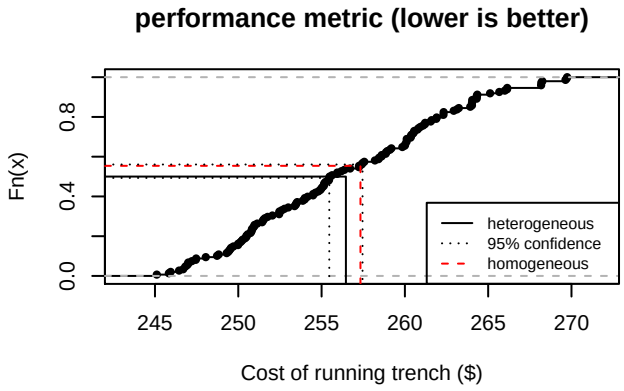

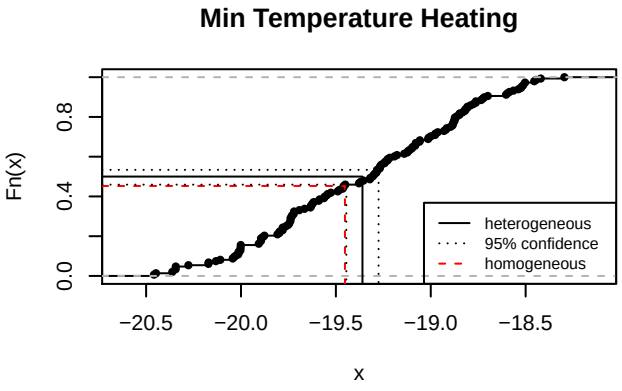

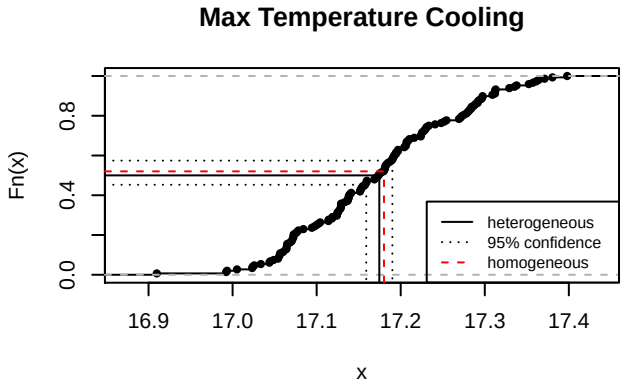

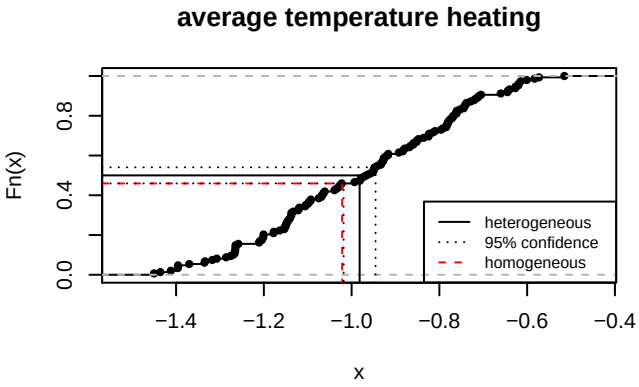

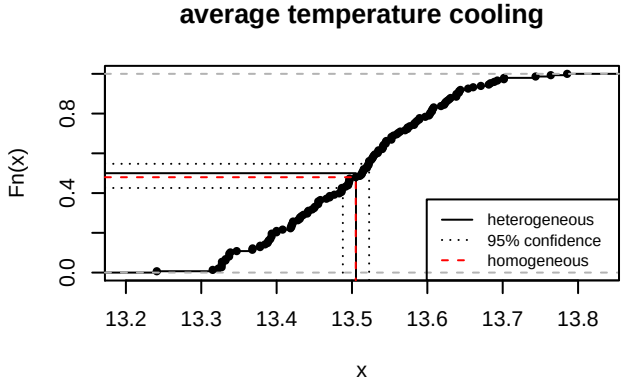

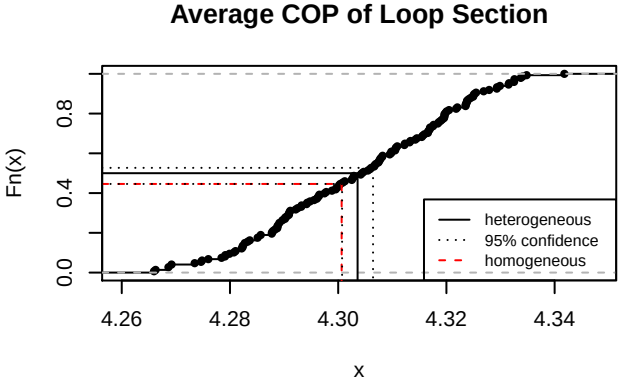

I.3.2 2.0 m below ground surface

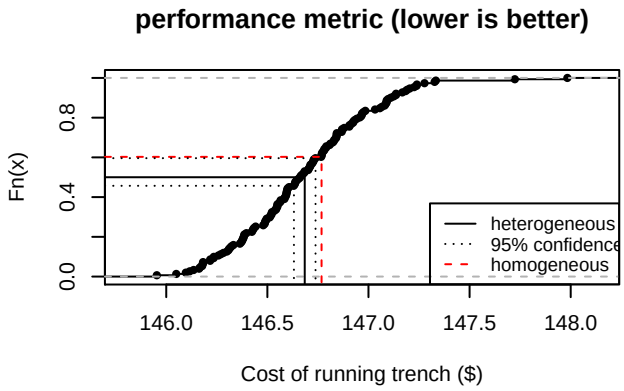

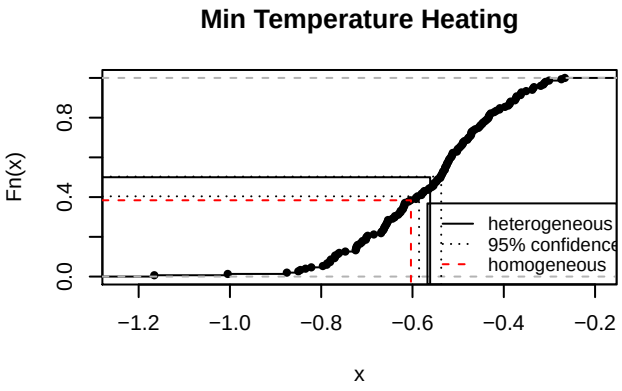

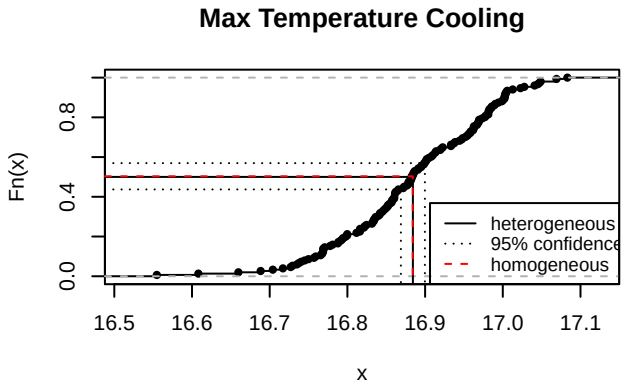

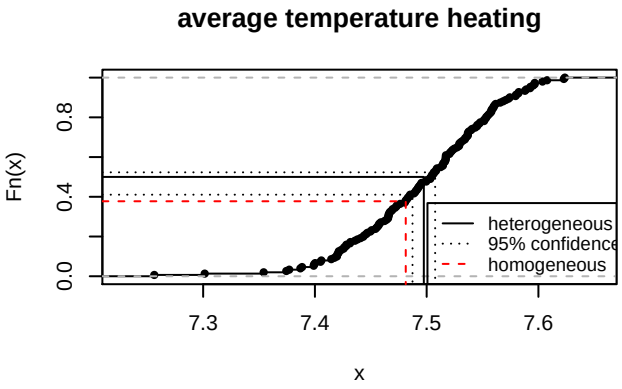

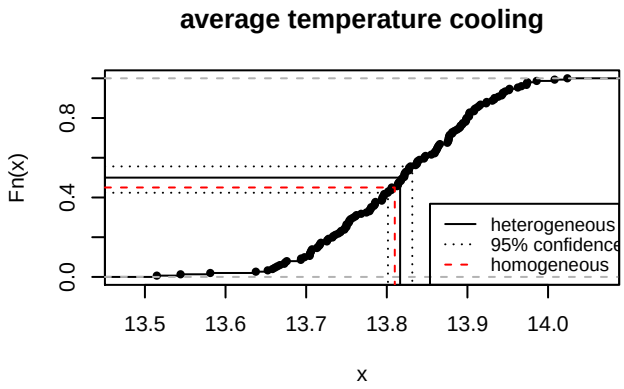

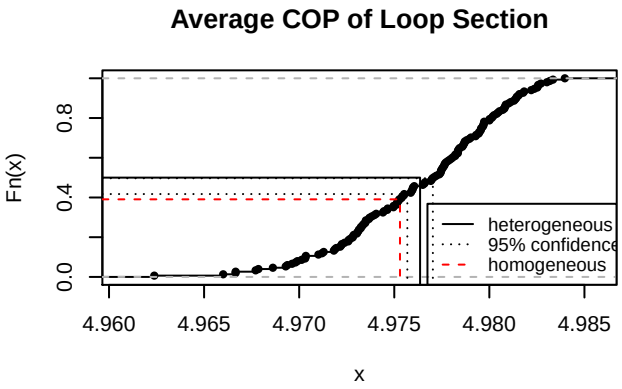

I.3.3 1.0 m below ground surface

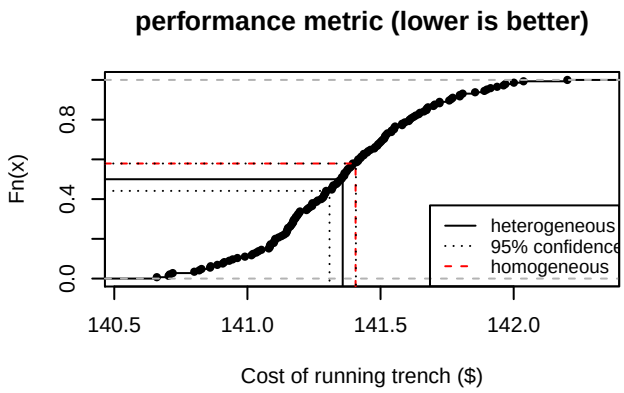

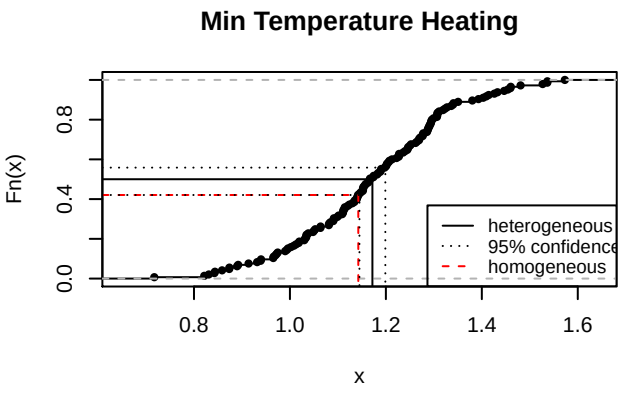

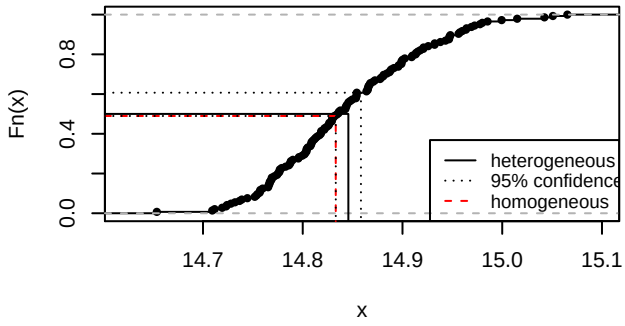

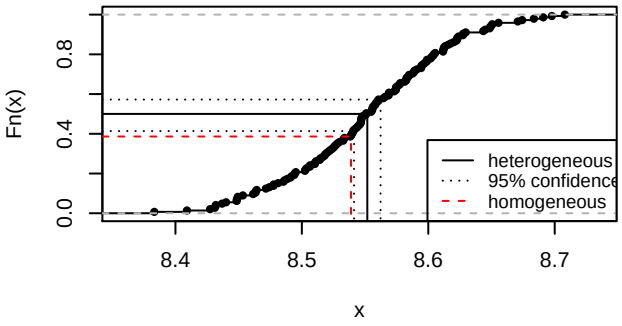

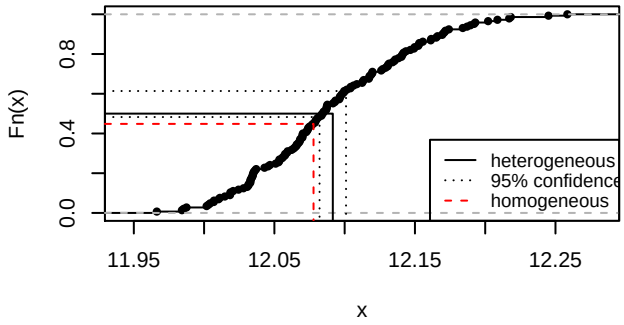

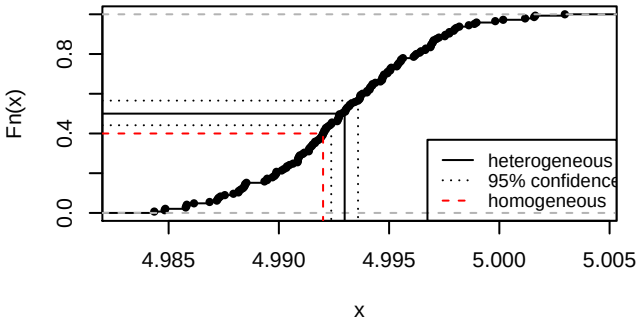

I.4 Heterogeneity Correlation Lengths

I.4.1 Double correlation length

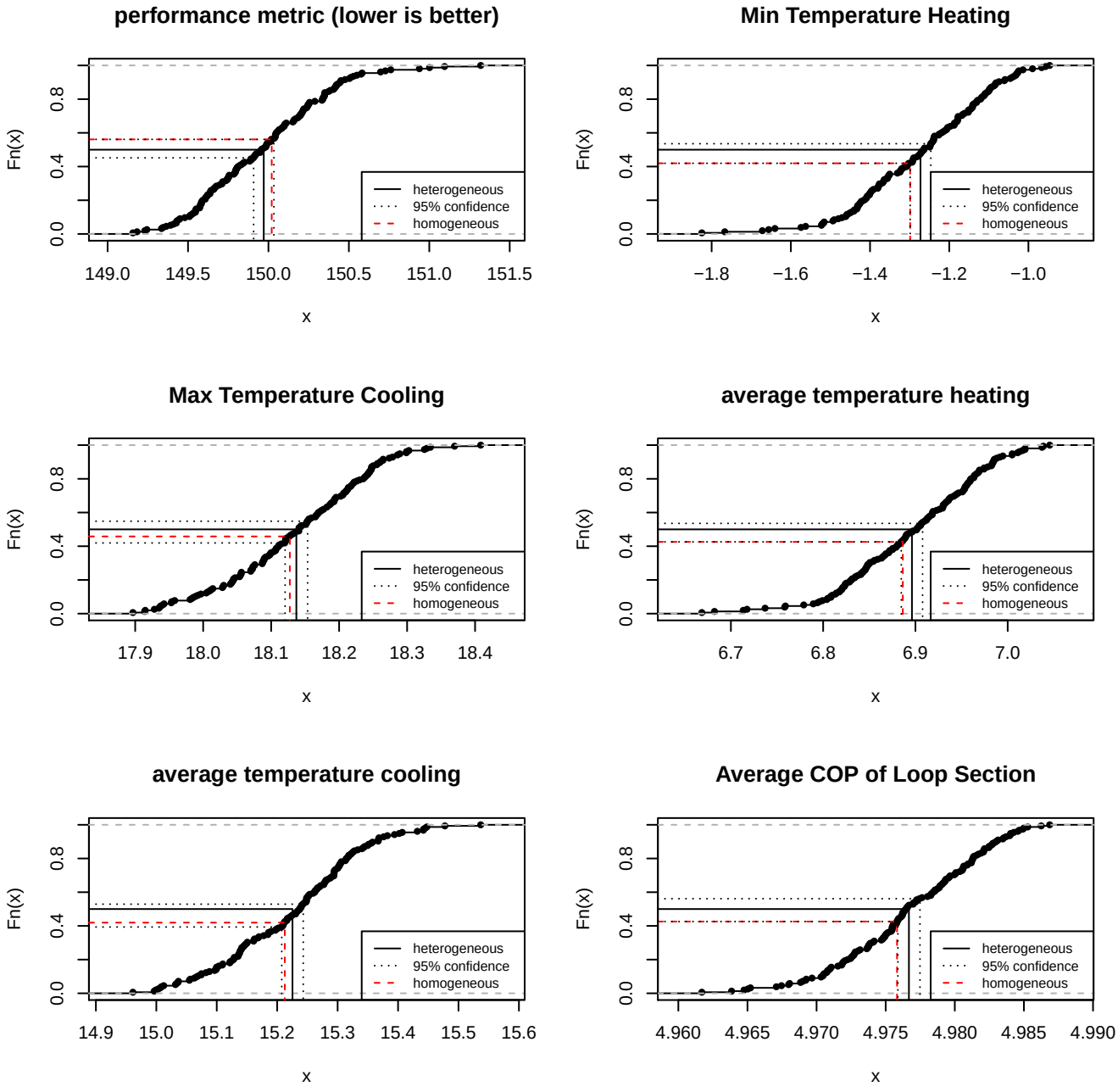

I.4.2 Normal correlation length

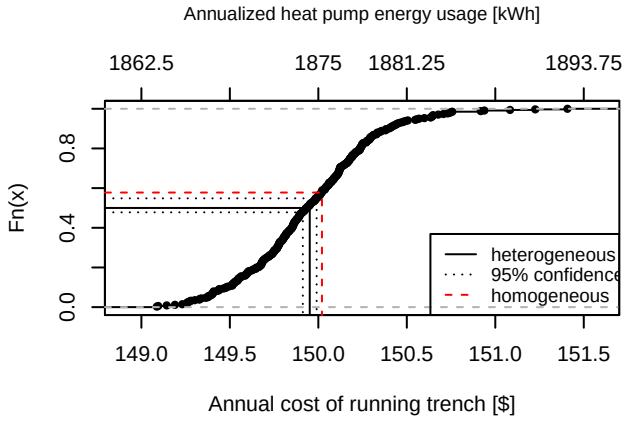

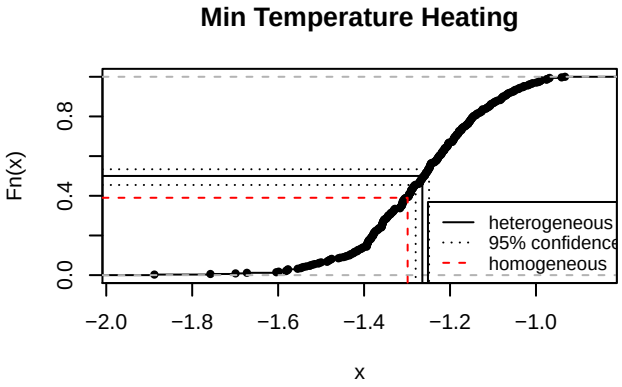

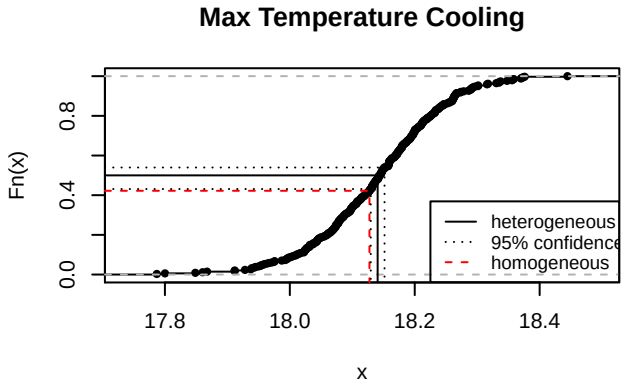

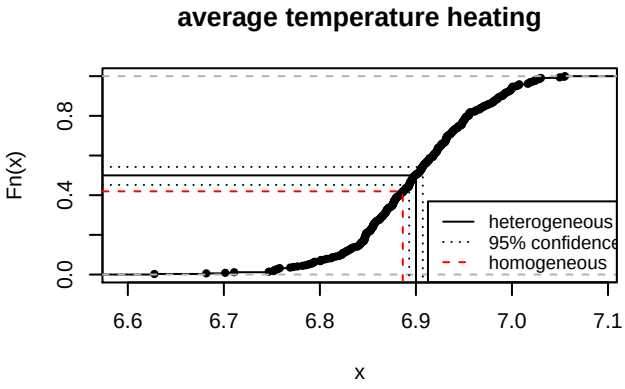

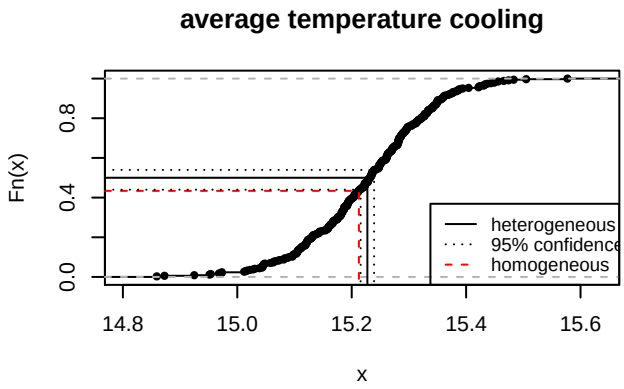

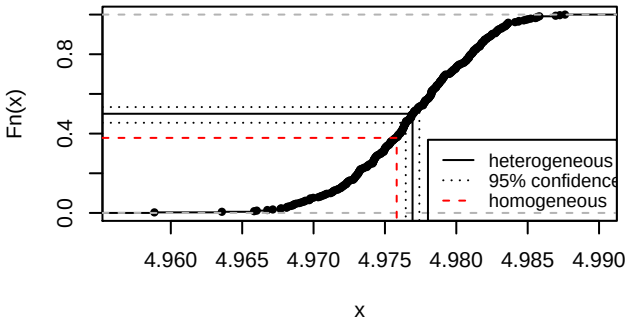

I.4.3 Half correlation length

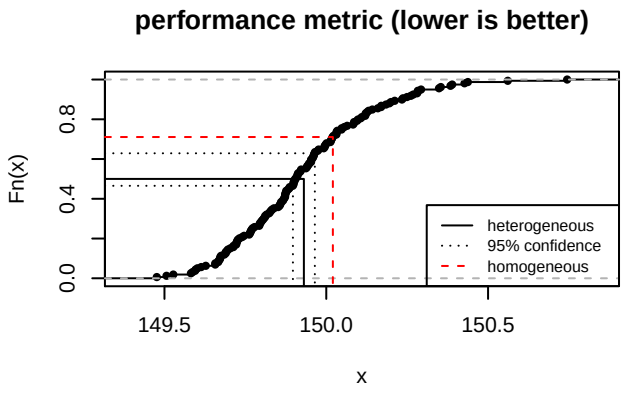

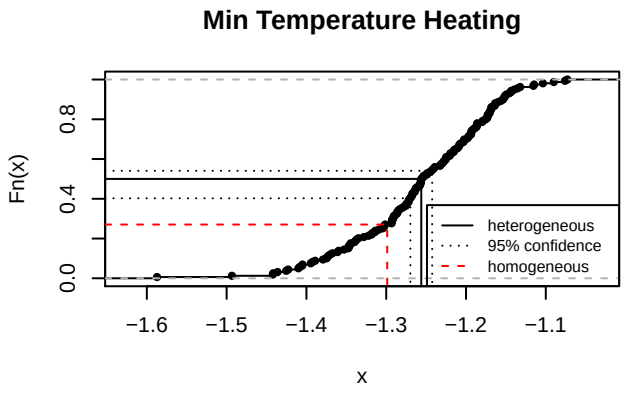

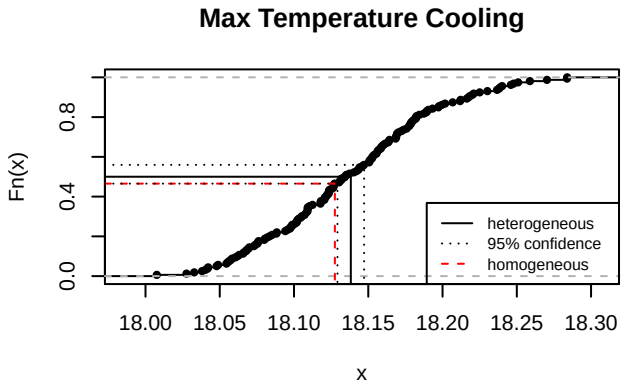

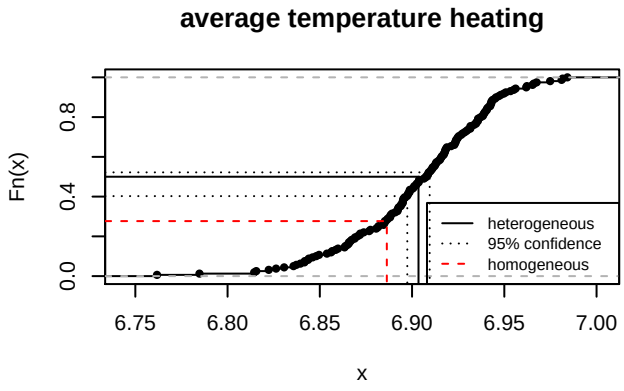

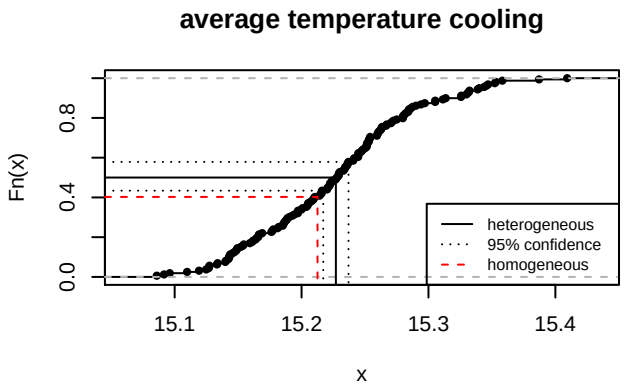

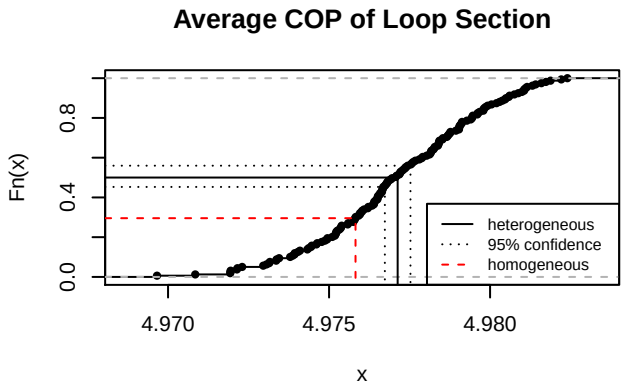

I.4.4 Zero correlation length

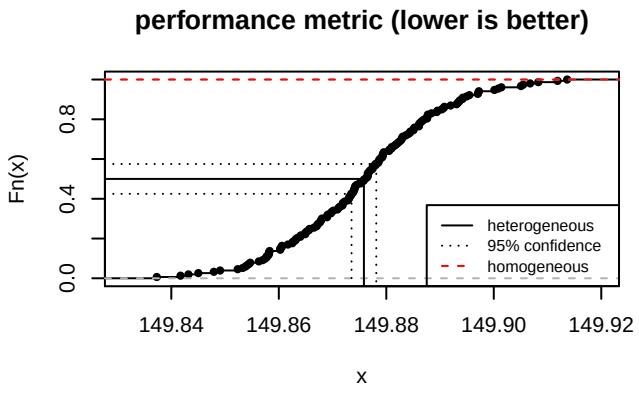

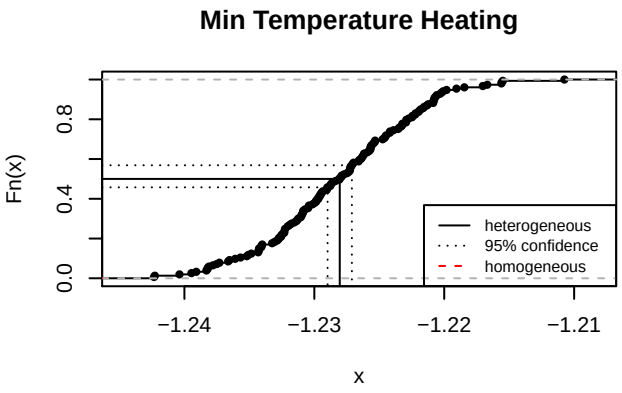

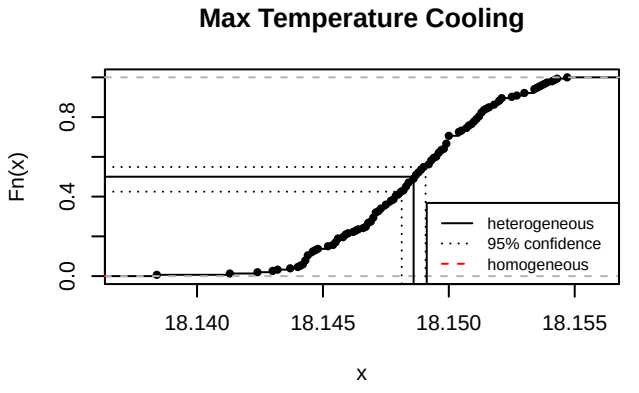

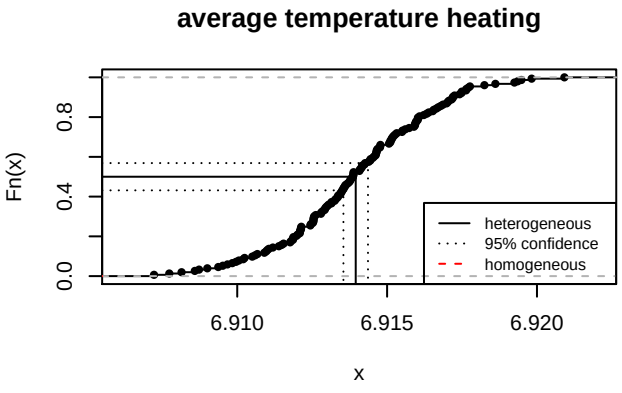

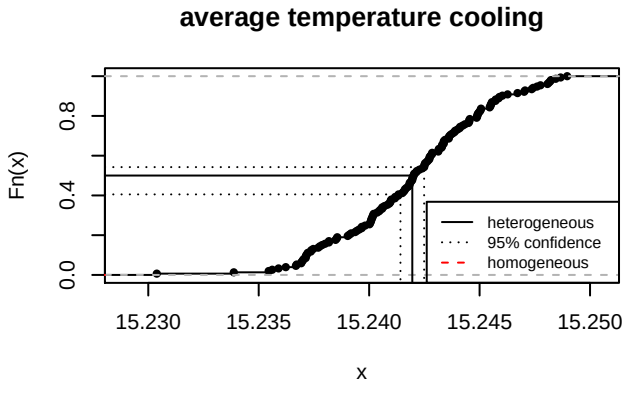

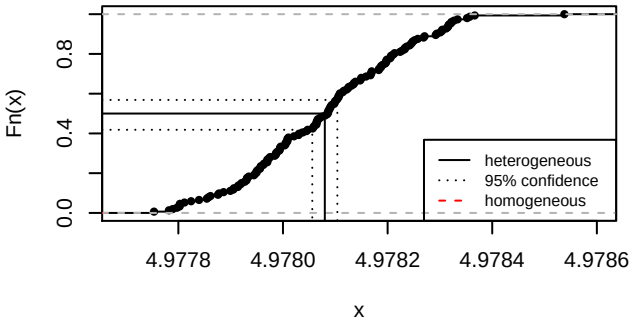

I.5 Different mean conductivities

I.5.1 1.5 W/m K thermal conductivity

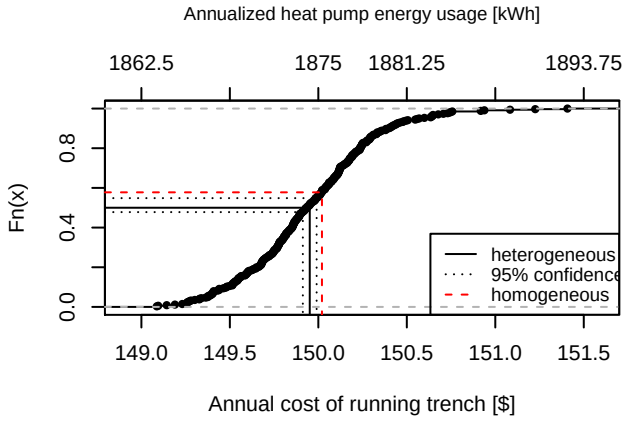

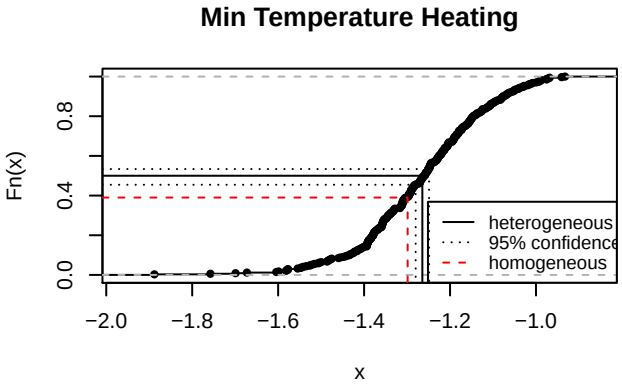

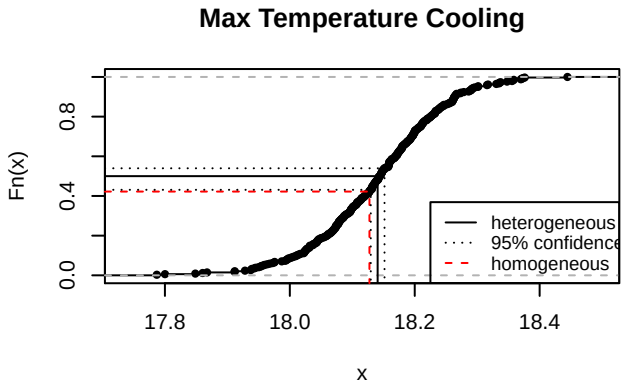

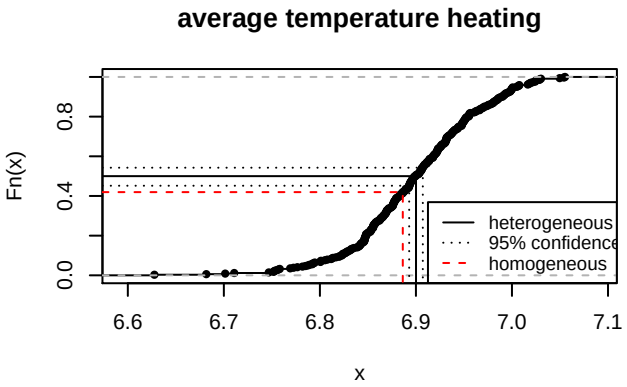

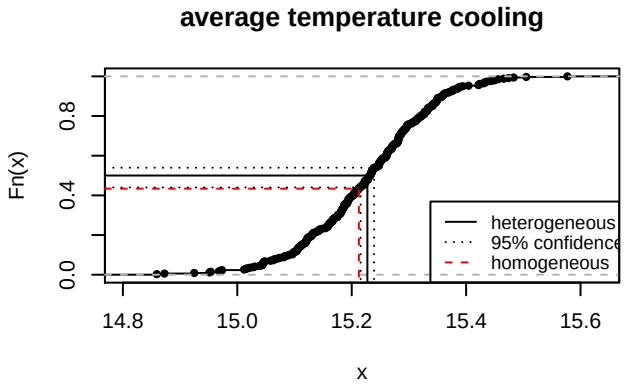

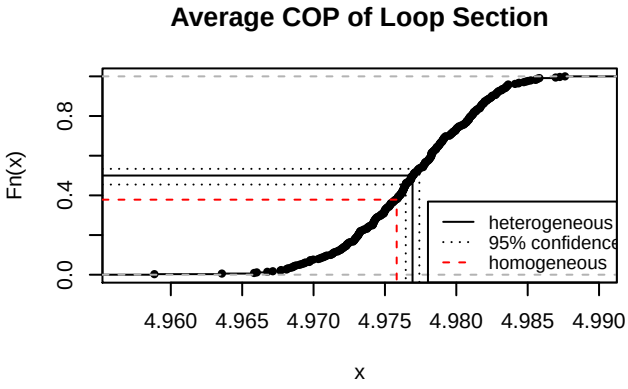

I.5.2 1.25 W/m K thermal conductivity

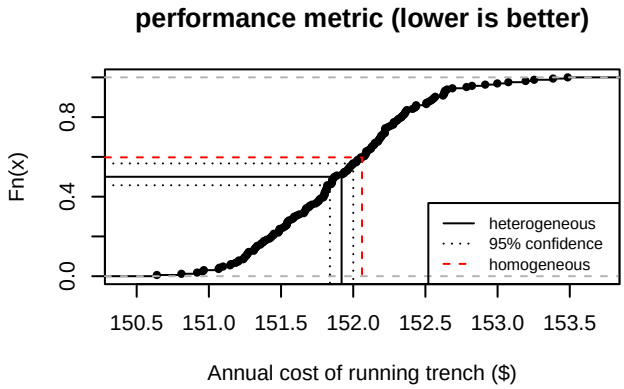

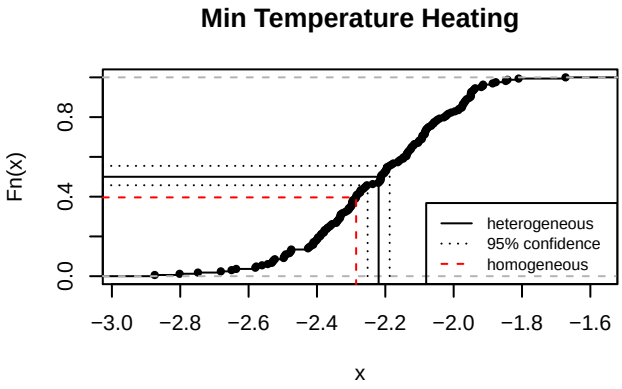

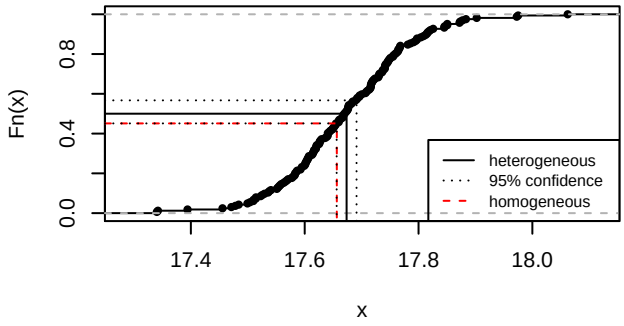

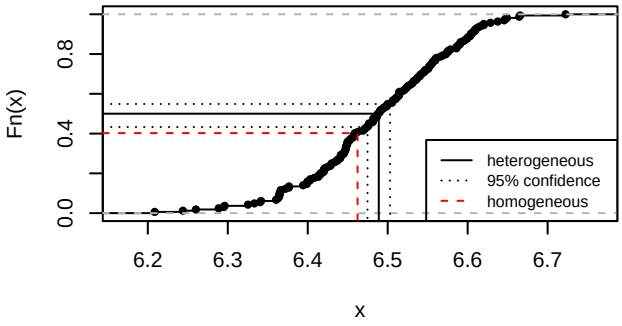

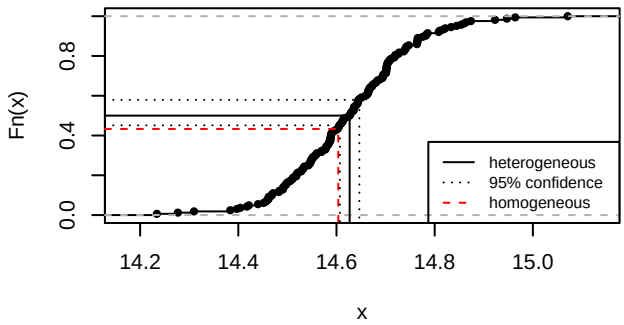

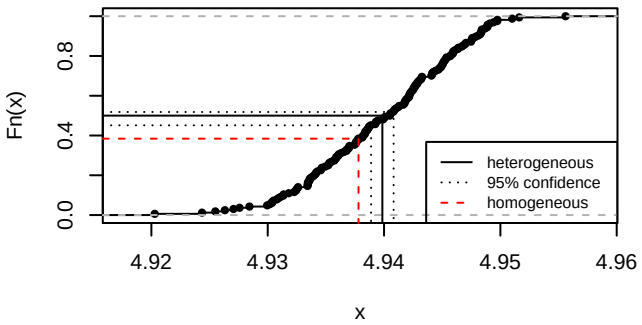

I.5.3 1.0 W/m K thermal conductivity

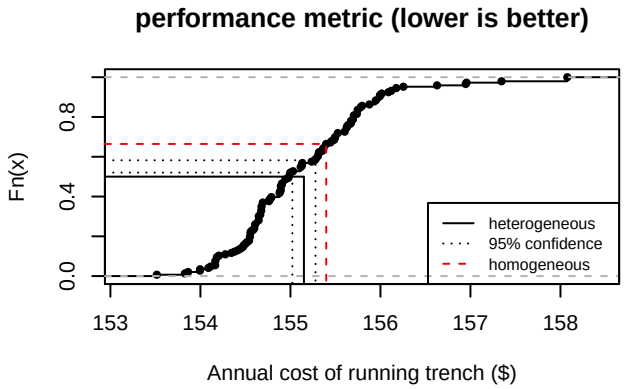

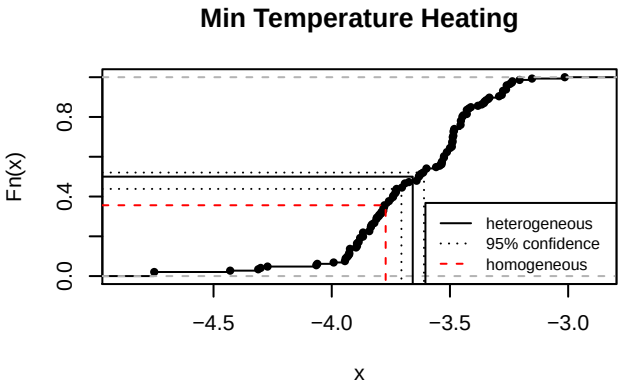

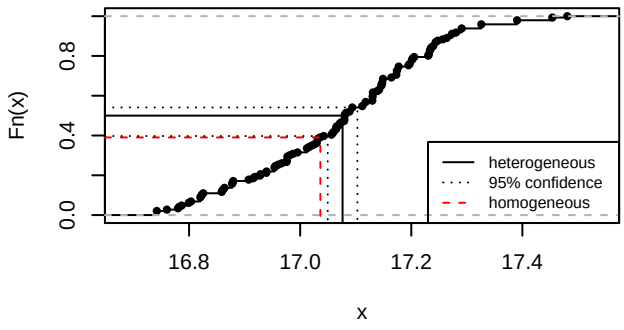

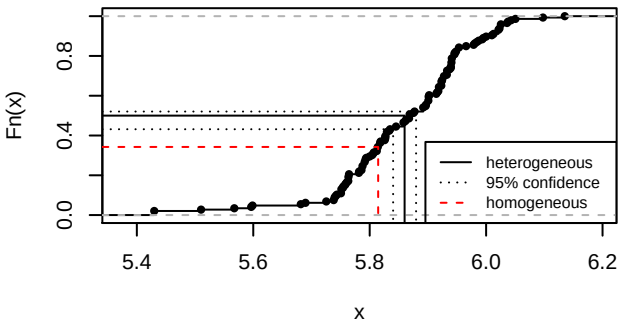

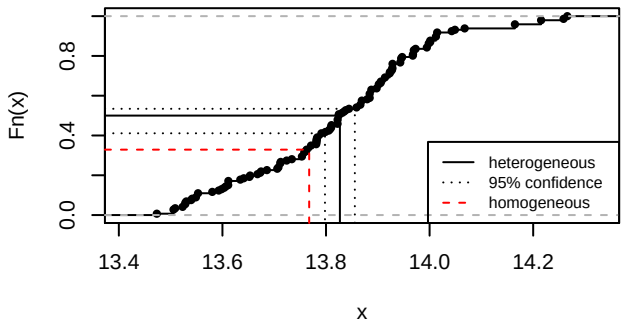

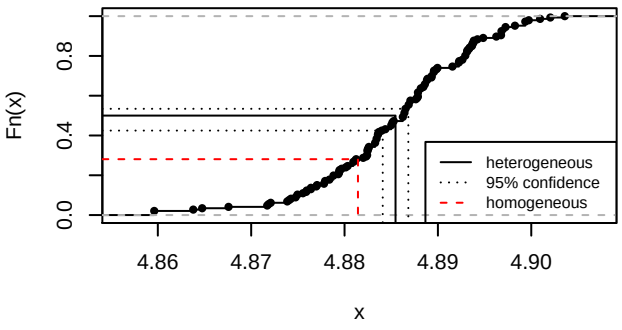

I.5.4 0.75 W/m K thermal conductivity

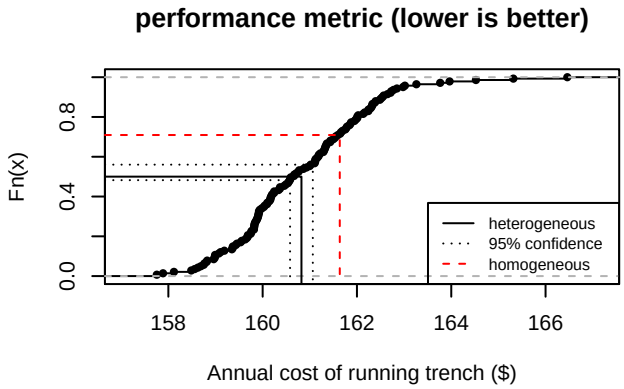

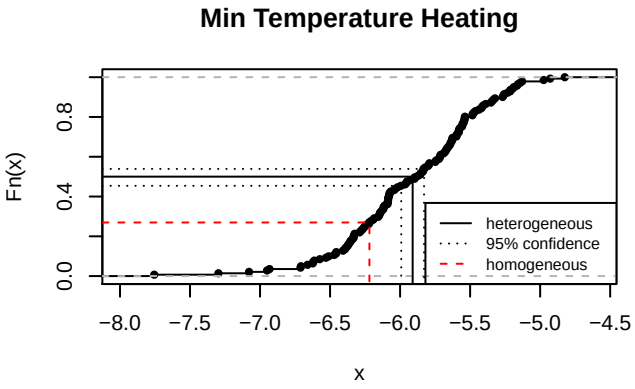

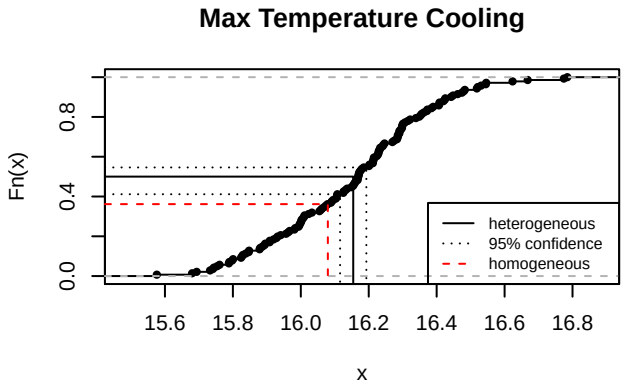

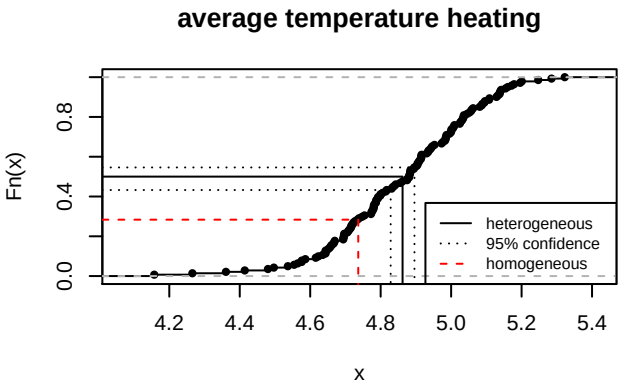

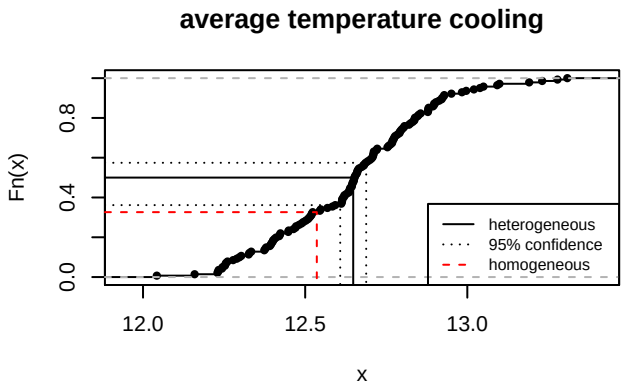

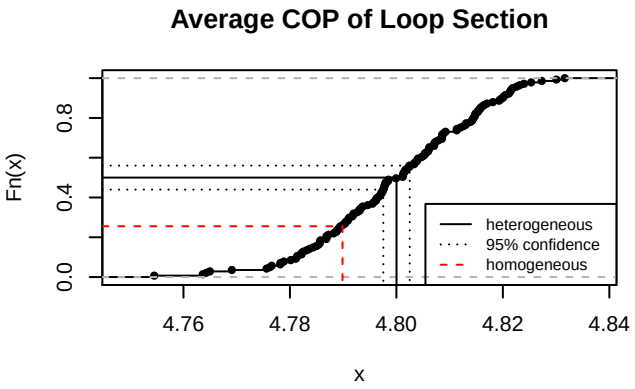

I.5.5 0.5 W/m K thermal conductivity

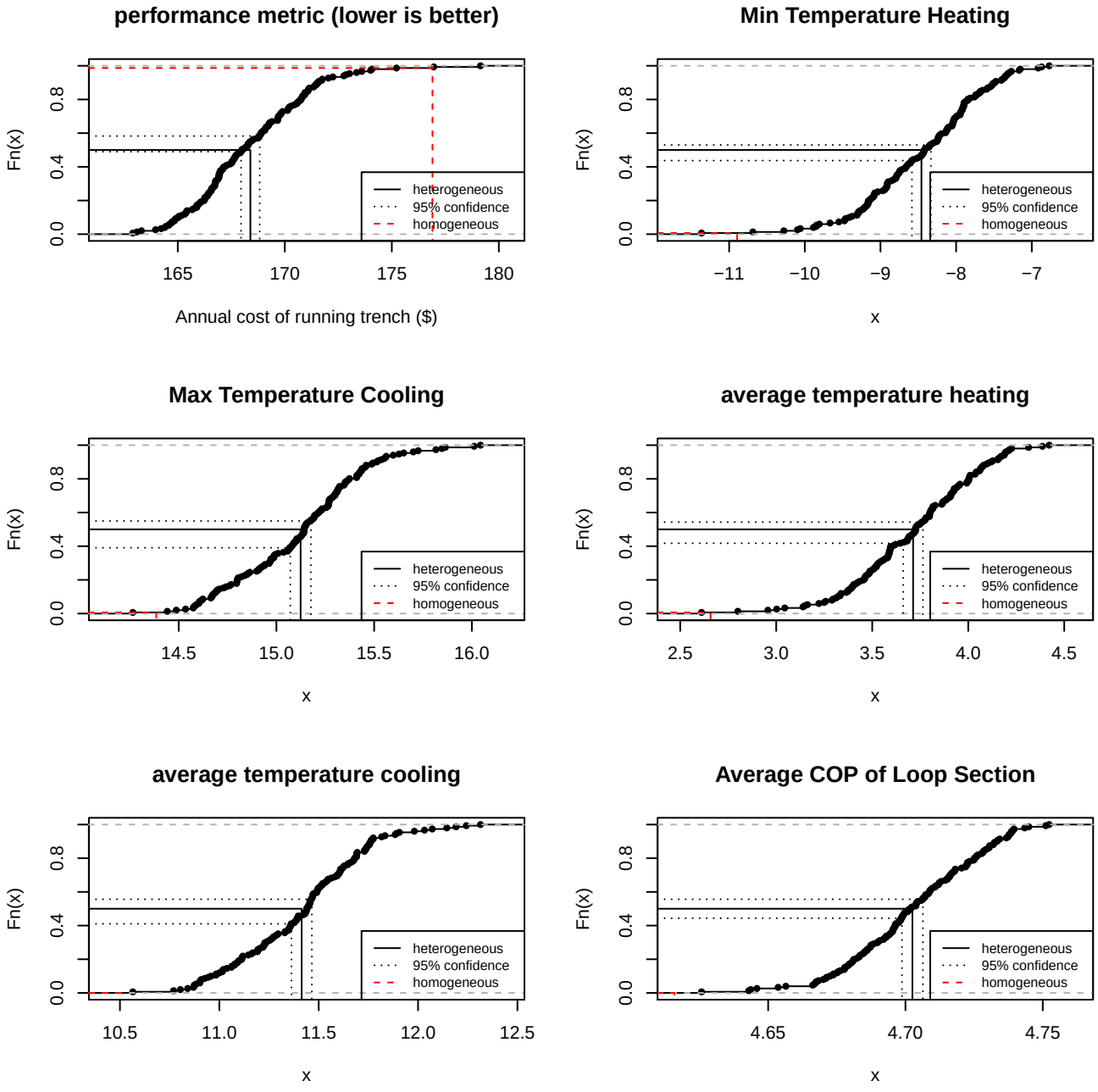

I.6 Different standard deviations

I.6.1 0.6 W/m K standard deviation

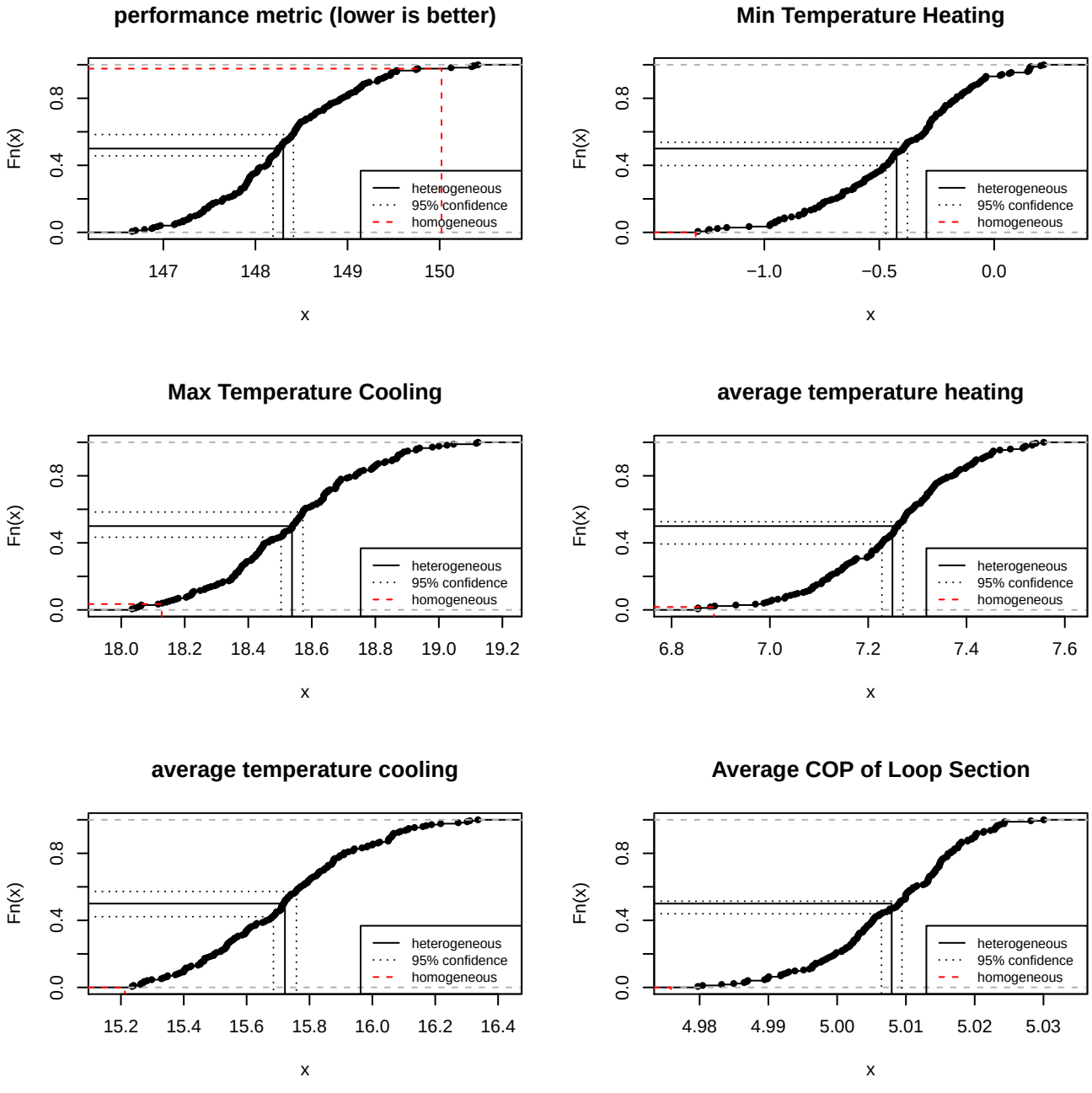

I.6.2 0.4 W/m K standard deviation

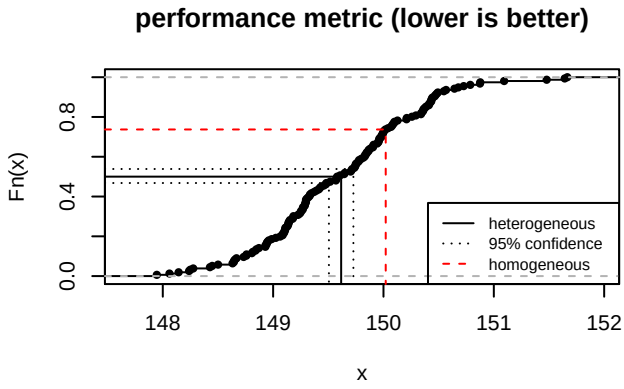

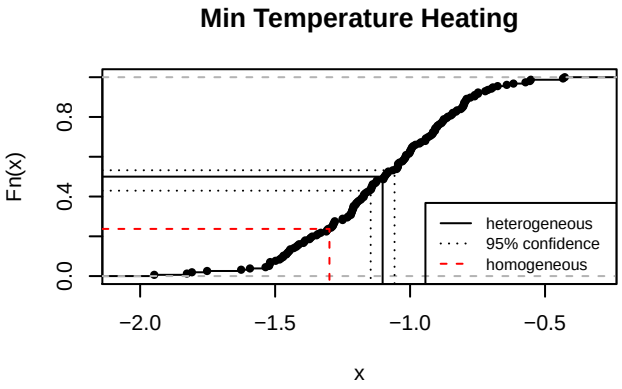

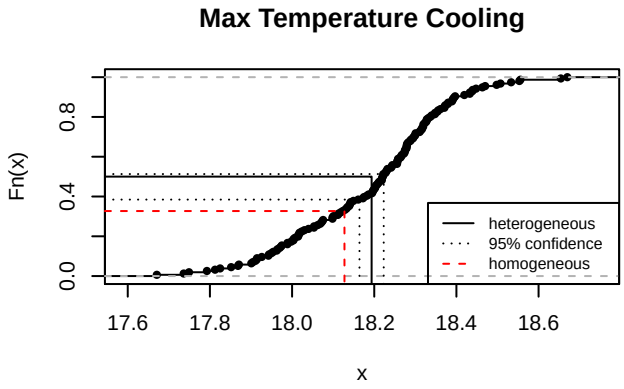

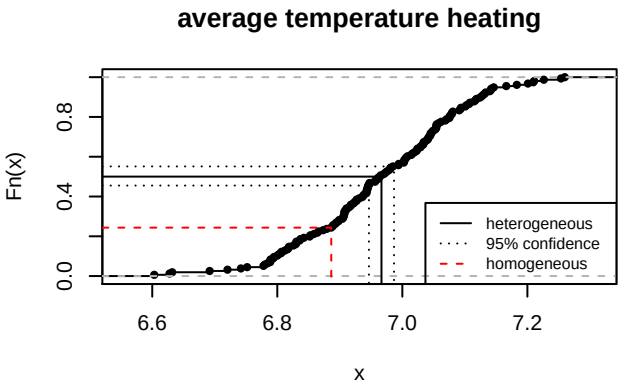

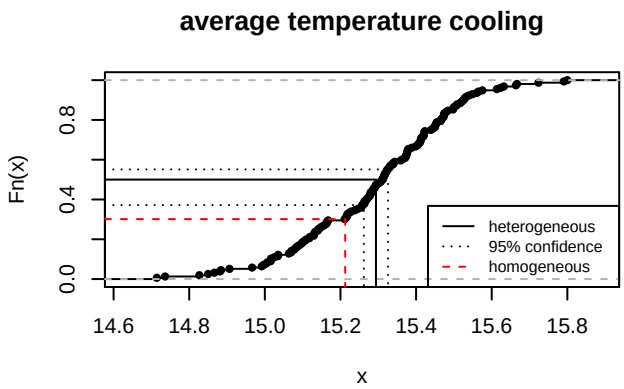

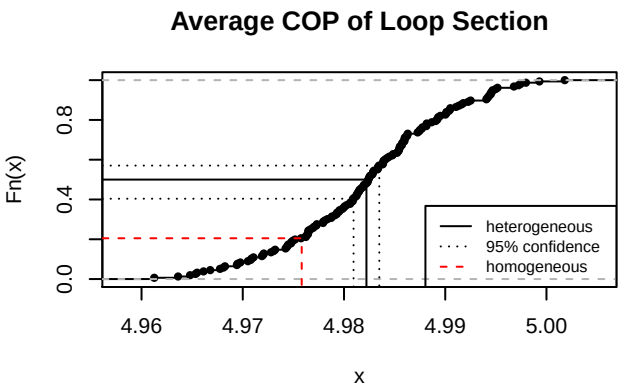

I.6.3 0.1 W/m K standard deviation

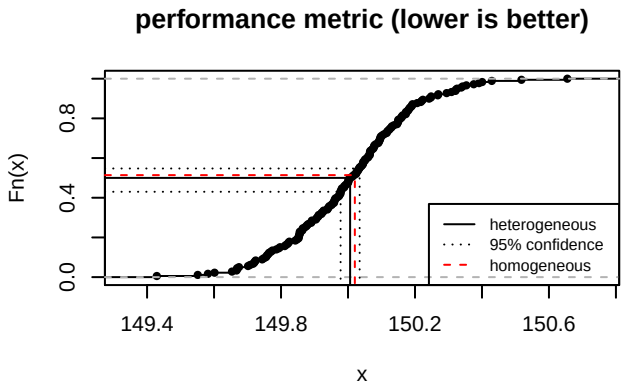

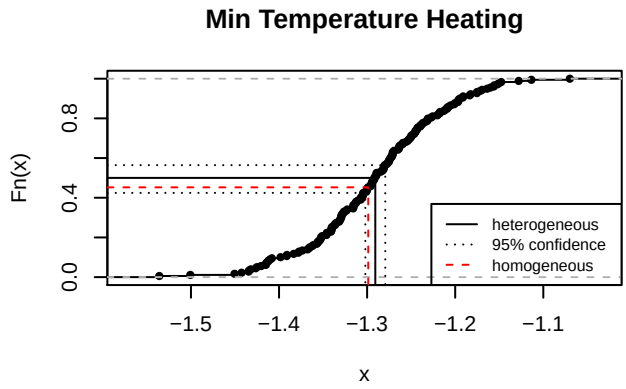

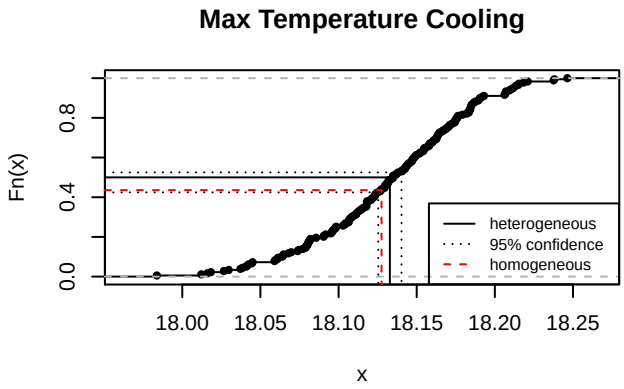

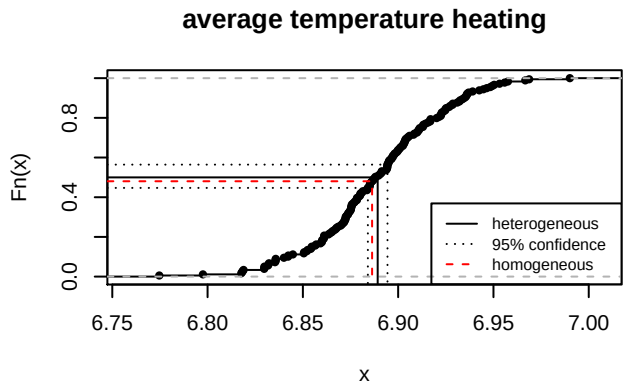

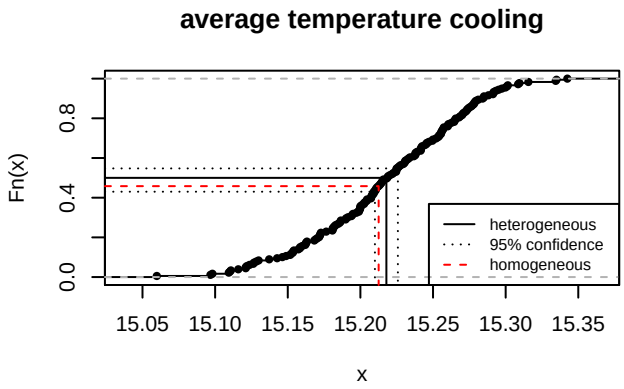

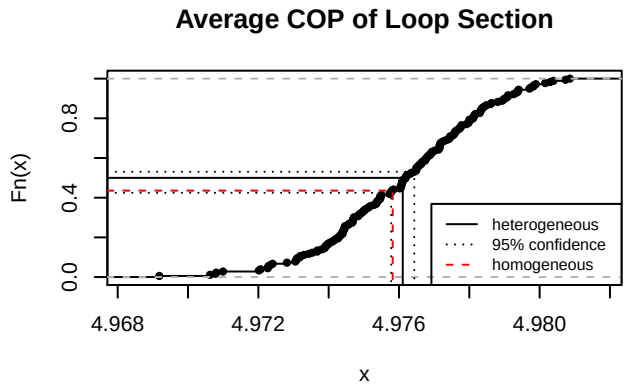

I.7 Pipe spacing in heterogeneous fields

I.7.1 0.3 m pipe spacing

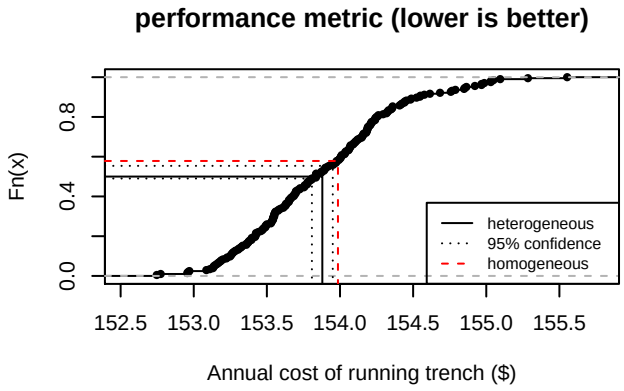

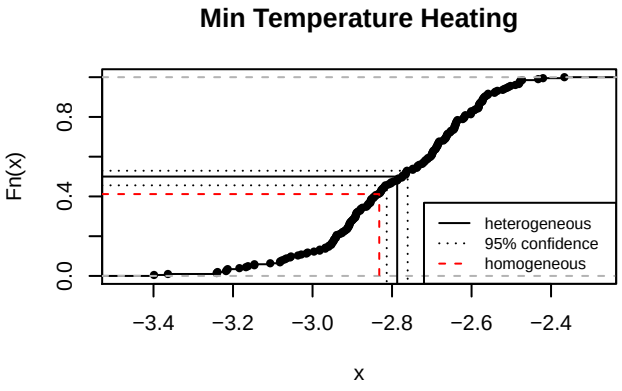

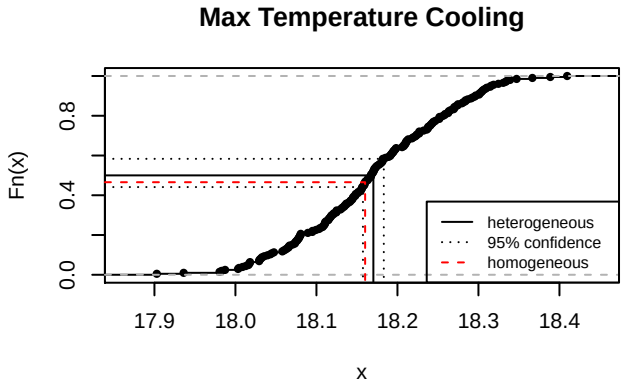

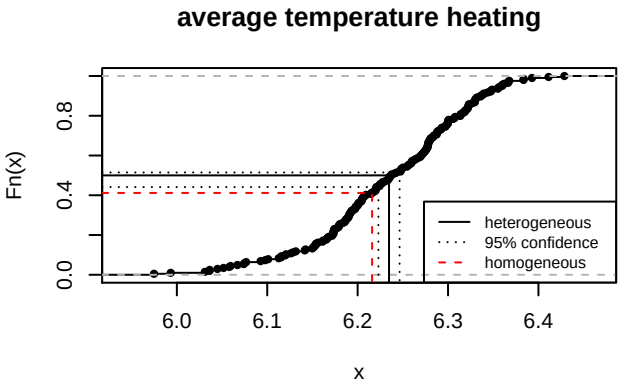

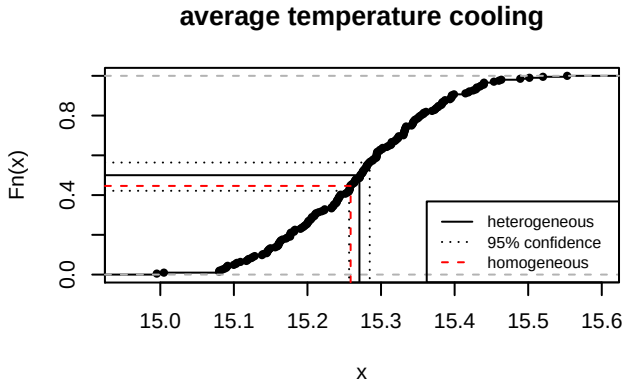

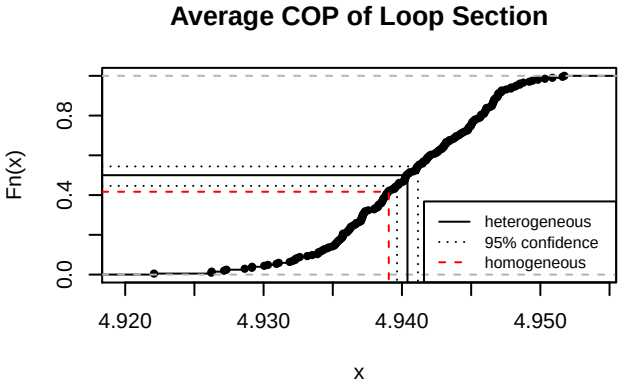

I.7.2 0.4 m pipe spacing

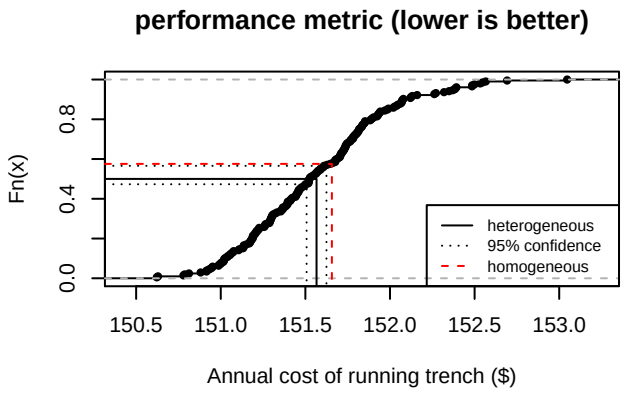

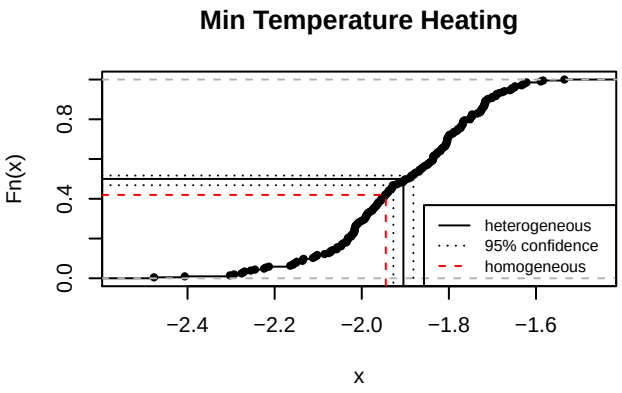

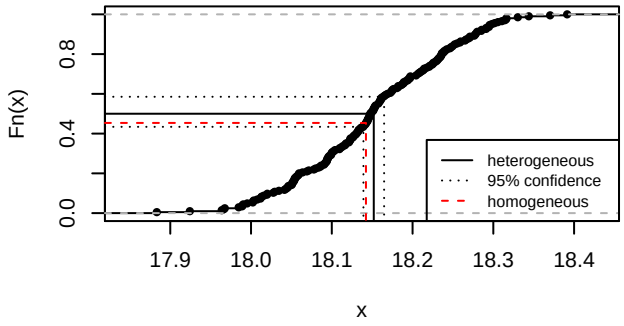

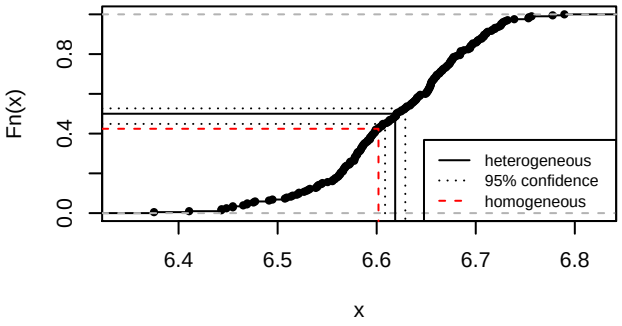

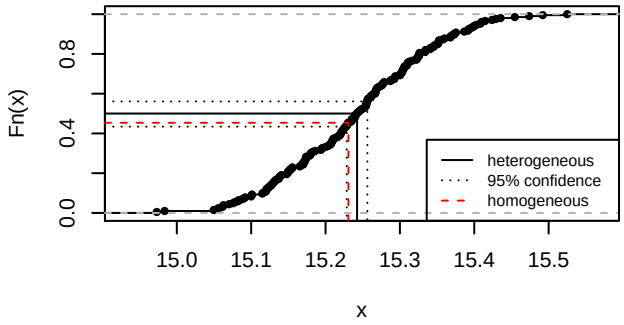

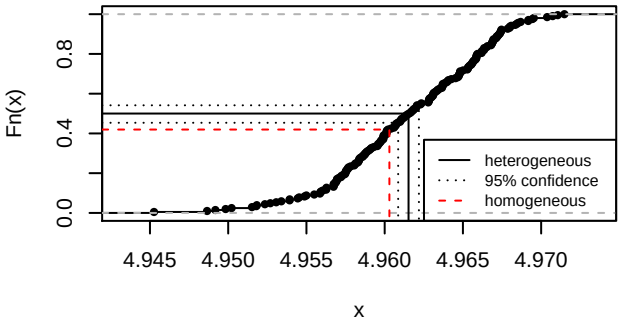

I.8 Pipe loading in heterogeneous fields

I.8.1 125% pipe load

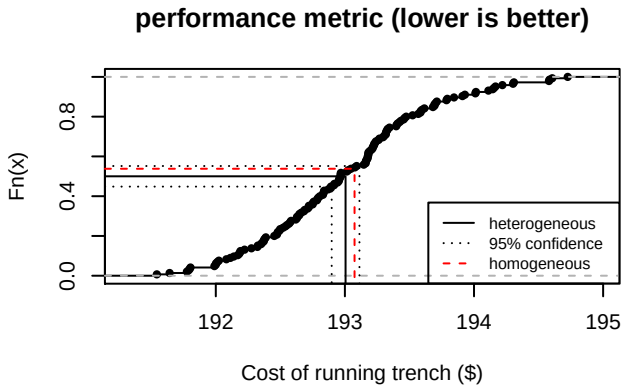

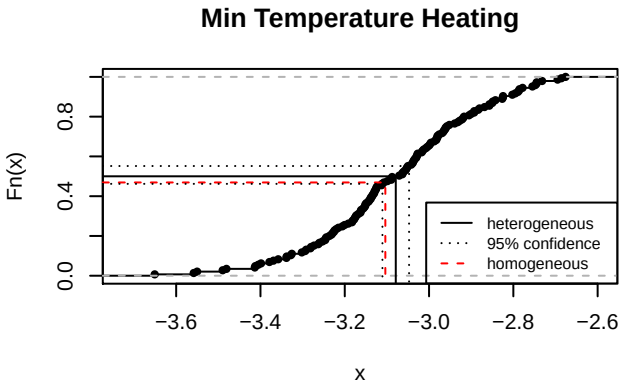

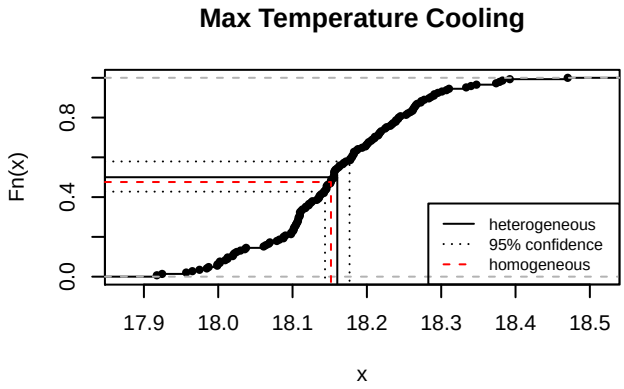

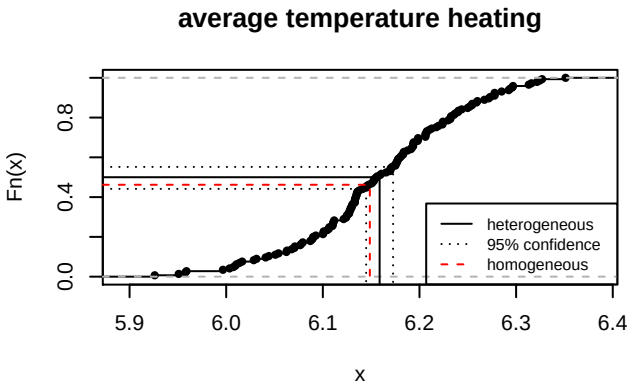

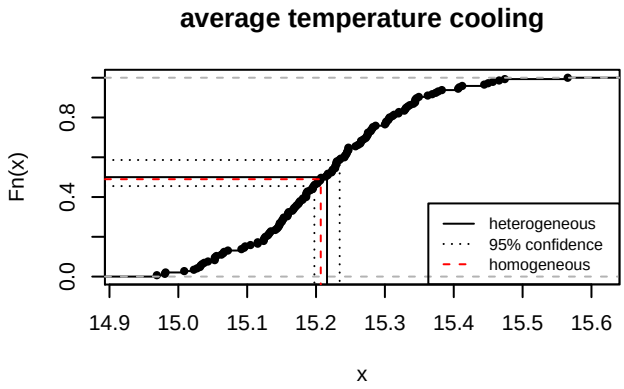

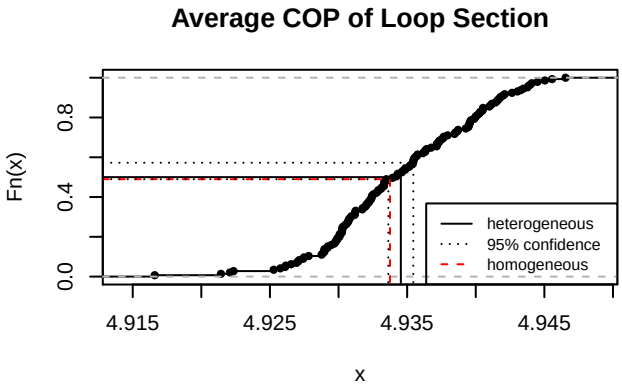

I.8.2 150% pipe load

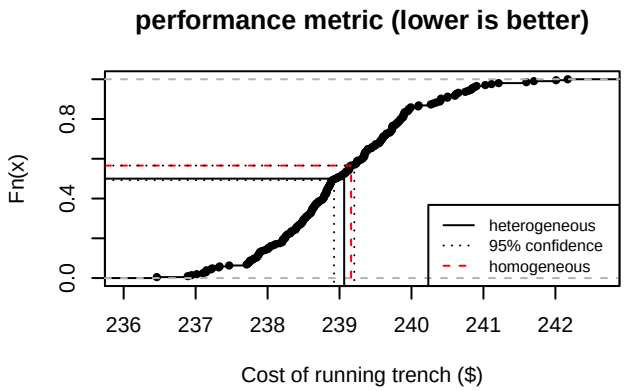

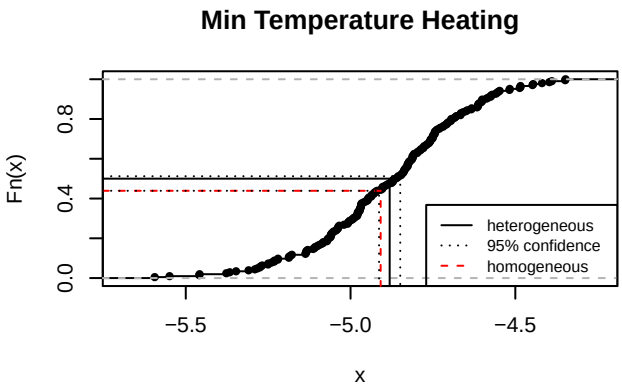

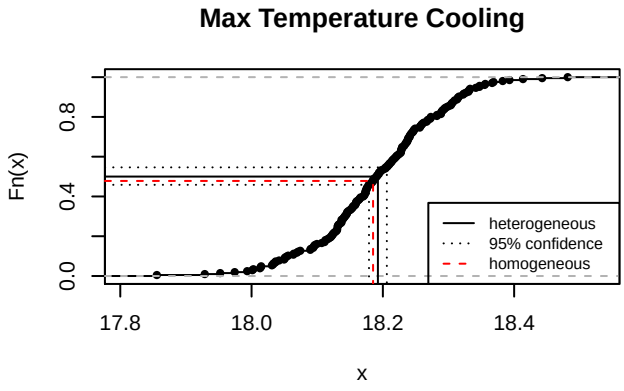

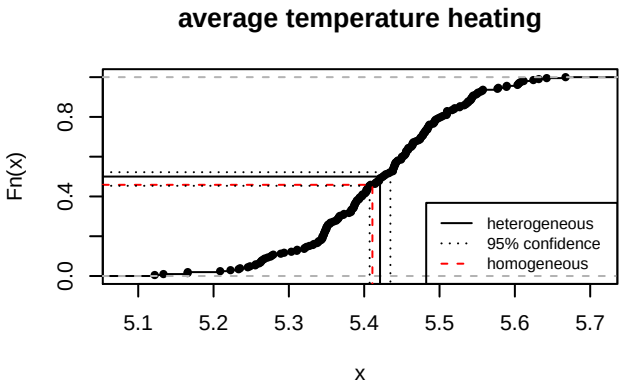

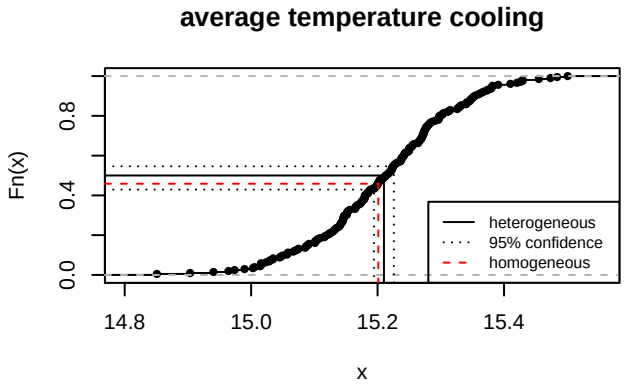

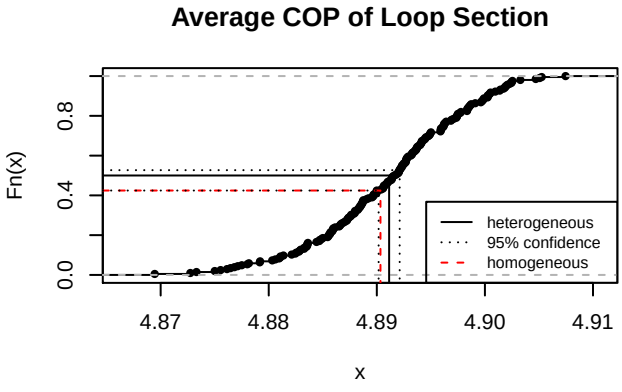

I.8.3 200% pipe load

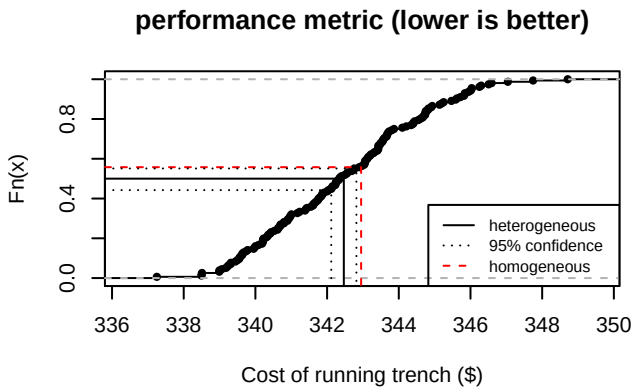

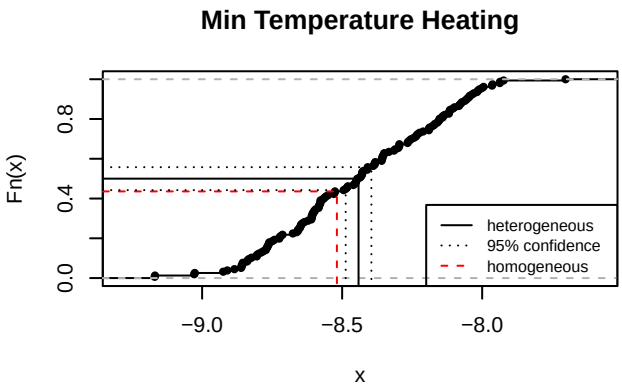

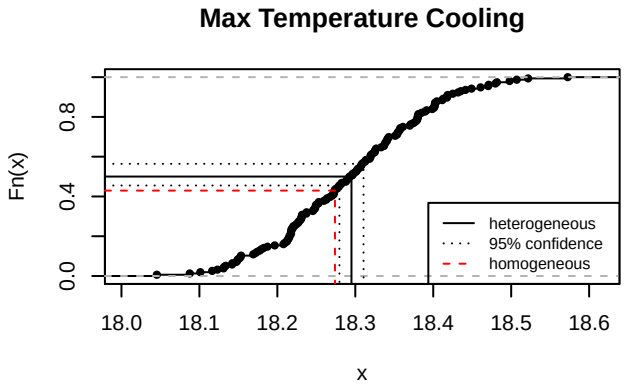

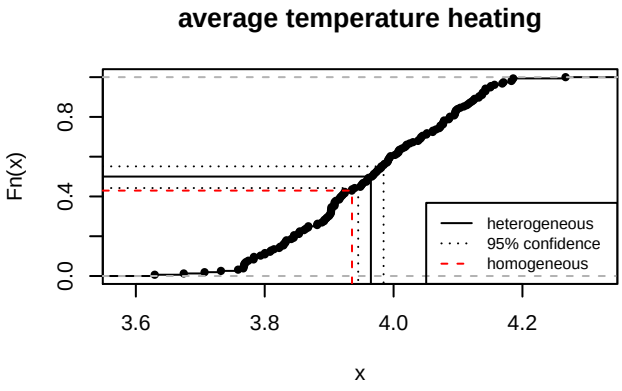

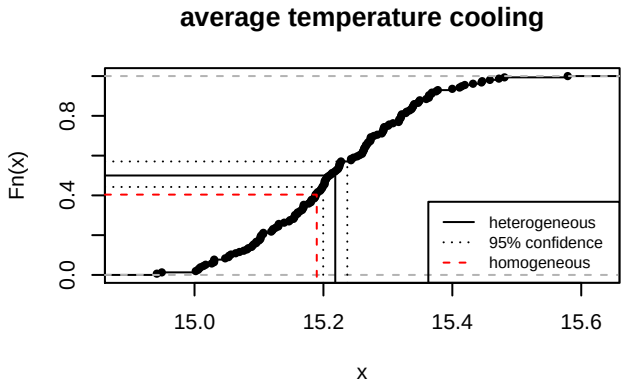

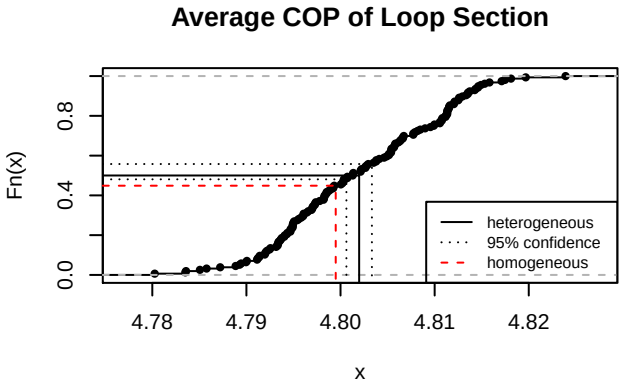

I.9 Multitrench GLHE in heterogeneous fields

I.9.1 Triple trench ECDFs

batch performance of the three pipe system in a heterogeneous field:

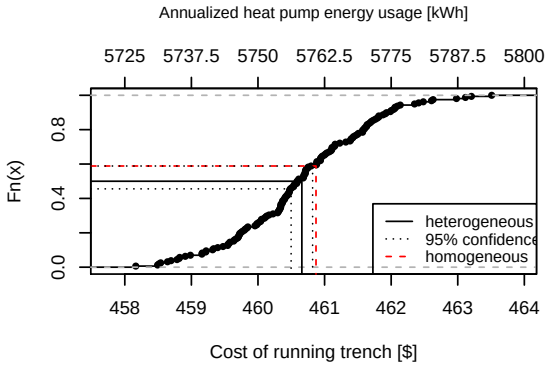

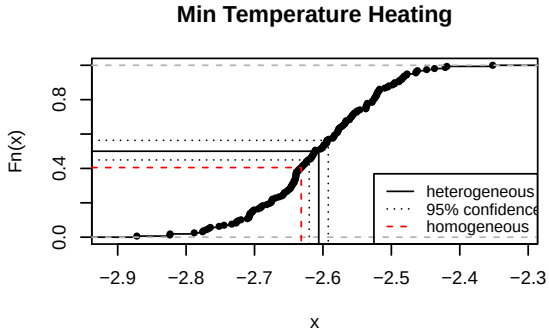

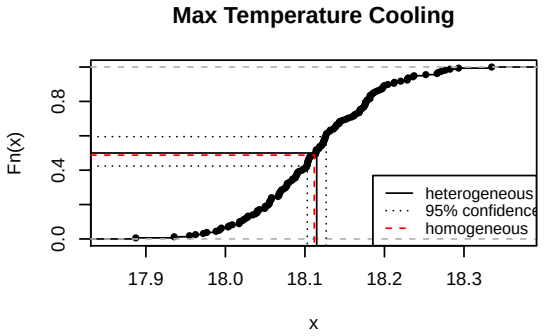

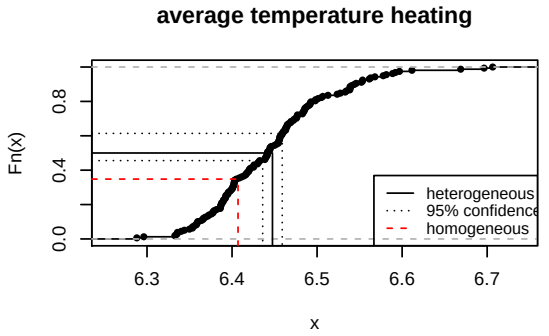

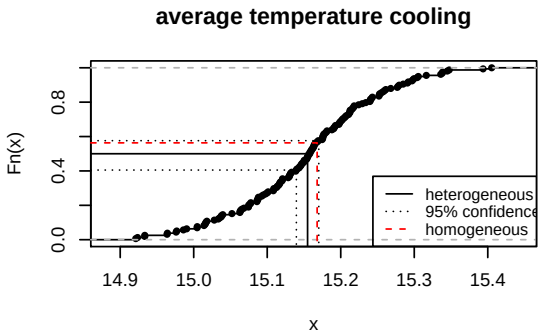

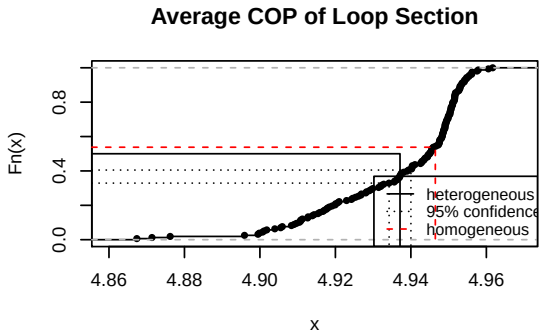

batch performance for the middle trench of the three trench system:

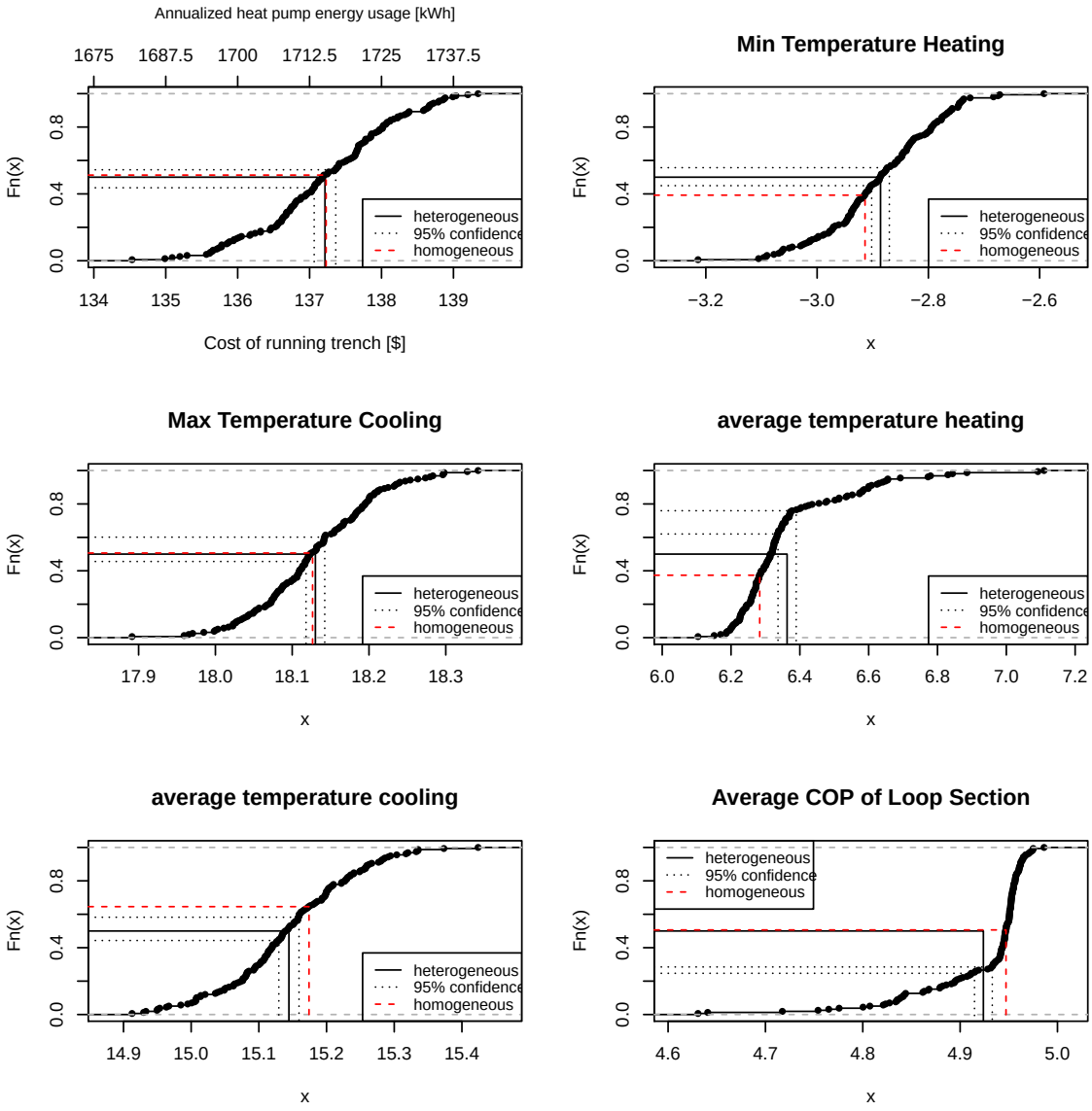

I.9.2 Triple trench days of exceedence

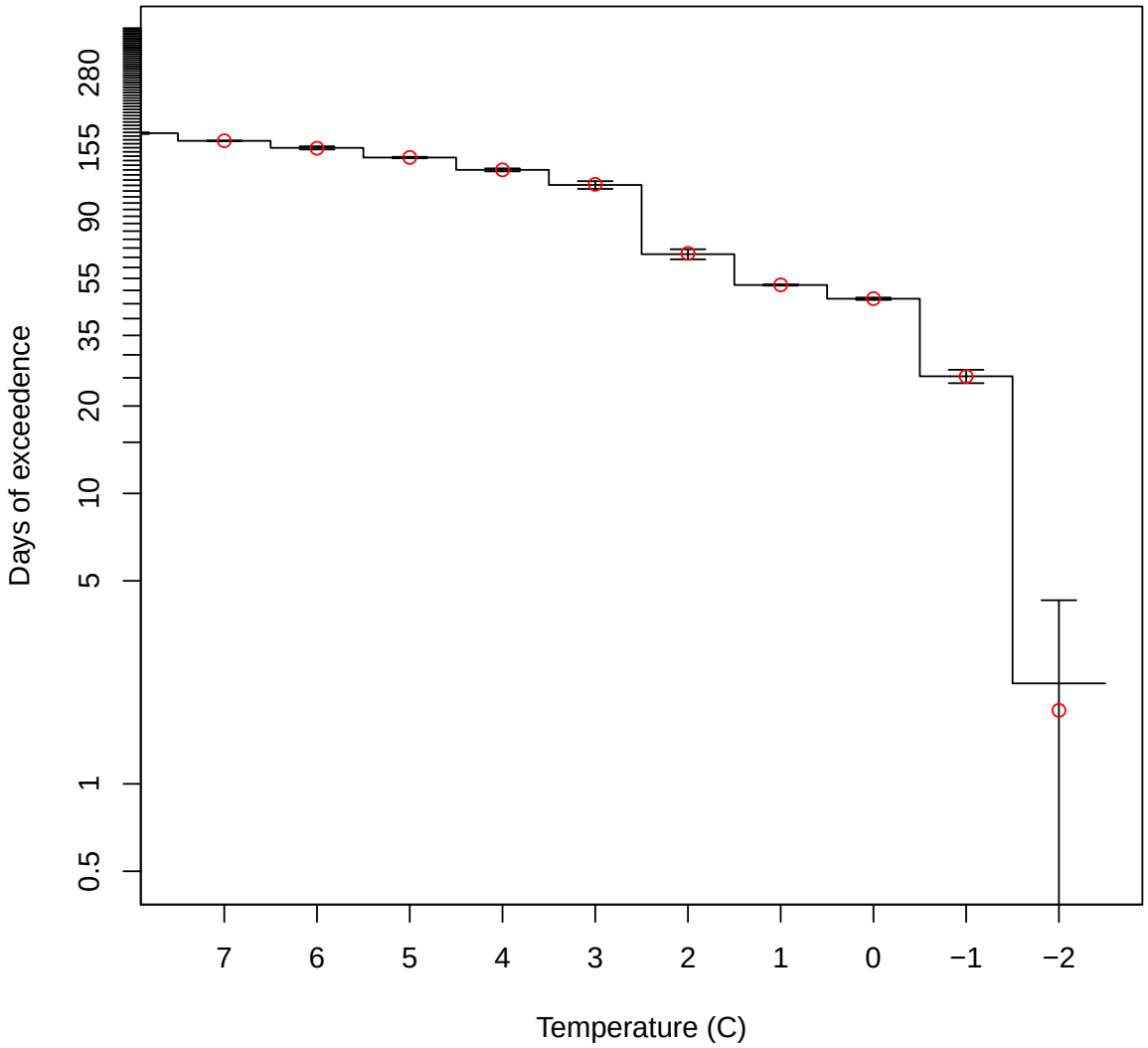

I.9.3 Triple trench temperature profile

The horizontal profile shows interesting variation with distance. Note that the grid is only well refined near the one trench. The second trench going away has a poorly defined grid and as such the gradients near it aren't captured by the limited number of monitoring points used to generate the chart

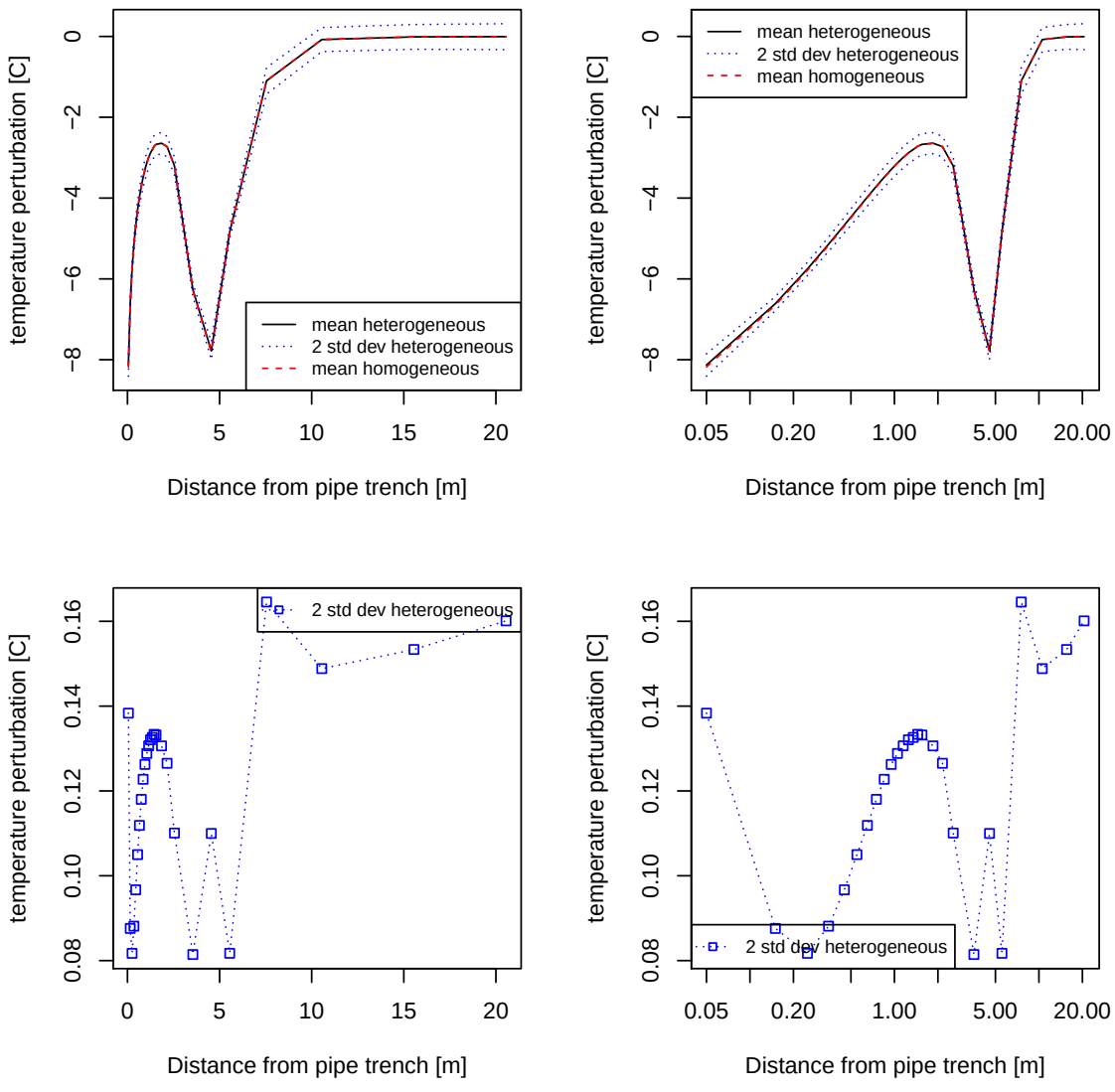

Appendix J

Thermal properties of natural soils

Material	Remarks	Thermal Conductivity $Jm^{-1}K^{-1}s^{-1}$	Volumetric Heat Capacity $Jm^{-3}K^{-1} \times 10^6$	Density $kgm^{-3} \times 10^3$	Specific Heat Capacity $Jkg^{-1}K^{-1} \times 10^3$	Thermal Diffusivity $m^2s^{-1} \times 10^{-6}$
Sandy soil (40% pore space)	Dry	0.30	1.28	1.60	0.80	0.24
	Saturated	2.20	2.96	2.00	1.48	0.74
Clay soil (40% pore space)	Dry	0.25	1.42	1.60	0.89	0.18
	Saturated	1.58	3.10	2.00	1.55	0.51
Peat soil (80% pore space)	Dry	0.06	0.58	0.30	1.92	0.10
	Saturated	0.50	4.02	1.10	3.65	0.12
Snow	Fresh	0.08	0.21	0.10	2.09	0.10
	Old	0.42	0.84	0.48	2.09	0.40
Ice	$0°C$, pure	2.24	1.93	0.92	2.10	1.16
Water	$4°C$, still	0.57	4.18	1.00	4.18	0.14
Air	$10°C$, still	0.025	0.0012	0.0012	1.01	20.50
	Turbulent	125	0.0012	0.0012	1.01	$\sim 10 \times 10^6$
Quartz	Crystal	8.4	1.92	2.65	0.72	4.38
Soil organic matter	Average	0.25	2.51	0.46	5.46	0.10

Table J.1: Thermal properties of natural materials reproduced from Oke (1987) and Farouki (1986) and Labs (1979b)

Study	Porosity	Thermal Conductivity	Volumetric Heat Capacity	Thermal Diffusivity
	%	$Jm^{-1}K^{-1}s^{-1}$	$Jm^{-3}K^{-1} \times 10^6$	$m^2s^{-1} \times 10^{-6}$
Collected by Taniguchi (1993)				
Taniguchi (1993)	30	1.59	2.73	0.583
Andrews and Anderson	48	1.76	3.01	0.58
Lapham	40	1.71	2.51	0.68
Lovering and Goode	...	1.0	1.75	0.57
Palmer et al. (1992)	35	2.1	2.84	0.75
Taniguchi (1985)	30	1.58	2.73	0.578
Collected by Palmer et al. (1992)				
Moench and Evans	...	2.49	2.76	0.903
Van Duin	40	2.0	2.82	0.71
Molz et al	25	2.29	1.81	1.27
Geiger	...	1.67	2.39	0.70

Table J.2: Thermal properties of aquifers from several studies

References

Al-Khoury, R., Bonnier, P. G., 2006. Efficient finite element formulation for geothermal heating systems. Int. J. Numer. Meth. Engng. 67 (5), 725–745. 7

Al-Khoury, R., Bonnier, P. G., Brinkgreve, R. B. J., 2005. Efficient finite element formulation for geothermal heating systems. part i: steady state. Int. J. Numer. Meth. Engng. 63 (7), 988–1013. 7, 9

Al-Khoury, R., Klbel, T., Schramedei, R., Oct. 2010. Efficient numerical modeling of borehole heat exchangers. Computers & Geosciences 36 (10), 1301–1315. 7

Al-Temeemi, A., Harris, D., Mar. 2004. A guideline for assessing the suitability of earth-sheltered mass-housing in hot-arid climates. Energy and Buildings 36 (3), 251–260. 53

Banks, D., 2009. Introduction to Thermogeology: Ground Source Heating and Cooling. Wiley-Blackwell, Hoboken, NJ, USA. 2

Belytschko, T., Gracie, R., Ventura, G., Jun. 2009. A review of extended/generalized finite element methods for material modeling. Modelling and Simulation In Materials Science and Engineering 17 (4), 043001. 148

Bertani, R., Jan. 2012. Geothermal power generation in the world 2005-2010 update report. Geothermics 41 (0), 1–29. 1

Bundschuh, J., Arriaga, M. C. S., 2010. Introduction to the numerical modeling of groundwater and geothermal systems: fundamentals of mass, energy, and solute transport in poroelastic rocks. Vol. 2 of Multiphysics modeling. CRC Press. 87

Chiasson, A., Rees, S., Spitler, J., 2000. A preliminary assessment of the effects of groundwater flow on closed-loop ground-source heat pump systems. ASHRAE Transactions 106, 380–393. 16

Claesson, J., Dunand, A., 1983. Heat extraction from the ground by horizontal pipes - A mathematical analysis. Department of Mathematical Physics, Lunds University, Sweden. 8

ClimateMaster, 2010. Tranquility 27 (TT) Series Specifications Manual. 105

Cocco Mariani, V., Coelho, L., 2009. Global optimization of thermal conductivity using stochastic algorithms. Inverse Problems in Science and Engineering 17 (4), 511–535. 47

Crank, J., Nicolson, P., 1947. A practical method for numerical evaluation of solutions of partial differential equations of the heat-conduction type 6 (1), 207–226–. 21

Dagan, G., 1994. The significance of heterogeneity of evolving scales to transport in porous formations. Water Resour. Res. 30 (12), 3327–3336. 93

de Vries, D. A., 1963. Thermal properties of soils. Physics of plant environment. North-Holland Publishing Company, Amsterdam. 93

Deutsch, C. V., Journel, A. G., 1992. GSLIB: Geostatistical Software Library and User's Guide, 1st Edition. Oxford University Press. 24, 91, 95, 187, 258

Diersch, m., Bauer, D., Heidemann, W., Rhaak, W., Schtzl, P., Aug. 2011a. Finite element modeling of borehole heat exchanger systems: Part 1. fundamentals. Computers & Geosciences 37 (8), 1122–1135. 7

Diersch, m., Bauer, D., Heidemann, W., Rhaak, W., Schtzl, P., Aug. 2011b. Finite element modeling of borehole heat exchanger systems: Part 2. numerical simulation. Computers & Geosciences 37 (8), 1136–1147. 7

Doherty, J., 1994. Pest: a unique computer program for model-independent parameter optimisation. Water Down Under 94: Groundwater/Surface Hydrology Common Interest Papers; Preprints of Papers, 551. 149

Esen, H., Inalli, M., Esen, M., Mar. 2007. Numerical and experimental analysis of a horizontal ground-coupled heat pump system. Building and Environment 42 (3), 1126–1134. 8, 87

Eskilson, P., 1987. Thermal analysis of heat extraction boreholes. Ph.D. thesis, University of Lund, Sweden. 87

Farouki, O. T., 1982. Evaluation of Methods for Calculating Soil Thermal Conductivity. U.S. Army Cold Regions Research and Engineering Laboratory Report 82-8, Hanover, NH. 60

Farouki, O. T., 1986. Thermal Properties of Soils. Vol. 11 of Series on Rock and Soil Mechanics. Trans Tech Publications, D-3392 Clausthal-Zellerfeld, Germany. 14, 89, 304

Ferguson, G., 2007. Heterogeneity and thermal modeling of ground water. Ground Water 45 (4), 485–490. 88, 89, 92, 117

Florides, G., Kalogirou, S., Dec. 2007. Ground heat exchangers – a review of systems, models and applications. Renewable Energy 32 (15), 2461–2478. 1, 3

Fujii, H., Nishi, K., Komaniwa, Y., Chou, N., 2012. Numerical modeling of slinky-coil horizontal ground heat exchangers. Geothermics 41 (0), 55 – 62. 1, 5, 9, 41, 148

Fujii, H., Okubo, H., Nishi, K., Itoi, R., Ohyama, K., Shibata, K., 2009. An improved thermal response test for u-tube ground heat exchanger based on optical fiber thermometers. Geothermics 38 (4), 399 – 406. 88, 92

Giardina, J., 1995. Evaluation of ground coupled heat pumps for the state of wisconsin. Master's thesis, University of Wisconsin-Madison. 87

Grasby, S., Majorowicz, J., Ko, M., 2009. Geothermal Maps of Canada Open File 6167. Geological Survey of Canada, Geological Survey of Canada 601 Booth Street Ottawa, Ontario K1A 0E8. xii, 19

Hart, P., Couvillion, R., 1986. Earth-Coupled Heat Transfer. National Water Well Association, Dublin, OH. 54, 59

Haslam, S., 2013. Improved tools and methods for ground heat exchanger design. Master's thesis, University of Waterloo. 5, 22, 26, 30, 35, 36, 46, 48, 51, 57, 62, 67, 68, 71, 76, 77, 80, 82, 84, 85, 86, 99, 105, 109, 110, 143, 149

Hendron, R., Engebrecht, C., September 2010. Building America House Simulation Protocols. National Renewable Energy Laboratory. 2

Hill, M. C., 2006. The practical use of simplicity in developing ground water models. Ground Water 44 (6), 775–781.
URL http://dx.doi.org/10.1111/j.1745-6584.2006.00227.x 75

Ingersoll, L., Plass, H., 1948. Theory of the ground pipe heat source for the heat pump. ASHVE Transactions 54, 339. 8, 87

Istok, J., 1989. Groundwater Modeling by the Finite Element Method. Water Resources Monograph 13. American Geophysical Union, Washington, DC. 20, 21, 153, 154, 155, 159, 167

Jarny, Y., Ozisik, M., Bardon, J., 1991. A general optimization method using adjoint equation for solving multidimensional inverse heat conduction. International Journal of Heat and Mass Transfer 34 (11), 2911 – 2919. 47

Johansen, O., 1975. Thermal conductivity of soils. Master's thesis, Trondheim, Institute for Kjoleteknikk. 24, 88

Kitanidis, P., May 1997. Introduction to Geostatistics. Cambridge University Press, Cambridge, UK. 90

Kopp, G., Lean, J. L., Jan. 2011. A new, lower value of total solar irradiance: Evidence and climate significance. Geophys. Res. Lett. 38 (1), L01706–. 18

Kovalenko, Y., Flanders, S., May 1991. Thermal conductivity of porous media and soils: a review of soviet investigations. U.S. Army Cold Regions Research and Engineering Laboratory Special report, 9–12, in English. Refs. p.9-12. Originator No: ADA-238 780. GeoRef Acc. No: 182958. 14

Labs, K., 1979a. The underground advantage: climate of soils. In: Proceedings of the Fourth National Passive Solar Conference. American Section of ISES, Kansas City, MO. 59

Labs, K., 1979b. Underground building climate. Solar Age 4 (10), 44–50. 14, 52, 304

LeBlanc, D. R., Garabedian, S. P., Hess, K. M., Gelhar, L. W., Quadri, R. D., Stollenwerk, K. G., Wood, W. W., 1991. Large-scale natural gradient tracer test in sand and gravel, Cape Cod, Massachusetts: 1. experimental design and observed tracer movement. Water Resour. Res. 27 (5), 895–910. 93

Lund, J. W., Freeston, D. H., Boyd, T. L., Sep. 2011. Direct utilization of geothermal energy 2010 worldwide review. Geothermics 40 (3), 159–180. 1

Matott, L. S., 2010. Ostrich: an Optimization Software Tool, Documentation and User's Guide, Version 1.8. University of Waterloo, Department of Civil and Environmental Engineering, Waterloo, Ontario. 103

Mei, V. C., 1986. Horizontal ground-coil heat exchanger theoretical and experimental analysis. Report No. ORNL/CON-193, Dec, Oak Ridge National Laboratory, Oak Ridge, Tenn., 1. 87

Mohanty, B. P., Kanwar, R. S., Horton, R., 1991. A robust-resistant approach to interpret spatial behavior of saturated hydraulic conductivity of a glacial till soil under no-tillage system. Water Resour. Res. 27 (11), 2979–2992. 93

Morgan, M., Henrion, M., 1992. Uncertainty: A Guide to Dealing with Uncertainty in Quantitative Risk and Policy Analysis. Cambridge University Press. 106, 107

Nam, Y., Ooka, R., Hwang, S., 2008. Development of a numerical model to predict heat exchange rates for a ground-source heat pump system. Energy and Buildings 40 (12), 2133–2140. 21, 22

Nicolsky, D. J., Romanovsky, V. E., Tipenko, G. S., 2007. Using in-situ temperature measurements to estimate saturated soil thermal properties by solving a sequence of optimization problems. Cryosphere 1 (1), 41–58. 47, 48

Oke, T. R., 1987. Boundary Layer Climates, 2nd Edition. Methuen, London and New York. 14, 54, 304

Palmer, C. D., Blowes, D. W., Frind, E. O., Molson, J. W., 1992. Thermal energy storage in an unconfined aquifer: 1. field injection experiment. Water Resour. Res. 28 (10), 2845–2856. 305

Penner, E., 1963. Anisotropic thermal conduction in clay sediments. In: International Clay Confernece. 13

Philippe, M., Bernier, M., Marchio, D., Lopez, S., 2011. A semi-analytical model for serpentine horizontal ground heat exchangers. HVAC&R Research 17 (6), 1044–1058. 5, 8

Piechowski, M., 1999. Heat and mass transfer model of a ground heat exchanger: theoretical development. Int. J. Energy Res. 23 (7), 571–588. 4

Rawlings, J., 1996. Subterranean heat exchange units comprising multiple secondary conduits and multi-tiered inlet and outlet manifolds. 3

Raymond, J., Therrien, R., Gosselin, L., Lefebvre, R., 2011a. A review of thermal response test analysis using pumping test concepts. Ground Water, 1–14. 83, 84, 89

Raymond, J.and Frenette, M., Leger, A., Magni, E., Therrien, R., 2011b. Numerical modeling of thermally enhanced pipe performances in vertical ground heat exchangers. ASHRAE Transactions 117, 899+–. 42, 44, 45

Rehfeldt, K. R., Boggs, J. M., Gelhar, L. W., 1992. Field study of dispersion in a heterogeneous aquifer: 3. geostatistical analysis of hydraulic conductivity. Water Resour. Res. 28 (12), 3309–3324. 93

Saad, Y., 2000. Iterative Methods for Sparse Linear Systems, 2nd Edition. Self Published. 10, 29

Sanderson, C., September 2010. Armadillo: An open source C++ linear algebra library for fast prototyping and computationally intensive experiments. Technical report, NICTA, St Lucia, Australia. 30

Schroeder, W., Martin, K., Loerensen, W., 2003. The Visualization Toolkit. Kitware Inc., 3rd Edition. 24

Schwartz, F. W., Zhang, H., 2002. Fundamentals of Ground Water. John Wiley & Sons, Ltd., Chapter 3. 93

Sharqawy, M., V, J. H. L., Zubair, S., 2010. Thermophysical properties of seawater: A review of existing correlations and data. Desalination and Water Treatment 16 (1-3), 354–380. 14

Shen, P. Y., Pollack, H. N., Huang, S., Wang, K., 1995. Effects of subsurface heterogeneity on the inference of climate change from borehole temperature data: Model studies and field examples from Canada. J. Geophys. Res. 100 (B4), 6383–6396. 88

Signorelli, S., Bassetti, S., Pahud, D., Kohl, T., 2007. Numerical evaluation of thermal response tests. Geothermics 36 (2), 141 – 166. 88

Sittel, C. N., Threadgill, W. D., Schnelle, K. B., 1968. Longitudinal dispersion for turbulent flow in pipes. Industrial & Engineering Chemistry Fundamentals 7 (1), 39–&. 25, 27

Spitler, J. D., 2005. Ground-source heat pump system research - past, present, and future (editorial). International Journal of HVAC&R Research 11 (2), 165–167. 4, 8

Sudicky, E. A., 1986. A natural gradient experiment on solute transport in a sand aquifer: Spatial variability of hydraulic conductivity and its role in the dispersion process. Water Resour. Res. 22 (13), 2069–2082. 93

Sugawara, A., Yoshizawa, Y., 1961. An investigation on thermal conductivity of porous materials and its application to porous rock. Australian Journal of Physics 14 (4), 468–&. 14

Taniguchi, M., 1985. Effects of snow cover and infiltrated meltwater on soil and groundwater temperature in and around Nagoaka City. Geographical Review Japan 58 (6), 370–384. 22, 305

Taniguchi, M., 1993. Evaluation of vertical groundwater fluxes and thermal properties of aquifers based on transient temperature-depth profiles. Water Resour. Res. 29 (7), 2021–2026. 305

Theis, C. V., 1935. The relation between the lowering the piezometric surface and rate and duration of discharge of a well using groundwater storage. Trans. Am. Geophys. Union 2, 519–524. 25, 181, 182

Therrien, R., McLaren, R. G., Sudicky, E. A., Panday, S. M., 2005. HydroGeoSphere: a three dimensional numerical model describing fully-integrated subsurface and surface flow and solute transport. Groundwater Simulations Group, University of Waterloo, Waterloo, Ontario, Canada. 7

Tolson, B. A., Shoemaker, C. A., Jan. 2007. Dynamically dimensioned search algorithm for computationally efficient watershed model calibration. Water Rsr. Res. 43 (1), W01413. 49

TRNSYS, 2010. TRNSYS 17 manual. The TRNSYS Group. 8

Usowicz, B., Kossowski, J., Baranowski, P., 1996. Spatial variability of soil thermal properties in cultivated fields. Soil and Tillage Research 39 (1-2), 85 – 100. 92, 93, 94

van der Vorst, H. A., 1992. Bi-CGSTAB: A fast and smoothly converging variant of Bi-CG for the solution of nonsymmetric linear systems. SIAM Journal on Scientific and Statistical Computing 13 (2), 631–644. 10, 29

Woodbury, A. D., Sudicky, E. A., 1991. The geostatistical characteristics of the Borden aquifer. Water Resour. Res. 27 (4), 533–546. 93, 94